Measuring and Understanding Grain Boundary Properties of Engineering Ceramics

Andrew Norton

St Edmund Hall



Supervisor:

Professor Richard Todd

Department of Materials

University of Oxford

Trinity Term 2013

Measuring and Understanding Grain Boundary Properties in Engineering Ceramics

A thesis submitted for the degree of Doctor of Philosophy at the University of Oxford

Andrew Norton, St Edmund Hall Oxford

Trinity Term 2013

This thesis aims to measure the mechanical properties of ceramics on the microscale using microcantilever beams. Focussed Ion Beam milled triangular cross-sectional beams (approximately 3 x 5 x 20μm) were fractured using a nanoindenter to measure the Young's modulus, fracture strength, and fracture toughness. By developing the technique with a sapphire bicrystal, it was found that the mechanical properties could be successfully ascertained if correction factors were used. Experiments and theoretical work showed that sapphire and polycrystalline alumina beams undergo moisture assisted sub-critical crack growth when tested in air. Whilst corrections for the Young's modulus have been previously reported, this is the first reported attempt to correct for the notch tip residual stress and the first to consider sub-critical crack growth.

Once these factors were characterised using the sapphire bicrystal, the technique was applied to a range of different ceramics, such as polycrystalline α-alumina and silicon nitride. These are the first reported direct measurements the grain boundary toughness of these ceramics using microcantilever beams.

The grain boundary toughness was correlated with the macroscopic fracture properties and the characteristics of the ceramic (grain boundary composition, impurities, and fracture mode). Two grades of α-alumina were used and the macro- and micro-scale properties extensively compared. The damage evolution during uniaxial compression of alumina was investigated in depth, and compared to a previous reported microcrack evolution model using the measured grain boundary toughness. Investigation of whether deformation twins formed during loading was undertaken and the phenomenon was shown to not occur.

Acknowledgements

I owe much of this project to the guidance and supervision of Professor Richard Todd. His unerring enthusiasm and thoughtful insight have made this work possible. Thank you for all that you have done during my time in Oxford.

Thanks must also go to the RIT group, past and present, for their help and support: to Dr Claire Dancer and Prof Amartya Mukhopadhyay for showing me the ropes early on, and to Dr Geoffrey Otieno and Noor Yahya for teaching me how to successfully produce the microcantilever beams. Thank you also to Simone Falco (Department of Engineering) for performing the Finite Element simulations, without which so much of the analysis could not have been performed.

I am also indebted to the work of other members of the Department of Materials. Dr Gareth Hughes and Dr David Armstrong have been very supportive in all things FIB and nanoindenter related. Dr Gabriella Chapman undertook so much of my electron microscopy training, for which I am very thankful. The EELS work could not have happened without Ron Doole, Prof Peter Nellist, and Dr Adam Papworth, and I am very thankful for their continued enthusiasm in hunting for those elusive edges! I am very grateful to Jack Severs and Dr Neil Young for performing the high-resolution TEM and nanodiffraction. An enormous thank you has to go to Steve Lett, who has been instrumental in the TEM sample preparation and was always willing to offer advice and guidance on any number of practical endeavours. Thanks to everyone in Materials, St Edmund Hall, and in Oxford in general who have been so supportive during my DPhil time.

Many thanks to my parents and sisters, who infallible support has allowed this work to happen.

Finally, a huge, huge thank you has to go to my wife Karen and my daughter Lily. Whilst the latter has provided giggles and fun to keep me sane, the former has been unfathomably

supportive and kind, even during those days of seemingly endless writing and all of those FIB nights. Truly, this would not have happened without you. And for that, and so much else, I am eternally thankful.

Preface

This thesis is an account of the work carried out by the author in the Department of Materials, University of Oxford (2009 – 2013) under the supervision of Professor Richard I. Todd.

No part of this work has been previously submitted for a degree at this or any other university. The work of others has been freely drawn upon and is duly acknowledged and referenced in the relevant points in the text. A full list of references is given at the end of the thesis.

Parts of the work described in the thesis have been presented at the following conferences

A. D. Norton, R. I. Todd, *Microcracking in Alumina due to Uniaxial Compression.*

Poster presentation at SCERN Meeting, University of Surrey, 25th April 2012.

A. D. Norton, R. I. Todd, *Grain Boundary Toughness in Alumina: Measuring and Understanding.*

Poster presentation at the Gordon Research Conference on "Solid State Studies in Ceramics: New Insights and New Paradigms in Fracture and Deformation", Mt. Holyoke College, South Hadley, Massachusetts, August 2012

A. D. Norton, R. I. Todd, *Measuring and understanding the fracture toughness in ceramics at the microstructural scale using microcantilever beams.*

Oral presentation at 37th International Conference & Exposition of Advanced Ceramics & Composites (ICACC), Daytona Beach, Florida, January – February 2013.

A. D. Norton, R. I. Todd, *Measuring fracture toughness in ceramics using microcantilever beams.*

Oral presentation at 13th ECERS International Conference, Limoges, France, June 2013

Contents

1.			**Introduction**	**19 – 22**
2.			**Literature Review**	**23 – 61**
2.1.			Aluminium Oxide	23 – 26
	2.1.1.		Twinning in Aluminium Oxide	24
	2.1.2.		Stress required to form deformation twins	25
	2.1.3.		Twins and doping	25 – 26
2.2.			Silicon nitride	26 – 27
2.3.			Complexions	27 – 32
2.4.			Mechanical Testing	32 – 36
	2.4.1.		Uniaxial Compression – Introduction to microscopic damage	32
	2.4.2.		Uniaxial Compression – Nucleation of a crack	32 – 36
2.5.			Acoustic Emission	36 – 37
2.6.			Microcantilever Beams	37 – 56
	2.6.1.		Focussed Ion Beam production method	38 – 40
	2.6.2.		Elastic modulus	40 – 42
	2.6.3.		Fracture strength	42 – 43
	2.6.4.		Fracture toughness	43 – 47
	2.6.5.		Notch bluntness	47 – 49
	2.6.6.		Gallium Implantation and other FIB effects	50 – 54
	2.6.7.		Subcritical crack growth	54 – 56
2.7.			Optical Fluorescence Microscopy	56 – 58
2.8.			Summary of objectives	58 – 61
3.			**Materials & Methods**	**62 – 84**
3.1.			Materials	62 – 64
	3.1.1.		AES-11C alumina (with and without chromia dopants)	62
	3.1.2.		TM-DAR alumina	63 – 64
		3.1.2.1.	TM-DAR with and without carbon	63 – 64
		3.1.2.2.	TM-DAR with and without chromia doping	64
	3.1.3.		Silicon Nitride	64
	3.1.4.		Single Crystal Sapphire	64
	3.1.5.		Diffusion Bonded Sapphire	64
3.2.			Transmission Electron Microscopy Sample Preparation	65 – 66

	3.2.1.		Dimple Grinding	65
	3.2.2.		Focussed Ion Beam (FIB)	65 – 66
3.3.			Characterisation of Materials	67 – 71
	3.3.1.		Mean grain size analysis	67
	3.3.2.		Density	67 – 68
	3.3.3.		X-ray diffraction	68 – 70
		3.3.3.1.	Lattice parameter determination	68 – 69
		3.3.3.2.	Pole figure determination	69 – 70
	3.3.4.		Energy Dispersive X-ray Spectroscopy (EDX)	70
	3.3.5.		Electron Energy Loss Spectroscopy (EELS)	70
	3.3.6.		Optical Fluorescence Microscopy (OFM)	70 – 71
	3.3.7.		Electron Back-scatted Diffraction (EBSD)	71
3.4.			Macroscopic Mechanical Testing - Sample Preparation	72 – 73
	3.4.1.		Uniaxial Compression	72
	3.4.2.		Tungsten Carbide Platens	72
	3.4.3.		Four-point bending beams – Fracture Strength	73
	3.4.4.		Four-point bending beams – Fracture Toughness	73
3.5.			Macroscopic Mechanical Testing	74 – 75
	3.5.1.		Uniaxial Compression	74
	3.5.2.		Four-point bending – Flexural Strength & Toughness	74 – 75
	3.5.3.		Four-point bending – Weibull analysis	75
3.6.			Microcantilever Beam production	76 – 78
	3.6.1.		FIB milled notches	78
3.7.			Nanoindenter Method	78 – 83
	3.7.1.		Fracturing Microcantilever Beams	78 – 79
		3.7.1.1.	Fracturing beams submerged in water or silicone oil	80
		3.7.1.2.	Determining the mechanical properties of the microcantilever beams	81 – 83
		3.7.1.3.	Determining the fracture toughness of the microcantilever beams	83
	3.7.2.		Nanoindentation	83
3.8.			Relative Humidity during microcantilever beam testing	84
4.			**Characterisation of Materials**	**85 – 136**
4.1.			Grain size analysis	86 – 90
	4.1.1.		Pressurelessly sintered AES-11C at 1600^{o}C & 1750^{o}C	86
	4.1.2.		AES-11C with chromia doping pressurelessly sintered at 1600^{o}C	86 – 87

	4.1.3.	AES-11C with chromia doping pressurelessly sintered at 1750^{o}C	88
	4.1.4.	Pressurelessly Sintered TM-DAR at 1600^{o}C and 1750^{o}C	88 – 89
	4.1.5.	Pressurelessly Sintered TM-DAR at 1500^{o}C in vacuum	89
	4.1.6.	Pressurelessly Sintered TM-DAR with 0.012wt% carbon at 1500^{o}C in vacuum	89
	4.1.7.	Pressurelessly Sintered TM-DAR with varying amounts of chromia	90
4.2.		X-Ray Diffraction and Density of materials	90 – 93
	4.2.1.	Pressurelessly sintered AES-11C	91
	4.2.2.	Pressurelessly Sintered AES-11C with varying amounts of chromia	91 – 92
	4.2.3.	Pressurelessly Sintered TM-DAR – sintered in air	92 – 93
	4.2.4.	Pressurelessly Sintered TM-DAR – sintered in vacuum	93
	4.2.5.	Pressurelessly Sintered TM-DAR with varying amounts of chromia dopant	93
	4.2.6.	Pressurelessly Sintered TM-DAR with 0.012wt% Carbon	93
4.3.		Transmission Electron Microscopy of the alumina samples	93 – 102
	4.3.1.	Undoped, Unstressed, Pressurelessly Sintered AES-11C	94 – 95
	4.3.2.	Undoped, pressurelessly sintered TM-DAR	95 – 96
	4.3.3.	Chromia doped, Unstressed, Pressurelessly Sintered AES-11C	96 – 98
	4.3.4.	Energy Dispersive X-ray Spectroscopy of twins	98 – 99
	4.3.5.	Diffraction Analysis of the twinned grains	99 – 102
4.4.		Optical Fluorescence Microscopy (OFM)	102 – 106
	4.4.1.	Variation in peak position and width on a single point	103
	4.4.2.	Variation in peak position and width across sapphire	103
	4.4.3.	Variation in peak position and width across polycrystalline AES-11C	103 – 104
	4.4.4.	Variation in peak position and width with chromia doping	104 – 106
4.5.		Diffusion Bonded Sapphire	106 – 109
	4.5.1.	Transmission Electron Microscopy	106 – 108
	4.5.2.	Electron Backscattered Diffraction (EBSD)	108
	4.5.3.	Energy Dispersive X-ray Spectroscopy (EDX)	109
4.6.		Analysis of the material change due to the focussed ion beam	109 – 116
	4.6.1.	Redeposited Material due to Focussed Ion Beam	110 – 113
	4.6.1.1.	Transmission Electron Microscopy & Electron Diffraction	110 – 111

		4.6.1.2.	Energy Dispersive X-ray Spectroscopy (EDX)	111 – 113
	4.6.2.		Implanted Material due to Focussed Ion Beam	113 – 116
		4.6.2.1.	Transmission Electron Microscopy & Electron Diffraction	114 – 115
		4.6.2.2.	Energy Dispersive X-ray Spectroscopy (EDX)	116
4.7.			Electron energy-loss spectroscopy (EELS) of doped TM-DAR samples	117 – 123
	4.7.1.		Comparison with standard materials	117
	4.7.2.		EELS of Undoped TM-DAR	117 – 119
	4.7.3.		0.012wt% doped TM-DAR	120 – 123
4.8.			Energy Dispersive X-ray Spectroscopy (EDX) of alumina grain boundaries	123 – 127
	4.8.1.		Undoped AES-11C sintered to 1600^{o}C	124 – 125
	4.8.2.		Undoped AES-11C sintered to 1750^{o}C	126
	4.8.3.		Undoped TM-DAR sintered to 1600^{o}C	126
	4.8.4.		2wt% chromia doped AES-11C sintered to 1600^{o}C	126 – 127
4.9.			Annealing in vacuum	127 – 130
4.10			Nanoindentation	130 – 134
	4.10.1		Nanoindentation of AES-11C alumina	130
	4.10.2		Nanoindentation of FIB altered sapphire	131 – 134
		4.10.2.1	Nanoindentation of gallium implanted sapphire	131 – 133
		4.10.2.2	Nanoindentation of redeposited material	133 – 134
4.11			Summary of properties	135 – 136
	4.11.1		Summary of properties – polycrystalline alumina	135
	4.11.2		Summary of properties – FIB altered materials	136
5.			**Macroscopic Mechanical Property Measurements**	**137 – 160**
5.1.			Acoustic emission – initial tests	137 – 139
5.2.			Macroscopic four-point bending tests	139 – 143
	5.2.1.		Undoped AES11-C sintered at 1600^{o}C – fracture strength	139 – 140
	5.2.2.		5wt% chromia doped AES11-C sintered at 1600^{o}C – fracture strength	141
	5.2.3.		Fracture strength - Combined Data	141 – 143
5.3.			Macroscopic fracture toughness tests	143
5.4.			Uniaxial Compression of Alumina	144 – 160
	5.4.1.		Failure Strength of samples	144 – 146
		5.4.1.1.	Combined data – compressive strength	146
	5.4.2.		Damage evolution analysis during compression	146 – 148

		5.4.1.2.	Optical Microscopy	147 – 149
		5.4.2.2.	Optical Fluorescence Microscopy	150
	5.4.3.		Microcracking in polycrystalline alumina	150 – 152
		5.4.3.1.	Frequency and types of flaws in untested AES-11C alumina	152
	5.4.4.		Transmission Electron Microscopy of Compressed Samples – Undoped AES-11C	153 – 157
	5.4.5.		Transmission Electron Microscopy of Compressed Samples – Chromia doped AES-11C	157 – 158
	5.4.6.		Compression testing – Summary	158 – 160
5.5.			Macroscopic data – summary	160
6.			**Stress Intensity Factor Equations for Microcantilever Beams**	**161 – 177**
6.1.			Straight Through Notches	161 – 175
6.2.			Controlled Flaws	175 – 177
7.			**Understanding the Microcantilever Beam Testing**	**178 – 196**
7.1.			Diffusion Bonded Sapphire	178 – 185
	7.1.1.		Un-notched beams across the boundary	179 – 180
	7.1.2.		Notched away from the boundary	180 – 181
	7.1.3.		Straight through notch at the boundary	181 – 182
	7.1.4.		Chevron notch at the boundary	182 – 183
	7.1.5.		Controlled flaw at the boundary	184 – 185
7.2.			Residual stress due to gallium implantation	185 – 189
	7.2.1.		Optical Fluorescence Microscopy (OFM)	185 – 188
	7.2.2.		Nanodiffraction	188 – 189
7.3.			Notch bluntness	189 – 196
	7.3.1.		Varying notch radii – beams in a-plane sapphire parallel to $< 1\bar{1}00 >$	190 – 192
	7.3.2.		Varying notch radii – beams in a-plane sapphire parallel to $[0001]$	192 – 193
	7.3.3.		Effect on mechanical properties	194 – 196
7.4.			Moisture assisted sub-critical crack growth	197 – 200
	7.4.1.		Modelling the crack growth under dynamic loading in Region I	197
	7.4.2.		Using experimental data	197 – 198
	7.4.3.		Microcantilever Beams submerged in liquids	198 – 200
		7.4.3.1.	Fracturing on m-plane in water	198 – 200

		7.4.3.2.	Fracturing on m-plane in oil	200
7.5.			Sapphire beams annealed in vacuum	201 – 206
7.6.			Microcantilever beam testing – Summary	206 – 207
8.			**Mechanical properties of Microcantilever Beams in various ceramics**	**208 – 233**
8.1,			Single crystal sapphire	208 – 213
	8.1.1.		Single crystal sapphire – Fracturing on the a-plane	208 – 210
	8.1.2.		Single crystal sapphire – Fracturing on the m-plane	210 – 211
	8.1.3.		Single crystal sapphire – Fracturing parallel to the c-plane	211 – 212
	8.1.4.		Single crystal sapphire – Fracturing away from known planes	212 – 213
8.2.			Microcantilever beams in undoped polycrystalline AES-11C alumina	213 – 220
	8.2.1.		Strength	213 – 215
	8.2.2.		Toughness of grains	215
	8.2.3.		Toughness of grain boundaries using straight through notches	215 – 216
	8.2.4.		Toughness of grain boundaries using controlled flaws	216 – 218
	8.2.5.		Consideration of misorientations	218 – 220
	8.2.6.		AES-11C alumina – combined data	220
8.3.			Microcantilever Beams in 2wt% chromia doped AES-11C beams	220 – 221
	8.3.1.		Toughness of grains	220 – 221
	8.3.2.		Toughness of grain boundaries	221
8.4.			Microcantilever beams in vacuum sintered TM-DAR	222 – 225
	8.4.1.		Undoped TM-DAR	211 – 213
		8.4.1.1.	Strength	222
		8.4.1.2.	Toughness of grain boundaries	223 – 224
	8.4.2.		0.012wt% carbon doped TM-DAR – Grain Boundary Toughness	224 – 225
8.5.			Rare-earth doped silicon nitride	225 – 232
	8.5.1.		Strength and Young's modulus	225 – 228
	8.5.2.		Toughness of grain boundaries	228 – 232
8.6.			Summary of properties	232 – 233
9.			**Discussion**	**234 – 287**
9.1.			Microcantilever beam testing & its validity	235 – 261
	9.1.1.		Redeposited Material	235 – 239

	9.1.2.		Gallium Implanted region	239 – 243
	9.1.3.		Microcantilever beams - Young's modulus	244 – 245
	9.1.4.		Microcantilever beams – strength	245 – 248
	9.1.5.		Microcantilever beams – notch types	248 – 251
	9.1.6.		Microcantilever beams – stress intensity factors at failure	251 – 260
		9.1.6.1.	Subcritical crack growth	251 – 253
		9.1.6.2.	Residual stress & Notch bluntness	253 – 256
		9.1.6.3.	Effect of annealing	256 – 260
	9.1.7.		Microcantilever beams –Summary	260 – 261
9.2.			Sapphire	262 – 263
9.3.			AES-11C and TM-DAR	263 – 278
	9.3.1.		Grain boundary composition and microstructure	265 – 269
	9.3.2.		Mechanical Properties	269 – 273
	9.3.3.		AES-11C – Damage Evolution	273 – 278
9.4.			TM-DAR with and without carbon	278 – 281
9.5.			Chromium oxide doping	281 – 284
9.6.			Silicon Nitride	284 – 287
10.			**Conclusions and Further Work**	**288 – 292**

Appendices

A3.1	Mechanical Properties of microcantilever beams	293 – 295
A3.2	Correlation of correction factor for Young's modulus with aspect ratio of microcantilever beams	296 – 297
A4.1	Calibration of JEOL 2000FX TEM	298 – 299
A4.2	Standard EELS spectra	300 – 303
A4.3	Atomic Force Microscopy of c-plane sapphire	304
A6.1	Geometric function M for semi-elliptical surface flaws	305 – 306
A7.1	Determining the stress intensity factors for blunt notches with residual stress at the tip due to gallium implantation	307 – 309
A7.2	Deriving the crack extension with dynamic loading due to moisture assisted sub-critical crack growth in Region I	310 – 312
A7.3.	Relating change in compliance with crack growth	313

References

For Karen and Lily

Glossary of Symbols

α	Notch depth in microcantilever beam top surface
α'	Ratio of notch depth to height of beam
γ	Free surface energy per unit area
$\Delta\nu$	Photoluminescence frequency shift in alumina
η	Ratio between the long and short crack stress intensity factors used in compliance calibration analysis
θ_{m0}	Slope at fixed of microcantilever beam due to bending moment
θ	Angle between incident ray and scattering planes in x-ray diffraction
λ	σ_3/σ_1 in uniaxial compression, X-ray wavelength in diffraction work
μ	Coefficient of friction
ν	Poisson's ratio
Π_{ij}	Piezospectroscopic coefficient of alumina matrix
ρ	Focussed ion beam notch radius
ρ_{sample}	Density of alumina disk from Archimedes' method
$\rho_{AES\text{-}11C,\ TM\text{-}DAR}$	True density of AES-11C and TM-DAR alumina, measured from XRD
σ	Tensile stress on top surface of microcantilever beam
σ_{ga}	Stress in gallium implanted region
$\sigma_{1,3}$	Applied compressive stresses in uniaxial compression
σ_{xx}, σ_{xy}	Normal and shear stresses in uniaxial compression
$\sigma_{\theta\theta}$	Tensile stresses in front of crack tip in uniaxial compression
σ'_{xy}	Effective shear stress on the crack plane
σ_I	Stress at wing crack initiation during uniaxial compression
β_n	Dimensionless constant related to Poisson's ratio used in uniaxial compression equations
σ_f	Failure strength
σ_y	Yield stress
σ_{res}	Residual stress in front of FIB notch

$\dot{\sigma}$	Stress rate
Φ	Angle between inclined flaw and direction of microcrack
φ	Angle between inclined flaw and principal stress during uniaxial compression
ψ	Geometric factor (1.12 for edge crack)
χ	Angle between edge of elliptical flaw and top surface
a	Flaw size, lattice parameter of alumina
$a_{0,1,2,3,4}$	Polynomial fitting factors relating C' and α' from compliance calibration
A	½ ($S_0 - S_i$)
b	Half-width of elliptical flaw
b_{foil}	Breadth of TEM foil
$b_{1,2,3,4}$	Polynomial fitting factors relating η and α'
B	Breadth of beam in four-point bending
B_s	Beam spreading in TEM
B_d	Beam diameter in TEM
C	Compliance
C'	Reduced compliance (= CEh)
c	Lattice parameter of alumina
c_m	Atomic percent of Cr_2O_3 in Al_2O_3
$C(x, t)$	Concentration of atoms during diffusion
d	Spacing of diffracting planes
$d\alpha$	Characteristic notch tip crack length
d_{foil}	Thickness of TEM foil
D_0	Initial level of damage before uniaxial compression
D	Displacement of microcantilever beam at indenter position
D_{ga}	Diffusivity of gallium into sapphire
D_{true}	Displacement of microcantilever beam at indenter position negating indentation of tip onto top surface
d_m	Mean grain size
E	Young's modulus

F	Indenter load during microcantilever beam testing
$F\left(\frac{\alpha}{h}\right)$	Dimensionless factor relating stress intensity factor and load in microcantilever beam testing
G	Mechanical energy release rate
h	Height of microcantilever beam
h_{foil}	Height of foil in OFM
h^*	$^2/_3 h$
h, k, l	Miller indices
H	Height of beam in four-point bending
I	Second moment of area
K	Stress intensity factor
K_I	Mode I stress intensity factor
K_{I0}	Stress intensity factor at start of Region I
K_{Ic}	Critical stress intensity factor
$K_{Ic,\,gb}$	Critical stress intensity factor of grain boundaries, measured using microcantilever beams
K_{max}	Maximum stress intensity factor on inclined flaw during uniaxial compression
l	Wing crack length
L	Wing crack length, l, divided by the flaw size, a
L_{el}	Indenter tip to fixed end distance in microcantilever beam testing
L_{fr}	Indenter tip to broken point distance in microcantilever beam testing
L_{cam}	Camera length in transmission electron microscope
M	Sum of various factors relating stress intensity factor and load for elliptical flaws on surface of microcantilever beams
m_{dry}	Dry mass of alumina disk
m_{damp}	Mass of alumina disk after boiling, with surface water removed
$m_{submerged}$	Mass of alumina disk submerged in water held in a cage
n	$\log V / \log K$
N_A	Number of cracks per unit area

N_f	Rank of strength used in Weibull statistics
P	Load in four-point bending
P_f	Failure probability used in Weibull statistics
Q	Number of supplied atoms per unit area
r	Radius of curvature
r_{hkl}	Distance between diffraction spots from TEM
r_c	Critical distance in front of blunt notch
R	Plastic zone size
R_s	Spatial resolution
R_{max}	$(B_s + B_d)^{1/2}$
$S_{o,\,I}$	Outer and inner spans of four-point bending tests
t	Time
t_{ga}	Thickness of gallium implanted region
u	Displacement of beam under applied load
U_E	Stored elastic energy
U_m	Mechanical energy
V	Volume of alumina unit cell
V_0	Velocity of crack at start of Region I
w	Width of microcantilever beam
w_{foil}	Width of TEM foil
X	Distance from top of triangle to a given horizontal plane
y	Distance across ruby foil in OFM
Y	Dimensionless factor relating stress intensity factor and load or stress, $\left[\frac{1}{2}\frac{dC'}{d\alpha'}\right]^{\frac{1}{2}}$
Z	Atomic number

Abbreviations

AES-11C	Commercially available alumina, 99.8% pure
AGG	Abnormal Grain Growth
CIP	Cold isostatic press
EDX	Energy-dispersive X-ray spectroscopy
EELS	Electron energy-loss spectroscopy
ELNES	Energy-loss near-edge structure
FEA	Finite Element Analysis
FIB	Focussed Ion Beam
HRTEM	High-resolution Transmission Electron Microscopy
OFM	Optical Fluorescence Microscopy
PIPS	Precision Ion Polishing System
RH	Relative humidity
SCG	Slow / sub-critical crack growth
SEI	Secondary electron image
SEM	Secondary Electron Microscopy
TEM	Transmission Electron Microscopy
TM-DAR	Commercially available alumina, >99.99% pure

Chapter 1 Introduction

Ceramics have been used in civilisations for millennia; clay figurines, pottery vessels, and clay bricks for kilns have been used from around 26000BC. They have a number of very useful properties, such as their high temperature capabilities (making them perfect for use in kilns) and their lustre (porcelain has been a prized possession for centuries). More recently, ceramics have been used as coatings for cutting tools because of their high hardness, and in high performance ball bearings due to their excellent wear properties. However, the strong directional bonds that give ceramics their low density and high hardness also result in the material showing a low ductility and brittle fracture properties.

The fracture strength of materials is often dictated by the critical flaw size. Macroscopic specimens in bending, for example, can often fail from polishing defects, scratches, sintering flaws and so on. These act as the critical defect, and failure is initiated from them. Whether or not a given flaw is large enough to be a critical defect is dependent upon the toughness of the material; this is shown by the Griffith equilibrium condition (Equation 1.1) [1]:

$$\sigma_f = \left(\frac{E\gamma}{\psi\pi\alpha}\right)^{\frac{1}{2}} = \frac{K}{\psi(\pi\alpha)^{\frac{1}{2}}} \qquad (1.1)$$

where σ_f is the fracture strength, E the Young's modulus, γ the free surface energy per unit area, α the critical flaw size, ψ a geometrical factor, and K the fracture toughness. Inspection of the equation shows that as the toughness decreases, the critical flaw size α decreases too. Whilst careful polishing and handling can make the flaws on the surface a sample smaller and smaller, the inherent toughness of the material also has a part to play in the failure strength.

Ceramics generally have low fracture toughnesses: for example, 3 – 4 $MPam^{1/2}$ for polycrystalline alumina [2] and around 3 - 7 $MPam^{1/2}$ for silicon nitrides [3]. These values are

considerably lower than those of metals, such as steel, which can have a toughness of 100 $MPam^{1/2}$ [4]. As a result, the critical flaw size in ceramics (using Equation 1.1) can often be of the order of microns [5, 6], which cannot be easily detected before failure. This makes the failure strength difficult to predict.

Understanding and improving the toughness of a ceramic is thus vitally important for its use in many applications. Many different methods have been used to try and improve toughness, such as the use of layers with different residual stresses [7], transformation toughening (such as in partially-stabilised zirconia, [8]), and crack bridging (e.g. using silicon carbide whiskers [9]). These methods improve the toughness by manipulating the microstructure such that energy is dissipated as the crack propagates. Another method of improving mechanical properties is by keeping the microstructure somewhat constant, but improving the toughness of the grain boundaries. Doping the grain boundaries with carbon, for example, has been shown to change the fracture mode from intergranular to transgranular [10] as the carbon presumably increases the toughness of the grain boundaries by altering the grain boundary structure (or “complexion”). Similarly, changing the rare-earth doping of the silicon nitride grain boundaries improves the macroscopic toughness without affecting microstructural features such as grain size and elongation [11]. Being able to understand the reasons for the improved toughness is hugely important to the field of ceramics.

Previous work has used Focussed Ion Beams (FIB) to produce microcantilever beams on the surface of different materials to measure the toughness of grain boundaries [12, 13]. The technique was used in this project on single crystal and polycrystalline ceramics; no previous work has been reported measuring the fracture toughness of ceramics using notched microcantilever beams. After developing the technique using a model grain boundary (sapphire bicrystal) with different notch types, the validity of the technique was assessed in light of the notch bluntness, residual stress, environmental assisted sub-critical crack growth, and flexure in the fixed end during loading. Once these properties were analysed and

relevant correction factors determined, the critical stress intensity factors of different ceramics were ascertained. Using the method set out in this work, the toughnesses of a variety of ceramics can be determined which will provide a wealth of information to the ceramics community.

By using this technique to quantitatively measure the grain boundary toughness of different ceramics, the macroscopic failure properties could be understood. Work was performed to explain the macroscopic results from previous authors [10, 11]. Furthermore, the mechanical properties of different ceramics, measured on the micro- and macro-scale, were correlated. Properties such as flexural strength, uniaxial compressive strength, and macroscopic fracture toughness were determined on a range of different ceramics, and attempts made to explain the properties in light of their grain boundary toughness.

One key uses of the measured grain boundary toughness in this work was to correlate the microcrack evolution during uniaxial compression with the model of Ashby and Hallam [14]. The original work uses the long crack toughness; this work considered whether using the directly measured grain boundary toughness is more appropriate.

Previous work by Lankford [15] shows that microcracking is related to deformation twins that had formed during uniaxial compression. The presence of such twins was investigated and the relationship, or lack of, with microcracking assessed.

Before describing this research, the relevant literature is reviewed. After assessing the literature on the properties of the ceramics (e.g. twinning, grain boundaries) used in this work, the previous model of damage evolution during uniaxial compression is discussed. The physical reason for acoustic emission (used in all macroscopic tests here) and how to use the technique experimentally are considered. Thereafter, the literature on microcantilever beams is presented, together with previous work on important factors such as ion

implantation, notch radii, and moisture assisted sub-critical crack growth. Previous work on removing residual stress by annealing is also described.

Chapter 2 Literature Review

2.1 Aluminium Oxide

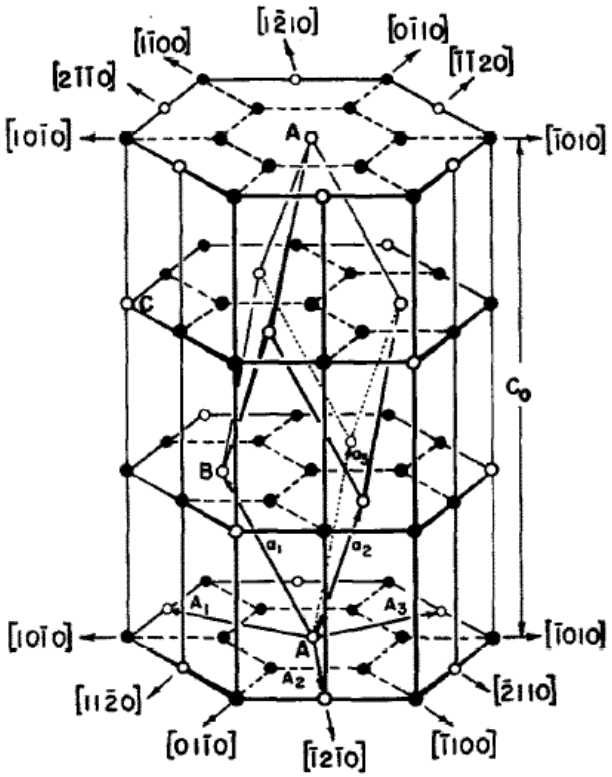


Figure 2.1: Hexagonal lattice of aluminium ions. The unit cell in the centre is rhombohedral, which is enclosed by the more convenient hexagonal cell. From [20]. Permission to reproduce this figure has been granted by Elsevier.

Aluminium Oxide, Al_2O_3, is a common engineering ceramic often referred to as *alumina,* and in single crystal form as *sapphire*. Its most common polymorph, and the one used in this project, is α-Al_2O_3. It has the *corundum* structure with the space group $R\bar{3}c$ [16] with many favourable properties as a ceramic, such as good chemical and thermal stability, electrical and thermal insulating characteristics, and hardness [17]. Hence, aluminium oxide has been used in a variety of applications such as refractory blocks [17], street lamps [18] and ceramic armour [19].

The crystal system of the structure is trigonal [21], but it is convenient to use a hexagonal rather than rhombohedral unit cell (Figure 2.1). The crystal structure corresponds closely to oxygen ions (O^{2-}) in hexagonal-closed packing with aluminium ions (Al^{3+}) in two out of three octahedral interstitial positions [21].

2.1.1. Twinning in Aluminium Oxide

Whilst alumina may be a brittle ceramic, twinning can still occur. A deformation twin is when part of the crystal transforms (under a shear stress) to a different position. The structure of the parent and twin is the same, and they are joined by a coherent boundary. Twinning can be defined by different symmetry operations: reflection across a mirror plane (twin plane), rotation about an axis or line (twin axis), or inversion through a point (twin centre) [21, 22]. Deformation twinning needs shear stresses to occur; when samples are in tensile or compressive tests, for example, this shear stress can still be generated due to the resolved stress at a grain boundary. There are several types of deformation twins that can be formed in alumina; the most common are rhombohedral and basal twins, on the $\{10\bar{1}2\}$ and (0001) planes [23], and in the $\langle 10\bar{1}1\rangle$ and $\langle 10\bar{1}0\rangle$ directions [24] respectively.

Growth, or annealing, twins [25, 26] can also occur in alumina. Both basal and rhombohedral annealing twins can form [26], with the former forming often in liquid phase sintered alumina [27, 28], although the liquid itself does not wet the twin boundaries [27].

An interesting sub-set of twins is when the twin boundaries accommodate different ions, such that twin planes have ordered ions between them (Figure 2.2) [29]. This is chemical twinning, and the resultant structure in aluminium oxide can be described as being "β-Al_2O_3" [29] (the example in Figure 2.2 is β'''-Al_2O_3 where the number of dashes relates to the number of spinel blocks per unit cell [30]). Whilst there is a large

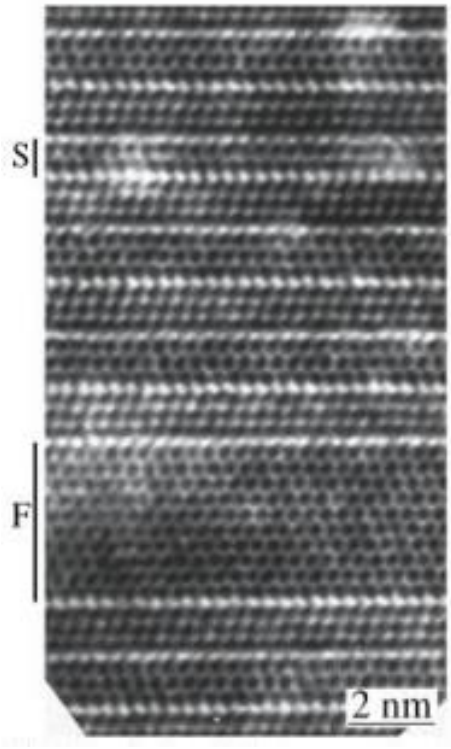


Figure 2.2: β'''-Al_2O_3 formed of chemical twin boundaries.

S: spinel, F: stacking fault. From [29]. Permission to reproduce this figure has been granted by Springer Science and Business Media.

body of literature on deformation and annealing twins, there is very little on such exotic twins.

2.1.2. Stress required to form deformation twins

Opinion is divided over whether basal or rhombohedral twins form at the lowest stress. In some papers, basal twinning was reportedly the most probable [31, 32] in sapphire or alumina [33], whereas others claim it is rhombohedral [34, 35]. Lagerlöf et al [24] claimed that basal twins were activated first, and rhombohedral filled the spaces between them.

For single crystal aluminium oxide, basal twinning was predicted to occur at resolved shear stresses of 7.3GPa [32] or 7.7GPa [36], and rhombohedral at between 3GPa [23] and 3.6GPa [32]. The key mechanism for basal twinning is the double-cross-slip of partial dislocations [36, 37]. The ability of the partial dislocations to undergo this slip mechanism will affect whether twins are present. Temperature and grain size impact on this mechanism and affect whether twins are present. For example, twins have been seen to occur at -196^{o}C [38], but the higher the temperature the more likely twinning is to occur [21, 23, 36, 39, 40]. In polycrystalline alumina, the twinning nucleated at 130MPa in tension [39], or between 283MPa [39] and 1400MPa [39] in compression. Twins appear to form more easily in larger grained ceramics [41, 42] (due to the increased ability for partial dislocations to form).

Which type of twin forms during loading, and the stress at which it occurs, depends on the stress mode (uniaxial compression, indentation etc.), material (single crystal v polycrystalline), temperature, grain size etc.

2.1.3. Twins and doping

Levengood [43] discusses the change in the critical stress to form deformation twins with the concentration of chromium ions. The critical stress for basal twinning in sapphire is 283MPa, but adding around 2% Cr^{3+} reduces the critical stress by around 50% [43]. However, more recent work has shown that the introduction of 9540ppm chromium to the sapphire increases

the twinning-resolved stress by a factor of 3, when tested between 800 – 1000°C [44]. This was due to chromium hindering the cross-slip of dislocations [44]. Indentation work [45] shows that the number and length of the twins decreases with increasing chromium content, but only above 1.09 at% chromium. Below this, the length and number of twins *increases* with chromium [45].

It is unclear why there was such a variation in results relating to chromium additions. In part this must be due to the stress mode, temperature, and the extent of chromium additions. Whilst the most likely explanation was that cross-slip was being hindered, the influence of other phenomena (such as dislocation movements and "crowdion plasticity" [45]) during loading could have affected the propensity for twinning [45].

2.2. Silicon Nitride

There are three crystallographic forms of silicon nitride: α-, β-, and γ-phases. Only β- is considered here. This has a hexagonal crystallographic structure [46]. When sintered with certain oxide additions, these materials tend to be self-reinforcing, due to their rod-like grains which have grown preferentially along the c-axis (Figure 2.3) [47]. Between these grains is a glassy phase [11, 47-49] made of 1) the surface oxide on the silicon nitride powders and 2) additives used to aid densification [47]. As the crack propagates through such materials, there is a large amount of frictional bridging and grain pull-out [11] (although recent

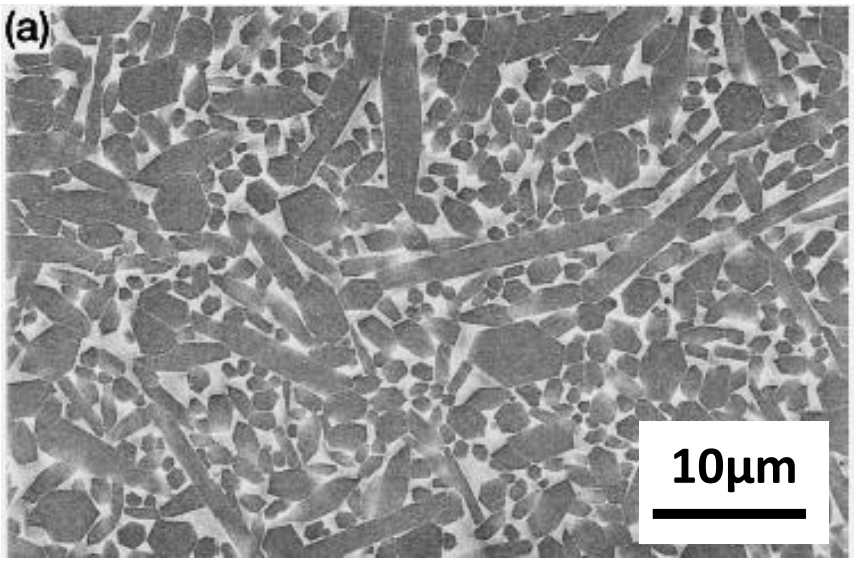


Figure 2.3: SEI of a typical β-Si_3N_4 microstructure, showing the elongated grains used to reinforce the material. From [48]. Permission to reproduce this figure has been granted by John Wiley & Sons, Inc.

theoretical work has suggested that elastic bridges with no debonding are also important [50]). This leads to an increasing toughness as the crack increases in length (or “R-curve” behaviour) [11, 47, 51, 52]. This macroscopic behaviour relies upon a low-toughness boundary for the crack to propagate along; if the boundary toughness is too high, crack bridging does not occur and a relatively low macroscopic toughness is recorded [11].

2.3. Complexions

The structure of a grain boundary is often termed its “complexion”. Whilst not being a phase in the orthodox sense (owing to the inability to truly disassociate it from the neighbouring grains), it has a specific structure, thermodynamic variables, and misorientation [53]. It is

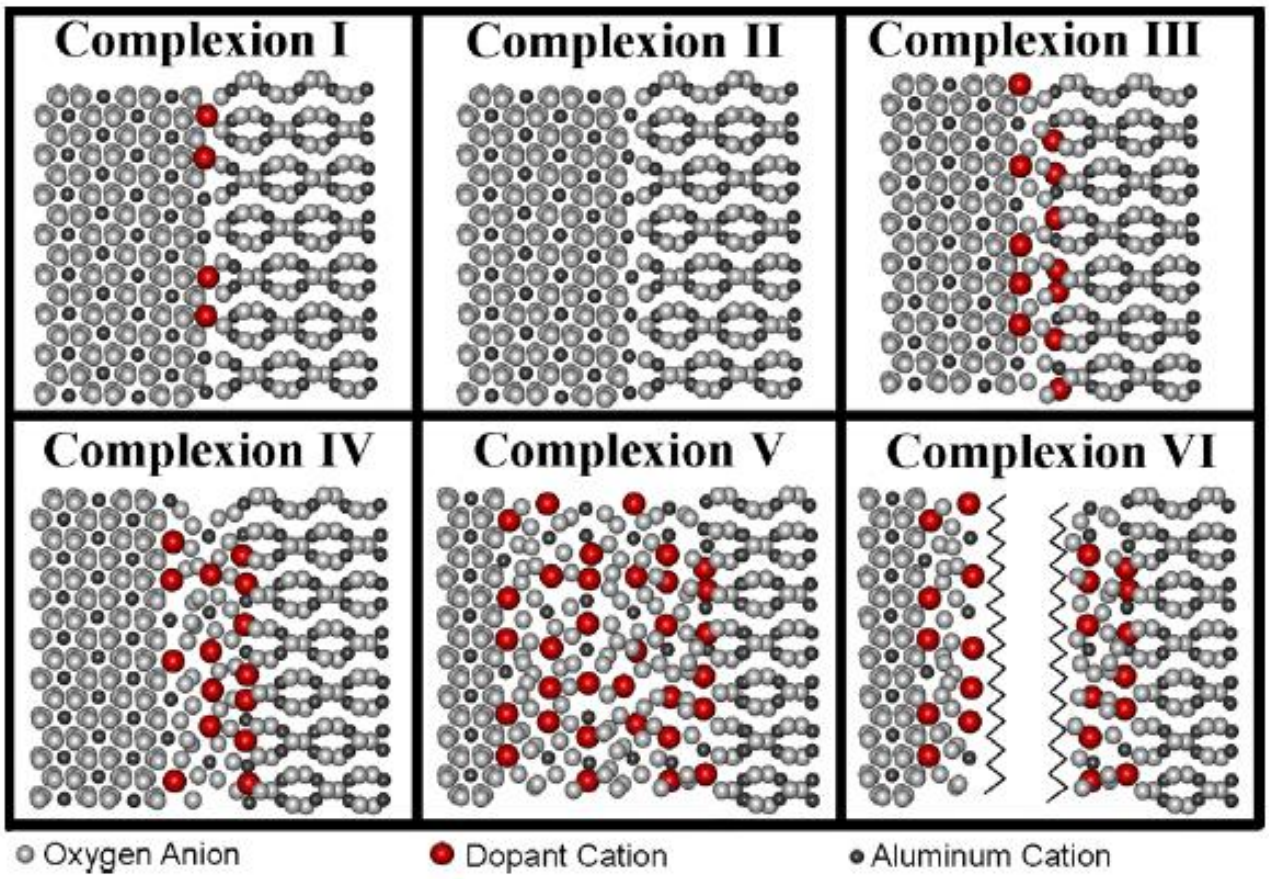


Figure 2.4: Illustration of the different classes of grain boundary complexions in alumina. From [53]. Permission to reproduce this figure has been granted by Elsevier.

proposed [53] that there are 6 distinguishable classes of complexions (Figure 2.4):

I – sub-monolayer adsorption

II – clean grain boundary

III – bilayer adsorption

IV – multi-layer adsorption

V – equilibrium amorphous intergranular film

VI – wetting film

These were determined from high-resolution transmission electron microscopy (HRTEM) of various boundaries in alumina. There is some overlap between these groups, and the specific chemistry at the boundary will determine the actual grain boundary complexion, but the six classes are a useful guide. In general, it is noted by Dillon and Harmer [54] that if two or more of these classes of complexions are present in a given microstructure, abnormal grain growth is likely to occur. This is due to the average grain boundary mobility varying greatly between the different complexions.

The complexions theory can explain various effects of the dopants in alumina. Magnesium oxide, MgO, is a beneficial sintering aid [55-57] whereas calcium oxide, CaO, and silicon dioxide, SiO_2, have a detrimental effect on the sintering of alumina [58-60]. Calcium segregation to free surfaces of sapphire crystal is highly anisotropic, segregating strongly to the prismatic planes but not to the basal planes [61] and hence the concentration at grain boundaries varies markedly [62]. This variation in segregation can lead to abnormal grain growth (AGG). Conversely, doping with 0.25wt% of MgO reduces the extent of AGG [55] by reducing the grain boundary mobility [63-64]. It has been shown that magnesia stabilises one low mobility complexion thus 1) reducing the overall extent of grain boundary migration and

2) reducing the variation in migration from boundary to boundary [53, 65]. By stabilising one grain boundary complexion, the extent of AGG is reduced. Hence, the microstructural features of alumina, and the effect of dopants, can be explained by complexions theory. A range of complexion types has been noted in differently doped silicon nitrides [66, 67] (although authors do not always use the phrase “complexion” to describe the grain boundary composition and structure).

The complexion of the grain boundary has an impact on the mechanical properties. Different complexions have different grain boundary energies [69-71] (and thus toughnesses). Hence, the toughness of a boundary will be related to the local chemistry. An example of this is

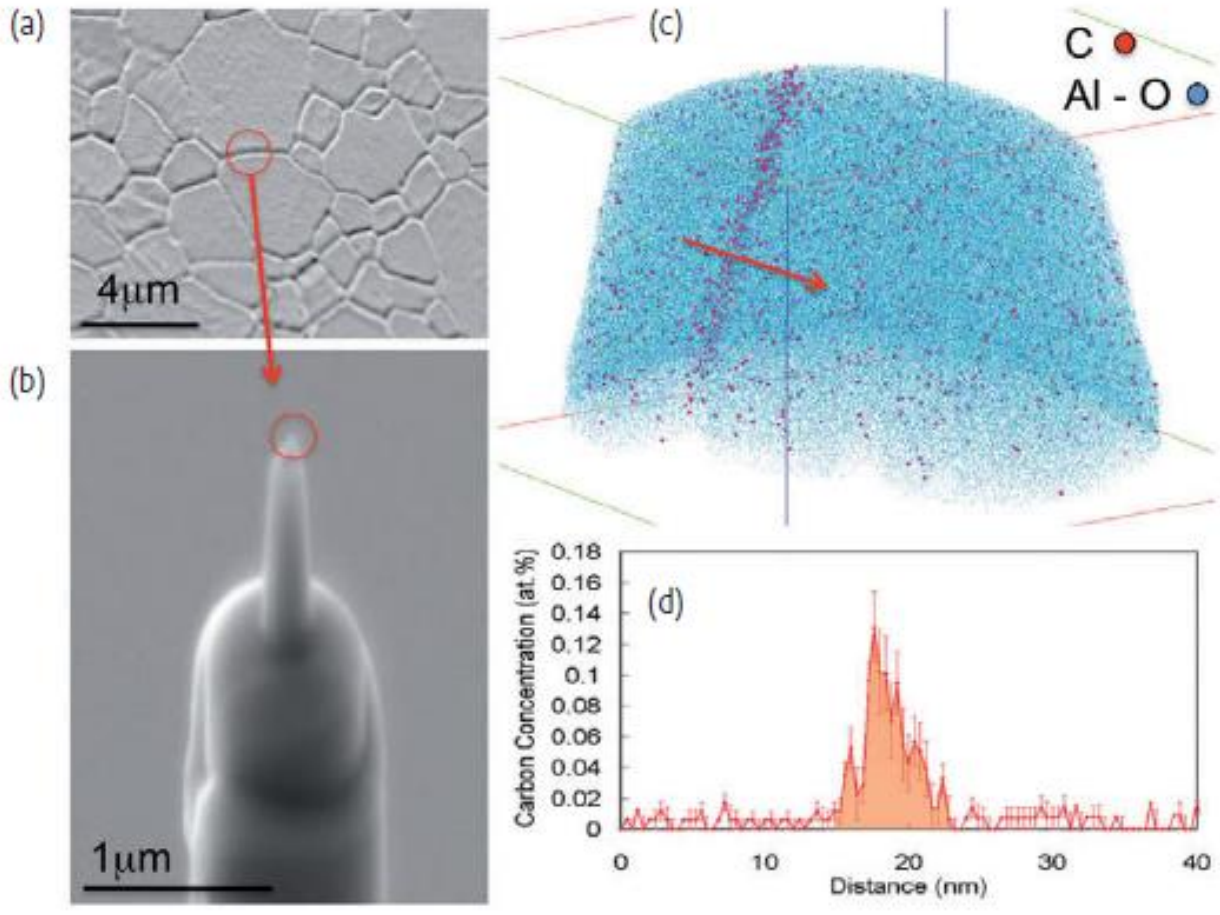


Figure 2.5: Atom-probe tomography of a carbon doped alumina grain boundary. c & d show the higher level of carbon at the grain boundary compared to the surrounding grain. From [68].

carbon doped alumina grain boundaries. Atom probe tomography (Figure 2.5) shows that carbon segregates preferentially to the alumina grain boundaries when sintered in vacuum

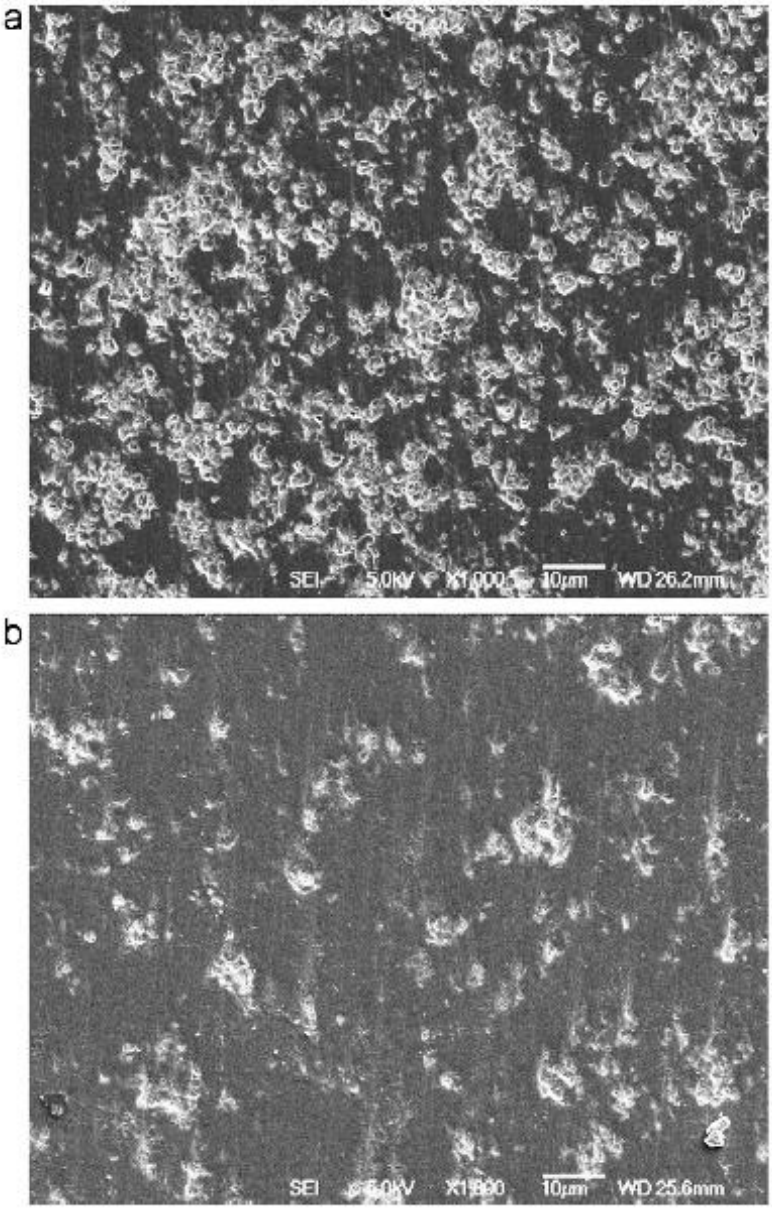


Figure 2.6: SEI of the surface of polycrystalline alumina after wear testing: a) without doping and b) with 0.012wt% carbon doping. From [10]. Permission to reproduce this figure has been granted by Elsevier.

[68].Whilst the authors did not perform HRTEM to consider the specific complexion of the boundary, it is likely that the carbon will have affected structure at the boundary, even though the amount of carbon present is low (1.5 +/- 0.5 atom/nm^2 [68]). The authors only measured one grain boundary, owing to the time intensive nature of the technique, so it is unclear whether all grain boundaries have the same level of carbon segregation.

The resultant impact on the mechanical properties was to alter the fracture mode during wear testing (Figure 2.6) [10]. The worn surface of undoped alumina (Figure 2.6a) indicates intergranular failure and large amounts of grain pull-out, whereas small (0.012wt%) amounts of carbon doping changes the fracture mode to transgranular with a reduced amount of damage on the surface (Figure 2.6b). Hence, the grain boundary complexion and the resultant mechanical properties are intimately linked.

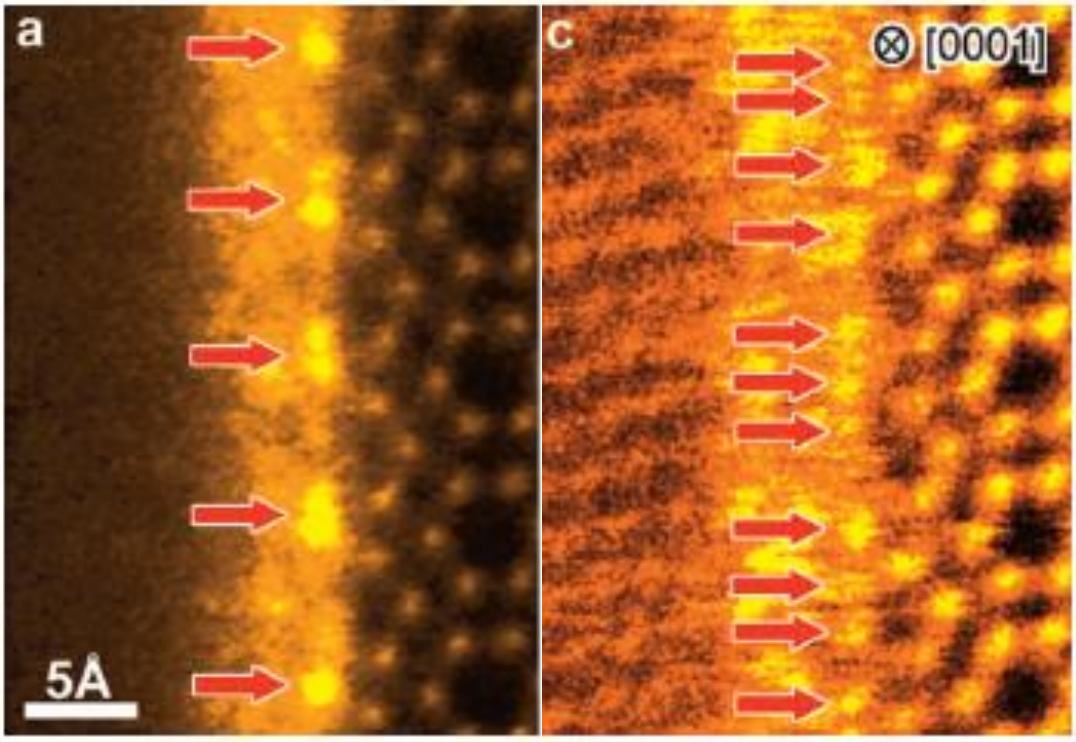


Figure 2.7: Atomic STEM image of a) Lu- and b) La- doped silicon nitride, indicating the number of occupied sites per repeating unit. Reprinted with permission from [67] as follows: N. Shibata, G. S. Painter, R. L. Satet, M. J. Hoffmann, S. J. Pennycook, and P. F. Becher. *Physical Review B* 72, no. 14 (2005): 140101. Copyright (2005) by the American Physical Society.

A further example where the change in complexion affects the mechanical properties is with rare-earth doped silicon nitrides. Atomic resolution scanning transmission electron microscope (STEM) images of the boundaries of Lu- and La- doped silicon nitride boundaries indicates that the complexions are different; Lu occupies fewer sites (one per repeating interface “unit cell”) compared to La (which occupies as many as three) [67]. These are indicated with arrows (Figure 2.7). The variation in complexion with rare-earth doping affects the mechanical properties of the material [11]. Although the microstructure (i.e. size and frequency of elongated silicon nitride grains) is consistent between the two rare-earth doping types, the macroscopic toughness is higher for the La-doped silicon nitride. The complexion is altered, leading to a different grain boundary phase energy, which results in a difference in

the measured macroscopic fracture toughness. This is an excellent example of the importance of the interplay between complexion and mechanical properties.

2.4. Mechanical Testing

2.4.1. Uniaxial Compression – Introduction to microscopic damage

During uniaxial compression of the monolithic ceramic samples, there is crack evolution both on the micro- and macro-scale. Macroscopically, the cracks propagate parallel to the applied compression [14, 72-74], often nucleating at the sample-platen interface. The stability of these depends upon whether the material is loaded in uniaxial, biaxial, or triaxial compression [14]. Herein, only uniaxial compression is considered where stable crack propagation can occur.

Microcracks can nucleate and propagate during loading. These are of significant interest to this project for several reasons. Firstly, the nucleation, growth, interaction, and coalescence of microcracks may lead to failure. The ability to produce these microcracks must in turn be related to the properties of the grain boundaries; as they propagate intergranularly, the toughness of the boundary affects the ease of nucleation and propagation. Secondly previous work showed that deformation twin / grain boundary interactions lead to the production of microcracks [15, 42]. Deformation twins may form during loading (Section 2.1.2.) and thus may be involved in the damage evolution. Hence, understanding the microscopic damage evolution is important for this project.

2.4.2. Uniaxial Compression – Nucleation of a crack

Two main defects are considered in the literature to understand how a crack nucleated; a spherical pore [75] and a sharp-inclined crack [14, 72, 76-78]. Both have some merit as both

flaw shapes are present in polycrystalline samples. For the discussion herein, only the inclined crack will be considered; whilst pores were present in the alumina, in this work

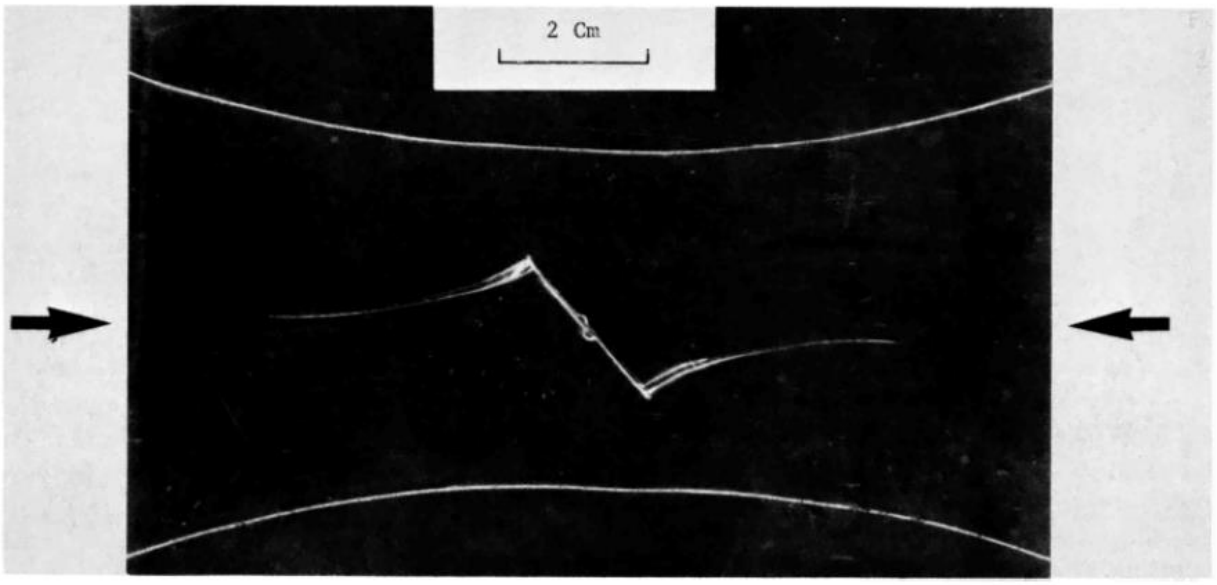


Figure 2.8: An inclined flaw in a brittle solid which, under a compressive load, nucleates wing cracks. These propagate parallel to the major compressive direction. From [76]. Permission to reproduce this figure has been granted by John Wiley & Sons, Inc.

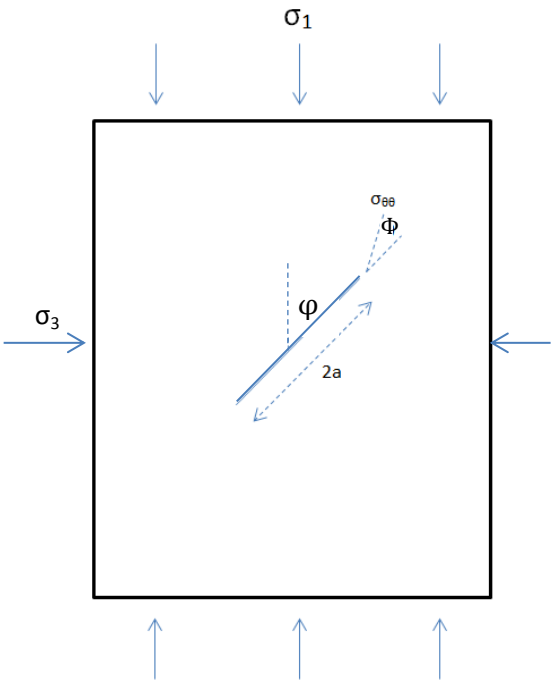


Figure 2.9: Inclined flaw under uniaxial compression, after Ashby and Hallam [14]. Permission to reproduce this figure has been granted by Elsevier.

microcracks were often not associated with them.

Many authors showed experimentally and theoretically that wing cracks were nucleated at an inclined flaw during loading (Figure 2.8) [14, 72-78]. Ashby and Hallam [14] present several useful equations for determining the maximum stress intensity factor around an inclined flaw (Figure 2.9). These are presented herein and are used in this project to analyse microcracks.

When loading the body in compression, the normal (σ_{xx}) and shear (σ_{xy}) stresses on a crack plane at an angle φ to the principal loading direction are:

$$\sigma_{xx} = \frac{\sigma_3 + \sigma_1}{2} + \frac{\sigma_3 - \sigma_1}{2}\cos 2\varphi \tag{2.1}$$

$$\sigma_{xy} = \frac{\sigma_3 - \sigma_1}{2}\sin 2\varphi \tag{2.2}$$

where $\sigma_{1,3}$ are the applied compressive stresses (Figure 2.9). The tensile stress $\sigma_{\Phi\Phi}$ a distance r in front of the crack tip is:

$$\sigma_{\theta\theta} = \frac{3}{2}\frac{\sigma'_{xy}\sqrt{\pi a}}{\sqrt{2\pi r}}\sin\Phi\cos\frac{\Phi}{2} \tag{2.3}$$

where $2a$ is the flaw size (Figure 2.9). σ'_{xy} is the effective shear stress on the crack plane:

$$\sigma'_{xy} = \sigma_{xy} + \mu\sigma_{xx} \tag{2.4}$$

where μ is the coefficient of friction, typically between 0.1 and 1. By analogy with the stress field ahead of a Mode I crack, it can be seen that the effective Mode I stress intensity in the direction Φ [79] is:

$$K_I = \frac{3}{2}\sigma'_{xy}\sqrt{\pi a}\sin\Phi\cos\frac{\Phi}{2} \tag{2.5}$$

When $K_I > K_{Ic}$, the wing crack is nucleated. The equation was in good accordance with previous work [80].

During continued loading, wing cracks extend parallel to the compressive direction [14, 73, 76, 81-88]. Further sliding due to the applied stress causes the cracks to wedge open. These sliding displacements could be separated into normal displacements and shearing displacements yielding two stress intensity factors: 1) K_I^n, due to the normal displacements on the wing crack, 2) K_I^s due to shearing displacements on the original inclined flaw. The former is due to the wedging action and dominates when L (the wing crack length, l, divided by a) is long. This yields three regimes, which can be related to the value L. At low values of L, the stress intensity factor is dominated by the shear of the initial crack. When L is

approximately 1, the stress intensity factor is dominated by the wedging effect. When L is large, the value of K_I is dominated by the confining stress σ_3. Using L, Ashby and Hallam [14] derived an equation for the stress intensity factor for wing crack growth:

$$K_I = \frac{\sqrt{\pi a}}{(1+L)^{\frac{3}{2}}}\left(\frac{2}{\sqrt{3}}(\sigma_{xy}+\mu\sigma_{xx})\right)\left(\beta_n L + \frac{1}{(1+L)^{\frac{1}{2}}}\right) \quad (2.6)$$

where β_n is a dimensionless constant related to the Poisson's ratio, ν, ($= 2/(1+\nu)$ in plane stress, $= 2(1-\nu)$ in plane strain [89]). The equation is very similar to that of Nemat-Nasser and Horii [80].

Finally, Sammis and Ashby [75] considered the interaction of propagating wing cracks. The parallel cracks split the sample into many struts; the behaviour of the struts was used to assess the interaction of the wing cracks. Initially, when the cracks are short, the struts are short and wide. Under these conditions, the stress intensity factor at the tip of a propagating crack (Equation 2.6) is unaffected by the other cracks. As the cracks extend, the struts become longer and thinner; these undergo bending and the stress intensity factors at the tips are not equal to those of isolated cracks.

When the cracks do interact, the stress intensity factor contribution becomes [75]:

$$K_I = -\frac{\sqrt{2}}{\pi} D_0^{\frac{1}{2}}(L+\Theta)^{\frac{1}{2}}\sigma_1\sqrt{\pi a}\left(\left(1-\frac{8}{\pi}D_o\lambda(L+\Theta)^3\right)\left(1-\frac{2}{\pi}D_o\lambda(L+\Theta)^3\right)\right)^{\frac{1}{2}} \quad (2.7)$$

where D_0 is the initial level of damage $= \pi a^2 N_A$ where N_A is the number of cracks per unit area, and Θ is a dimensionless constant $\left(\frac{1}{\sqrt{2}}\right)$ [14]. The total stress intensity factor is the sum of Equations 2.5.and 2.7. With a finite level of damage, the cracks become unstable above a specific value of L. The predicted failure stress is [72, 87]:

$$\frac{\sigma_f}{\sigma_i} = \frac{\left(1 + \frac{\left(1 - {D_0}^{\frac{1}{2}}\right)}{(1 - D_0)}\right)}{1 + \left(\frac{\left(1 - {D_0}^{\frac{1}{2}}\right)}{(1 - D_0)}\right){D_0}^{\frac{1}{2}}} \quad (2.8)$$

where σ_i is the stress when wing crack initiation occurred.

These equations were used to assess the damage evolution during uniaxial compression. One key aspect of Ashby & Hallam's [14] work (and others, such as [80]) is that the wing crack was expected to nucleate when the stress intensity factor is greater than or equal to the critical stress intensity factor K_{Ic}. It is unclear from the literature what value of K_{Ic} to use: the long crack value, which includes toughness contributions from crack bridging etc. [5], or the grain boundary toughness itself. Presumably, in lieu of details of the grain boundary toughness, the former is used. This model is applied to the microcrack generation in alumina in this project using the grain boundary toughness, and its validity assessed. Furthermore, whilst the above model was generated using a continuum material, the microstructure of the ceramic can have an effect on the crack propagation route [90-93]; if the crack propagates intergranularly, the local microstructure will affect the ability of the microcrack to propagate exactly parallel to the applied stress direction. This effect was considered in this work.

2.5. Acoustic Emission

Acoustic emission (AE) is a technique that can be readily used to detect changing defects in ceramic materials [94-96]. The system uses a piezoelectric transducer with a resonant frequency to detect emissions from a few hundred kilohertz to a few thousand kilohertz [94]. AE relies on the movement or growth of sub-structures during the test [97]. For example, a growing crack will cause the material around it to relax, and so releases a stress wave. Hence, the change in the internal defects or cracks can be assessed, making acoustic emission a useful technique for studying the formation of deformation twinning and the propagation of microcracks.

Two key features of the acoustic emission were utilised in this work. The Kaiser effect is the phenomenon that if a material is loaded and unloaded, acoustic emission only restarts once the previous maximum load is reached and surpassed [98-101]. The phenomenon is due to the elastic response of the material under compression [101] or due to low level damage mechanisms due as local crushing of debris [98].

At higher loads, the Felicity effect occurs whereby emission occurs at loads lower than the previous maximum [100, 102]. The effect often occurs in composite materials [102], but can occur in brittle materials either due to sliding on pre-existing flaws or the formation of new defects such as cracks [103]. The latter generally results in continuous acoustic emission bursts [103]. Given the nucleation and propagation of micro- and macro-cracks as discussed in Section 2.4, this would be expected to be the cause of the Felicity effect in uniaxial compression of brittle materials.

In general, micro- and macro-cracking is the expected cause of acoustic emission [104] especially at high loads [98]. Acoustic emission may also be due to the formation of deformation twins (2.1.2.). In general, the papers reviewed made no mention of twinning being a cause of acoustic emission. The only author who appears to consider twinning as a cause of acoustic emission during loading of polycrystalline alumina is Lankford [15, 39]. Microstructural analysis in this project should shed further light on the interplay, if any, of twinning and acoustic emission during loading.

2.6. Microcantilever Beams

A very useful method for testing the properties of materials on the length scale of the microstructure is by using microcantilever beams. The original microcantilever beams were produced in silicon using etchants such as KOH [105-108]. There are drawbacks to etchant techniques, such as the difficult in controlling the sample thickness [109]. Furthermore, for ceramics, such selective etching is often not possible; techniques such as Focussed Ion

Beam (FIB) are more appropriate. FIB-produced microcantilever beams were manufactured in this work. The literature on FIB manufactured beams is discussed, as well as some important findings from previous work on etched silicon beams.

2.6.1. Focussed Ion Beam production method

A Focussed Ion Beam microscope (FIB) has similarities to a scanning electron microscope but, rather than accelerating electrons, uses a liquid metal ion source (often gallium) [110]. The ions are accelerated through the column and through condenser and objective lenses. Between the lenses, a set of apertures are used to define the probe size and hence the beam current [110]. With time, apertures increase in diameter due to erosion by the gallium ions; this will affect the size of the probe focussed on the sample surface and thus needs careful monitoring.

The focussed gallium ion probe is able to mill away the surface atoms of the sample [111] due to physical sputtering of the target. Di Maio and Roberts [12] developed the following technique for producing microcantilever beams in silicon:

1. A coarse staircase mill (3000pA) of two rectangles, 4µm apart and 7µm deep, produced on the surface of the material.
2. A rectangle section milled at one end of the beam to a depth of 7µm (resultant beam was around 10µm long)
3. Vertical sides produced by performing rectangular milled sections to a depth of 7µm.
4. Sample titled to 45^{o} and base milled away to produce a pentagonal cross section.

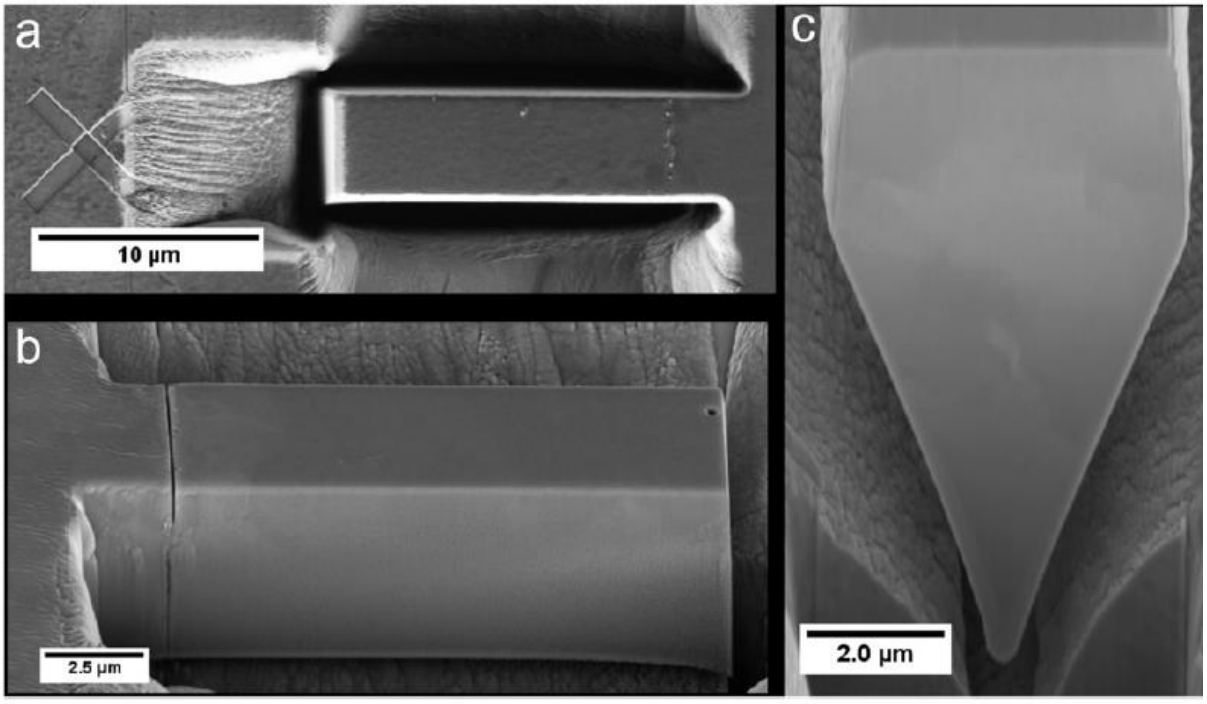


Figure 2.10: Microcantilever beam in copper showing the pentagonal cross section and the outline of the grain structure (due to channelling contrast). From Armstrong et al [13]. Permission to reproduce this figure has been granted by Taylor & Francis.

This method was used to produce microcantilever beams in silicon and tungsten carbide [12] and many authors have followed the same general method although with some slight variations. For example, some authors used a rectangular mill section in Step 1 and cleaning stages to remove redeposited material after Step 4 (Figure 2.10) [13, 112]. Other authors have opted for a similar method, but using triangular [113-116] or rectangular [117-121] cross-sectional beams. There is currently no standard method for producing microcantilever beams, unlike with macroscopic samples, and direct comparison between work can be difficult (mechanical data can depend greatly on beam size [108, 115]). Although direct comparisons may not always be possible, qualitative comparisons are.

Several authors have previously performed micromechanical testing to measure different properties in engineering ceramics. Bulk metallic-glasses (BMGs) have been tested using micropillars [122-128]; Mg-based BMGs tend to show brittle behaviour under compression [122, 124-125]. Micropillar testing has also been performed on GaAs [129], InP [130], Laves phases [131-132] (which undergo plastic, not brittle, deformation on the small scale), SiC

reinforced SiC matrix [133], VN and TiN thin films [134], cubic SiC [135], and even wood [136]. In general, there are fewer articles in the literature regarding microcantilever beam testing in engineering ceramics. Ceramics that have been tested using microcantilever beam testing include WC [12], Ti_2AlC [137], teeth [116], SiC & GaAs single crystals [138], and CrN & CrAlN/Si_3N_4 [138] coatings. Single crystal alumina and polycrystalline alumina and silicon nitride does not appear to have been considered previously.

Whilst some studies have focussed on the microcantilever properties of ceramics, there is a relatively sparse range of literature compared to metals and silicon. As such, these materials will be considered in the following sections alongside ceramics.

2.6.2. Elastic modulus

For unnotched microcantilever beams, simple beam theory has been used previously by Armstrong et al for triangular cross-sectional beams [115]:

$$C = \frac{D}{F} = \frac{{L_{el}}^3}{3EI} \tag{2.9}$$

where C is the compliance, F the indenter load, D the displacement of the beam at the indenter position, L_{el} the fixed end to indenter tip distance, E the Young's modulus, and I the second moment of area (= $h^3w/36$ for a triangular cross section, where h is the height and w the width of the microcantilever beam). However, as the fixed end is not fully constrained by the support behind the fixed end, there is an additional compliance term (i.e. the beam is less stiff that expected). Ignoring lower order terms [115]:

$$C = \frac{{L_{el}}^3}{3EI} + \theta_{m0}{L_{el}}^2 \tag{2.10}$$

where θ_{m0} is the slope at the fixed end due to the bending moment. When L_{el} is large the first term dominates and the compliance of the beam tends to that from Equation 2.9. It was

determined that an aspect ratio of L_{el}:w > 6 [115] was required to use the simple beam approach for triangular beams; below this the Young's modulus was greatly underestimated. This was seen experimentally. For example, Namazu et al [107] found that the Young's modulus of the microcantilever beam remained constant for different sized beams, so long as the length-to-width ratio was large, whereas beams with an aspect ratio much lower than 6:1 showed a lower value for microcantilever beams than from nanoindentation [116]. Ti_2AlC beams [137] of approximately 6:1 ratio appeared to give sensible modulus values.

Rather than just ensuring that beams had an aspect ratio of >6:1, the flexure in the fixed end can be accounted for. Matoy et al [118] found that analytical methods underestimated the modulus of silicon by up to 30% due to lack of consideration of the shear stresses and the behaviour of the fixed end. Using Finite Element Analysis (FEA) to account for the behaviour of the fixed end resulted in the correct Young's modulus being achieved. FEA was used by Gong and Wilkinson [113] to compensate for the fixed end in titanium; Young's modulus

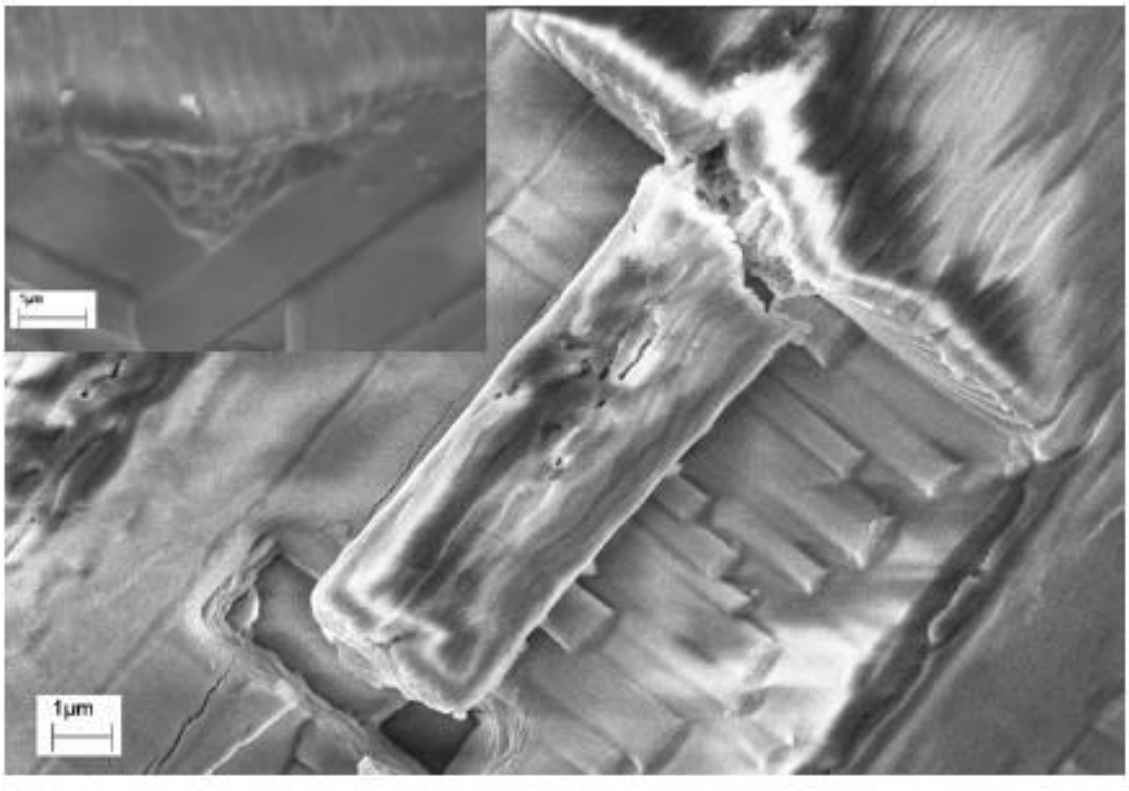


Figure 2.11: SEI of microcantilever beam in dentin-enamel junction (DEJ) from [116]. Permission to reproduce this figure has been granted by Elsevier.

values were in very good accordance to the macroscopically measured values for different metals, despite the length-to-width ratio being between 4.5 and 6.

It is imperative to account for the behaviour of the fixed end to ascertain a correct value for the Young's modulus. The most rigorous approach was to use FEA which avoids the requirement of a fixed aspect ratio of the beam. This was the approach used in this work.

2.6.3. Fracture strength

Measuring the fracture strength on the microscale has been performed by a number of authors. By loading the microcantilever beam using a nanoindenter tip, the sample fails near the fixed end and the fracture strength can be determined. The beams tend to fail from a critical flaw (Equation 1.1). For example, Ericson and Schweitz [139] tested silicon microcantilever beams after a series of different grades of mechanical polishing, and found that the expected flaw size corresponded well to the TEM analysis of the damage from polishing. Often, though, the critical flaw is difficult to determine after failure [108].

There are many advantages to measuring the strength on the small scale, especially for material which cannot be produced in the size and shape of orthodox testing samples. For example, the strength anisotropy in dentin-enamel junctions in teeth [116], the phenomenon of stress corrosion cracking [112], or the strength anisotropy with crystallographic orientation in Ti_2AlC [137] can be determined using microcantilevers.

Whilst testing the strength is very interesting, there are some issues. Several beams presented in the published work show beams that have failed very close to, and overlapping with, fixed end (e.g. Figure 2.11). As the maximum tensile stress is at the fixed end, this is liable to happen. Interpretation of the true fracture strength from bending is difficult when beams fail in this way; it is unlikely to be in true bending at failure. Hence, care must be taken to ensure that the fracture point is far enough away from the fixed end to be confident that the expected stress state is obeyed by the sample.

Plasticity before failure has been seen for different metals using microcantilever beams, with a strong dependence on beam dimensions [114, 117] (Figure 2.12). It is possible that plasticity (e.g. deformation twinning or slip) occurs in ceramic microcantilever beams during loading (Section 2.1.2.) especially due to the small critical flaw sizes and high strengths [108, 117]. Micropillar work, for example, has shown that Laves phases [131-132], which behave in a brittle manner macroscopically, can undergo plastic deformation on the small scale; hence, ceramic microcantilever beams may deform plastically (although this was not seen in Ti_2AlC [137]). Relating the ability to form twins on the macro- and micro-scales will further shed light on the plasticity properties of these ceramic materials under loading.

2.6.4. Fracture toughness

To the author's knowledge, there is no equation in the literature to determine the stress intensity factor at failure for triangular shaped microcantilever beams. As a result, an

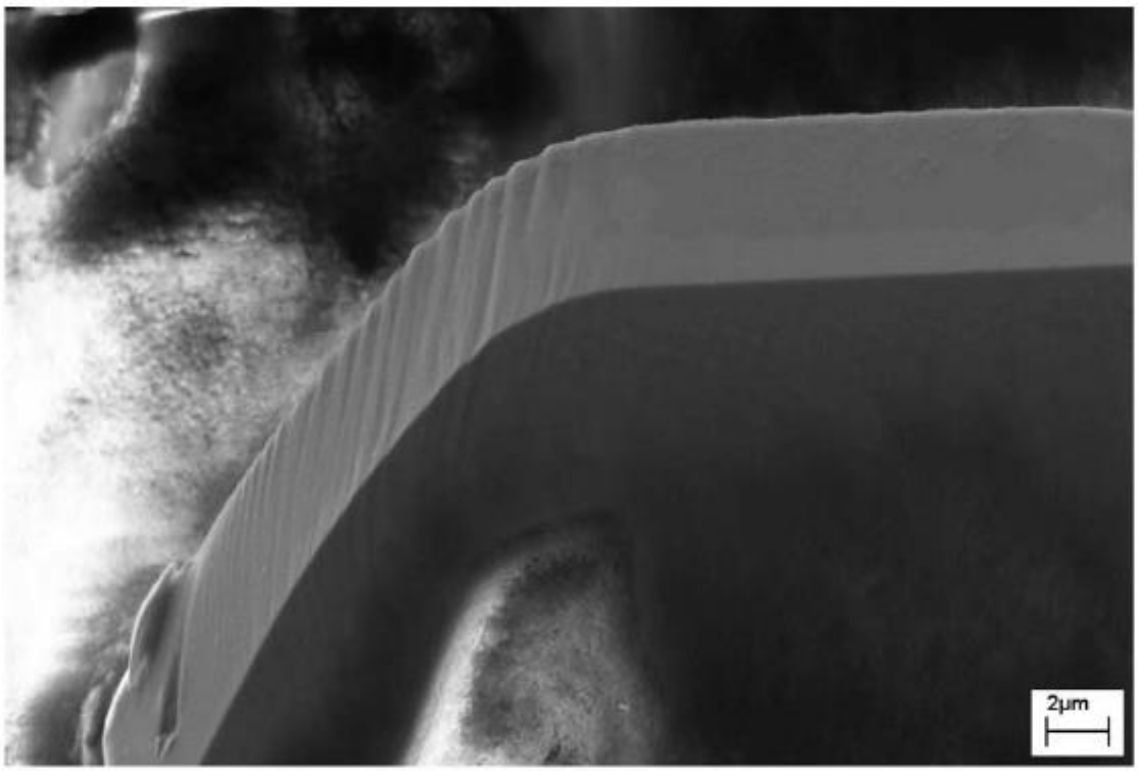


Figure 2.12: Deformed microcantilever beam in copper showing slip lines on the top surface from [117]. Permission to reproduce this figure has been granted by Elsevier.

equation is derived in this work.

Many authors have shown great interest in measuring the fracture toughness using notched microcantilever beam. Di Maio [12] used a straight through notch on the surface of pentagonal cross-section beams silicon beams and, by using a boundary element method to determine the dimensionless factor $\mathrm{F}\left(\frac{\alpha}{\mathrm{h}}\right)$ (in Equation 2.11), a fracture toughness of silicon was measured as 1.1 +/- 0.016 MPam$^{1/2}$:

$$\mathrm{K_{Ic}} = \sigma_f \sqrt{\pi\alpha}\ \mathrm{F}\left(\frac{\alpha}{\mathrm{h}}\right) \qquad (2.11)$$

where α is the notch depth and h the height of the beam. The authors noted that the value was slightly higher than previous work; this was attributed to notch bluntness (Section 2.6.5.).

Straight through notches on the surface of pentagonal shaped beams in copper were produced by Armstrong et al [13] (Figure 2.13). Due to the channelling contrast of the metal [111], the grain boundaries could be resolved prior to milling. Hence, beams were constructed such that the crack propagation

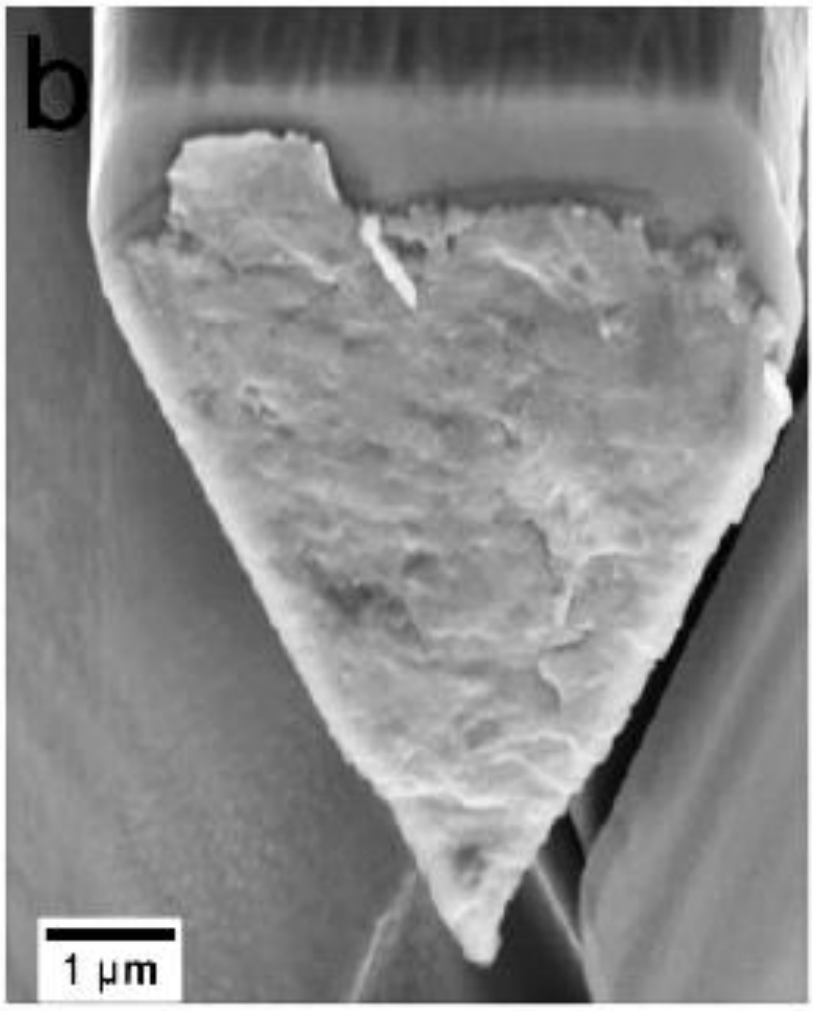


Figure 2.13: Fracture surface with straight through notch in copper (from Armstrong et all [13]). Permission to reproduce this figure has been granted by Taylor & Francis.

occurred along a grain boundary perpendicular to the surface. Fracture surfaces were fairly flat (Figure 2.13). However, the notch is not even across the width of the beam, with the notch depth greater at the edge of the beam. This is due to the additional free surface, which allows milling to occur more rapidly (an effect known as “curtaining” [140]). Presumably this was not taken into consideration in the Finite Element Analysis used to determine the stress intensity factor of the notched beam; the additional depth may have impacted on the measured mechanical properties.

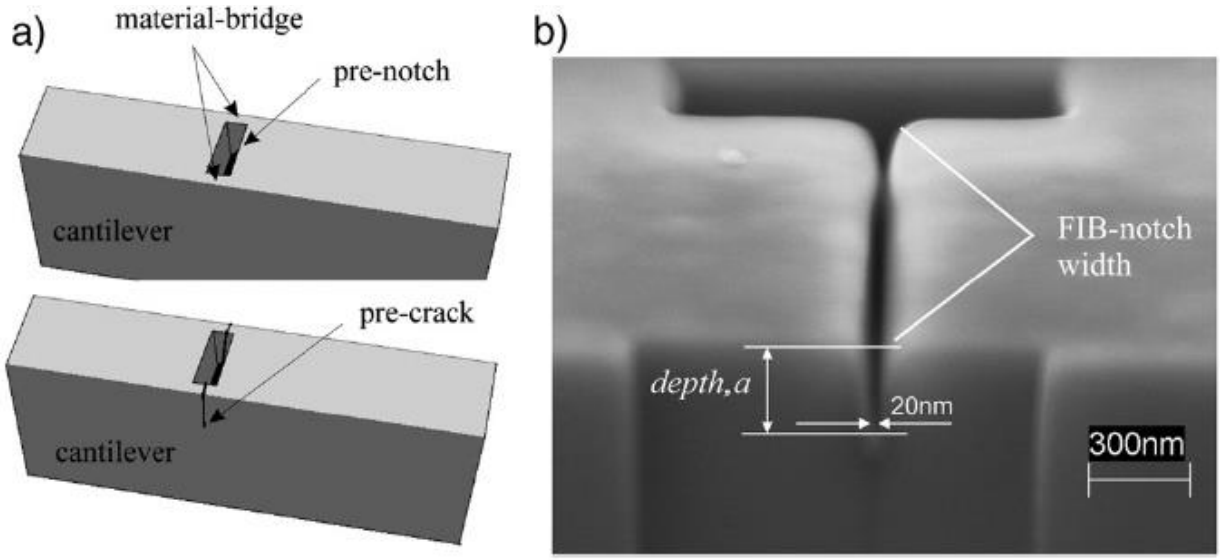


Figure 2.14: Schematic and SEI of a controlled flaw, or pre-notch, method used to avoid the issue of curtaining (from [118]). Permission to reproduce this figure has been granted by Elsevier.

A variation on the straight through notch method that avoids the effect of the curtaining is using a “controlled flaw” approach (Figure 2.14) [118]. The thin material “bridge” either side of the notch was thought to fail in loading and the crack to extend either side of the flaw. The authors suggested that as a result a sharp crack was produced at the base of the notch; aside from avoiding the curtaining issue, the failure should also occur from a sharp crack rather than a FIB produced notch. However, the authors did not report a change in compliance during loading which should occur if the crack extended stably during loading

[141]. Furthermore, the factor $F\left(\frac{\alpha}{h}\right)$ is ascertained assuming the notch was across the whole beam; there is no factor relating to the width of the notch [118]. The assumption was that cracking would occur stably along the material-bridges (Figure 2.14) and the beam fails from effectively a straight through notch. Whilst it is difficult to reconcile these assumptions with the experimental results (especially the lack of compliance change and the ambiguity of images such as Figure 2.14b showing that the crack had extended), the ascertained values of the fracture toughness / surface energy are consistent with those measured macroscopically and, hence, there are merits to the method.

A more appropriate method of determining the fracture toughness using these notches (Figure 2.14) is perhaps to use some of the literature equations for surface flaws under bending. Many of these are for semi-elliptical or semi-circular flaws. Newman and Raju [142] and Raju and Newman [143] derive an equation for a semi-elliptical surface flaw under bending, which includes variables relating the notch depth, width, beam height, and beam width. More recent work by Strobl et al [144] has used finer computational meshes to produce a more rigorous analytical equation for the stress intensity factor of surface flaws. Both semi-elliptical and semi-circular flaws can be used in the equation, but the former fails at the base of the flaw and the latter on the side [144].

For a FIB flaw, whether it is more appropriate to use the Strobl et al [144] approach or assume a straight through notch (as Matoy et al [118] do) depends on the width of the flaw relative to the beam. If the flaw is small, it is effectively an isolated surface flaw that is not affected by the shape of the microcantilever beam. If the flaw is very wide, the effect of the remaining material (“material-bridge” in Figure 2.14) is minimal. Consideration is given in this project as to when it is appropriate, given the flaw dimensions, to use these two approaches.

Hence, both the straight through notch and the controlled flaw methods were used in this current work. Both have their advantages and disadvantages, and the merit of each will be

investigated in this project. However, unlike previous authors [118], the controlled flaws were analysed using equations for surface flaws.

2.6.5. Notch bluntness

Various authors have noted or discussed the effect of the notch bluntness on the resultant fracture toughness from the microcantilever beam. The overall consensus is that the FIB notches in silicon appear blunt, and as such the apparent fracture toughness is increased [12, 118, 145]. Interestingly, the toughness is often underestimated for ductile materials [119, 121, 146] due to the plastic zone being approximately the same size as the specimen (and linear elastic fracture mechanics underestimates the fracture toughness in this regime [119]). For sapphire, the size of the plastic zone can be estimated to be 6nm (Equation 2.12) using a value of toughness of 3MPam$^{1/2}$ [147] and a value of the yield stress of ≈ E / 10 (40 GPa):

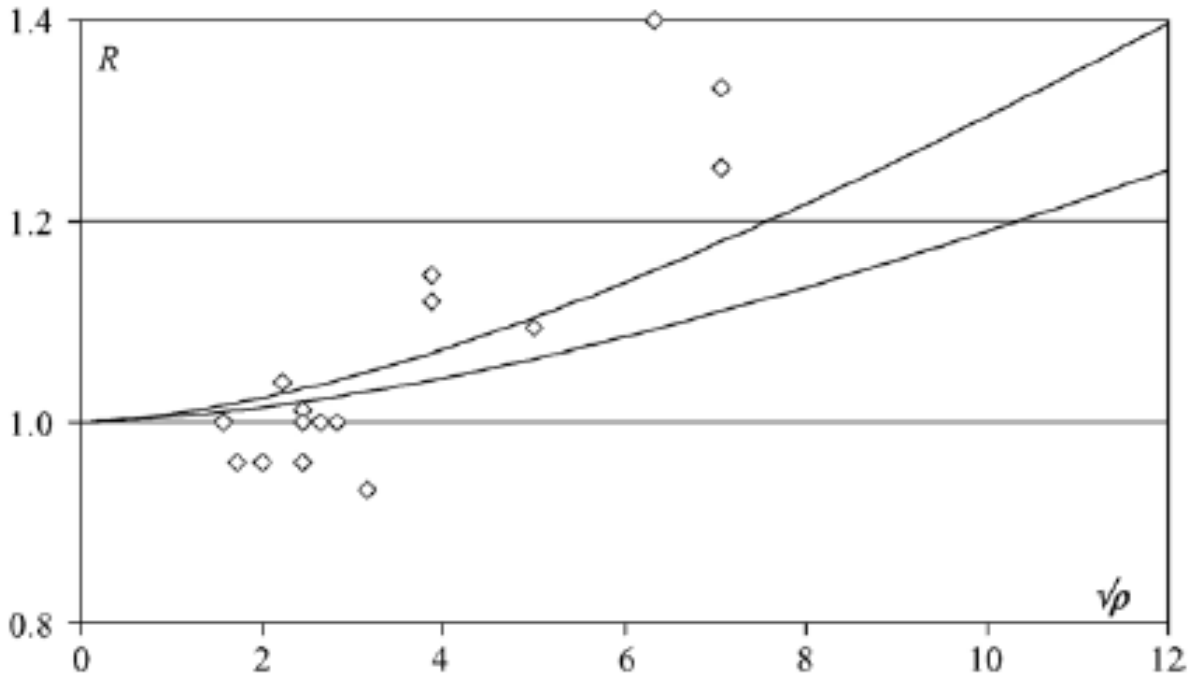


Figure 2.15: R (= K^{app} / K) against the square root of the notch root radius (in μm$^{1/2}$), indicating that FIB notches should give toughness values close to the true values. Diamonds are experimental results, and the lines are the predictions. From [148]. Permission to reproduce this figure has been granted by Elsevier.

$$R \approx \frac{K^2}{\sigma_y^2} \tag{2.12}$$

The plastic zone size is expected to be far smaller than the size of specimen, and so the ceramic microcantilever beams are likely to behave differently to those in metals. However, it is worth contemplating the contrasting effects of the plastic zone size and the notch bluntness in metals. If the notch bluntness increases the apparent fracture toughness but, because of the plastic zone, toughness is underestimated, it is possible that these effects cancel out to give the correct value but for the wrong reasons. The same effect could be possible in brittle materials; notch bluntness may increase the applied stress intensity factor at failure but effects such as environment assisted sub-critical crack growth decrease it.

Several authors [118, 120], having noted that the FIB produced notch may be blunt rather than sharp, used the correction factor discussed by Picard et al [148]. This method applies both stress and energetic failure criteria on a notched sample. Inspection of the change in the value of $R\ (= K^{app} / K)$ against $\rho^{1/2}$ ($\mu m^{1/2}$) (Figure 2.15) shows that a small notch radius such as those produced by FIB (e.g. 10s of nm [118]), will give a stress intensity factor very close to the true value. Hence, whilst this correction was used by several authors [118, 120] the impact on the values was small. The validity of this approach is considered in this work.

An alternative to the above method is proposed by Fett et al [149]. For a notch depth α with a sharp flaw of length $d\alpha$ extending beyond the notch tip, the apparent stress intensity factor can be determined using Equation 2.13.

$$K^* = \sigma_f \sqrt{\pi(\alpha + d\alpha)}\, F\left(\frac{\alpha}{h}\right) \tag{2.13}$$

K^* is the true stress intensity factor only when the length $d\alpha$ is much larger than the notch root radius, ρ. In the case of the microcantilever beams, where this does not always hold, the toughness determined from Equation 2.13 does not closely relate to the true toughness of

the material. If the notch root radius ρ is smaller than α, then the true stress intensity factor K can be given as Equation 2.14 [149, 150]

$$K \cong K^{*} \tanh\left(2.243\sqrt{\frac{d\alpha}{\rho}}\right) \qquad (2.14)$$

The critical factor for these equations is the value of $d\alpha$. For macroscopic samples, the length is generally taken to be around 2 – 3 d_m, where d_m is the mean grain size [151]. For microcantilever beams, especially those in single crystals, it is not possible simply to take the length $d\alpha$ as that of the grain size. Assuming the FIB notch is 10nm in radius [12, 118], the ratio of the true stress intensity factor to the apparent stress intensity factor (= R) can be determined for a range of values of $d\alpha$ (Figure 2.16). If the characteristic notch tip crack length $d\alpha$ is of the order of 10nm, the measured toughness is close to the toughness for the material. The merit of using this approach will depend upon how long the edge crack is; this will need to be determined experimentally.

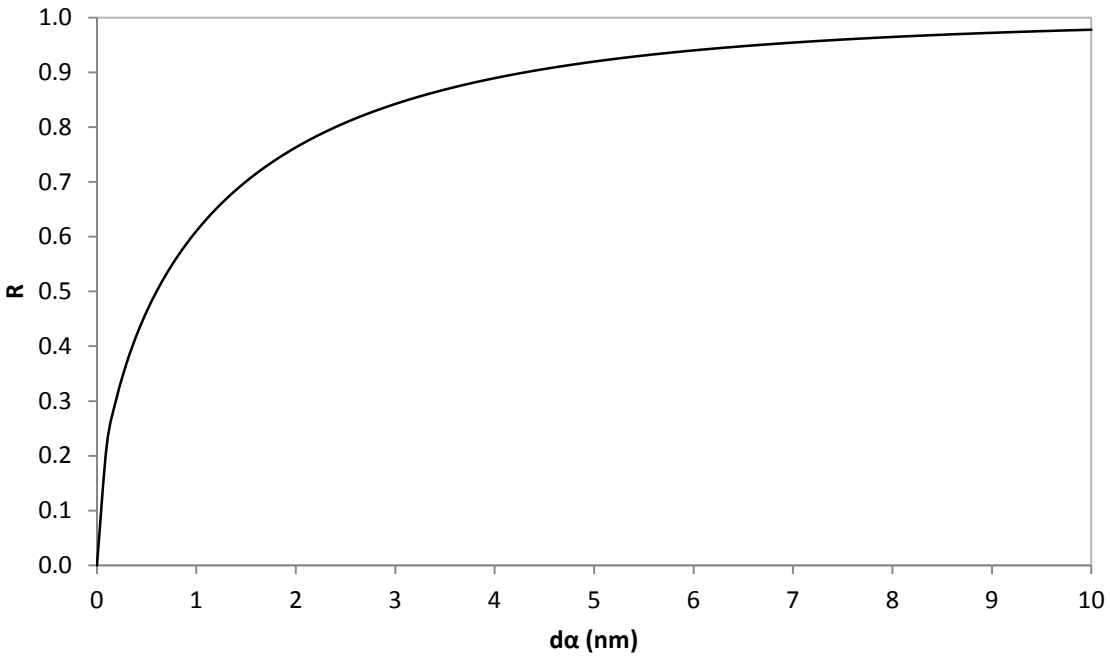


Figure 2.16: Change in the value of $R\ (= K / K^{*})$ with different values of the length $d\alpha$, using Equation 2.14.

2.6.6. Gallium Implantation and other FIB effects

Whilst many authors have used Focussed Ion Beams to produce the mechanical testing samples, few have considered the impact of the gallium ions on the material itself. There is a considerable amount of research on the subject of implantation, redeposition etc., but there have been few researchers who have drawn upon this work to discuss the microcantilever beam mechanical properties. The possible FIB related effects are firstly discussed, followed by the previous work on microscale mechanical testing that considered such effects.

One effect, common in metals, is that the energetic bombardment by ions can produce a high dislocation density region underneath the surface [152] which dislocations can pile-up at [153] and which in turn can lead to an increased hardness [154].

Another possible effect of the gallium implantation is surface amorphisation (Figure 2.17). Research in this field is almost exclusively focussed on silicon, but several features may also

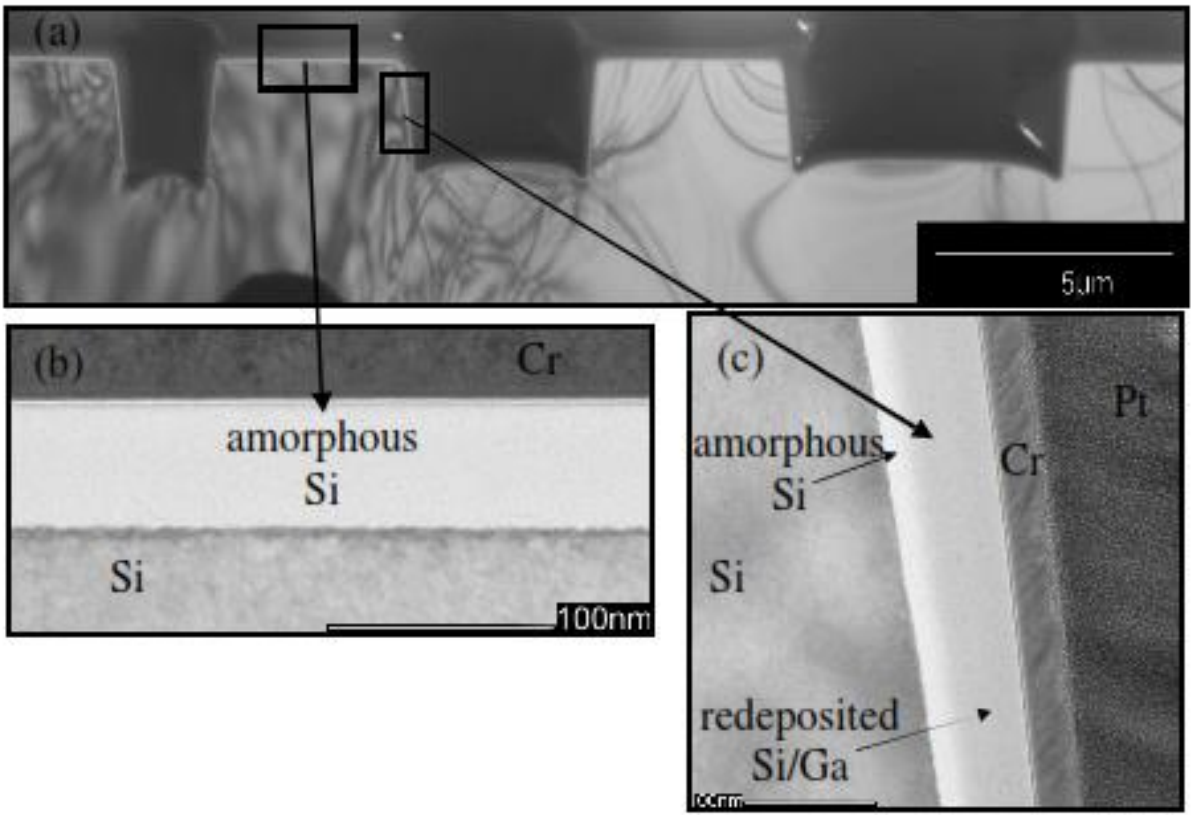


Figure 2.17: A layer of amorphous silicon present due to the bombardment of gallium ions on the surface. From [155]. Permission to reproduce this figure has been granted by Cambridge University Press

be applicable to the ceramic materials studied here. If the displacement of atoms (due to the collision with the gallium ions) is sufficient then long range crystal order is lost [155]. Various factors determine the ability of the surface to amorphise, such as the unit cell size, the width of the phase field between the substrate and gallium [156, 157] and bonding type [157]. Wider phase fields, fewer atoms per unit cell, and non-directional bonding (such as in metals) favour implantation over amorphisation [157]. In silicon, amorphisation readily occurs (Figure 2.17) [155, 157-161], although it was often found to be difficult to fully determine exactly the properties of the region; both redeposition and amorphisation occur somewhat simultaneously (Figure 2.17). Several authors have found that the amorphised layer also contains redeposited material [157, 162]. Overall, the amorphised region was between 17nm [158] and 22nm thick [159], although there is some variation depending on the nature of the FIB work [159].

The final effect that may have a significant impact on the mechanical properties is residual stress due to ion implantation. No authors have discussed the mechanical properties of the microcantilever beams with respect to residual stress caused by implantation. In metals, any residual stress due to implantation may simply be alleviated by the formation of dislocations (hence the high dislocation density at the surface, as discussed above). In silicon, the only other material to receive serious interest in terms of microcantilever beams, the presence of residual stress has not been reported. In ceramics, which will neither readily form dislocations nor amorphise, there may be a significant amount of residual stress due to the ion implantation. Authors try to reduce the beam current when working with ceramic beams [12, 137, 138] to reduce the extent of implantation; however, no work has looked at what the FIB may be doing to the ceramic during microcantilever beam milling.

Burnett & Page [164] implanted the surface of polished sapphire with titanium and yttrium ions at 300keV, to a depth of 0.5µm. This resulted in a residual stress, due to both the formation of vacancy / interstitial pairs and the injection of atoms into the surface, of a

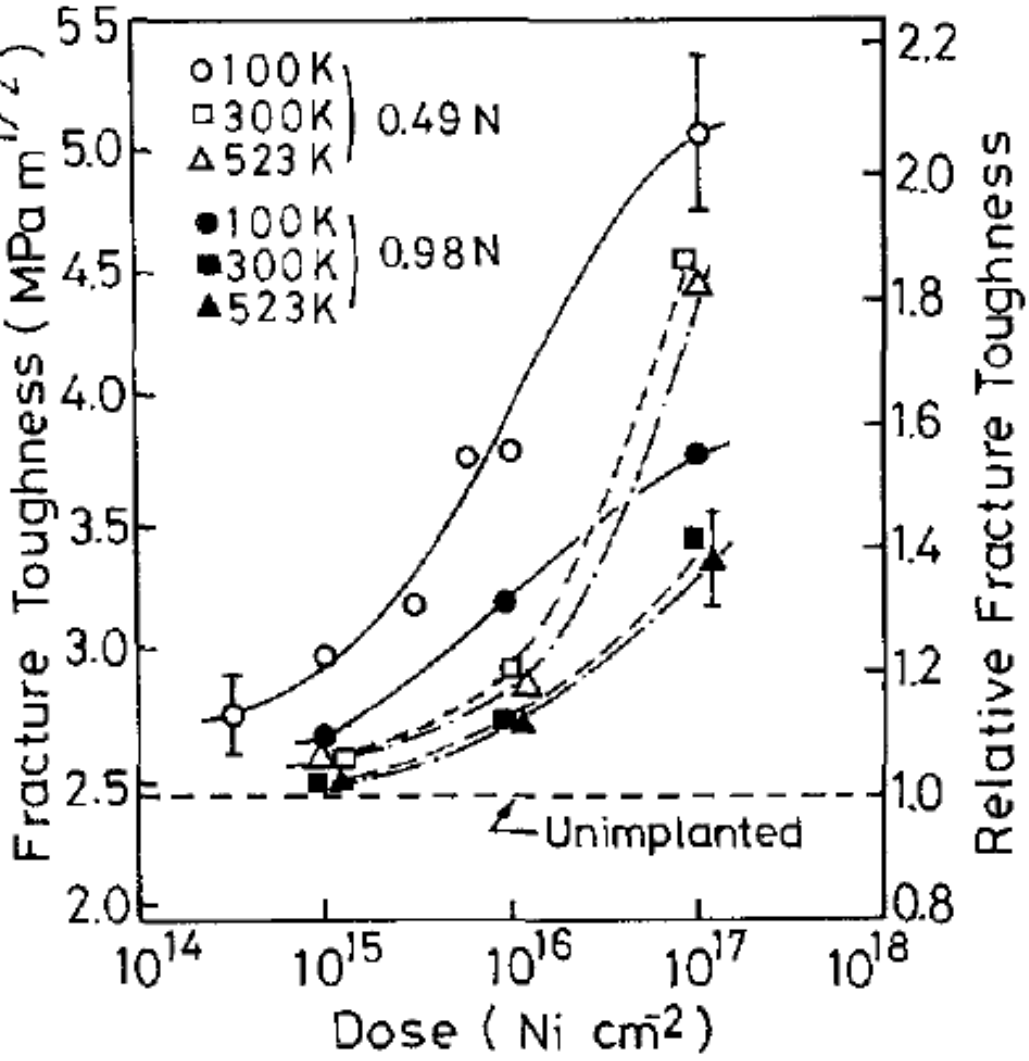


Figure 2.18: Change in the fracture toughness (measured from indentation) with implantation of nickel ions on the surface of sapphire. From [163]. Permission to reproduce this figure has been granted by Springer Science and Business Media.

maximum of 6.4 and 7.6GPa for titanium and yttrium doping respectively [164]. The use of nickel ions at 300keV gave a residual stress of 2GPa (at 10^{15} cm^{-2} dosage) [163] as well as an increase in hardness and fracture toughness (Figure 2.18). Implantation of chromium at 280keV gave a residual stress of 1GPa [165, 166]. The fluences (ions/cm^2) used in previous experiments [163 – 166] are around the same order, if not lower, as those that could be expected to be achieved using gallium Focussed Ion Beams (10^{17} - 10^{18} cm^{-2}) [167, 168]. As such, the residual stresses are expected to be of the same order, if not higher, due to gallium Focussed Ion Beams.

The variation in the residual stress is due to the variation in the specific ion, accelerating voltage, and fluence used for the implantation. Nonetheless, it is clear that the residual compressive stress due to the ion implantation is on the order of a few GPa. If the same is true for the microcantilever beams, the effect on the mechanical properties will be huge. For example, the increase in the fracture toughness due to implantation was significant [163] (Figure 2.18). To fully understand the mechanical properties on the microscale, the residual stress needs to be measured.

Annealing of the implanted sapphire in nitrogen at 900^{o}C appeared to reduce the residual stress, by 60% for $[01\bar{1}0]$ and by 80% for $[0001]$ orientation, with the latter assisted by basal slip [169]. There is also some work that shows that annealing removes gallium from the surface of ceramics ($BaTiO_3$) [170]. Hence, although the residual stress may be a problem for the microcantilever beams, annealing of the beams may reduce the effect. Hence, both annealed and unannealed beams were considered in this study.

Overall, it is clear that the FIB can significantly affect the underlying material, and hence the mechanical properties. Understanding the extent of dislocation generation, amorphisation, and implantation-induced residual stress is imperative for microscale testing. In the field of microcantilever beams, little consideration has been given. Armstrong et al [13] discussed the impact of the gallium ions on copper beams. It was noted that, whilst gallium damage is likely to occur, the damaged layer will be thin (Kiener et al [152] found it to be of the order of 50nm). Hence, the crack was assumed to readily propagate through this region and so the effect was minimal [12]. Other authors also concluded that the damaged area was negligible [116], although certain materials are particularly susceptible to severe damage from gallium ions (aluminium, for example, undergoes grain boundary embrittlement due to the gallium ions [120]).

In the field of FIB-produced micropillars, some consideration to the FIB effects has been given. In general, the production method uses grazing rather than perpendicular bombarding

gallium ions [171 - 173]; the effect on the mechanical properties of metals is uncertain, but has been given some consideration [154, 174, 175]. Ceramic micropillars have been produced using FIB [133, 171, 172], but the effect of the gallium ions on the ceramic was not fully considered or accounted for. As the micropillar deformation is fundamentally different to the microcantilever beams, gallium ion effects may be substantially less important. Moreover, as the beam glances the surface during production, the gallium implantation and hence surface effects may be less significant than underneath a FIB notch produced by direct bombardment of the gallium ions. If there is going to be any effect of the implantation / amorphisation / residual stress it will underneath the FIB notch. Although the effect of the gallium ions at notches is generally ignored by authors, careful work was undertaken in this thesis to understand the effects of the gallium ions and the impact on the mechanical properties.

2.6.7. Subcritical crack growth

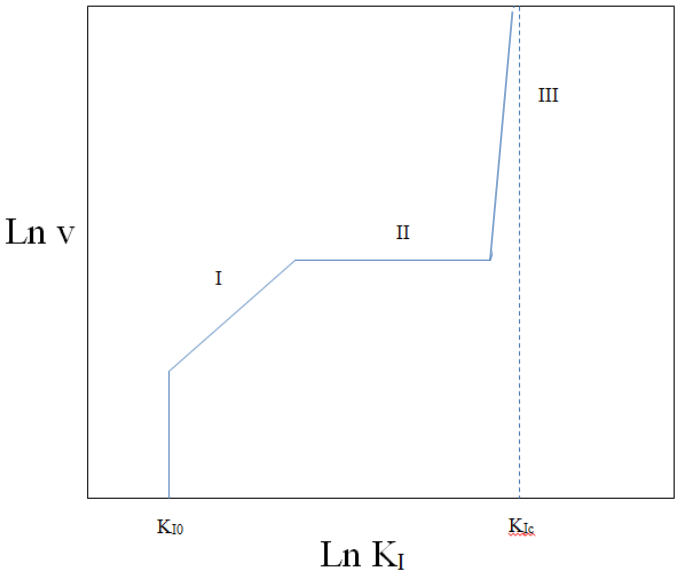


Figure 2.19: Generalised crack velocity against stress intensity factor curve showing three distinct regions during sub-critical crack growth

A further issue regarding the testing of the notched microcantilever beams in ceramics is the extent to which moisture assisted subcritical, or slow, crack growth (SCG) occurs before failure. Sapphire and other ceramics readily undergo SCG during loading (depending on the environment and loading rate), resulting in a stress intensity factor at failure far below the K_{Ic} [2, 5]. There are generally four

regions (Figure 2.19). Below K_{I0}, no crack growth occurs. In Region I, the velocity of the crack growth greatly depends upon the stress intensity factor, and is associated with water chemically breaking the ceramic bonds. Hence, the specific environment has a huge impact on the properties of Region I [2, 176]. The plateau of Region II occurs as the diffusion of attacking environment, such as water molecules, from the crack opening to the crack tip limits the rate and the system advances under transport limited conditions. Region III is associated with the bond rupture without the chemical attack of the environment (i.e. fast fracture, K_{Ic}). In reality, Region III is not seen in slow-crack growth experiments unless very low humidities are used, such as 0.02% (Figure 2.20) [176-178].

The fracture of microcantilever beams occurs with a relative low crack velocity, although no reports in the literature specify exact values. Analysis is required to determine which region oxide ceramics fail in and what the stress intensity factor at failure is expected to be (Figure 2.20).

There are uncertainties as to the environmental effects on silicon nitride. According to some, silicon nitride does not undergo environment assisted sub-critical crack growth if the grain boundaries are oxynitride [179]. However, other authors [180] suggest that silicon nitride crack propagation is sensitive to environmental factors when the crack growth rate is low (i.e. the regime microcantilever beams are probably in), although others argue that the sensitivity is low [181]. The properties of the grain boundaries clearly have a huge effect on whether environment assisted sub-critical crack growth (SCG) occurs. The interplay between the complexion (Section 2.3) and the extent of SCG is unknown. In this project, La- and Lu-doped silicon nitrides were used, which had different complexions; this was possible that these also reacted differently to the environment.

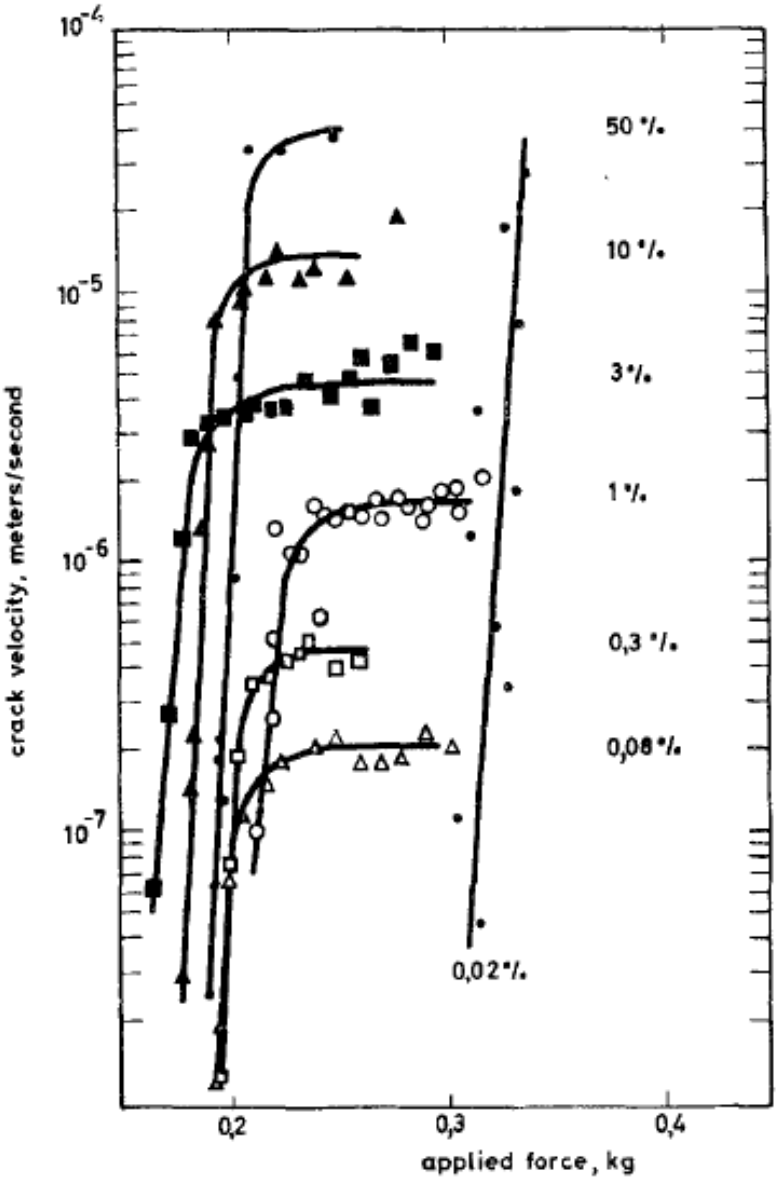


Figure 2.20: Crack velocity against applied force (or stress intensity factor) for sapphire fracturing on the rhombohedral plane in different relative humidities (from Wiederhorn [176]). Permission to reproduce this figure has been granted by Springer Science and Business Media.

2.7. Optical Fluorescence Microscopy

Optical fluorescence has been used previously to determine the residual stresses in polycrystalline alumina by considering the peak position of the ruby (R) line due to trace amounts of chromium ion (Cr^{3+}). First discussed by Grabner [182], the technique was developed by Ma & Clarke [183, 184]. The use of the technique relies on the substitution of

Cr^{3+} ions onto the Al^{3+} sites in the lattice; this can readily occur, due to the like charges and the similar ionic radii [182-184]. The fluorescence of Cr^{3+} on the Al^{3+} sites gives rise to the ruby line (R) due to the $^2E - {}^4A_2$ transition, which is split into two peaks, R_1 and R_2, due to splitting of the ^2E level [184]. These are centred around 14400cm^{-1} [182]. As stress distorts the atoms around the Cr^{3+} ion, the oxygen-chromium bond length changes which results in a change in the radiative transitions between the ^2E and $^4A_2$ levels. This can be recorded as a shift in the peak frequency (Figure 2.21). Hence, the frequency shift of the ruby lines, $\Delta\upsilon$, can be converted into a stress, σ_{ij}, using Equation 2.15 [182-184].

$$\Delta\upsilon = \Pi_{ij}\sigma_{ij} \tag{2.15}$$

where Π_{ij} are the piezospectroscopic coefficients. The piezospectroscopic coefficient for the matrix, Π_m ($= \Pi_{11} + \Pi_{22} + \Pi_{33}$) was found to be 7.59 $cm^{-1}GPa^{-1}$ [185]. Hence, by determining

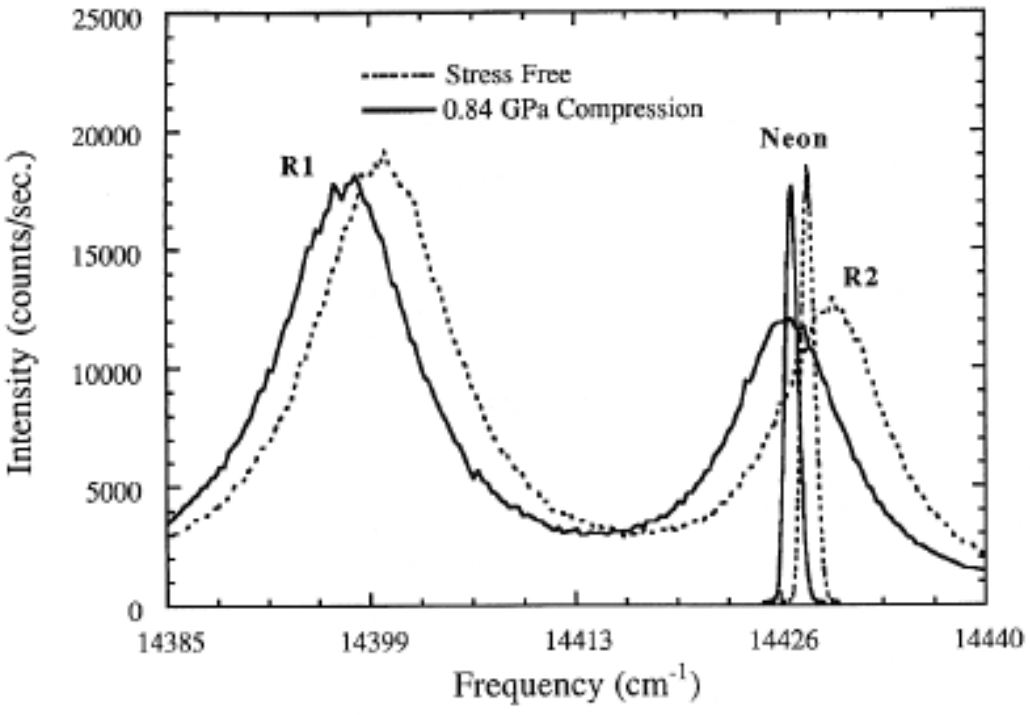


Figure 2.21: R1 and R2 peaks, and the shift due to stress, from the Cr^{3+} ions substituting onto the aluminium oxide lattice. From [185]. Permission to reproduce this figure has been granted by John Wiley & Sons, Inc.

the stress state of a given material, the residual stress can be related to the peak shift.

An alternative use of the technique is to consider the peak width. The broadening of the R1 peak can be due to plastic deformation such as dislocations or twins [147, 186-189]. In general, any microstructural feature that leads to variations in local stresses can cause additional scattering will yield an increase in the peak breadth.

2.8 Summary of Objectives

Whilst extensive microcantilever beam work has been undertaken on metals and silicon, no previous work has been published on ceramics. As many of the macroscopic mechanical properties of ceramics are dependent upon grain boundary characteristics, the technique of measuring the grain boundary toughness directly using microcantilever beams is undertaken in this project. The key objectives are:

1) There is no equation in the literature to determine stress intensity factors at failure for triangular shaped microcantilever beams in ceramics. Using compliance values from Finite Element Analysis an equation for the stress intensity factor of a triangular shaped microcantilever beam (with a straight through notch on the top surface) is derived. The stress intensity factors at failure for microcantilever beams with controlled flaws are determined using equations by Strobl et al [144] and the validity of using these equations is considered in view of the flaw dimensions relative to the beam. The approach of Matoy et al [118], which assumes the beam (with a controlled flaw) fails like one with a straight through notch, is also considered.
2) Although much of the microcantilever beam community ignore effects such as notch bluntness, notch tip residual stress, and environment assisted sub-critical crack growth, these effects are considered here. Previous corrections for notch bluntness, by Picard et al [148] and Fett and Munz [149, 150], are used and their validity assessed. The residual stress due to ion implantation is measured using optical

fluorescence microscopy, and the value is compared to previous literature values (albeit those which use different ions and fluences). Beams are tested submerged in different liquids to assess the extent of environment assisted sub-critical crack growth. Using microcantilever beams on the surface of a model sapphire grain boundary, the validity of the microcantilever beam testing technique on ceramics is considered. This is the first report of attempts to validate the technique in either metals or ceramics.

3) Using correction factors generated to take into consideration the effects described in 2), the mechanical properties of different engineering ceramics (single crystal sapphire, undoped and undoped aluminium oxide, and rare-earth doped silicon nitride) are obtained. To the author's knowledge, this is the first attempt to find fracture toughnesses of these ceramics using microcantilever beams.
4) The macroscopic fracture properties, such as flexural and compressive strength, of different ceramics are determined, and discussed in relation to the grain boundary fracture toughness and composition.
5) The damage evolution during uniaxial compression is determined ex-situ using TEM. The extent of deformation twinning before and after loading is ascertained, and discussed in light of the grain size and the ability of the double-cross slip of partial dislocations to occur. Previous work has shown contradictory results on how chromium affects the ability of deformation twins to form; hence, chromium-doped aluminium oxide is tested micro- and macro-scopically and the extent of deformation twinning determined.

The presence of microcracking after loading is considered in light of the equations by Ashby and Hallam [14]. The compressive strength of different ceramics is discussed with regards to the extent of microcracking, and the model is used to predict the fracture strength based on the propagation and interaction of microcracking during

uniaxial compression. As the equations were developed for continuum materials, the validity of the use of the equations for polycrystalline materials is discussed.

The results and discussion of these five objectives are presented in the following chapters:

In Chapter 3, the materials and techniques used in this project are outlined.

Chapter 4 presents the characteristics (such as grain size and microstructure, density, and composition) of the different materials used in this project.

In Chapter 5 the macroscopic mechanical properties, such as flexural and compressive strength, and the fracture toughness, are shown, together with the damage evolution during uniaxial compression.

Chapter 6 uses compliance values (from Finite Element Analysis) to derive an equation for the stress intensity factor of microcantilever beams with a straight through notch on the top surface. It also presents the equations from Strobl et al [144] for the stress intensity factor of a controlled flaw on the surface of a microcantilever beam.

In Chapter 7, the validity of the microcantilever beam testing is assessed. Qualitative comparison of the stress intensity factors of microcantilever beams notched at and away from a sapphire grain boundary is made. The properties such as notch bluntness, residual stress, and environment assisted sub-critical crack growth are investigated, and suitable correction factors ascertained. Finally, provisional assessment of the stress intensity factors of vacuum annealed sapphire beams is made.

Chapter 8 uses the correction factors ascertained in Chapter 7 to determine the mechanical properties of different engineering ceramics using microcantilever beams.

In Chapter 9, the various macroscale mechanical properties are discussed in light of the microscale measurements of the grain boundary toughnesses. Furthermore, the change in the grain boundary toughness with doping is discussed in view of the change in grain boundary complexions.

Chapter 10 outlines the key conclusions from the project, and suggests further experiments to be undertaken.

Chapter 3 Materials & Methods

3.1 Materials

3.1.1. AES-11C α-alumina (with and without chromia dopants)

AES-11C (Sumitomo, Japan) consisted of:

- H_2O = 0.1%
- Fe_2O_3 = 0.01%
- SiO_2 = 0.06%
- Na_2O = 0.04%
- MgO = 0.05%
- Al_2O_3 = 99.8%

Particle Size (D_{50}) = 0.45µm

Samples were produced with and without dopants. Various amounts of Cr_2O_3 (Sigma-Aldrich, 99.99%) were added; 2.0, 3.0, and 5.0wt%. Slurries with water were produced (70 wt% power), and dispersant (Dispex, 0.25wt% of powder) and binding agent (PEG, 2.0wt% of powder) were added.

Powders were ball-milled in a polyethylene bottle using alumina milling media for 24 hours (25 vol% slurry, 50 vol% media). The resultant slurry was freeze dried to remove the liquid and leave an unagglomerated powder. Powders were subsequently sieved and calcined (600^{o}C, 1 hour) to remove residual organic material, uniaxially cold-pressed (50MPa, 5 minutes, 32mm diameter die), cold isostatically pressed (CIP) (200MPa), and sintered in air (Lenton Furnace, 1600^{o}C, 2 hours, 10^{o}C/min heating rate).

Several samples were sintered at higher temperature to increase the mean grain size. An induction heated graphite chamber was used to sinter the samples (1750^{o}C, 30 minutes,

argon). As the samples were reduced by sintering in the graphite chamber, they were then annealed in air (1550^{o}C, 3 hours). Herein, these are referred to as being sintered at 1750^{o}C.

3.1.2. TM-DAR α-alumina

Taimicron TM-DAR (Taimei Chemicals Co., Ltd, Tokyo, Japan) was used to produce α-alumina samples both with and without carbon. The powder purity was >99.99% and the starting mean particle size was 150nm:

- Si = 10ppm
- Fe = 8ppm
- Na = 8ppm
- Cu = 1ppm
- Mn < 1ppm
- Th < 0.005ppm
- K = 3ppm
- Ca = 3ppm
- Mg = 3ppm
- Cr < 1ppm
- U < 0.004ppm

Two sets of samples were produced using this powder: 1) sintered in vacuum with and without carbon and 2) sintered in air, with and without chromia additions.

3.1.2.1. TM-DAR with and without carbon

0.012wt% carbon (KS6, Lonza, Germany, 6μm) was used to dope the TM-DAR powder. Undoped and doped TM-DAR powders were ball milled in a polyethylene bottle (24 hours): 100g powder, 400g alumina milling balls, 350ml ethanol, 0.25wt% MgO (UBE, Japan, 120nm mean particle size). Slurries were dried in a rotary evaporator (IKA RV10, Jencons, Germany). In order to break down agglomerates, dry ball milling was performed for 24 hours. Powders were sieved (150μm holes), and calcined (250^{o}C, 2 hours for doped, 600^{o}C for 1 hour for undoped) to remove any organic material.

Powders were uniaxially compressed (50MPa, 5 minutes, 32mm diameter die), cold isostatically pressed (200MPa), and sintered in vacuum under a graphite powder bed (Lenton Furnaces, 1500^{o}C, 1 hour, 10^{o}C/min heating and cooling rate). The graphite bed

ensured that there was no oxidation of the carbon in the doped sample. After sintering, discs were flat-bed ground to remove approximately 0.75mm of material from each face (i.e. carbon diffused region). For the SEM and FIB work, samples were cut from the inner region of the disc.

3.1.2.2. TM-DAR with and without chromia doping

The method was similar to 3.1.1. Undoped and 2.0 & 5.0wt% doped Cr_2O_3 (Sigma-Aldrich, 99.99%) slurries were produced and a dispersant (Dispex, 0.25wt%) and a binding agent (PEG, 2.0wt%) added. Powders were ball milled, pressed, CIPed, and sintered in the manner described in 3.1.1.

3.1.3. Silicon Nitride

The silicon nitride used in this project was provided by Prof. Dr. Michael J. Hoffmann from the Institute for Applied Materials, *Karlsruher Institut für* Technologie. The details of the production method are in [11].

3.1.4. Single Crystal Sapphire

Single crystal sapphire was from two sources. The microcantilever beams were milled by the author on m-, c-, and a-plane sapphire from Shinkosha, Japan. c-plane sapphire used for the diffusion bonded specimen was from Fluoroware Inc. Both were polished prior to purchase.

3.1.5. Diffusion Bonded Sapphire

Two pieces of c-plane sapphire (3.1.4.) were ultrasonically cleaned in acetone for 2 hours and annealed in air at 1200^{o}C. The pieces were diffusion bonded together with a twist angle of ≈ 20^{o} by hot-pressing (1550^{o}C, 30minutes, 20MPa, argon). The boundary was difficult to view in optical or electron microscopes; hence, after polishing with diamond lapping films to a finish of 1µm, the sample was thermal etched (1400^{o}C, 10min).

3.2. Transmission Electron Microscopy Sample Preparation

3.2.1. Dimple Grinding

Samples for microstructural analysis, including electron energy-loss spectroscopy (EELS), energy dispersive x-ray spectroscopy (EDX), and high-resolution transmission electron microscopy (HRTEM), were produced using the following method. 3mm discs were drilled from a thick (>1mm) block, and ground (SiC papers) and polished (diamond lapping films) to a finish of 1μm. The sample was turned over and thinned using SiC papers to around 200μm thickness, then to 60μm using diamond lapping film (with a finish of 1μm). The sample was dimple ground (Gatan Dimple Grinder, 3 to 1μm diamond paste) to give a central depth of 15μm. The dimple was polished for an hour on 1μm and an hour on ¼ μm diamond paste (ethanol lubricant). The sample was removed from the stub, cleaned in acetone, and ion milled (Gatan Precision Ion Polishing System (PIPS)) until a small hole appeared in the centre. A thin carbon coating was applied to reduce charging in the TEM.

To analyse the damage after uniaxial compression tests, transmission electron microscopy samples were cut from the post-tested cuboids: ≈ 1.5 (wide) x 2.5 (long) x 0.5mm (thick). Samples were thinned and dimpled in the manner described above. As the sample was too small to be placed directly into the TEM holder, the sample was secured onto a copper ring using a small amount of resin prior to ion milling.

3.2.2. Focussed Ion Beam (FIB)

A number of TEM samples were produced using Focussed Ion Beam milling (FEI FIB200). To protect the top surface during the sample preparation, a layer of platinum was deposited (Figure 3.1a). A two stage deposition was used; 0.1μm using 10pA, then 2μm using 300pA.

Material was removed on either side of the platinum using a step-pattern (≈ 15μm, beam current of 7000pA) (Figures 3.1b and c). After thinning the sample from both sides to around 200nm using a cleaning stage of 1000pA (Figure 3.1d), “goalposts” were produced in the sample by tilting to 45^{o} (300pA) (arrowed in Figure 3.1e). This had two purposes: 1) to allow

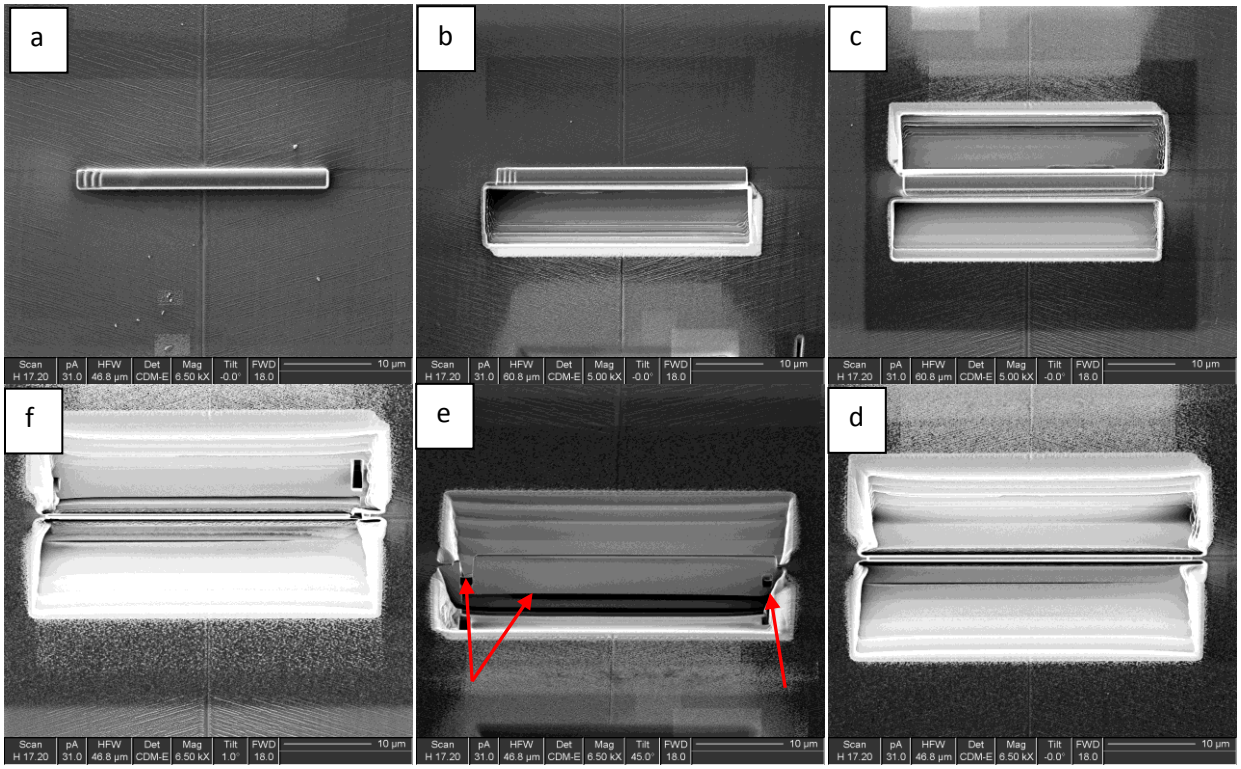


Figure 3.1: FIB images of production of a TEM sample. Clockwise from top left: a) Deposition of a Pt strip on region of interest; b) step pattern on one side and c) on the other; d) the sample is thinned to around 200nm before; e) the sample is tilted to 45° and the goalposts produced.

the sample to be removed at a later stage, and 2) allowing relaxation of the material. Thereafter, the sample was not tilted beyond 1° in order to reduce the amount of gallium implantation in the bulk of the material. The sample was thinned to 60 - 80nm using cleaning stages (1000 – 500pA). Images (short exposure times) were regularly taken through this final stage to ensure that the beam / sample had not drifted. Finally, the material above the goalposts was removed using block patterns (300pA) (Figure 3.1f).

Ex-situ liftout was performed to place the foil onto a grid. A very thin glass needle was produced and coarsely lowered to around 1mm above the foil (x5 lens). The needle was finely lowered into the trench (x40 lens). The foil attached itself to the needle due to electrostatic interactions. The needle was lifted away from the sample surface, and positioned above an amorphous carbon / copper grid. The needle was carefully lowered and, when the tip touched the carbon film, the foil detached itself. Due to the electrostatic interactions, the foil remained secured on the surface of the carbon film.

3.3. Characterisation of Materials

3.3.1. Mean grain size analysis

The mean grain size was determined using the mean-linear-intercept method (ASTM Standard E 112-88). Lines, covering at least 40 grains, were drawn over scanning electron micrographs. The number of intersections was counted, assigning 1 for every grain boundary intersected, ½ if the line ends on a grain boundary, and 1½ for triple point intersections. The mean 3-D grain size was determined using a factor of 1.57 [190]. Five different images were used per sample; the average and error presented here represented the mean and standard deviation of the five grain sizes.

3.3.2. Density

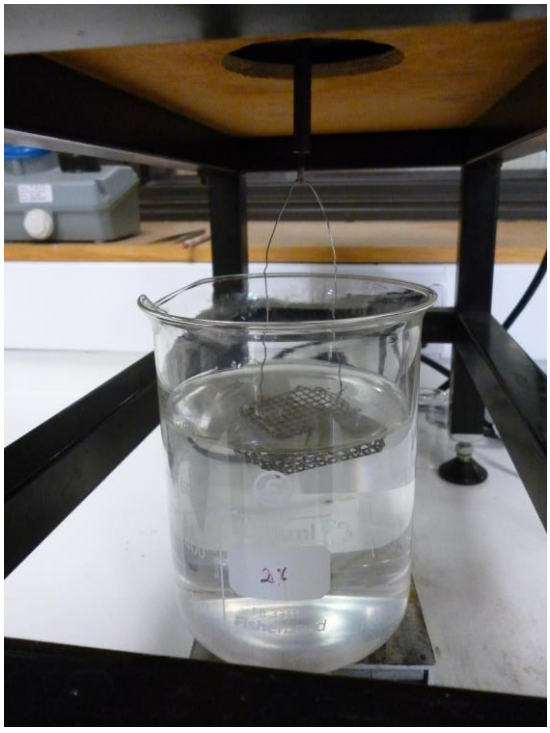


Figure 3.2: Cage in distilled water used to measure the mass of the alumina disk submerged in water.

The density of the ceramic samples was measured using the Archimedes principle. After sintering, disks were ground and polished (Buehler EcoMet 300) to a finish of 1µm. These were baked (100^{o}C, 1 hour) to remove any moisture. Subsequently, the dry mass m_{dry} was measured ten times. Samples were boiled (1 hour) to fill the internal pores with water.

A cage was suspended in distilled water, with a thin wire attached to the underneath of the weighing scales (Figure 3.2). After boiling, samples were removed and placed immediately in the cage to measure $m_{submerged}$. After the measurement was recorded, samples were replaced in the boiling water for two minutes to re-fill any pores, and the submerged mass recorded again. This was repeated ten times.

The damp mass m_{damp} was recorded by removing the sample from the water, placing both sides on filter paper and recording the mass in air. This method removed the water from the surface and surface pores.

The density of the sample was calculated using Equation 3.1.

$$\rho_{sample} = \frac{m_{dry}}{m_{damp} - m_{submerged}} \times \rho_{H2O} \quad (3.1)$$

3.3.3. X-ray diffraction

3.3.3.1. X-Ray Diffraction – Lattice parameter determination

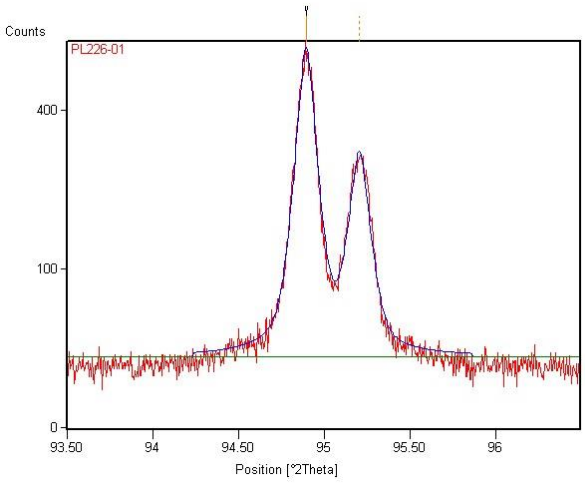


Figure 3.3: Outputted scan for the {226} planes in undoped AES-11C alumina (red) overlayed by the curve fitting (X'Pert HighScore) (blue)

The lattice parameters a & c of the α-Al_2O_3 unit cells were determined using X-ray diffraction (XRD) (Philips PW1729 X-ray Diffractometer). Scans were performed for the following planes: $\{110\}$, $\{220\}$, $\{300\}$, $\{113\}$, and $\{226\}$ (Figure 3.3). An extrapolation method was used [191, 192] to determine the lattice parameters. This alleviates the effect of absorption, a principal source of error [192].

d-spacings were calculated using Bragg's Law (Equation 3.2) and, by noting the relationship between the lattice parameters and the d-spacings for sapphire (Equation 3.3, from [193]), the lattice parameter determined.

$$d = \frac{\lambda}{2 \sin \theta} \quad (3.2)$$

$$d_{hkl} = \left[\frac{4(h^2 + k^2 + hk)}{3a^2} + \frac{l^2}{c^2}\right]^{-\frac{1}{2}} \quad (3.3)$$

where λ is the X-ray wavelength, and h, k, and l the Miller indices.

Three values of the lattice parameter a were determined for $\{110\}$, $\{220\}$, $\{300\}$. These were plotted against $\frac{\cos^2\theta}{\sin\theta} + \frac{\cos^2\theta}{\theta}$ [191, 192], and extrapolated back to zero (e.g. Figure 4.9a). Thus, an accurate value of a was ascertained.

The spacing of the $\{113\}$ planes (d_{113}) were found using the $\{113\}$ and $\{226\}$ peaks. These were plotted against the extrapolation function $\frac{\cos^2\theta}{\sin\theta} + \frac{\cos^2\theta}{\theta}$ (e.g. Figure 4.9b) and an accurate value of the d_{113} spacing found by extrapolating to zero. By noting the accurate value of a (from above), the lattice parameter c was found using Equation 3.3.

As the unit cell of the sapphire is hexagonal, the volume of the unit cell is:

$$V = a^2 c \sin 60^o \quad (3.4)$$

Thus, by noting the number and type of atoms in a unit cell, the density was found.

3.3.3.2. X-Ray Diffraction – Pole figure determination

The plane and orientation of the single crystal sapphires were determined using x-ray diffraction (Philips X'PERT MRD X-ray Diffractometer). The value of 2θ was defined for a given set of planes, and the pole figure generated by varying angles phi and psi (Figure 3.4) and recording the x-ray intensity:

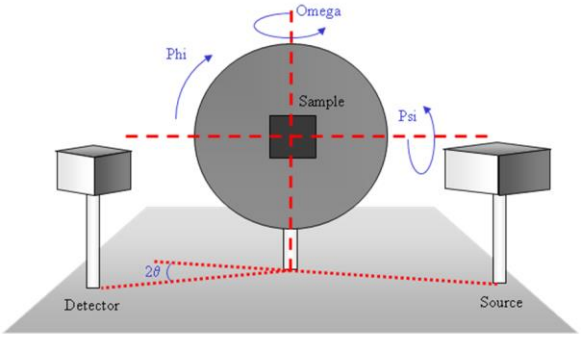


Figure 3.4: Schematic of X-ray diffraction set-up, showing Phi and Psi angles.

- Phi: - Start: 0^o End: 360^o

		-	Step size:	1^o	Time per step:	1s
-	Psi	-	Start: 0^o		End: 80^o	
		-	Step size:	1^o	Time per step:	1s.

3.3.4. Energy Dispersive X-ray Spectroscopy (EDX)

EDX in the transmission electron microscopy (TEM-EDX) was performed using JEOL 2000FX (200kV, LaB_6 source, "4L" spot size = 75nm FWHM). Spectra were analysed using INCA software with a Cliff-Lorimer thin ratio quantification method [194] (i.e. absorption and fluorescence ignored as sample is thin).

3.3.5. Electron Energy Loss Spectroscopy (EELS)

EELS was performed by Mr Ron Doole (Department of Materials, University of Oxford) using a VG HB501 microscope with a cold field emission electron source:

- Accelerating Voltage: 100kV
- Objective aperture: 3
- Condenser lens C2 7
- Spot size 4.5 – 5nm
- Convergence semiangle, α 8 mrad
- Divergence semiangle, β 13 mrad
- Beam current 150pA
- Exposure time: 2s for 270V offset spectra, 10s for 1000V offset spectra

Samples were baked *in-situ* before imaging to remove organic material.

3.3.6. Optical Fluorescence Microscopy (OFM)

Optical Fluorescence Microscopy was performed using a confocal Raman microscope (System 1000, Renishaw, UK, 633nm He-Ne laser) to assess the peak position of the Cr^{3+} fluorescence (Section 2.7). Firstly, A silicon wafer, which has a well-defined peak at $520cm^{-1}$,

was used to calibrate the set-up. Thereafter, spectra of the surface were taken centred at 14400cm^{-1}, with the stage moving the sample between each point. FocusTrack was used to ensure the spot was always focussed on the top surface.

The in-built curve fitting software was used to fit the R1 and R2 curves. In order to successfully curve fit the spectra, an intensity > 5000 a.u. was required. However, the detector was saturated if the intensity > 150000 a.u.. Hence, the exposure and laser power was optimised for each series of experiments.

3.3.7. Electron Back-scattered Diffraction (EBSD)

The relationship between the misorientation angle across grain boundaries in polycrystalline AES-11C and the measured stress intensity factor at failure was investigated (Section 8). As the thin layer of platinum, deposited prior to microcantilever beam production to reduce the drift, was too thick to successfully record Kikuchi patterns, the following procedure was used:

1. Produce an array of nanoindents (MTS NanoindenterXP, Berkovich tip) on the surface of thermally etched AES-11C.
2. Deposit a thin layer of carbon on the surface.
3. Record several EBSD maps (JEOL JSM-6300, EDAX-TSL EBSD system) at 20kV and 6 x 10^{-8} Å.
4. Deposit 10nm of platinum on the tip surface.
5. Using the nanoindents as location markers, locate the grain boundaries recorded in the EBSD maps. Produce microcantilever beams at these boundaries.

EBSD was also performed on the diffusion bonded sapphire to determine the misorientation angle. The sample was coated with a thin layer of carbon prior to EBSD analysis.

3.4. Macroscopic Mechanical Testing - Sample Preparation

3.4.1. Uniaxial Compression

Disks were produced and flatbed ground to give parallel sides (≈ 4mm thick), and polished to a finish of 1µm (Buehler EcoMet 300) on both sides. These were the faces in contact with the anvils during compression.

A disk was fixed into an aluminium holder using wax, and cut every 4mm (Buehler Isomet 5000). The holder was rotated 90^{o}, and the sample cut again giving perpendicularly sided cuboids.

The blocks were removed, and polished on the four cut faces (Buehler EcoMet 300) to a finish of 1µm. The resultant cuboid size was around 3.5 x 3.5 x 4mm. Optical microscopy was performed to assess the polishing finish and to determine the shape of the block. Samples with a corner angle lower than 90^{o} and / or sides that were not parallel were not tested.

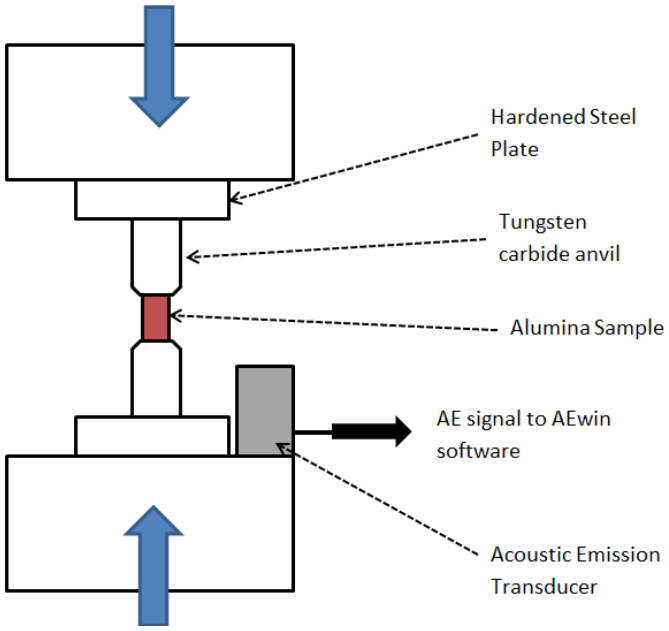


Figure 3.5: Schematic of uniaxial compression set-up.

3.4.2. Tungsten Carbide Platens

Tungsten carbide (Hartmetall-Gesellschaft, Grade K20, Vickers Hardness HV30 = 1700) anvils were produced to compress the alumina cuboids (Figure 3.5). Cylinders (15mm long, 10mm in diameter) were flat bed ground on both circular faces to give parallel, defect free surfaces. A taper of angle 34^{o} was produced (Figure 3.5); this reduced the spalling away of WC during loading.

3.4.3. Four-point bending beams – Fracture Strength

Disks were flat bed ground and polished (Buehler EcoMet 300) on both faces to a finish of 1µm. These were cut (Buehler Isomet 3000) into beams of around 14mm x 2mm x 1.5mm. Beams were polished on the other two sides (Buehler EcoMet 300) to a finish of 1µm. Optical microscopy was performed to assess the finish and whether the beams were parallel sided.

3.4.4. Four-point bending beams – Fracture Toughness

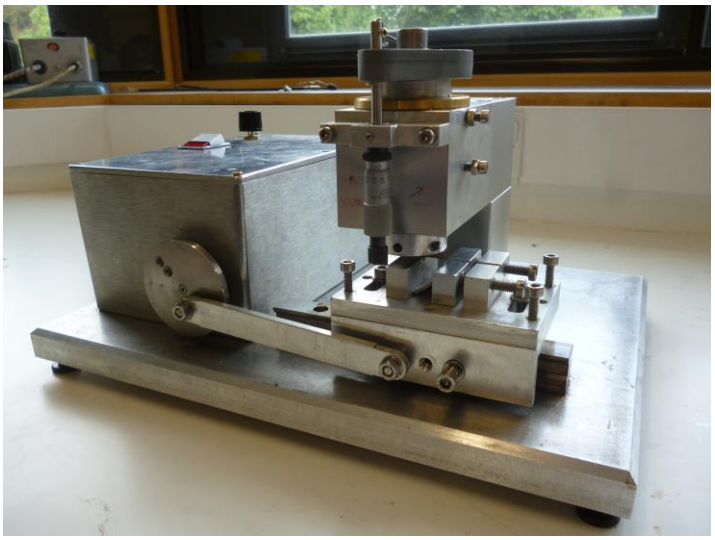


Figure 3.6: In house produced notching machine used to produce macroscopic fracture toughness samples

Disks were flat bed ground and polished on one side (Buehler EcoMet 300) to a finish of 1µm and cut (CapCo) to a size of 25mm x 3.5mm x 2.5mm.

An in-house produced notching machine (Figure 3.6) was used to notch the polished face of the beam. A razor blade was attached to the head, and lowered onto the surface of the beam. A coarse notch (≈ 0.5mm deep) was produced using 6µm diamond paste with ethanol lubricant, and subsequently polished using a new razor blade with ¼µm diamond paste. The resultant notch was both long (thus minimising the errors in the calculations) and sharp. Optical microscopy was performed to image the notch.

3.5. Macroscopic Mechanical Testing

3.5.1. Uniaxial Compression

Alumina samples were uniaxially compressed (Instron 5582 UTM, 100kN load cell, 5μm/s) between tungsten carbide anvils (Figure 3.5). An acoustic emission sensor (R15α, Physical Acoustics, 150kHz resonant frequency) was placed close to the anvil, and coupled with the steel base using vacuum grease. Load and displacement (Bluehill) and acoustic emission (AEwin for USB Version E3.34, Physical Acoustics) were recorded throughout a test. Several samples were tested until failure, whereas others were stopped at various loads.

3.5.2. Four-point bending – Flexural Strength & Toughness

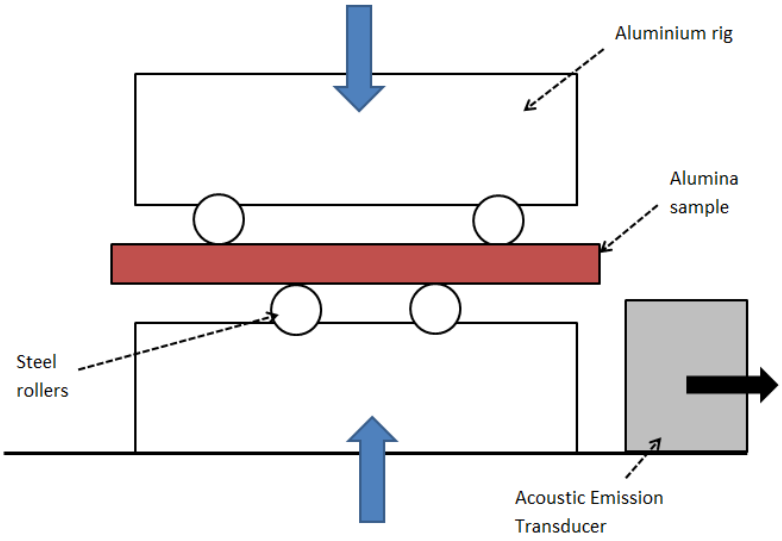


Figure 3.7: Schematic of flexural strength and toughness set-up.

Alumina samples were tested in four-point bending (Denison-Mayes rig, 3kN load cell) using an aluminium rig with steel rollers (Figure 3.7). An extensometer was used to externally measure the displacement during loading. An acoustic emission sensor (R15α, Physical Acoustics) was coupled to the steel base using vacuum grease.

Beams were tested using the following rigs (S_i & S_o are the inner and outer spans respectively). Strength: S_o = 10.05mm, S_i = 5.95mm. Fracture toughness: S_o = 20mm, S_i = 10mm.

The load and displacement (Rubicon), and acoustic emission (AEwin for USB Version E3.34, Physical Acoustics) was recorded throughout the test. Samples were tested until failure.

The fracture strength, σ_f, is determined from Equation 3.5.

$$\sigma_f = \frac{3PA}{BH^2} \tag{3.5}$$

where P is the load, $A = ½ (S_o - S_i)$, B the breadth and H the height of the beam [3].

For the notched beams, the fracture toughness, K_{Ic}, is:

$$K_{Ic} = \frac{F(S_o - S_i)}{bh^{1.5}} \frac{3\sqrt{\alpha'}}{2(1-\alpha)^{1.5}} Y \tag{3.6}$$

S_o and S_i are the outer and inner spans, $\alpha' = \alpha/h$ where α is the notch depth, and $Y = 1.9887 - 1.326\alpha' - (3.49 - 0.68\alpha' + 1.35\alpha'^2)\alpha'(1-\alpha')(1+\alpha')^{-2}$ [195].

3.5.3. Four-point bending – Weibull analysis

Due to the variation in size and type of flaw in a ceramic and the fact that it is difficult to determine the critical flaw size prior to loading, an empirical distribution is used to describe the strengths. This is the Weibull distribution [196].

The following approach was undertaken to assess the distribution of failure strengths:

1) Rank the failure strengths for a given material from lowest to highest (N_f).
2) The failure probability for each, P_f, is given by the median rank plotting positions: $P_f = 1 - \frac{N_f - 0.3}{N + 0.4}$ where N was the total number of samples [197, 198].
3) Plot $\ln\ln\left(\frac{1}{1-P_f}\right)$ against $\ln(\sigma_f)$. The gradient of the curve is the Weibull modulus, m.

3.6. **Microcantilever Beam production**

Microcantilever beams with a uniform triangular cross-section were produced using Focussed Ion Beam milling (FEI FIB200, 30kV).

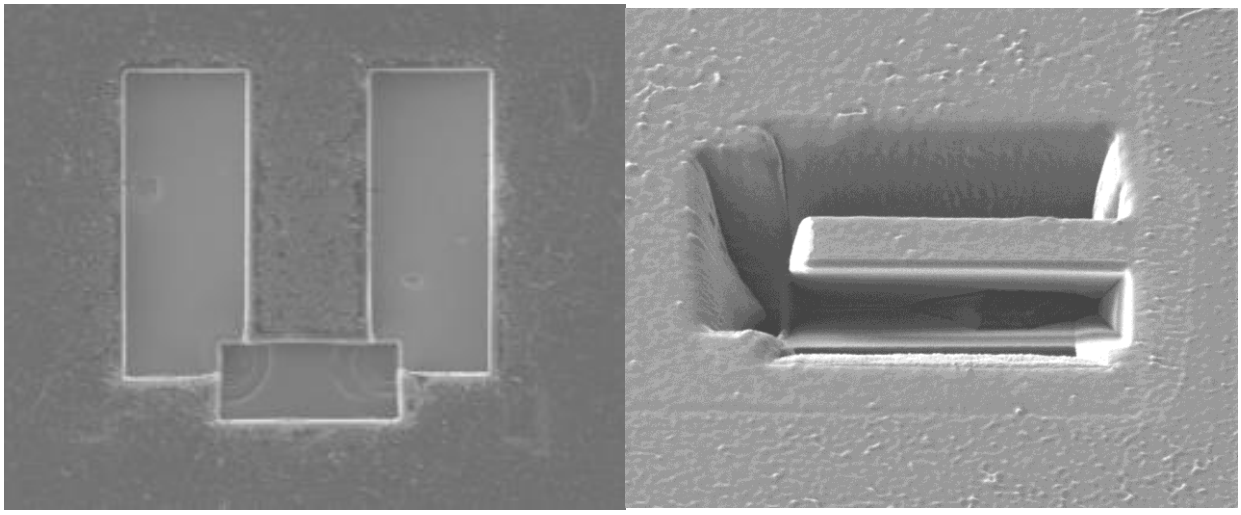


Figure 3.8: FIB produced microcantilever beam: a) coarse trenches milled at the surface, and b) after undercutting at 45^{o}

To reduce the extent of drifting during FIB milling, a 10nm layer of platinum was deposited on the top surface prior to milling (Cressington 208HR high resolution sputter coater).

Firstly, a U-shaped series of trenches was produced (7000pA beam current); the two long trenches were ≈ 5 x 25µm the short trench ≈ 4 x 8µm (all around 8µm deep) (Figure 3.8a). Beams were tilted to 45^{o}, and rotated 90^{o}. The x-direction was aligned with the edge furthest from the screen (top edge in Figure 3.8b) (this reduced beam tapering). The beam was undercut (5000pA) to a

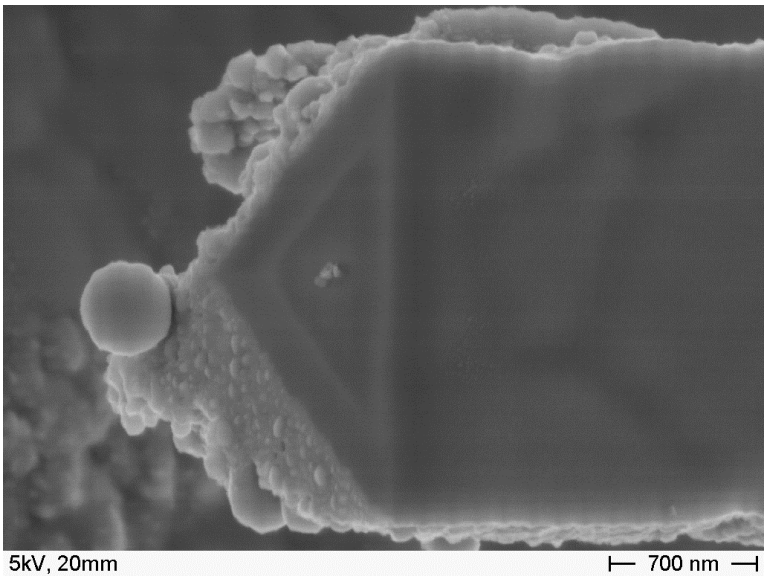


Figure 3.9: SEI (JEOL 840F) of microcantilever beam, titled to 50^{o}, showed redeposited material underneath beam after undercut

depth of ≈ 10µm. The sample was rotated 180° and the process repeated.

There was a significant amount of redeposited material on the underneath of the beam after the undercut (Figure 3.9). This was removed by tilting to 45° and using a clean-up cut (CUC) (1000pA, 10µm deep). The sample was rotated 180° and the process repeated.

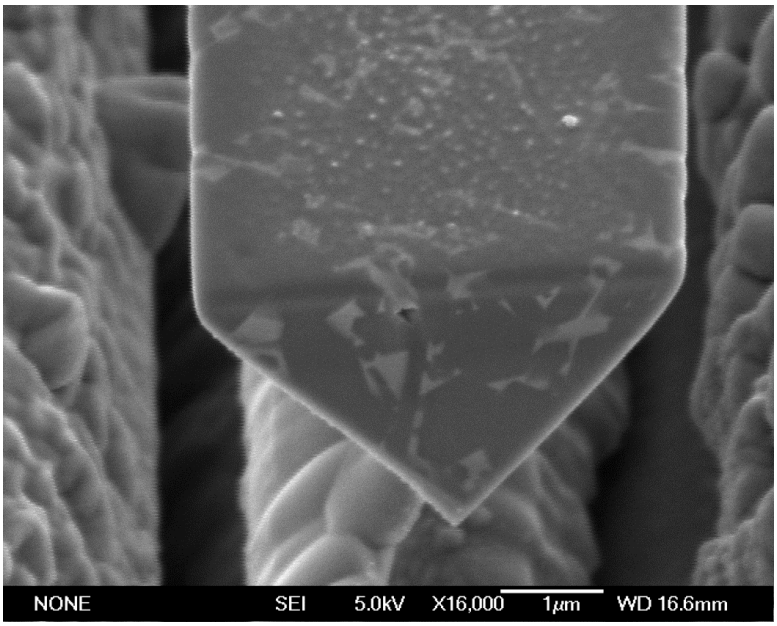


Figure 3.10: SEI (JEOL 6500F) of silicon nitride microcantilever beam, tilted to 50°, showing the triangular cross section and the relative lack of redeposited material after the final clean

Thereafter, the redeposited material at the free end of the beam was removed (0° tilt, 1000pA, 10µm depth, cleaning towards the fixed end).

Often, after the final cleaning of the free end, redeposited material had formed underneath the beam again. The sample was tilted to 45° and the CUC repeated. This produced a beam with a uniform triangular cross section, of dimensions approximately 3 x 4 x 25µm, that was relatively free of redeposited material (Figure 3.10).

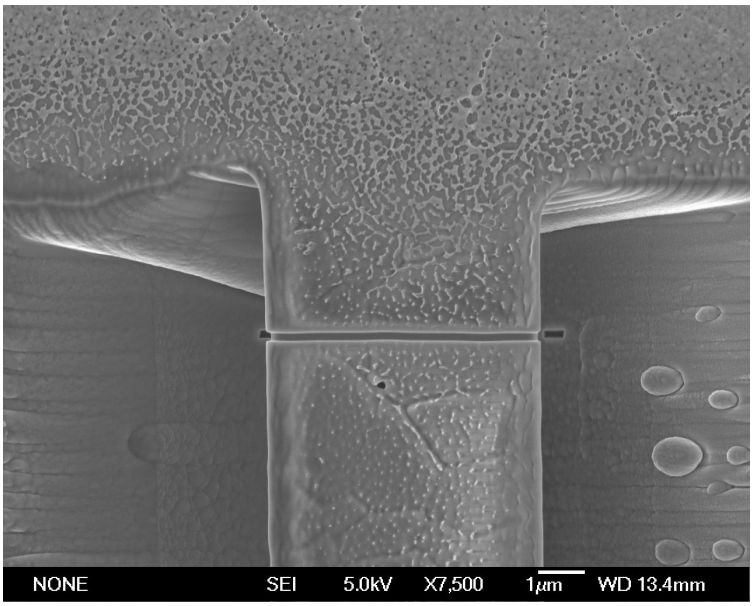


Figure 3.11: SEI (JEOL 6500F) of the top surface of a microcantilever beam showing a straight through milled FIB notch

Throughout the production, images were taken to ensure that the beam had not drifted. As the FEI FIB200 was not a dual-beam FIB/SEM, the gallium ions were used to image the

beam. Short exposures were performed to restrict this additional damage to the beam surface.

3.6.1. FIB milled notches

FIB (FEI FIB200, 30kV) notches were milled into the top surface of the beam. Most of notches were milled with 10pA, with several beams notched with 100 and 1000pA.

At a zero degree tilt, a straight line mill section was drawn across the beam and milled to a depth of around 0.3µm (Figure 3.11). Some notches were produced which did not cross the whole beam; these were termed “controlled flaws”. The same straight line mill was used for these.

3.7. Nanoindenter Method

3.7.1. Fracturing Microcantilever Beams

NanoindenterXP MTS (Berkovich tip) was used to scan and indent the surface of the microcantilever beam. The sample was placed in a metal holder, and mounted into the

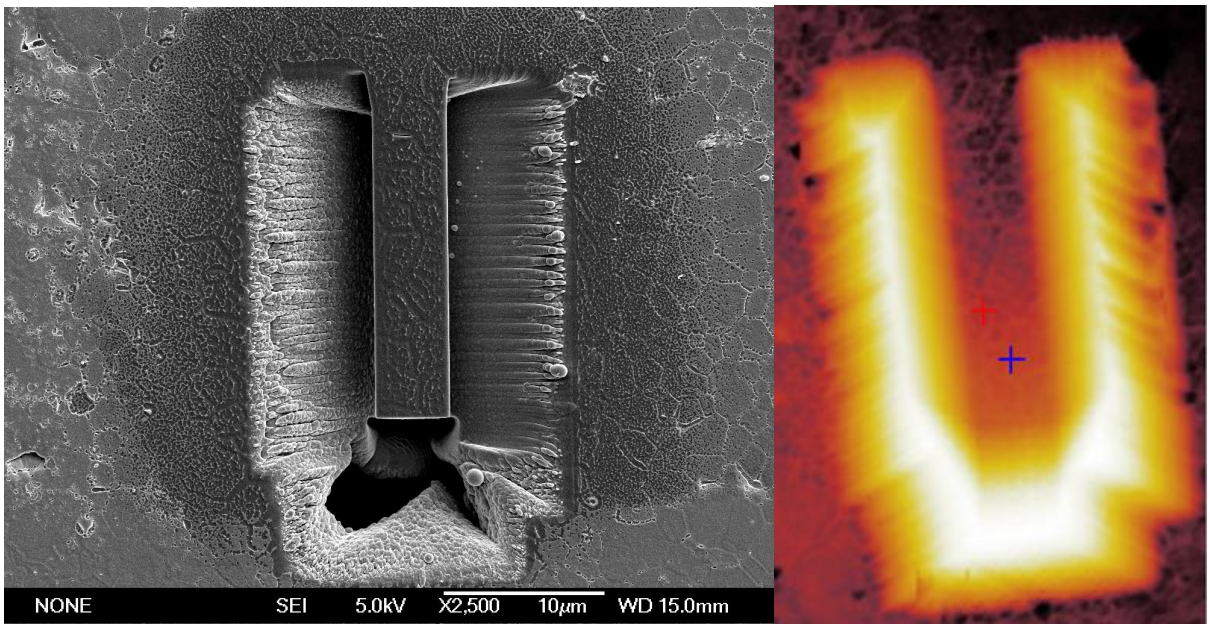


Figure 3.12: a) SEI (JEOL 840F) of a polycrystalline alumina beam, and b) the surface profile of the beam from the nanoindenter. The red cross was the centre of the scan, and the blue cross was the position of indentation.

NanoVision stage (flatness of travel 1-2nm, accuracy 0.01%). This was loaded into the nanoindenter, and the stage initialized. After locating the surface of the sample (x10 lens), the indenter tip-to-microscope calibration was performed (this correction was imperative in order to place the indenter tip on the desired part of the surface). Once performed, the optical lens was changed to x40 and the calibration repeated.

The indenter tip was engaged on to the sample surface, typically 30 - 35µm away from and 7-8 µm above the centre of the beam. The beam was scanned using the following parameters:

- Scan X Data Dimension: Scan line every ¼ µm
- Scan Y Data Dimension: 250
- Scan Y Scan Time: 2s
- Scan Load: 3µN
- Surface Stiffness: 250 N/m

One common problem during scanning was that, although the tip successfully engaged with the surface, it lost contact during the first few initial scans. When this occurred, the load and the scan time were increased in order to help the tip stay in contact with the surface. Scanning was vastly improved if the scan started from the fixed end of the beam and ran parallel to the beam. The beam was indented (at blue cross in Figure 3.12b):

- Displacement rate: 5nm/s
- Surface approach velocity: 10nm/s
- Surface approach detection stiffness: 200N/m

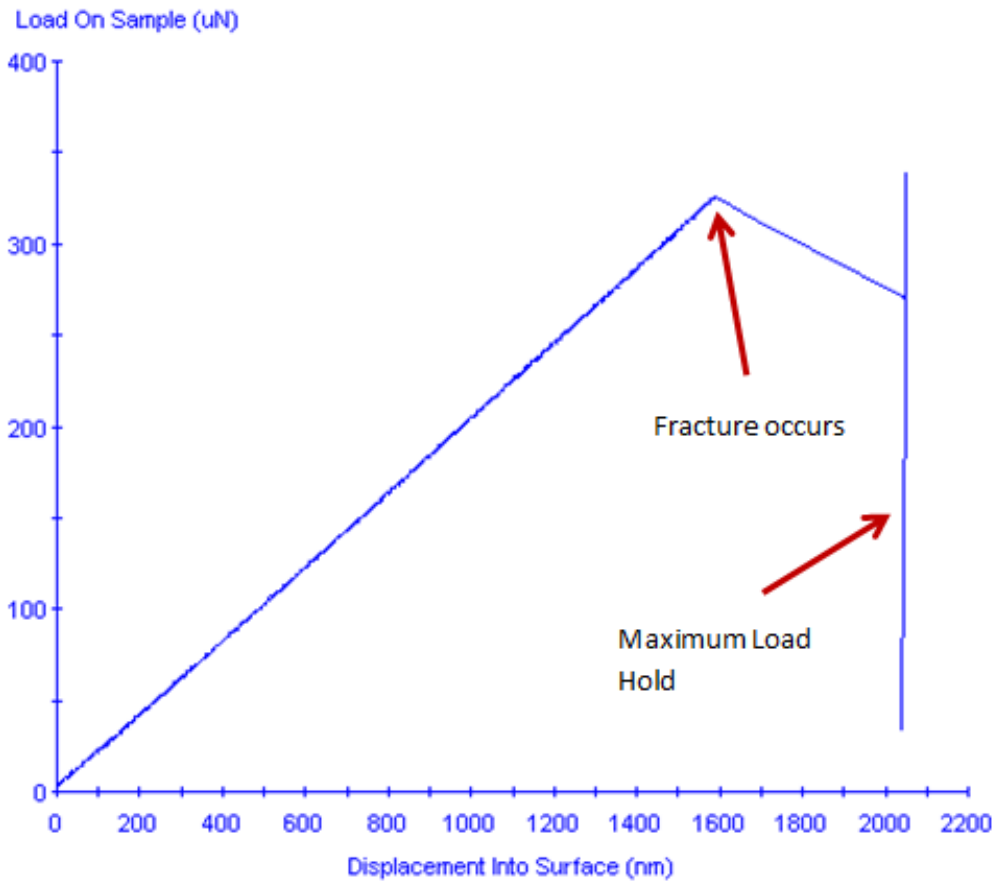


Figure 3.13: A typical load-displacement curve for a microcantilever beam

After failure, the NanoVision software held the maximum load and measured the thermal drift. Thereafter the sample was unloaded and the tip returned to the engage height. The load-displacement curves (Figure 3.13) were generated and exported for analysis.

3.7.1.1. Fracturing beams submerged in water or silicone oil

Tests were performed submerged in water or silicone oil following a similar method to that described above. The x40 lens was not used because the working distance was very small. After locating the position of the beams using the x10 lens and performing the calibration, several drops of liquid were placed on the surface of the sample. The tip engage was performed through the liquid; the liquid covered the tip throughout the test.

3.7.1.2. Determining the mechanical properties of the microcantilever beams

The width and height of the beam were measured from scanning electron micrographs of the free end, tilted at an angle of 50^o (e.g. Figure 3.10). The correct height was ascertained by dividing by $\sin(50^o)$. Occasionally there was a tapering of the beam. To overcome this, the dimensions of the fracture surface were measured. The height could not be accurately measured from fracture surfaces, due to the effect of the cantilever curl [199, 200]. Hence, the width of the beam at the fracture end was measured and, by determining the height-to-width ratio from the free end, the height of the beam at the fracture surface estimated. These were the dimensions used to determine the mechanical properties. From inspection of Equations 3.7 and 3.8, the height and width of the beam have a large effect on the ascertained mechanical property. The resolution of the scanning electron images was such that there was some error in measuring the dimensions. This was further hampered with the presence of redeposited material at the sides or underneath the beam (Figure 3.9). Hence, dimensions were measured carefully and consistently.

The following method was used to determine the distance from the fixed end to the indenter tip:

1. Four characteristic distances were measured on the SEI (in microns) (Figure 3.14a). From left to right: 26.7, 32.7, 31.8, and 27.7µm.
2. The same characteristics lengths were measured on the scan profile (in pixels) (Figure 3.14b). From left to right: 284.5, 361.0, 356.4, and 312.8.
3. By comparing the two sets of lengths, a conversion for pixels per micron was found: 11.15, 11.04, 11.21, 11.30, giving an average of 11.17 pixels per micron.
4. The indenter position to fix end length was measured on the scan profile in pixels (202.81), and converted into microns: 18.15µm.

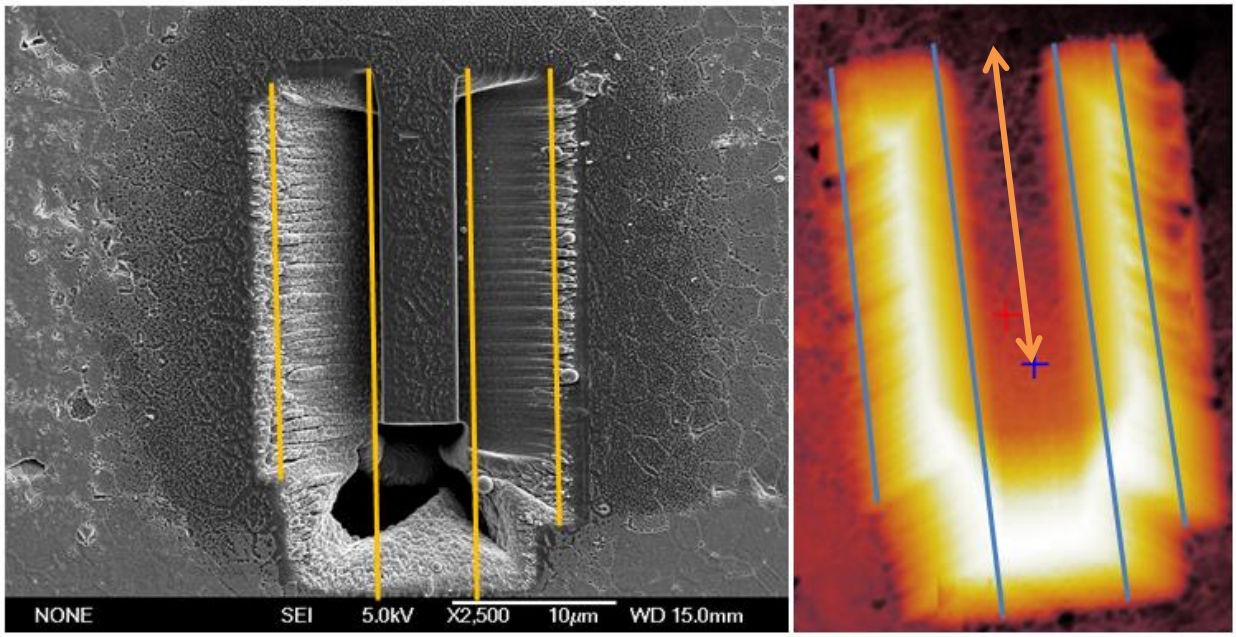


Figure 3.14: Comparison of SEI and surface profile showing how the indenter position to fixed end length was measured

Equations 3.7 and 3.8 were used to determine the Young's modulus, E, and strength, σ_f, respectively (see Appendix 3.1)

$$E = \frac{F}{D_{true}} \frac{12L_{el}^3}{wh^3} \tag{3.7}$$

$$\sigma_f(L_{fr}) = \frac{12F_{max}L_{fr}}{wh^2} \tag{3.8}$$

where F_{max} is the maximum indenter tip load, D_{true} the displacement of the beam at the indenter tip when $F = F_{max}$, $L_{el,\,fr}$ the indenter tip to fixed end and broken point distance respectively, and w & h the width and height of the beam respectively.

Finite Element Modelling (LS-DYNA) analysis (performed by Simone Falco, Engineering Department, University of Oxford) of the deflection of the microcantilever beam showed that there was a discrepancy between the Young's modulus of a perfectly encastré beam (fully bound at the fixed end) and a more realistically supported beam with deflections in the material behind the fixed end possible; this was discussed in Section 2.6.2. The extent of this discrepancy correlated with the aspect ratio (fixed-end-to-indenter-tip length to beam width)

(Appendix 3.2). Hence, as the simple beam theory (Equation 3.7) underestimated the Young's modulus of the microcantilever beam, a correction factor was used; the value of this was dependent upon the aspect ratio of the beam.

3.7.1.3. Determining the fracture toughness of the microcantilever beams

Using Finite Element Modelling (LS-DYNA) to simulate the stiffness of the beam with varying notch depths and position, a compliance calibration method (Section 2.7) was used to determine the stress intensity factor at failure with the various beam properties (Section 6.1) (Equation 3.9).

$$K = \frac{13.44\sqrt{\pi}\, L_{fr} F\sqrt{\alpha}}{h^2 w}\left(1 + 0.123\alpha' + 5.456\alpha'^2 + 0.073\alpha'^3 - 0.023\alpha'^4\right) \quad (3.9)$$

where $\alpha' = \alpha/h$, with α being the depth of the notch measured using SEM after fracturing.

3.7.2. Nanoindentation

Nanoindentation on the surface of the sample was performed (NanoindenterXP MTS, Berkovich tip) using the following method:

1. After loading the sample in the stage, the surface of the sample was found (x10 lens).
2. An indenter-to-microscope calibration was performed by indenting the surface 3 or 5 times, and manually selecting the position of the central indent.
3. The x40 lens was inserted, and the calibration repeated.
4. Using the Batch mode, the position of several indents can be made on the surface. The indentation depth of each of these was pre-defined.

The following parameters were used:

- Amplitude of oscillation of tip 2 nm
- Frequency of oscillation of tip 45 Hz
- Projected area of indent (100nm depth) after calibration 0.78 μm^2

- Ratio of projected nanoindent area to projected area if perfect Berkovich (= 24.5 x 100nm^2) 3.17
- Projected area of indent (1100nm depth) after calibration 35.84 μm^2
- Ratio of projected nanoindent area to projected area if perfect Berkovich (= 24.5 x 1100nm^2) 1.21

Continuous stiffness and hardness measurements were recorded due to the harmonic force applied to the tip during loading.

3.8. Relative Humidity during microcantilever beam testing

The relative humidity was measured (OMEGAETTE HH311, OMEGA) over the microcantilever beam testing. Excluding results from the first 30 minutes for each test (during which the system acclimatised), there was little variation during a day. However, there was significant variation day-to-day (seemingly independent of the external weather). Averaging over results from several days, the relative humidity was (52 +/- 8) %.

Chapter 4 Characterisation of Materials

In this chapter, the following characteristics of the single crystals and polycrystalline ceramics used in this project are detailed:

1) Grain size of polycrystalline alumina
2) Density (from X-ray diffraction) and relative density (from Archimedes method) of polycrystalline alumina
3) Microstructural analysis of polycrystalline alumina using Transmission Electron Microscopy
4) Energy-dispersive x-ray spectroscopy (EDX) and electron diffraction analysis of annealing twins
5) Optical fluorescence microscopy (OFM) of sapphire and alumina
6) Diffusion bonded sapphire: TEM, Electron back-scattered diffraction (EBSD), and EDX
7) Analysis of FIB affected regions in sapphire: Redeposited and Implanted
8) Composition of polycrystalline alumina grain boundaries: Electron energy-loss spectroscopy (EELS) and EDX
9) Characteristics of FIB-affected sapphire after vacuum annealing
10) Nanoindentation response of polycrystalline alumina and FIB damaged sapphire

4.1 Grain size analysis

Following the Mean-Linear-Intercept (MLI) method described in Section 3.3.1., the mean grain size was determined from scanning electron images (SEI).

4.1.1. Pressurelessly sintered AES-11C at 1600°C & 1750°C

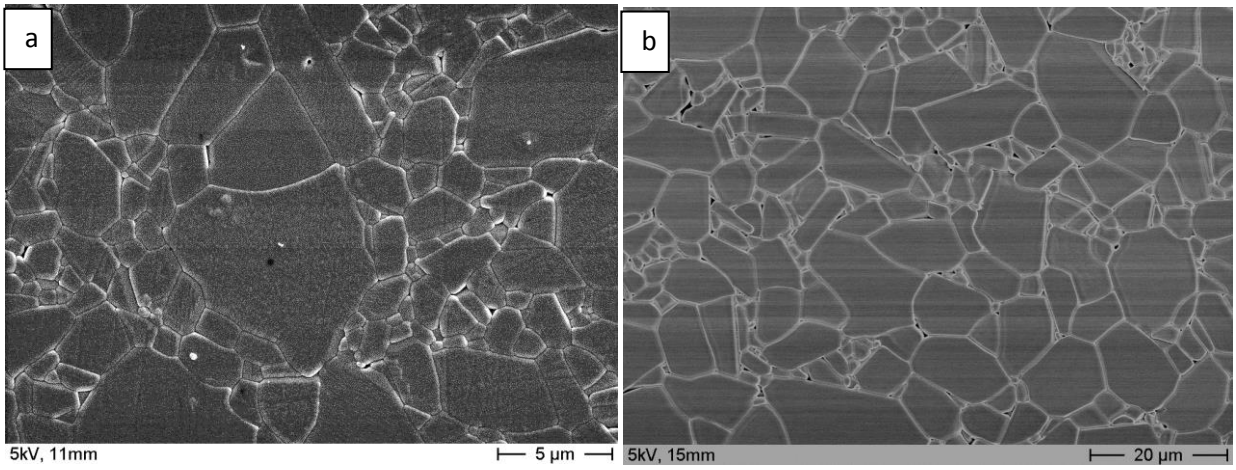


Figure 4.1: SEI (JEOL 840F) of microstructure of undoped AES-11C; a) sintered at 1600C for 2 hours and b) annealed at 1750°C in argon for 30minutes then 1550°C in air for three hours (both thermal etch at 1550°C for 30min)

The mean grain size was (2.7 +/- 0.9) µm for 1600°C and (7.6 +/- 2.1) µm for 1750°C. SEIs of the two microstructures (Figure 4.1 a&b) showed a wide range of grain sizes; undoped AES-11C was bimodal with a significant number of abnormal grains.

4.1.2. AES-11C with chromia doping pressurelessly sintered at 1600°C

AES-11C alumina with varying levels of Cr_2O_3 additions (2.0, 3.0, 5.0 wt%) was pressurelessly sintered at 1600°C. The was a change in the mean grain size with amount of chromia (Figure 4.2). The distribution of grain sizes reduced with the addition of chromium oxide, with fewer abnormal grains being present in the high chromia alumina (Figure 4.3)

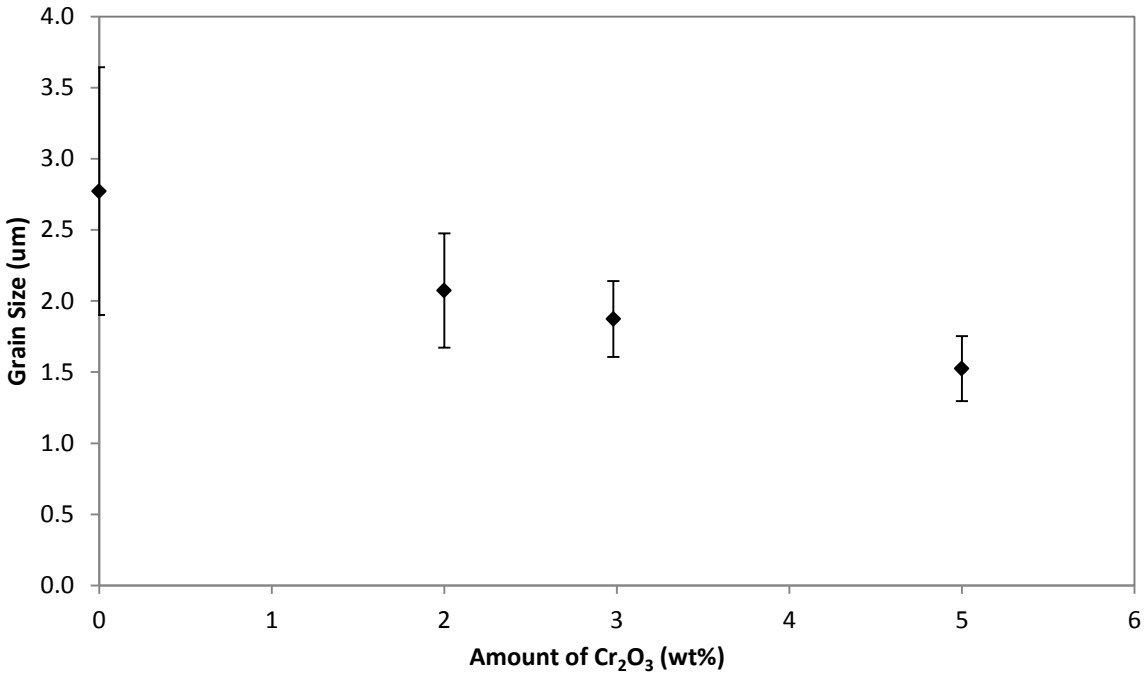


Figure 4.2: Change in the mean grain size (with standard deviation) in AES-11C with the addition of Cr_2O_3.

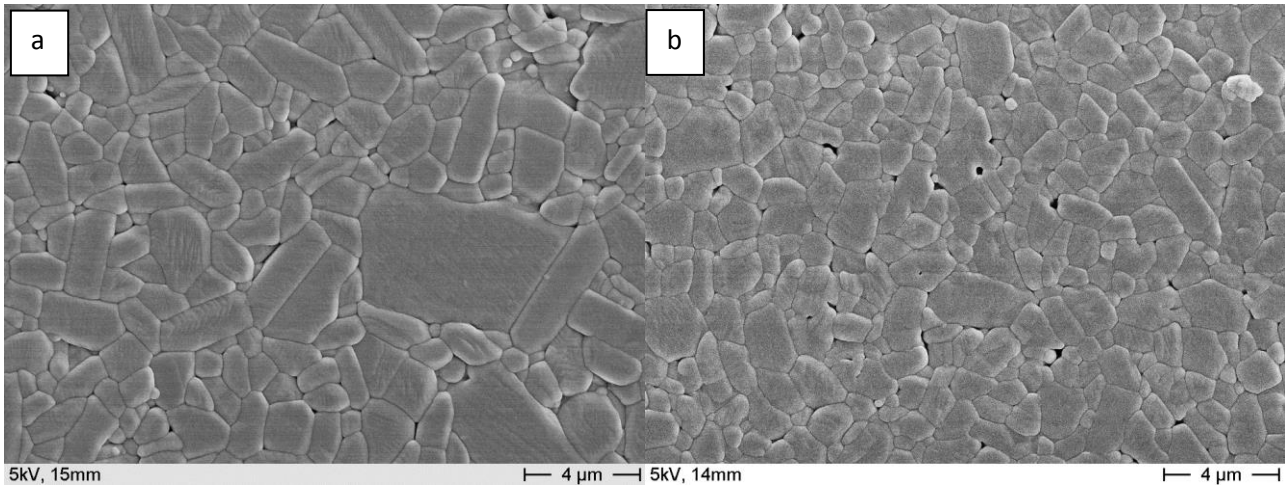


Figure 4.3: SEI (JEOL 840F) of microstructure of a) 3.0wt% and b) 5.0wt% Cr_2O_3 doped AES-11C, sintered at 1600C for 2 hours (thermal etch at 1550°C for 30min)

4.1.3. AES-11C with chromia doping pressurelessly sintered at 1750°C

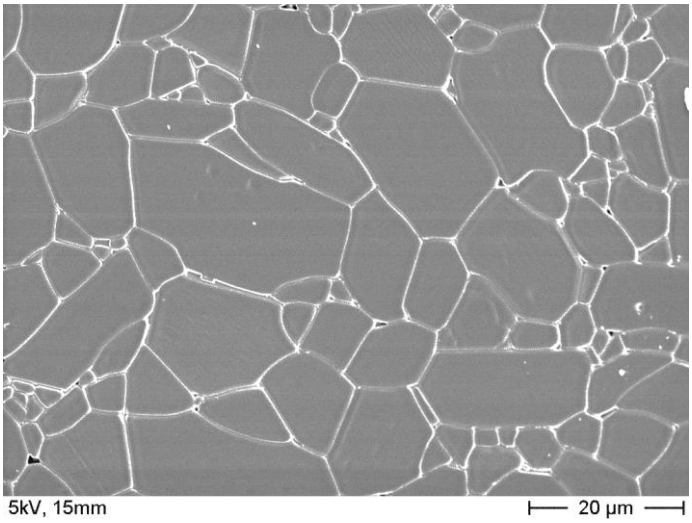


Figure 4.4: SEI (JEOL 840F) of microstructure of 2.0wt% Cr_2O_3 doped AES-11C annealed at 1750°C in argon

AES-11C with 2.0wt% Cr_2O_3 additions was sintered at 1750°C (Figure 4.4). The average grain size was (10.6 +/- 2.9) µm. Although, after sintering at 1600°C, the grain size was lower for the 2.0wt% doped than the undoped AES11-C, after the 1750°C anneal the grain size was significantly larger than the undoped equivalent.

4.1.4. Pressurelessly Sintered TM-DAR at 1600°C and 1750°C

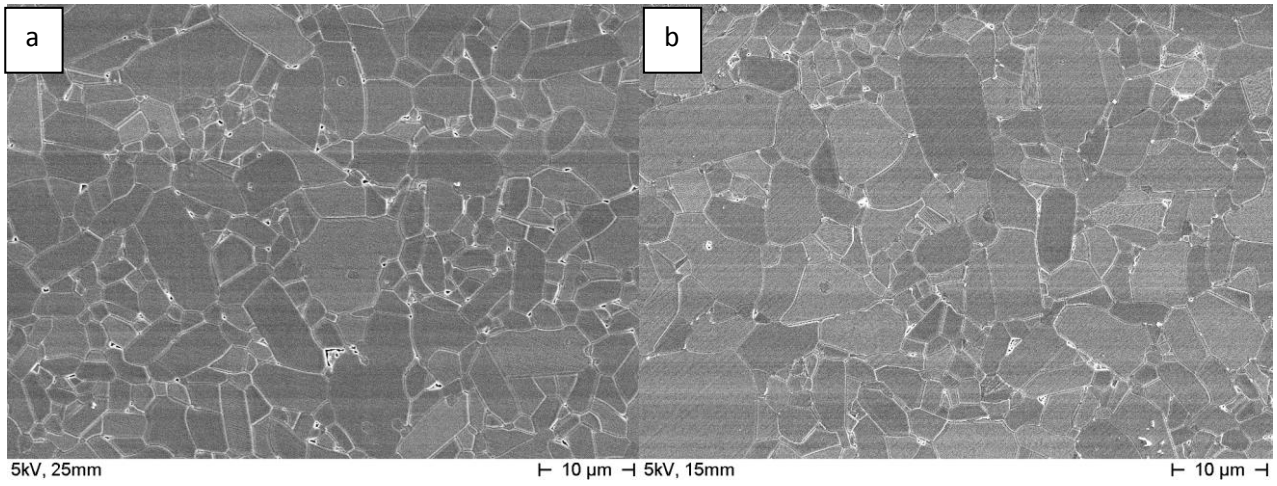
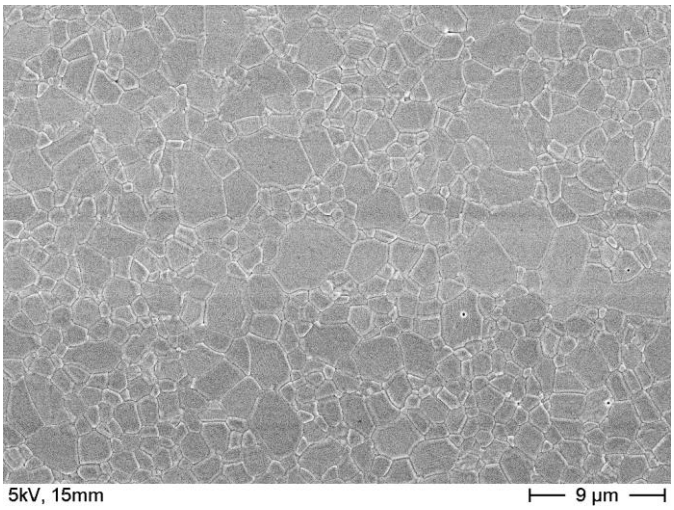


Figure 4.5: SEI (JEOL 840F) of TM-DAR sintered a) at 1600°C in air and b) at 1750°C in argon, then 1550°C in air.

The mean grain size was determined as (4.3 +/- 0.7) µm and (5.1 +/- 0.9) µm for the 1600°C and 1750°C sintered undoped TM-DAR respectively. The annealing at 1750°C in argon had a much smaller impact on the mean grain size and distribution than occurred in AES-11C

(Figure 4.5). Although there was still some abnormal grain growth, the extent was far lower than in AES-11C for both annealing temperatures.

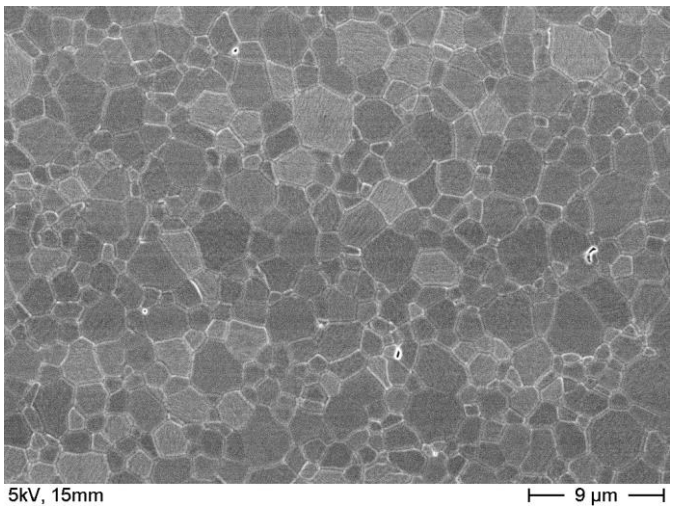
4.1.5. Pressurelessly Sintered TM-DAR at 1500°C in vacuum



TM-DAR was sintered in vacuum at 1500°C for 1 hour. The mean grain size was (2.2 +/- 0.2) µm. This value, and the shape of the grains, was consistent with work performed previously which used the same processing techniques [10].

Figure 4.6: SEI (JEOL 840F) of undoped TM-DAR sintered at 1500°C in vacuum

4.1.6. Pressurelessly Sintered TM-DAR with 0.012wt% carbon at 1500°C in vacuum



TM-DAR doped with 0.012wt% carbon was sintered in vacuum at 1500°C for 1 hour (Figure 4.7). The mean grain size was determined as (2.4 +/- 0.2) µm; within the standard deviation, this was consistent with the undoped TM-DAR.

Figure 4.7: SEI (JEOL 840F) of 0.012wt% carbon doped TM-DAR sintered at 1500°C in vacuum

4.1.7. Pressurelessly Sintered TM-DAR with varying amounts of chromia

The addition of chromia to TM-DAR, sintered at 1600^{o}C in air, reduced the mean grain size. The mean grain size was (3.9 +/- 0.5) µm and (3.8 +/- 0.4) µm for 2.0 and 5.0wt% dopant respectively.

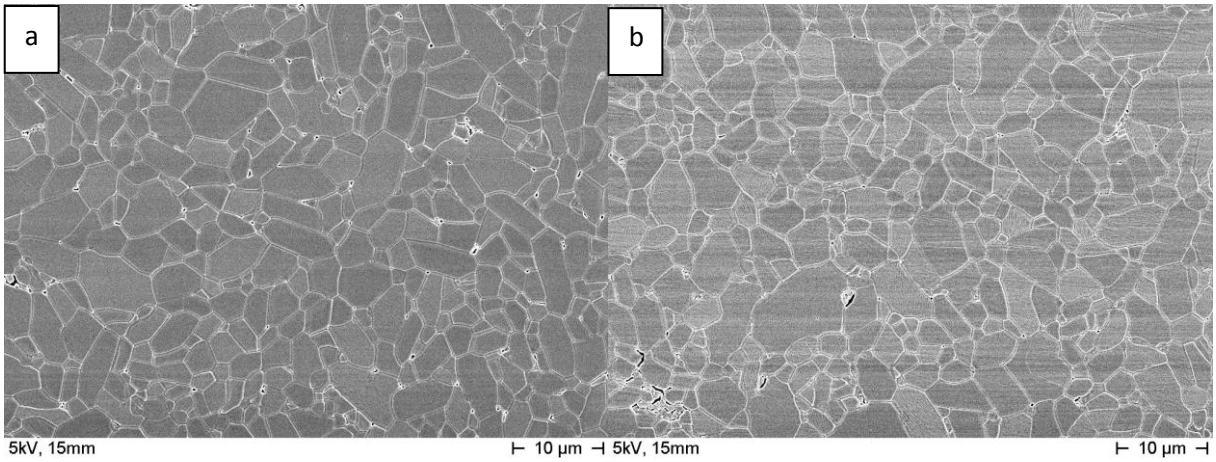


Figure 4.8: SEI (JEOL 840F) of a) 2.0wt% and b) 5.0wt% Cr_2O_3 doped TM-DAR sintered at 1600^{o}C in air

4.2. X-Ray Diffraction and Density of materials

Using the extrapolation function method (Section 3.3.3.1.), the lattice parameters of the different aluminas were determined. By using these to find the true density of the material, the relative density was found (assuming no significant impurities, vacancies etc.).

The following terms are used:

- *True Density*: Measured from XRD, this represents the maximum possible density achievable.
- *Measured Density*: Measured from Archimedes principle.
- *Relative Density*: Measured density / true density

4.2.1. Pressurelessly Sintered AES-11C

The lattice parameter a and the d_{113} spacings for pressurelessly sintered AES-11C were found (Figure 4.9): a and c were (4.7673 +/- 0.0001) Å and (13.0268 +/- 0.0009) Å respectively. The true density of AES-11C was (3.9620 +/- 0.0003) gcm^{-3}.

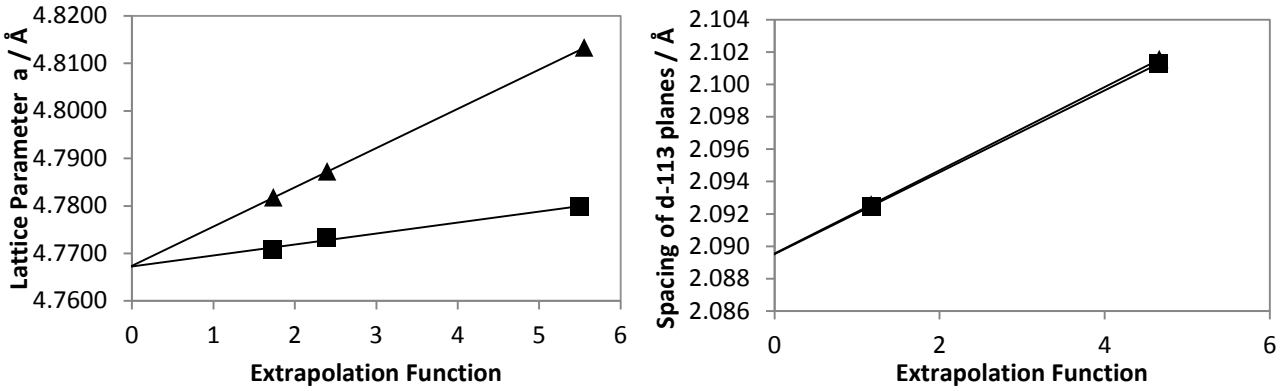


Figure 4.9: Determination of the lattice parameters using the extrapolation function for undoped, pressurelessly sintered AES-11C

Using the Archimedes method (Section 3.3.2.), the measured density of AES-11C sintered at 1600°C was (3.95 +/- 0.04) gcm^{-3}. The relative density was (99.7 +/- 0.7) %.

The measured density of the alumina sintered at 1750°C was (3.96 +/- 0.03) gcm^{-3}, giving a relative density of (99.9 +/- 0.6) %.

4.2.2. Pressurelessly Sintered AES-11C with varying amounts of chromia

Lattice parameters a and c were (4.7695 +/- 0.0002) Å and (13.045 +/- 0.003) Å for 2.0wt%, (4.7744 +/- 0.0003) Å and (13.012 +/- 0.003) Å for 3.0wt%, and (4.777 +/- 0.001) Å and (13.026 +/- 0.007) Å for 5.0wt% respectively. The volume of the unit cell increased with the addition of the chromium ions.

AES-11C true density, $\rho_{AES-11C}$ increased with at% Cr_2O_3, c_m (Figure 4.10). The increase (Equation 4.1) was very similar to that by Jan et al [201]:

$$\rho_{AES-11C} = 3.9620(1 + 0.318c_m) \quad (4.1)$$

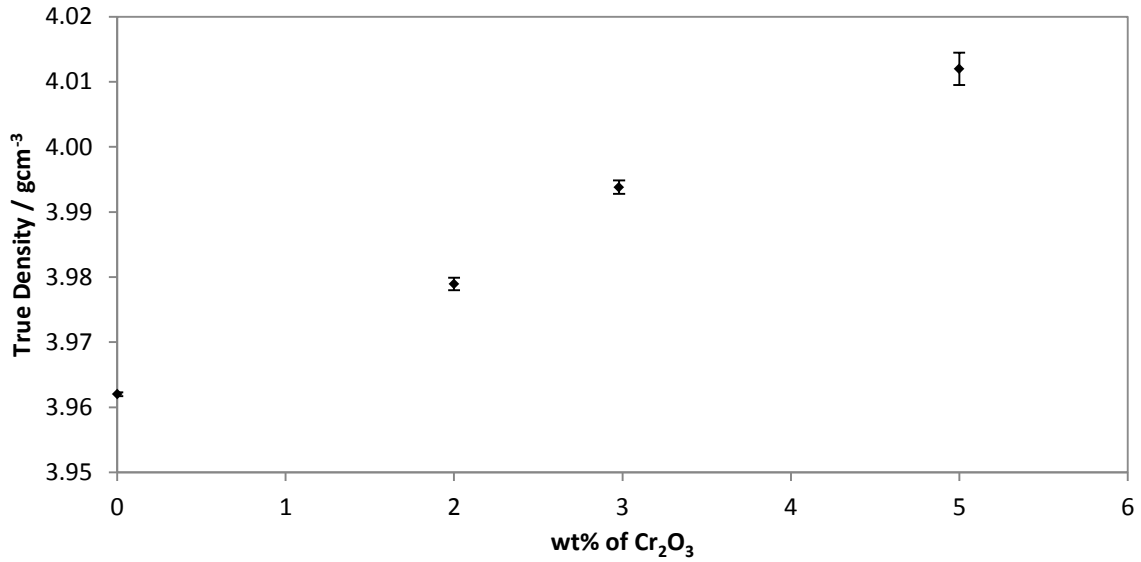


Figure 4.10: Change in true density of AES-11C alumina with chromia doping.

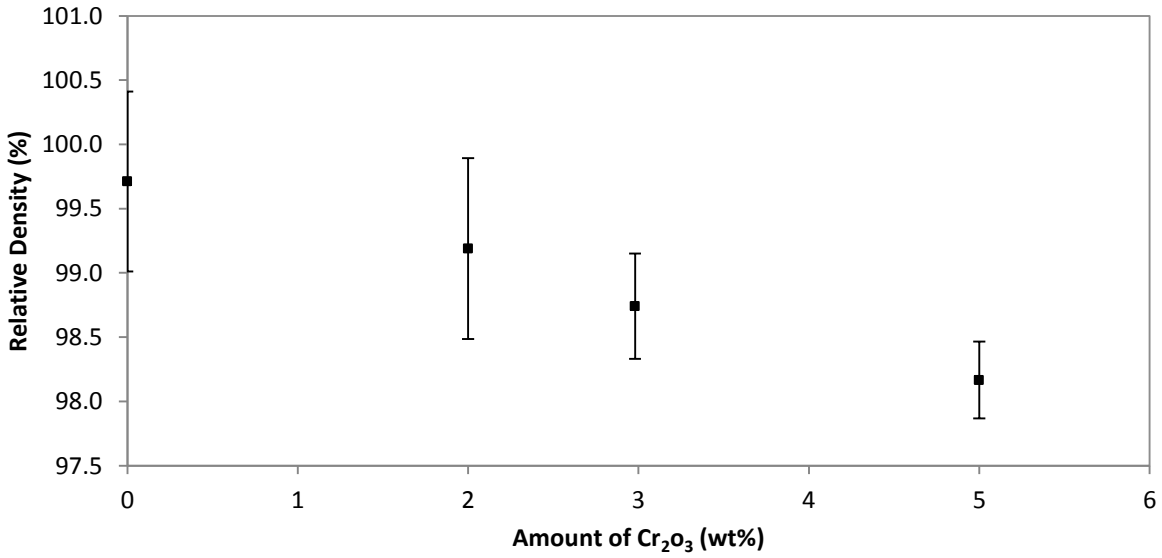


Figure 4.11: Change in the relative density of AES-11C alumina with chromia doping.

Although the errors were relatively large, there was a general trend of decreasing relative density with increasing Cr_2O_3 (Figure 4.11).

4.2.3. Pressurelessly Sintered TM-DAR – sintered in air

Lattice parameters a & c for the undoped TM-DAR sintered at 1600^{o}C were (4.7701 +/- 0.0004) Å and (12.992 +/- 0.003) Å respectively. The true density was (3.968 +/- 0.001) gcm^{-3}.

The measured density was (3.96 +/- 0.03) gcm^{-3}, and the relative density (99.8 +/- 0.8) %.

4.2.4. Pressurelessly Sintered TM-DAR – sintered in vacuum

It was assumed that the true density of the material, measured by XRD, was the same for the TM-DAR regardless of being sintered in air or vacuum. The measured density was (3.968 +/- 0.002) gcm^{-3} and (using the true density from Section 4.2.3.) the relative density was (99.997 +/- 0.002) %.

4.2.5. Pressurelessly Sintered TM-DAR with varying amounts of chromia dopant

The lattice parameters a and c were (4.7729 +/- 0.0007) Å and (12.992 +/- 0.006) Å for 2.0wt% Cr_2O_3 TM-DAR, and (4.7773 +/- 0.0007) Å and (13.004 +/- 0.002) Å for 5.0wt% Cr_2O_3 TM-DAR respectively. The true density of the material increased with chromia content (Equation 4.2) in a similar manner to that of AES-11C.

$$\rho_{\mathrm{TM-DAR}} = 3.9681(1 + 0.315c_m) \qquad (4.2)$$

The relative densities were: 2% = (98.4 +/- 0.9) %, 5% = (97.1 +/- 0.7) %.

4.2.6. Pressurelessly Sintered TM-DAR with 0.012wt% Carbon

The lattice parameters a and c for TM-DAR doped with 0.012wt% carbon were (4.7703 +/- 0.0001) Å and (12.998 +/- 0.002) Å respectively. The difference between the doped and undoped lattice parameters a & c were 0.004% and 0.05% respectively. Hence, the doping did not affect the lattice parameters nor the unit cell volume. The measured density was (3.9665 +/- 0.0006) gcm^{-3}, and the relative density (100.01 +/- 0.01) %.

4.3. Transmission Electron Microscopy of the alumina samples

Although secondary electron microscopy assessed the variation in the grain size and its distribution, many of the key microstructural features of these aluminas were only determinable using transmission electron microscopy (TEM). Once these as-sintered

aluminas are characterised, it is possible to assess the extent of damage after macroscopic stress testing (Section 5).

4.3.1. Unstressed, Pressurelessly Sintered AES-11C

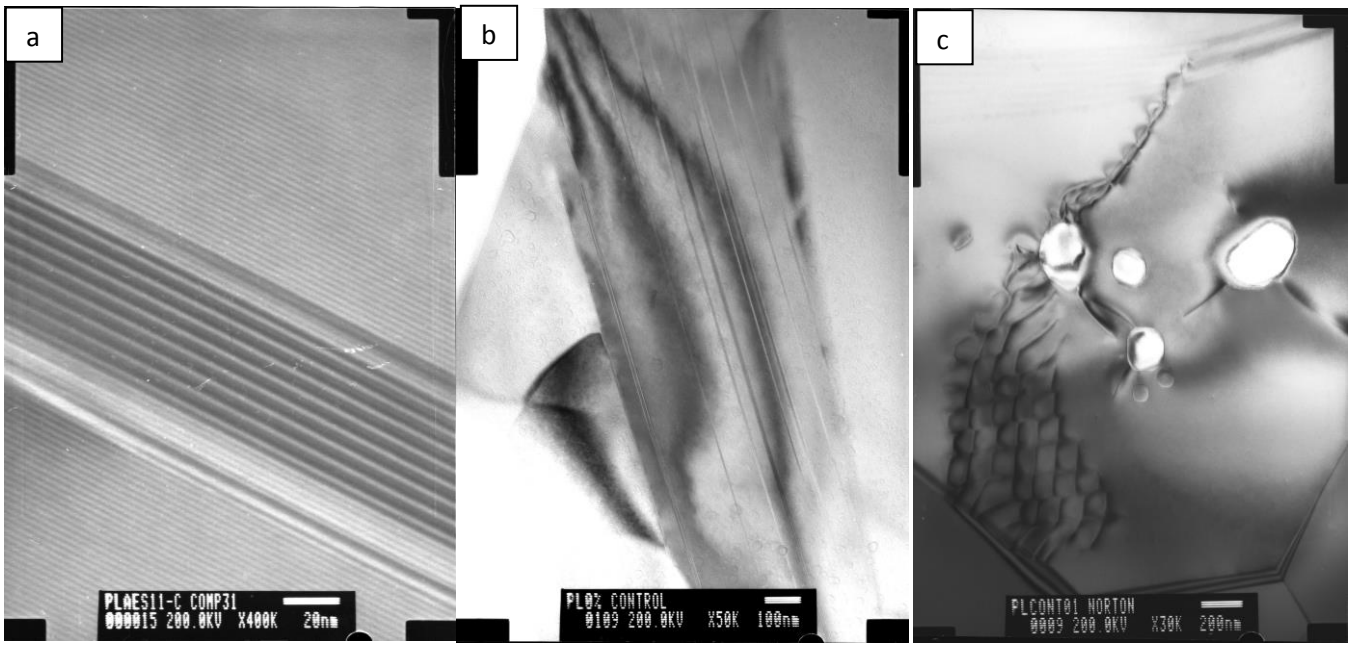


Figure 4.12: Transmission Electron Microscopy (TEM) images (JEOL 2000FX) of an untested, pressurelessly sintered, undoped AES-11C sample, sintered at 1600°C for 2 hours. Microstructural features included: a) and b) twinned grains, and c) grains with dislocations in.

There were several key features of undoped, pressurelessly sintered AES-11C (1600°C, 2h) (Figure 4.12). There were a wide range of examples of dislocations, some of which were associated with pores (Figure 4.12c). There were single dislocations which branched away from the pore, interconnected dislocations, and others that were associated with neither a pore nor other dislocations.

Several grains in a single foil were twinned (Figure 4.12a & b); they were always long, thin, and aligned in a certain orientation in the grain. Diffraction analysis of these twins was performed and shown in Section 4.3.5.

Pores often were present in the twinned grains (Figure 4.13b). These did not appear to interact with the twins, suggesting that either the grains were fairly deep compared to the size of the pore (and so the twins looped around the pore), or the hole in the foil had been

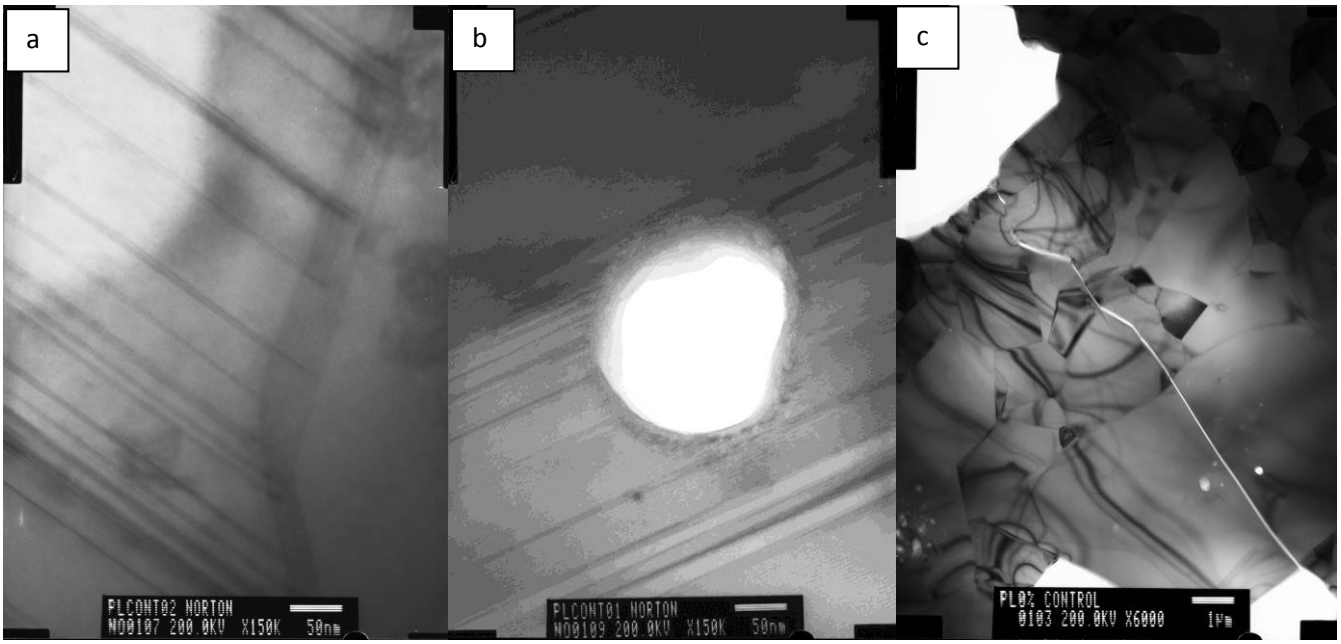


Figure 4.13: Transmission Electron Microscopy (TEM) (JEOL 2000FX) images of a) basal twins at a grain boundary, b) twins and an intragranular pore, c) a transgranular crack that occasionally were present in the foil

created during the ion milling stage. There were grains with pores and no twins, and grains with twins and no pores, and hence the two microstructural features were not related. Occasionally, there were twinned regions with dislocations in the grains; these were difficult to image owing to the diffraction conditions of the two features being different.

In a typical TEM sample, there were around 4 – 8 twinned grains out of 500+ grains that could be imaged. The width of the twins was consistent: (2.1 +/- 0.4) nm.

A few microcracks were present in some of the foils of the unstressed material (Figure 4.13c). These cracks were almost exclusively transgranular, suggesting that the sample has cracked during the production of the TEM sample. The frequency was low; in two samples of around a thousand grains altogether, there were three different cracks. They formed/ended at the central hole in the film.

4.3.2. Undoped, pressurelessly sintered TM-DAR

There were a number of dislocations in the TM-DAR grains (Figure 4.14). The frequency of a grain with dislocations in was fairly similar to that of AES-11C. Many of these dislocations

were associated with pores (Figure 4.14a), but the two features were not mutually interdependent.

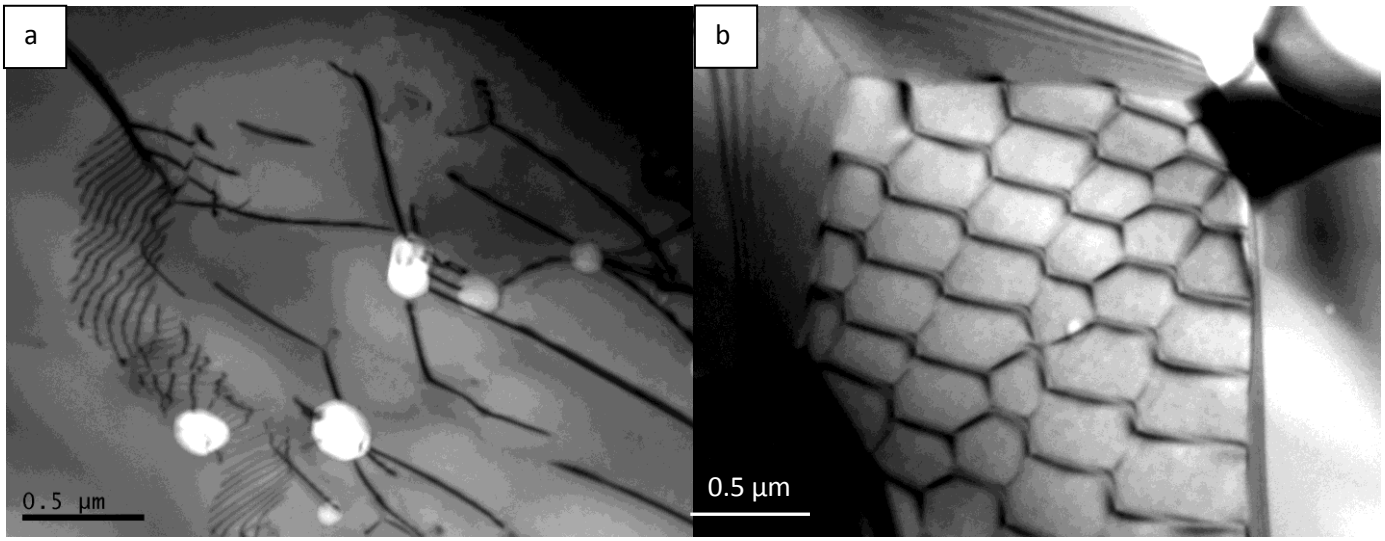


Figure 4.14: Microstructural features of undoped pressurelessly sintered TM-DAR; there were a number of dislocation arrays in the grains

The key difference between the TM-DAR and AES-11C materials was the lack of basal twins in TM-DAR. Many hundreds of TM-DAR grains were imaged, but none was twinned.

4.3.3. Chromia doped, Unstressed, Pressurelessly Sintered AES-11C

The number of grains with basal twins decreased as the amount of Cr_2O_3 increased. In the undoped sample, there were typically around 5 or 6 grains containing twins in around five hundred grains imaged. With 2.0wt% Cr_2O_3 addition, the number of grains with twins was 4 or 5 out of around 500 (Figure 4.15b & c). In the 3.0wt% sample, there were around 2 twinned grains per 500. At 5.0wt%, although three different control samples were analysed (each which had around 500 imageable grains), no twins were found.

.

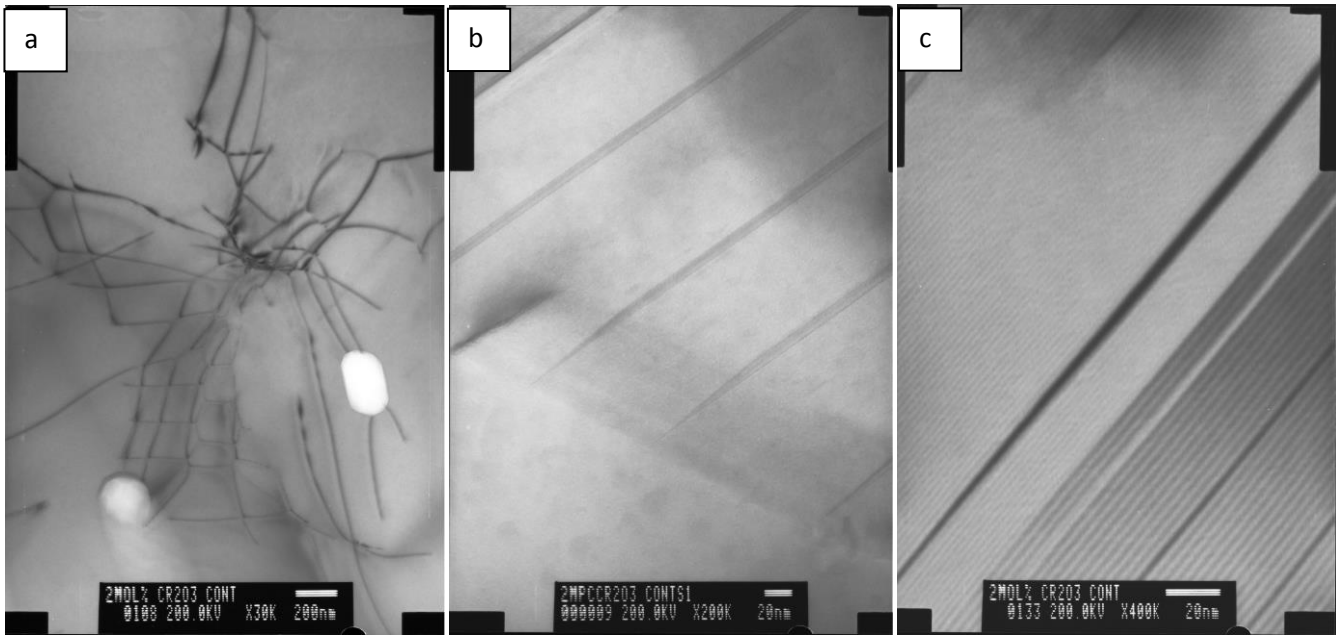


Figure 4.15: Transmission Electron Microscopy (JEOL 2000FX) images of 2wt% Cr_2O_3 doped AES-11C, pressurelessly sintered at 1600°C for 2 hours; a) a lot of dislocation density was found intragranularly, and b) & c) there were a number of twinned grains

The number of grains with dislocations increased with chromia doping. In the undoped sample, there were dislocations every 5th or 6th grain. In the 5wt% sample, there were dislocations in every 2nd grain (Figure 4.16). Not only were there more grains with

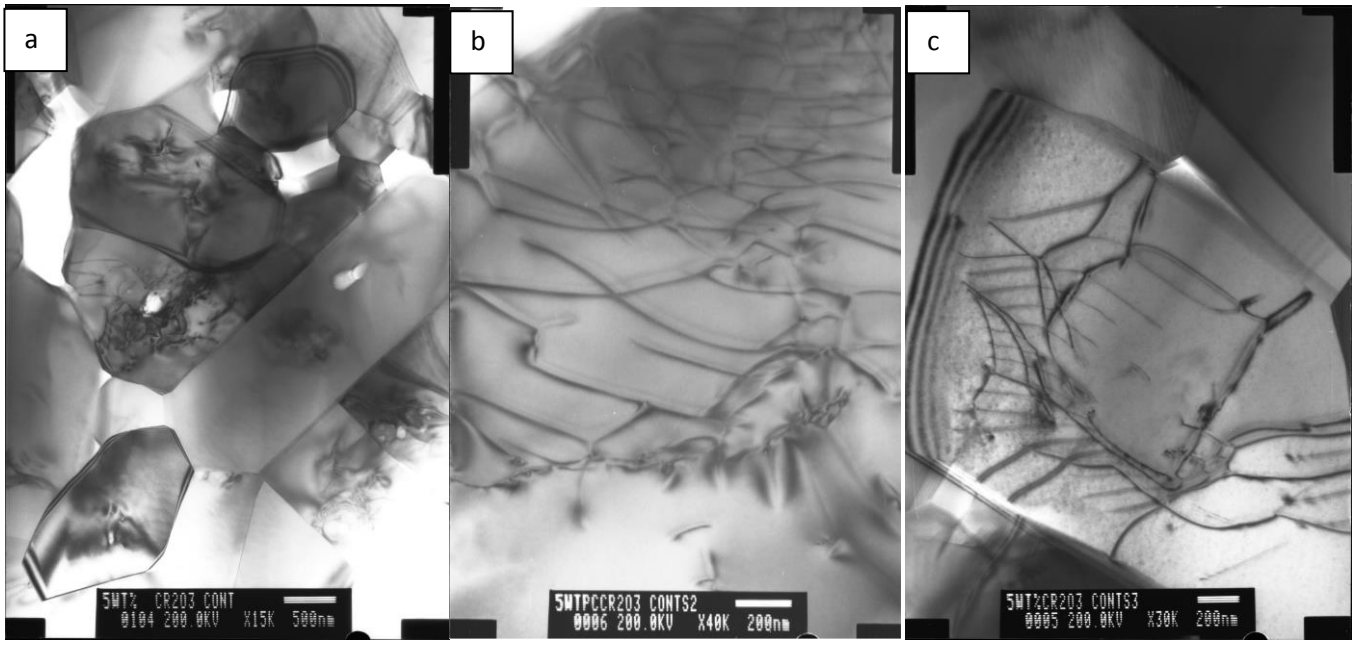


Figure 4.16: TEM images of unstressed 5wt% Cr_2O_3 doped AES11-C, sintered at 1600°C for 2 hours. a) Many grains appear to have dislocations located inside them. Around eight grains here appear to have dislocations, b) & c)

dislocations, each grain with dislocations in had a greater dislocation density (Figure 4.16b).

4.3.4. Energy Dispersive X-ray Spectroscopy of twins

Energy-dispersive x-ray spectroscopy (EDX) was performed (JEOL 2000FX) on un-twinned and twinned grains (Section 3.3.4).

	1	2	3	4	5	6	7
O	61	63	63	57	58	57	57
Al	38	36	38	43	42	42	42
Cr	-	1	-	-	-	-	-
Fe	2	-	-	-	-	-	-
Mg	-	-	-	-	-	1	1
Al/O	0.6	0.6	0.6	0.8	0.7	0.7	0.7

Table 4.1: Composition (at%) of a variety of un-twinned grains in undoped pressurelessly sintered AES-11C

Seven un-twinned grains were analysed (Table 4.1). There were several elements present; each was an expected impurity/additive (Section 3.1.1).

Several twinned grains were considered. The EDX probe was placed inside five twinned grain (over many twin/matrix boundaries), and twice on the edge of the twinned grain boundary (Table 4.2).

	Twin 1	Twin 2	Twin 3	Twin 4	Twin 5	GB 1	GB 2
O	56	61	60	52	52	53	53
Al	36	34	36	45	45	46	46
Cr	5	3	-	-	-	-	-
Mg	-	-	-	1	-	1	1
Ca	-	-	-	0.4	0.3	-	-
K	3	3	3	2	3	0.1	-
Al/O	0.64	0.55	0.60	0.87	0.88	0.87	0.87

Table 4.2: Composition (at%) inside five twinned grains (Twin), and two grain boundaries of twinned grains (GB), in undoped pressurelessly sintered AES-11C

Potassium was present in all the twinned grains (Table 4.2, Figure 4.17) at (3 +/- 1) at%. There were occasionally small amounts of Cr, Mg, and Ca. K was present at the twin/matrix boundary, but not at the grain boundaries of the twinned grains.

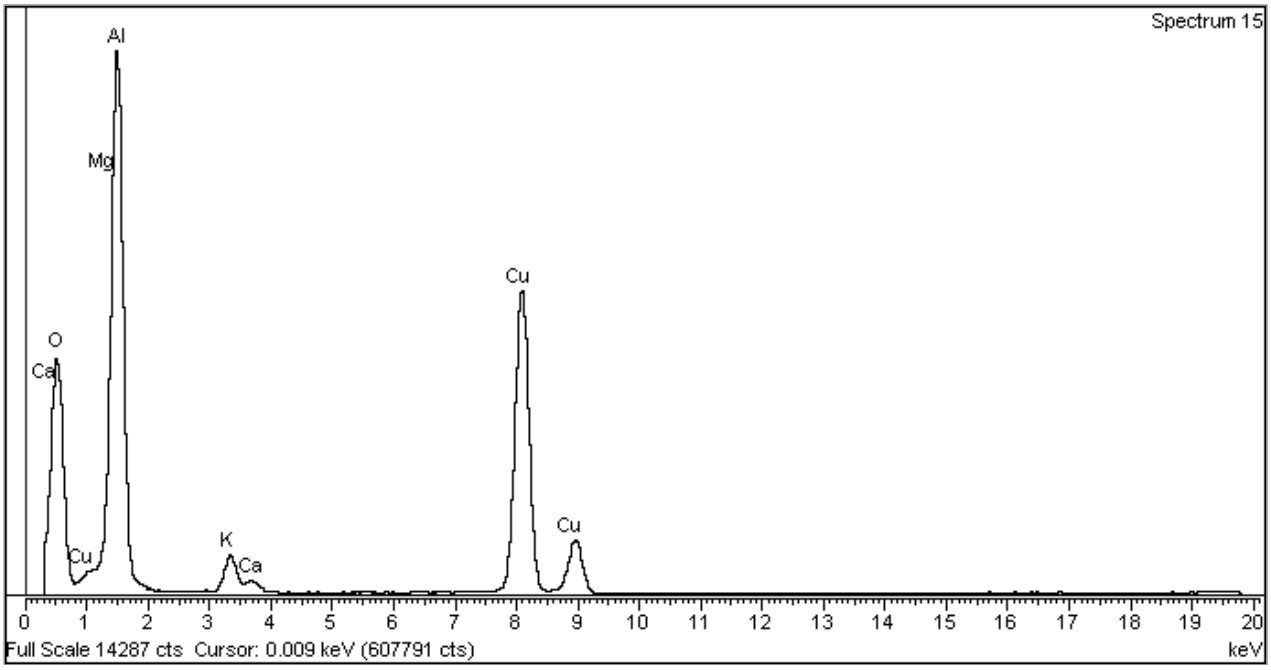


Figure 4.17: A typical TEM-EDX spectra (JEOL 2000FX) of twin/matrix boundary in AES-11C.

4.3.5. Diffraction Analysis of the twinned grains

Electron diffraction patterns (JEOL 2000FX) were taken of the twinned grains in as-sintered AES-11C. Previous work shows that additional diffraction spots are present due to twins [26, 202, 203]. Diffraction patterns oriented down two zone axes (in one grain) are given in Figure 4.18. The two diffraction patterns were orientated 37^{o} apart. d_{hkl} was determined from the diffraction spots using Equation 4.1.

$$d_{hkl} = \frac{\lambda L}{r_{hkl}} \qquad (4.1)$$

where λ is the wavelength of the electron beam (2.5pm [202] for 200kV), L the camera length (tabulated in Appendix 4.1), and r_{hkl} the distance measured on the diffraction pattern. The measured d-spacings from the two zone axes (from one twinned grain) are given in Table 4.3: ”Axis 1” = Figure 4.18a, “Axis 2” = Figure 4.18b.

There are no planes (with allowed reflections) in the sapphire crystal with a d-spacing of 22 - 23Å (Table 4.3); the highest d-spacing, using Equation 3.3 and sapphire lattice parameters [193], is 12.99 Å due to $\{100\}$. Thus, some of the diffraction spots must be due to twins.

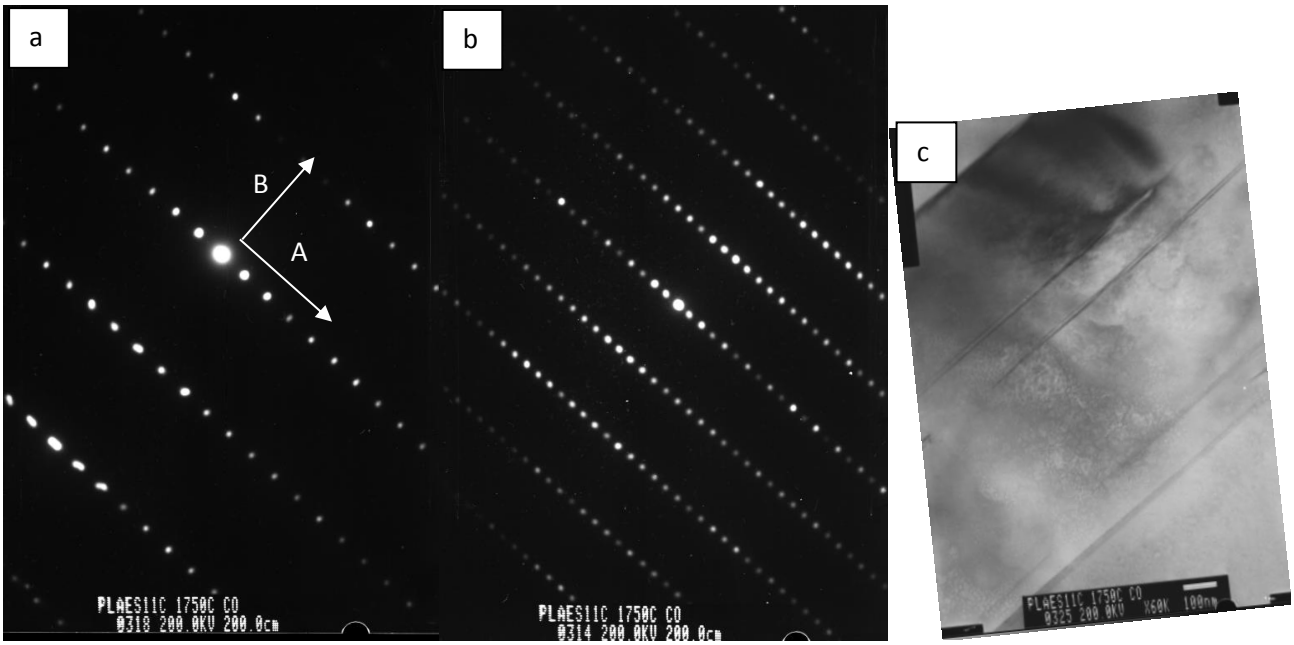


Figure 4.18: a & b) Two diffractions from the same twinned grain (A and B show notation for Table 4.3): c) The bright field image showing the orientation of the twins relative to the diffraction pattern.

	Axis 1 1	Axis 1 2	Axis 1 3
A1 (Å)	11.2	11.1	11.5
A2 (Å)	5.6	5.5	5.8
A3 (Å)	3.7	3.7	3.8
B1 (Å)	2.8	2.8	2.8

	Axis 2 1	Axis 2 2	Axis 2 3
A1 (Å)	22.5	23.1	22.4
A2 (Å)	11.3	11.6	11.2
A6 (Å)	3.8	3.9	3.7
B1 (Å)	4.9	4.9	4.9
B2 (Å)	2.5	2.4	2.4

Table 4.3: The measured d-spacings for two zones axes (1 & 2) for 3 twinned grains. "A" = spots in A-direction (Figure 4.18a), "B" = spots in B-direction. "1" = 1st spot, "2" 2nd etc.

The electron diffraction patterns are a composite between spots due to the twins and those due to the grain. To determine the orientation of the grain, diffraction patterns were analysed using the following features, and the results compared to the expected values for sapphire to find a best match:

1) Measured d_{hkl} values from diffraction patterns (Table 4.3).
2) The ratios between length of diffraction vectors g_{hkl} for different hkl values
3) The angle between g_{hkl} vectors for different hkl
4) The angle between the zone axes (37^{o})

Using these method, it was shown that Axis 1 = ⟨210⟩ and Axis 2 = ⟨110⟩. The twins are on the (006) planes. The labelled diffraction patterns for ⟨210⟩ and ⟨110⟩ are shown in Figures 4.19a and b respectively. The presence of such twins is discussed in Section 9.3.1.

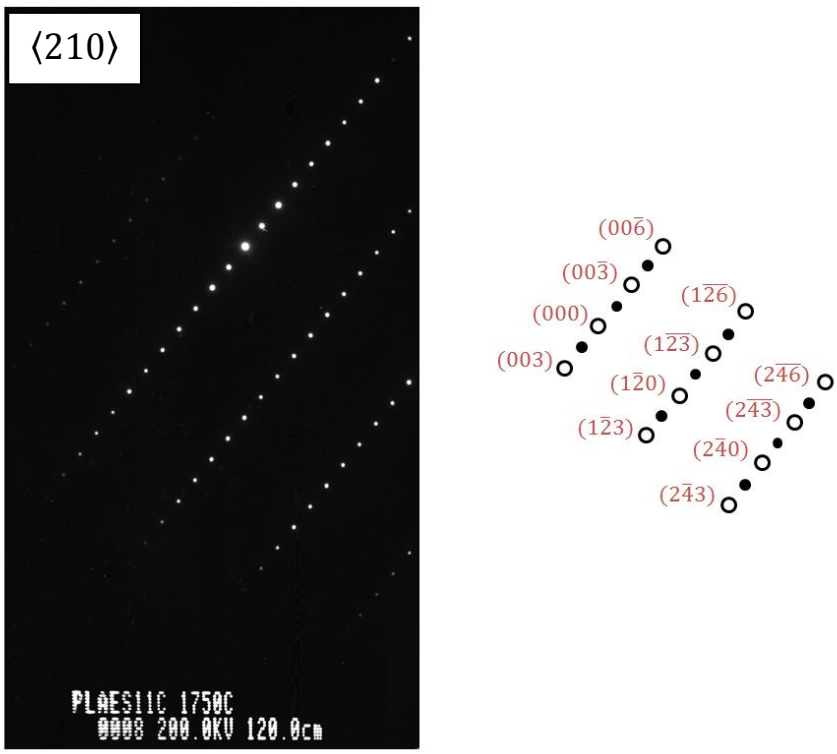


Figure 4.19a: Diffraction pattern along the ⟨210⟩ zone axis. The diffraction spots were labelled: ○ represented spots from the grain, ● those of the twins.

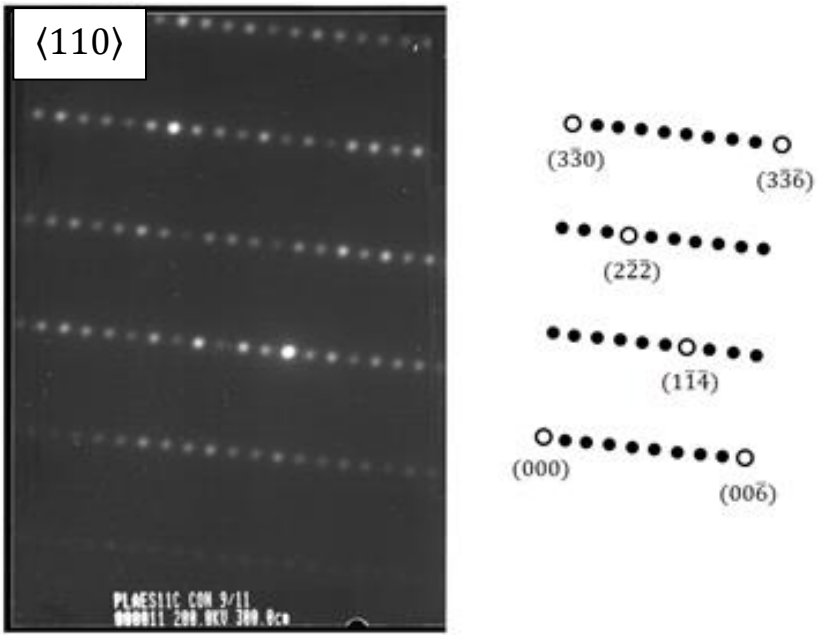


Figure 4.19b: Diffraction pattern along the ⟨110⟩ zone axis. The diffraction spots were labelled: ○ represented spots from the grain, ● those of the twins.

4.4. Optical Fluorescence Microscopy (OFM)

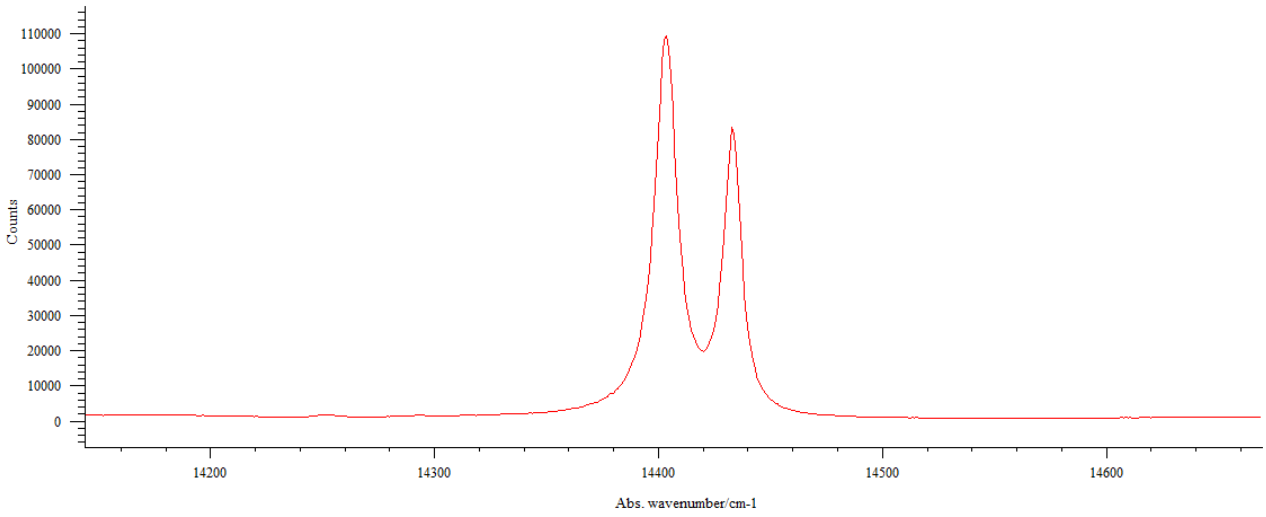


Figure 4.20: Optical Fluorescence Spectra of the Cr^{3+} transition in single crystal aluminium oxide (sapphire).

Optical fluorescence microscopy (OFM) was used to measure the residual stresses in compression tested alumina, assess the residual stress due to gallium implantation etc. After

considering the accuracy of the technique using sapphire (Section 4.41. and 4.4.2.), the peak position and width of various aluminas were determined.

4.4.1. Variation in peak position and width on a single point

The variation in the peak position and peak width for repeated spectra on a single point was considered. 100 spectra were taken on a single point on the sapphire surface. The peak position and width were (with standard deviation) (14403.51 +/- 0.05) cm^{-1} and (11.6 +/- 0.2) cm^{-1} respectively.

4.4.2. Variation in peak position and width across sapphire

608 points were taken (1µm spacing between points) over the surface of c-plane sapphire (confocal, power 100%, exposure time per point 360s). FocusTrack was used at every point to ensure that each point was in focus. The mean peak position and width was (14403.58 +/- 0.04) cm^{-1} and (11.5 +/- 0.2) cm^{-1} respectively. Using Equation 2.15, the deviation in peak position is due to a hydrostatic stress variation of +/- 5 MPa. This is the limit to the hydrostatic stress resolution; values larger than this are deemed to be genuine.

4.4.3. Variation in peak position and width across polycrystalline AES-11C

AES-11C was diamond lapped to a finish of 1µm. The mean peak position and peak width was, respectively, (14403.03 +/- 0.18) cm^{-1} & (12.88 +/- 0.17) cm^{-1}. The addition of the grain boundaries affected both the peak position and the peak width. The mean peak position was moved to a lower wavenumber, but the variation increased, suggesting a small &

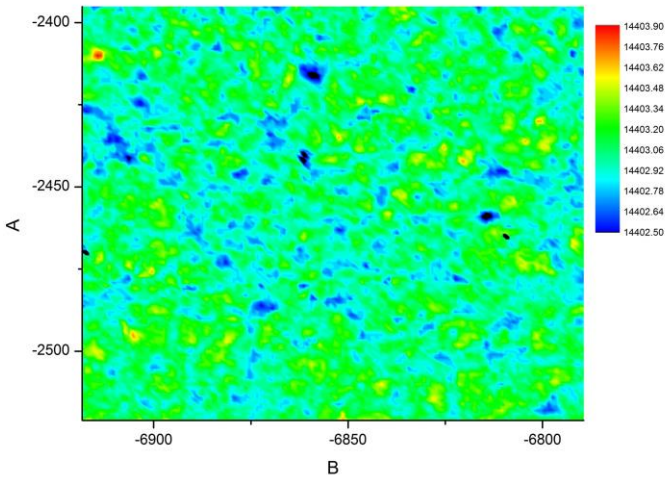


Figure 4.21: OFM peak position map of the surface of uncompressed AES-11C alumina (axes in microns)

varying residual compressive stress across the surface; using Equation 2.15, the hydrostatic stress variation is +/- 24MPa. However, the stress was not uniform over the surface (Figure 4.21). Several regions, whose size was of the order of the grain size, were ≈ 0.5cm^{-1}, or 71MPa, below the mean.

4.4.4. Variation in peak position and width with chromia doping

A large number of points was taken in confocal mode over a polished surface of 2.0, 3.0, and 5.0wt% chromia doped AES-11C. As the amount of chromium oxide increased, the fluorescence intensity increased. To avoid saturating the detector, the exposure time was adjusted: 2s per point (undoped), 0.1s (chromia doped).

The peaks become noticeably broader with increasing chromia doping (Figure 4.22), and had features at lower wavenumbers that were not resolvable in the undoped alumina (Figure 4.22). These were the N-lines due to transitions in Cr^{3+}-Cr^{3+} pairs, which shift depending on

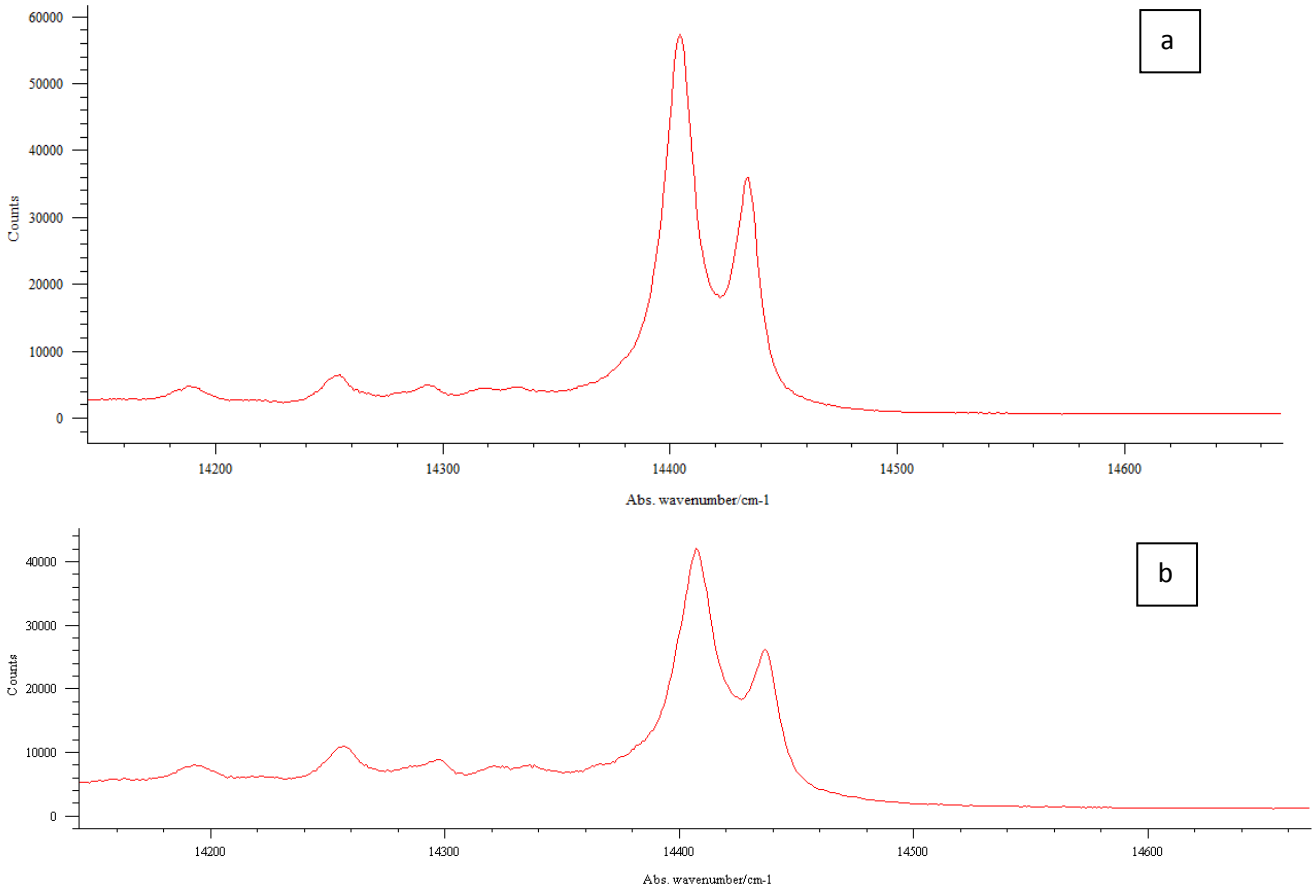


Figure 4.22: R1 and R2 peaks for a) 2wt% and b) 5wt% chromia doped AES-11C

the extent of doping [204]. For example, the N_1 (transition between third removed neighbouring pairs) is at (14198.4 +/- 1.71C) cm^{-1} and the N_2 (transition between fourth removed neighbouring pairs) is at (14263.1 +/- 1.26C) cm^{-1}, where C is the chromium concentration in wt% [204].

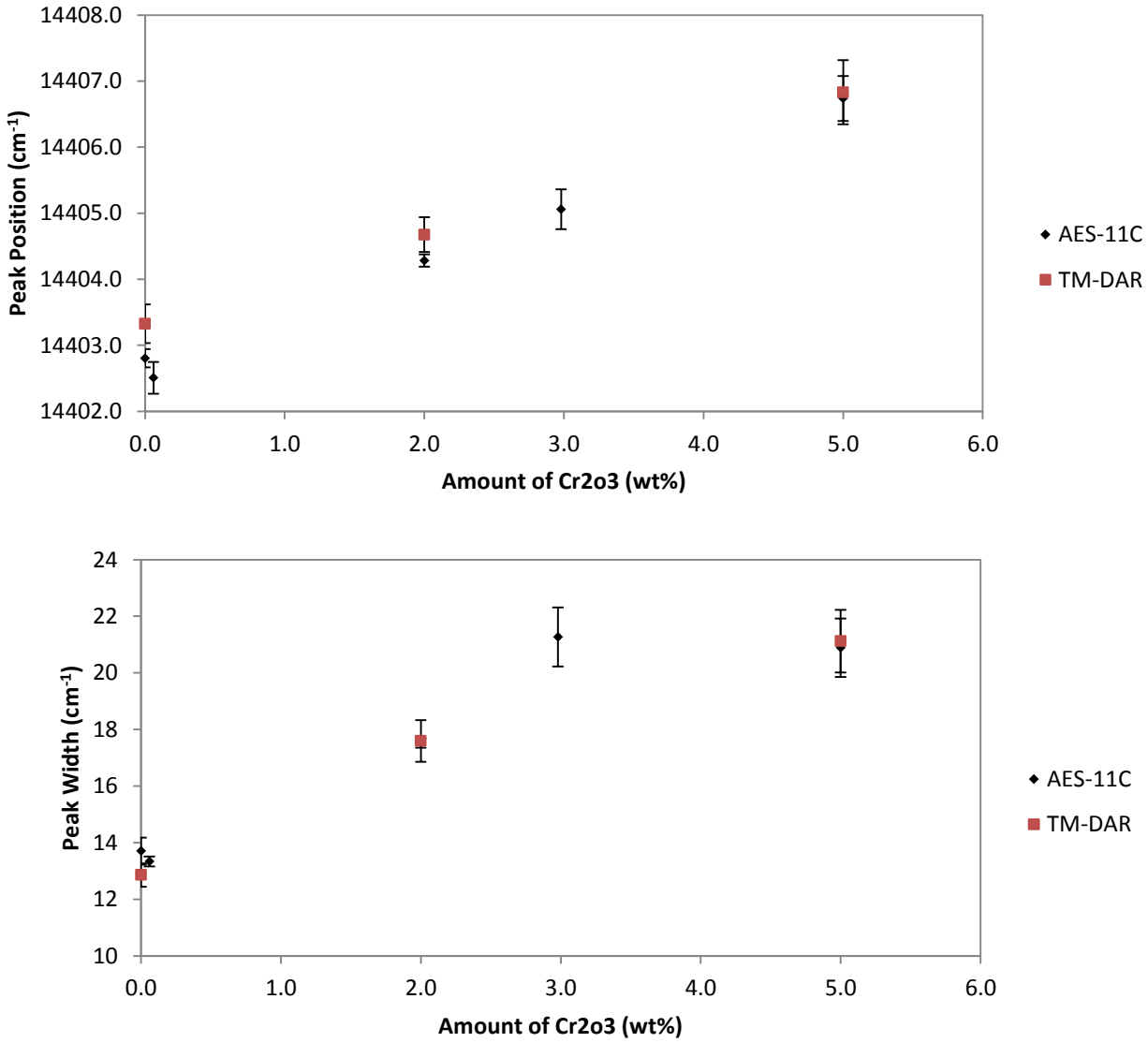


Figure 4.23: The R1 peak position and peak width for increasing levels of chromium oxide additions in AES-11C and TM-DAR alumina

Increasing the amount of chromium oxide increased the peak position for AES-11C and TM-DAR (Figure 4.23a) due to lattice expansion [204] (Section 4.2.2.). Plotting the peak shift against the chromium content, the relationship was $\Delta\nu = 111c_m$, where c_m was the wt% of chromium ions. This dependence was close to that seen by other authors [183, 204]. The peak broadening (Figure 4.23b) was related to the local deformation of the Al_2O_3 lattice around the Cr^{3+} ions; the elastic lattice deformation increased with the number of chromium ions [204].

4.5. Diffusion Bonded Sapphire

4.5.1. Transmission Electron Microscopy

A FIB produced foil (Section 3.2.2., Figure 4.24a) of the diffusion bonded sapphire was imaged using high-resolution TEM (JEOL 3000F; all HRTEM here were by Jack Severs,

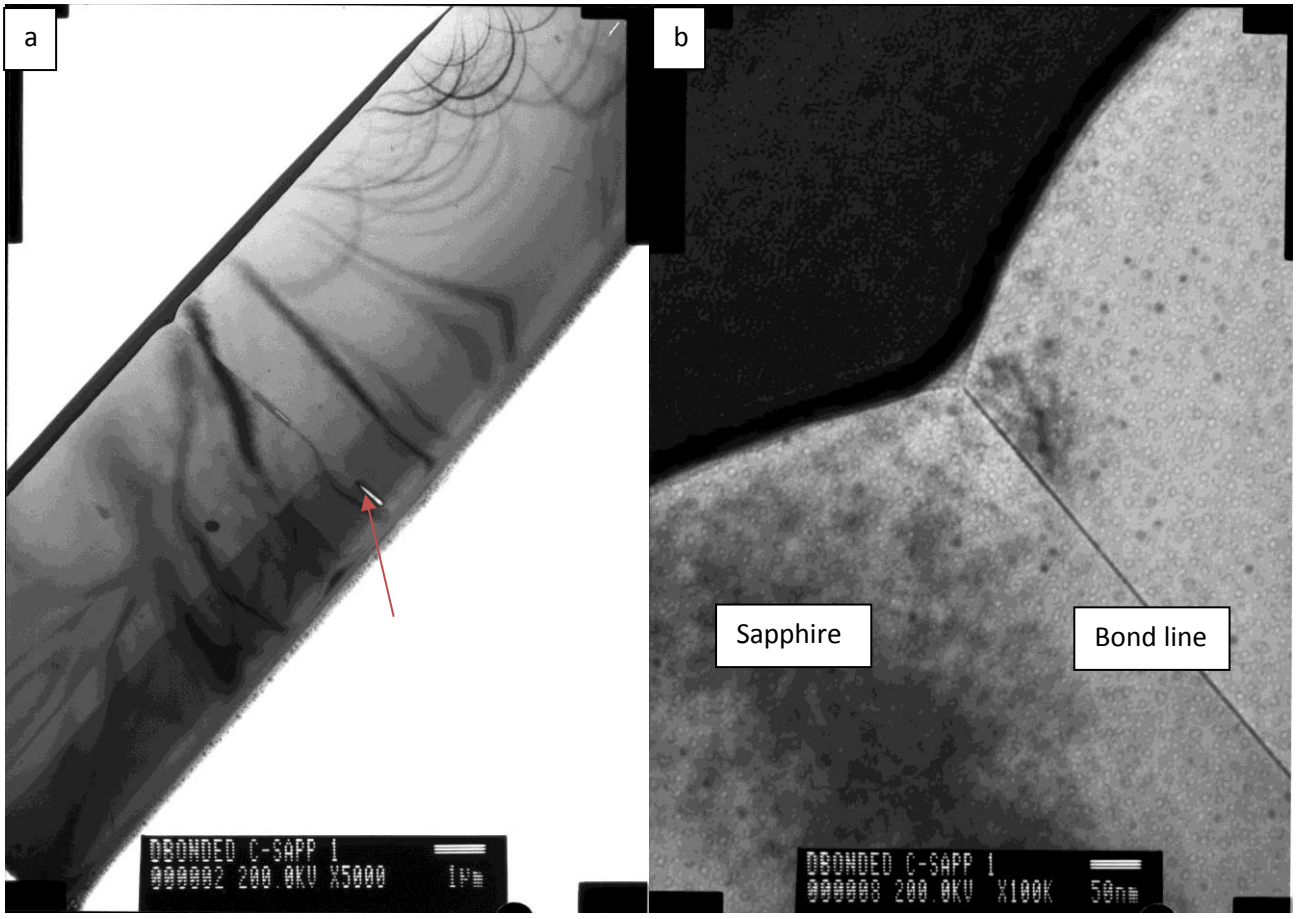


Figure 4.24: TEM (JEOL 2000FX) of a FIB produced foil in diffusion bonded sapphire

Department of Materials, University of Oxford) and was found to have a boundary of (3.5 +/- 0.7) nm (Figure 4.25a). However, it was possible that the boundary was not flat or aligned parallel to the beam and thus the boundary appeared wider than it was in reality. For the same reasons, it was difficult to interpret the boundary structure; whilst the fringes at the boundaries appeared to be ordered, suggesting that the complexion had a specific structure,

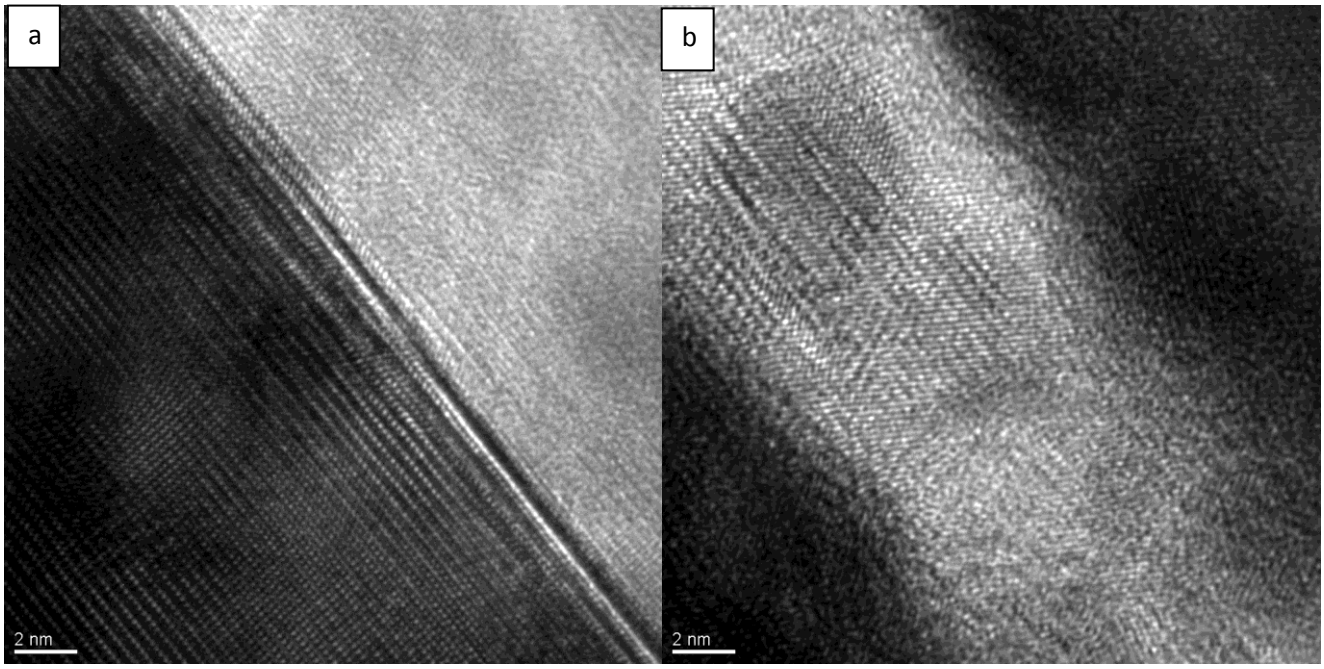


Figure 4.25: High resolution transmission electron microscopy (JEOL 3000F) of a) the diffusion bonded sapphire boundary, and b) a hole in the diffusion bonded boundary, indicating that there was material present in the unbounded gap.

the fringes may have been due to the boundary not being aligned parallel to the beam.

There was part of the boundary that was not well bonded (arrowed in Figure 4.24a). HRTEM suggested that it was filled with material (Figure 4.25b); it was more likely redeposited material from the FIB-TEM foil production than impurities present during bonding. In the three TEM foils produced in the diffusion bonded sapphire, this was the only un-fused section. Whilst it was not a common feature, it may have a bearing on the microcantilever beam work; beams may have failed with a low stress intensity factor due to an un-fused boundary section underneath the notch.

Electron diffraction was used to determine the twist angle across the boundary. The zone axis $\langle 100 \rangle$ for the left hand grain (Figure 4.24) was at the x- and y-tilt -18^o & -16^o, and at x- and y-tilt of -32^o & y = -29^o for the right hand grain. To tilt the first grain onto the second, an x-tilt of -14^o and a y-tilt of -13^o would be required, thus giving twist angle of 19^o.

For the zone axis $\langle 75\bar{1} \rangle$ the left grain was aligned at an x- and y-tilt of +31^o and -7^o, and the right hand grain aligned with an x- and y-tilt of +17^o and 20^o. Hence, to tilt one grain onto the other required an x- and y-tilt of +14^o and 13^o, giving an overall tilt of 19^o.

Hence, the two pieces of c-plane sapphire were diffusion bonded together with a twist angle of (19 +/- 2)^o.

4.5.2. Electron Backscattered Diffraction (EBSD)

An EBSD map was made over the diffusion bonded sapphire surface (Section 3.3.7.) (JEOL 6300, 20kV). After the Kikuchi patterns were indexed (OIM software), the misorientation of the boundary was determined by drawing a line segment over the boundary (OIM software). Six measurements were taken across the boundary (Table 4.4) and the misorientation angle and planes ascertained. The mean misorientation angle and standard deviation was (19.7 +/- 0.9) ^{o}.

Line	Angle	Axis			Plane 1			Plane 2		
		h	k	l	u	v	w	u	v	w
1	18.9	-4	1	26	1	0	-30	1	0	30
2	20.2	0	7	-27	0	0	1	0	1	28
3	21.0	3	-5	20	0	0	-1	1	-1	30
4	20.2	2	-3	20	0	0	-1	0	1	30
5	19.4	1	-4	15	0	0	-1	0	1	30
6	18.6	-1	-4	23	0	0	-1	0	1	30

Table 4.4: Misorientation across the diffusion bonded boundary EBSD

4.5.3. Energy Dispersive X-ray Spectroscopy (EDX)

The chemical composition of the boundary was measured using TEM-EDX (JEOL 2000FX) (Figure 4.26) (mean of several spectra):

- Al = (34 +/- 2) %
- O = (60 +/- 1) %
- Ca = (2 +/- 1) %
- Ga = (0.3 +/- 0.1) %
- Si = (4 +/- 2) %

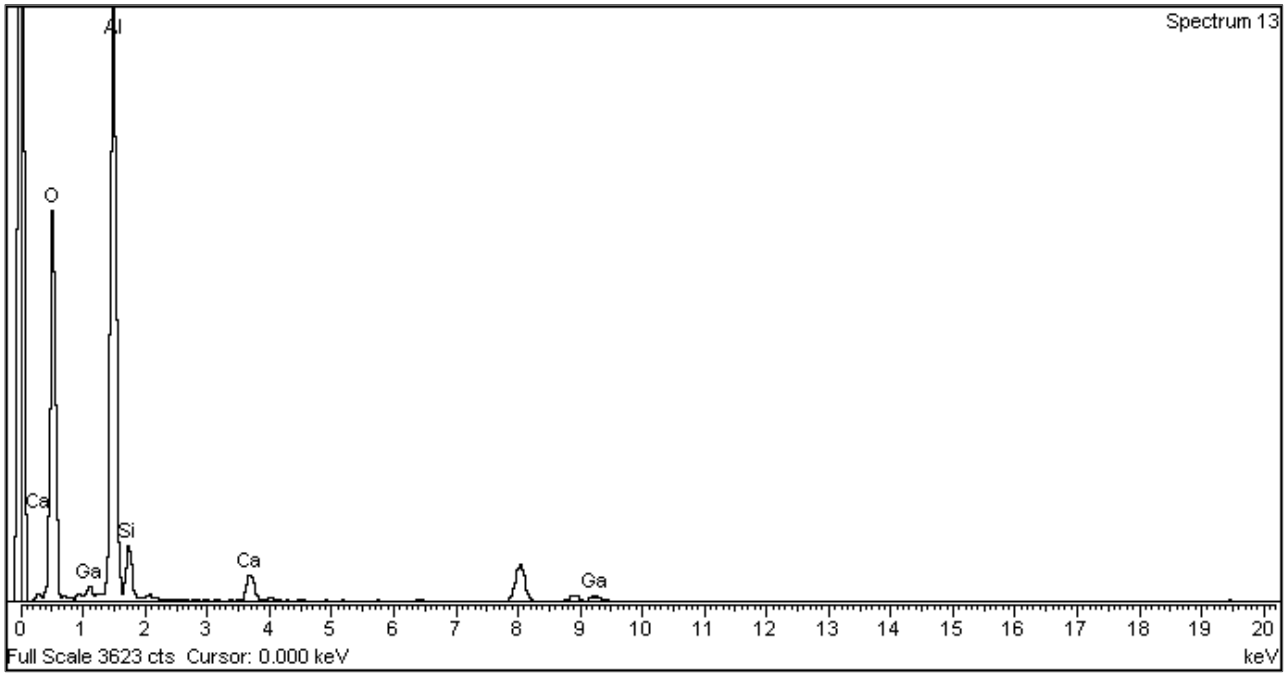


Figure 4.26: A typical TEM-EDX spectra of bond in the diffusion bonded sapphire

Silicon and calcium were likely to have been on the sapphire prior to bonding.

4.6 Analysis of the material change due to the focussed ion beam

Several changes occurred to the material during the focussed ion beam work. These were investigated in turn, using transmission electron microscopy, electron diffraction, and energy dispersive x-ray spectroscopy (EDX).

4.6.1. Redeposited Material due to Focussed Ion Beam

The redeposited material was prevalent during the FIB work, both underneath the microcantilever beams and at the base of the FIB-milled notches (Figure 4.33). The characteristics were important for the understanding of the microcantilever beams.

4.6.1.1 Transmission Electron Microscopy & Electron Diffraction

The redeposited material formed globule shapes (Figure 4.27) which did not appear to have the same microstructure as the initial material. Electron diffraction patterns were taken of the redeposited material and of the carbon on which the TEM foil was placed (Figure 4.28).

The diffraction pattern of amorphous carbon was diffuse (Figure 4.28c), although a broad ring was present (arrowed). This was converted into d-spacings using Equation 4.1: 1.89 - 2.36 Å.

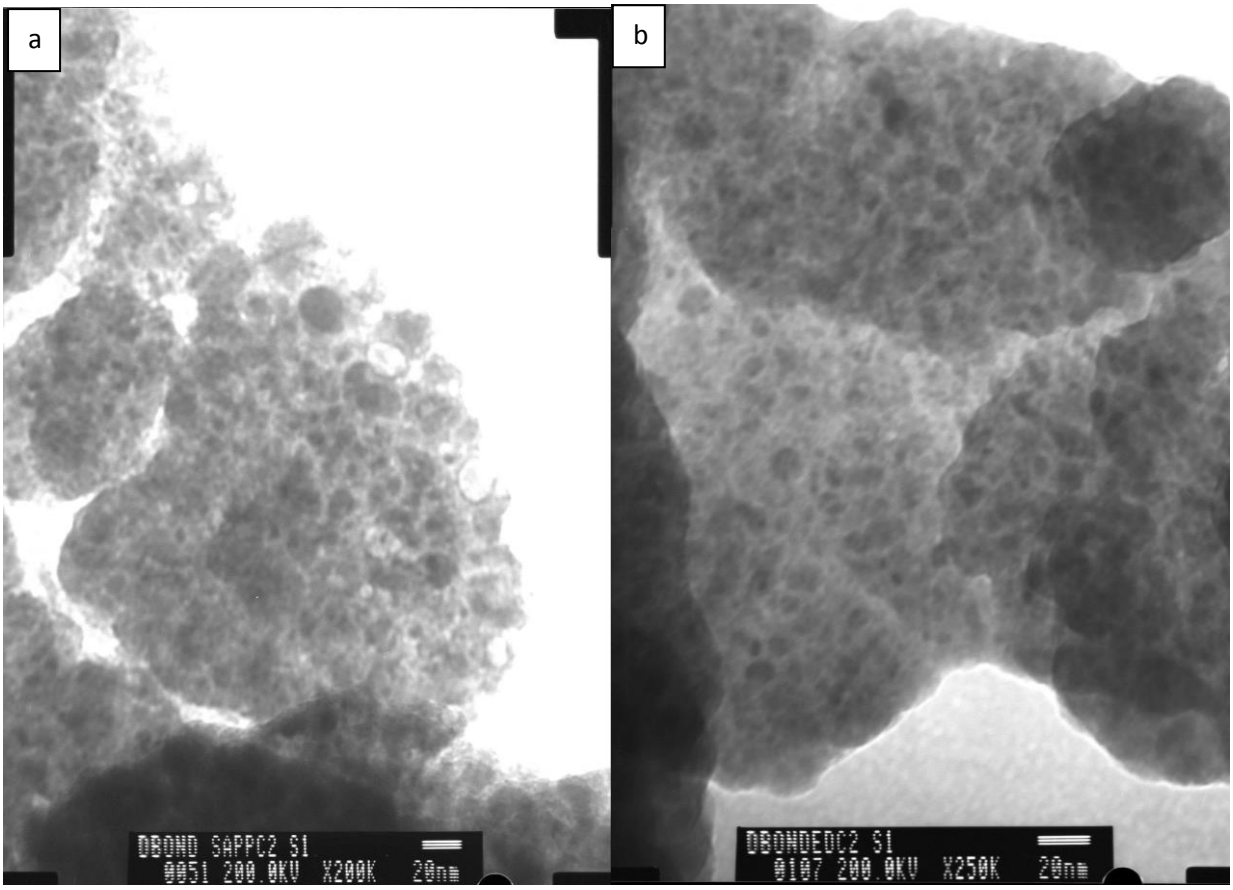


Figure 4.27: TEM (JEOL 2000FX) of redeposited material showing the globule shapes of the material

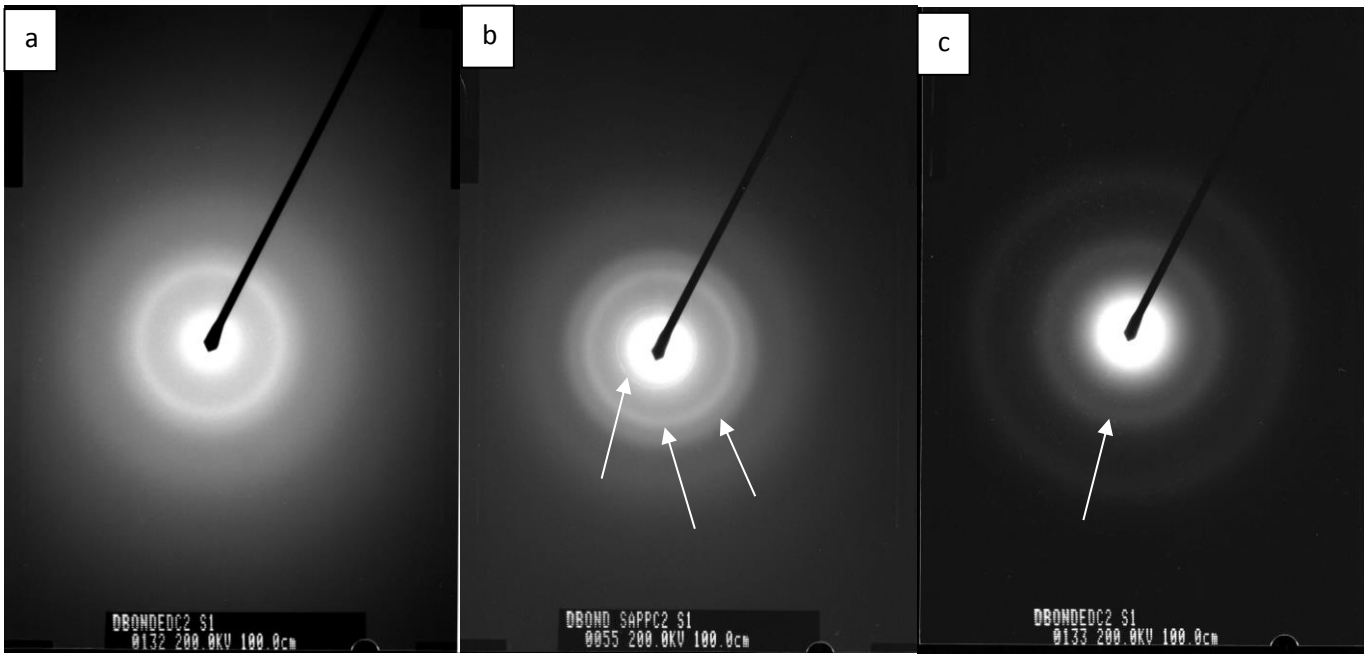


Figure 4.28: Electron diffraction pattern of a) the redeposited region, b) a second redeposited region, and c) the amorphous carbon grid under the sample.

The d-spacings of the redeposited material showed some variation (Table 4.5). Some rings occurred in some regions of redeposited material but not in others (Figure 4.28a&b). The majority of the regions of redeposited material considered (Table 4.5) had: 1) a sharp diffraction ring close to the centre spot, corresponding to a d-spacing of (4.2 +/- 0.2) Å, 2) a more diffuse ring with a d-spacing of (2.47 +/- 0.08) Å and 3) a diffuse ring with a d-spacing of (2.0 +/- 0.1) Å (all arrowed in Figure 4.28b).

Region	D1	D2	D3
1	4.39	2.43	1.94
2	4.38	2.44	1.92
3	4.23	2.45	1.91
4	3.94	2.43	1.91
5	N/A	2.62	2.18

Table 4.5: d-spacings for the rings in the electron diffraction patterns of the redeposited material

These are analysed, in light of the EDX, in Section 9.1.1.

4.6.1.2 Energy Dispersive X-ray Spectroscopy (EDX)

Before considering the composition of the redeposited material, the composition of the FIB-produced TEM foil (Section 3.2.2.), far away from the redeposited or implanted material, was determined (Figure 4.29).

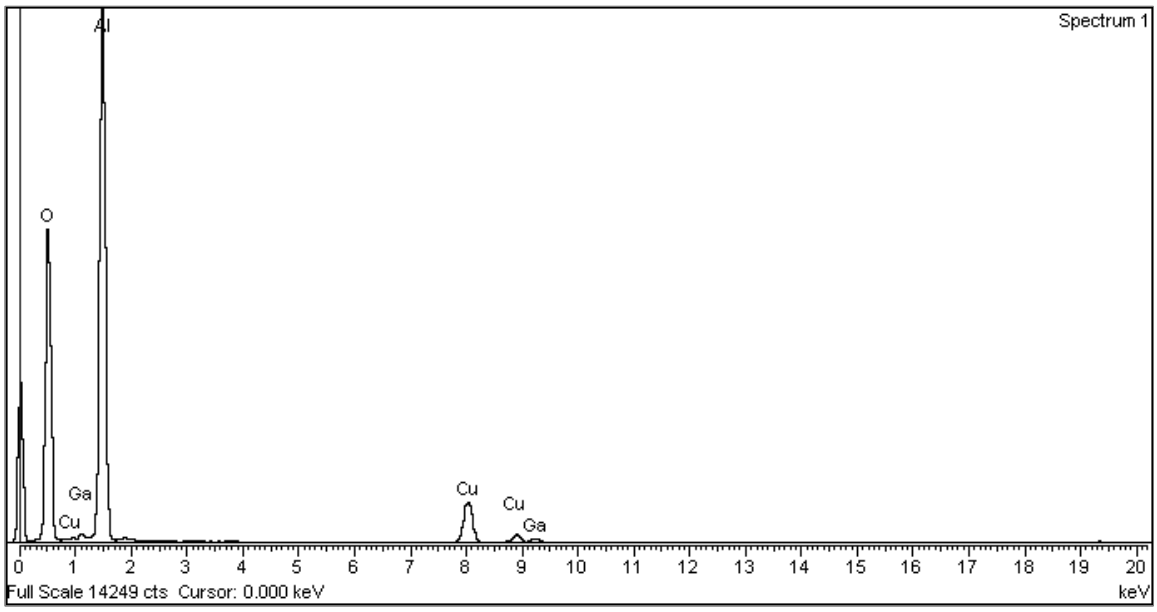


Figure 4.29: A typical TEM-EDX spectra (JEOL 2000FX) of sapphire material in FIB produced TEM foil.

Four elements were present: aluminium, oxygen, gallium, and copper. The first two were from the sapphire, the copper was from the grid, and the gallium was due to implantation during the FIB sample production.

Spectra from three regions were ascertained and the values averaged:

- Ga = (0.4 +/- 0.1) at%
- Al = (40 +/- 1) at%
- O = (59 +/- 1) at%

The concentration of gallium was low, suggesting that there was very little implantation during the FIB sample production. The gallium ions “glanced” the side and did not implant as readily as compared to a more head-on collision.

The elements present in the EDX spectra of the redeposited material (Figure 4.30) were copper (from the grid), gallium, aluminium, and oxygen. Spectra from several regions were ascertained and the values of the different elements averaged:

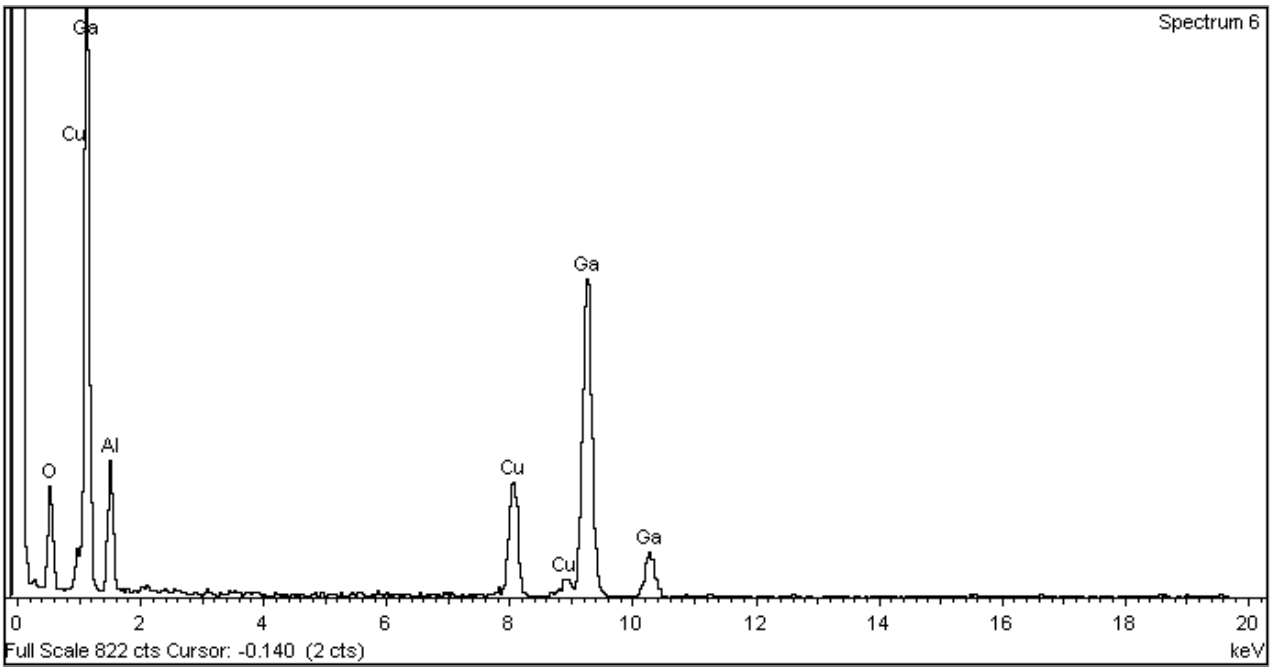


Figure 4.30: A typical TEM-EDX spectra (JEOL 2000FX) of the redeposited material.

- Ga = (37 +/- 10) at%
- Al = (20 +/- 2) at%
- O = (43 +/- 8) at%

The Al/O ratio was 0.47 which was lower than the expected ratio of Al_2O_3. To maintain charge neutrality, both elemental gallium and gallium in solid solution with alumina must have been present. This is discussed in Section 9.1.1.

4.6.2 Implanted Material due to Focussed Ion Beam

Due to the high energy gallium ions hitting the surface in the FIB process, surface material was removed. Gallium ions also implanted into the top surface. The characteristics of the implanted region were very important for microcantilever beams. Two regions underwent ion

implantation: the top surface of the foil or microcantilever beam, and the base of the FIB milled notch.

4.6.2.1 Transmission Electron Microscopy & Electron Diffraction

The low magnification transmission electron microscopy image (Figure 4.31a) shows a darker band due to the implantation; HRTEM showed that this region was crystalline (Figure 4.31b). There was also some redeposited material present underneath the top surface.

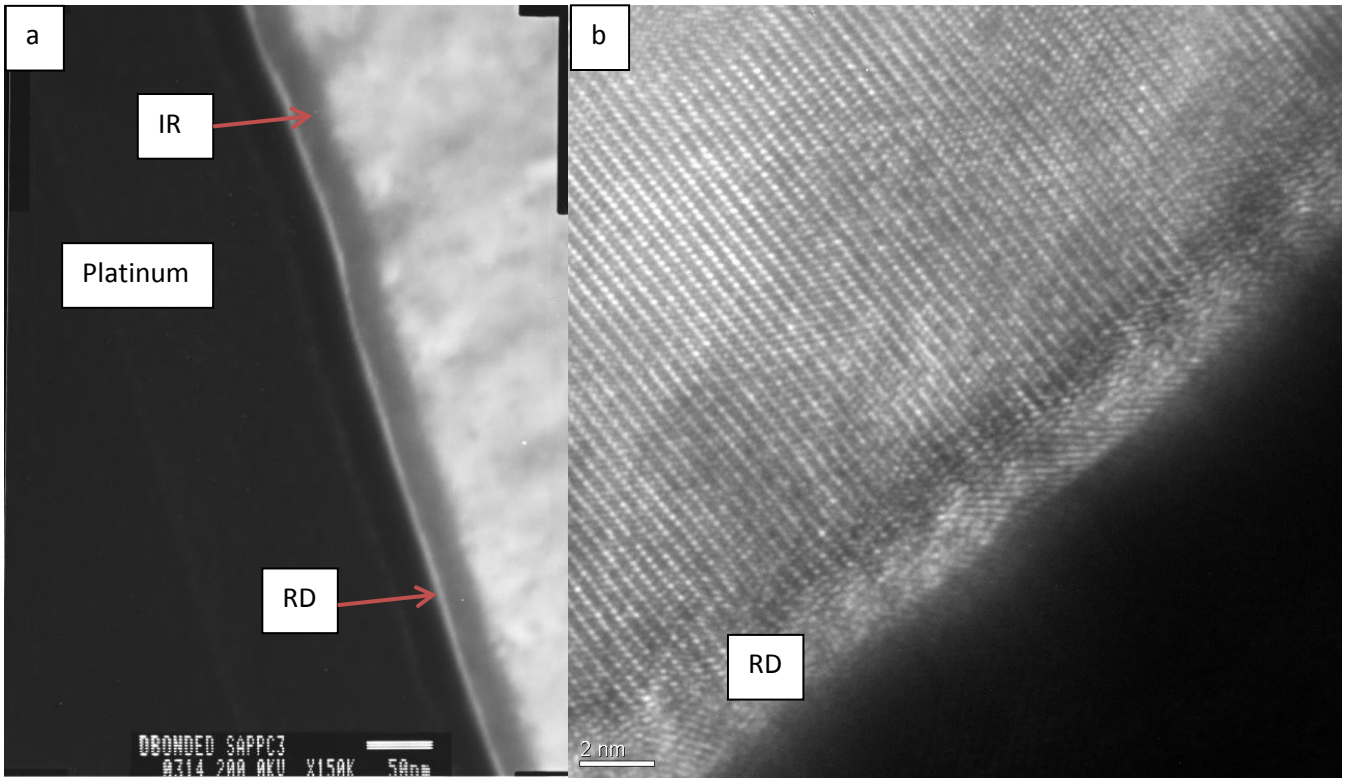


Figure 4.31: Implanted region on the top surface of the sapphire TEM foil; a) low magnification TEM (JEOL 2000FX), b) HRTEM (JEOL 3000F). IR = implanted region, RD = redeposited material.

Nanobeam diffraction of the implanted region was performed (JEOL 2010, by Dr Neil Young, Department of Materials, University of Oxford) with a probe size ≈ 5nm (200kV, 15cm camera length). The ordered arrangement of the diffraction spots showed that the region was crystalline (Figure 4.32)

Underneath the FIB notches was a layer of implanted material at the same depth as that at the top layer of the foil (Figure 4.33). The depth of the implanted region was the same for each beam current as the beam voltage, which determined the implantation depth, was 30kV throughout: (20.5 +/- 1.5) nm for 10pA, (20.7 +/- 0.9) nm for 100pA, and (20.4 +/-1.1) nm for 1000pA. The depth of redeposited material was (29 +/- 2), (27 +/- 1) and (23 +/- 1) nm for 10, 100, and 100pA respectively.

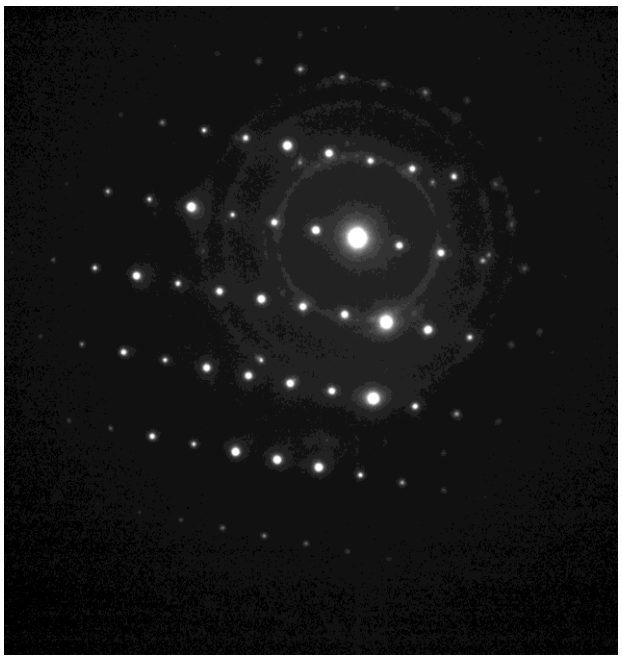


Figure 4.32: Nanobeam diffraction (JEOL 2010) of the implanted region in sapphire

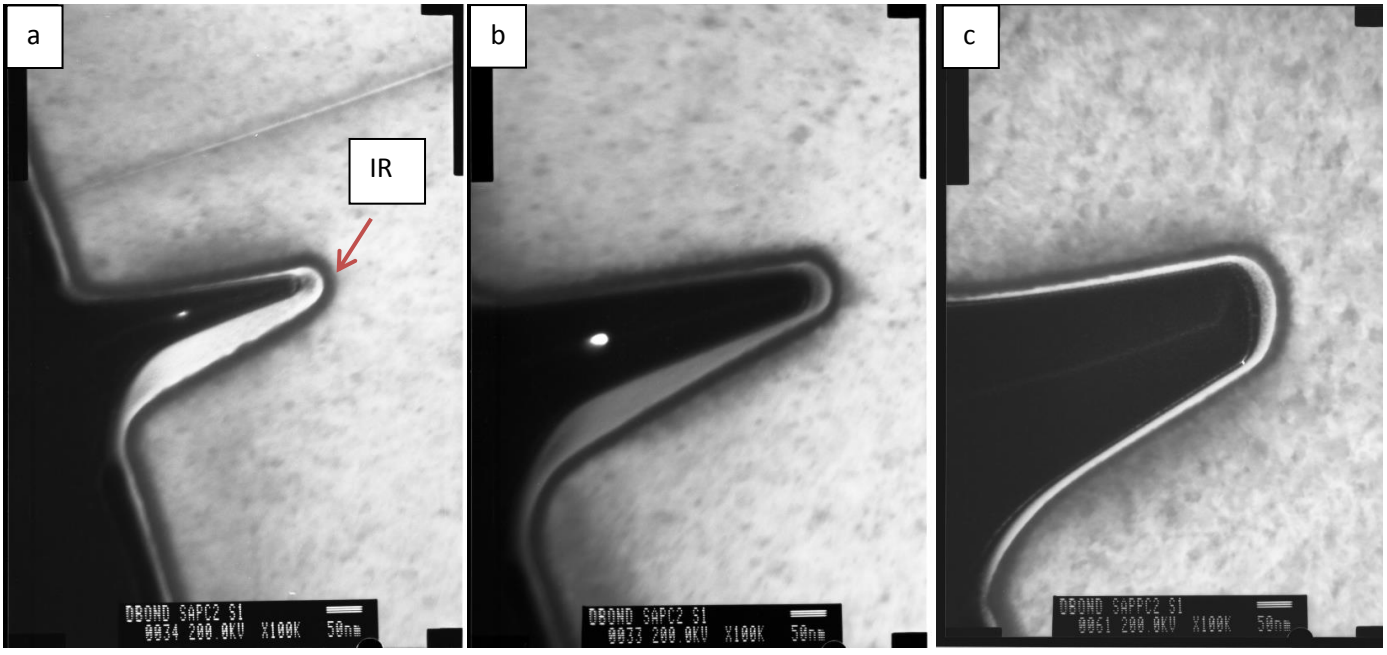


Figure 4.33: TEM (JEOL 2000FX) of FIB produced notches, filled with platinum, at the surface of sapphire at beam currents of: a) 10pA, b) 100pA, and c) 1000pA. The implanted region (IR) was present underneath each notch.

4.6.2.2 Energy Dispersive X-ray Spectroscopy (EDX)

The composition of the implanted region at 1) the tip of the notch and 2) underneath the top surface was ascertained. The compositions for both regions were the same. The results here were for taken from the implanted material at the tip of the notch.

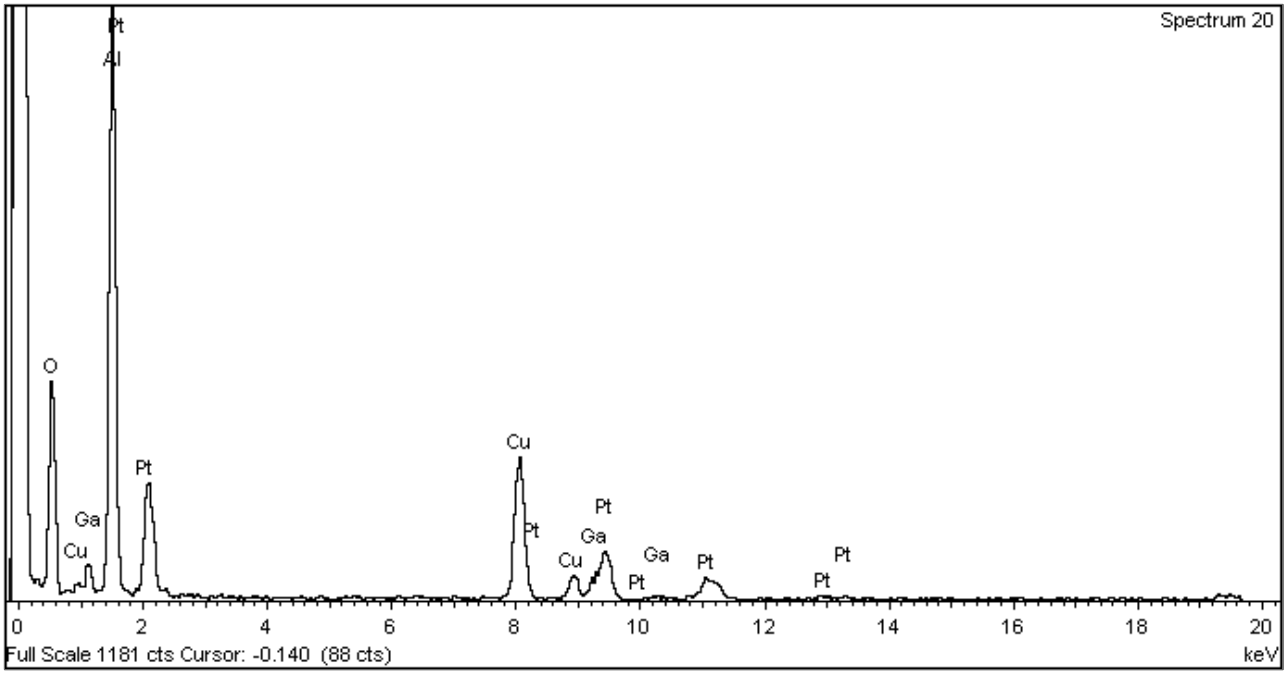


Figure 4.34: A typical TEM-EDX spectra (JEOL 2000FX) of the implanted material.

As the FWHM of the EDX probe was 72nm (i.e. larger than the implanted region), some of the counts came from neighbouring material. Hence, some platinum was analysed. EDX of the implanted region (Figure 4.34), averaged over several scans, was:

- Ga = (3 +/- 1) at%
- Al = (33 +/- 1) at%
- O = (49 +/- 3) at%
- Pt = (15 +/- 5) at%

The ratio between the aluminium and oxygen was 0.67. The gallium content was lower than for the redeposited material but higher than when the beam glanced the surface (Figure 4.29).

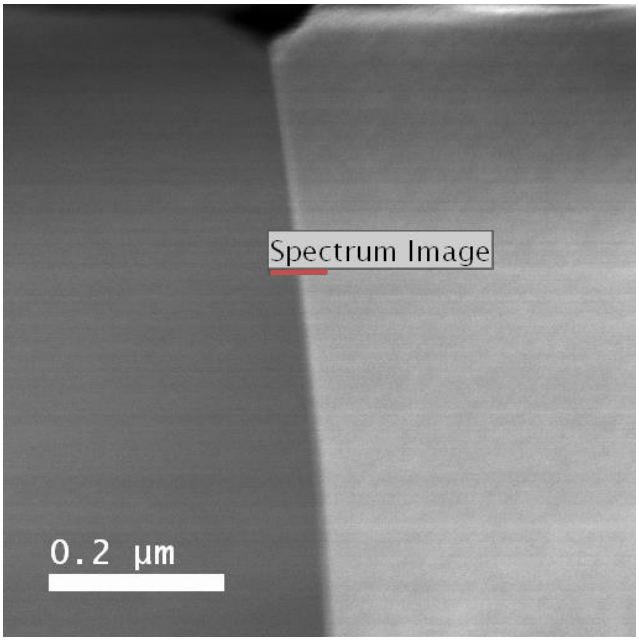
4.7 Electron energy-loss spectroscopy (EELS) of doped TM-DAR samples

The composition of grain boundaries in undoped and 0.012wt% carbon doped TM-DAR was determined using electron energy-loss spectroscopy (EELS) (Section 3.3.5.); the technique was better at detecting elements of a low atomic number than EDX [205, 206]. Aside from trying to detect carbon, other elements were also considered: aluminium and oxygen, magnesium, and silicon, calcium, and potassium (the latter three elements may be present in small amounts and could have interacted with the carbon).

4.7.1 Comparison with standard materials

Unlike the case with techniques such as EDX, there was not a readily available technique to identify the peaks in EELS, due to the importance of the background removal [206]. However, there was an atlas of EELS spectra (Appendix 4.2) which were used to determine the edges and energy-loss near-edge structure (ELNES) in this project.

4.7.2 EELS of Undoped TM-DAR



Several undoped TM-DAR grain boundaries were investigated. A typical grain boundary is discussed herein (Figure 4.35). For each species, spectra were generated at and away from the grain boundary. These were subsequently compared.

Figure 4.35: TEM (VG-STEM HB501) of grain boundary in undoped TM-DAR, with a line indicating the region where the spectra was generated from

The energy-loss of the edge and the energy-loss near-edge structure (ELNES) was identical for aluminium at and away from the boundary (Figure 4.36); there was no edge showing the presence of magnesium. There was an edge due to oxygen (Figure 4.37); there was no edge for carbon (284eV). Furthermore, there were no edges due to silicon (99 & 1835eV), calcium

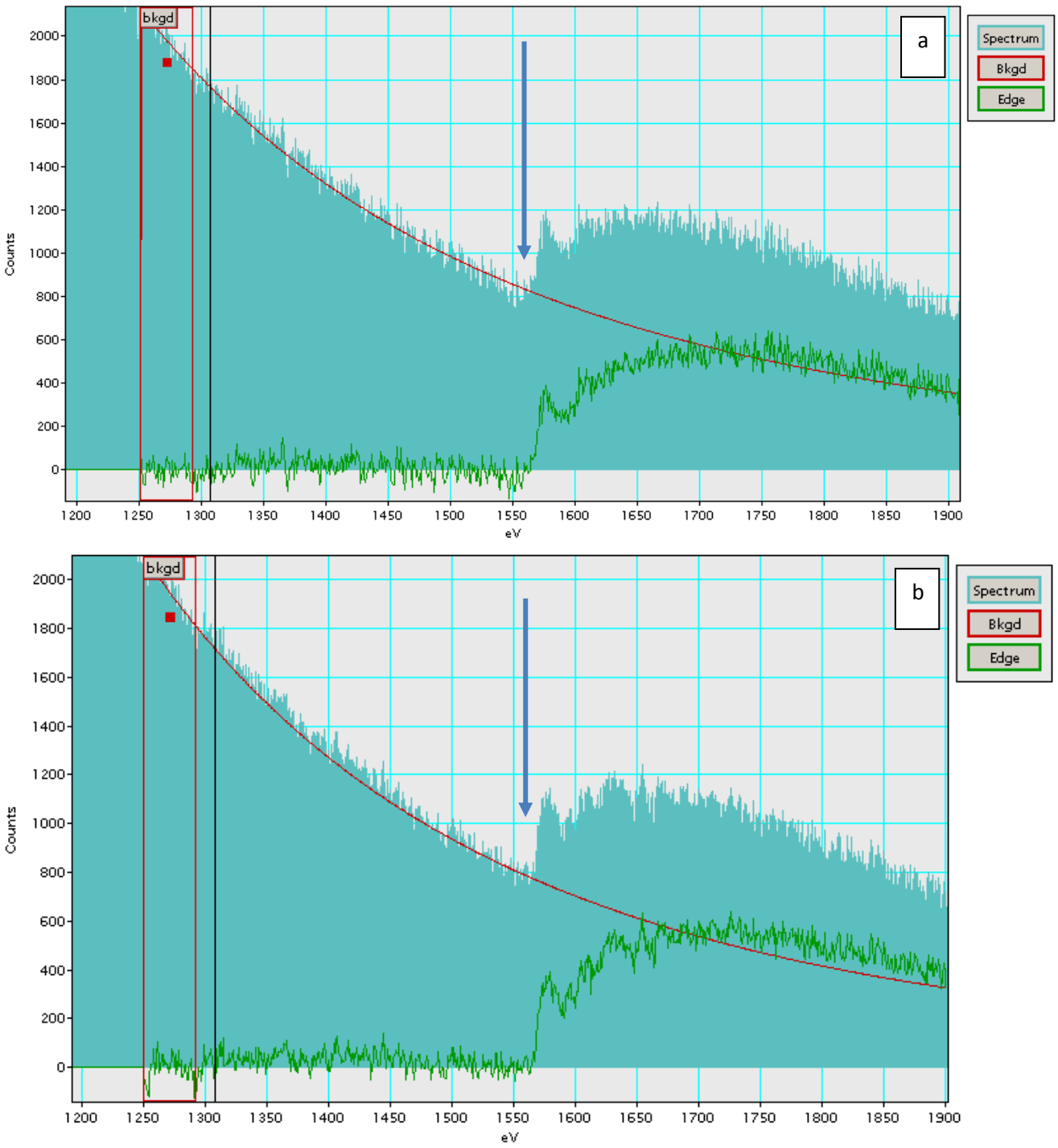


Figure 4.36: EELS spectra for magnesium (at 1310eV, indicated with the black line) and aluminium (indicated with arrow) a) away and b) at the boundary in undoped TM-DAR. The red line "bkgd" was the background removal, and the green spectra "edge" was the resultant spectra after the background removal

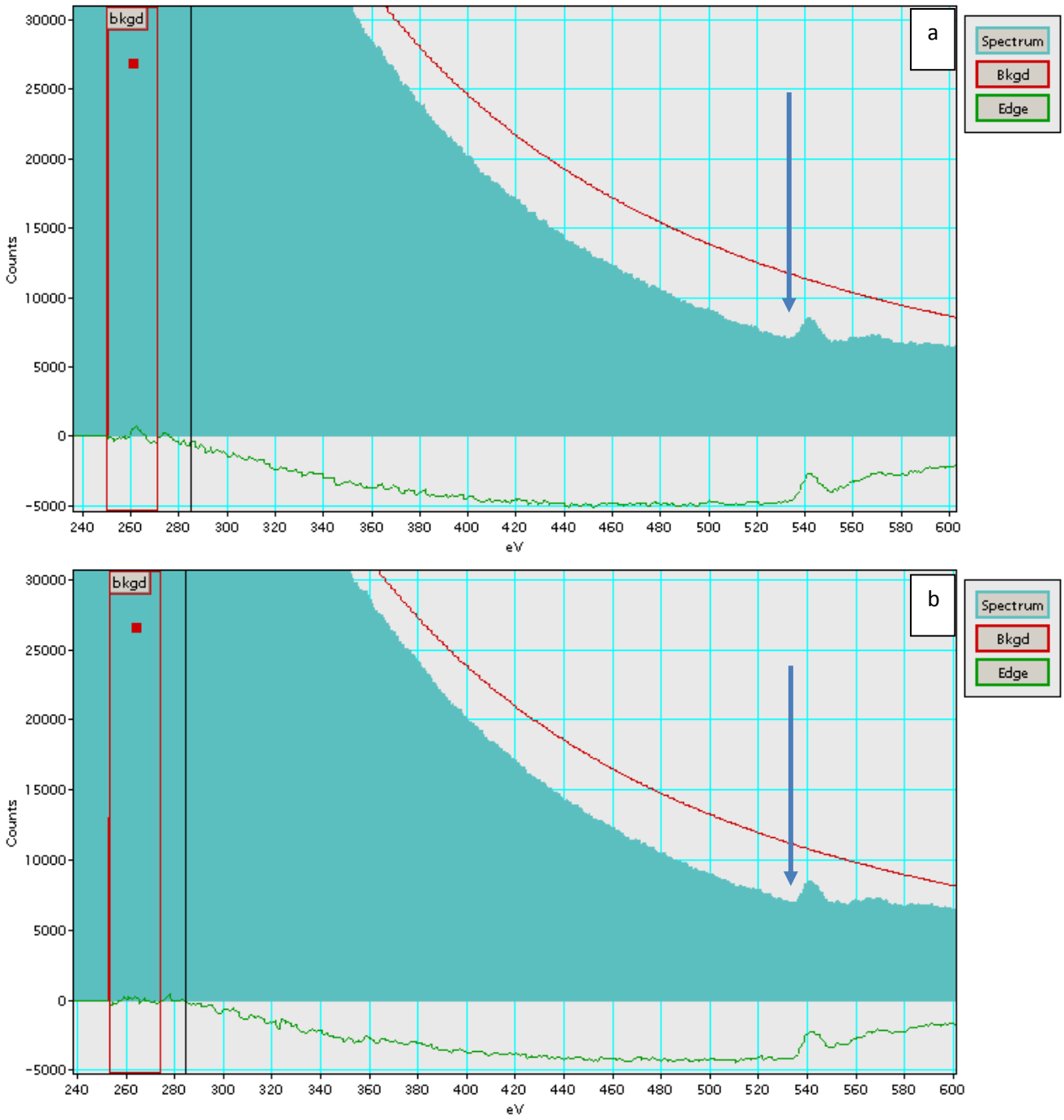


Figure 4.37: EELS spectra for carbon (at 284eV, indicated with the black line) and oxygen (at 535eV, arrowed) a) away and b) at the boundary in undoped TM-DAR. The red line "bkgd" was the background removal, and the green spectra "edge" was the resultant spectra after the background removal

(350eV) (Figure 4.37), or potassium (300eV) (Figure 4.37).

4.7.3 0.012wt% carbon doped TM-DAR

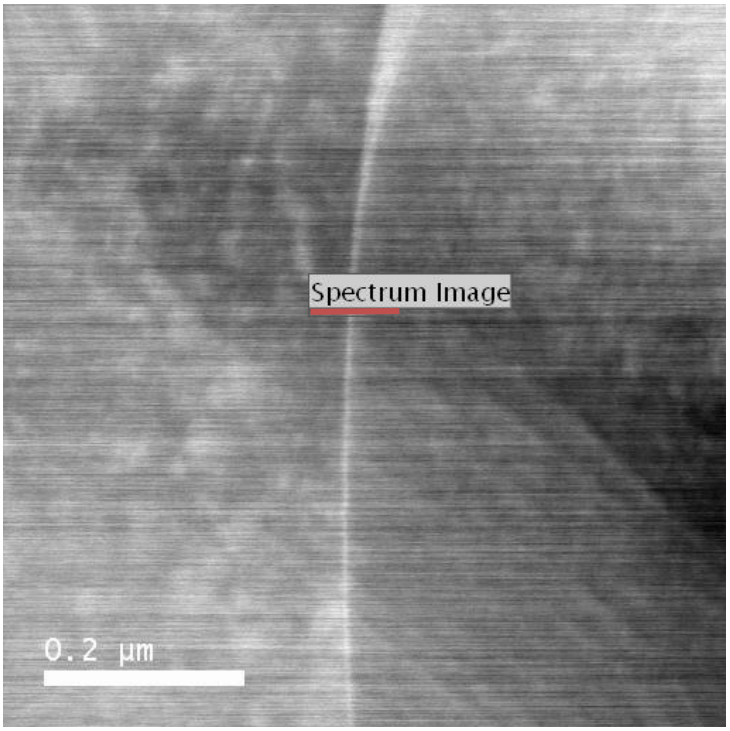


Figure 4.38: TEM (VG-STEM HB501) of grain boundary in 0.012wt% TM-DAR, with a line indicating the region where the spectra was generated from

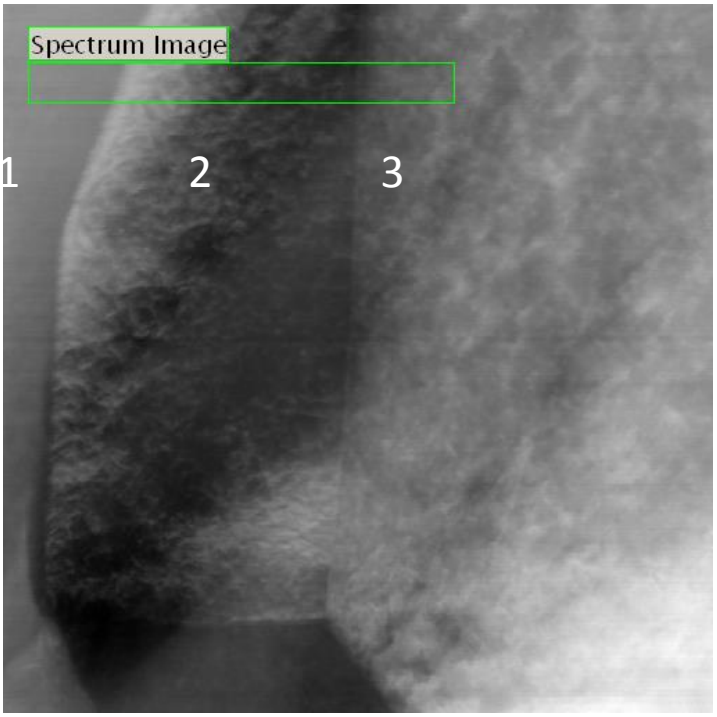


Figure 4.39: TEM image of Mg rich grain, with arrows indicated regions used for EELS analysis

Several grain boundaries were examined in the 0.012wt% carbon doped TM-DAR alumina. A typical boundary (Figure 4.38) is discussed herein.

The energy loss of the edge and the ELNES were the same for aluminium (Figure 4.40) and oxygen (Figure 4.41) at and away from the boundary.

There were no edges associated with carbon in any of the spectra (Figure 4.41). This result was consistent over several grain boundaries. There were no edges present for any of the other elements: magnesium, silicon, calcium, and potassium.

One grain showed different characteristics to the others (Figure 4.39). The edges and ELNES for oxygen and aluminium were the same in Grains 1, 2, and

3. There was a significant concentration of magnesium in Grain 2 (Figure 4.42). This was most likely a grain of $MgAl_2O_4$ spinel; some EELS of this material has been reported previously [207]. Electron diffraction work would be required to confirm this. If a significant proportion of magnesium was forming such grains, the concentration at the grain boundaries may have been substantially lower than expected.

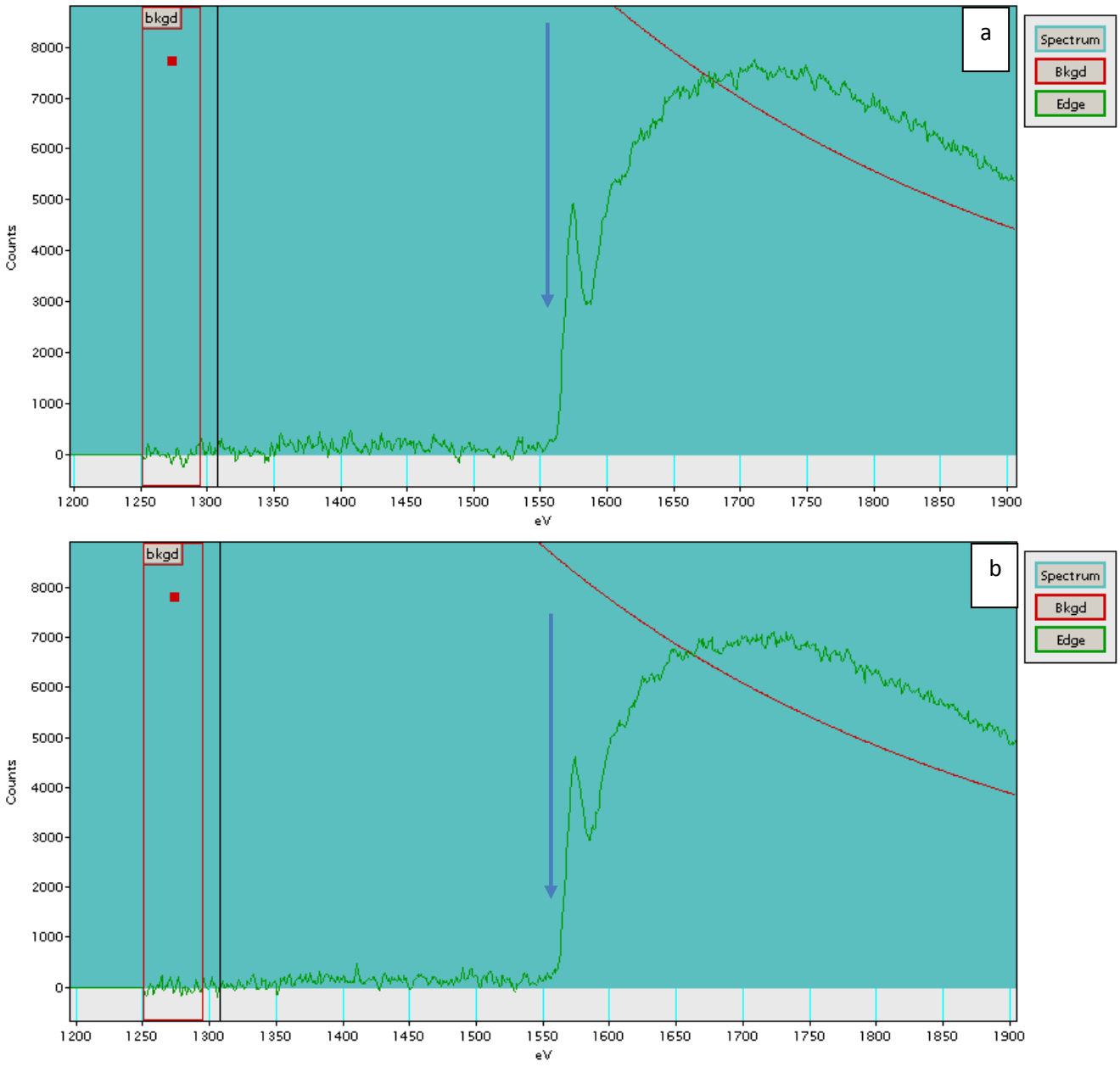


Figure 4.40: EELS spectra for magnesium (at 1310eV, indicated with a black line) and aluminium (arrowed) a) away and b) at the boundary in 0.012wt% carbon doped TM-DAR. The red line "bkgd" was the background removal, and the green spectra "edge" was the resultant spectra after the background removal

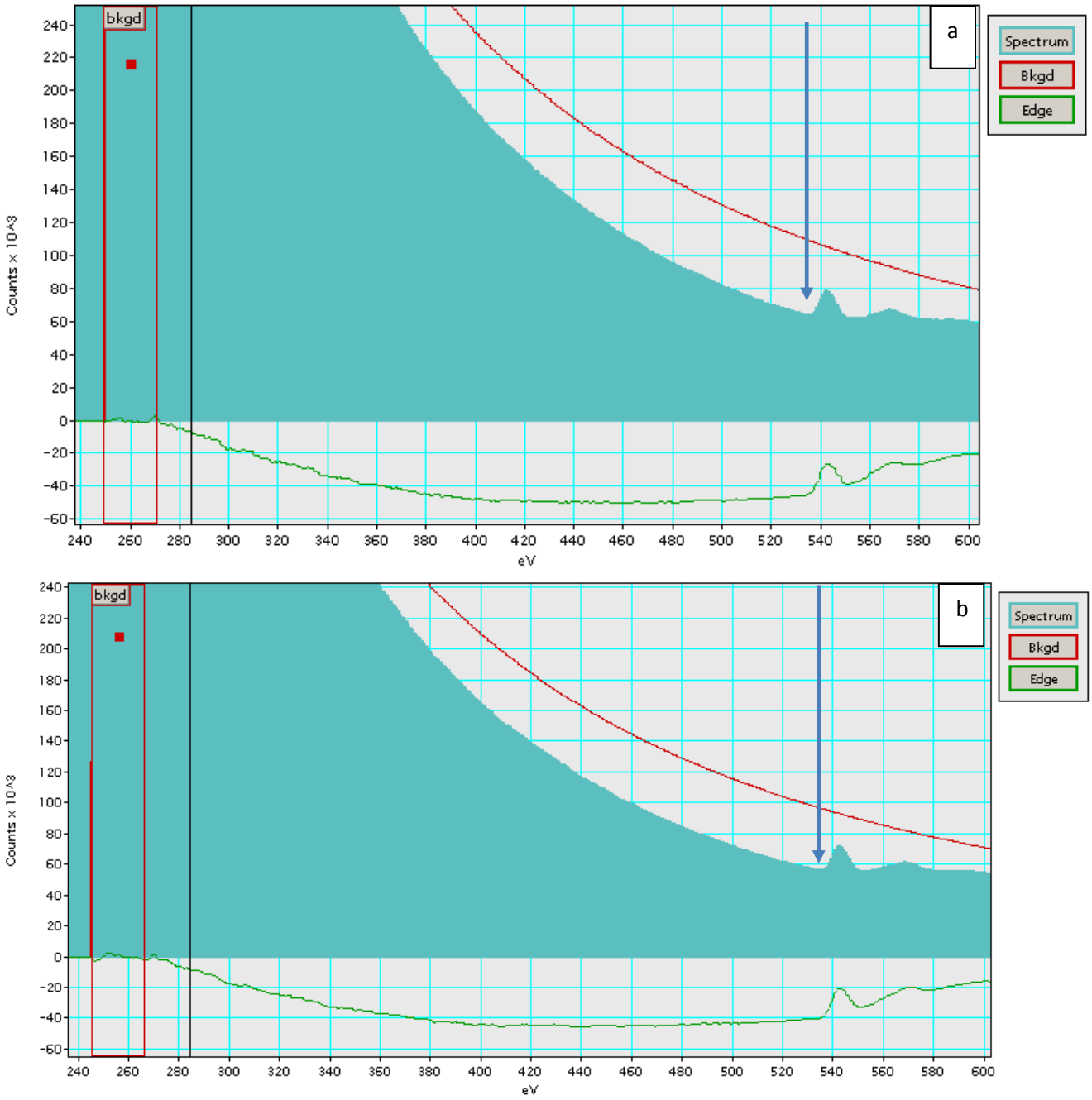


Figure 4.41: EELS spectra for carbon (at 284eV, indicated with a black line) and oxygen (arrowed) a) away and b) at the boundary in 0.012wt% carbon doped TM-DAR. The red line "bkgd" was the background removal, and the green spectra "edge" was the resultant spectra after the background removal

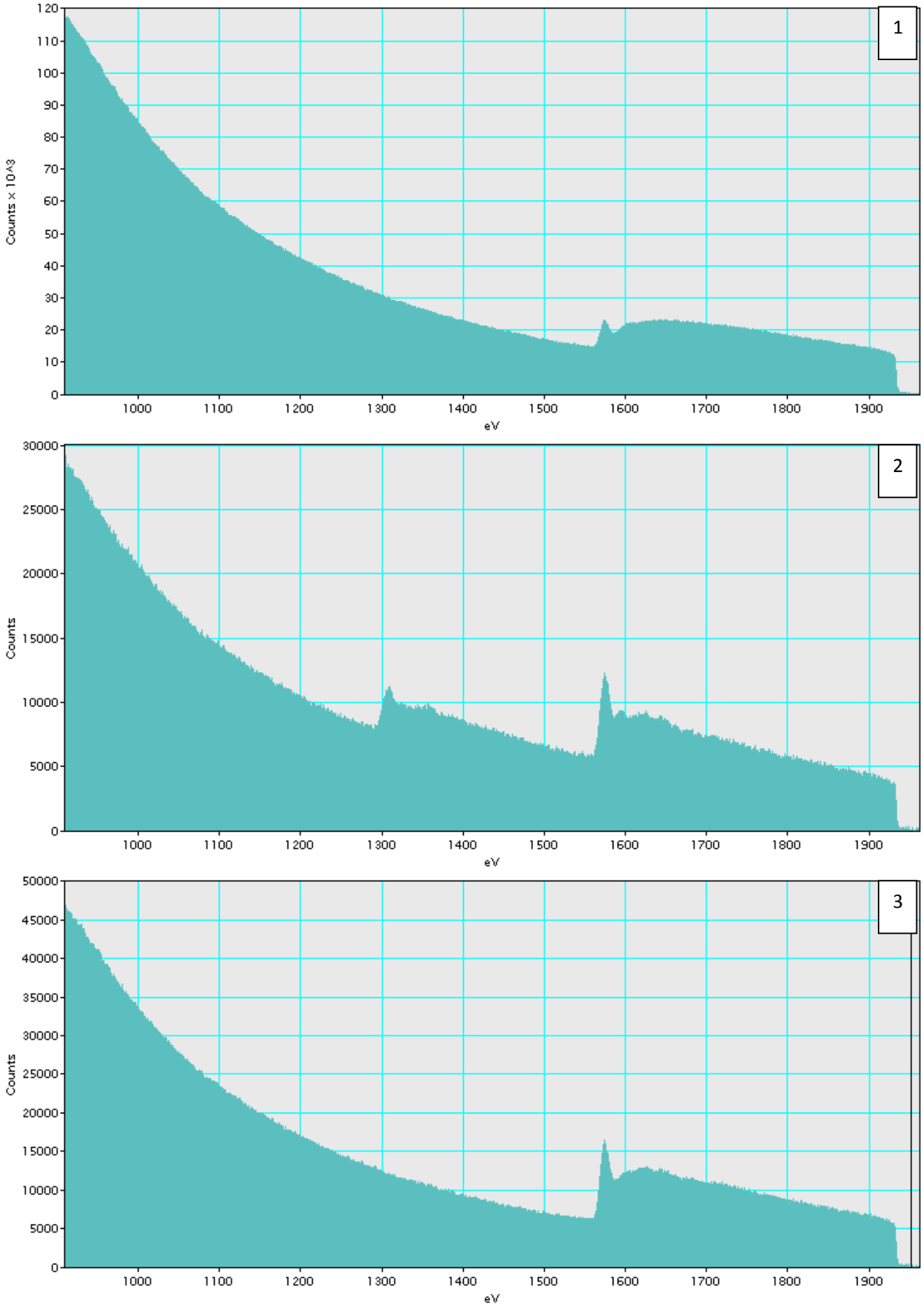


Figure 4.42: EELS spectra for magnesium (at 1300eV) and aluminium (at 1560eV) taken from Grains 1, 2, and 3 (Figure 4.39) in 0.012wt% carbon doped TM-DAR.

4.8. Energy Dispersive X-ray Spectroscopy (EDX) of alumina grain boundaries

The compositions of several grain boundaries in both undoped AES-11C and undoped TM-DAR were tested using TEM-EDX.

4.8.1. Undoped AES-11C sintered to 1600°C

Several grain boundaries were analysed in AES-11C (Figure 4.43); most had a small amount of silicon (Figure 4.44a&b), although the quantitative value varied. The amount of magnesium was difficult to determine due to the overlap between the Mg and Al peaks (Figure 4.44), and was thus not considered.

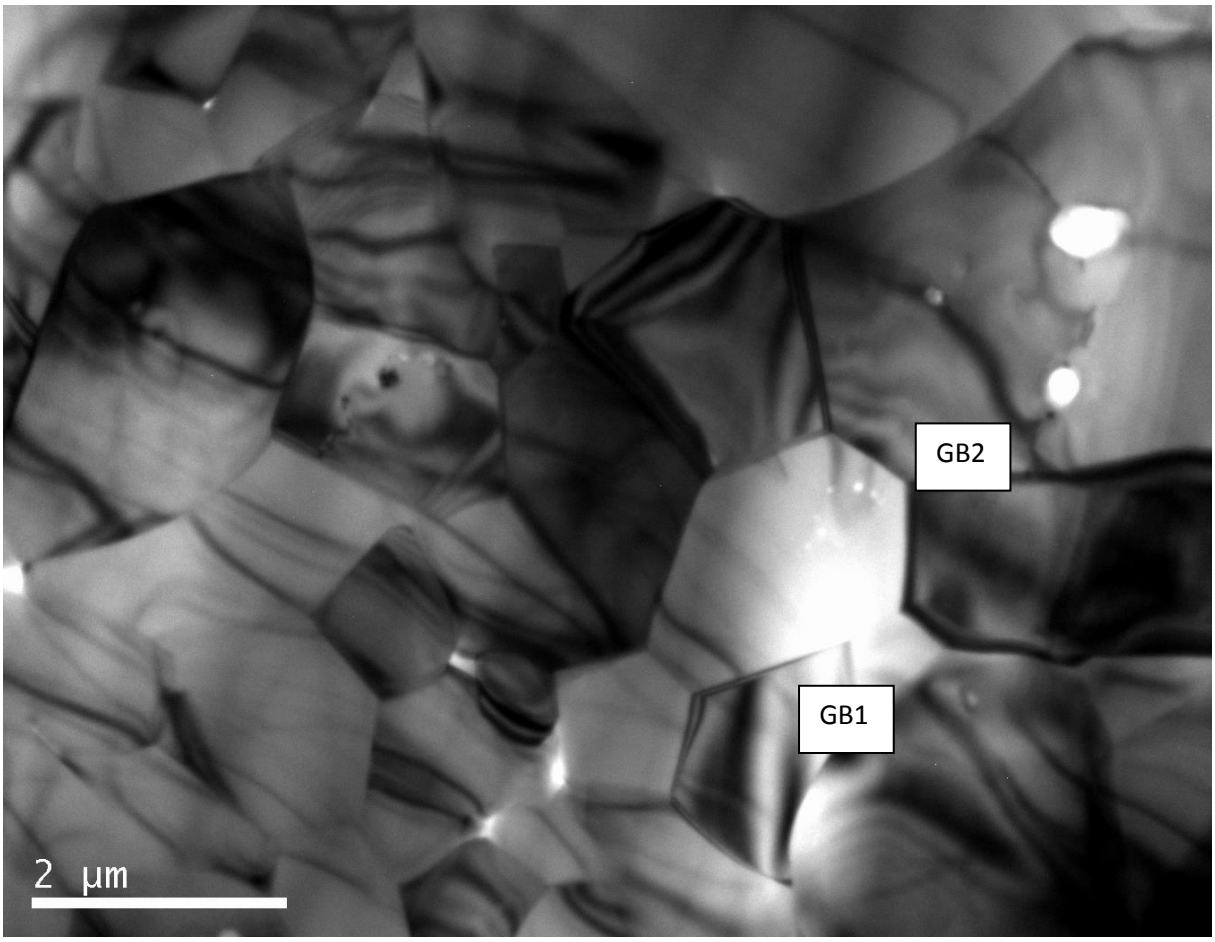


Figure 4.43: TEM (JEOL 2000FX) of undoped AES-11C sintered to 1600°C showing where EDX spectra were taken from

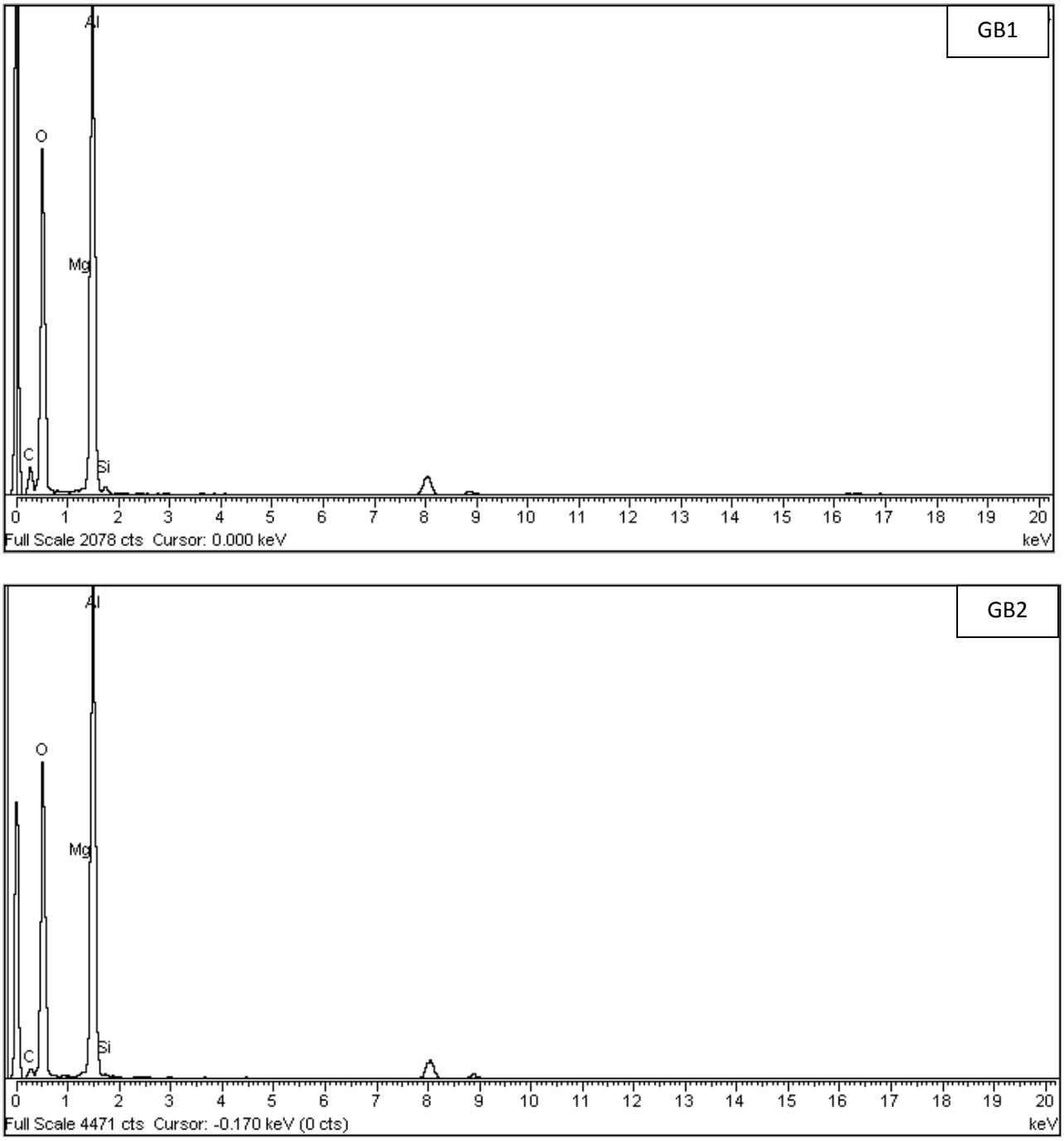


Figure 4.44: TEM-EDX (JEOL 2000FX) of AES-11C (1600°C) grain boundary a) GB1 and b) GB2 in Figure 4.43

The amount of silicon was averaged over 18 boundaries: (0.14 +/- 0.08) at%. No other elements were detected at the grain boundaries.

4.8.2. Undoped AES-11C sintered to 1750°C

14 grain boundaries were analysed with TEM-EDX (JEOL 2000FX). The amount of silicon at the boundaries was (0.05 +/- 0.02) at%.

4.8.3. Undoped TM-DAR sintered to 1600°C

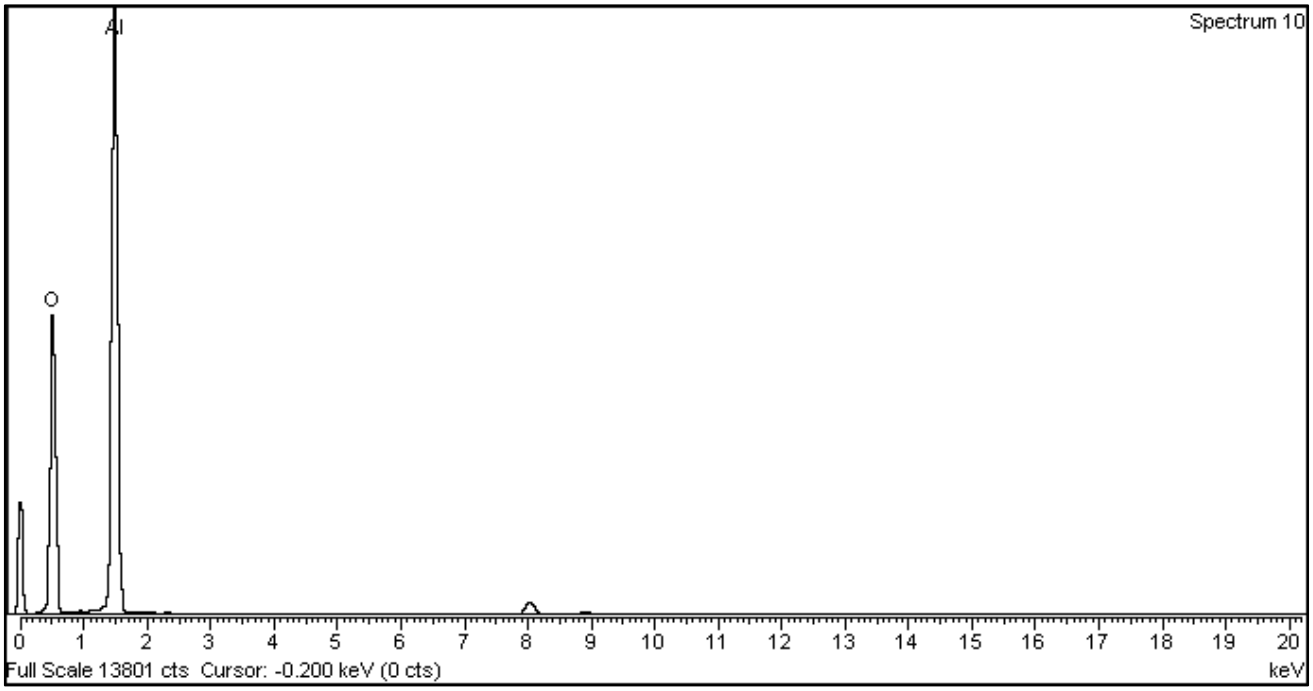


Figure 4.45: TEM-EDX (JEOL 2000FX) of typical TM-DAR (1600°C) grain boundary

10 grain boundaries were analysed in TM-DAR using TEM-EDX (Figure 4.45). In general, only aluminium, oxygen, and carbon (due to coating) peaks were present. There was no determinable peak due to silicon.

4.8.4. 2wt% chromia doped AES-11C sintered to 1600°C

Probing inside the chromia doped AES-11C grains, the amount of chromium was (0.6 +/- 0.2) at% (averaged over 14).

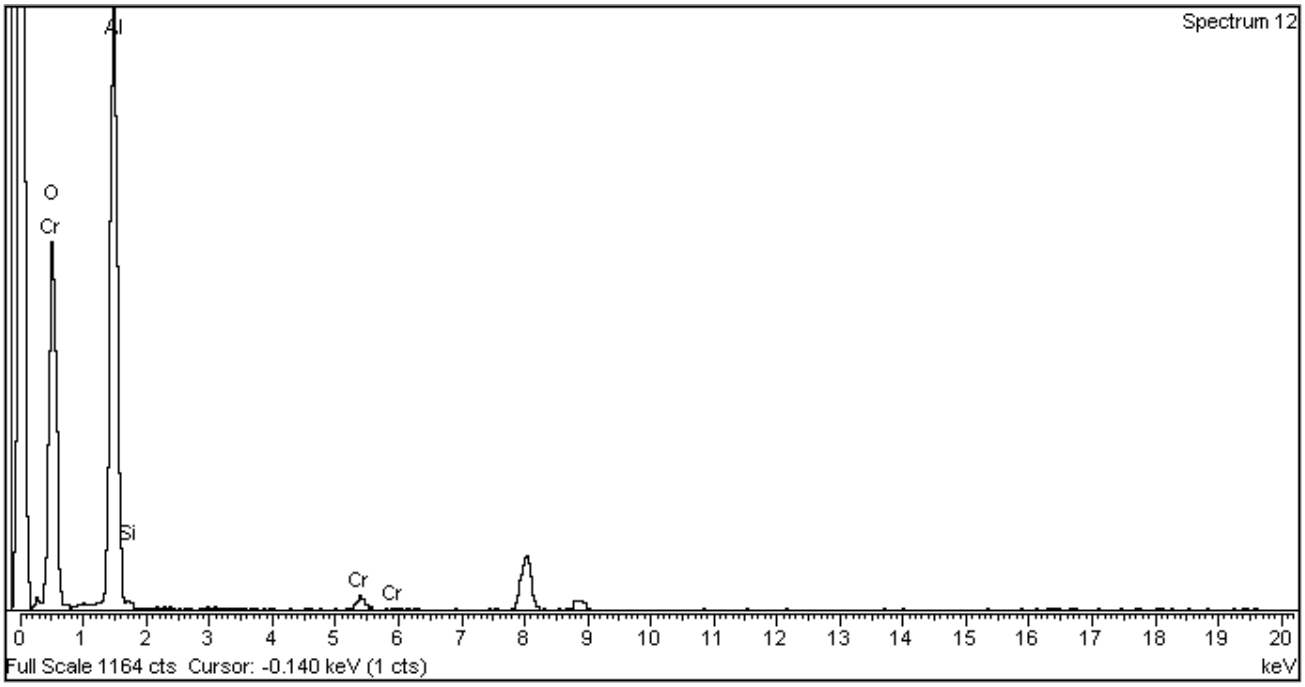


Figure 4.46: TEM-EDX (JEOL 2000FX) of grain boundary of 2wt% Cr_2O_3 doped AES-11C

Analysis of the grain boundaries was also performed, which showed a silicon peak similar to that in undoped AES-11C (Figure 4.46). The amount of chromium and silicon was (0.6 +/- 0.1) and (0.3 +/- 0.2) at% respectively.

4.9. Annealing in vacuum

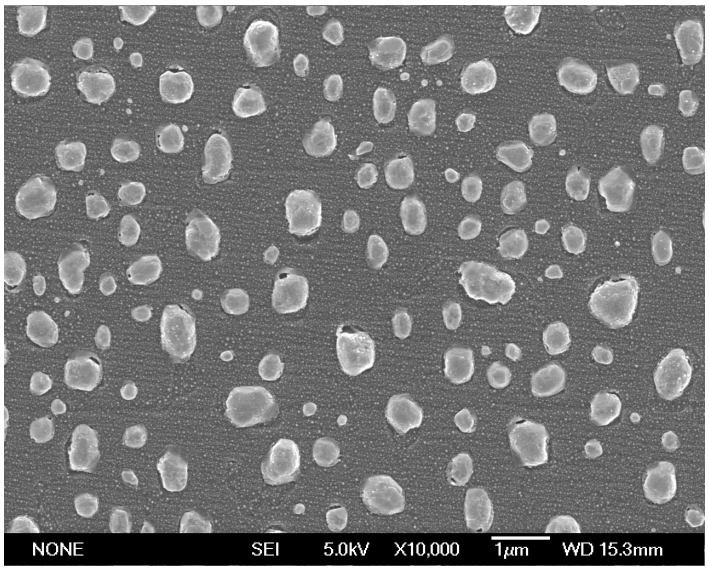


Figure 4.47: SEI (JEOL 6500F) of sapphire after 1000°C anneal

After annealing in vacuum, the thin layer of platinum that was deposited prior to the microcantilever beam production had formed regions on the surface (Figure 4.47); it was seemingly more energetically favourable to de-wet the surface of

the sapphire and form “droplets” on the surface.

SEM-EDX (Figure 4.48b) showed that the particles were very rich in platinum, whereas the surrounding material had a significantly less platinum.

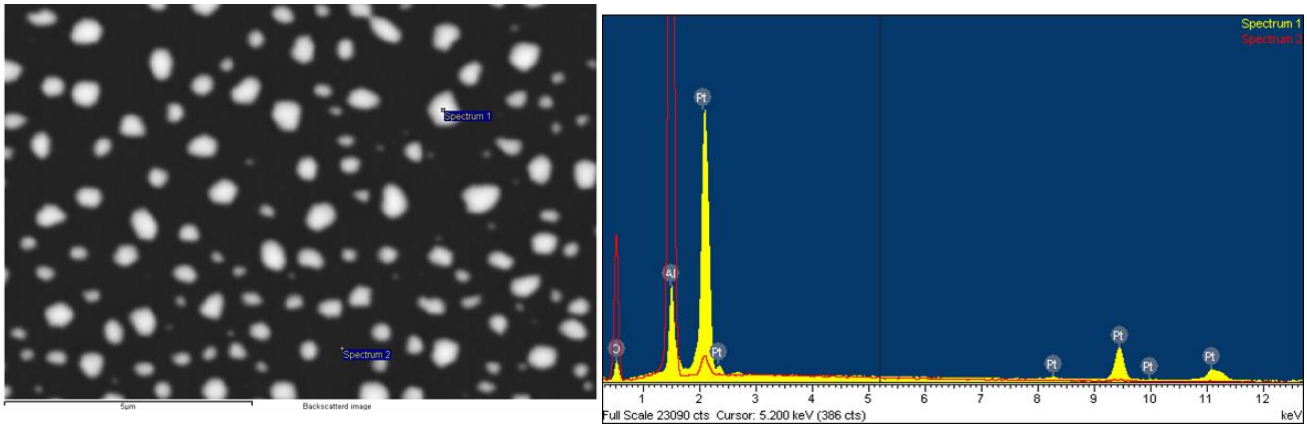


Figure 4.48: a) Back-scattered electron image for top surface of sapphire after 1000°C anneal, and b) SEM-EDX of a surface particle and the surrounding material (JEOL 840A)

In order to further understand the change in the platinum due to the annealing, sapphire TEM foils were produced (Section 3.2.2). Rather than performing ex-situ liftout, the sample was left in place and annealed in vacuum (Figure 4.49). The roughness that was apparent on the surface of the foil due to the FIB cleaning was far less apparent after annealing. The large striations, such as those underneath the right hand notch, were not resolvable after annealing (Figure 4.49b).

There was a substantial change in the redeposited material during annealing. However, whilst the morphology of the redeposited globules was altered (Figure 4.49), it was difficult to determine if there was a reduction in the overall amount of the material. Behind the foil, for example, large regions of redeposited material were either removed or made significantly smaller due to the anneal; however, there were other regions where the amount of redeposited material seemingly increased.

The notches milled on the surface of the sapphire before the platinum deposition did not change structure during annealing. Although the platinum inside the notch was altered, the depth and radius were not.

A second TEM foil was produced to measure the annealed notches. After producing a notch on the bulk sapphire surface at 10pA, the sample was annealed at 1000^{o}C. Thereafter, platinum was deposited on the top surface and the TEM sample produced. After ex-situ liftout, TEM-EDX was performed to determine the properties of the notch; spectra were taken at and away from the tip of the notch. The gallium content was:

- At tip (average of 2): (4 +/- 1) at%
- Centre ≈ 100nm away (average of 2): (0.3 +/- 0.2) at%
- Centre ≈ 300nm away (average of 2): (0.02 +/- 0.02) at%

The notch radii for the annealed beams was measured to be (107 +/- 10) nm (Figure 4.50) which corresponded well to the value of (95 +/- 20) nm (Figure 4.49). Thus, the notch did not broaden during annealing, but the 10pA beam produced broader notches (probably due to the aperture becoming larger over time).

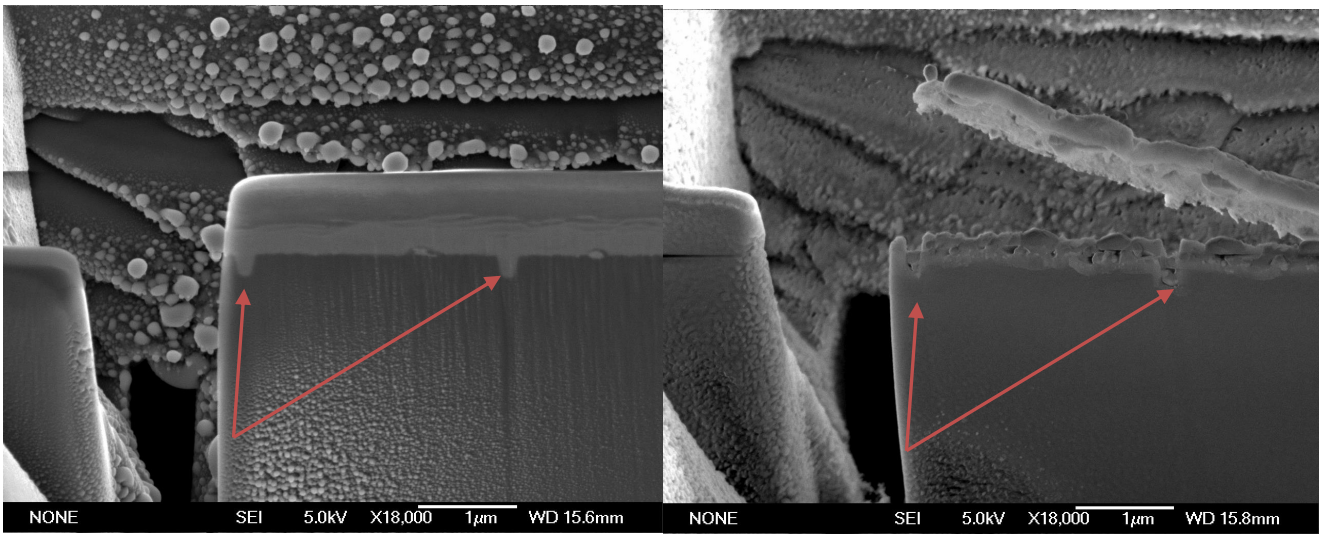


Figure 4.49: SEI (JEOL 6500F) of a thinned sapphire with notches (arrowed) a) before and b) after a 1200^{o}C anneal in vacuum. The surface of the sapphire was affected by the annealing. Tilted to 50^{o}.

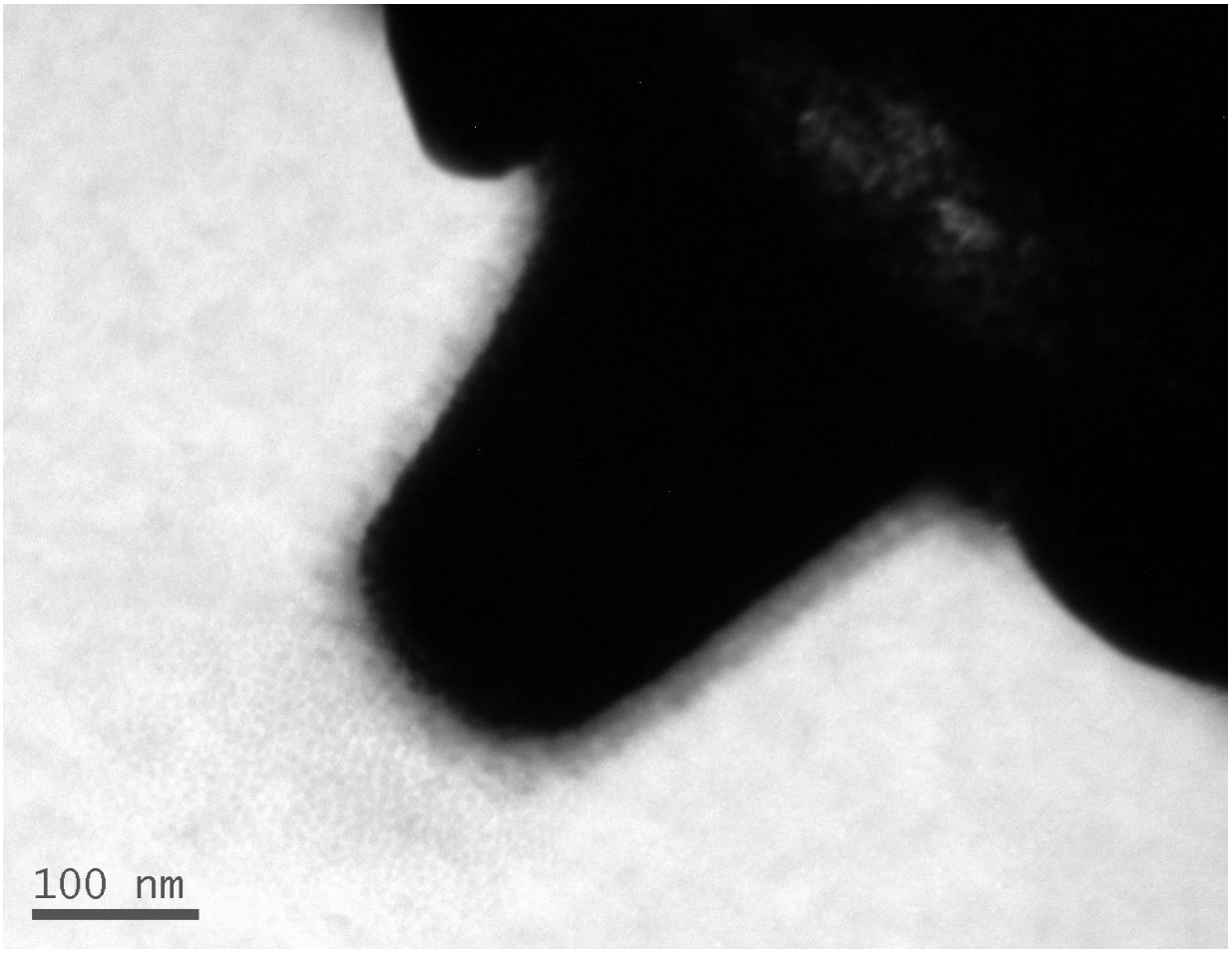


Figure 4.50: TEM (JEOL 2000FX) image of the notches annealed in vacuum

4.10 Nanoindentation

4.10.1 Nanoindentation of AES-11C alumina

16 indents were produced on the surface of AES-11C alumina (MTS NanoindenterXP) (Section 3.7.2.). The depth was 1100nm which gave a maximum load of ≈ 482mN. Indentations in silica to the same depth were used to calibrate the indenter tip (Analyst, MTS Systems). The average modulus was (442 +/- 20) GPa.

4.10.2 Nanoindentation of FIB altered sapphire

The mechanical properties of the FIB damaged material were analysed using nanoindentation with continuous stiffness analysis. Two materials were considered: the gallium implanted region, and the redeposited material.

4.10.2.1 Nanoindentation of gallium implanted sapphire

25 nanoindents, to a depth of 100nm, were made on the surface of an undamaged piece of c-plane sapphire (MTS NanoindenterXP). The mechanical properties were corrected using silica calibration (Analyst, MTS systems). The stiffness and hardness were measured during loading; the mean properties with depth were determined by averaging over the 25 indents.

The top surface of an uncoated piece of c-plane sapphire was imaged 15 times with the ion beam (FEI FIB200, 1000pA beam current). Very short exposure times were used; this was to reproduce the type of damage expected to occur on the top surface of a microcantilever

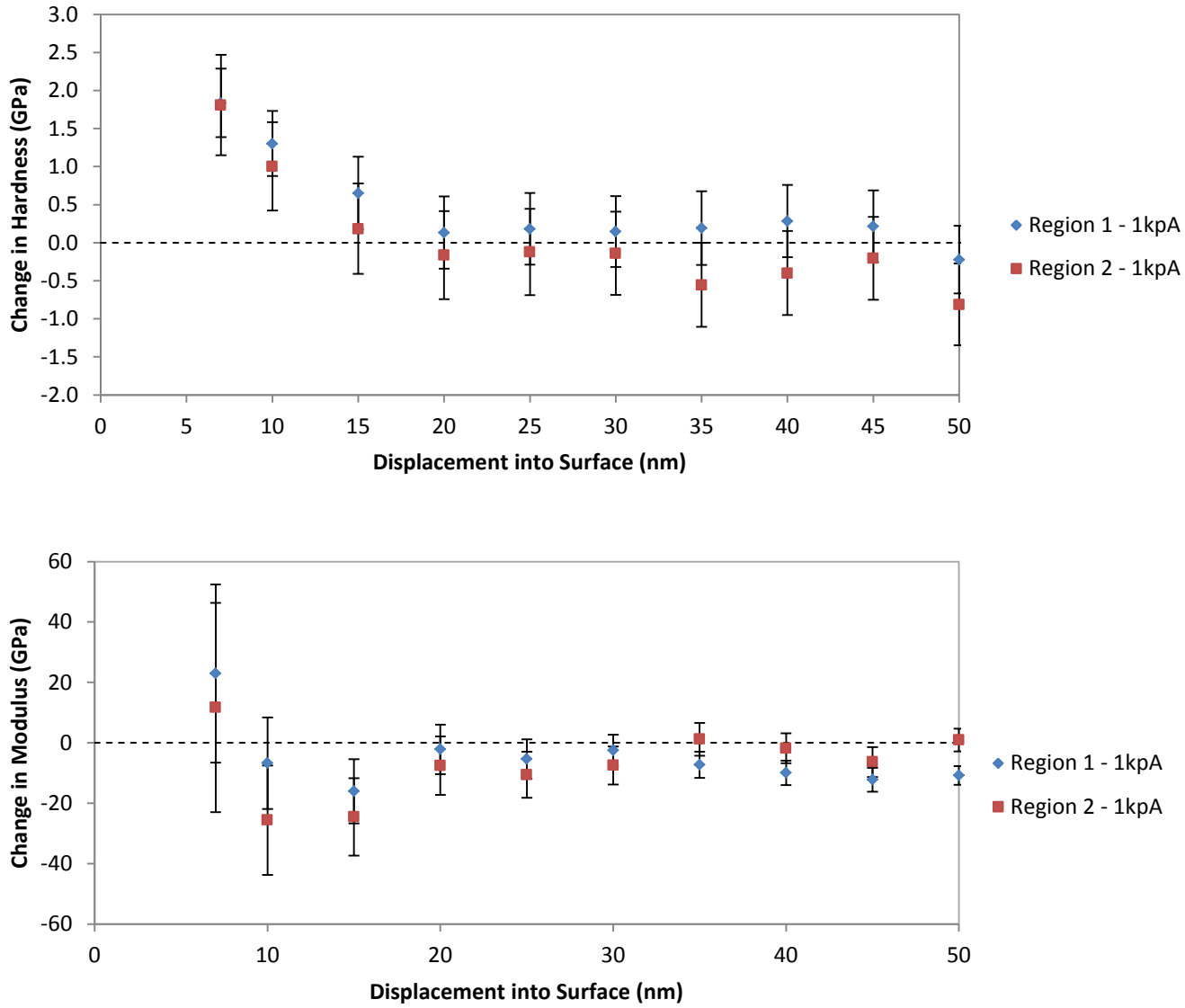


Figure 4.51: Difference in a) hardness and b) modulus between a region damaged by 15 exposures of a 1kpA FIB (FEI FIB200) beam and undamaged sapphire.

beam. Thereafter, 25 indents were made on the top surface of the damaged sapphire. The change in properties due to the FIB was determined for different nanoindentation depths (Figure 4.51). The mean hardness or modulus was determined at each indentation depth by averaging over the 25 indents.

There was a slight increase in the hardness due to the gallium implantation. Previous implantation work [163] has shown a variation in hardness with implantation, such that at low doses the hardness increases above nominal (around 1.6 times larger), but then decreases to around 0.6 times the nominal at higher doses. As the decrease was due to amorphization of the top surface (not seen in this work), it is expected that gallium implantation due to the FIB (and thus residual stress) increases the indentation hardness. The residual stress due to gallium implantation was measured as (13 +/- 5) GPa (Section 7.2.1.); this is comparable to the aforementioned previous work [163] and, as such, it would be expected that the hardness would increase above nominal.

Any change in the modulus was less clear. There was a value lower than the undamaged sapphire between 10 and 20nm (of up to around 25GPa). However, due to the effect of the underlying sapphire and the implanted region being very thin, it was difficult to differentiate the properties of the implanted region and the sapphire.

Other artefacts will also be affecting the nanoindentation results, due to the small indentation depths. If the tip is blunt, the measured mechanical properties will be affected; the indentation width and load are larger if the tip is blunt. The extent of bluntness is apparent by noting the ratio of projected areas between the tip used here and a perfect Berkovich (3.17, Section 3.7.2.). Whilst indentation area calibration was performed on silica, there are errors in the calibration and it is probable that mechanical properties from small indent will have relatively large errors associated with them. Furthermore, the sensitivity of the tip to residual stress in the top surface is reduced by the tip bluntness. As such, although the residual

stress in the top surface may have been large, the blunt tip was not sensitive enough to detect this stress.

Another source of error may be related to the displacement noise floor [208], which determines the minimum useable indent depth. This is generally 20 times the value of the average roughness (Ra), such that the outputted mechanical properties are well above the noise. For the sapphire used here, Ra was found to be (0.16 +/- 0.05) nm (Pacific Technology Nano-R AFM, Appendix 4.3). Hence, providing the indent is greater than 3.1nm, the mechanical properties from the indentation should be valid [208]. Thus, this effect should not contribute to the errors in the nanoindentation.

Overall, analysis of the nanoindentation is difficult due to the associated errors, especially the effect of the substrate and the indenter tip bluntness.

4.10.2.2 Nanoindentation of redeposited material

The uncoated piece of c-plane sapphire had several large, deep boxes milled onto the surface using 1000pA beam current (FEI FIB200). 25 indents were made per box, and the results for a given depth were averaged. Using the aforementioned undamaged sapphire values, the difference in the properties due to the milling was determined (Figure 4.52).

As the redeposited material is globular (Figure 4.49a, for example), the trenches are not evenly filled. Also, it is possible that the redeposited material at the bottom of the trench is different to that at the top. In Figure 4.49a, for example, there are some redeposited globules sitting on top of a smooth region. Furthermore, whilst the boxes may have been deep, the underlying sapphire may still have had an effect on the elastic response especially at large indentation depths. As a result, the indentation response was not uniform with depth (Figure 4.52).

As it was unclear how the material was responding during loading (e.g. densifying, globules being pushed together, effect of the underlying sapphire), it was difficult to determine what

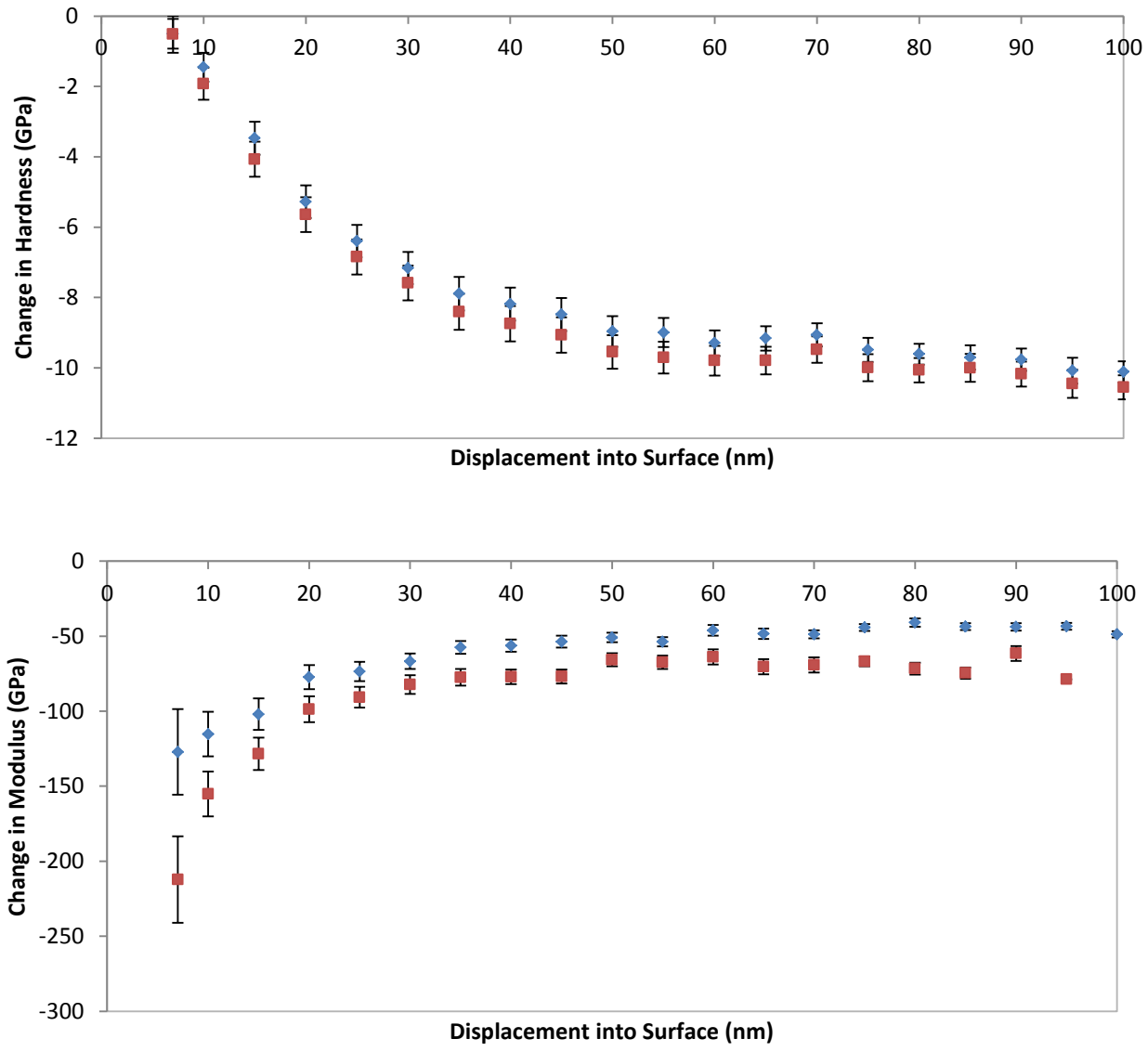


Figure 4.52: Difference in average hardness (between damaged and undamaged) with displacement (100nm) for two FIB-milled regions. Errors bars were a combination of standard errors from the undamaged sapphire and the damaged sapphire samples.

the elastic modulus and hardness of the redeposited material was. However, the two key results are that 1) the modulus is lower than the sapphire at all depths, and 2) the modulus is not insignificant. The latter is important; if the redeposited material has a non-negligible elastic modulus, the presence of the material under the microcantilever beams may affect the measured beam stiffness.

4.11. Summary of characteristics

Several properties of the different materials used in this project are discussed above. These are summarised in the following tables.

4.11.1. Summary of characteristics – polycrystalline alumina

Alumina	Sint Temp (°C)	Grain Size (μm)	Density (%)	Twins?	Dislocations?	Composition
AES-11C	1600	2.7 +/- 0.9	99.7 +/- 0.7	1 per 100	1 per 5	Si @ GB, K & Ca @ Tw
AES-11C	1750	7.6 +/- 2.1	99.9 +/- 0.6	1 per 100	1 per 5	Si @ GB, K & Ca @ Tw
2%Cr AES	1600	2.1 +/- 0.4	99.2 +/- 0.7	1 per 125	1 per 4	Cr in grains, Si @ GB, K & Ca @ Tw
2%Cr AES	1750	10.6 +/- 2.9	99.3 +/- 0.3	-	-	-
3%Cr AES	1600	1.9 +/- 0.3	98.7 +/- 0.4	1 per 250	1 per 3	-
5%Cr AES	1600	1.5 +/- 0.2	98.2 +/- 0.3	None	1 per 2	-
TMDAR	1600	4.3 +/- 0.7	99.8 +/- 0.8	None	1 per 5	No impurities detected (EDX)
TMDAR	1750	5.1 +/- 0.9	99.7 +/- 0.4	None	1 per 5	-
TMDAR - v	1500	2.2 +/- 0.2	100.0 +/- 0.1	-	-	No impurities detected (EELS/EDX)
0.012%C TMDAR - v	1500	2.4 +/- 0.2	100.01 +/- 0.01	-	-	No impurities detected (EELS/EDX)
2%Cr TM	1600	3.9 +/- 0.5	98.4 +/- 0.9	-	-	-
5%Cr TM	1600	3.8 +/- 0.4	97.1 +/- 0.7	-	-	-

Table 4.6: Master table of properties for the alumina materials tested in this project. Cr = Cr_2O_3, C = carbon, GB = grain boundaries, Tw = twin boundaries, v = vacuum. Twins: approximate number of twinned grains to untwined. Dislocations: approximate number of grains with dislocations in to those without.

4.11.2. Summary of properties – FIB altered materials

Material	Structure	Composition	Where	Depth	Modulus
Before annealing					
Implanted	Crystalline	Ga: (3 + 1) at%	Under top surface / notch (below redeposited)	≈ 21nm (beam current independent)	Difficult to determine
Redeposited	Amorphous	Ga: (37 +/- 10) at%	Under top surface / notch (above implanted)	Beam current dependent: 10pA ≈ 29nm, 100pA ≈ 27nm 1000pA ≈ 23nm	140 to 220GPa below sapphire at small indent depths 50 to 70GPa below sapphire at large indent depths
After annealing					
Implanted	-	Ga: (4 +/- 1) at%	Under top surface / notch (below redeposited)	≈ 19nm	

Table 4.7: Master table of properties of FIB damaged materials, before and after annealing

Chapter 5 Macroscopic Mechanical Property Measurements

The following macroscopic tests were performed in this work on different aluminas: four-point flexure, single-edged V-notched beam fracture toughness, and uniaxial compression tests. The results of these tests are the focus of this chapter.

5.1 Acoustic emission – initial tests

In order to differentiate between acoustic emission from the bulk and that from the contact between the rollers / platens, preliminary tests were performed. Samples were loaded to a point before failure, unloaded, and re-loaded. Two effects were expected (Section 2.5):

- **Kaiser effect**: Little or no acoustic emission until at and above previous maximum load (Figure 5.1) as the material behaves either elastically or there is local crushing that does not occur during the re-loading stage [209]. This often occurs up to around 75 – 85% of the failure strength [209].

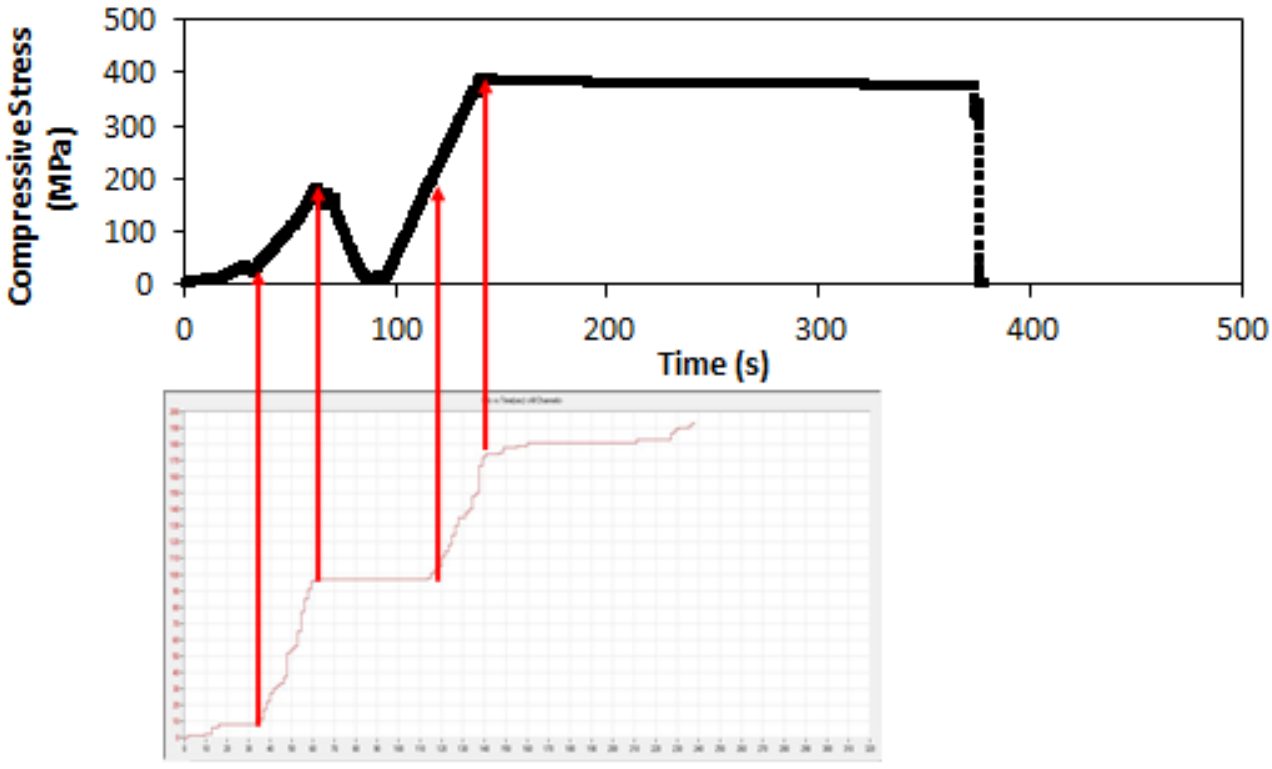


Figure 5.1: a) Compressive stress against time and b) Cumulative number of hits against time for compressed AES-11C sample showing the Kaiser effect.

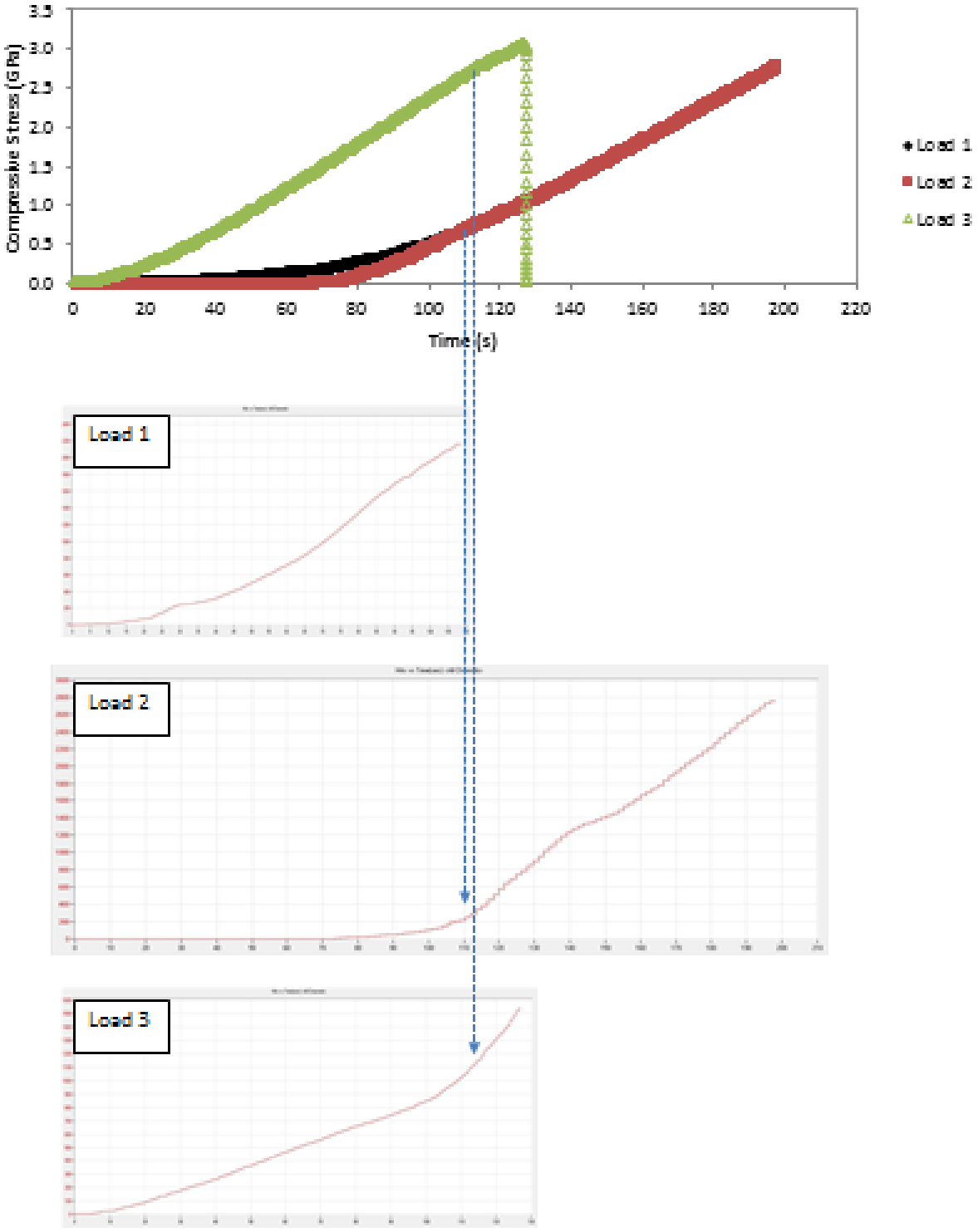


Figure 5.2: a) Stress against time and b) Cumulative hits against time for an AES-11C sample in compression showing the Felicity effect.

- **Felicity effect**: Significant acoustic emission below previous maximum load [209] (Figure 5.2). In Figure 5.2, Load 1 is stopped at 0.7GPa. During Load 2, little acoustic emission is recorded below this stress (i.e. Kaiser effect); furthermore, the hits are low-amplitude. Load 2 is stopped at 2.8GPa. A considerable amount of acoustic emission is detected below this stress during Load 3 (i.e. Felicity effect), although all hits are <76dB. At around 2.8GPa during Load 3, the number and amplitude of hits increases dramatically until failure occurred. The acoustic emission during the latter stages of Load 2 is probably due to inelastic behaviour (e.g. crack nucleation, propagation).

Thus, the acoustic emission response is defined into two characteristic groups:

A) At low loads (approx. <1GPa), the acoustic emission showed the Kaiser effect and is due to elastic response of sample and local crushing between platen / rollers and sample.
B) At higher loads (approx. >1GPa), the acoustic emission shows the Felicity effect due to inelastic response of material (i.e. crack nucleation and propagation).

These groups were a useful guideline for determining whether the acoustic emission is due to elastic or non-elastic response of the material.

5.2 Macroscopic four-point bending tests

Following the method described in Section 3.4.3., flexural strength tests were performed using four-point bending. Undoped and 5wt% doped AES-11C are considered in detail; thereafter the key results of all materials are shown in Table 5.1.

5.2.1 Undoped AES11-C sintered at 1600^{o}C – fracture strength

The mean flexural strength and standard error from the 27 AES-11C samples were (331 +/- 13) MPa.

The Weibull plot of the flexural samples was constructed (Section 3.5.3.) (Figure 5.3). Two regions were determined with Weibull moduli, m, of 12 and 3.

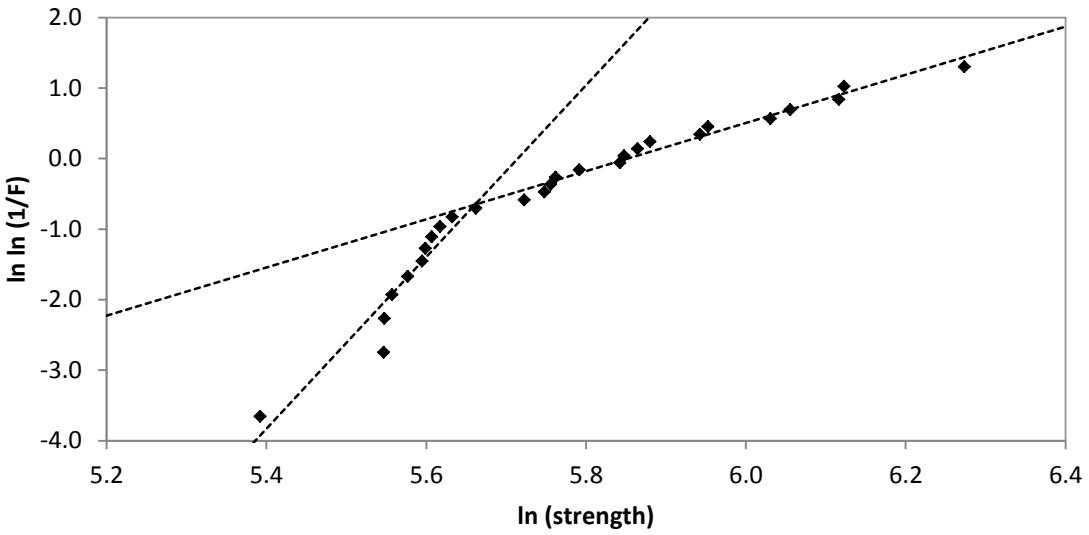


Figure 5.3: Weibull plot for the undoped AES-11C flexural test samples, indicating two regimes with two different Weibull moduli.

Fracture surfaces (Figure 5.4) of samples with low and high strengths showed different fracture origins. For the low strength samples (m = 12 region) the fracture origin was identifiable as a defect on the surface (Figure 5.4a). It was difficult to identify failure origins of samples with high strengths (m = 3)

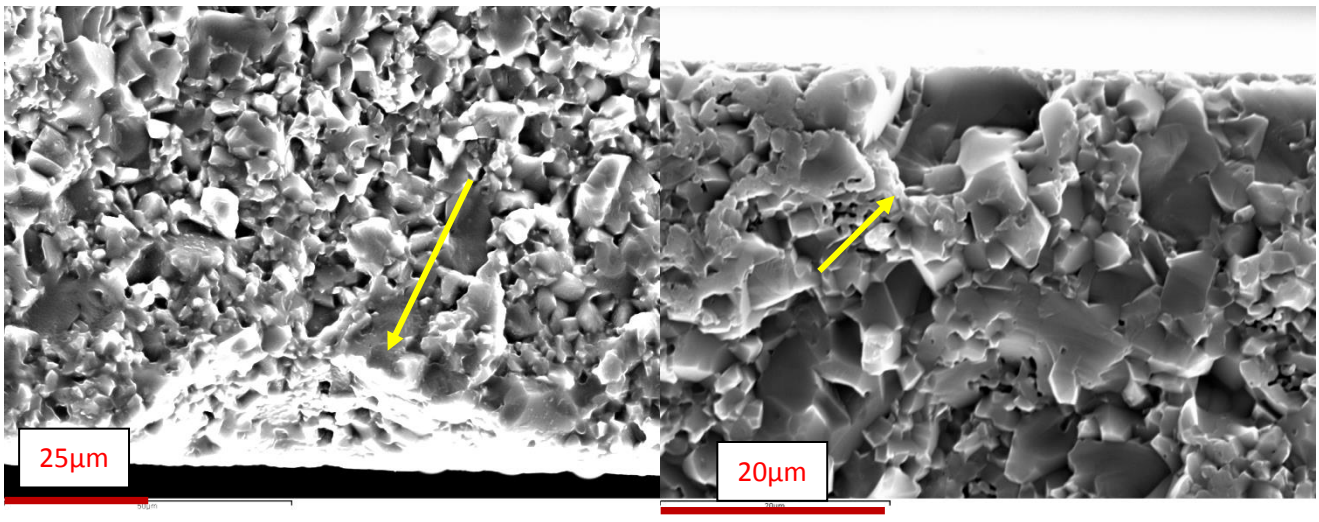


Figure 5.4: Fracture surfaces (JEOL 6300) of AES-11C flexural samples fractured at a) 259 and b) 416 MPa. Probable failure origins are arrowed.

5.2.2. 5wt% chromia doped AES11-C sintered at 1600°C – fracture strength

Seventeen 5wt% Cr_2O_3 doped AES-11C samples were tested: the mean flexural strength and error were (277 +/- 19) MPa. The Weibull modulus (Figure 5.5) was 4.

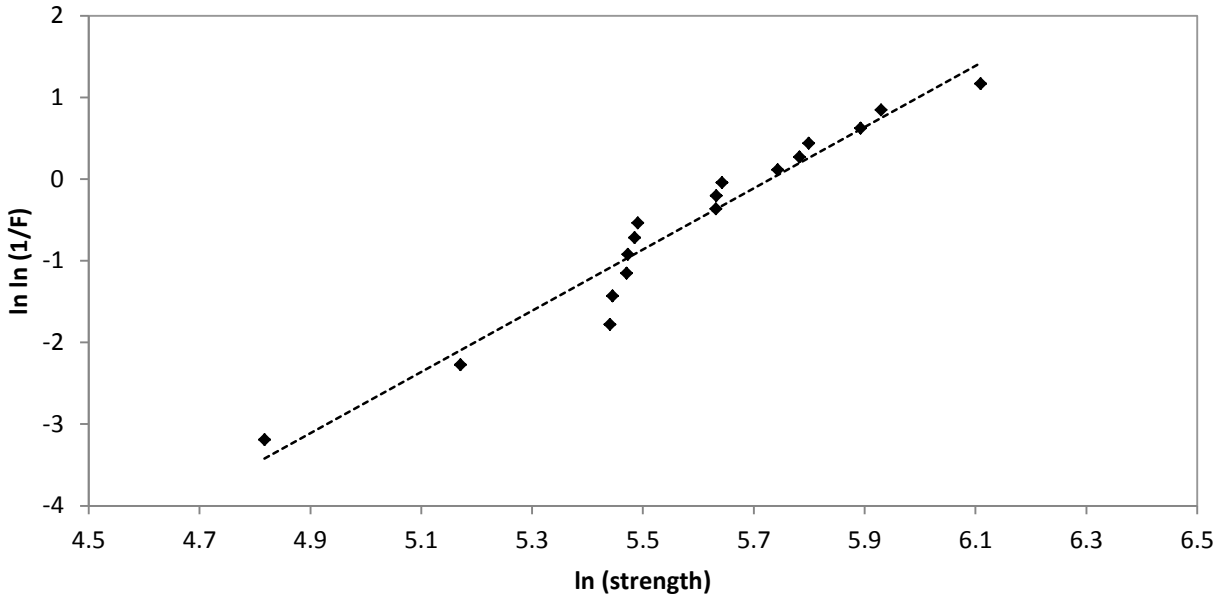


Figure 5.5: Weibull plot for 5wt% Cr_2O_3 doped AES11-C flexural test samples

5.2.3. Fracture strength - Combined Data

The failure strength and Weibull moduli for the different sample sets are shown in Table 5.1. Only undoped AES-11C showed two Weibull regions.

Sample set	Failure strength (MPa)	Number of regions	m (1)	m (2)
Undoped AES-11C	331 +/- 13	2	12	3
2wt% Cr_2O_3	266 +/- 7	1	11	
3wt% Cr_2O_3	288 +/- 13	1	7	
5wt% Cr_2O_3	277 +/- 19	1	4	

Table 5.1: The flexural mechanical properties for the different AES-11C sample sets

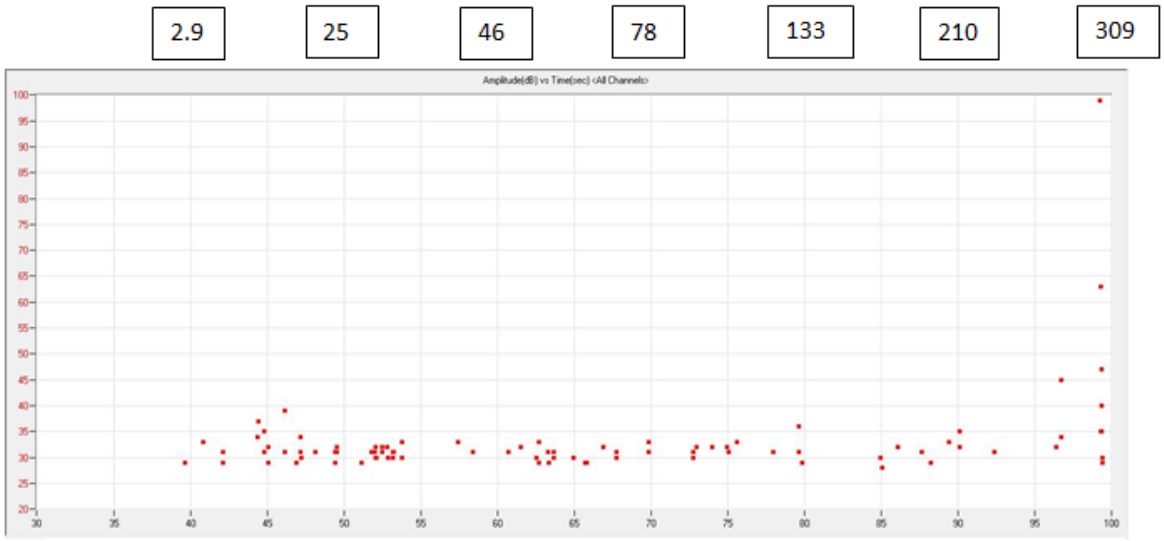


Figure 5.6: A typical acoustic emission plot during flexural loading. Values above the plot represented the load (in MPa) during the test

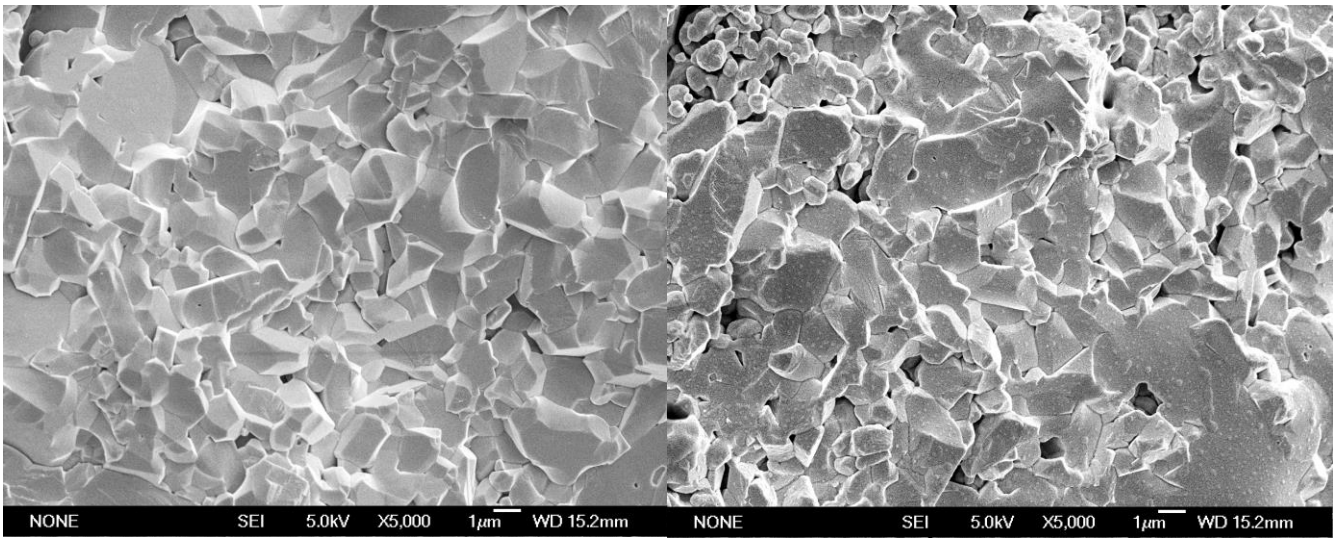


Figure 5.7: SEI (JEOL 6500F) of fracture surfaces of a) undoped and b) 5wt% chromia doped AES-11C, showing the intergranular fracture

The acoustic emission (Figure 5.6) showed a number of low-amplitude hits during loading. Failure was accompanied with mid- to high-amplitude hits. This plot was typical for all sample sets; there was no significant acoustic emission difference between the different aluminas.

The fracture surfaces (Figure 5.7) showed that all the alumina samples tested in four-point bending failed mostly intergranularly. The addition of the chromia had no effect on the preferred crack propagation route.

5.3 Macroscopic fracture toughness tests

The SEVNB fracture toughness measurement technique (Section 3.5.2.) was used to determine the stress intensity factor at failure, K_{Ic}, for different alumina samples (Table 5.2). The stress intensity factors were corrected for notch bluntness using the tanh weighted function by Fett and Munz [149, 150] (Equation 2.14) by assuming that the notch tip crack length dα was 2.5 times that mean grain size [151] (Section 2.6.5.).

Sample	Number of samples	Average notch radius (μm)	K_{Ic} (MPa . $m^{1/2}$)
Undoped AES-11C	10	6 +/- 1	3.5 +/- 0.2
2wt% Cr_2O_3 in AES-11C	4	4 +/- 1	3.7 +/- 0.2
Undoped TM-DAR	4	7 +/- 1	3.8 +/- 0.1
0.012wt% carbon doped TM-DAR	4	8 +/- 1	4.3 +/- 0.1

Table 5.2: Combined SEVNB results for different alumina samples.

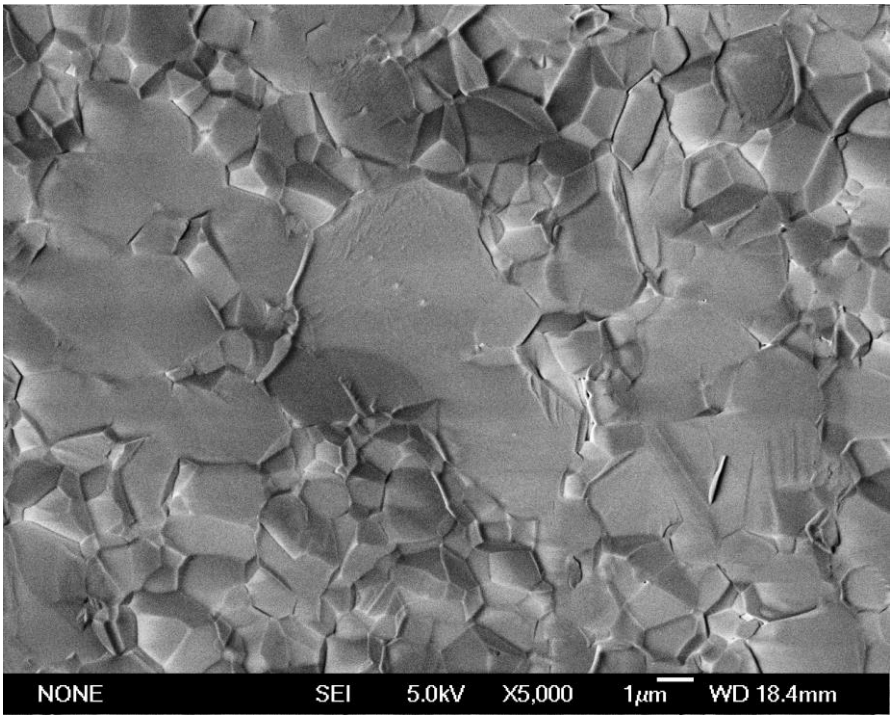


Figure 5.8: SEI (JEOL 6500F) of fracture surface of 0.012wt% carbon doped TM-DAR, showing mostly transgranular fracture.

The carbon doping increased the value of K_{Ic}; the corresponding fracture surface (Figure 5.8) showed a considerable amount of transgranular fracture.

5.4 Uniaxial Compression of Alumina

Uniaxial compression samples (Section 3.4.1.) were either loaded to failure or unloaded after a given load to determine the damage evolution (Section 3.5.1).

5.4.1 Failure Strength of samples

Alumina samples were uniaxially compressed to failure. In order to understand the damage evolution, acoustic emission was recorded for each sample. The data for undoped AES-11C are given in detail below; the key results of the other samples are given in Table 5.3.

12 undoped AES-11C samples, sintered to 1600^{o}C for 2 hours, were tested until failure (Table 5.3).

Sample	Failure Strength (GPa)	Sample	Failure Strength (GPa)
A – 16 – F1	3.88	A – 16 – F7	2.90
A – 16 – F2	5.14	A – 16 – F8	2.97
A – 16 – F3	3.71	A – 16 – F9	1.41
A – 16 – F4	3.45	A – 16 – F10	2.98
A – 16 – F5	2.68	A – 16 – F11	2.80
A – 16 – F6	3.17	A – 16 – F12	3.06

Table 5.3: Summary of the uniaxial compression failure strengths for the undoped AES11-C sintered at 1600^{o}C

There was a large variation in the failure strengths; the mean and standard error were (3.2

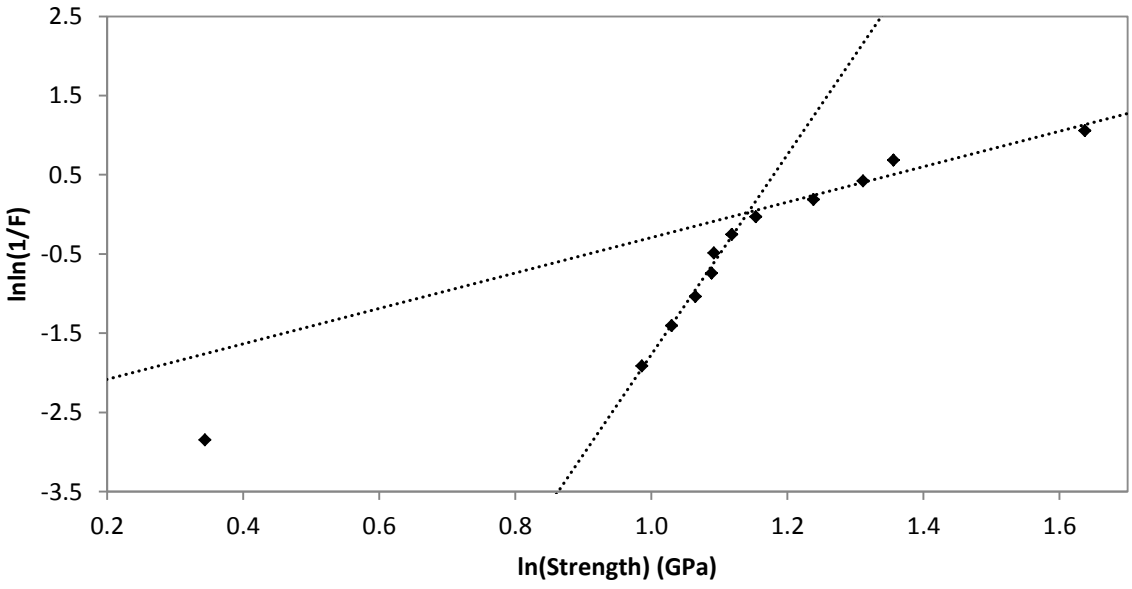


Figure 5.9: Weibull plot of uniaxial compression failure strengths of undoped AES-11C samples (Table 5.3).

+/- 0.3) GPa. There were two Weibull regimes with moduli of 18 and 3 (Figure 5.9). The sample that failed at 1.41 GPa did not fit on the Weibull slope.

A typical plot of the cumulative number of hits against time is shown in Figure 5.10a. There were low amplitude hits at low stress due to the contact of the platen and surface interfaces (Kaiser effect). Thereafter, there was a steady rise in the number and amplitude of hits with stress. Just before failure, there were very high amplitude hits together with hundreds of low-amplitude hits (or 10^4 - 10^5 low- to mid-amplitude counts, as in Figure 5.10). Hence, the

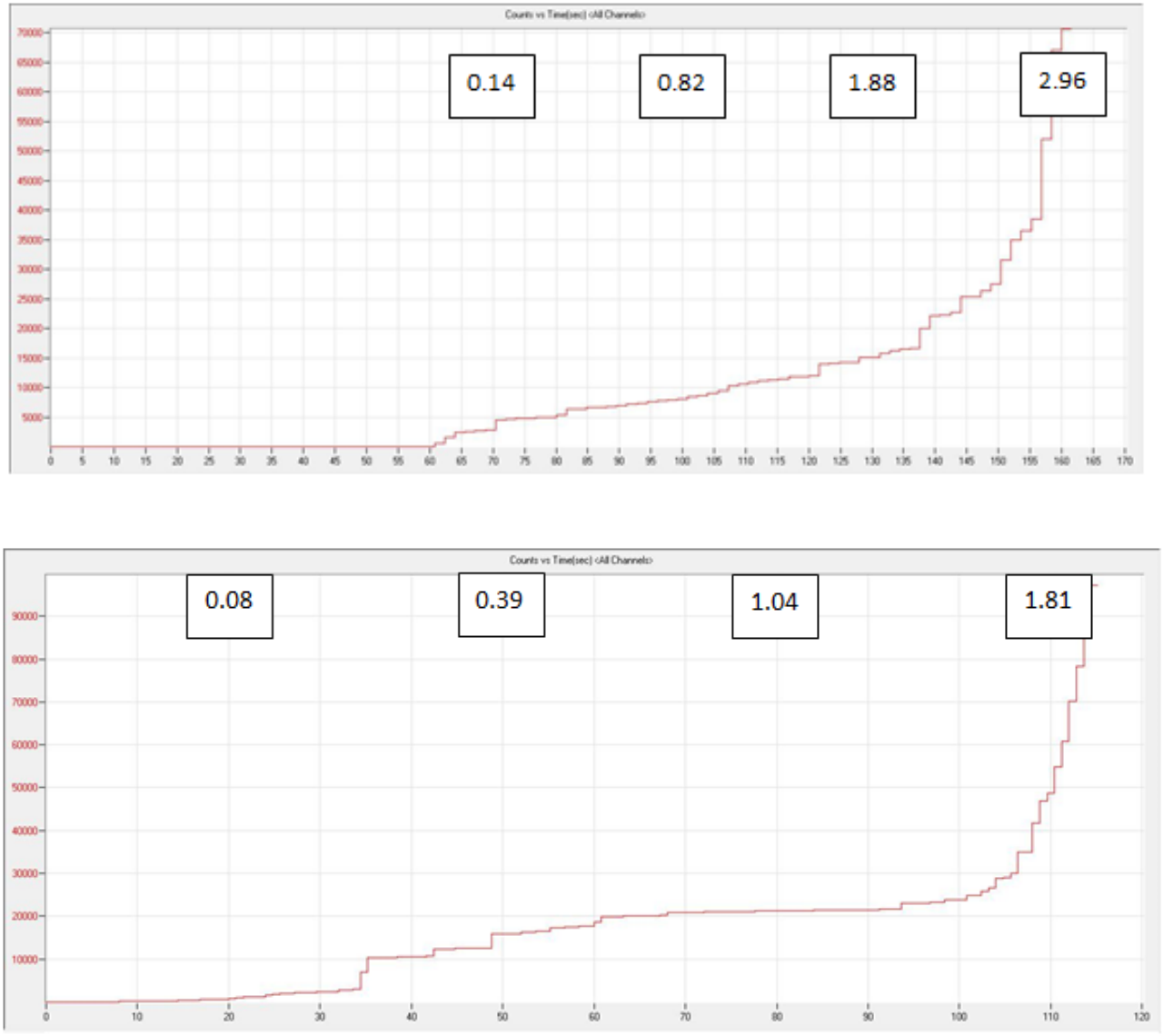


Figure 5.10: Cumulative number of counts against time for uniaxial compressed undoped AES11-C sintered at a) 1600°C and b) 1750°C. Superimposed are the compression stresses during the loading (in GPa). Start of loading is arrowed.

cumulative number of hits rapidly increased until failure due to non-elastic response of the material (Section 5.1).

5.4.1.1. Combined data – compressive strength

Despite the spread of strengths for each alumina (e.g. Table 5.4), there was significant variation between the compressive strengths of the different aluminas (Table 5.5). All samples had similar acoustic emission plots; those that failed at lower stresses had an increase in the number and amplitude of hits at lower stresses (Figure 5.10b).

Sample	Number of tests	Weibull modulus	Failure Strength (GPa)
Undoped AES-11C 1600^{o}C	12	18, 3	3.2 +/- 0.3
Undoped AES-11C 1750^{o}C	6	5	1.7 +/- 0.1
2wt% Cr_2O_3 doped AES-11C 1600^{o}C	19	9, 3	2.4 +/- 0.1
2wt% Cr_2O_3 doped AES-11C 1750^{o}C	4	-	2.3 +/- 0.3
3wt% Cr_2O_3 doped AES-11C 1600^{o}C	8	4	2.3 +/- 0.2
5wt% Cr_2O_3 doped AES-11C 1600^{o}C	21	4	1.7 +/- 0.1
Undoped TM-DAR 1600^{o}C	8	5	3.7 +/- 0.3
Undoped TM-DAR 1750^{o}C	8	6	2.6 +/- 0.2
2wt% Cr_2O_3 doped TM-DAR 1600^{o}C	8	28, 2	3.2 +/- 0.2
2wt% Cr_2O_3 doped TM-DAR 1750^{o}C	6	10	3.6 +/- 0.1
5wt% Cr_2O_3 doped TM-DAR 1600^{o}C	9	4	2.5 +/- 0.2

Table 5.5: Summary of the uniaxial compression failure strengths for different alumina samples. Standard error used for failure strength. Weibull moduli were only given for samples with a suitable number of data points

5.4.2. Damage evolution analysis during compression

In order to determine the evolution of damage during loading, AES-11C samples were compressed to a given load and then unloaded. The damage was assessed in various ways:

optical microscopy to assess the macroscopic damage, optical fluorescence microscopy to measure the residual stress, and transmission electron microscopy to consider the extent of microcracking and twinning. These were compared to the acoustic emission during loading.

Undoped AES-11C was used. Samples were stopped at the following stresses: 1.1, 1.5, 1.8, 2.0, 3.1, 3.6, and 3.8 GPa.

5.4.2.1. Optical Microscopy & Acoustic Emission

Compressed to 1.1, 1.5, and 1.8GPa

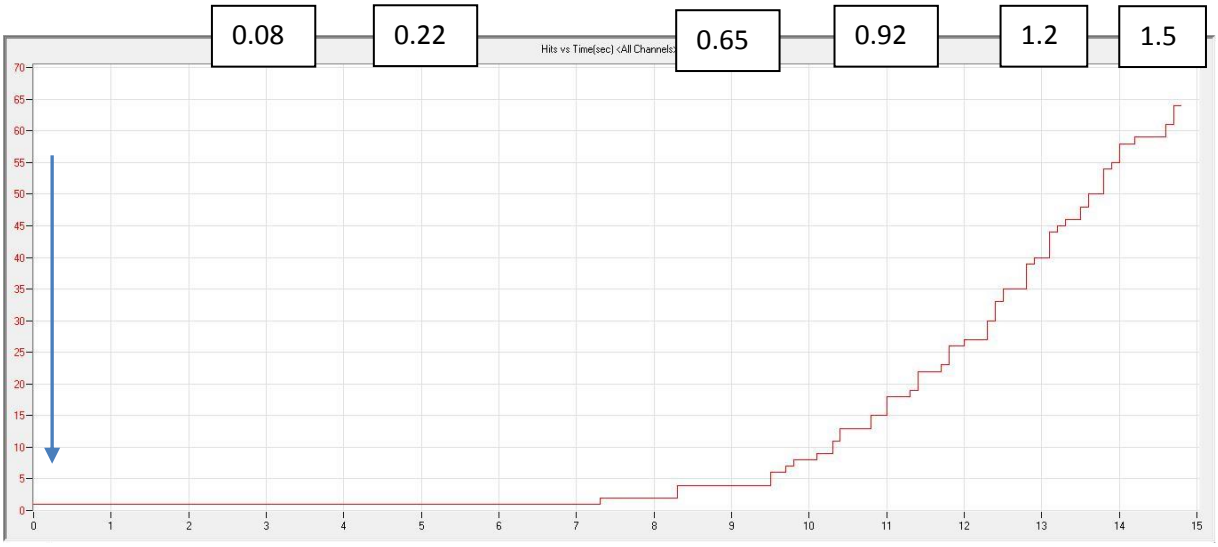


Figure 5.11: Cumulative number of hits with time for undoped AES-11C compressed to 1.5GPa and unloaded. Start of loading was arrowed. Loads are shown in GPa.

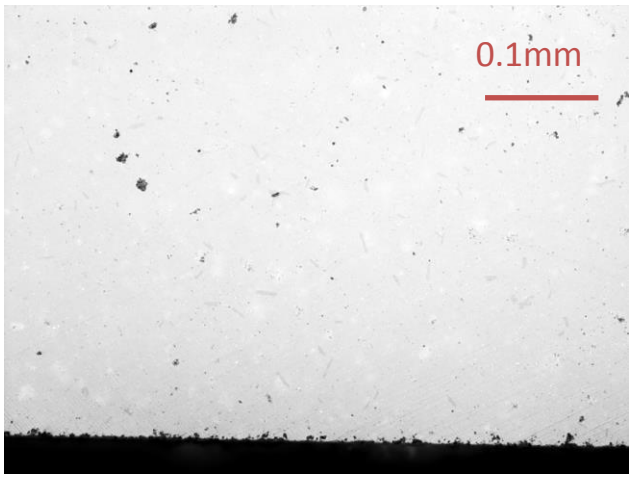
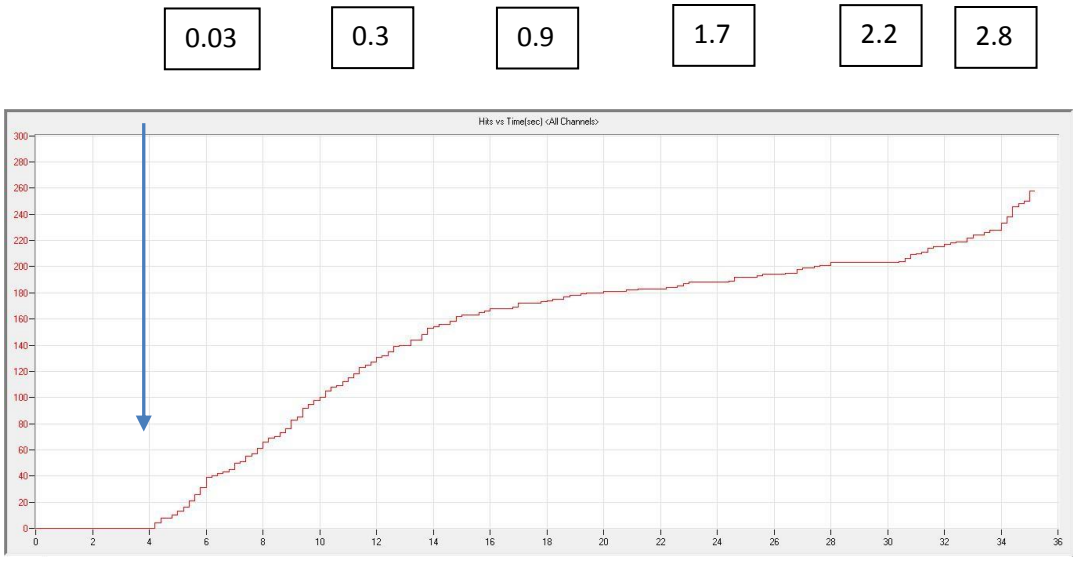


Figure 5.12: Optical microscopy of AES-11C sample compressed to 1.5GPa and unloaded

Before unloading, there were hits in the low- to mid-amplitude range and the cumulative number of hits increased linearly with time (Figure 5.11). There was no macroscopic change to the sample, with the sample showing no signs of cracking, spalling etc. (Figure 5.12).

Compressed to 2.0 and 3.1GPa

After the initial rise in hits (as seen in Figure 5.11), the rate of hits decreased (between 0.4 and 2.2 GPa in Figure 5.13). Thereafter, the cumulative number of hits increased rapidly prior to unloading (2.5 GPa in Figure 5.13).



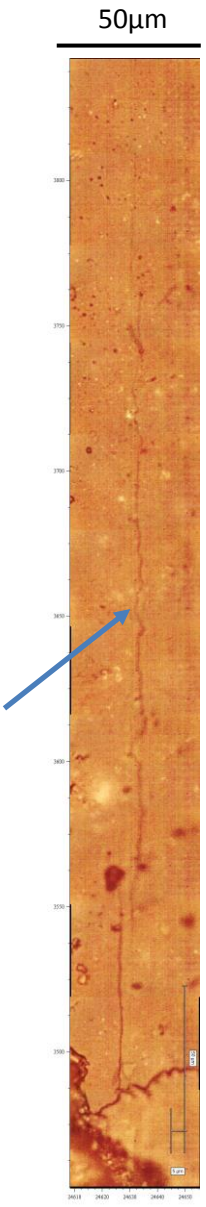


Figure 5.13: a) Cumulative number of hits with time for undoped AES11-C compressed to 3.1GPa and unloaded. b) Optical micrograph of a crack (arrowed) from the surface of the sample parallel to the uniaxial compression direction (vertical in figure). Start of loading is arrowed, and stresses given above in GPa.

Whilst there was no spalling or falling apart of the sample, there were a few cracks that had grown parallel to the uniaxial compression direction (Figure 5.13b). These appeared to have propagated stably and had not caused failure of the sample.

Compressed to 3.6 and 3.8GPa

As seen in Figure 5.13, the rate of hits increased at high loads. This is also seen in Figure 5.14. There were a large number of hits in the high-amplitude range prior to unloading suggesting some energetic process. Optical micrographs indicated both cracking (Figure 5.15a) and spalling (Figure 5.15b). The sample was still intact after unloading.

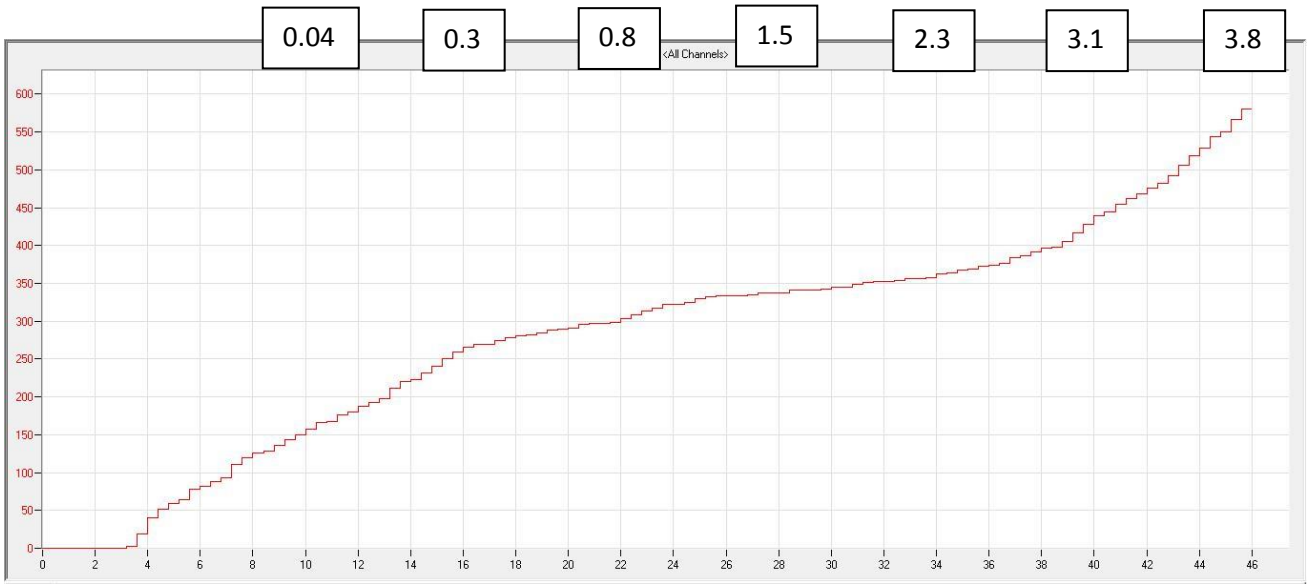


Figure 5.14: Amplitude of hits with time for undoped AES-11C compressed to 3.8GPa and unloaded. Start of loading is arrowed and the stresses given above in GPa.

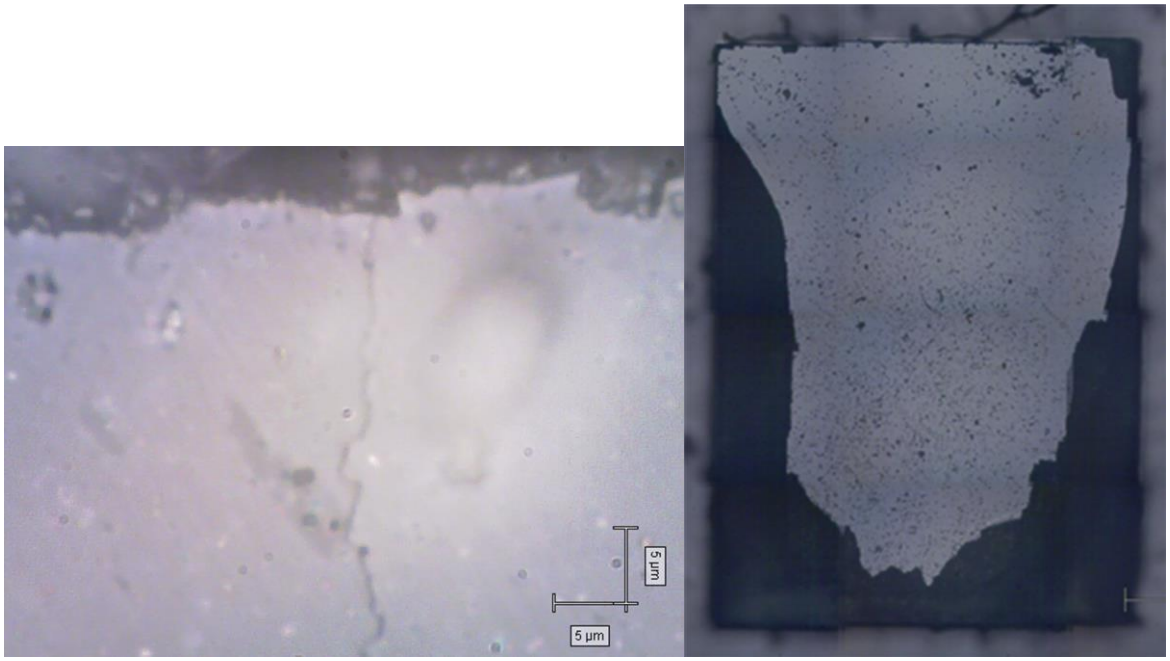


Figure 5.15: Optical micrographs of AES-11C sample compressed to 3.8GPa then unloaded: a) crack from the surface, b) spalling of material. Direction of loading is vertical.

5.4.2.2. Optical Fluorescence Microscopy (OFM)

After compressing the AES-11C samples to various loads, samples were removed and assessed using optical fluorescence microscopy (Section 3.3.6.). Confocal maps were produced across the surface (several thousand points per sample); there was no change in the mean peak position and width (both in cm^{-1}) with the maximum stress reached before unloading. There were the same local variations in peak position (Figure 5.16) seen in the control sample (Figure 4.21), although some regions of variation were seemingly related to microcracking (arrows in Figure 5.16).

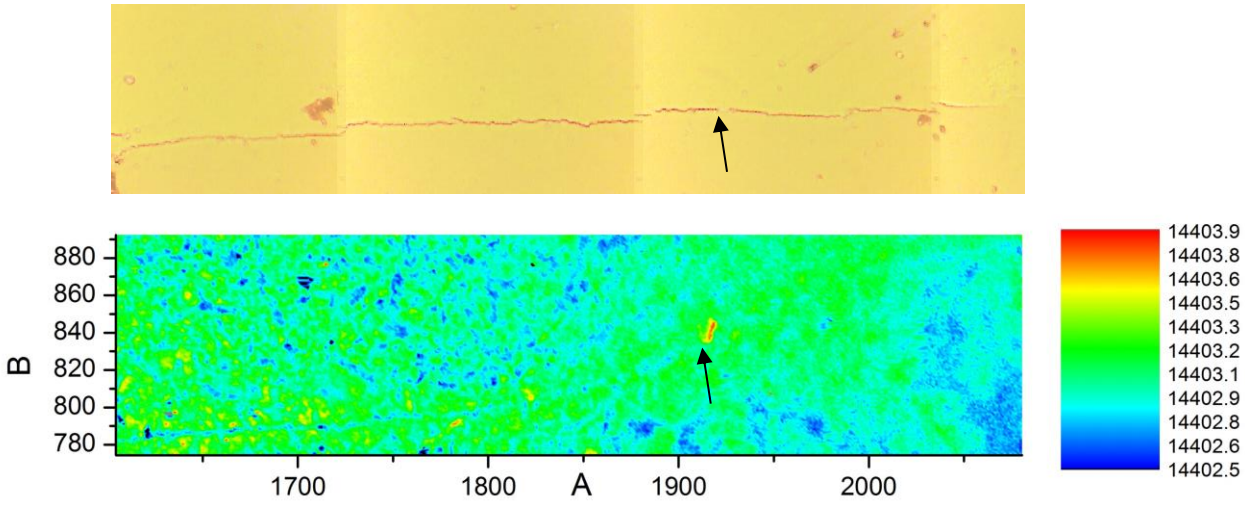


Figure 5.16: a) Optical micrograph and b) OFM peak position map on surface of AES-11C sample compressed to 3.5GPa. Compressive stress direction horizontal in images. Dimensions in µm.

5.4.3. Microcracking in polycrystalline alumina

During the uniaxial compression, microcracks appeared to form (and were imaged in TEM) which were not present in the control, unstressed sample. In order to understand this behaviour during uniaxial compression, the wing crack model developed by Ashby and Hallam [14] was used; this was outlined in Section 2.4.2. The following factors were considered in analysing the damage in a given sample:

1	By ascertaining the size and inclination of the flaw, whether the stress intensity factor, K_I, (due to the applied compressive stress) (Equation 2.5) was enough to nucleate wing cracks by fulfilling the criterion $K_I > K_{Ic,\ gb}$. (the critical stress intensity factor of the grain boundaries)
2	If the criterion was fulfilled, whether the wing cracks were in the correct orientation to maximise the stress intensity factor ($\approx 71^o$, from Equation 2.5).
3	By considering the stress intensity factor to propagate a wing crack through a continuum material (Equation 2.6), whether the applied stress was sufficient to propagate a wing crack to the length measured using TEM.
4	As the wing cracks should propagate parallel to the compressive direction, whether those imaged using TEM were in the correct orientation relative to the applied stress.

Whilst Ashby and Hallam used the long crack critical stress intensity factor, K_{Ic}, (3.5 $MPam^{1/2}$ for AES-11C, Section 5.3), a more appropriate value is the toughness of the grain boundary itself, $K_{Ic,gb}$. The difference is discussed in more detail in Section 9.3.2. The grain boundary toughness of alumina was measured using microcantilever beams (Section 8.2.6.). However, the microcantilever beams underwent moisture assisted sub-critical crack growth and so the measuring stress intensity factor was lower than $K_{Ic,gb}$. By estimating the relationship between the critical stress intensity factor for samples undergoing sub-critical crack growth and K_{Ic} (see Section 8.2.6.), $K_{Ic,gb}$ is estimated to be (1.4 +/- 0.4) $MPam^{1/2}$. The coefficient of friction was estimated to be 0.4 +/- 0.05 (friction at room temperature, 2GPa load) [210].

After first considering the type and frequency of flaws in an uncompressed AES-11C sample, the damage after compression is assessed.

5.4.3.1. Frequency and types of flaws in untested AES-11C alumina

TEM analysis (Figure 5.17) showed several flaws at grain boundaries in AES-11C alumina. These flaws tended to be between 1 - 3µm.

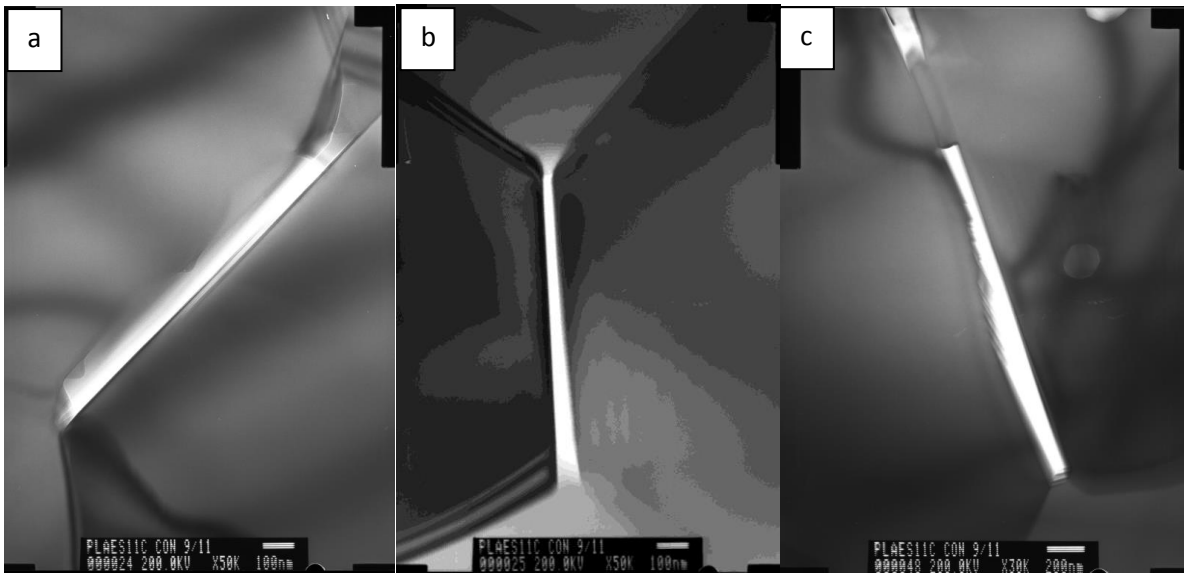


Figure 5.17: TEM (JEOL 2000FX) of several grain boundary flaws in uncompressed AES-11C, which could initiate wing cracks under loading

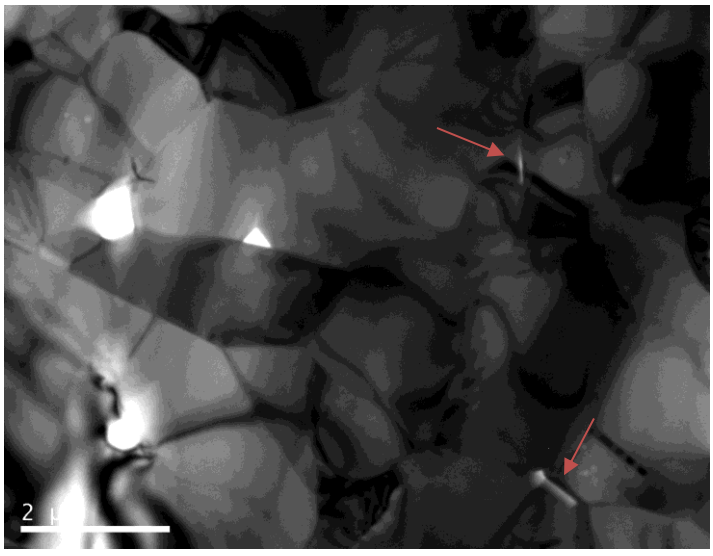


Figure 5.18: TEM (JEOL 2000FX) of AES-11C (1600°C) with some of the flaws arrowed.

The frequency of these flaws was assessed using low-magnification TEM (Figure 5.18). The number of flaws 1) per unit area and 2) per number of grains imaged in a TEM sample was ascertained. For AES-11C sintered at 1600°C, there were flaws every 13 grains or 35µm^2. Sintered at 1750°C, this was 12 grains and 310 µm^2. In TM-DAR: 16 grains or 160µm^2.

5.4.4. Transmission Electron Microscopy of Compressed Samples – Undoped AES-11C

In order to understand the evolution of damage during loading, samples were loaded to a given stress &unloaded, before a TEM foil was produced (Section 3.2.1) and viewed in the TEM.

For each TEM image, the compression direction is vertical.

For each microcrack, the initial flaw is unclear. It is possible that the initial flaw was removed during the ion milling or, due to the grain boundary flaws being planar and not linear, the flaw was not obvious in the TEM foil. These issues were discussed in Section 9.3.3. However, an estimation for the initial flaw is taken and this used to assess the microcracking.

Compressing to 1.1GPa, there was no microstructural change (Figure 5.19). Inclined flaws were present, but there was no wing crack nucleation.

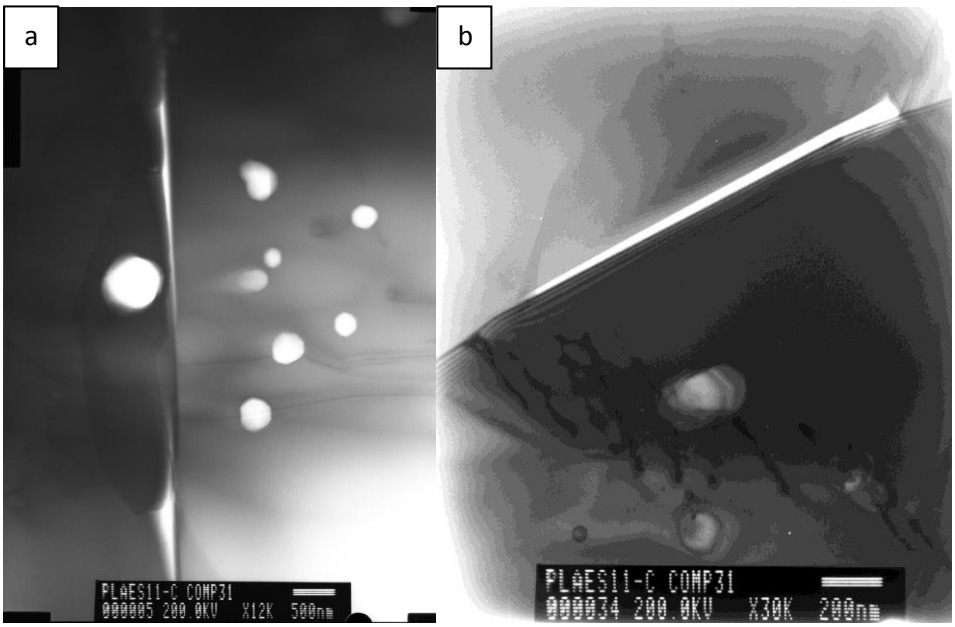


Figure 5.19: TEM (JEOL 2000FX) of flaws A & B present in the alumina. The compression to 1.1GPa was not great enough to initiate wing cracks at these, or any other, flaws. Compression direction is vertical.

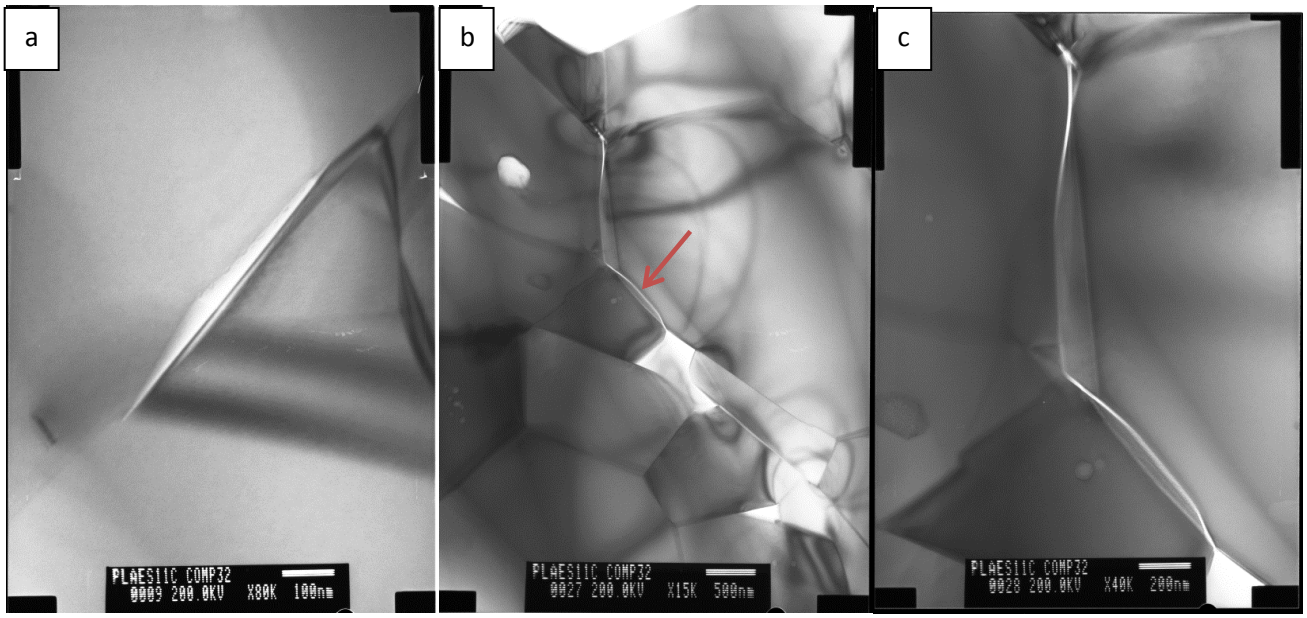


Figure 5.20: TEM (JEOL 2000FX) of flaws A present in the alumina, with no wing cracks associated with it after the 1.5GPa loading. B & C showed two magnifications of a microcrack which appeared to have propagated during loading. Compression direction is vertical.

Compressing to 1.5 GPa, one flaw appeared to have initiated wing cracks during loading (Figure 5.20b). It was unclear which section was the initial flaw, and the presence of the holes (which could be either pre-existing pores or damage during the ion milling) hindered the analysis. The most likely section was arrowed in Figure 5.20b. Using the four criteria in Section 5.4.3.:

1) Noting that a (= half width of flaw) was 0.6µm and the angle to applied stress was 50^{o}, the maximum stress intensity factor was 0.7 $MPam^{1/2}$ (Equation 2.5). This was < $K_{Ic,gb}$. No other microcrack section had a sufficiently high stress intensity factor to nucleate wing cracks.
2) The wing cracks were orientated in approximately the correct direction to maximise the stress intensity factor.
3) If the arrowed section was the initial flaw, the ratio L (i.e. wing crack length, l, divided by a) was ≈ 5. Using Equation 2.6, the applied stress required to give L = 5 before the stress intensity factor driving the wing crack propagation < $K_{Ic,gb}$ is 18GPa. This is greater than the applied compressive stress.

4) The angle of the microcrack to the applied stress direction was 24°.

Whilst a microcrack was present in the foil, it does not fulfil three of the four requirements set out in Section 5.4.3. Each microcrack presented herein was analysed in the same manner; no microcracks fulfilled all four requirements.

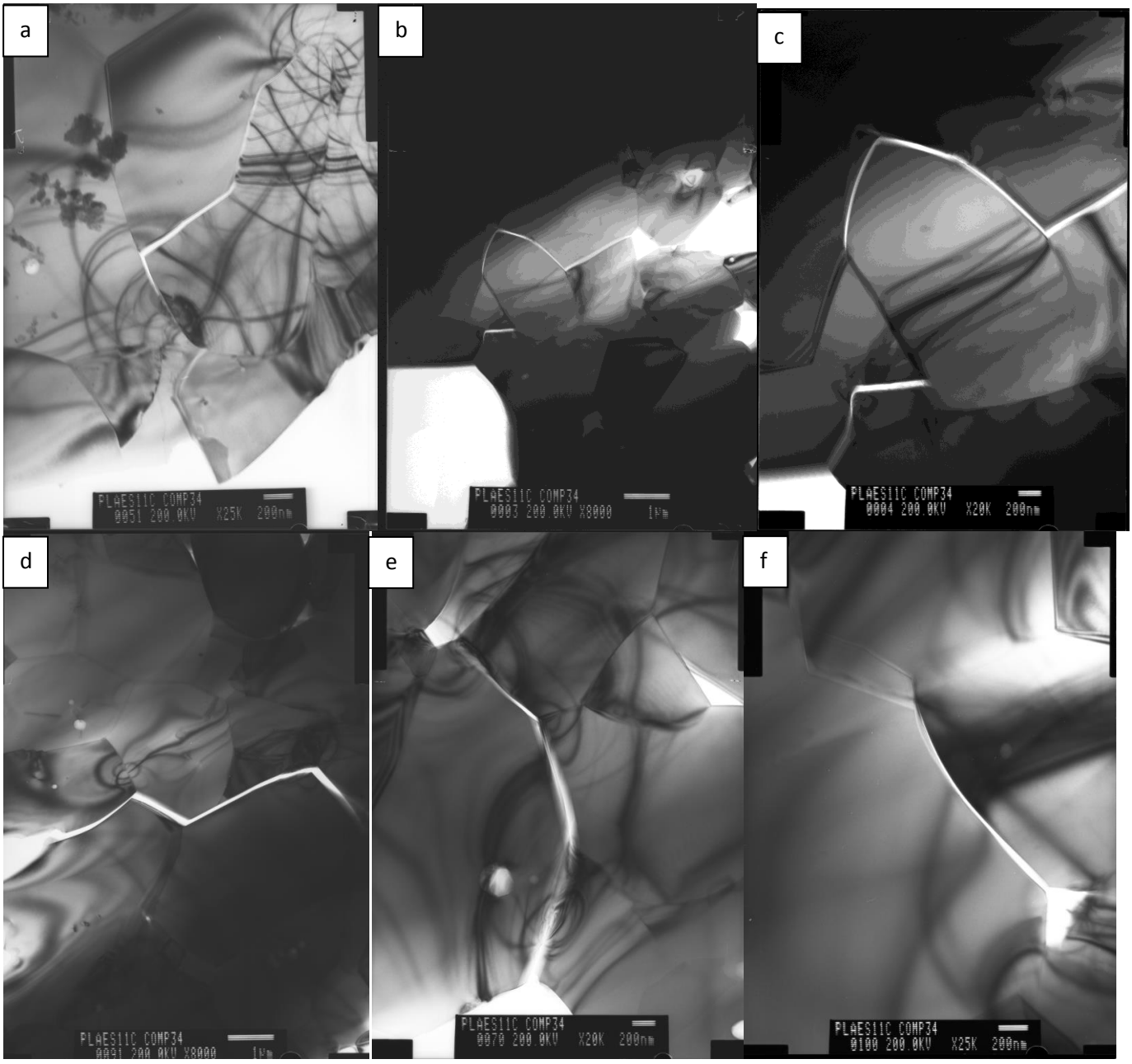


Figure 5.21: TEM (JEOL 2000FX) of microcracks in AES-11C previously loaded to 1.8GPa. Compression direction is vertical.

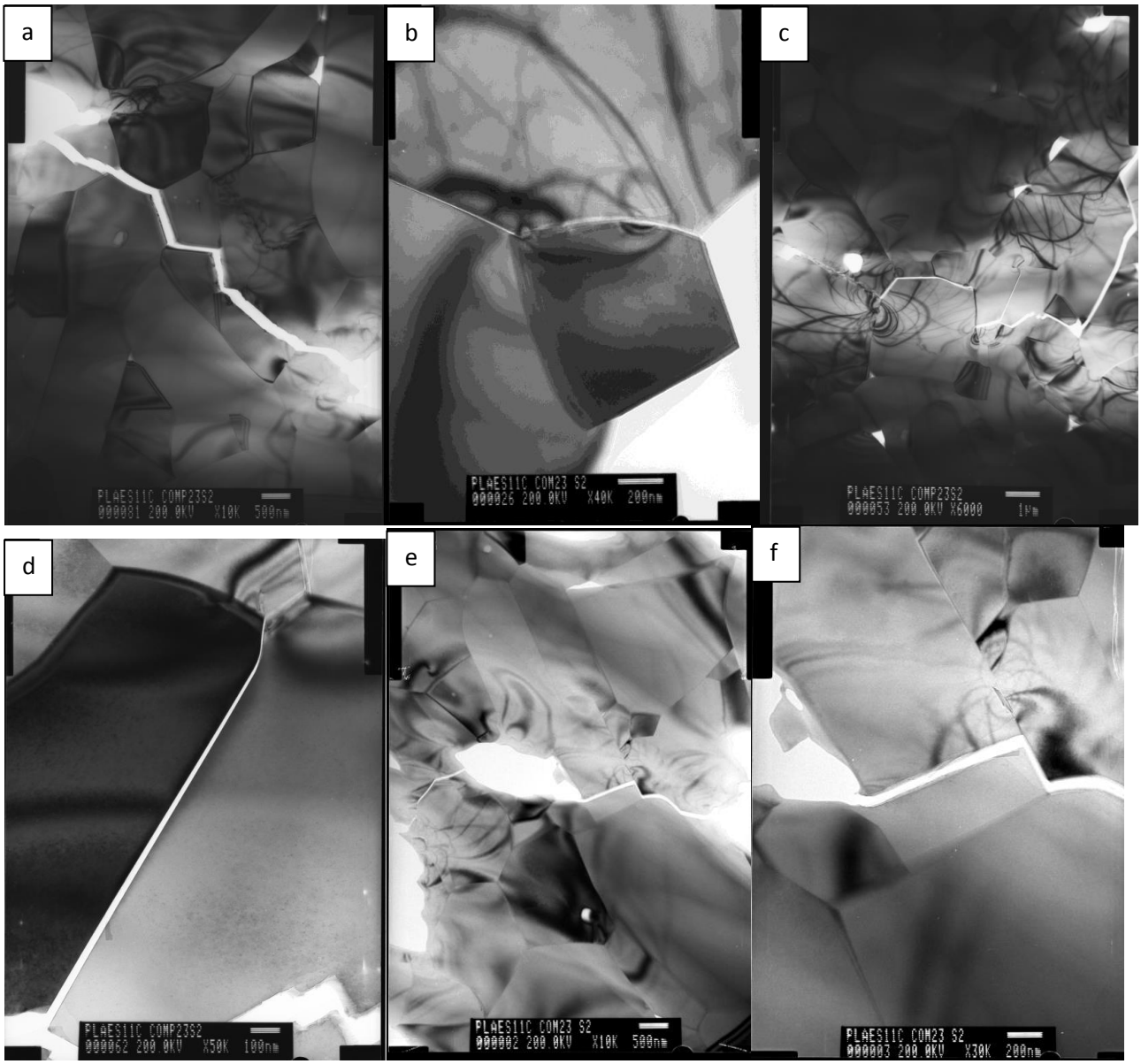


Figure 5.22: TEM (JEOL 2000FX) of microcracks in AES-11C previously loaded to 3.1GPa. Compression direction is vertical.

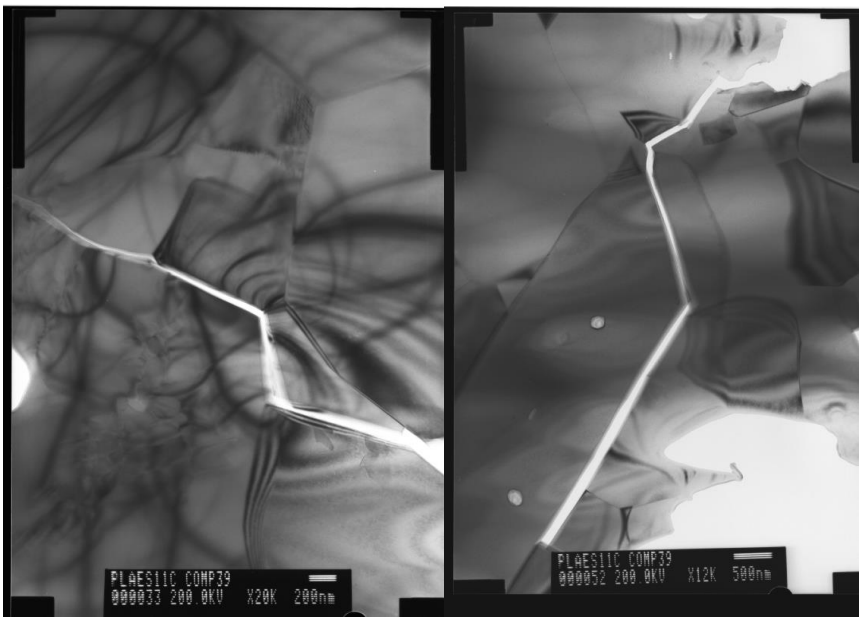


Figure 5.23: TEM (JEOL 2000FX) of microcracks in AES-11C previously loaded to 3.8GPa. Compression direction is vertical.

The microcracks in Figures 5.21 – 5.23 were analysed using the four requirements (Section 5.4.3.). Whilst some of the flaws had a maximum stress intensity factor greater than $K_{Ic,gb}$, the lengths of the microcracks were typically significantly longer than the length predicted from Equation 2.6. Furthermore, several did not have wing cracks in the direction that would maximise the stress intensity factor (Figure 5.21d, Figure 5.22f, Figure 5.23a for example) or did not propagate parallel to the applied stress direction (Figure 5.21b&c, Figure 5.22c&e). The use of the model to assess these microcracks is considered in further detail in Section 9.3.3.

No deformation twins were present in any of the compressed samples.

5.4.5. Transmission Electron Microscopy of Compressed Samples – Chromia doped AES-11C

Four 2wt% Cr_2O_3 doped AES-11C (sintered to 1600^{o}C) samples were compressed and unloaded: 2.0, 2.5, 2.7 and 3.0GPa. The extent of microcracking was similar to the undoped described above. There were no deformation twins present in the TEM foils.

Three 3wt% Cr_2O_3 doped AES-11C (sintered to 1600^{o}C) samples were compressed and unloaded: 2.0, 2.1, and 2.2GPa. No deformation twins were present.

5.4.6. Compression testing – Summary

Whilst the microcracks imaged using TEM may not have corroborated to the Ashby and Hallam [14] model, some microcracking may have occurred during loading. To estimate the propensity for wing crack nucleation and microcracking at different loads, the maximum stress intensity factor to nucleate a wing crack from a flaw was estimated and compared to $K_{Ic,gb}$. The maximum stress intensity factor on a flaw K_{max} was calculated (Equation 2.5) by assuming that there was an internal flaw (i.e. 2a) equal to the mean grain size of AES-11C (i.e. 2.7µm). The range of φ values indicate the spread of inclination angles (to the applied stress) which result in stress intensity factors above $K_{Ic,gb}$ of (1.4 +/- 0.4) $MPam^{1/2}$ (Section 9.3.2.).

Compressive Load (GPa)	AE	Macro change?	Estimate K_{max} ($MPam^{1/2}$)	Range of φ	Number of microcracks	Total Microcrack Length (µm)
1.1	Few low- to mid-amplitude	No	0.9	-	-	-
1.5			1.3	-	1	3.1
1.8			1.6	24 - 44	5	28
2.0	Some mid- and high-amp	Occasional crack from surface	1.7	21 - 48	1	0.4
3.1			2.6	12 - 56	5	24
3.6	A number of high amp hits	Cracking & spalling	3.0	10 - 58	-	-
3.8			3.2	9 - 59	5	15

Table 5.6: Properties of samples loaded in uniaxial compression then unloaded. AE was a measure of the acoustic emission prior to unload. The length of each microcrack was determined by measuring the individual sections; these were added to give the total length.

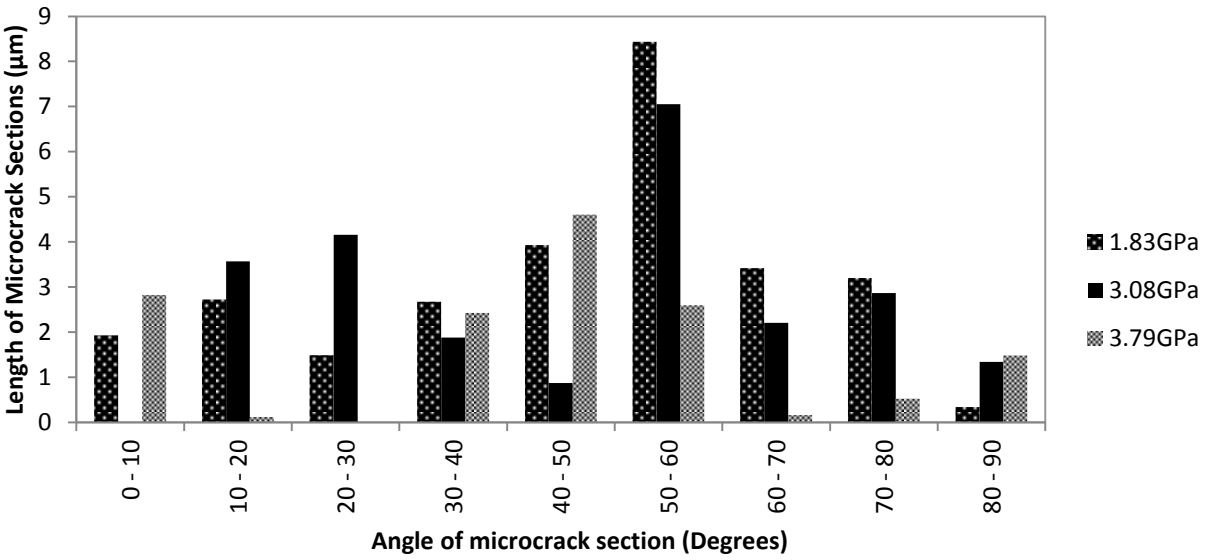


Figure 5.24: Distribution of microcrack segment lengths with angle from the compression direction.

Both the total microcrack length and angle, and the individual microcrack segment length and angle, were obtained. The former was performed by determining the end points of the total microcrack length. The latter was determined by estimating each microcrack segment, and measuring each length and angle to the applied stress. These were shown in Figures 5.24

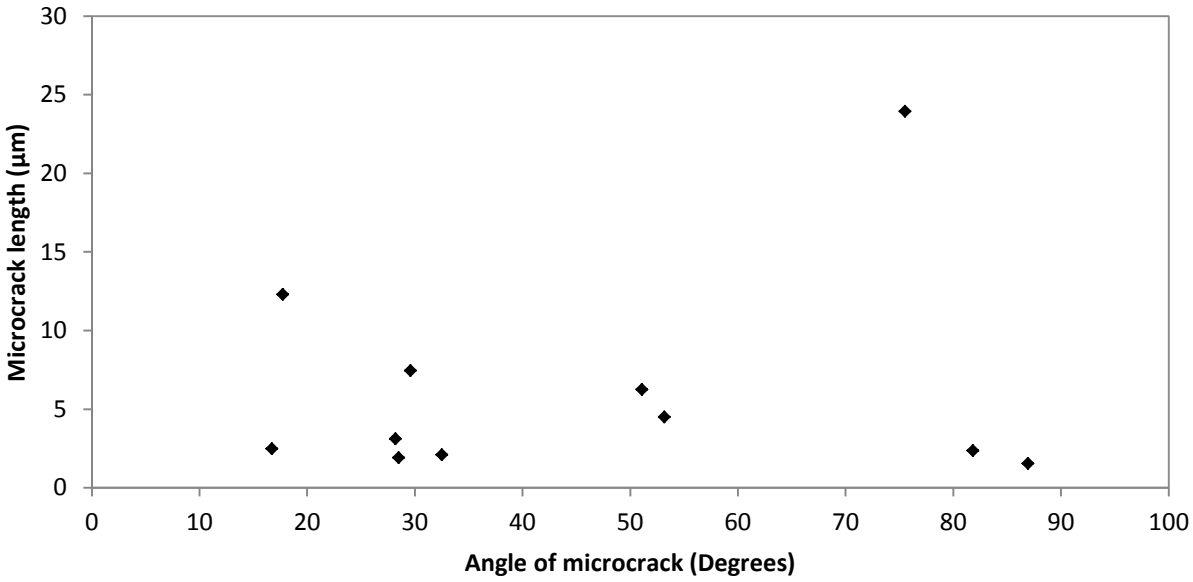


Figure 5.25: Total microcrack lengths and angle to the compressive direction for all samples.

and 5.25. Microcracks should propagate parallel to the uniaxial compression (Section 2.4.2.). Measuring the individual crack sections, there was a peak at 50 – 60^{o} (Figure 5.24). However, the angles for the total lengths were not close to the uniaxial compressive direction (Figure 5.25).

5.5. Macroscopic data – summary

The macroscopic properties of the various alumina based materials discussed above are tabulated (Table 5.7). The mean grain size and relative density (% ρ) are also given; the error in these values is given in Table 4.6.

Alumina	Sint Temp (^{o}C)	Grain size (μm)	% ρ	Flexural Strength (MPa)	Weibull moduli (Flexure)	K_{Ic} (MPam$^{1/2}$)	Uni Comp Strength (GPa)	Weibull moduli (Comp)
AES-11C	1600	2.7	99.7	331 +/- 13	12, 3	3.5 +/- 0.2	3.2 +/- 0.3	18, 3
AES-11C	1750	7.6	99.9	-	-	-	1.7 +/- 0.1	5
2%Cr AES	1600	2.1	99.2	266 +/- 7	11	3.7 +/- 0.2	2.4 +/- 0.1	9, 3
2%Cr AES	1750	10.6	99.3	-	-	-	2.3 +/- 0.3	-
3%Cr AES	1600	1.9	98.7	288 +/- 13	7	-	2.3 +/- 0.2	4
5% Cr AES	1600	1.5	98.2	277 +/- 19	4	-	1.7 +/- 0.1	4
TMDAR	1600	4.3	99.8	-	-	-	3.7 +/- 0.3	5
TMDAR	1750	5.1	99.7	-	-	-	2.6 +/- 0.2	6
2%Cr TM	1600	3.9	98.4	-	-	-	3.2 +/- 0.2	28, 2
2%Cr TM	1750	4.6	98.5	-	-	-	3.6 +/- 0.1	10
5%Cr TM	1600	3.8	97.1	-	-	-	2.5 +/- 0.2	4
TMDAR – v	1500	2.2	100.0	-	-	3.8 +/- 0.1	-	-
0.012%C TMDAR - v	1500	2.4	100.0	-	-	4.3 +/- 0.1	-	-

Table 5.7: Table of mechanical properties of the aluminas tested. Cr = Cr_2O_3, C = carbon.

Chapter 6 Stress Intensity Factor Equations for Microcantilever Beams

6.1. Straight Through Notches

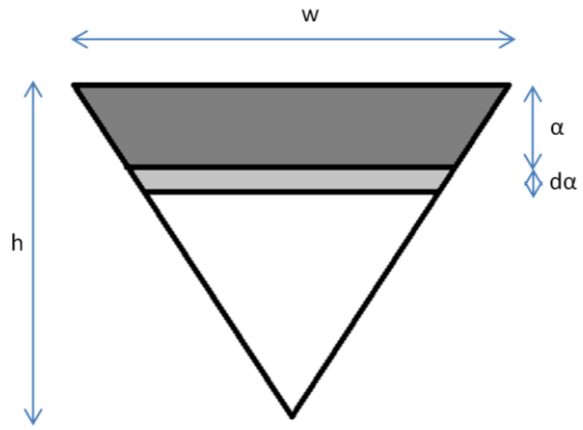


Figure 6.1: Schematic diagram of notch to determine the stress intensity factor using a compliance calibration method

The method used herein followed the general compliance calibration method outlined by [89, 141, 211-214]. By simulating the deflection of a triangular cross-section microcantilever beam with notches of different depths and positions, and calculating the compliance of each one, a suitable calculation for the stress intensity factor of the beams was determined.

The relationship between the Young's modulus, E, and the compliance, C, of an un-notched beam is (Appendix 3.1):

$$E = \frac{F}{D_{true}} \frac{12L_{el}^3}{wh^3} = \frac{1}{C} \frac{12L_{el}^3}{wh^3} \quad (6.1)$$

The mechanical energy release rate for a notched triangular shaped beam under bending was found as follows. The displacement of the beam, u, under an applied load, F, is:

$$u = FC \quad (6.2)$$

The stored elastic energy, $U_E = ½\, u\, F$, so:

$$U_E = \frac{1}{2} F^2 C \quad (6.3)$$

Assuming that the crack grows but $du = 0$ (i.e. the loading system does no work), the change in the mechanical energy, U_m, is:

$$dU_m = dU_E = \frac{\partial}{\partial C}\left(\frac{\frac{1}{2}u^2}{C}\right)dC = -\frac{\frac{1}{2}u^2}{C^2}dC = -\frac{1}{2}F^2dC \tag{6.4}$$

The mechanical energy release rate, G, is given by:

$$G = -\frac{dU_m}{dA} \tag{6.5}$$

Given the dimensions of the beam and notch (Figure 6.1), the change in crack area due to a growth of notch $d\alpha$ is:

$$dA = d\alpha\, w\frac{h-\alpha}{h} \tag{6.6}$$

Thus,

$$G = -\frac{\frac{1}{2}F^2dC}{\frac{w(h-\alpha)}{h}d\alpha} = \frac{F^2}{2w}\frac{h}{h-\alpha}\frac{dC}{d\alpha} \tag{6.7}$$

This was used to determine the value of G for a given notch depth. In order to perform this calculation, dimensionless values of the compliance and the crack length were defined: $\alpha' = \alpha/h$ and $C' = CEh$. Hence:

$$G = \frac{F^2}{2w}\frac{h}{h-h\alpha'}\frac{1}{Eh^2}\frac{dC'}{d\alpha'} = \frac{F^2}{2h^2wE}\frac{1}{1-\alpha'}\frac{dC'}{d\alpha'} \tag{6.8}$$

As the stress intensity factor, K, is related to the mechanical energy release rate by the equation $K = \sqrt{GE}$, then:

$$K = \frac{F}{h\sqrt{w}}\left(\frac{1}{2}\frac{dC'}{d\alpha'}\right)^{\frac{1}{2}}\left(\frac{1}{1-\alpha'}\right)^{\frac{1}{2}} \tag{6.9}$$

Alternatively, if the reduced compliance was taken as CEw,

$$K = \frac{F}{w\sqrt{h}} \left(\frac{1}{2}\frac{dC'}{d\alpha'}\right)^{\frac{1}{2}} \left(\frac{1}{1-\alpha'}\right)^{\frac{1}{2}} \quad (6.10)$$

(The stress intensity factors determined using $C' = CEh$ and $C' = CEw$ were within about 2% of each other, and thus the particular dimension considered was unimportant).

The factor $\left(\frac{1}{2}\frac{dC'}{d\alpha'}\right)^{\frac{1}{2}}$ is often referred to as the dimensionless factor Y [89, 141, 211-214]. Using the compliance calibration method, this factor was determined and thus the stress intensity factor calculated.

The simulations were performed using LS-DYNA by Simone Falco, Engineering Department, University of Oxford, with the following properties:

- Extruded 2D discretisation of triangular section in brick elements (Figure 6.2).
- Majority of elements were hexahedral, with some (< 1%) pentahedral elements when necessary to avoid distortion.
- Back face (furthest from indenter tip) fully constrained. All other faces unconstrained.
- Convergence testing: The deformation of the un-notched beam has been compared with the analytical calculation (Euler-Bernoulli theory) showing complete agreement, therefore the element size has been considered acceptable. No analysis of the sensitivity to loading geometry was considered.
- Crack generated by duplicating the nodes above the height of the notch (for a given notch position). No mesh refinement was considered at notch tip, as the compliance calibration is insensitive to the mesh at the notch.
- The indenter was simulated with a force on 9 nodes (approx. 150μm in diameter)
- The recorded displacement was the average across the loaded nodes.
- Beams were constructed to behave with isotropic elasticity. Some work was performed by Simone Falco to explore anisotropy; the value of Young's modulus (from simulations) changed with angle between beam and sapphire c-axis as expected. With the compliance calibration approach, the values of the compliance

from simulations (related to anisotropy) is insignificant; it is the relative curve of compliance against notch depth that is required.

The beam parameters were:

- Height, h = 2.5 mm
- Width, w = 4.2 mm
- Total length = 30 mm
- L_{el} = 20 mm
- L_{fr} = Variable
- E = 398 GPa
- ν = 0.22

The dimensions of the beam were in mm to speed up the simulation; the time step in FEA is proportional to the minimum element length over the speed of sound in the material. FEA of a beam (dimensioned in μm) showed that using mm for most beams was valid for the compliance calibration analysis route used here.

The encastré beam from FEA gave a Young's modulus with 0.07% away from that ascertained using simple beam theory (Equation 3.7).

The analysis hereafter was performed by the author and supervisor.

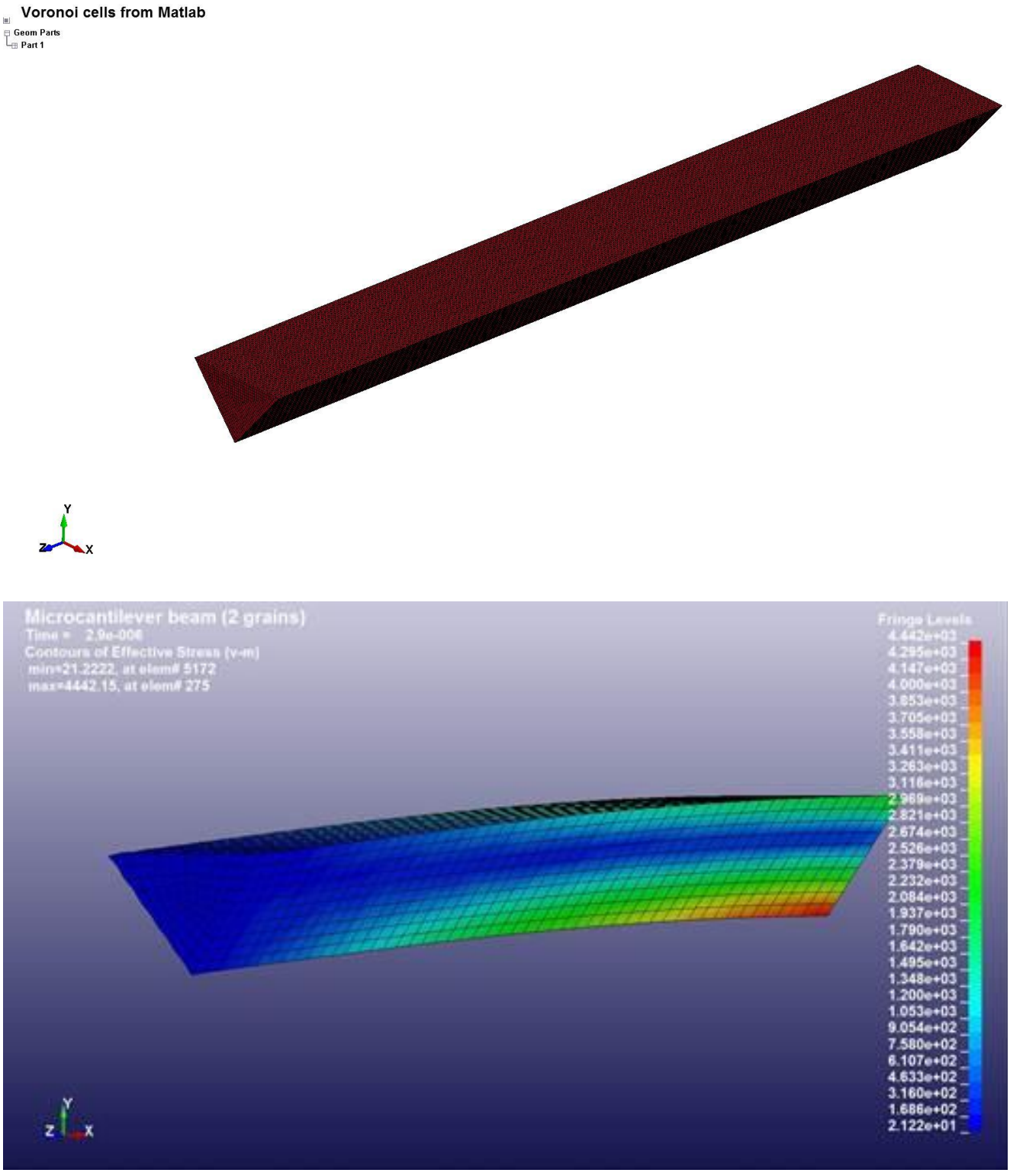


Figure 6.2: a) Encastre microcantilever beam constructed for compliance calibration analysis, b) beam during loading with indenter tip, showing deformation.

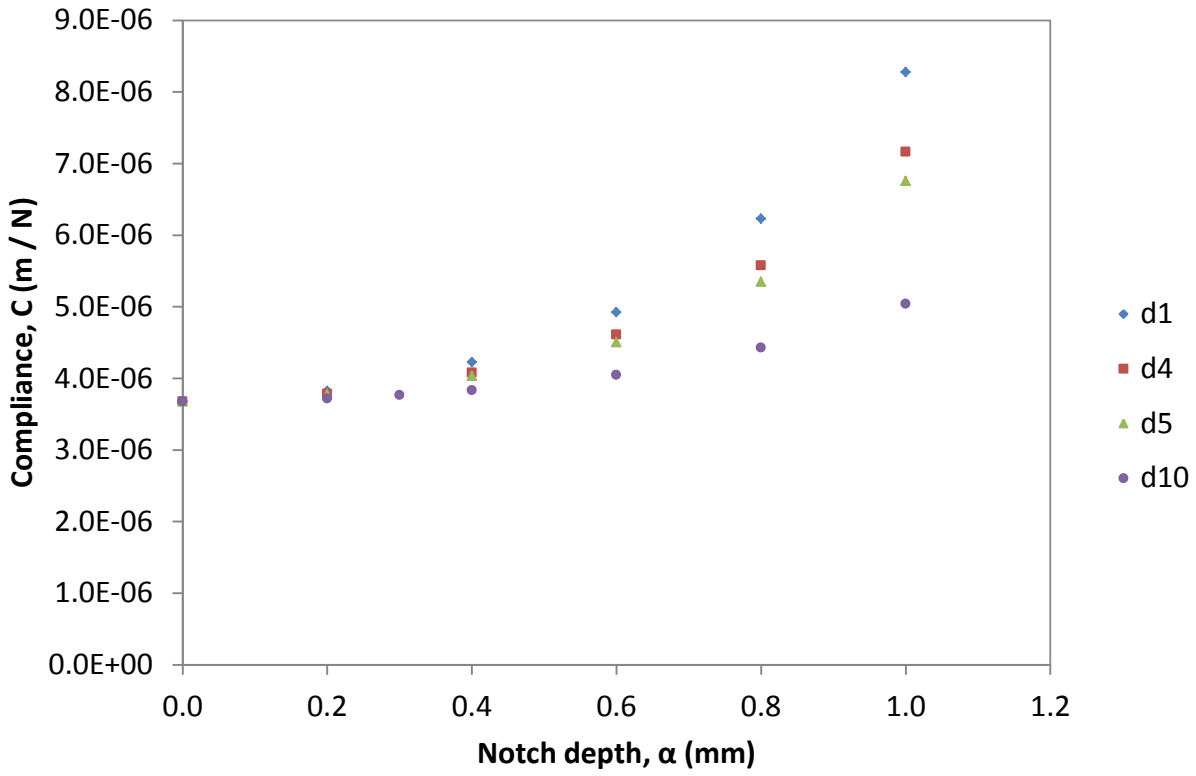


Figure 6.3: Change in compliance with depth of notch for different distances between the fixed end and the notch; d1, 4, 5, 10 represent 1, 4, 5, and 10mm respectively.

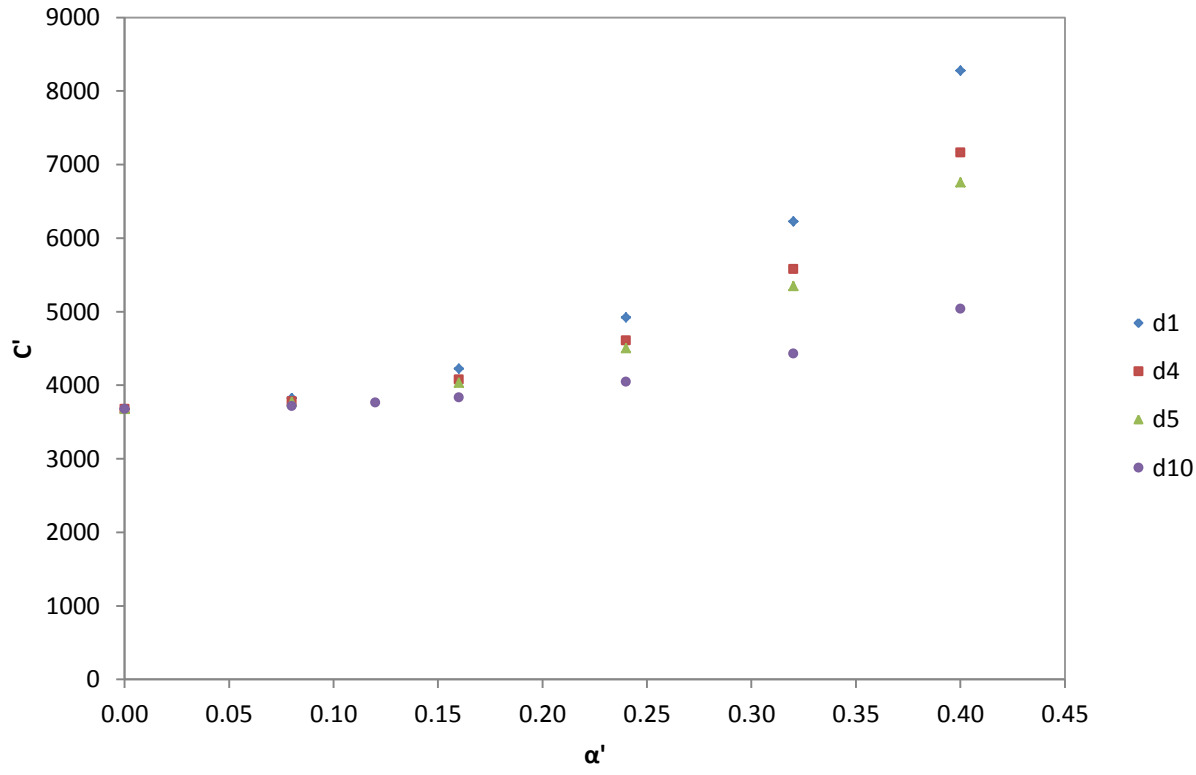


Figure 6.4: Change in the reduced compliance with reduced depth of notch for different distances between the fixed end and the notch; d1, 4, 5, 10 represent 1, 4, 5, and 10mm respectively.

The value of the compliance increased as simulated notch depth increased (Figure 6.3), and the compliance was greater for a smaller distance between the fixed end and the notch. In order to determine a value of the dimensionless factor, Y, Figure 6.3 was re-plotted as C' against α' (Figure 6.4). As the dimensionless factor $Y = \left[\frac{1}{2}\frac{dC'}{d\alpha'}\right]^{\frac{1}{2}}$, the points in Figure 6.4 were fitted with a fourth order polynomial:

$$C' = a_0 + a_1\alpha' + a_2\alpha'^2 + a_3\alpha'^3 + a_4\alpha'^4 \qquad (6.11)$$

and differentiated. For very short cracks, the stress intensity factor should reduce to $K = \psi\sigma\sqrt{\pi\alpha}$ where ψ is a geometric factor (1.12 for a through-thickness surface crack). a_1 and a_2 can be determined in the following way. From Appendix 3.1:

$$\sigma(L_{fr}) = \frac{12FL_{fr}}{wh^2} \qquad (6.12)$$

where σ is the tensile stress on the top surface of the beam a distance L_{fr} from the load point. Hence the stress intensity factor for a short notch a distance L_{fr} from the load point is:

$$K = 1.12\sqrt{\pi}\frac{12FL_{fr}}{wh^2}\sqrt{h\alpha'} \qquad (6.13)$$

The stress intensity factor for the short notch equals that derived from the mechanical energy release rate (Equation 6.9). Equation 6.13 was rearranged to have a similar form to Equation 6.9:

$$K = 13.44\sqrt{\pi}\frac{F}{h\sqrt{w}}\frac{L_{fr}}{\sqrt{hw}}\frac{1}{\sqrt{1-\alpha'}}\sqrt{\alpha'(1-\alpha')} \qquad (6.14)$$

Hence, comparing Equations 6.9 and 6.14:

$$\left(\frac{1}{2}\frac{dC'}{d\alpha'}\right)^{\frac{1}{2}} = 13.44\sqrt{\pi}\frac{L_{fr}}{h}\left(\frac{h}{w}\right)^{\frac{1}{2}}\sqrt{\alpha'(1-\alpha')} \qquad (6.15)$$

For very small values of α',

$$\left(\frac{1}{2}\frac{dC'}{d\alpha'}\right)^{\frac{1}{2}} \rightarrow 13.44\sqrt{\pi}\frac{L_{fr}}{h}\left(\frac{h}{w}\right)^{\frac{1}{2}}\sqrt{\alpha'} \quad (6.16)$$

Hence,

$$\frac{dC'}{d\alpha'} = 2(13.44^2)\pi\left(\frac{L_{fr}}{h}\right)^2\left(\frac{h}{w}\right)\alpha' \quad (6.17)$$

Integrating:

$$C' = (13.44^2)\pi\left(\frac{L_{fr}}{h}\right)^2\left(\frac{h}{w}\right)\alpha'^2 + a_0 \quad (6.18)$$

Thus, $a_1 = 0$, and $a_2 = (13.44^2)\pi\left(\frac{L_{fr}}{h}\right)^2\left(\frac{h}{w}\right)$

The reduced compliance was fitted using Equation 6.11 using a four order polynomial; a_1 and

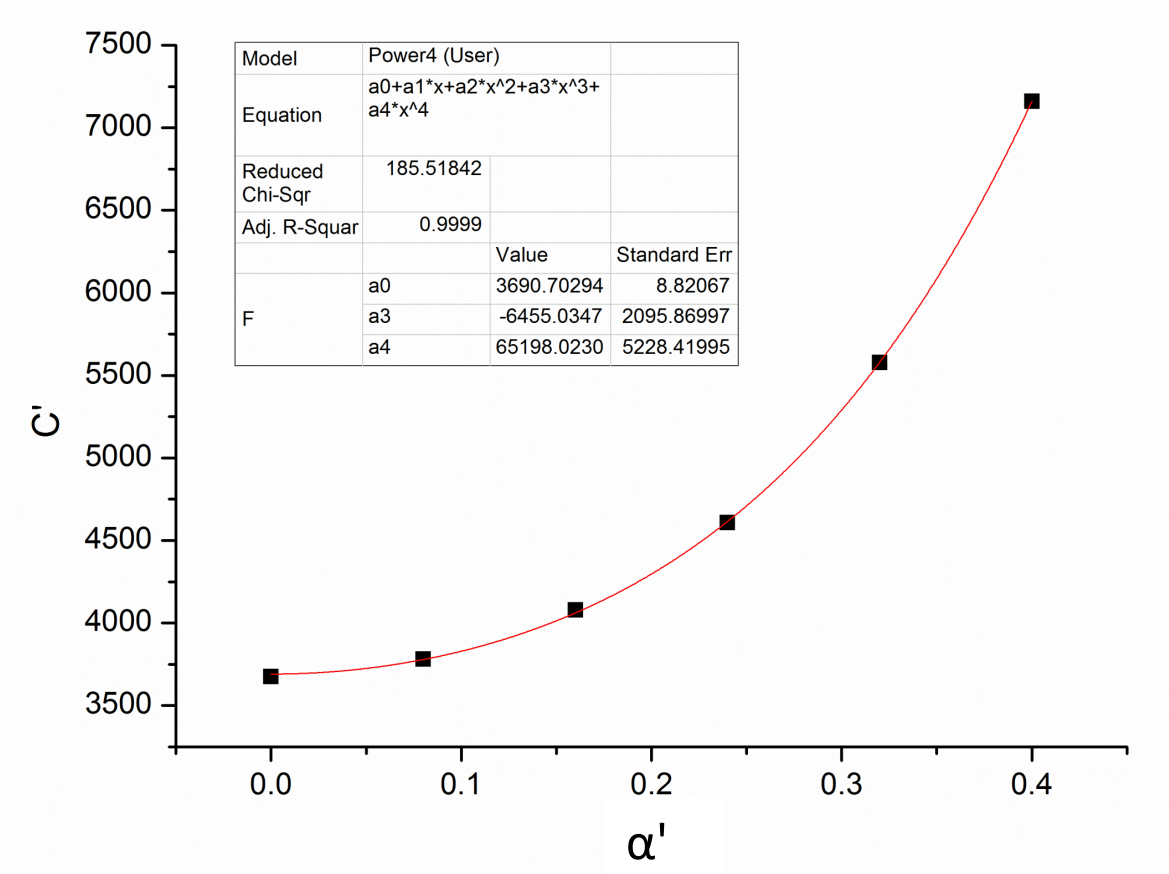


Figure 6.5: Graph of reduced compliance against reduced notch depth for d4 showing the curve fit, after setting $a_1 = 0$ and defining a_2.

a_2 were defined, and a_0, a_3 and a_4 were free (Figure 6.5). The fit was good, with an adjusted R^2 value of 0.99994.

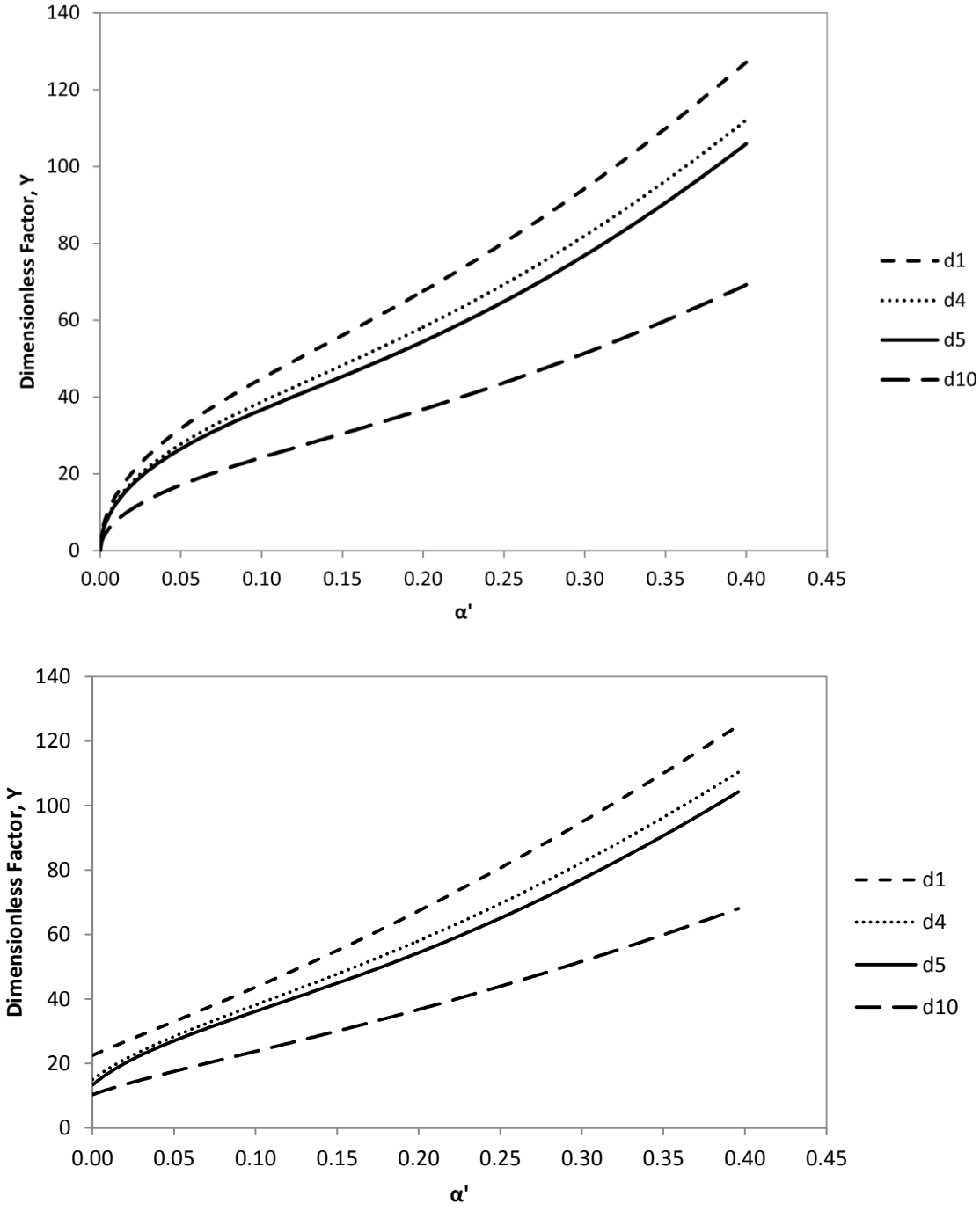


Figure 6.6: Change in the dimensionless factor Y with the reduced notch depth for different distances between the fixed end and the notch; d1, 4, 5, 10 represent 1, 4, 5, and 10mm respectively. a) Constrained a_1 and a_2 values, b) Unconstrained a_1 and a_2 values.

For comparison, fits were also considered without constraining either a_1 or a_2. Using the derivative of the polynomial fits, the dimensionless factor Y was determined for each the notch position (Figure 6.6). Whilst the constrained and unconstrained curves tend to the same values of Y at large α', the behaviour at small values was markedly different. Considering the short crack solution (Equation 6.15), as $\alpha' \rightarrow 0$, $Y \rightarrow 0$. Without the constraining terms, the behaviour was not correctly modelled for short cracks. Thus, only fits with a_1 and a_2 constrained were considered herein.

C' curves were fitted with a five power polynomial with a_1 and a_2 constrained. The graphs for Y were very similar to those where C' was fitted with a four power polynomial (Figure 6.6a). Further comparison of the four and five power fits was made forthwith.

There was variation in the value of Y with notch position (for a given depth). Short crack stress intensity factors (Equation 6.9) should be independent of notch position. To take the variation in notch position into account, an approximation was used that included the value L_{fr}; the new parameter is η. From Equation 6.15,

$$Y = 13.44\sqrt{\pi}\frac{L_{fr}}{h}\left(\frac{h}{w}\right)^{\frac{1}{2}}\sqrt{\alpha'(1-\alpha')} \qquad (6.19)$$

The parameter η was defined

$$\eta = \frac{Y}{13.44\sqrt{\pi}\frac{L_{fr}}{h}\left(\frac{h}{w}\right)^{\frac{1}{2}}\sqrt{\alpha'(1-\alpha')}} \qquad (6.20)$$

Thus, $K = K_0\eta$ where K_0 is the stress intensity factor for short cracks given by Equation 6.13.

The assumption that the long crack solution for any notch position can be accounted for by η was tested by plotted η against α' for different notch positions (Figure 6.7).

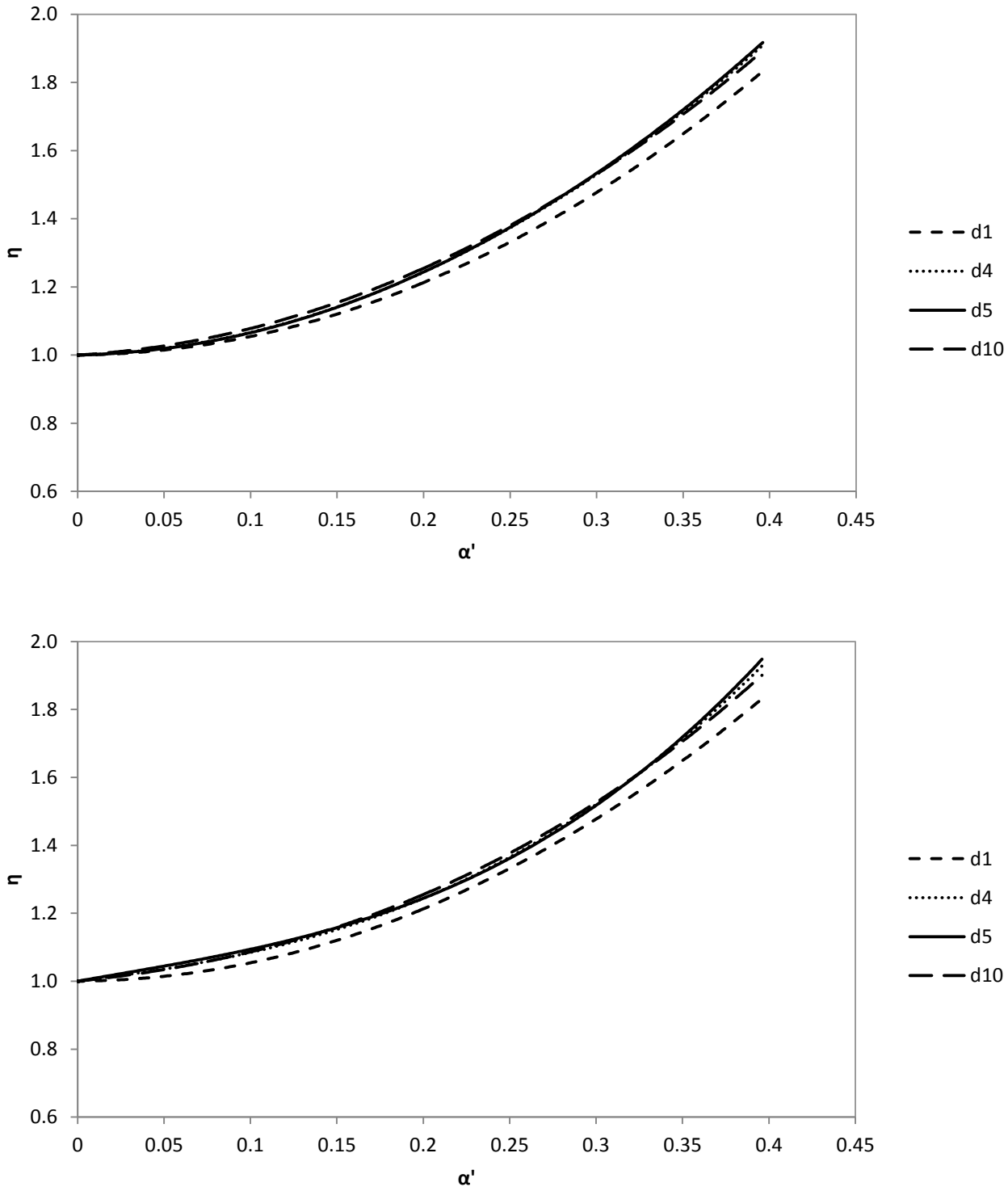


Figure 6.7: Change in the dimensionless factor η with the reduced notch depth for different distances between the fixed end and the notch; d1, 4, 5, 10 represent 1, 4, 5, and 10mm respectively. a) with four-order and, b) with five-order polynomial fit of C'

There was a small variation in η between the curves for the different notch positions as well as between the four- or five-order polynomial fit of C'.

d_1 was notably different from the other curves (Figure 6.7) for both four- and five-order polynomial fits, due to the effect of the fixed end which altered the local stress in the vicinity of the notch.

Whilst at large values of α' the curves were similar between the four- and five-order polynomial fits, there was a difference in the gradient at short crack depths. The gradient was ≈ 0 for short cracks using the four-order fit of C', but was finite using the five-order fit. Using the five-order fit of C' and using the following method, there was around 0.7% error from the four-order fit. As the C' curve had six points, fitting a five-order polynomial to it may have over-fitted the curve. Thus, only the four-order polynomial fitting of C' was considered herein.

The η curves were fitted with a four-order polynomial using the following equation:

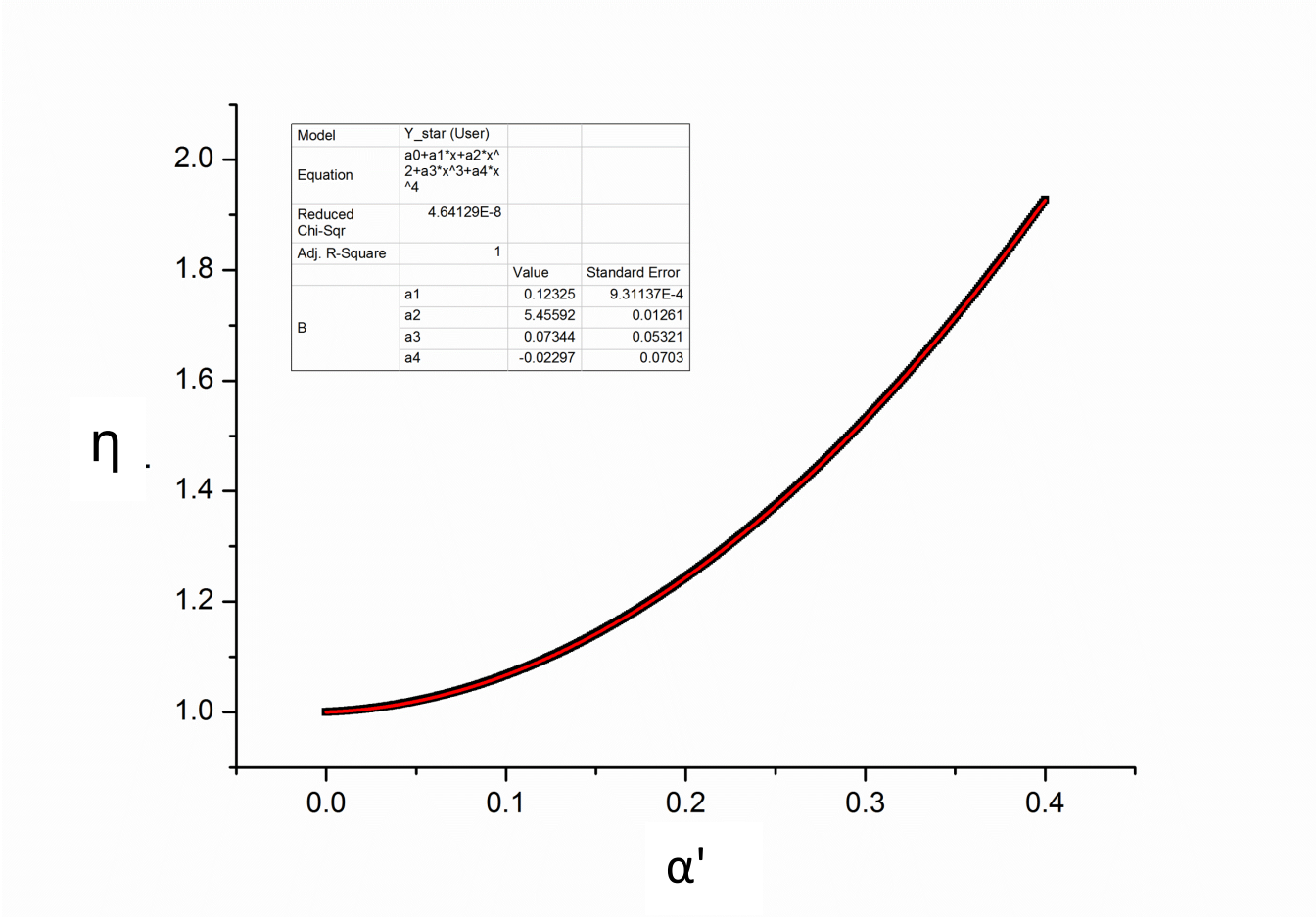


Figure 6.8: Change in η with α' for a notch position of d4, with a polynomial fitted using OriginLab.

$$\eta = 1 + b_1\alpha' + b_2\alpha'^2 + b_3\alpha'^3 + b_4\alpha'^4 \quad (6.21)$$

Equation 6.21 fitted the η curves with a good accuracy (Figure 6.8). η was determined, and thus Y was ascertained using Equation 6.20. This was substituted in Equation 6.9 to give Equation 6.22.

$$K = \frac{13.44\sqrt{\pi}\, L_{fr} F\sqrt{\alpha}}{h^2 w}\left(1 + b_1\alpha' + b_2\alpha'^2 + b_3\alpha'^3 + b_4\alpha'^4\right) \quad (6.22)$$

As $\alpha' \rightarrow 0$,

$$K = \frac{13.44\sqrt{\pi}\, L_{fr} F\sqrt{\alpha}}{h^2 w} \quad (6.23)$$

Using Equation 6.12, this can be seen to give,

$$K = 1.12\sqrt{\pi}\,\sigma(L_{fr})\,\sqrt{\alpha} \quad (6.24)$$

which is the stress intensity factor for short cracks under a tensile stress of σ, as required.

For a given microcantilever beam, the stress intensity factor needed to be determined. A unifying equation (of the form of Equation 6.22) needed to be ascertained for any notch

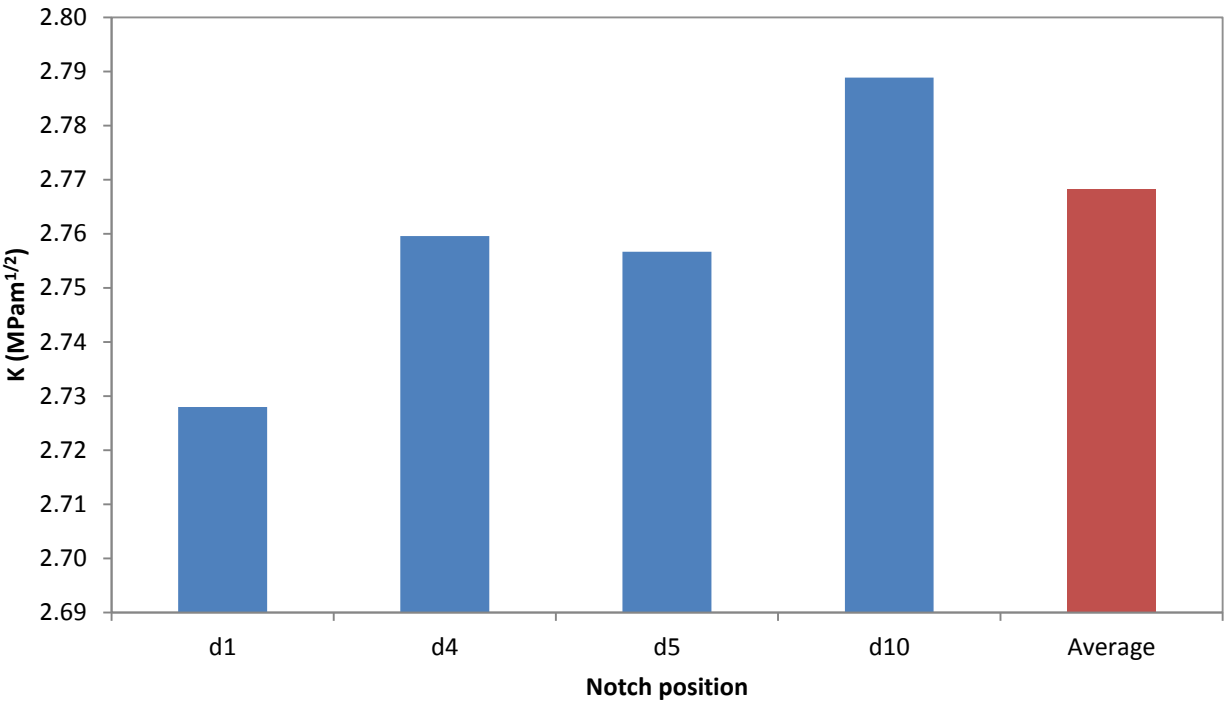


Figure 6.9: Variation in stress intensity factor K using Equation 6.22. All variables were kept constant apart from the polynomial factors from Equation 6.21.

position, beam dimensions etc.

The factors b_1 to b_4 from Equation 6.21 were determined for the different notch positions. These values were used in Equation 6.22 using: L_{fr} = 19µm, F = 300µN, h = 2.5µm, w = 4.2µm, and α = 0.1 for each curve (Figure 6.9).

Excluding d1, due to the influence of the fixed end, the mean stress intensity factor was (2.75 +/- 0.02) MPam$^{1/2}$. The range of values corresponded to an error of +/- 0.6%.

As d4 was the most realistic distance from the fixed end used in this project, Equation 6.25 was determined using the η fit from the d4 curve:

$$K = \frac{13.44\sqrt{\pi}\, L_{fr} F\sqrt{\alpha}}{h^2 w}\left(1 + 0.123\alpha' + 5.456\alpha'^2 + 0.073\alpha'^3 - 0.023\alpha'^4\right) \qquad (6.25)$$

At short notch depths, Equation 6.25 corresponded well with the short crack equations

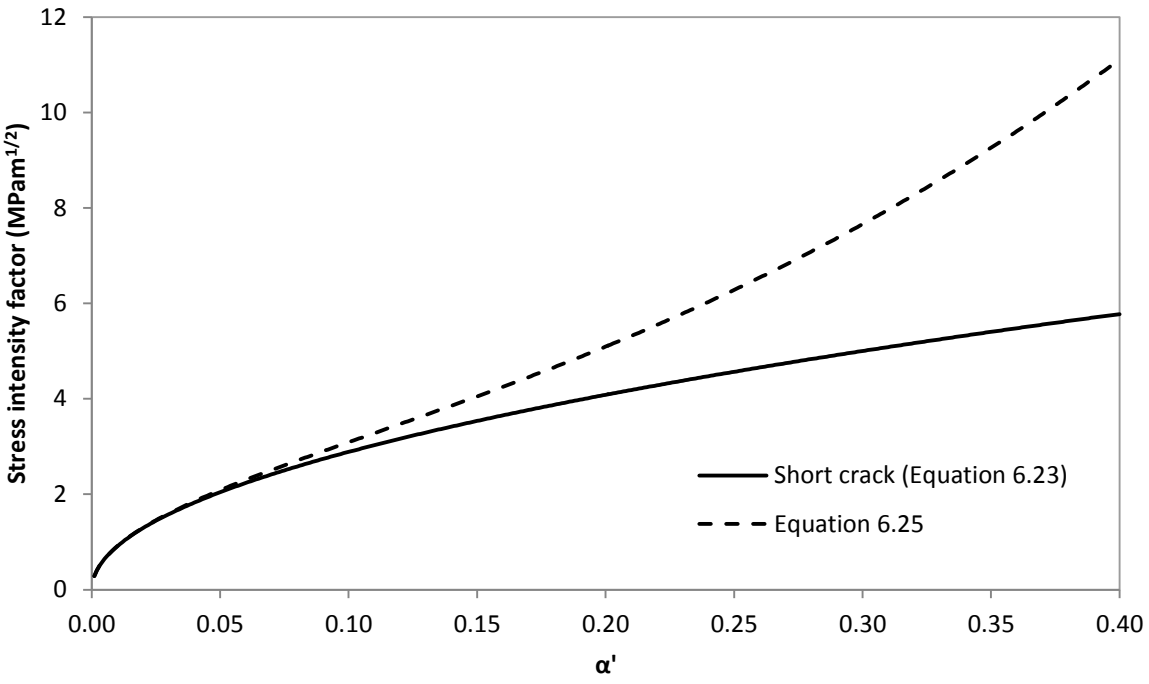


Figure 6.10: Stress intensity factor for short crack (Equation 6.23) and long crack (Equation 6.25) for different reduced notch depths.

(Figure 6.10). The deviation between the short and long crack equations was notch depth dependent.

The validity of the equations were tested by working backwards from the stress intensity factor (Equation 6.25) to determine the reduced compliance for a given notch depth. The discrepancy between this value of C' and the original C' (from Finite Element Analysis, Figure 6.4) was <0.8%. Equation 6.25 was used hereafter to determine the stress intensity factors of the straight through notched Focussed Ion Beam microcantilever beams in this project. The validity of the generated values of the stress intensity factors was discussed in Section 9.1.5.

6.2. Controlled Flaws

The most rigorous approach for determining the stress intensity factors of controlled flaws would be to perform Finite Element Analysis simulations and use the approach in Section 6.1. In the absence of these simulations, this was not possible. Instead, previous equations for semi-elliptical flaws [144] were used (the controlled flaws were approximated to ellipses).

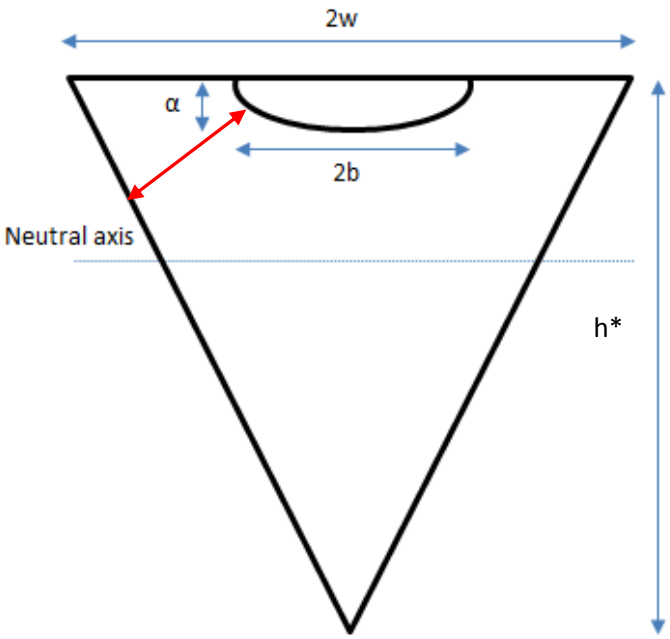


Figure 6.11: Schematic of microcantilever beam with flaw

This approach was valid for two reasons. Firstly, the stress intensity values ascertained for sapphire beams with controlled flaws (Section 7.1.5.) using the equations in this chapter were consistent with those of sapphire beams with straight through notches using Equation 6.25 (Section 7.1.3). Secondly, if the flaw half-width b << w (where w is the beam half-width) (Figure 6.11), then the notch acts as an isolated surface flaw and the equations presented herein are expected to be

correct. Thus, whilst not the most rigorous method, it was valid for the experiments performed in this work.

Strobl et al [144] used five different factors relating to the ratios of $\frac{\alpha}{b}$, $\frac{\alpha}{h^*}$, $\frac{b}{w}$, θ, ν (Poisson's ratio) and χ (the angle between the edge of the elliptical flaw and the top surface) such that:

$$K = \sigma(L_{fr})\sqrt{\pi\alpha}\, M = \sigma(L_{fr})\sqrt{\pi\alpha} f\, f_b f_\nu f_\chi f_\theta \qquad (6.26)$$

The five factors that make up M are given in full in Appendix 6.1.

In the original paper [144], rectangular beams are used. As the neutral axis of a rectangular beam is different to a triangular beam, a conversion is required. The height used in the equations, $h^* = {}^2/_3 h$, where h is the true height of the beam. This is discussed in Appendix 6.1.

Equation 6.26 is valid for specific dimensional ratios (Table 6.1) due to the limits used in the Finite Element Analysis by the authors [144].

Dimensional ratio	Range of values for which Equation 6.26 is valid
$\frac{\alpha}{h^*}$	0.01 – 0.5
$\frac{\alpha}{b}$	0.4 – 1.2
$\frac{b}{w}$	0.1 – 0.5
χ	70^o – 110^o

Table 6.1: Range of dimensional ratios for which the controlled flaw equations [144] are valid

The values in Table 6.1 are a useful guide to determining if the stress intensity factor at failure of a beam, determined using Equation 6.26, is valid. Superimposed onto these requirements are ones specific for the triangular shaped beam:

1) To reduce the effect of the edge of the beam, controlled flaws should be placed (where possible) in the centre of width of the beam.
2) As α and b become larger, the effect of the edge of the beam is greater than in the rectangular beams (due to the shape). If the distance from the bottom corner of the flaw to the edge of the beam (red arrow in Figure 6.11) > b, the flaw should be acting as a surface flaw independent of the edges of the beam (i.e. Saint-Venant's principle) and the equations are valid
3) To ensure that the maximum stress intensity factor is at the base of the notch (and not at the edges), $\frac{\alpha}{b} < 0.6$ was used (from equations from [144]).

By using the above three requirements, and those in Table 6.1, Equation 6.26 is confidently used to determine the stress intensity factor at failure for controlled flaws on the surface of microcantilever beams. For the flaws used in this project, $\frac{\alpha}{b} < 0.6$ and $\frac{\alpha}{h^*} < 0.2$. Thus, from [144], the maximum stress intensity was at the bottom of the controlled flaw; the factor $f_\theta = 1$. As $\chi = 90^o$, $f_\chi = 1$.

Chapter 7 Understanding and Validating the Microcantilever Beam Testing

The equations for stress intensity factors of notched microcantilever beams (Chapter 6) can be used to determine the toughnesses of different ceramics. Before doing this, the microcantilever beam technique was validated. The following sections focus on:

1) Determining the fracture strength and Young's modulus of sapphire
2) Comparing qualitatively the stress intensity factors at failure for beams notched at and away from a boundary on a diffusion bonded sapphire (or bicrystal) sample.
3) Ascertaining the residual stress in the gallium implanted region, using optical fluorescence microscopy and nanodiffraction, and determining a suitable correction for the stress intensity factor correction at failure.
4) Understanding how the stress intensity factor at failure changes with notch radii, and finding suitable correction factors.
5) Investigating the effect of moisture assisted sub-critical crack growth on the measured stress intensity factor at failure.
6) Considering the change in the mechanical properties after vacuum annealing.

These six considerations were the focus of this chapter. The tests were performed on either a diffusion bonded sapphire boundary or on the surface of sapphire.

7.1. Diffusion Bonded Sapphire

Microcantilever beams were produced using Focussed Ion Beam (FIB) milling (Section 3.7). In order to understand the technique, beams were manufactured across a diffusion bonded sapphire boundary (Section 3.1.5., characterised in Section 4.6). As the sapphire bicrystal

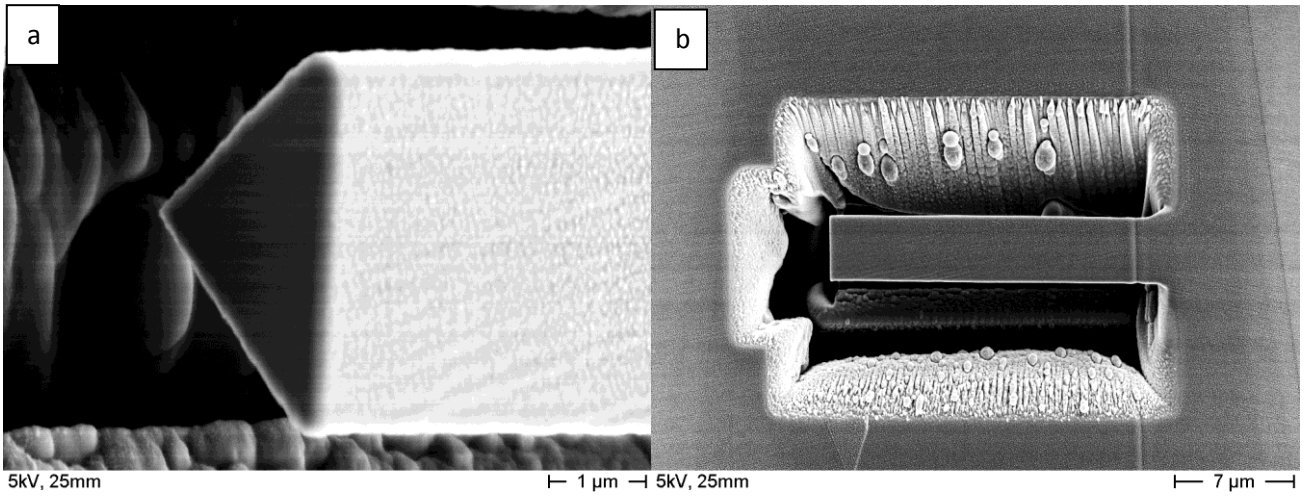


Figure 7.1: SEI (JEOL 840F) of an un-notched microcantilever beam in diffusion bonded sapphire: a) the free end, tilted to 50 degrees, and b) the beam in its trench before loading

was several millimetres long, many beams were produced across the grain boundary. The grain boundary structure and composition was expected to be fairly consistent along its length, and so the toughnesses measured along it should be constant. Notches of different types were made and their validity compared.

7.1.1. Un-notched beams across the boundary

Three microcantilever beams were produced on the surface of the diffusion bonded sapphire, orientated parallel to the c-axis. They were uniform in cross-section along their lengths and generally free from redeposited material (Figure 7.1a); some redeposited material was apparent at the fracture surface (Figure 7.2) indicating the difficulty in eradicating it entirely. Beams were unnotched in order to measure fracture strength (Equation 3.6) and Young's modulus (simple beam theory (Equation 3.5) and corrected to allow for the

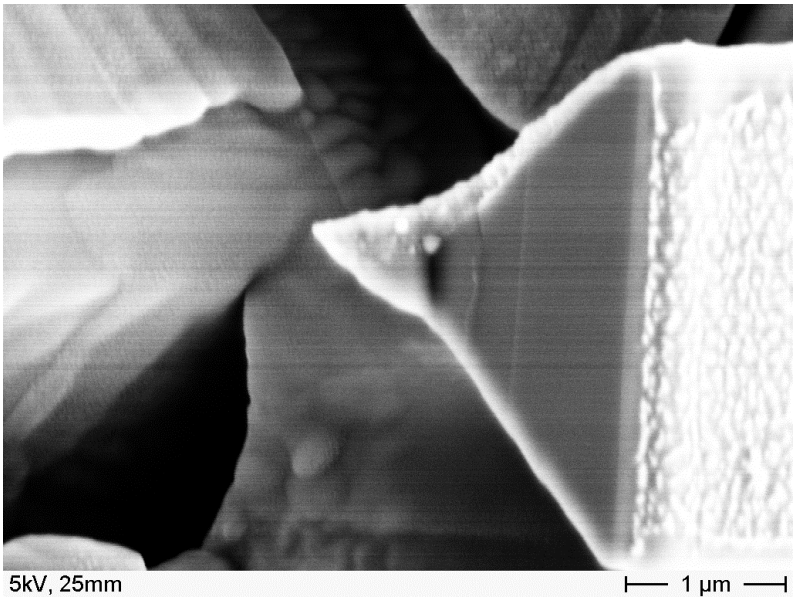


Figure 7.2: SEI (JEOL 840F) of broken microcantilever beam in diffusion bonded sapphire. Tilted to 50°

deflection in the support behind the fixed end (Section 3.7.1.2)).

Beam	Modulus (GPa)	Fracture Strength (GPa)
Un-notched 1	443	5.4
Un-notched 2	457	5.0
Un-notched 3	493	5.0

Table 7.1: Mechanical properties of un-notched beams fractured across a diffusion bonded sapphire boundary

The mean Young's modulus and standard error was (465 +/- 25) GPa. The expected modulus (using elastic constants from Wachtman et al [215]) was 463GPa. The mean fracture strength was (5.2 +/- 0.1) GPa. The fracture surfaces (Figure 7.2) were smooth, indicating that the crack had nucleated at the grain boundary thermal groove and propagated along the diffusion bonded boundary.

7.1.2. Notched away from the boundary

To determine whether the recorded stress intensity factor at failure was reduced due to the presence of the boundary, microcantilever beams were produced and notched in the sapphire matrix (parallel to the c-plane). Beams were manufactured with a straight through notch (10pA beam current). The resultant fracture surface (Figure 7.3) was faceted; as the c-plane was unfavourable to fracture along [147], the crack propagated along planes which were close to, but not, the basal plane (this is similar to that seen by [137]). .

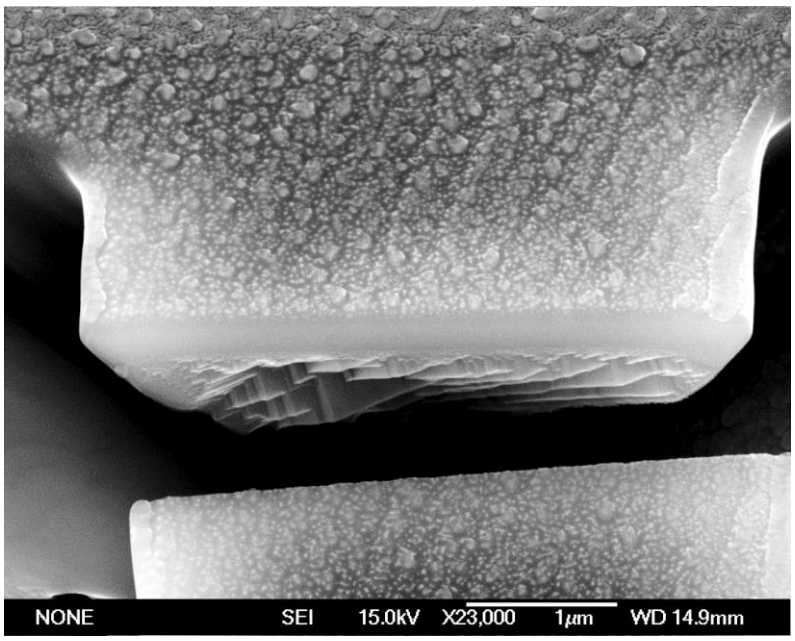


Figure 7.3: SEI (JEOL 6500F) of microcantilever beam in diffusion bonded sapphire notched and fractured away from the boundary. Tilted to 50°.

Load-displacement curves were linear until failure. The nominal strength of the beams (Table 7.2) was lower with the notch than without. The average stress intensity factor at failure of the notched beams, K_{fail}, (using Equation 6.25) was (3.8 +/- 0.1) $MPam^{1/2}$.

Beam	Notch Depth (μm)	Nominal Strength (GPa)	α'	K_{fail} ($MPa.m^{1/2}$)
Notch – Matrix 1	0.35	2.8	0.12	3.7
Notch – Matrix 2	0.34	3.1	0.11	3.9
Notch – Matrix 3	0.31	3.2	0.12	3.8

Table 7.2: Microcantilever beams in diffusion bonded sapphire notched away from the boundary. α' = ratio between the notch depth and the height of the beam, K_{fail} = stress intensity factor at failure

7.1.3. Straight through notch at the boundary

Straight through notches were milled across the diffusion bonded boundary (10pA beam current). Load-displacement curves were linear until failure. The fracture surface was smooth (Figure 7.4), indicating that the crack had nucleated at the FIB notch and propagated along the bicrystal boundary. The stress intensity factor at failure was (2.9 +/- 0.1) $MPa.m^{1/2}$.

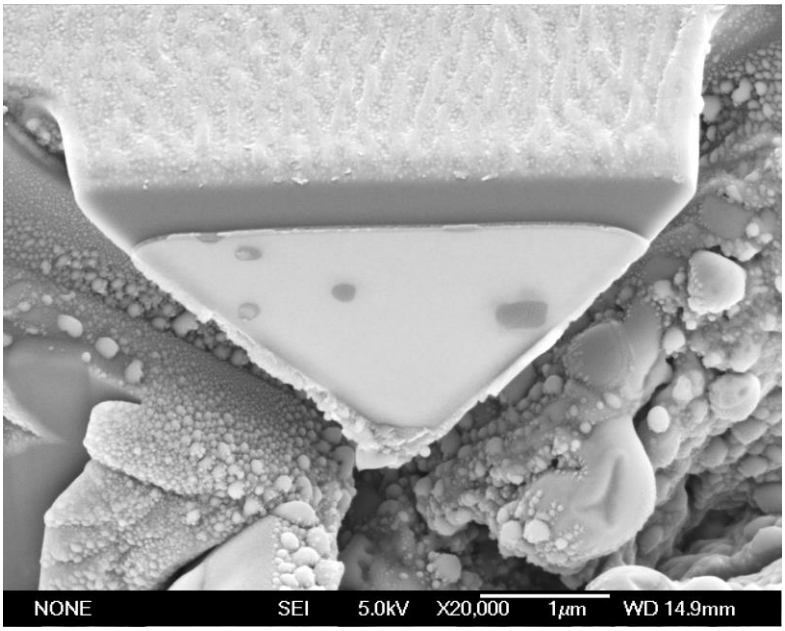


Figure 7.4: SEI (JEOL 6500F) of microcantilever beam in diffusion bonded sapphire with a straight through notch at the boundary. Tilted to 50°

Beam	Notch Depth (μm)	Nominal Strength (GPa)	α'	K_{fail} (MPa.m$^{1/2}$)
Str – GB - 1	0.16	3.7	0.11	3.1
Str – GB - 2	0.43	2.0	0.21	3.4
Str – GB - 3	0.12	3.8	0.06	2.6
Str – GB - 4	0.12	3.7	0.05	2.6
Str – GB - 5	0.34	2.5	0.13	3.2
Str – GB - 6	0.45	1.8	0.16	2.7
Str – GB - 7	0.45	1.9	0.13	2.8
Str – GB - 8	0.24	2.7	0.10	2.8

Table 7.3: Results from the microcantilever beams in diffusion bonded sapphire with a straight through notch at the boundary

7.1.4. Chevron notch at the boundary

Ceramic beams with single-edge chevron notches undergo stable crack growth macroscopically [3]. Similar notches were produced on microcantilever beams to assess the extent of stable crack growth. Final failure should have initiated from a sharp crack rather than a notch, and may have resulted in a different K_{fail}.

Several samples were manufactured but failed during scanning (Section 3.7.1.). One sample was successfully produced with a chevron notch at the diffusion bonded boundary (Figure 7.5a). The load-displacement curve did not show any stable crack growth prior to failure

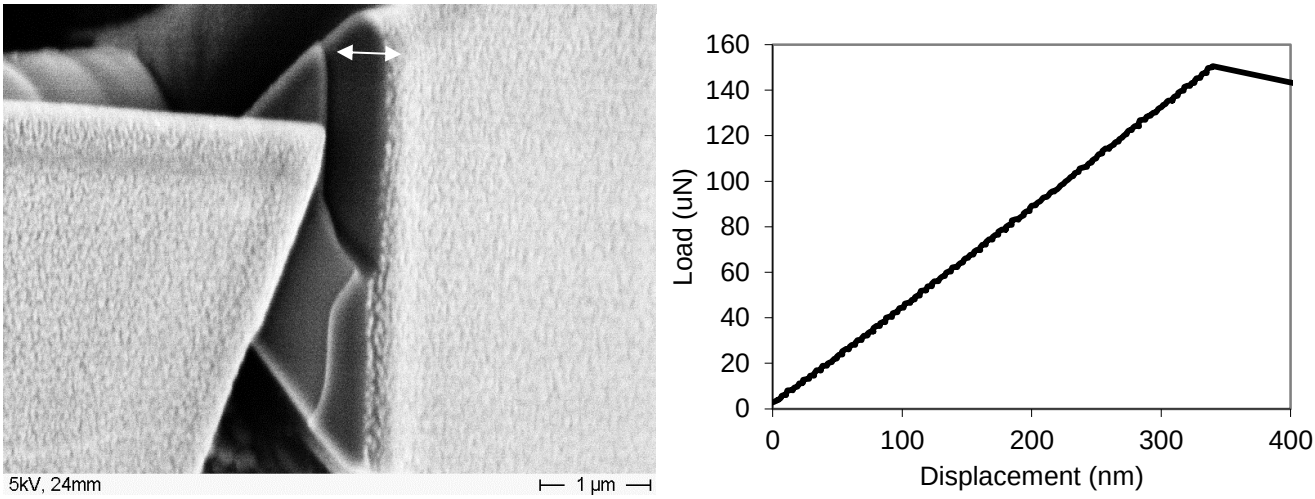


Figure 7.5: a) Fracture surface of chevron notch at diffusion bonded sapphire boundary, with arrow indicating the notch depth used to determine the stress intensity factor at failure, b) Load-displacement curve for beam showing no stable crack growth before failure.

(Figure 7.5b). This was due to either 1) the nanoindenter being essentially under load control and, once cracking began to occur and the load dropped, the tip attempted to maintain the load on the top surface and drove the crack front forward, or 2) the residual stress at the notch tip did not allow stable crack growth to occur (Section 7.2).

The stress intensity factor at failure was determined (Equation 6.25) by assuming that failure occurred from a flat notch of depth equal to the deepest part of the FIB-ed chevron (i.e. arrow in Figure 7.5a).

Beam	Notch Depth (μm)	Strength (GPa)	α'	K_{fail} (MPa.m$^{1/2}$)
Chevron - 1	0.85	1.1	0.34	3.5

Table 7.4: Mechanical properties of a microcantilever beam with a chevron notch at the boundary

The stress intensity factor at failure was higher than the straight through notch. Furthermore, its key feature (of stable crack growth before failure) was not apparent. Thus it was ruled out as a viable testing method.

A variant of the technique was to produce a straight through type notch at the boundary with an un-notched section in the middle, or “pseudo-chevron” (Figure 7.6). Stable crack propagation should occur in a similar way to the chevron notch. The key difference was that the crack should nucleate from the top surface which had not been altered by the gallium implantation. In practice, there was no stable crack growth prior to failure and it was difficult to produce consistent notches. Thus, it was not considered further in this work.

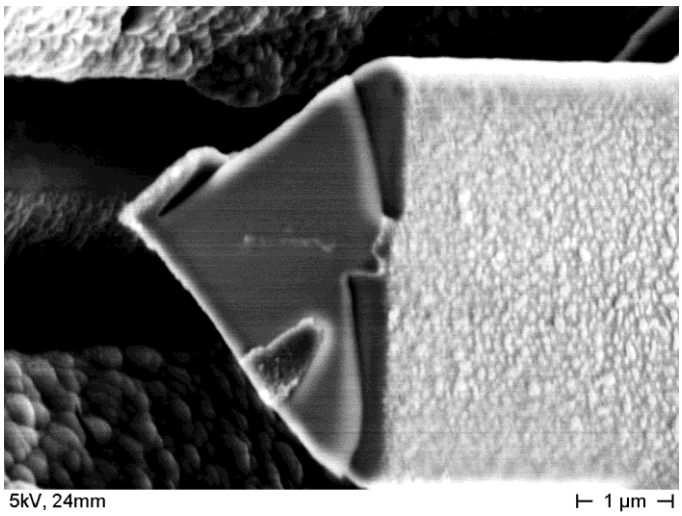


Figure 7.6: SEI (JEOL 840F) of pseudo-chevron notch in polycrystalline alumina. Tilted to 50°

7.1.5. Controlled flaw at the boundary

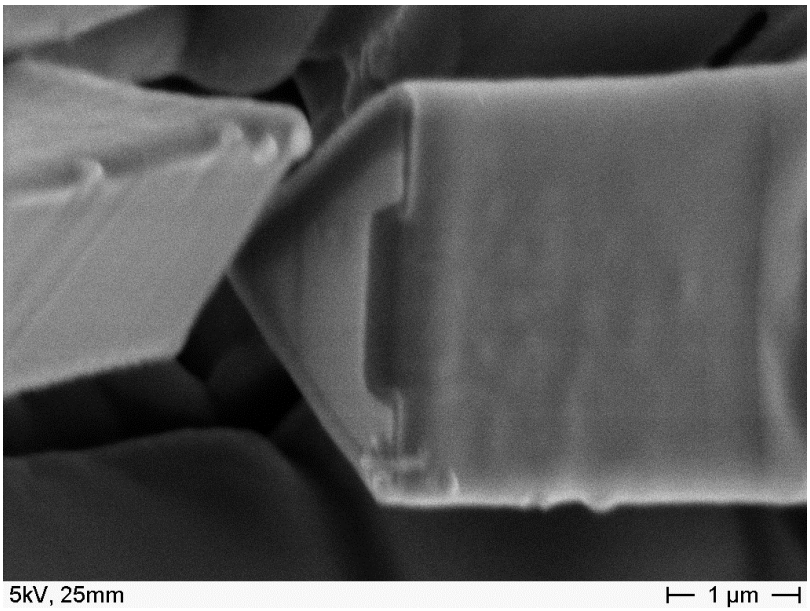


Figure 7.7: SEI (JEOL 840F) of controlled flaw at the boundary of diffusion bonded sapphire (tilted at 50°).

The controlled flaw method had many potential benefits over the straight through notch, due to the possibility of placing a notch on a section of a polycrystalline boundary and avoiding the problem of a boundary which was not flat and straight. It also avoided the curtaining effect (Section 2.6.4.). Hence, the method was tested on the diffusion bonded boundary; the values generated must be the same as those for the straight through notch.

The load-displacement curves were linear until failure. The fracture surfaces of the controlled flaws at the diffusion bonded sapphire showed that the samples fractured along the grain boundary due to a crack being nucleated at the flaw (Figure 7.7). The stress intensity factors were determined following the method described in Section 6.2 (from [144]), ensuring that the dimensional ratios etc. were within the requirements set out in Section 6.2. The stress intensity factor at failure was (2.7 +/- 0.4) MPa.m$^{1/2}$ (Table 7.5).

Beam	α/b	b/w	α'	M	K_{fail} (MPa.m$^{1/2}$)
Flaw - 1	0.44	0.27	0.09	0.77	2.5
Flaw – 2	0.30	0.35	0.11	0.84	3.1
Flaw – 3	0.50	0.46	0.18	0.69	3.6
Flaw – 4	0.42	0.50	0.17	0.75	2.1
Flaw – 5	0.42	0.44	0.14	0.76	2.3

Table 7.5: Mechanical properties of microcantilever beams with controlled flaws at the boundary. M is value calculated using Equation A6.1.1.

The stress intensity factors at failure were also calculated using the equation for a straight through notch (as Matoy et al [118] proposed). The mean value of K_{fail} was (4.7 +/- 0.2)

MPam$^{1/2}$. This was much higher than the value for genuine straight through notches (Section 7.1.3.) and, as such, was deemed an inappropriate approach for controlled flaws. Hence, the Strobl [144] equations were used instead.

7.2. Residual stress due to gallium implantation

7.2.1. Optical Fluorescence Microscopy (OFM)

In order to understand the impact that the Focussed Ion Beam has on 1) the top surface of the sample (due to imaging during microcantilever beam production) and 2) the properties at the base of the FIB-milled notch, the residual stress of a FIB produced liftout sample was measured using optical fluorescence microscopy (OFM). Due to greater chromium content, and hence clearer OFM signal, ruby was chosen over sapphire.

The liftout foil, produced using the method described in Section 3.2.2. was located inside the Renishaw System 1000 Optical Fluorescence Microscope. The following parameters were used:

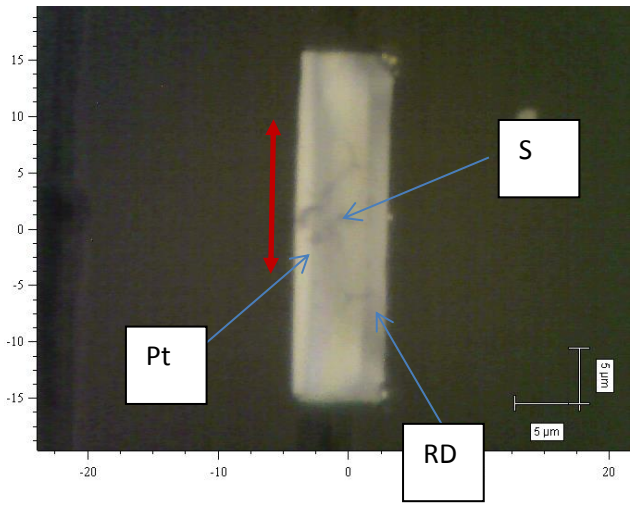


Figure 7.8: Optical image of the ruby liftout sample. The platinum (Pt), sapphire (S) and a small amount of redeposited material overlapping the sapphire (RD) can be seen. Uniaxial stress expected in the direction of arrow.

- Laser power: 1%
- Exposure time: 3s
- Step size: 0.1µm
- Scan type: Snake

Horizontal line scans were taken over the foil. Owing to the small size of the specimen, FocusTrack was not used; the spot remained in focus over the surface .

The top surface of the foil (underneath the platinum strip) underwent gallium implantation. Due to the implanted ions, in its relaxed state the region would effectively takes up a larger volume than before. In order for the implanted region and unimplanted ruby substrate to be attached, it can be imagined

that a compressive force must have been applied to the implanted region and a tensile force to the unimplanted substrate [216]. The resultant effect is that 1) the implanted region is in compression, 2) the unimplanted ruby foil underneath the implanted region is in tension (red arrow in Figure 7.8), and 3) the unimplanted ruby foil located by the redeposited material is in compression. These stresses can be measured, and used to determine the compressive stress in the gallium implanted region by using Stoney's equation [216] (as the foil was in uniaxial stress, no $(1-\nu)$ factor, where ν is the Poisson's ratio, is included [217]):

$$\sigma_{ga} = \frac{E_{ruby} {h_{foil}}^2}{6 t_{ga}} \frac{1}{r} \tag{7.1}$$

- σ_{ga} and t_{ga} are the stress and thickness of the gallium implanted region respectively (the latter was measured previously (Section 4.6.2.1.) to be (20.5 +/- 1.5) nm)
- E_{ruby} is the Young's modulus of the ruby (400GPa),
- h_{foil} is the height of the foil (including implanted region): (5.0 +/- 0.5) µm
- r is the radius of curvature (measured from the line scans, and determined using Equation 7.2):

$$\frac{1}{r} = \frac{\sigma}{Ey} \tag{7.2}$$

where y is the distance across the foil (from Pt strip to redeposited material in Figure 7.8). It is expected that there is a linear relationship between stress across the foil and distance y, and hence Equation 7.2 can be used. This is apparent from Figure 7.9 for y between -0.5 and 3µm (there was a trough in the peak position at around -1.5µm; this was consistent for all horizontal line scans across the foil).

To determine r from the line scans (e.g. Figure 7.9), the following method was used.

1) The slope Δpeak position / Δy (between -0.5 and 3µm) was ascertained

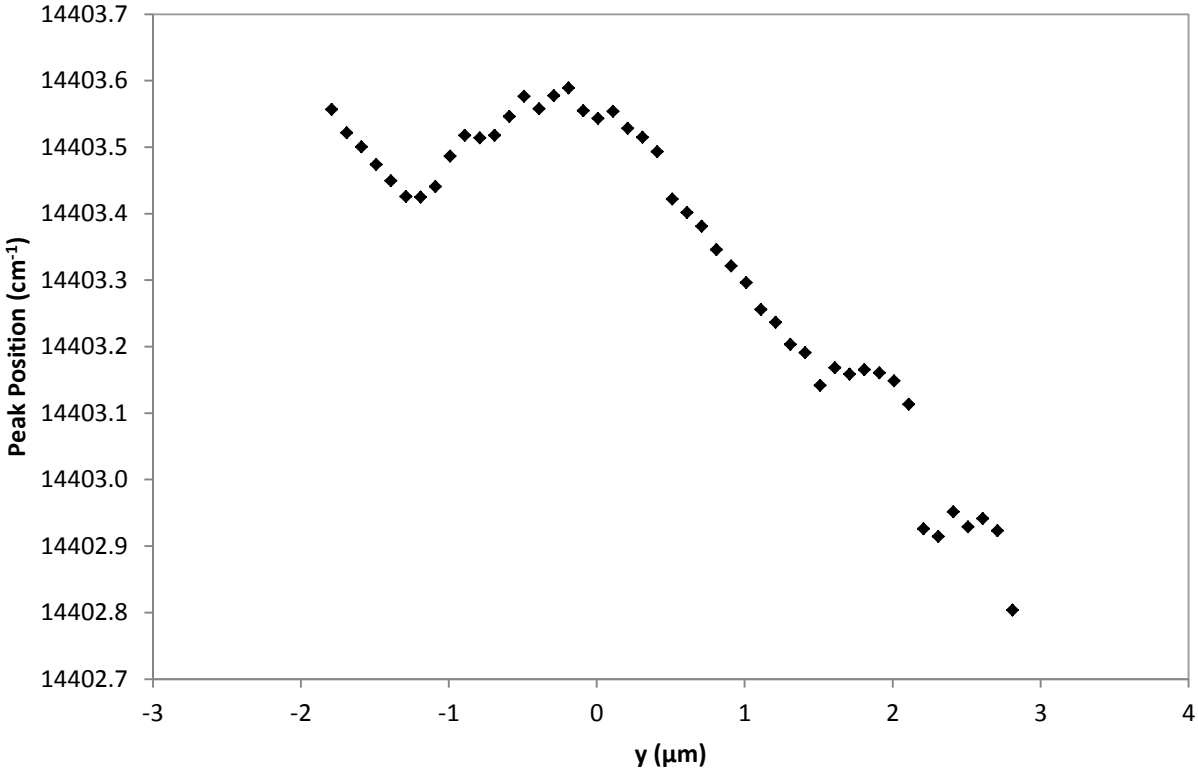


Figure 7.9: Peak position change across the middle of ruby foil (taken at 5µm in Figure 7.8)

2) This was converted to a value of $\Delta\sigma/\Delta y$ by noting that the relationship between peak shift and stress (Equation 2.15). It was assumed that the foil was in uniaxial stress state, and so a value of $\frac{1}{3}\Pi_m$ should be used [218] in Equation 2.15.
3) This was substituted into Equation 7.2 to find $1/r$.
4) Using the value of $1/r$, the stress in the implanted region was determined using Equation 7.1.

Several lines scans were performed. Following Steps 1 & 2 and Equation 7.2, the value of $1/r$ was determined: (222 +/- 76) m^{-1}. Thus, using Equation 7.1, the stress in the implanted region was found to be (18 +/- 6) GPa. This is most likely the stress on the uppermost part of the foil; as the extent of gallium implantation will reduce exponentially with distance away from the surface, it is likely that the stress decreases in a form similar to that in Equation 7.3.

$$\sigma = \sigma_{ga}\, e^{-x/20} \qquad (7.3)$$

where x is the distance into the implanted region (in nm) and 20nm is the approximate depth of the implanted region. The key stress is that at the depth equal to the characteristic notch tip crack length $d\alpha$ (7nm, Section 7.3.3.). At 7nm deep, the stress is (13 +/- 5) GPa.

This stress was considered, in light of wrinkling, delamination, and buckling, in Section 9.1.

There was also a change in the peak width across the ruby foil. At the implanted region, the peak width was much greater than in the middle of the foil (Figure 7.10). This was due to the gallium implantation; an increase in the range of stresses present in the sample increases the peak width. If elemental gallium was present interstitially in the corundum lattice, the variable lattice distortion will lead to a range of local stresses and thus peak positions.

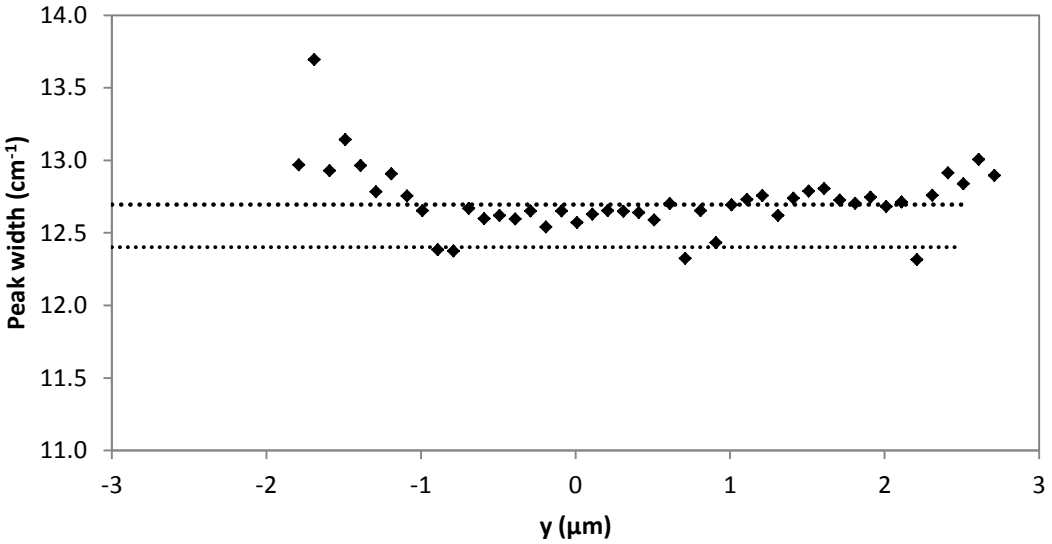


Figure 7.10: Peak width change across the middle of ruby foil. The dotted lines represented the mean peak width +/- one standard deviation for bulk ruby

7.2.2. Nanodiffraction

A sapphire foil, produced in an identical way to that of the ruby, had an implanted region at the top surface. Nanodiffraction (JEOL 2010, 5nm probe size) was performed by Dr Neil Young (Department of Materials, University of Oxford) to probe the implanted region. A typical diffraction pattern is given in Figure 4.32. The zone axis was $\langle 1\bar{1}0 \rangle$. After determining

the calibration for the TEM using the known lattice parameters of gold, the d-spacings of planes $\{1\bar{2}0\}$ and $\{003\}$ from the implanted region were determined as (2.48 +/- 0.02) and (4.55 +/- 0.04) Å respectively. For undamaged sapphire, the d-spacings (termed $d_{hkl,0}$) are 2.381 and 4.330 Å (using lattice parameters from [193]).

There were two possible contributions to the d-spacing change: gallium implanted into the lattice and residual stress. The relationship between d-spacings and gallium substitution into the corundum lattice (i.e. solid solution $(Ga, Al)_2O_3$) was considered by Hill et al [219]. However, as the gallium content was (3 +/- 1) at% (Section 4.6.2.2.), there was expected to be no change in the d-spacing due to the gallium.

Assuming that the increase in the d-spacings was due to the residual stress, the lattice strains, $\varepsilon_{\text{lattice}} = \frac{d_{hkl} - d_{hkl,0}}{d_{hkl,0}}$, were determined. The residual stress was ascertained using $\sigma_{res} = E\varepsilon_{\text{lattice}}$ where E is the Young's modulus: (14.8 +/- 0.2) and (18.0 +/- 0.2) GPa using $\{1\bar{2}0\}$ and (003) planes respectively. Although the magnitude of the stresses was similar to that from OFM, the technique ascertained a tensile residual stress from the implanted region. The most likely explanation was that gallium was situated interstitially in the lattice. This may have increased the lattice parameters (and thus d-spacings) to a greater extent that that predicted by [219]. Overall, as the technique could not determine the compressive nature of the implanted region, the results are not used here.

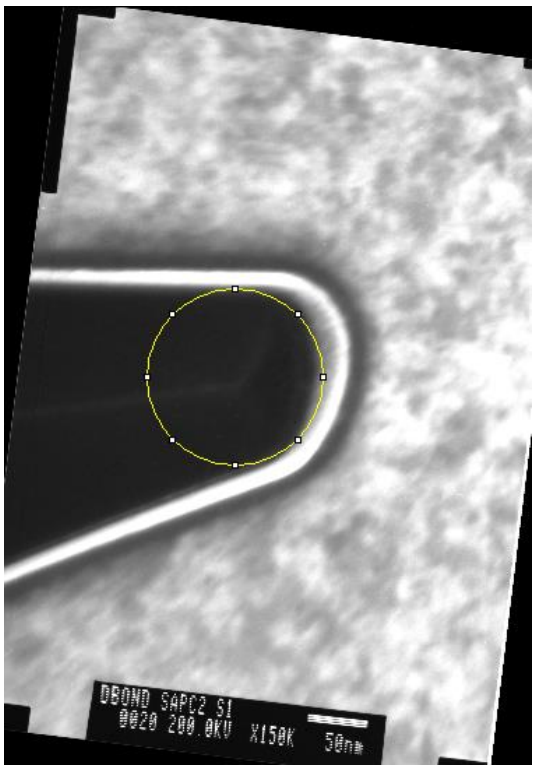


Figure 7.11: TEM image (JEOL 2000FX) of a FIB produced sapphire foil, showing the analysis of the notch root radius

7.3. Notch bluntness

As discussed in Section 2.7.5., previous authors have noted the effect of the notch bluntness on the

apparent fracture toughness. In order to determine if this is an issue in ceramics, microcantilever beams with different notch radii were loaded until failure and the stress intensity factors at failure compared.

Beams were produced in a-plane sapphire (Section 3.1.4.) after the plane and orientation were confirmed using XRD (Section 3.4.2.2.) These were notched with three beam currents: 10, 100, and 1000pA. In order to determine the notch radii of these beams, notches of the same beam currents were produced on the top surface of sapphire and a FIB-milled TEM foil, following the method in Section 3.3.2, produced (Figure 4.33).

The notch root radius was measured using an image analysis tool (ImageJ) (Figure 7.11). The relationship between the beam current and the notch root radius is shown in Table 7.6:

Beam current (pA)	Radius (nm)	+/- (nm)
10	14.5	0.1
100	31.6	0.5
1000	75.9	1.9

Table 7.6: Relationship between the beam current (FEI FIB200) and the notch root radius

As the beam current increased the notch root radius increased. These notches were produced on the surface of microcantilever beams oriented in two directions: parallel to $< 1\bar{1}00 >$ and to $[0001]$.

7.3.1. Varying notch radii – beams in a-plane sapphire parallel to $< 1\bar{1}00 >$

Tables 7.7, 7.8, and 7.9 outline the results from fractured beams notched with 10, 100, 1000pA beam currents, respectively. All load-displacements curves were linear until failure.

Beam	Nominal Strength (GPa)	Notch depth (μm)	α'	K_{fail} (MPa.m$^{1/2}$)
Str – m – 10pA - 1	4.7	0.19	0.04	4.1
Str – m – 10pA – 2	3.1	0.37	0.12	4.1
Str – m – 10pA – 3	2.7	0.34	0.14	3.5
Str – m – 10pA – 4	2.9	0.32	0.12	3.5

Table 7.7: Properties of microcantilever beams in a-plane sapphire oriented parallel to the $< 1\bar{1}00 >$ direction, with a 10pA notch

Beam	Nominal Strength (GPa)	Notch depth (μm)	α'	K_{fail} (MPa.m$^{1/2}$)
Str – m – 100pA - 1	2.3	0.69	0.14	4.3
Str – m – 100pA – 2	3.5	0.40	0.16	5.1
Str – m – 100pA – 3	3.2	0.43	0.13	4.7
Str – m – 100pA – 4	2.7	0.49	0.16	4.4

Table 7.8: Properties of microcantilever beams in a-plane sapphire oriented parallel to the $< 1\bar{1}00 >$ direction with a notch produced with a beam current of 100pA

Beam	Nominal Strength (GPa)	Notch depth (μm)	α'	K_{fail} (MPa.m$^{1/2}$)
Str – m – 1000pA – 1	2.7	0.92	0.18	6.1
Str – m – 1000pA – 2	5.7	0.24	0.10	5.9
Str – m – 1000pA - 3	5.9	0.22	0.06	5.6

Table 7.9: Properties of microcantilever beams in a-plane sapphire oriented parallel to the $< 1\bar{1}00 >$ direction with a notch produced with a beam current of 1000pA

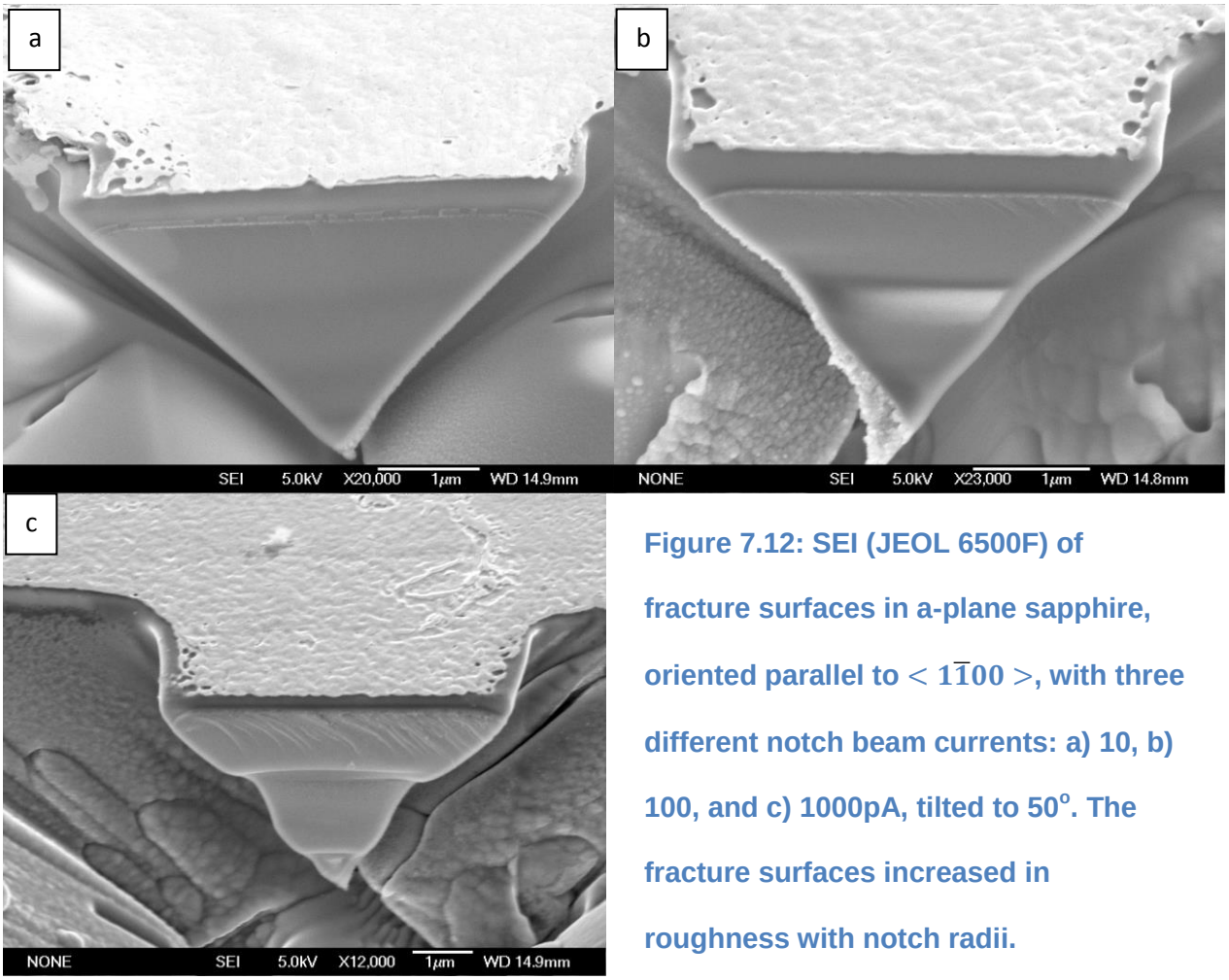


Figure 7.12: SEI (JEOL 6500F) of fracture surfaces in a-plane sapphire, oriented parallel to $< 1\bar{1}00 >$, with three different notch beam currents: a) 10, b) 100, and c) 1000pA, tilted to 50°. The fracture surfaces increased in roughness with notch radii.

Although the strength depends upon the notch depth and beam dimensions, in general the nominal strength increased with notch radius. The fracture surfaces differed between the sample sets (Figures 7.12a, b & c). A 10pA notch resulted in a fracture surface that was very flat, indicating that the crack propagated along the m-plane. The number of striations on the fracture surface increased with notch radius; these may be due to crack branching effects. Field [220] noted that cracks propagating in brittle materials have a longer path before branching for lower failure stresses. Ericson and Schweitz [139] also noted that beams that fail at low strength (i.e. from a large flaw) were smooth, whereas high strength beams were rougher. Thus, the notch radii had an effect on the fracture surfaces.

7.3.2. Varying notch radii – beams in a-plane sapphire parallel to [0001]

Tables 7.10, 7.11, and 7.12 outline the fractured beams notched with 10, 100, 1000pA beam currents, respectively. All load-displacements curves were linear until failure.

Beam	Nominal Strength (GPa)	Notch depth (μm)	α'	K_{fail} (MPa.m$^{1/2}$)
Str – c – 10pA - 1	3.4	0.26	0.06	3.5
Str – c – 10pA - 2	3.6	0.27	0.07	3.7
Str – c – 10pA – 3	3.1	0.32	0.12	3.8
Str – c – 10pA – 4	3.1	0.36	0.11	3.9
Str – c – 10pA – 5	2.9	0.41	0.12	4.0
Str – c – 10pA – 6	2.4	0.49	0.14	3.7

Table 7.10: Properties of microcantilever beams in a-plane sapphire oriented parallel to the [0001] direction, with a 10pA notch

Beam	Nominal Strength (GPa)	Notch depth (μm)	α'	K_{fail} (MPa.m$^{1/2}$)
Str – c – 100pA - 1	2.7	0.55	0.13	4.4
Str – c – 100pA – 2	3.0	0.48	0.15	4.7
Str – c – 100pA – 3	3.6	0.42	0.12	4.9

Table 7.11: Properties of microcantilever beams in a-plane sapphire oriented parallel to the [0001] direction with a notch produced with a beam current of 100pA

Beam	Nominal Strength (GPa)	Notch depth (μm)	α'	K_{fail} (MPa.m$^{1/2}$)
Str – c – 1000pA – 1	2.7	0.79	0.17	5.5
Str – c – 1000pA – 2	4.3	0.31	0.11	6.1
Str – c – 1000pA – 3	6.7	0.22	0.07	6.5

Table 7.12: Properties of microcantilever beams in a-plane sapphire oriented parallel to the $[0001]$ direction with a notch produced with a beam current of 1000pA

As with the samples oriented parallel to $< 1\bar{1}00 >$, there was an increasing stress intensity factor with notch radii. The fracture surfaces (Figure 7.13) were consistently facetted as the crack propagated along planes close to, but not, the c-plane. There was no difference between the fracture surfaces; there was no increase in the extent of bifurcation with notch radii as was seen in the beams parallel to $< 1\bar{1}00 >$.

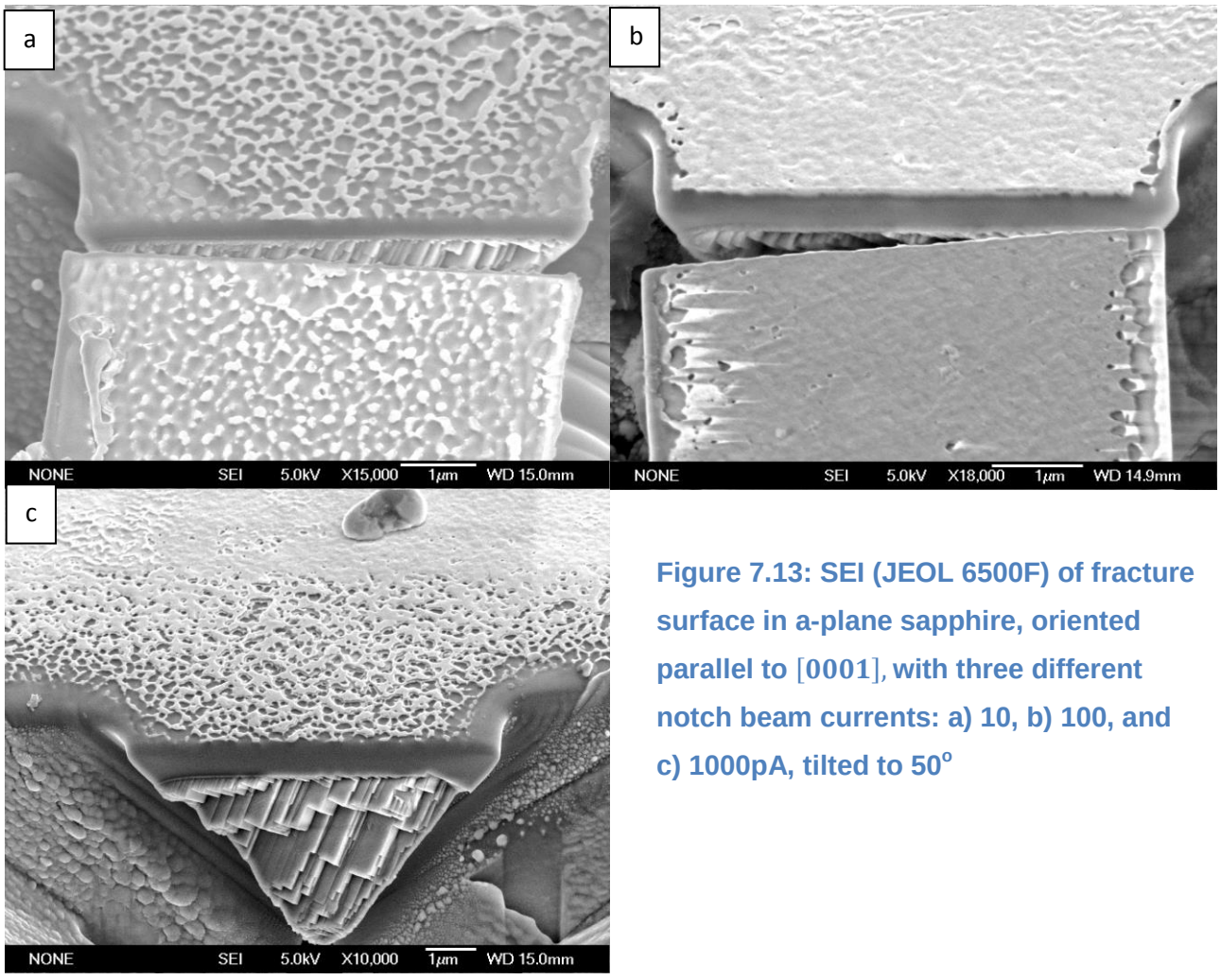


Figure 7.13: SEI (JEOL 6500F) of fracture surface in a-plane sapphire, oriented parallel to $[0001]$, with three different notch beam currents: a) 10, b) 100, and c) 1000pA, tilted to 50°

7.3.3. Effect of notch radius and residual stress on mechanical properties

The measured stress intensity factor at failure was increased due to 1) the residual stress caused by the gallium implantation (as an increased stress was required to propagate the notch tip crack through the compressive region) and 2) the notch bluntness. Two different methods can be used to correct for bluntness: Picard et al [148] and Fett and Munz [149, 150].

Using Picard's [148] method, the correction term for a FIB-milled notch of 15nm is ≈ 1 (this is apparent from inspection of Figure 2.15). Furthermore, the method cannot explain the change in measured stress intensity factor at failure with notch radius; notches of 32 and 76nm also have correction terms of ≈ 1. Hence, the method is inappropriate for FIB-milled notches used in this work.

The method of Fett and Munz [149, 150] was considered instead. To analyse the effects of notch bluntness and residual stress, Equation 7.4 was used (see Appendix 7.1 for detail). The assumption is that there is a sharp notch tip crack of length dα in front of the notch tip. If the notch tip crack is smaller than the implanted region, the stress intensity factor contribution due to the residual stress is assumed to be given as $\sigma_{res}\ \psi\ \sqrt{\pi\ d\alpha}$, where σ_{res} is the residual stress in the implanted region, such that,

$$K = K_{app}\ \tanh\left(2\ \psi\ \sqrt{\frac{d\alpha}{\rho}}\right) + \sigma_{res}\ \psi\ \sqrt{\pi\ d\alpha} \qquad (7.4)$$

K_{app} is the applied stress intensity factor (from Equation 6.25), ψ = 1.12, and ρ is the notch radius. Noting that σ_{res} was (13 +/- 5) GPa (Section 7.2.1.), and using the mean values of K_{app} from Tables 7.7 – 7.12, the corrected stress intensity factor was correlated with dα (using

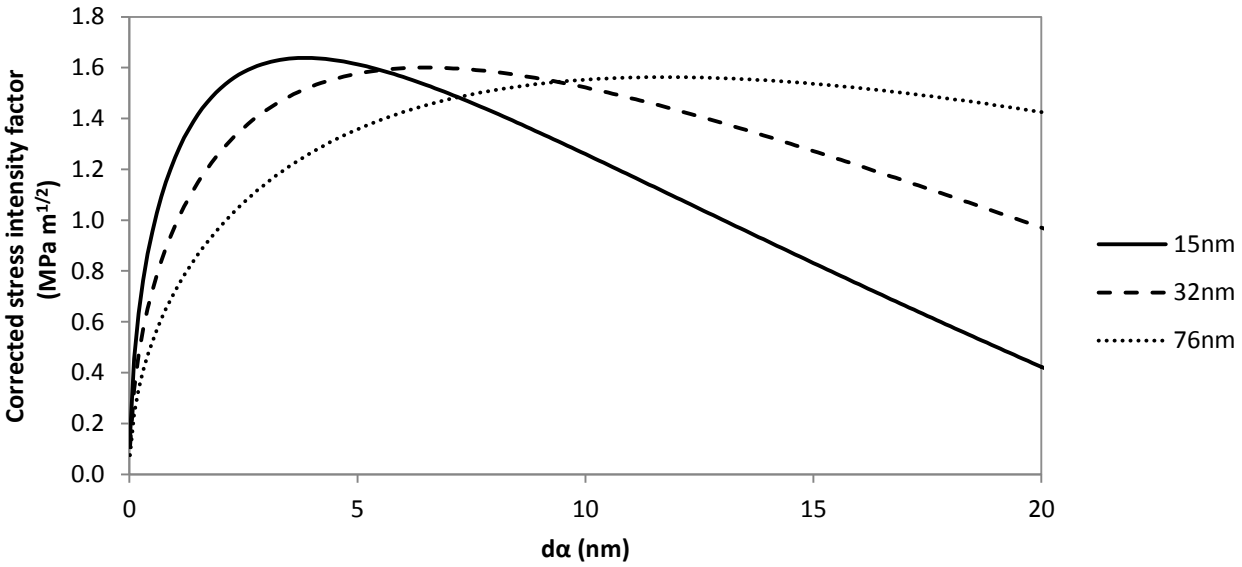


Figure 7.14: Corrected stress intensity factor, using Equation 7.3, for beams oriented parallel to $< 1\bar{1}00 >$ with three different notch radii. The curves used the mean SIFs for each sample set

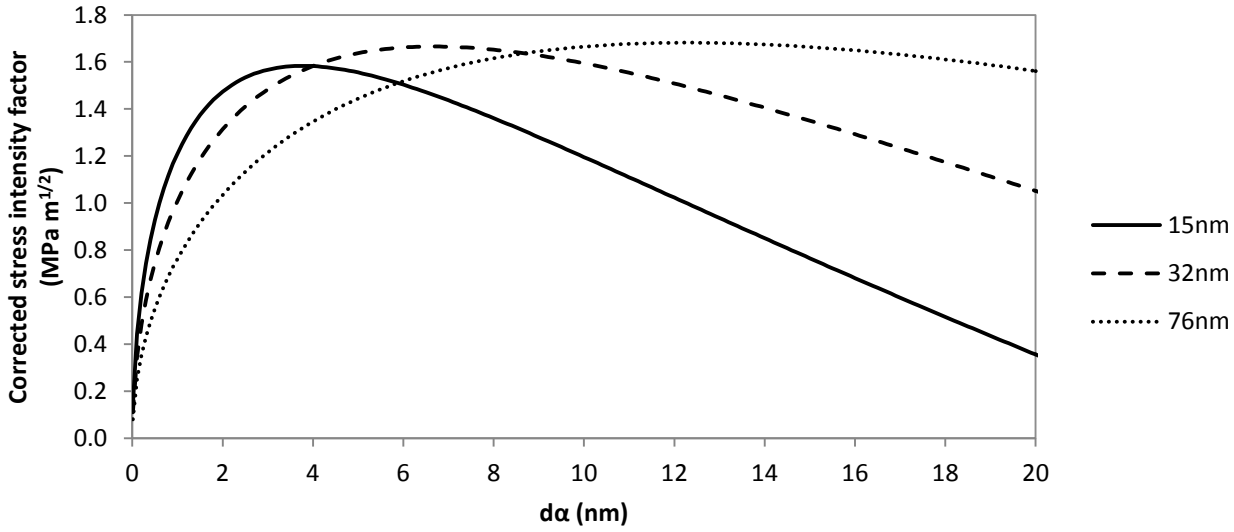


Figure 7.15: Corrected stress intensity factor, using Equation 7.3, for beams oriented parallel to $[0001]$ with three different notch radii. The curves used the mean SIFs for each sample set

Equation 7.4) (Figures 7.14 and 7.15) [1].

[1] The crack length used to determine K_{app} in Equation 7.4 was $\alpha - \frac{\rho}{2}$. The tanh correction (Appendix 7.1) used the Creager and Paris [221] solution for blunt notch which considered the stress intensity factor a distance r in front of a blunt notch; r = 0 was taken ρ/2 behind the notch tip [221]. As in general ρ << α, the effect was small. For 15nm notch radii, the difference in K_{app} between using $\alpha - \frac{\rho}{2}$ and α was 1.3%, but increased up to 6.6% for 76nm notch radii. See Appendix 7.1 for more details.

As the toughness of the material was the same for each sample set (regardless of notch radius), it was assumed that the value of dα could be determined from the three curve intersections: for beams fracturing along the m-plane, dα was (7 +/- 2) nm (standard deviation). For the c-plane, the value was (6 +/- 2) nm. The value of the notch tip crack length was not necessarily expected to be the same for the three radii, but the results suggest that the lengths were of the same order. The physical interpretation for the notch tip crack was discussed in Section 9.1.6.2.. The value of dα was smaller than the implanted region (≈ 20nm), and so the residual stress had a direct effect on the stress intensity factor on this crack.

Using Equation 7.4, the corrections were as follows:

- Stress intensity factor contribution due to the compressive region (using second part of Equation 7.4 with the 6 values of dα): (1.9 +/- 0.3) $MPam^{1/2}$.
- Notch bluntness correction (using first part of Equation 7.4 with the 6 values of dα):
    - (0.89 +/- 0.05) for 15nm radii (10pA)
    - (0.76 +/- 0.07) for 32nm radii (100pA)
    - (0.57 +/- 0.07) for 76nm radii (1000pA)

Using the corrections for residual stress and notch bluntness, the corrected stress intensity factors at failure for the diffusion bonded sapphire were: (0.7 +/- 0.1) & (1.2 +/- 0.1) $MPa.m^{1/2}$ for the boundary and matrix respectively. Beams fracturing on the m-plane (Tables 7.7 – 7.9) and notched parallel to the c-plane (Tables 7.10 – 7.12) had a stress intensity factors at failure of (1.5 +/- 0.2) and (1.5 +/- 0.2) $MPa.m^{1/2}$ respectively.

The stress intensity factors at failure presented from now on are corrected for the residual stress and notch bluntness.

7.4. Moisture assisted sub-critical crack growth

7.4.1. Modelling the crack growth under dynamic loading in Region I

The possible effect of moisture assisted sub-critical (or slow) crack growth on measured properties is discussed in Section 2.6.7. Considering Figure 2.20, it is very probable that the microcantilever beams failed in Region I due to moisture assisted sub-critical crack growth. This means that the measured stress intensity factors at failure should be close to K_{I0} and not K_{Ic} (i.e. the critical stress intensity factor due to fast fracture).

To determine if beams do fail in Region I, the slow crack growth phenomenon under dynamic loading was modelled. By first assuming the relationship between the velocity of the crack growth and the stress intensity factor, the crack length and stress was given as Equation 7.5 (see Appendix 7.2 for derivation).

$$\alpha = \left[{\alpha_0}^{1-\frac{n}{2}} - \left(\left(\frac{\sigma\psi(\pi\alpha_0)^{\frac{1}{2}}}{K_{I0}} \right)^{n+1} - 1 \right) \frac{V_0 K_{I0}(n-2)}{2\dot{\sigma}\pi^{\frac{1}{2}}{\alpha_0}^{\frac{n+1}{2}}(n+1)} \right]^{\frac{1}{1-\frac{n}{2}}} \qquad (7.5)$$

where α is the crack length, α_0 the original flaw size, $\dot{\sigma}$ the loading rate, ψ = 1.12, K_{I0} and V_0 the stress intensity factor and crack tip velocity at the start of Region 1, and $n = \frac{\log V}{\log K}$. Using Equation 7.5, the stress on the sample and the crack length were correlated for a typical test. K_{I0}, V_0, and n were taken from literature data [222].

7.4.2. Using experimental data

The properties of a typical beam were taken: c_0, = 258nm, $\dot{\sigma}$ = 10.7MPa/s. For Region I, K_{I0} = 0.894MPa.m$^{1/2}$, n = 46, and V_0 = 5 x 10^{-7}m/s [222]. Using Equation 7.5, the variation of the theoretical crack length with stress was determined (Figure 7.15).

As the stress increased, the crack did not grow until the stress was around 0.9931GPa. The failure strength was 0.99326GPa, giving a stress intensity factor at failure of 0.894MPam$^{1/2}$. The ratio of this stress intensity factor to K_{I0} was 1.00025.

If the loading rate was increased by a factor of 1000, there was essentially no crack growth until 1.043 GPa. The failure strength of this sample was 1.0485 GPa, giving a stress intensity factor of 0.944 $MPam^{1/2}$. The ratio of this value to K_{I0} was 1.056, suggesting that this sample would also fail early in Region I.

Thus, the microcantilever beams undergo moisture assisted sub-critical crack growth when tested in air. The stress intensity factors at failure are close to K_{I0}, and not K_{Ic}.

7.4.3. Microcantilever Beams submerged in liquids

In order to assess the extent of moisture assisted sub-critical crack growth experimentally, sapphire beams were tested in oil and water to measure the stress intensity factor at failure.

7.4.3.1. Fracturing on m-plane in water

A single sample was produced on the surface of c-plane sapphire notched parallel to the m-plane. This was tested to fracture in water (Section 3.7.1.1.).

Notch depth = 0.31µm

α' = 0.13

K_{fail} = 1.0 $MPa.m^{1/2}$

The load-displacement curve (Figure 7.17) showed a kink at around 180nm, but no subsequent change in the compliance. The most likely cause was that the tip slipped on the surface due to the water.

Three samples were produced on the surface of a-plane sapphire (notched parallel to the m-plane) (Table 7.13). The average stress intensity factor at failure was (0.9 +/- 0.2) $MPa.m^{1/2}$. The mean of the four samples fracturing on the m-plane was (0.9 +/- 0.2) $MPam^{1/2}$.

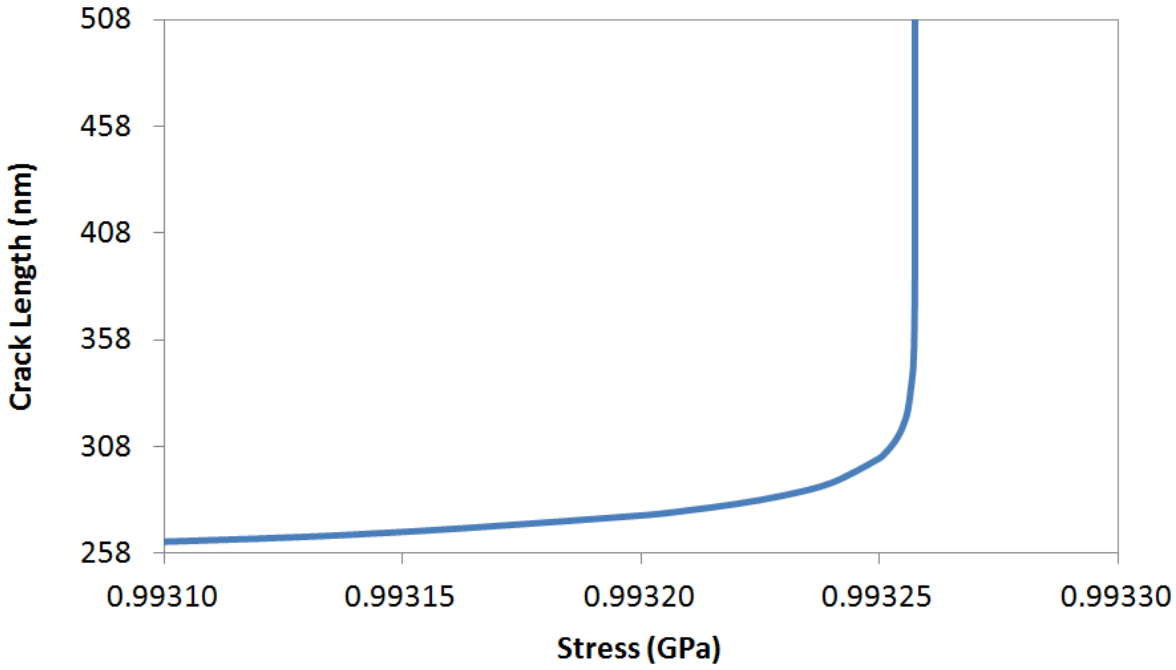


Figure 7.16: Plot of the crack length against stress in Region I using data from a real microcantilever sample

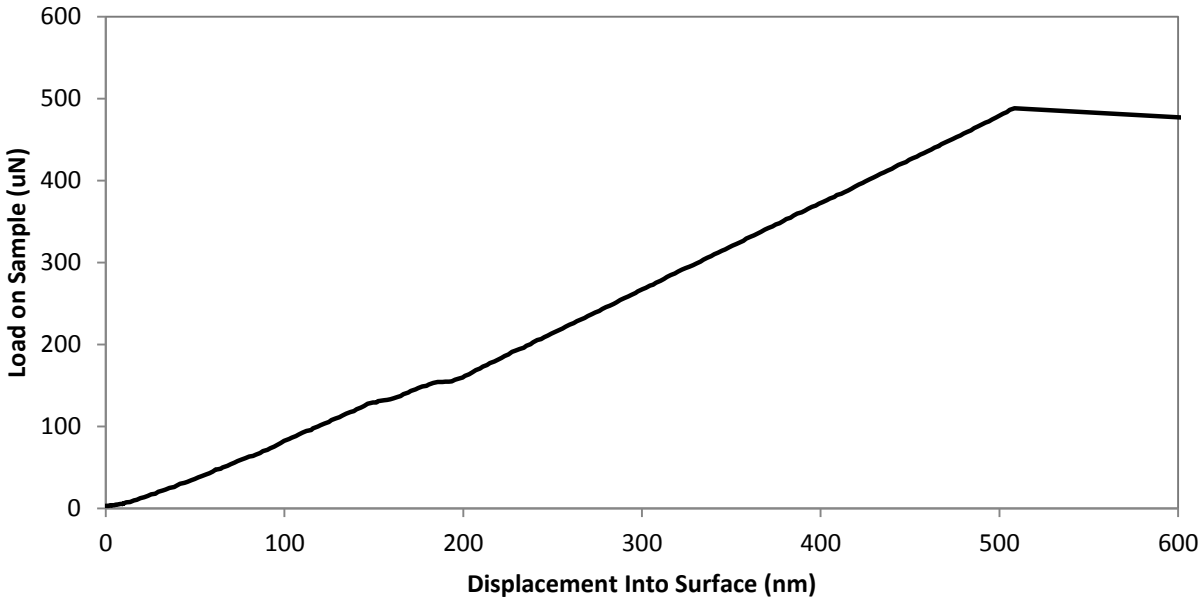


Figure 7.17: Load-displacement curve of beam in c-plane sapphire, oriented parallel to $\langle 11\bar{2}0 \rangle$, submerged in water during testing

Beam	Nominal Strength (GPa)	Notch depth (µm)	α'	K_{I0} (MPa.m$^{1/2}$)
M – water- S1	2.5	0.28	0.14	1.0
M – water- S2	2.5	0.30	0.15	0.7
M – water- S3	2.8	0.30	0.08	0.9

Table 7.13: Mechanical properties of beams notched parallel to the m-plane fractured when submerged in water

7.4.3.2. Fracturing on m-plane in oil

Two beams were fractured along the m-plane when submerged in silicone oil (Table 7.14).

The average stress intensity factor at failure was (3.4 +/- 0.4) MPa.m$^{1/2}$.

Beam	Nominal Strength (GPa)	Notch depth (µm)	α'	K_{Ic} (MPa.m$^{1/2}$)
M – oil - S1	4.8	0.32	0.10	3.2
M – oil - S2	4.9	0.35	0.11	3.6

Table 7.14: Mechanical properties of beams notched parallel to the m-plane fractured when submerged in silicone oil

7.5. Sapphire beams annealed in vacuum

Beams on the surface of diffusion bonded sapphire were notched (straight through) at the boundary and in the sapphire matrix, before annealing in vacuum at 1000^{o}C to anneal away the residual stress. Several samples were broken, and the sample re-annealed at 1100^{o}C. Several samples were broken, the sample annealed to 1200^{o}C, and the remaining samples broken. Hence, the property changes due to each annealing temperature were determined.

The load-displacement curves of beams notched in the sapphire matrix were different to those without annealing. Whilst the compliance was constant for the majority of the loading regime, the compliance increased before failure (Figure 7.18). The beams notched parallel to the boundary did not increase in compliance prior to failure (Figure 7.19).

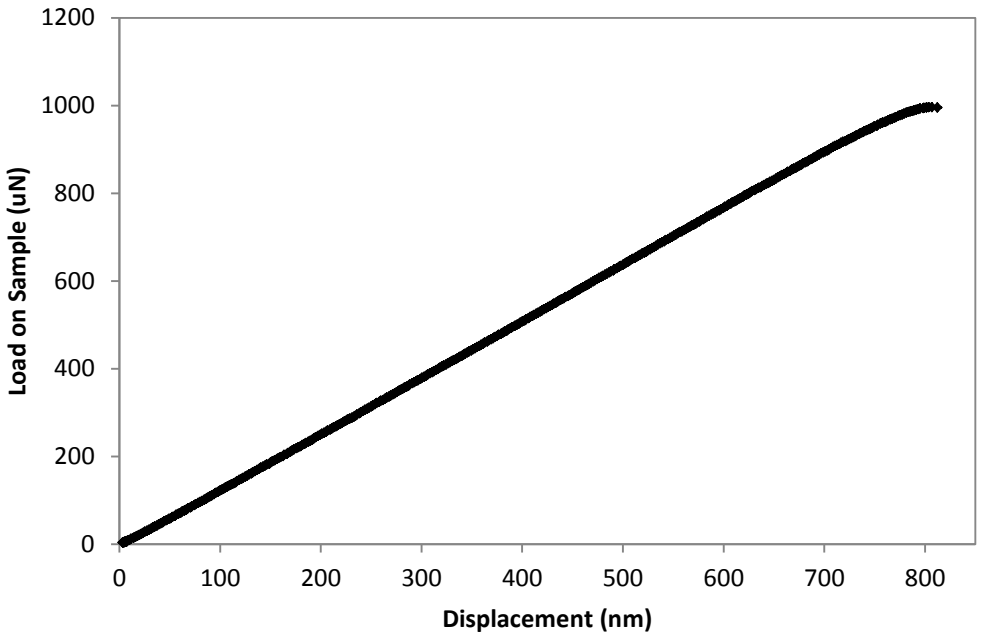


Figure 7.18: Load against displacement curve for a sapphire beam, notched away from the boundary, annealed in vacuum at 1000^{o}C.

There were two possible explanations for this change in compliance: crack extension or plasticity. Figure 7.20 shows the stress intensity factor for an annealed beam, analysed in two different ways:

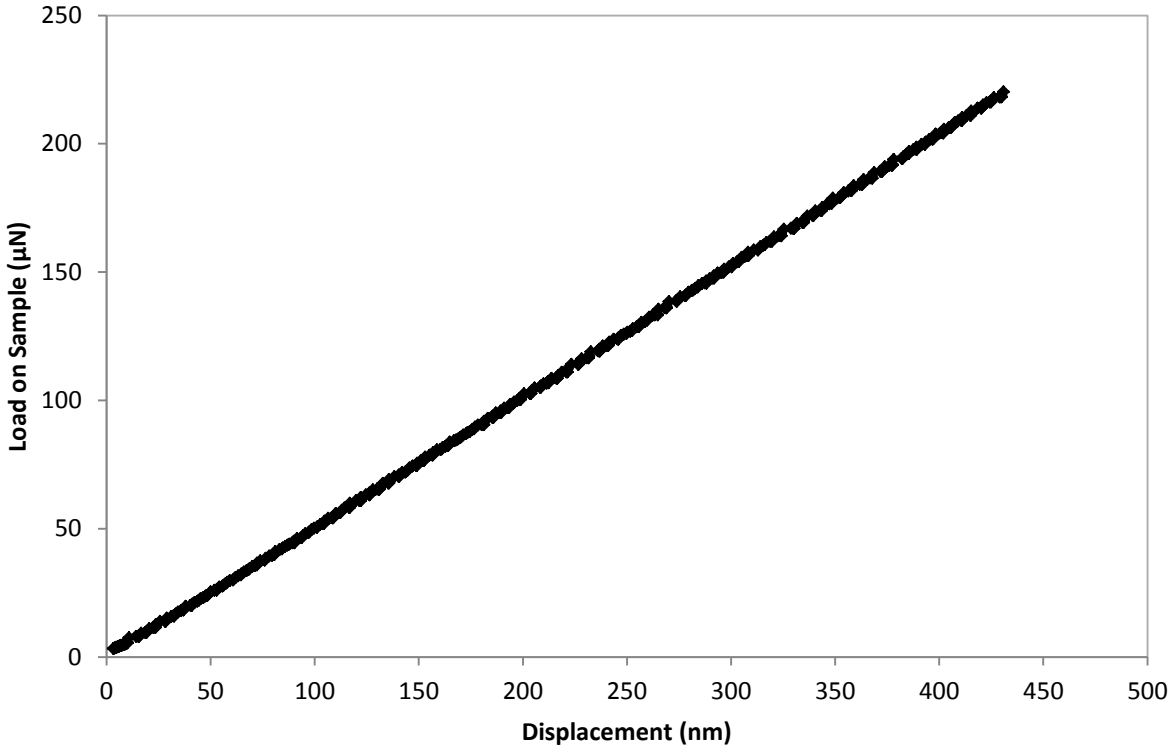


Figure 7.19: Load against displacement curve for a sapphire beam, notched at from the boundary, annealed in vacuum at 1000°C

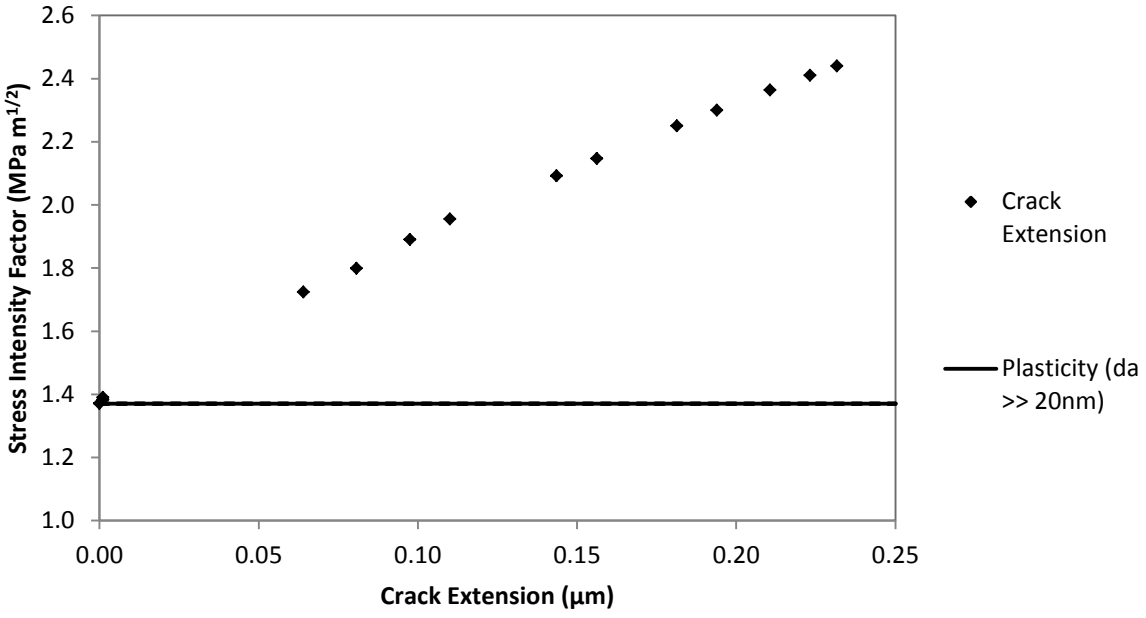


Figure 7.20: Stress intensity factor with crack extension for beam annealed at 1000°C (load-displacement curve in Figure 7.18)

1) Assuming that the compliance change was due to crack extension, the change in α' was found using Equation A7.3.4 (Appendix 7.3) by noting the change in compliance. The crack depth α used in Equation 6.25 (i.e. K_{app}) was taken as the original notch depth + the crack extension. As a result, the applied stress intensity factor increased with crack extension. As the notch tip crack length dα was not known, no tanh weighted function (for notch bluntness) could be used.
2) If the compliance change was due to plasticity, the crack depth α used in Equation 6.25 was taken as the original notch depth. The stress intensity factor at failure was calculated using the load at failure. As the value of dα was not known, no tanh weighted function could be used to correct for the notch bluntness.

These two methods are shown in Figure 7.20. For both curves, the residual stress was assumed to be zero. As discussed in Section 2.6.6., previous work showed that a large proportion, but not all, the residual stress was removed by the annealing. Whilst some

Sample	Max rel change in compliance	Notch depth (μm)	If crack extension			If plasticity
			Increase in crack length (μm)	$K_{I0, st}$ (MPa.m$^{1/2}$)	$K_{I0,fail}$ (MPa.m$^{1/2}$)	$K_{I0,fail}$ (MPa.m$^{1/2}$)
1000 – M - 1	4%	0.22	0.23	1.3	2.4	1.4
1000 – M - 2	5%	0.26	0.11	1.9	2.6	2.0
1000 – M – 3	12%	0.25	0.26	1.5	2.8	1.6
1000 – B – 1	-	0.12	-	-	0.7	0.7

Table 7.15: Mechanical properties of diffusion bonded sapphire beams annealed at 1000°C, notched at M (matrix) and B (boundary).

Sample	Max rel change in compliance	Notch depth (μm)	If crack extension			If plasticity
			Increase in crack length (μm)	$K_{I0,fail}$ (MPa.m$^{1/2}$)	$K_{I0,fail}$ (MPa.m$^{1/2}$)	$K_{I0,fail}$ (MPa.m$^{1/2}$)
1100 – M - 1	3%	0.20	0.21	0.9	1.9	1.2
1100 – M - 2	3%	0.24	0.16	1.9	2.7	2.1
1100 – M – 3	6%	0.26	0.18	1.9	2.6	1.9
1100 – B – 1	-	0.25	-	-	1.0	1.0

Table 7.16: Mechanical properties of diffusion bonded sapphire beams annealed at 1100°C, notched at M (matrix) and B (boundary).

Sample	Max rel change in compliance	Notch depth (μm)	If crack extension			If plasticity
			Increase in crack length (μm)	$K_{I0,fail}$ (MPa.m$^{1/2}$)	$K_{I0,fail}$ (MPa.m$^{1/2}$)	$K_{I0,fail}$ (MPa.m$^{1/2}$)
1200 – M - 1	2%	0.20	0.12	1.8	2.7	2.1
1200 – M - 2	4%	0.23	0.17	2.2	3.1	2.2
1200 – M – 3	7%	0.20	0.13	1.3	2.3	1.4
1200 – B – 1	-	0.19	-	-	0.9	0.9

Table 7.17: Mechanical properties of diffusion bonded sapphire beams annealed at 1200°C, notched at M (matrix) and B (boundary).

residual stress may still have been present, $\sigma_{res} \approx 0$ is a reasonable approximation.

Tables 7.15 – 7.17 show the data for the annealed beams, with details assuming both crack extension and plasticity. In lieu of a measure of dα after annealing (it would be erroneous to assume it was the same as before annealing), no correction for notch bluntness was used for beams notched either at the boundary or away from it.

If the compliance change was due to crack extension, the stress intensity factors at the start of crack extension & at failure (away from the boundary) were, respectively:

1000°C anneal: (1.6 +/- 0.2) and (2.6 +/- 0.3) MPam$^{1/2}$.

1100°C anneal: (1.6 +/- 0.4) and (2.4 +/- 0.4) MPam$^{1/2}$

1200°C anneal: (1.8 +/- 0.3) and (2.7 +/- 0.4) MPam$^{1/2}$.

If the compliance change was due to plasticity, the stress intensity factors at failure were:

1000°C anneal: (1.7 +/- 0.2) MPam$^{1/2}$.

1100°C anneal: (1.7 +/- 0.3) MPam$^{1/2}$

1200°C anneal: (1.9 +/- 0.3) MPam$^{1/2}$.

Most of the fracture surfaces were similar to those of unannealed beams (Figure 7.21). Several, but not all, beams showed a region (approximately 0.25μm) underneath the notch (Figure 7.22). This corresponded fairly well with the estimated crack extension (Table 7.15). All three beams annealed at 1000°C showed this but none of the beams annealed at higher

temperatures did. It was possible that the whole depth was the FIB notch, but the depth was far greater than would be expected given the FIB conditions (and was measured using TEM, Figure 4.50, and in SEM, Figure 8.24).

The cause of the compliance change is considered further in Section 9.1.

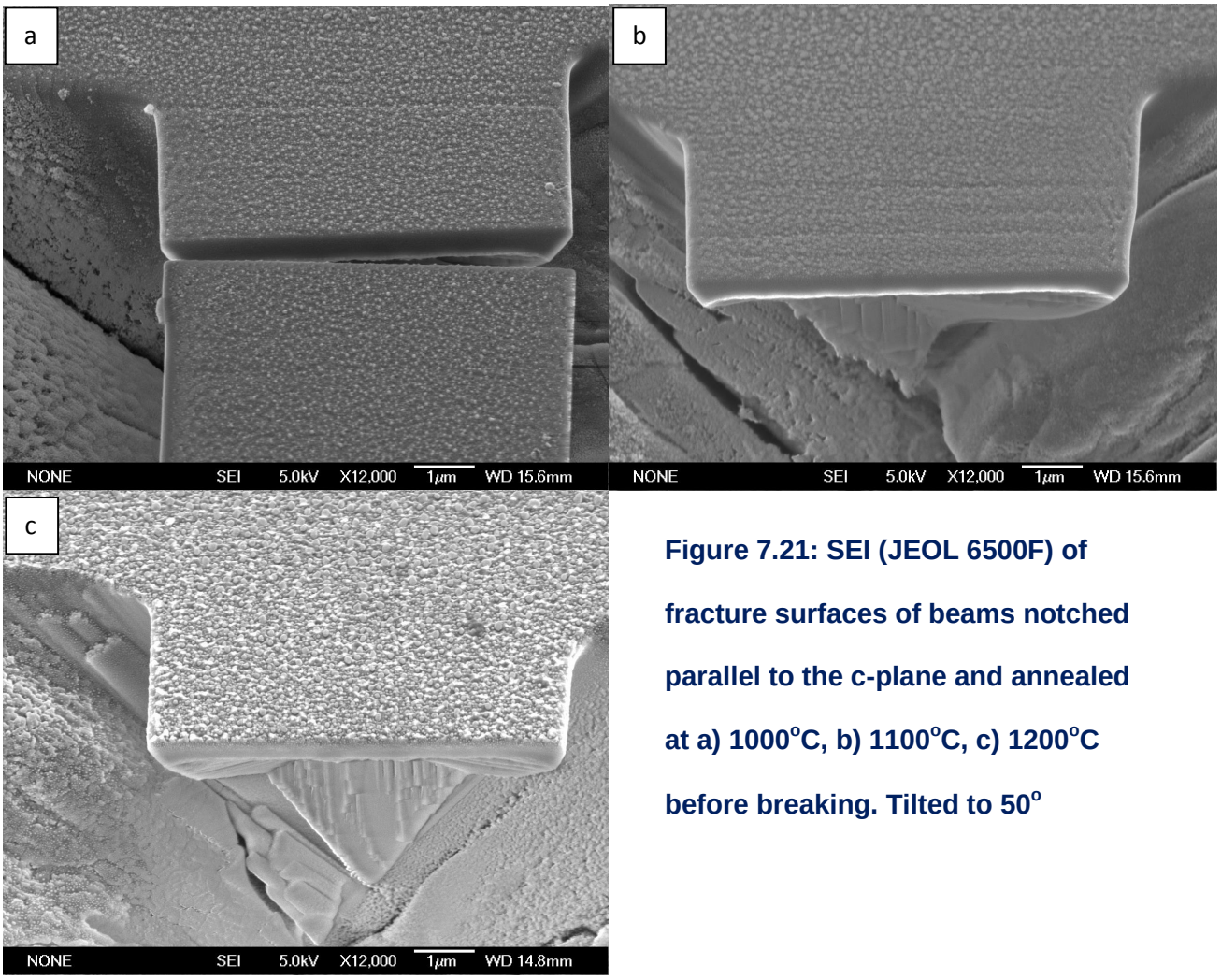


Figure 7.21: SEI (JEOL 6500F) of fracture surfaces of beams notched parallel to the c-plane and annealed at a) 1000^{o}C, b) 1100^{o}C, c) 1200^{o}C before breaking. Tilted to 50^{o}

The Young's modulus was calculated by correcting for 1) displacements in the fixed end (Appendix 3.2) and 2) the compliance change due to the notch (Appendix 8.1). Hence, the Young's modulus of 1000, 1100, and 1200^{o}C annealed beams was (503 +/- 62), (449 +/- 43), and (468 +/- 40) GPa respectively.

The stress intensity factor for beams notched at the boundary was (0.9 +/- 0.2) $MPam^{1/2}$ (averaging over the three beams, assuming the effect of the temperature was the same for each).

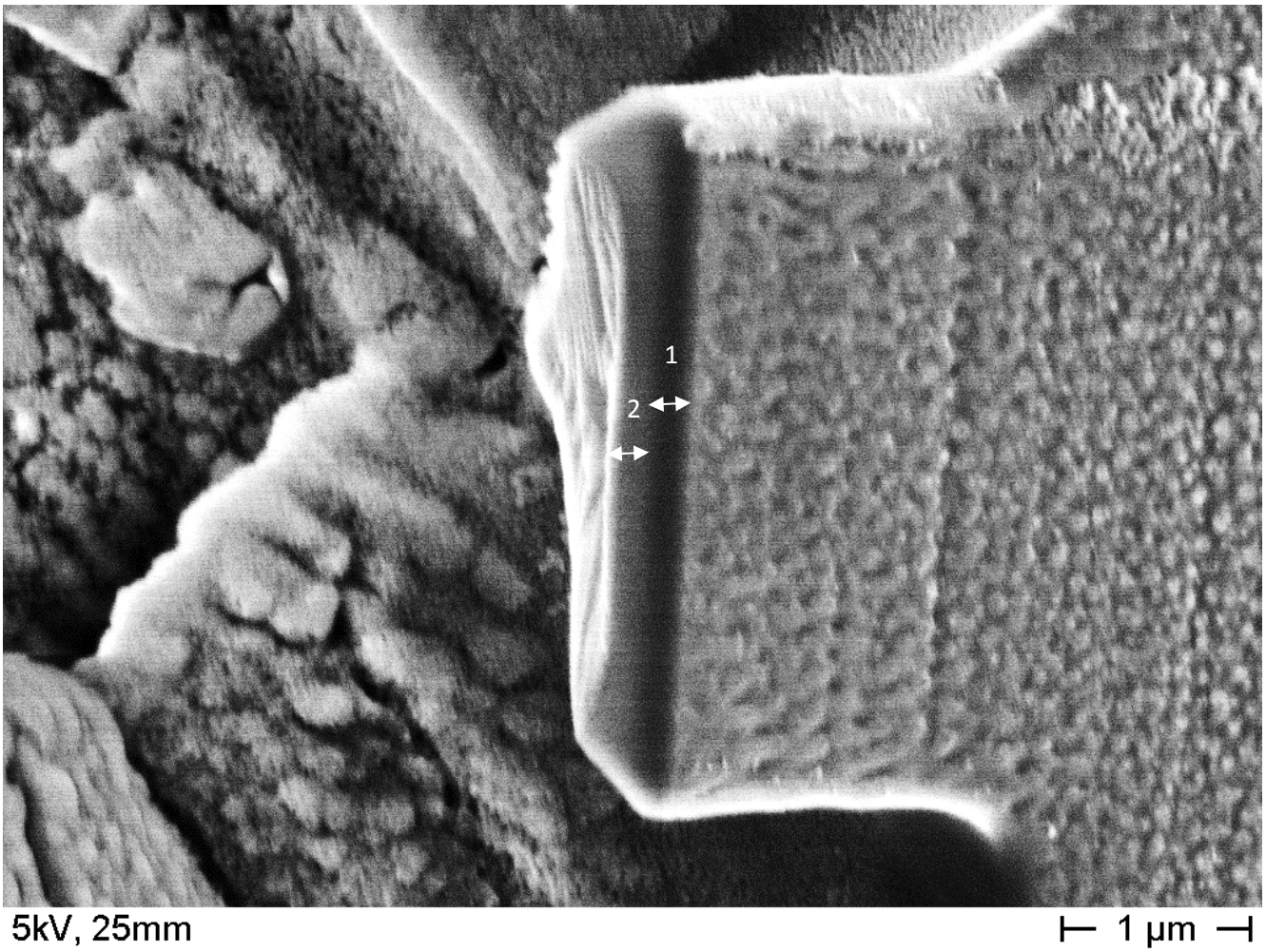


Figure 7.22: SEI (JEOL 840F) of fracture surface of annealed diffusion bonded sapphire beam "1000 – M – 2", tilted to 50°. There was a contrast difference on the notch suggesting that "1" was the FIB notch and "2" was due to crack extension during loading.

7.6. Microcantilever beam testing – Summary

Whilst much of the discussion on the validity of the microcantilever beam testing is presented in Section 9.1, the use of the technique on engineering ceramics (Chapter 8) depends upon the results in this chapter. As such, the key results are summarised here.

1) Un-notched beams failed at the diffusion bonded boundary, and had a failure strength of (5.2 +/- 0.1) GPa. The Young's modulus, after correction for flexure in the fixed end, was (465 +/- 25) GPa which corresponds well to the expected modulus using the elastic constants from [215].
2) Qualitatively, the stress intensity factor at failure was higher for beams notched away from the boundary than notched at the diffusion bonded boundary. Hence, the technique was able to differentiate between fracture in high and low toughness materials.
3) The residual stress of the gallium implanted region was measured (using optical fluorescence microscopy) to be (13 +/- 5) GPa. Nanodiffraction gave an incorrect value for the residual stress, presumably due to the increase in the lattice parameters due to inclusion of gallium into the unit cell. Noting that the notch tip crack length $d\alpha$ was (7 +/- 2) nm, the stress intensity factor correction term was (1.9 +/- 0.3) $MPam^{1/2}$.
4) The uncorrected stress intensity factor increased with notch radius. The correction term for a notch radius of 15nm (i.e. sharpest possible using FEI FIB200) was (0.89 +/- 0.05).
5) Beams tested in air underwent moisture assisted sub-critical crack growth. Hence, the stress intensity factor was close to K_{I0}.
6) After annealing, there was a compliance change before failure due either to crack extension or plasticity. Several factors were not known: $d\alpha$, the magnitude of the residual stress, the reason for the compliance change, the structure of the material after annealing (i.e. solid solution, gallium interstitials). In lieu of this information, beams in the rest of the project were not annealed.

Whilst various corrections are required, the microcantilever beam testing can be used to determine the toughness of different ceramics. This was the focus of Chapter 8. The stress intensity factor at failure was referred herein as K_{I0} due to the failure under moisture assisted sub-critical crack growth.

Chapter 8 Mechanical properties of Microcantilever Beams in various Ceramics

Microcantilever beams were produced on the surface of different single crystal and polycrystalline ceramics (Section 3.7). Using the beam dimensions, the load-displacement curve and the measurement of the notch depth after fracture, the applied stress intensity factor at failure was calculated (Equation 6.25), and corrected for the notch bluntness and residual stress at the notch tip (Equation 7.4). Due to the degradation of the FIB aperture with time, the notch radius was periodically measured.

The errors presented alongside the mean value include contributions from the standard error, error in notch bluntness factor, and error in correction for residual stress.

For the sapphire and alumina beams, two key assumptions were made:

1) Residual stress was (13 +/- 5) GPa for beams notched in single crystals and at grains boundaries; the stress intensity factor contribution was (1.9 +/- 0.3) $MPam^{1/2}$.
2) The notch tip crack length was (7 +/- 2) nm and was a characteristic of the aluminium oxide material, and could be used for beams notch in single crystals and at grain boundaries.
3) As the beams failed in air (50% RH) due to moisture assisted sub-critical crack growth, the stress intensity factors at failure are termed "K_{I0}".

These assumptions are considered further in Section 9.1.

8.1. Single crystal sapphire

8.1.1. Single crystal sapphire – Fracturing on the a-plane

Two pieces of sapphire, m- and c-plane (Section 3.1.4.), were used to produce beams parallel to the $\langle 11\bar{2}0 \rangle$ direction.

Beam	Nominal Strength (GPa)	Notch depth (μm)	α'	K_{I0} (MPa.m$^{1/2}$)
c-plane – A - 1	3.1	0.36	0.13	1.6
c-plane – A - 2	3.3	0.29	0.10	1.4

Table 8.1: Properties of microcantilever beams in c-plane sapphire oriented parallel to $\langle 11\bar{2}0 \rangle$ direction

Beam	Nominal Strength (GPa)	Notch depth / Width (μm)	α'	K_{I0} (MPa.m$^{1/2}$)
m-plane – A - S1	4.6	0.16	0.07	1.4
m-plane – A – S2	5.1	0.16	0.05	1.7
m-plane – A – S3	6.0	0.11	0.03	1.5
m-plane – A – S4	3.4	0.23	0.06	1.0

Beam	α/b	b/w	α'	M	K_{I0} (MPa.m$^{1/2}$)
m-plane – A - F1	0.39	0.10	0.03	0.86	1.7
m-plane – A – F2	0.60	0.09	0.05	0.75	1.1

Table 8.2: Properties of microcantilever beams in m-plane sapphire oriented parallel to $\langle 11\bar{2}0 \rangle$ direction. M is calculated using Equation A6.1.1. α' = α/h where α is the notch depth and h the height of the beam. S = straight, F = flaw.

The load-displacement curves were linear until failure for both straight through notched and controlled flaw beams (Figure 8.1). As the crack propagated along the a-plane, the fracture surfaces (Figure 8.1) were flat. However, there was some variation between the surfaces; the controlled flaw had a fracture surface noticeably less smooth than that for the straight through notched samples. Underneath the flaw, there was a smooth region, followed by increasing roughness below and to the side of this. These features were probably due to the acceleration of the crack through the sample, in a similar way to the mirror, mist, and hackle seen in macroscopic samples [5, 220].

The stress intensity factor at failure for the 8 beams fracturing on the a-plane was (1.4 +/- 0.2) MPam$^{1/2}$.

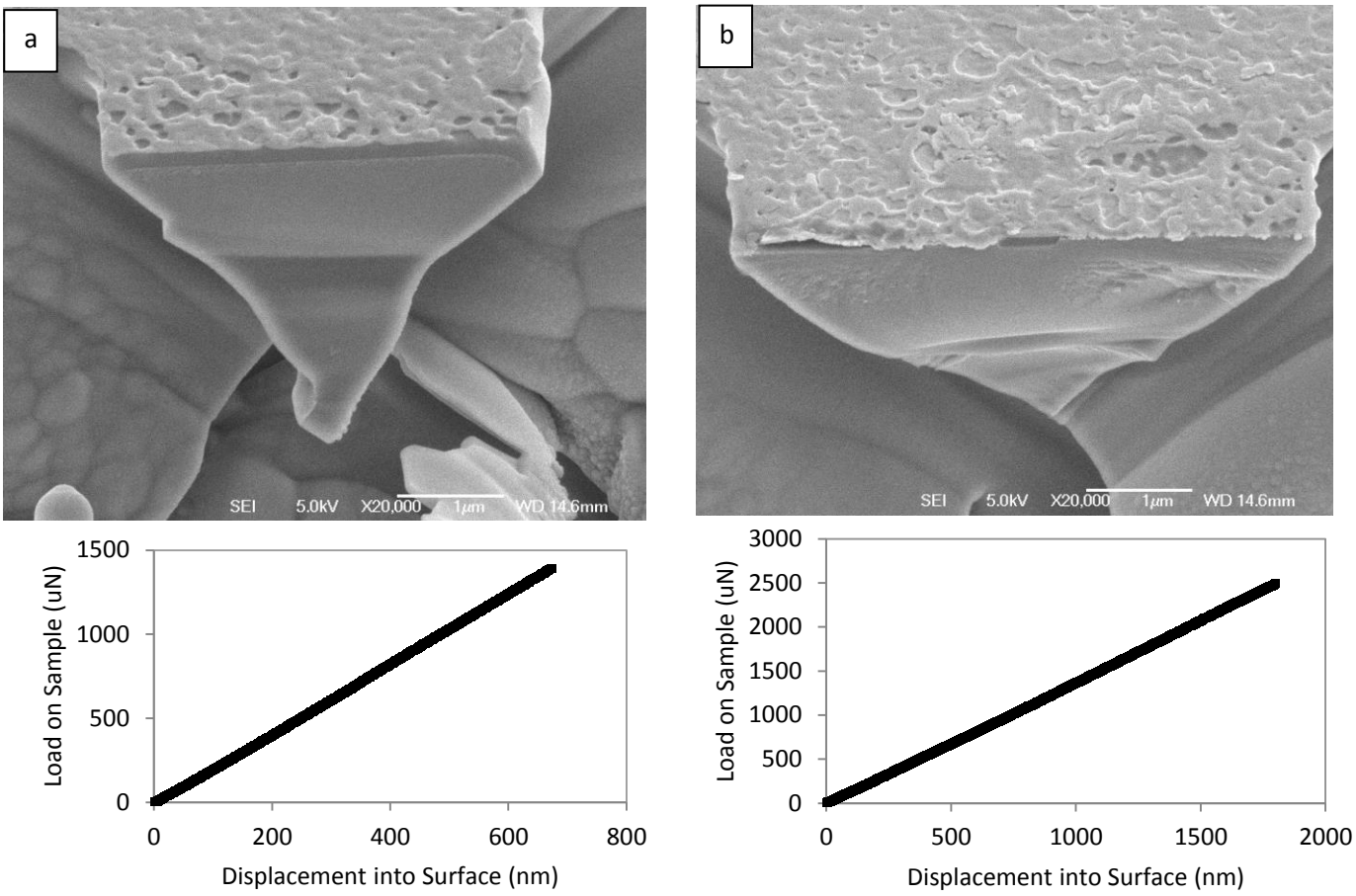


Figure 8.1: Fracture surfaces and load-displacement curves of beams in m-plane sapphire, oriented parallel to $\langle 11\bar{2}0 \rangle$, with a) straight through notch and b) controlled flaw, tilted to 50°

8.1.2. Single crystal sapphire – Fracturing on the m-plane

Results of microcantilever beams fracturing on the m-plane (made on the surface of a-plane sapphire) are presented in Tables 7.7 – 7.9 (and Figure 7.9). After correcting for the notch bluntness and residual stress, the mean stress intensity factor was (1.5 +/- 0.2) MPa.m$^{1/2}$.

Beams were produced in c-plane sapphire which fractured along the m-plane (Table 8.3).

Beam	Nominal Strength (GPa)	Notch depth (μm)	α'	K_{I0} (MPa.m$^{1/2}$)
c-plane – M – 1	3.5	0.28	0.12	1.7
c-plane – M – 2	3.4	0.27	0.15	1.6
c-plane – M - 3	2.3	0.44	0.11	0.9

Table 8.3: Properties of microcantilever beams in c-plane sapphire oriented parallel to $\langle 1\bar{1}00 \rangle$ direction

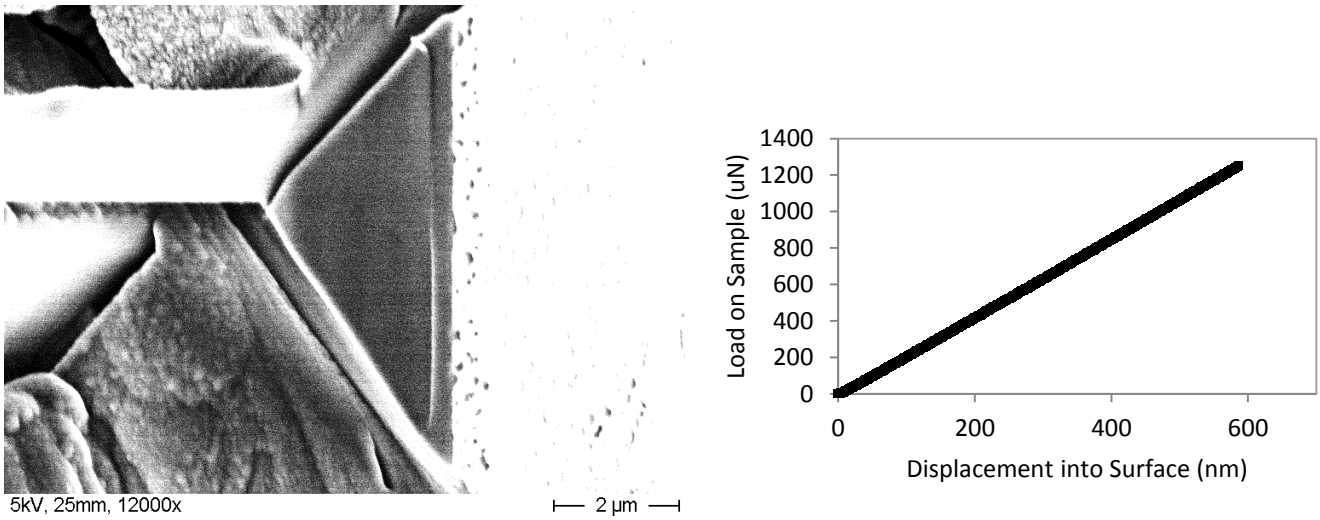


Figure 8.2: SEI (JEOL 840F) of fracture surface (tilted 50°) and b) load-displacement curve of beam in c-plane sapphire, oriented parallel to $\langle \bar{1}100 \rangle$.

The load-displacement curves were linear until failure and the fracture surfaces were flat (Figure 8.2). The mean value of the stress intensity factor at failure for the 14 beams fractured on the m-plane (Tables 7.7 – 7.9, 8.3) was (1.5 +/- 0.2) MPam$^{1/2}$.

8.1.3. Single crystal sapphire – Fracturing parallel to the c-plane

Results for the microcantilever beams produced on the a-plane sapphire that were notched parallel to the c-plane are presented in Tables 7.10 – 7.12 (and Figure 7.11). After correction, the 12 beams had mean stress intensity factor at failure of (1.5 +/- 0.2) MPam$^{1/2}$.

Three beams were produced on the surface of m-plane sapphire, notched parallel to the c-plane (Table 8.4).

Beam	Nominal Strength (GPa)	Notch depth (µm)	α'	K_{I0} (MPa.m$^{1/2}$)
m-plane – C – S1	4.4	0.16	0.05	1.2
m-plane – C – S2	3.9	0.23	0.07	1.5

Beam	α/b	b/w	α'	M	K_{I0} (MPa.m$^{1/2}$)
m-plane – C – F1	0.61	0.15	0.08	0.71	2.0

Table 8.4: Properties of microcantilever beams in m-plane sapphire oriented parallel to $[0001]$ direction. M is calculated using Equation A61.1.

The mean stress intensity factor of all beams notched parallel to the c-plane was (1.5 +/- 0.2) $MPam^{1/2}$.

8.1.4. Single crystal sapphire – Fracturing away from low index planes

Whilst notching parallel to the a- and m-planes yielded fracture surfaces that showed that cracks propagated along the specific plane of interest, it was interesting to measure the stress intensity factors for samples whose notches were not along specific planes. Comparison of the toughnesses helped to clarify whether the aforementioned results are genuinely for a- and m-planes.

Two beams were produced 30^o away & two beams 60^o from $[0001]$ (Table 8.5).

Beam	Nominal Strength (GPa)	Notch depth (μm)	α'	K_{I0} ($MPa.m^{1/2}$)
m-plane – 30 – S1	3.7	0.28	0.10	1.8
m-plane – 30 – S1	4.2	0.21	0.06	1.6
m-plane – 60 – S1	4.0	0.18	0.05	1.5
m-plane – 60 – S2	3.7	0.21	0.05	1.6

Table 8.5: Properties of microcantilever beams in m-plane sapphire oriented 30^o & 60^o from the $[0001]$ direction

The fracture surfaces for beams orientated 60^o $[0001]$ were facetted (Figure 8.3b) as the beam propagated along many planes. The mean stress intensity factor was (1.6 +/- 0.2) $MPam^{1/2}$.

Fracture surface for beams orientated 30^o $[0001]$ were smooth, suggesting that the crack propagated along a single low-index plane. Several beams were excluded as the crack nucleated at the edge of the beam and the crack propagated on a particular plane close to, but not parallel with, the notch (Figure 8.3a). The mean stress intensity factor of those that did fracture suitably at the notch was (1.7 +/- 0.3) $MPam^{1/2}$.

Hence, whilst the notch often nucleated a crack, the properties of the material (such as which planes were favourable to propagate along) often dominated.

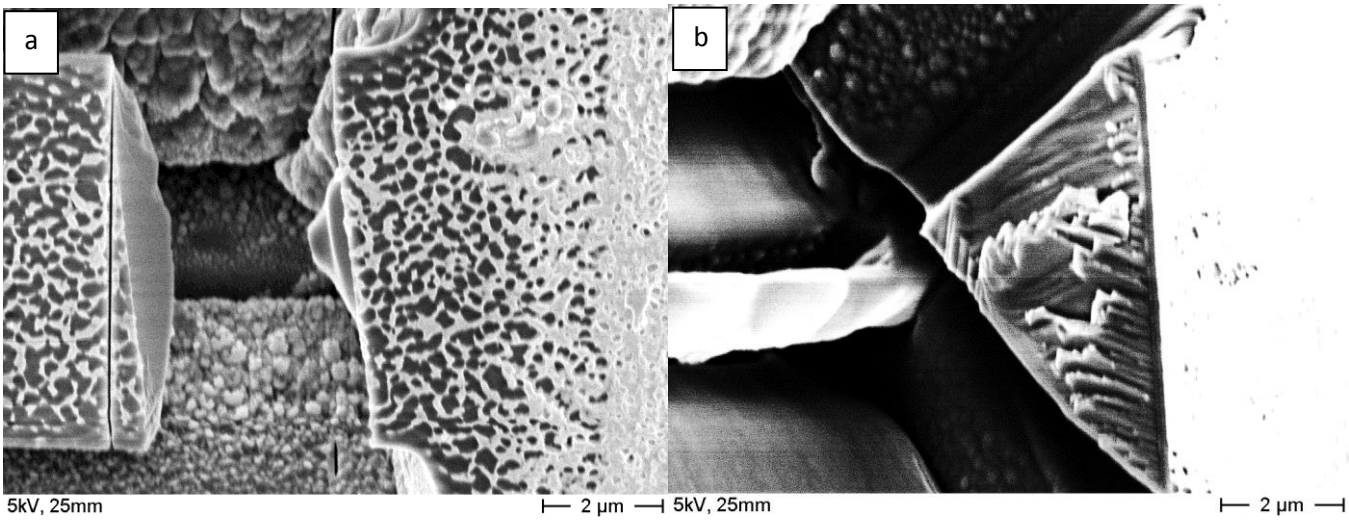


Figure 8.3: SEI (JEOL 840F) of fracture surfaces of beams in m-plane sapphire: a) orientated 30° to [0001] where the crack did not nucleate at the base of the notch, b) oriented 60° from [0001], with a facettered fracture surface (titled 50°).

8.2. Microcantilever beams in undoped polycrystalline AES-11C alumina

Microcantilever beams in polycrystalline AES-11C alumina were produced. Both controlled flaws and straight through notches were used, depending on the shape and form of the grain boundaries near the fixed end of the beam.

8.2.1. Strength

Twenty one un-notched beams were produced on the surface of polycrystalline AES-11C.

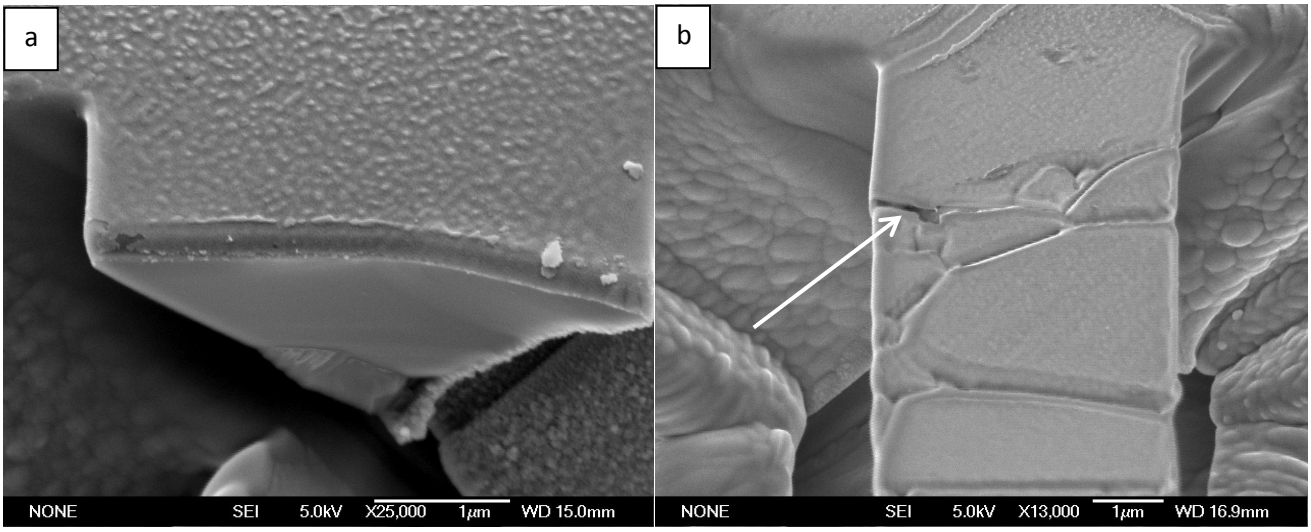


Figure 8.4: SEI (JEOL 6500F) of fracture surfaces of microcantilever beams (tilted to 50°) of a) Strength 16 and b) Strength 17 from Table 8.7

Fracture strength, modulus (corrected for flexure in fixed end using data in Appendix 3.2), the cause of failure & crack propagation route were considered (Table 8.6).

Beam	Young's Modulus (GPa)	Failure strength (GPa)	Failure origin
Strength 1	431	3.1	GB, Inter
Strength 2	413	4.0	GB, Inter
Strength 3	475	3.7	GB, Inter
Strength 4	506	3.1	GB, Inter
Strength 5	433	2.4	Flaw, Trans
Strength 6	430	4.1	GB, Inter
Strength 7	471	1.5	Flaw, Inter
Strength 8	466	4.2	GB, Trans
Strength 9	505	3.9	GB, Inter
Strength 10	418	3.5	GB, Inter
Strength 11	411	1.9	Flaw, Trans
Strength 12	423	4.3	GB, Inter
Strength 13	396	4.2	GB, Inter
Strength 14	478	2.2	Flaw, Trans
Strength 15	454	4.8	GB, Inter
Strength 16	404	5.1	GB, Inter
Strength 17	411	1.5	Flaw, Inter
Strength 18	381	3.9	GB, Inter
Strength 19	471	2.8	GB, Inter
Strength 20	454	3.1	GB, Inter
Strength 21	442	2.7	GB, Inter

Table 8.6: Mechanical properties of the microcantilever beams in polycrystalline AES-11C alumina. GB: failed at a thermal groove at a grain boundary, Flaw: failed at a flaw Inter/Trans: crack propagated intergranularly/transgranularly.

The mean Young's modulus and standard error of the microcantilever beams, after correction, was (447 +/- 38) GPa.

The majority of the 21 beams failed intergranularly with the failure origin appearing to be the thermal groove at the grain boundary (Figure 8.4a). Several failed from obvious flaws (arrow, Figure 8.4b). Weibull plots were produced for the strength measurements (Figure 8.5). The Weibull modulus for all data (21 samples) was 3.3; excluding samples that failed from flaws, this increased to 5.5 (for 16 samples).

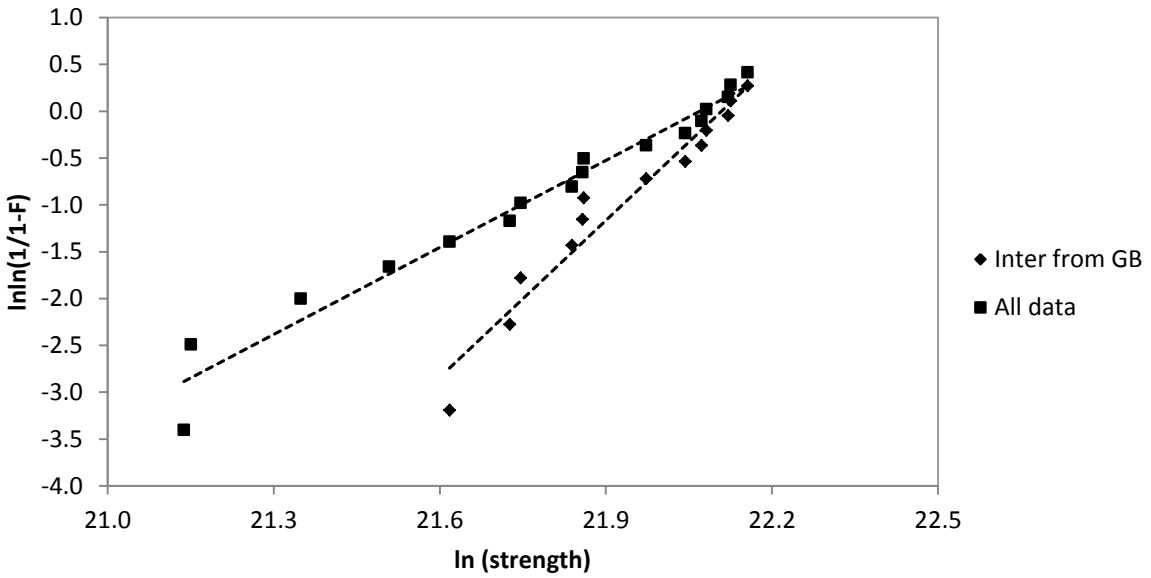


Figure 8.5: Weibull plots for microcantilever beams in AES11-C alumina: All 16 data points, and only including those failed from grain boundaries and propagated intergranularly

8.2.2. Toughness of grains

Straight through notches (10pA) were produced in five alumina grains (i.e. away from boundaries) to differentiate between the boundary and grain toughness in the material.

Beam	Nominal Strength (GPa)	Notch depth (μm)	α'	K_{I0} (MPa $m^{1/2}$)
AES-11C – G1	3.1	0.38	0.14	2.0
AES-11C – G2	2.4	0.45	0.14	1.2
AES-11C – G3	2.5	0.32	0.18	1.2
AES-11C – G4	3.2	0.31	0.11	1.5
AES-11C – G5	4.4	0.22	0.08	1.8

Table 8.7: Mechanical properties of microcantilever beams notched in AES-11C alumina grains

The average stress intensity factor at failure was (1.5 +/- 0.3) MPa $m^{1/2}$.

8.2.3. Toughness of grain boundaries using straight through notches

Although many of the grain boundaries in AES-11C were unsuitable to have a straight notch imparted upon them (due to the curvature of the grain boundary on the surface), several grain boundaries could accommodate such a notch (Figure 8.7). Three were produced at acceptable grain boundaries (Table 8.8).

Beam	Nominal Strength (GPa)	Notch depth (μm)	α'	$K_{I0, gb}$ (MPa.m$^{1/2}$)
AES-11C – GB1	2.0	0.44	0.16	0.8
AES-11C – GB2	1.9	0.37	0.20	0.6
AES-11C – GB3	3.2	0.20	0.06	0.7

Table 8.8: Results from the AES11-C microcantilever beams notched at the grain boundaries

The average stress intensity factor at failure of the grain boundary, $K_{I0, gb}$, was (0.7 +/- 0.1) MPa m$^{1/2}$.

As only large (and mostly abnormal) grains have a straight enough boundary for a straight through notch, the resultant grain boundary toughnesses may be biased towards those grain boundary structures / complexions related to such grain boundaries (Section 2.3).

Unlike the notches produced in the grain or in the single crystal, some notches were not parallel and of a uniform depth (Figure 8.6b). This could be due to certain grain boundaries being milled at a faster rate than others. In order to determine the stress intensity factor for this notched beam, the highest measured notch depth was taken. After the crack has been initiated underneath the notch, the crack propagated intergranularly; the large flat area (indicated by the arrow in Figure 8.6b) was likely to be the grain boundary of the large grain at the fixed end of the beam.

8.2.4. Toughness of grain boundaries using controlled flaws

Microcantilever beams were produced with controlled flaws at the grain boundaries (Table 8.9).

Beam	α/b	b/w	α'	M	$K_{I0, gb}$ (MPa.m$^{1/2}$)
AES-11C – GB1	0.48	0.75	0.22	0.78	1.2
AES-11C – GB2	0.44	0.22	0.14	0.73	0.5
AES-11C – GB3	0.62	0.22	0.11	0.68	0.6
AES-11C – GB4	0.35	0.45	0.13	0.80	0.6

Table 8.9: Results from the AES-11C microcantilever beams notched at the grain boundaries. M is calculated using Equation A6.1.1.

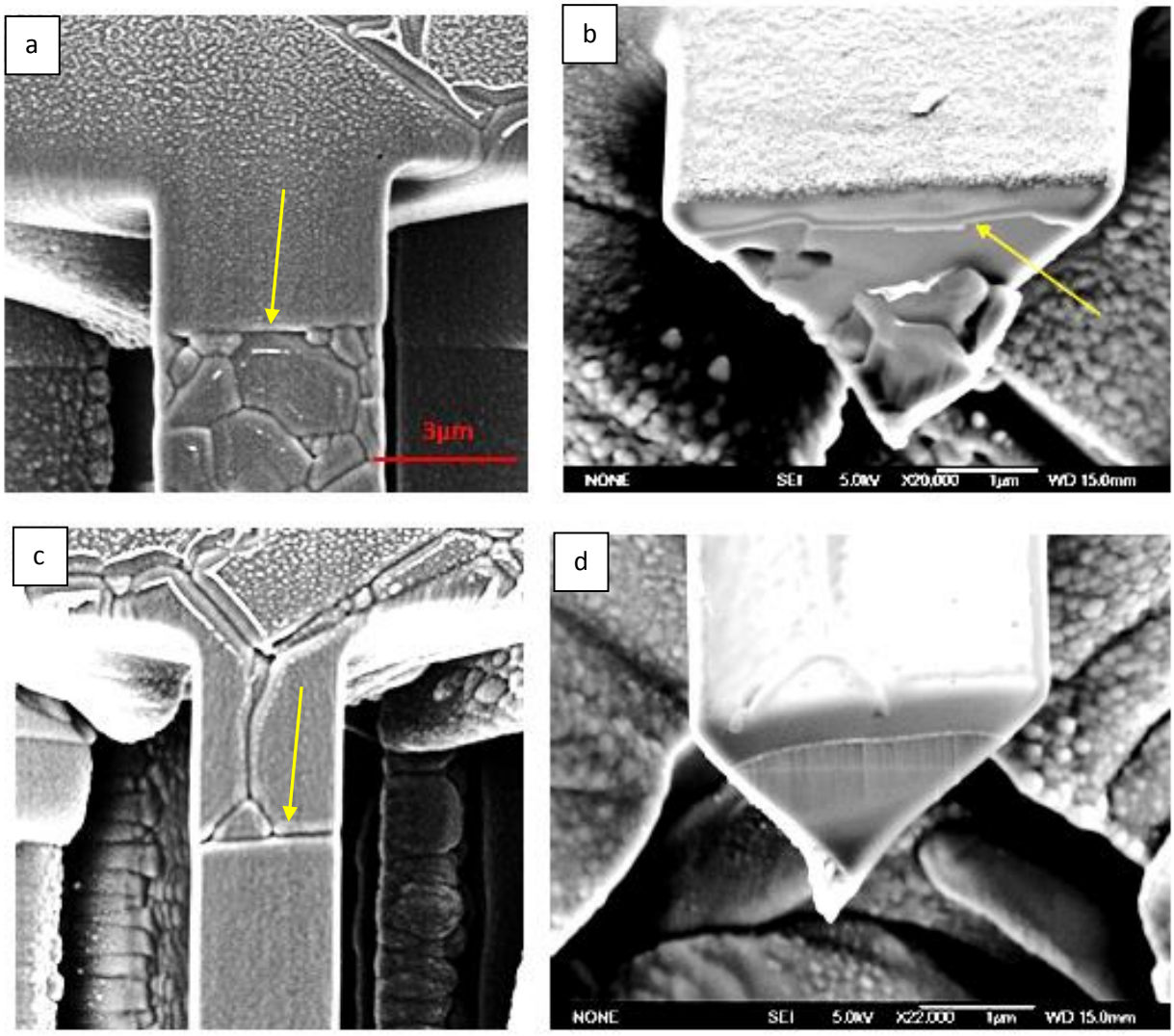


Figure 8.6: SEI (JEOL 6500F) of two beams fractured from straight through notches at the grain boundaries. A) and c) were taken before notching (arrows showing notch position), b & d) show fracture surfaces

.

Often the crack did not fail at the tip of the notch; ≈ 50% failed next to the notch but along neighbouring grain boundaries (Figure 8.7). This was in part due to the notch ending in a grain; it was impossible to determine the grain structure under the surface

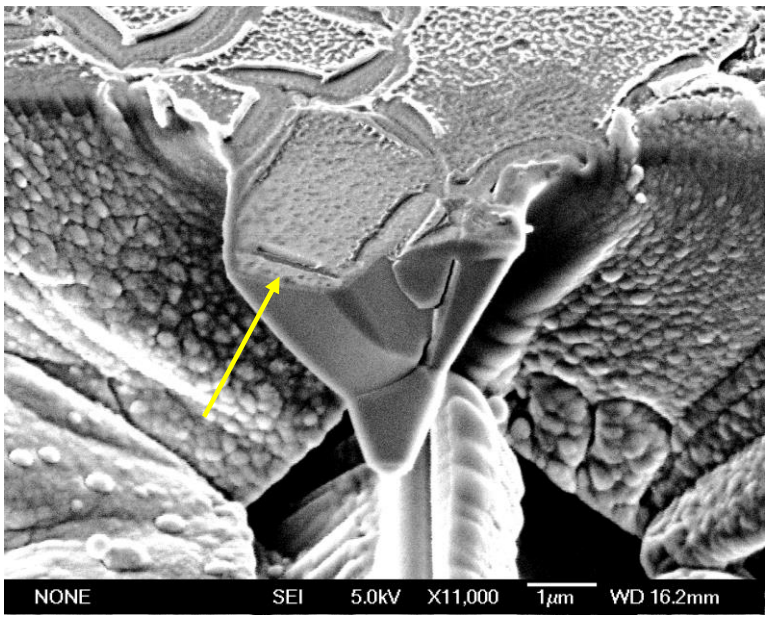


Figure 8.7: Polycrystalline AES-11C beam that failed near to, but not at, a flaw (arrowed). Titled to 50°

prior to notching. Four samples failed from the notch (Figure 8.8, Table 8.9). The values were corrected for notch bluntness and residual stress.

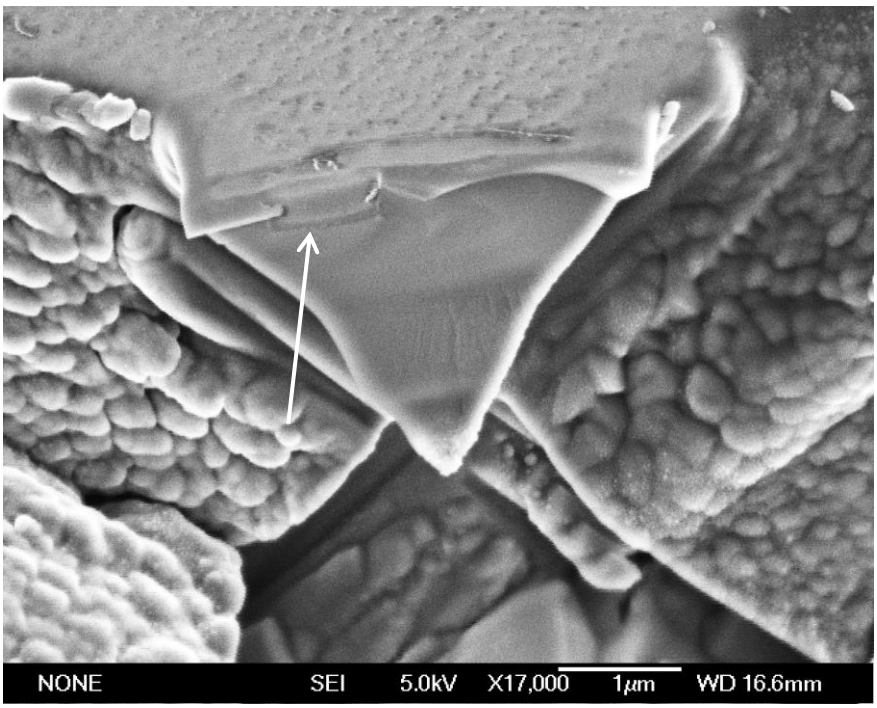


Figure 8.8: SEI (JEOL 6500F) of a microcantilever beam in AES11-C fractured from a controlled flaw (arrowed), tilted to 50°.

The value of b/w for GB1 (Table 8.9) was greater than the maximum b/w used in the simulations by Strobl et al [144] (Section 6.2). Hence, the value was excluded. The mean stress intensity factor was (0.6 +/- 0.1) MPa $m^{1/2}$. The fracture surfaces (Figure 8.8) indicated that the flaw was the cause of the crack nucleation. Several additional samples, not shown in Table 8.10, had flaws at grain boundaries but did not fracture from them.

8.2.5. Consideration of misorientations

In order to investigate whether the misorientations across a grain boundary was having an effect on the measured toughness (as has been seen in metals, for example [13]), Electron Back-scattered Diffraction (EBSD) of the polycrystalline alumina was performed (Section 3.4.6.) (Figure 8.9). The properties of the grain boundary were determined (OIM software). Using the nanoindenter markers, the specific grain boundaries on the surface of the alumina

were located and microcantilever beams produced. Hence, the relationship between the grain boundary misorientation and the stress intensity factor at failure was determined.

Only samples whose boundary was perpendicular to the top surface were used (determined after failure; channelling contrast was too low to determine the orientation of the grain boundary to the surface prior to milling) (Table 8.10).

Consideration of the fracture surfaces showed that A – EBSD – 3 (Table 8.10) failed in the grain rather than at the boundary, hence the large stress intensity factor at failure.

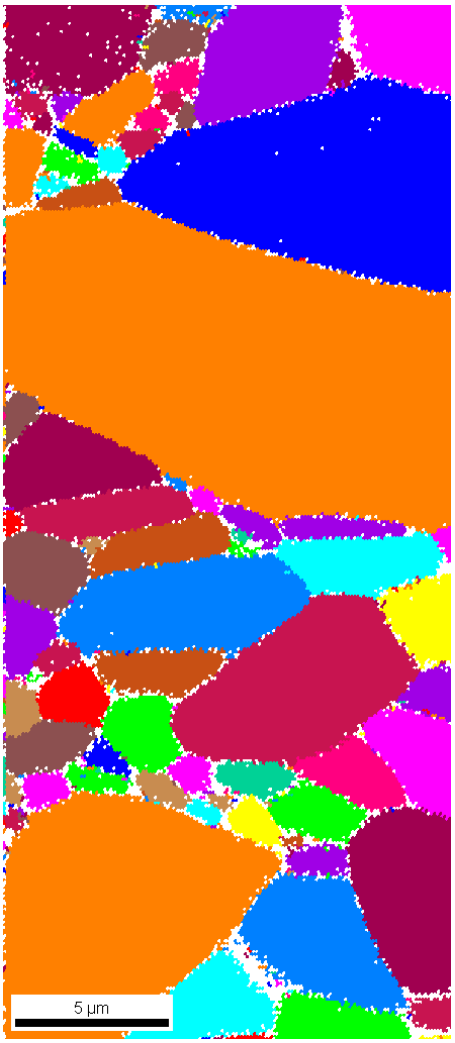


Figure 8.9: EBSD map (JEOL 6300) showing polycrystalline AES-11C alumina grains.

Beam	θ	Axis			GB plane 1			GB plane 2			Σ	$K_{I0,\ gb}$ (MPa.m$^{1/2}$)
		h	k	l	u	v	w	u	v	w		
A – EBSD - 1	67	-11	16	2	5	-8	26	16	9	19	-	0.5
A – EBSD – 2	84	21	-10	1	1	3	-6	-4	-1	19	-	0.3
A – EBSD – 3	84	-14	-7	-5	-1	-1	24	20	9	15	-	1.4
A – EBSD – 4	87	13	-8	-4	7	-18	-2	-14	3	25	-	0.3
A – EBSD – 6	63	-13	20	14	-16	5	22	2	-4	23	-	0.8

Table 8.10: Mechanical properties and misorientations angles for microcantilever beams in AES-11C alumina. θ = misorientation angle, Σ = special (low energy) boundaries

No special boundaries (including discarded beams) were detected. Although the sample set was small, there was no discernible relationship between the grain boundary misorientation and the boundary toughness. However, the experiments showed that it is possible to determine the misorientation across a boundary in alumina and produce microcantilever beams there, providing the EBSD is performed prior to microcantilever beam milling (following the procedure outlined in Section 3.4.6).

8.2.6. AES-11C alumina – combined data

Eleven samples had notches milled at grain boundaries in AES-11C alumina ; $K_{I0,gb}$ was (0.6 +/- 0.1) MPa $m^{1/2}$. By using the ratio of $K_{I0,\ air}/K_{Ic}$ from sapphire, K_{Ic} of the AES-11C boundaries was estimated to be (1.4 +/- 0.4) $MPam^{1/2}$ (see Section 9.3.2.).

8.3. Microcantilever Beams in 2wt% chromia doped AES-11C beams

Previous research (discussed in Section 2.1.3.) was unclear on whether chromium reduced or increased to propensity for deformation twinning. In order to 1) to determine if twinning could be induced during loading to high stresses and 2) to assess the change in macroscopic mechanical properties with chromium (Section 5), microcantilever beams of 2wt% chromia doped AES-11C were notched and loaded until failure.

8.3.1. Toughness of grains

Two beams were produced in the chromia doped grains with straight through notches (10pA) in the grains (Table 8.11).

Beam	Nominal Strength (GPa)	Notch depth (μm)	α'	K_{I0} ($MPam^{1/2}$)
2wt% - M - 1	3.0	0.32	0.12	1.4
2wt% - M - 1	2.9	0.38	0.15	1.7

Table 8.11: Mechanical properties of microcantilever beams produced in 2wt% chromia doped AES-11C and notched in the grains

The load-displacement curves were linear until failure. The mean stress intensity factor at failure was (1.6 +/- 0.3) MPa $m^{1/2}$. One fracture surface (Figure 8.9a) had several features underneath the notch; it was unclear what these were.

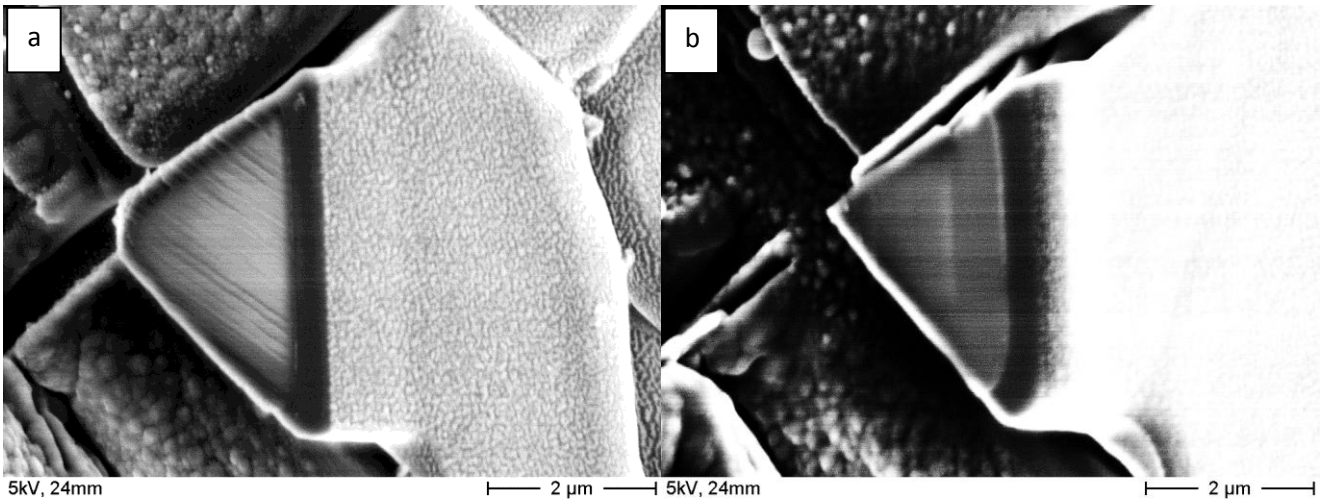


Figure 8.9: SEI (JEOL 840F) of a fracture surface of 2wt% chromia doped AES11-C with a) notch in a grain, b) notch at grain boundary. Tilted to 50^{O}

8.3.2. Toughness of grain boundaries

Two beams were produced and notched at the grain boundaries in the chromia doped AES-11C. The mean stress intensity factor of the grain boundaries was (0.8 +/- 0.2) MPa $m^{1/2}$. The fracture surface was smooth as the crack had propagated along the grain boundary (Figure 8.9b).

Beam	Nominal Strength (GPa)	Notch depth (µm)	α'	$K_{I0,\ gb}$ (MPam$^{1/2}$)
2wt% - GB – S1	2.4	0.38	0.13	0.9
2wt% - GB – S2	1.9	0.45	0.16	0.6

Table 8.12: Mechanical properties of microcantilever beams produced in 2wt% chromia doped AES-11C and notched at the grain boundaries

8.4. Microcantilever beams in vacuum sintered TM-DAR

Two TM-DAR samples were produced: one with 0.012wt% carbon doping and one without (see Section 3.1.2.1). Microcantilever beams were produced at the surface of these samples to measure the grain boundary toughness.

8.4.1. Undoped TM-DAR

8.4.1.1. Strength

Beams were produced on undoped TM-DAR and loaded until fracture (Table 8.13).

Beam	Young's Modulus (GPa)	Failure strength (GPa)	Failure origin
TM – Strength 1	523	5.8	GB, Inter
TM – Strength 2	446	7.0	GB, Inter
TM – Strength 3	458	5.1	GB, Inter

Table 8.13: Mechanical properties of microcantilever beams produced in undoped TM-DAR alumina. GB = failed at grain boundaries, Inter = crack propagated intergranularly

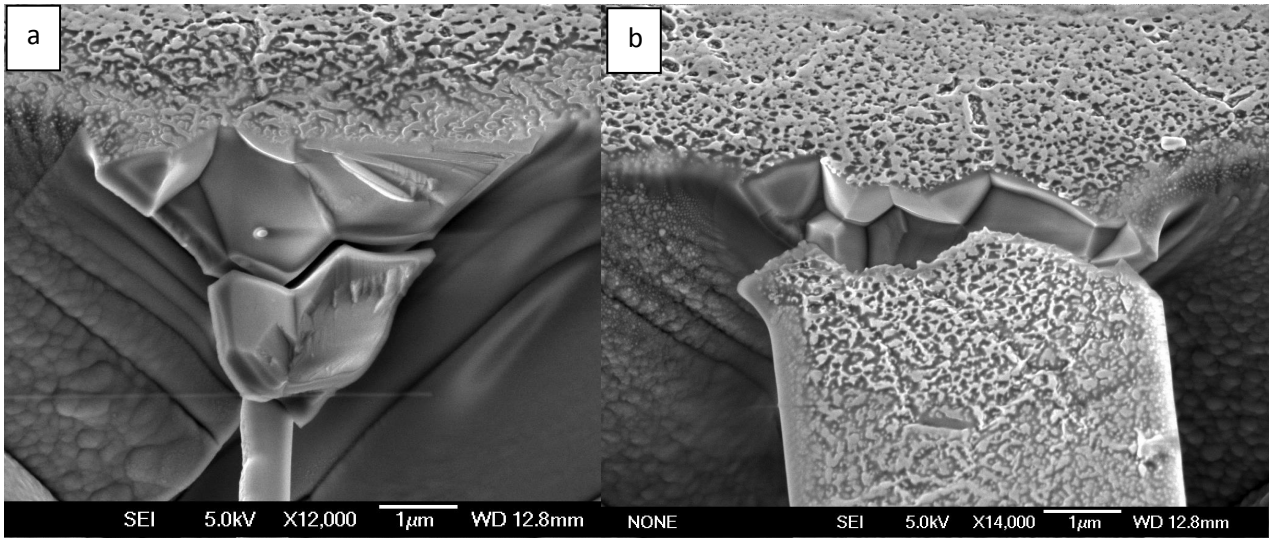


Figure 8.10: SEI (JEOL 6500F) of fracture surfaces of undoped vacuum sintered TM-DAR microcantilever beams, used for strength measurements. Tilted to 50°

The Young's modulus of the three beams, after correction (Appendix 3.2), was (475 +/- 41) GPa. The fracture surfaces showed that the crack appeared to have propagated mostly intergranularly (Figure 8.10).

8.4.1.2. Toughness of Grain Boundaries

Beams were produced to measure the grain boundary toughness in undoped TM-DAR (Table 8.14). Owing to the finer grain size, it was very difficult to find suitable boundaries to produce straight through notches; the majority of beams had controlled flaws.

Beam	Nominal Strength (GPa)	Notch depth (μm)	α'	$K_{I0,\ gb}$ (MPa.m$^{1/2}$)
TM – GB – S1	2.3	0.39	0.12	0.8

Beam	α/b	b/w	α'	M	$K_{I0,\ gb}$ (MPa.m$^{1/2}$)
TM – GB – F1	0.51	0.23	0.09	0.74	1.3
TM – GB – F2	0.58	0.16	0.08	0.72	1.7
TM – GB – F3	0.66	0.22	0.12	0.65	1.8
TM – GB – F4	0.44	0.24	0.08	0.79	0.8
TM – GB – F5	0.51	0.30	0.12	0.72	0.7
TM – GB – F6	0.65	0.18	0.09	0.69	0.7
TM – GB – F7	0.52	0.12	0.05	0.78	0.2
TM – GB – F8	0.48	0.14	0.05	0.80	0.8

Table 8.15: Mechanical properties of microcantilever beams produced in undoped TM-DAR alumina. M is calculated using Equation A6.1.1.

Beams F1 to F3 appeared to have a noticeably higher toughness than F4 to S1, despite similar values for M (i.e. the failure strengths were higher for F1 – F3 despite similar shaped

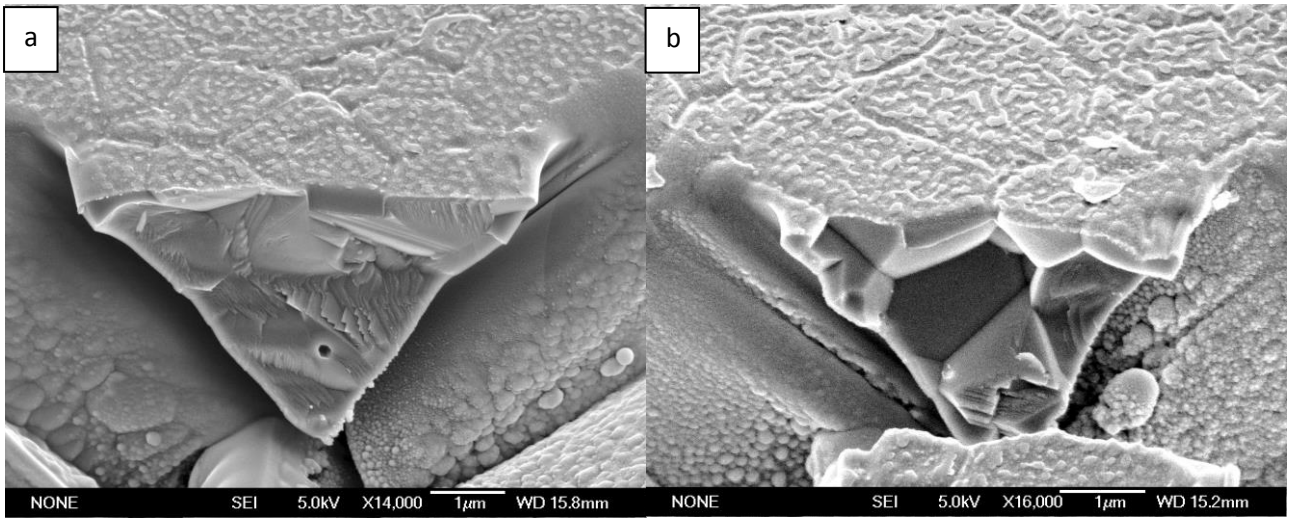


Figure 8.11: SEI (JEOL 6500F) of fracture surfaces of undoped vacuum sintered TM-DAR microcantilever beams: a) F2, showing mostly transgranular fracture and b) F4, showing mostly intergranular fracture. Tilted to 50°

and sized flaws). The fracture surfaces showed some differences between the different beams (Figure 8.11). Beams F1 to F3 showed mostly transgranular fracture, whereas F4 to S1 showed mostly intergranular fracture. The mean stress intensity factor at failure for all samples was (1.0 +/- 0.2) $MPam^{1/2}$. Excluding those that failed transgranularly, the value decreased to (0.7 +/- 0.1) $MPam^{1/2}$.

8.4.2. 0.012wt% carbon doped TM-DAR – Grain Boundary Toughness

Beams were produced at grain boundaries in 0.012wt% carbon doped TM-DAR. Four of the beams were notched with flaws at the grain boundaries, and four had straight through notches across the grains and the boundaries. The former were intended to directly measure the grain boundary toughness of a specific boundary. The latter allowed the beam to fracture along the boundary of the lowest toughness feature present under the notch.

Beam	Nominal Strength (GPa)	Notch depth (μm)	α'	$K_{I0,\ gb}$ ($MPa.m^{1/2}$)
TM + 0.012C – S1	4.0	0.23	0.08	1.6
TM + 0.012C – S2	3.1	0.33	0.10	1.4
TM + 0.012C – S3	2.5	0.46	0.11	1.2
TM + 0.012C – S4	1.2	0.38	0.11	-0.5

Beam	α/b	b/w	α'	M	$K_{I0,\ gb}$ ($MPa.m^{1/2}$)
TM + 0.012C – F1	0.56	0.22	0.09	0.72	0.9
TM + 0.012C – F2	0.48	0.35	0.13	0.73	1.8
TM + 0.012C – F3	0.51	0.16	0.04	0.89	0.6
TM + 0.012C – F4	0.23	0.40	0.07	0.92	1.4

Table 8.16: Mechanical properties of microcantilever beams produced in undoped TM-DAR alumina. M is calculated using Equation A6.1.1.

S4 (Table 8.16) failed at a much lower stress and stress intensity factor than the other samples, despite a similar depth notch. There was a small defect underneath the notch (Figure 8.12a); hence, the value was excluded.

The mean stress intensity factor at failure was (1.3 +/- 0.2) MPa $m^{1/2}$. The fracture surfaces (Figure 8.12) showed large areas of transgranularly fracture with some intergranular regions.

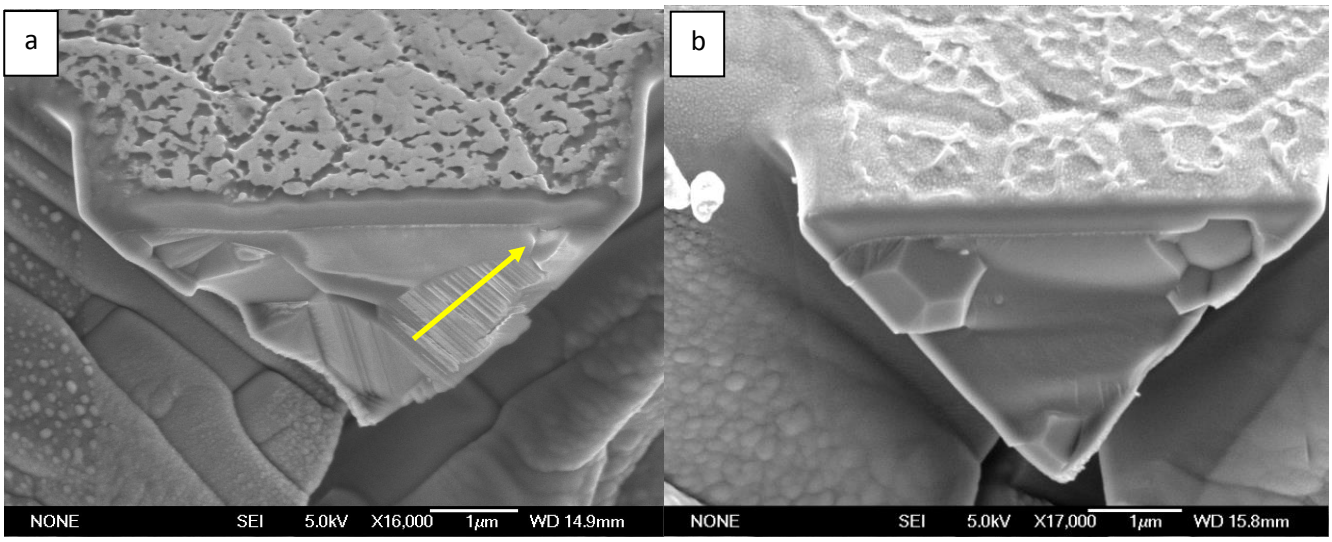


Figure 8.12: SEI (JEOL 6500F) of fracture surfaces of 0.012wt% carbon doped TM-DAR a) showing S4 with defect underneath notch, and b) a straight through notch across the beam. Tilted to 50°

8.5. Rare-earth doped silicon nitride

Two different rare-earth doped silicon nitride ceramics (discussed in Section 3.1.3.) were used: La- and Lu-doped. Several beams were produced per sample; some to measure strength and Young's modulus, and several to measure the grain boundary toughness.

8.5.1. Strength and Young's modulus

The mechanical properties are shown in Tables 8.17 (Lu-doped) and 8.18 (La-doped). The load-displacement curves of the silicon nitride samples often behaved differently to those of the sapphire and alumina. Rather than being a straight line until failure, several samples had a kink in the curve, with an increased compliance thereafter (Figure 8.13).

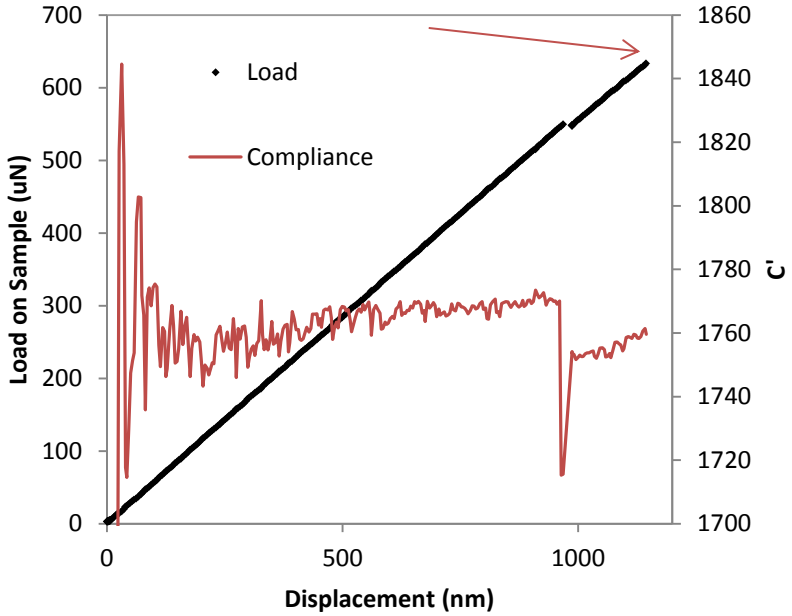


Figure 8.13: Load- & compliance-displacement curves for Lu-doped silicon nitride, which increased linearly until around 900nm. Failure occurred at the arrow.

The Young's moduli were calculated from the lower portion of the curve, and corrected for the displacements in the support structure (whilst the FEA was performed on isotropic alumina, in lieu of FEA on silicon nitride the correction in Appendix 3.2 was used). Failure strength was calculated at the failure load (arrow in Figure 8.13).

There was no change in compliance without a kink; only after the step change was there is change in the compliance. All samples that had kinks had a compliance change (Table 8.17 and 8.18). Not all samples showed a kink and a change in compliance during the loading, and there was not a correlation between whether the sample showed such behaviour and the failure strength. The crack extension was determined from Equation A7.3.4.

Beam	Relative change in compliance	Crack Extension (μm)	Young's Modulus (GPa)	Strength (GPa)
SN - Lu – 1	-	-	327	3.1
SN - Lu – 2	-	-	333	3.1
SN - Lu – 3	-	-	342	3.1
SN - Lu – 4	3.0%	0.22	378	2.8
SN - Lu – 5	2.6%	0.20	366	2.8

Table 8.17: Mechanical properties of the microcantilever beams in Lu-doped Si_3N_4

Beam	Relative change in compliance	Crack Extension (μm)	Young's Modulus (GPa)	Strength (GPa)
SN - La – 1	1.0%	0.14	306	2.4
SN - La – 2	1.9%	0.28	370	2.2
SN - La – 3	-	-	305	1.6

Table 8.18: Mechanical properties of the microcantilever beams in La-doped silicon nitride

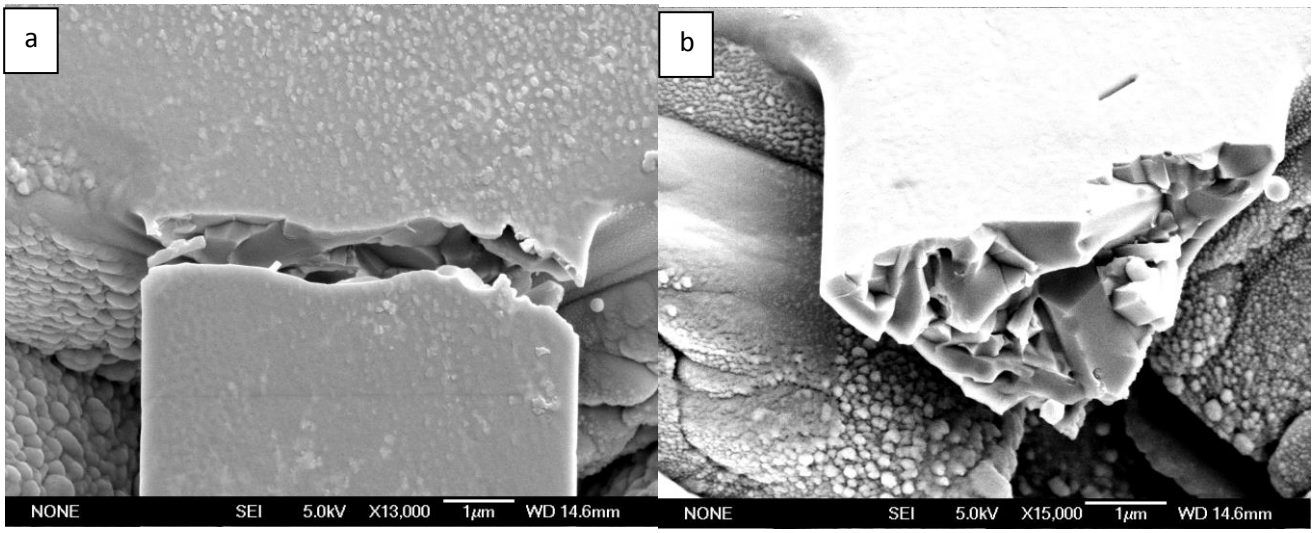


Figure 8.14: SEI (JEOL 6500F) of Lu-doped silicon nitride a) Beam 1 and b) Beam 2, tilted at 50° to show fracture surface

The frequency of the step change in compliance appeared to not be affected by the rare-earth doping.

The Young's moduli of the Lu- and La- doped silicon nitrides was (347 +/- 22) GPa and (327 +/- 38) GPa respectively. The strength of the Lu- and La-doped silicon nitrides was (3.0 +/- 0.2) GPa and (2.1 +/- 0.4) GPa respectively. Analysis of the fracture surfaces (Figures 8.14 and 8.15) showed that the crack propagated along the grain boundary phase (if it had propagated transgranularly, the fracture surfaces would be much smoother with far fewer facets); the strengths represent the inherent strength of the amorphous phase.

One noticeable feature of the silicon nitride beams was that the beam often (around 80% of the time) did not fall away from the fixed end; in sapphire and alumina, the beam almost always fell into trench and left the whole fracture surface viewable. In the silicon nitride, even though the load-displacement curve showed conclusively that the beam had failed, the beam

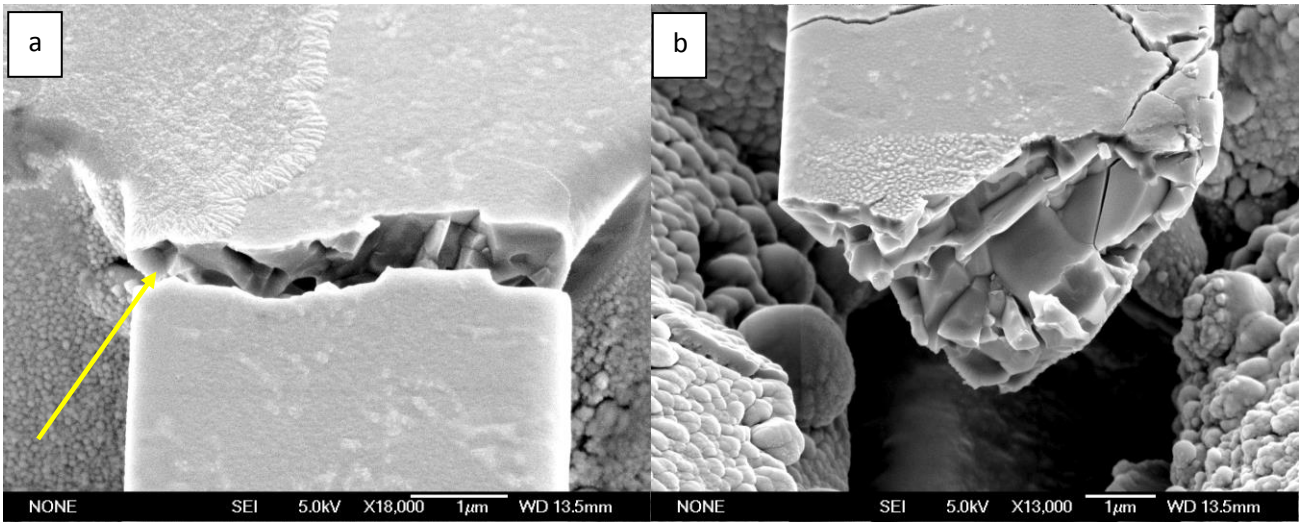


Figure 8.15: SEI (JEOL 6500F) of La-doped silicon nitride a) Beam 1 and b) Beam 2, tilted at 50° to show fracture surface. Arrow shows possible flaw.

remained close to the fixed end (Figures 8.15a). Presumably, there was enough crack bridging (due to microstructure size and frequency of elongated grains with sizes on the order of the beam) that the microcantilever beam could not fall away.

One other feature was the additional cracking (Figure 8.15b). This was atypical for the material and, as no change in compliance was detected during loading, perhaps occurred after failure.

It was often difficult to determine the failure origin from the silicon nitrides. Some small flaws were detectable at the top surface (e.g. arrowed in Figure 8.15a) but it was difficult to determine this conclusively.

8.5.2. Toughness of grain boundaries

Several beams were notched using both straight through notches and controlled flaws. In general, the controlled flaws were unsuccessful at nucleating a crack; the failure often happened away from the flaw along the grain boundary phase. The straight through notches were much more successful when placed across the beam; the crack propagated under the notch along the lowest toughness feature.

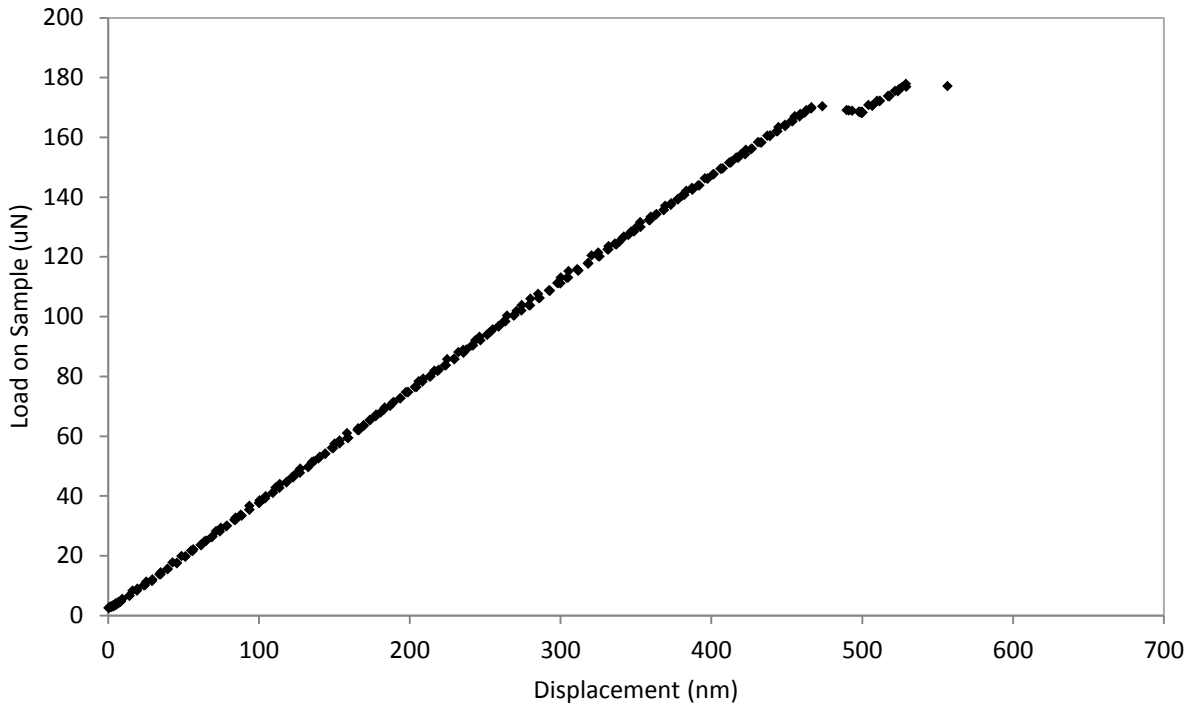


Figure 8.16: Load-displacement curve for notched La-doped silicon nitride beam, showing steps due to stable crack extension

The load-displacement curves often showed steps such as those seen for the strength tests. However, the behaviour was markedly different for the two silicon nitrides; none of the Lu-doped samples showed a change in compliance before failure, whereas 5 of the 11 La-doped beams underwent a change in compliance during loading (Figure 8.16).

Unlike with the stress testing, there was occasionally a compliance change before a kink in the load-displacement curve (Figure 8.17). Also unlike the stress tests, after the kink the compliance continued to increase before failure (i.e. the rate of change of compliance with displacements was not zero).

The crack extension, $\Delta\alpha$, was determined by considering the compliance change with relative notch depth (Equation A7.3.4). The initial FIB notch depth was determined from SEI of fracture surfaces.

There were three unknowns for rare-earth doped silicon nitrides: the notch tip crack length, dα, the residual stress, σ_{res}, and the depth of the implanted zone. It was not correct to simply assume that these values were the same as for sapphire (Section 7). In the absence of information, no corrections for notch bluntness and residual stress could be taken. Qualitative comparison was used instead.

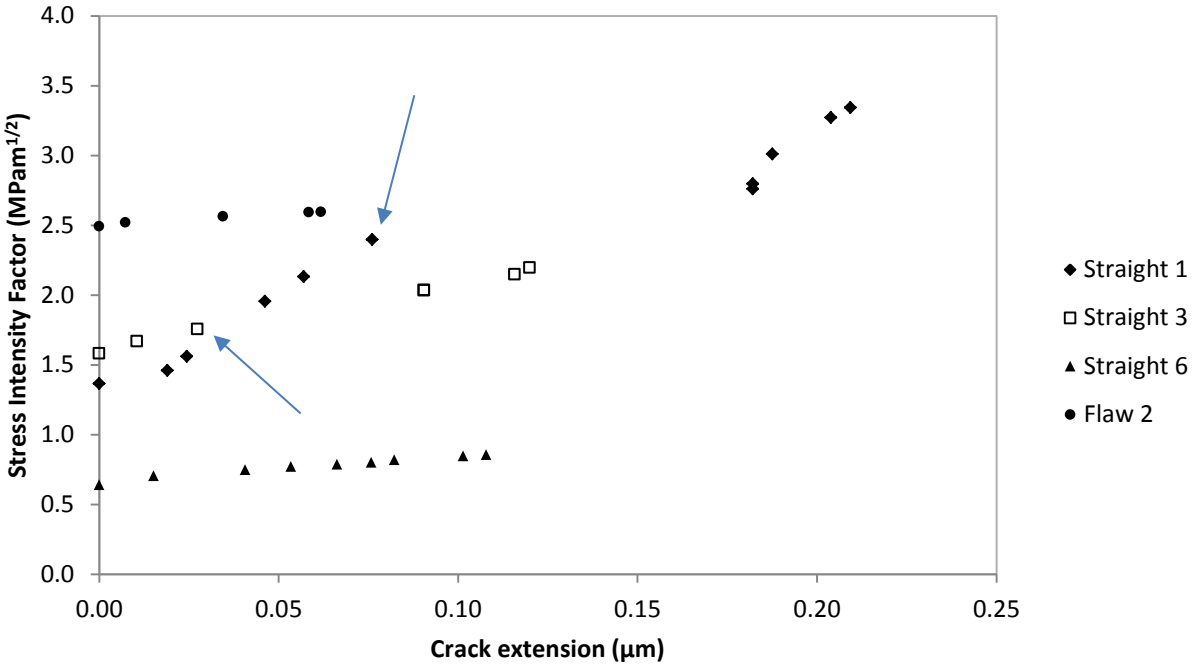


Figure 8.17: Change in stress intensity factor with crack extension for different La-doped silicon nitride beams. Arrows indicate data points when kinks in load-displacements occur

Sample	Relative compliance change	Crack extension (µm)	Notch depth (µm)	α'	K_{fail} (MPa.m$^{1/2}$)
Lu – Straight 1	-	-	0.42	0.11	2.3
Lu – Straight 2	-	-	0.55	0.18	3.1
Lu – Straight 3	-	-	0.69	0.27	3.5
Lu – Straight 4	-	-	0.39	0.14	2.7
Lu – Straight 5	-	-	0.65	0.30	3.2

Beam	α/b	b/w	α'	M	K_{fail} (MPa.m$^{1/2}$)
Lu – Flaw 1	0.49	0.27	0.11	0.74	2.6

Table 8.19: Mechanical properties of the notched microcantilever beams in Lu-doped silicon nitride. M is calculated using Equation A6.1.1.

Sample	Relative compliance change	Crack extension (μm)	Notch Depth (μm)	α' (Initial)	K_{ext}	K_{fail} (MPa.m$^{1/2}$)
La – Flaw 1	2%	0.06	0.38	0.11	2.5	2.6
La – Straight 1	23%	0.21	0.53	0.19	1.4	3.4
La – Straight 2	-	-	0.45	0.17	-	3.0
La – Straight 3	3%	0.05	0.22	0.11	1.6	2.2
La – Straight 4	44%	N / A	0.31	0.09	-	1.0
La – Straight 5	-	-	0.28	0.10	-	2.1
La – Straight 6	4%	0.11	0.43	0.13	0.7	0.9
La – Straight 7	-	-	0.33	0.19	-	1.9
La – Straight 8	-	-	0.26	0.12	-	2.2
La – Straight 9	-	-	0.35	0.13	-	2.1

Table 8.20: Mechanical properties of the notched microcantilever beams in La-doped silicon nitride

Fracture surfaces for the two materials are shown in Figures 8.18 and 8.19.

There was variation in the stress intensity factor at failure for La-doped beams (Table 8.20). La – Straight 4 (Figure 8.20a) did not break fully at the notch, and was excluded. La – Straight 6 had a small crack at the right hand side of the notch (see arrow). The sample probably failed at this point, rather than at the base of the straight through notch. La – Flaw 1 failed in a silicon nitride crystalline grain rather than at the grain boundary, and was also excluded. The mean stress intensity factor at failure for Lu- and La-doped silicon nitride was (2.9 +/- 0.2) MPam$^{1/2}$ and (2.4 +/- 0.2) MPam$^{1/2}$ respectively. The stress intensity factor for crack extension in La-doped was (1.5 +/- 0.1) MPam$^{1/2}$.

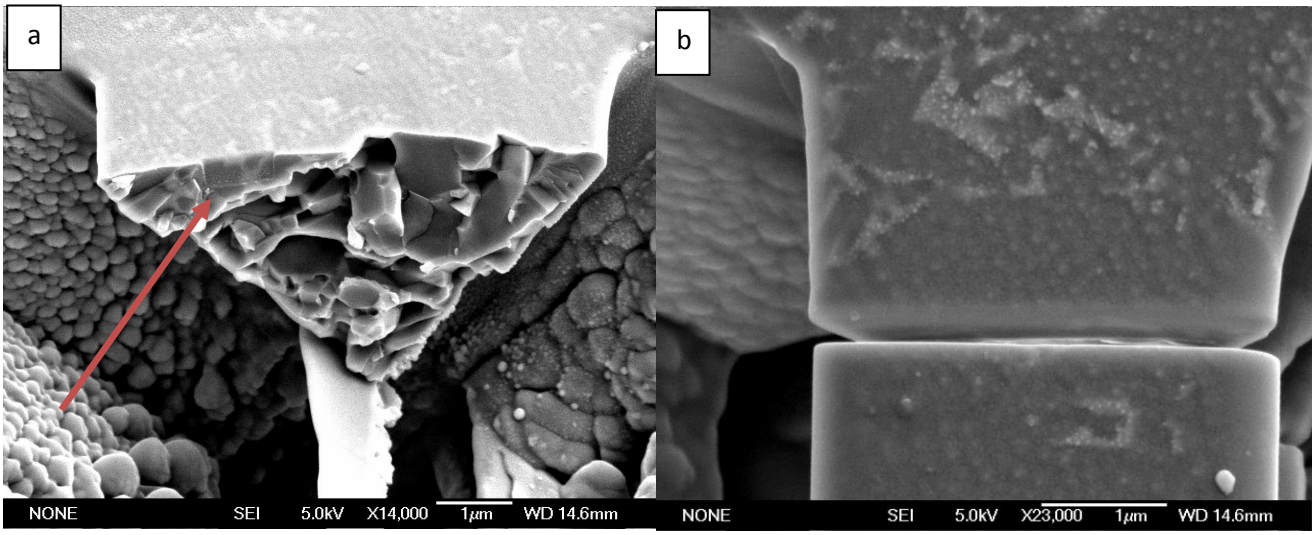


Figure 8.18: SEI (JEOL 6500F) of fracture surfaces of Lu-doped silicon nitride a) Flaw 1 and b) Straight 5, tilted at 50° and 20° degrees respectively. The FIB flaw in a) was indicated with an arrow

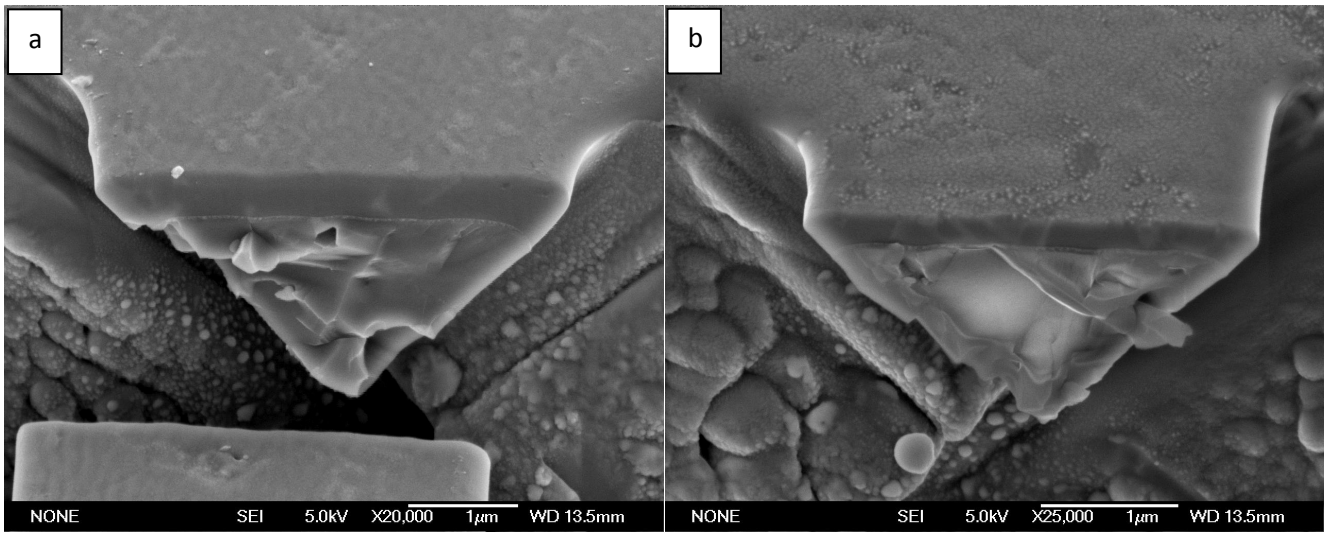


Figure 8.19: SEI (JEOL 6500F) of fracture surfaces of La-doped silicon nitride beams a) Straight 2 and b) Straight 3, tilted at 50° .

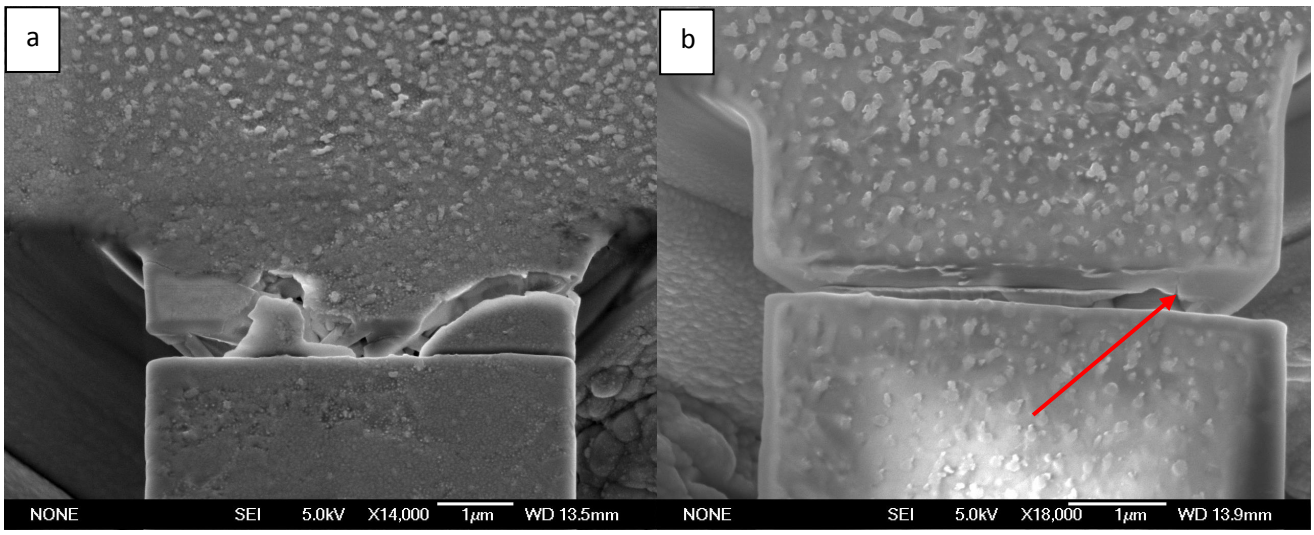


Figure 8.20: SEI (JEOL 6500F) of fracture surfaces of La-doped silicon nitride beams; a) Straight 4 (30° tilt), and b) Straight 6 (50° tilt).

The fracture surfaces appeared to be similar for the two materials (Figures 8.18 and 8.19).

8.6 Summary of properties

Microcantilever beams are produced in a variety of different ceramics. The mechanical properties are tabulated for comparison in Table 8.24.

Sample	Fracture on…	#	E (GPa)	σ (GPa)	K_{I0} ($MPam^{1/2}$)	Compliance change?
DBond sapphire	Matrix	3	465 +/- 25	-	1.4 +/- 0.2	No
	Boundary	3, 14		5.2 +/- 0.1	0.7 +/- 0.2	
Sapphire	m-plane	13	-	-	1.5 +/- 0.2	No
Water		4	-	-	0.9 +/- 0.2	
Oil		2	-	-	3.4 +/- 0.6	
Sapphire	a-plane	8	-	-	1.4 +/- 0.2	No
Sapphire	c-plane	7	-	-	1.5 +/- 0.2	No
Sapphire	60^o to [0001]	2	-	-	1.6 +/- 0.2	No
Sapphire	30^o to [0001]	2	-	-	1.7 +/- 0.3	No
Undoped AES-11C	Matrix	5	447 +/- 38	-	1.5 +/- 0.3	No
	Boundary	21, 17		3.9 +/- 0.7	0.6 +/- 0.1	
2wt% Cr_2O_3 AES-11C	Matrix	2	-	-	1.6 +/- 0.3	No
	Boundary	4	-	-	0.8 +/- 0.2	
TM-DAR – v	Boundary	3, 9	476 +/- 41	5.9 +/- 0.6	0.7 +/- 0.1	No
0.012wt% C TM-DAR – v	Boundary	8	-	-	1.3 +/- 0.2	No
Lu- Si_3N_4	Boundary	5, 6	347 +/- 22	3.0 +/- 0.2	2.9 +/- 0.2	Only un-notched
La- Si_3N_4	Boundary	3, 11	327 +/- 38	2.1 +/- 0.4	1.5 +/- 0.1, 2.4 +/- 0.2	≈ 50%

Table 8.24: Mechanical properties of tested microcantilever beams. For samples tested for both strength and toughness, two sets of numbers were given in "#" (number of samples): strength, toughness. If crack extension before failure occurred, stress intensity factors for 1) start of crack extension, 2) at failure were given.

Chapter 9 Discussion

Several key objectives of this project are outlined in Section 2.9. Many of these objectives rely upon the validity of the microcantilever beam testing. Thus, a sub-set of objectives and a summary of findings, regarding the various characteristics of the microcantilever beam technique, are given at the start and end of Chapter 7 respectively.

The shape of Chapter 9 is as follows:

1) Discussion of the validity of the microcantilever beam testing for ceramics (including the characteristics of the redeposited material and implanted region) focussing on: Young's modulus, strength, notch types, stress intensity factors at failure, and environment assisted sub-critical crack growth. The physical interpretation of the notch tip crack length $d\alpha$ is discussed, as well as the use of corrections for notch bluntness and notch tip residual stress. Tentative analysis of the change in properties due to vacuum annealing is given.
2) Using the microcantilever beam technique, the toughness results for different planes of sapphire are discussed.
3) Using the stress intensity factors at failure of different grain boundaries, as well as the macroscopic fracture properties, two different purity alumina ceramics are compared and contrasted. Consideration of the damage evolution during uniaxial compression is given, in view of the flaw distribution and the grain boundary toughness.
4) Focussing on the change in the grain boundary toughness, the change in properties due to the addition of carbon to polycrystalline alumina is discussed.
5) The micro- and macro-scopic properties after chromium doping in polycrystalline alumina is considered.
6) Qualitative discussion of the difference in silicon nitride microscale properties with rare-earth doping is given.

9.1. Microcantilever beam testing & its validity

9.1.1. Redeposited Material

The key considerations for the analysis of the redeposited material are:

1) Composition
2) Structure
3) Mechanical properties
4) Where and to what extent it forms, and the effect on the measured properties of the microcantilever beams

Composition

The redeposited material, always present during Focussed Ion Beam milling, had a significant amount of gallium present: (37 +/- 10) at% (Section 4.6.1.2). The cation-to-anion ratio of the redeposited material is around 1.3, compared to 0.67 for either Al_2O_3 or Ga_2O_3. Whilst quantitative analysis of EDX can often be prone to errors (e.g. due to absorption of x-rays or fluorescence [202]), this is a significantly different ratio.

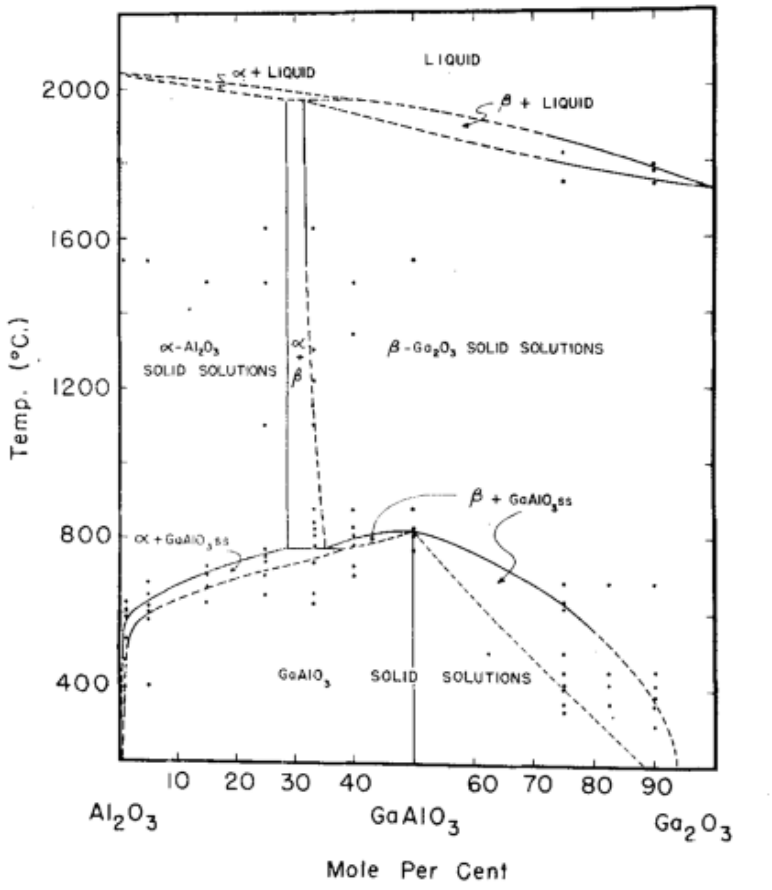


Figure 9.1: Equilibrium phase diagram between Al_2O_3 and Ga_2O_3 (from Hill et al [219]). Permission to reproduce this figure has been granted by John Wiley & Sons, Inc.

There could not have been a solid-solution of Ga^{3+}-Al^{3+}-O^{2-} (the nature of which is discussed by Hill et al [219]) as charge

neutrality would not be maintained; neutrality would have been attained if there was 10% Ga^{3+} in solid solution with Al-O (i.e. $Al_{1.5}Ga_{0.5}O_3$) and around 27% elemental gallium. These processes can be written as:

$$Ga^{+} \rightarrow Ga^{3+} + 2e^{-} \qquad 2Ga^{+} + 2e^{-} \rightarrow 2Ga$$

However, the composition of the redeposited material does not necessarily have to be uniform in all regions, so the true values are likely to vary from this stoichiometry.

Structure

Electron diffraction work of the redeposited material was performed (Table 4.5). There were several identifiable rings that were not present in the electron diffraction pattern of amorphous carbon (i.e. the material that the TEM foil was sitting on). As the rings were full and continuous, it was likely that the material was nano-crystalline [158].

Two d-spacings for redeposited material (not present in the amorphous carbon) were (4.2 +/- 0.2) Å and (2.47 +/- 0.08) Å (Table 4.5). It is possible that these were due to the gallia-alumina solid solution (Figure 9.1). Previous work [219] considers the d-spacings for different gallia-alumina solid solutions. Using this work, some estimation of the expected d-spacings (noting the composition) can be made (Table 9.1).

Planes	**Relative Intensity (%)**	**d-spacing (Å)**		
		Pure alumina	+ 10 at% gallium	+ 37 at% gallium
{110}	42	2.38	2.38	2.42
{104}	92	2.56	2.56	2.59
{012}	74	3.48	3.48	3.52
?	50	-	-	4.28

Table 9.1: d-spacings for different planes in alumina with different gallium content (in solid solution) using the data from [219]. Relative intensities of first three from X'Pert data sheet for pure alumina.

It was unclear why there was no variation in the d-spacing at 10at% (the change in d-spacing would be expected to be linear with gallium inclusion, in a similar way to chromium shown in Section 4.2.2); this may be down to experimental accuracy. Consideration of the d-spacings predicted from a solid solution (Table 9.1) shows that the measured d-spacing at (2.47 +/- 0.08) Å was probably due to either the $\{110\}$ or $\{104\}$ planes in 10 at% gallium-alumina solid solution (i.e. the estimated composition).

From [219], there are d-spacings at 4.28 Å (Table 9.1). However, the authors do not state which planes these are associated with. The measured d-spacing from electron diffraction of redeposited material at around 4.2 Å could be due to these planes; more work is required to elucidate what this d-spacing is due to. This could be done experimentally, by producing gallium doped alumina and performing X-ray diffraction, or theoretically, using a computer simulated x-ray diffraction pattern programme.

If there was also some elemental gallium present (see Composition), diffraction rings associated with this would be expected. Elemental gallium has d-spacings (amongst others) of 2.73 and 2.50 Å; these were in good accordance to the measured rings (Table 4.5).

Overall, the measured electron diffraction rings were broad and so both the elemental gallium rings and those of the solid-solution may have been present but, due to local changes in composition (and thus d-spacing, Table 9.1), individual rings could not be elucidated. Furthermore, and the probe size was large compared to the nano-crystalline features, many nano-crystals were diffracted giving rise to many electron rings.

The fringes from high-resolution TEM suggested that the redeposited material had some local order (Figure 4.31b). There were regions where the fringes appeared order, but others where the fringes showed no order. This further suggested that nano-crystalline nature of the material.

Mechanical Properties

The mechanical properties of the redeposited material were assessed using nanoindentation (Section 4.10.2.2.). At the start of indenting, the Young's modulus was between 130 and 220GPa below that of the original sapphire. This tended towards between 50 and 70GPa below sapphire at high indent depths. It was unclear what was occurring during indentation. It could be that the loosely compacted globules were being pushed together and densifying (especially at the start of loading). It was also unclear what the effect of the underlying sapphire was. Whilst the boxes were deep, the amount of redeposited material may have not been sufficiently thick enough to negate the effect of the substrate. Two key results are that 1) the modulus is lower than the sapphire at all depths, and 2) the modulus is not insignificant. This is important, as it means that the presence of such material may affect the measured microcantilever beam properties.

Discussion of the possible effect on the mechanical properties requires consideration of where the material actually is.

Location, extent of material, and effect on mechanical properties

The redeposited material was present in the following places:

- **At the base of the FIB notches (Figures 4.41):** The redeposited material was around 25nm thick (Figure 4.33). It was probable, given the nature of the material, that the toughness was less than that of the underlying sapphire. Thus, if the notch tip crack was extending through this at low stresses, the crack would be arrested once it met either the implanted region (in unannealed beams) or the crystalline ceramic (in annealed beams). As a result, the measured toughness was of the crystalline ceramic and not the redeposited material.
- **At the top surface (Figure 4.39b):** From TEM (Figure 4.31b), the depth of redeposited material was ≈ 2nm (i.e. 0.05% of the beam height) and as such had little impact on the Young's modulus. **Underneath the beam (Figure 3.9):** Attempts were

made to remove the latter as much as possible. If present in large amounts, the measured beam stiffness may be affected (as the material had a non-negligible Young's modulus). However, as the modulus was much lower than the sapphire, the error in the measured stiffness due to this effect may be small (especially in comparison to errors such as the beam dimension measurements).

-

Analysis could be done using Finite Element Analysis to determine what effect, if any, the redeposited material (both on the top surface and underneath the beam) had on the load-displacement curves, and thus the measured Young's modulus. If there was an effect, a correction term could be generated and subsequently used to negate the effect of the redeposited material.

Summary

Overall, the most likely structure of the redeposited material was that it was nanocrystalline gallia-alumina solid solution (e.g. $Al_{1.5}Ga_{0.5}O_3$) with around 27% elemental gallium in pockets. Each globule (Figure 4.27) may be a separate nano-crystalline pocket of either elemental gallium or solid solution. Due to the very large EDX/diffraction probe size compared to these features, the average composition and structure was ascertained.

Whilst the presence of the material at the base of the FIB notch and on the top surface of the microcantilever beams is inevitable, the effect on mechanical properties should be minimal. However, if there is material at the bottom of the microcantilever beam, the non-negligible elastic modulus may make a different to the measured beam stiffness. Thus, every attempt is made to remove this material.

9.1.2. Gallium Implanted region

The key considerations for the analysis of the gallium implanted region are:

1) Composition & Structure

2) Mechanical properties and residual stress
3) The effect on the microcantilever beam mechanical properties

Composition & Structure

The region was formed of (3 +/- 1) at% gallium. Full analysis of the atomic structure is difficult. It could be that the gallium was elemental and accommodated in the corundum interstices (this would maintain charge neutrality, and explain the increase in the d-spacings (Section 7.2.2.)). However, it could be that a solid solution had formed [219] with gallium ions replacing aluminium ions in the corundum lattice. If this was the case, it is unclear why such a large residual stress would be formed; 3 at% gallium in solid solution gives rise to no change in d-spacing (Table 9.1) and, as a result, no expected lattice strain. The most likely explanation was the former, but further investigation is required to confirm this.

HRTEM (Figure 4.31) and nanodiffraction (Figure 4.32) showed that the implanted region was crystalline. Thus, the region was distinguishable from the redeposited material on the top surface of the sapphire (Figure 4.31b) and at the tip of the notch (Figure 4.33).

This gallium implantation in ceramics was different to the previously reported work in the literature (which focusses on metals and silicon); to the author's knowledge, this is the first quantitative analysis of residual stress in ceramics due to Focussed Ion Beam. For metals and silicon, the properties are dictated by dislocations [152, 153] and amorphisation [155, 157-161] respectively. Thus, it is very likely that the mechanical response of ceramics due to gallium is different to those materials investigated previously.

Mechanical properties and residual stress

The mechanical properties of the gallium implanted region were estimated using nanoindentation (Figure 4.51). Noting that the implanted region was 20nm in thickness, the results suggested that the region had a lower modulus and a higher hardness than the pristine sapphire (the latter of which agreed with previous work on implanted sapphire [163]).

However, it was very difficult to interpret these indents. Aside from there being redeposited material above implanted material, nanoindentation was assessing the properties of the underlying sapphire as well as the damaged layers; previous authors have shown that the substrate thickness [223] or film thickness [224] impact on the measured properties. Hence, it was difficult to directly measure the properties of the implanted region.

The stress in the implanted region (from a sapphire foil) was estimated using Stoney's equation [216] (Section 7.2.1.) to be (13 +/- 5) GPa. The value was higher than those measured for implantation of various ions into the surface of sapphire [163-166] (typically 1 – 7.6 GPa), but was not unrealistically high. The fluences (ions/cm^2) of Focussed Ion Beams [167, 168, 225] are of the same order of magnitude, if not higher, to those used in previous work [163-166]: (10^{17} - 10^{18} cm^{-2}). The effect of the fluence on the mechanical properties is significant; inspection of Figure 2.18 shows that the toughness is doubled when the fluence is increased from 10^{15} to 10^{17} ions/cm^2. The relationship between the fluence and the mechanical properties explains why 1) there is such a variation in literature values, as different fluences are used, and 2) the residual stress may be much larger in this work than that previously measured as the FIB fluence was larger than those used in the literature.

It was possible that the foil could buckle if such a stress was on the top surface. The foil was assumed to be a strut under compressive loading (Figure 7.8 for dimensions). From [3], the critical force for the onset of buckling is, F_c:

$$F_c = \frac{\pi^2 E}{12} \frac{d_{foil} {b_{foil}}^3}{{w_{foil}}^2} \quad (9.1)$$

where d_{foil} is the thickness of the foil (≈ 100nm), b_{foil} the breadth (≈ 5μm), and w_{foil} the width (≈ 25μm). The critical force for buckling is 7 mN. If the residual stress was acting over the whole cross-section of the foil (i.e. $d_{foil}b_{foil}$), the force would be 6 mN. However, the stress was acting over an area of ($t_{ga}d$) in size (t_{ga} = 20nm); the force was thus 0.02 mN. The foil was unlikely to buckle, as seen in practice. Another possible outcome of the residual stress is

delamination from the sapphire [226]; this was also not seen in practice. Despite the high stress in the implanted region, the foil was expected to stay intact.

The accuracy of the residual stress measurement needs analysis. Firstly, it was possible that Poissonian stress relaxation occurred due to the foil production, and the measured stress is an underestimate. Secondly, the foil may not have been in uniaxial stress; some stress may have been accommodated in the thickness of the foil. This will affect the use of $\frac{1}{3}\Pi_m$ in Equation 2.15 (Π_m should be used if in triaxial stress) and the use of the Stoney equation (Equation 7.1). The overall effect would be that the measured residual stress is an overestimate. The thickness-to-height ratio was < 2%, suggesting that the uniaxial stress criterion was probably valid. Thirdly, the measured stress in the foil may have had a contribution from the inclusion of gallium ions. Although the gallium content due to a glancing beam was (0.4 +/- 0.1) at% (Section 4.6.1.2.), there may have been some variation in gallium across the foil (suggested the change in the peak width, Figure 7.10, which is indicative of a range of local stresses due to inclusions). However, the lattice stress due to inclusions should be minimal (Table 9.1).

It was unclear which of these effects would be the most significant; they may all be small relative to the experimental errors measuring the stress from the foil.

<u>The effect on the microcantilever beam mechanical properties</u>

The key effect of the gallium implantation is the resultant residual stress. There were several possible effects of the mechanical properties measured using microcantilever beams:

- **Young's modulus:** There will no effect of the residual stress on the measured beam stiffness.
- **Fracture strength:** The presence of the gallium implanted region (and thus residual stress) on the top surface of the beam may have altered the fracture strength. It is unclear was whether the implanted region is uniform across the top surface and

whether it is present underneath thermal grooves or other surface defects. If the implanted region is present under the thermal grooves, it is likely that the measured strength will be affected; a compressive stress of 12GPa across the top surface of the microcantilever beams would lower the stress intensity factor of the flaws and increase the measured fracture strength.

One way to understand if the residual stress had an impact on the fracture strength was by using the AES-11C beams that failed from flaws. Using the failure strength and the measured value of $K_{Ic,gb}$ (Section 8.2.6.), the flaw size was predicted using the Griffith equation (Equation 1.1.) and compared to the measured flaw size from SEM. From Figure 8.4, the measured flaw was 0.13µm deep and 0.29µm (i.e. 2c) wide. The expected flaw size using $K_{Ic,gb}$ = 1.4MPam$^{1/2}$ (Section 8.2.6.) is 0.06µm. For the other beams that failed from flaws, the predicted and measured sizes were within ≈ 20% of each other. Given the various errors involved (the precision of measuring the flaws, the accuracy of the value of $K_{Ic,gb}$), the correlation of the predicted and measured flaws was reasonable. However, further work is required to confirm whether the residual stress is affecting the fracture strength.

- **Stress Intensity Factor at failure:** The effect of the residual stress on the stress intensity factors at failure is huge for sapphire and polycrystalline alumina. As this effect is so important, and so interrelated to the notch bluntness, it is discussed in detail in Section 9.1.6.

Having considered two of the key FIB related effects for ceramics (formation of redeposited material and gallium implantation), the validity of measuring different mechanical properties with microcantilever beams can be discussed. Experimental data for sapphire and different engineering ceramics are given as examples; more detail of the microscale properties for each material is given in later sections.

9.1.3. Microcantilever beams - Young's modulus

Previous authors discuss the underestimation of the Young's modulus due to the aspect ratio (Section 2.6.2.). Rather than ensuring that the beam was of the correct aspect ratio, a more rigorous approach was taken in this work, The Young's moduli of the microcantilever beams were calculated by using simple beam theory (Equation 3.7) and corrected for the flexure in the fixed end using a factor dependent upon the aspect ratio (Appendix 3.2). The ability of the technique to correctly obtain the Young's modulus was assessed using un-notched beams in diffusion bonded sapphire (parallel to [0001]). The beams had a Young's modulus of (465 +/- 25) GPa; this corresponded well to the value determined from the elastic constants from Wachtman et al [215] of 463GPa.

One key drawback to the correction factors is that they were determined for an isotropic aluminium oxide material. Whilst this may be valid for polycrystalline materials with grains in different orientations, beams parallel to a single crystallographic direction may have a different magnitude of fixed end flexure. However, it is estimated that the magnitude of the fixed end flexure is proportional to the Young's modulus of the beam. As a result, the relative change in displacement due to fixed end flexure should be approximately the same for beams of different stiffnesses. Thus, using the results in Appendix 3.2 for all alumina based is reasonable. The issue with using it for other materials was that the Poisson's ratio may be different to alumina. However, as the Poisson's ratio for silicon nitride and alumina are almost identical [3], this effect is minimal.

The Young's moduli for un-notched beams on the surface of AES-11C and TM-DAR alumina were (447 +/- 38) and (476 +/- 41) GPa respectively. These corresponded well with each other, and showed that effects such as grain boundary composition had no effect on the modulus. Both also corresponded well with the modulus measurements from nanoindentation on AES-11C, (442 +/- 20) GPa (Section 4.10), as well as literature values for macroscopic tests: 380 [182], 402 [3] or (416 +/- 30) GPa [210].

The rare-earth doped silicon nitrides had moduli of (347 +/- 22) and (327 +/- 38) GPa for Lu- and La-dopant respectively. The moduli corresponded well to those of other rare-earth doped silicon nitrides: 318 – 342 GPa [227]. To the author's knowledge, Young's moduli of the same doped silicon nitrides are not in the literature for direct comparison.

In the absence of un-notched beams in annealed sapphire, the Young's moduli of notched beams were determined. An additional correction factor for the increased compliance due to the notch was determined using Equation A7.3.4., which considered both the position and the depth of the notch (in general, the effect on the Young's modulus was < 2%). The Young's moduli of beams parallel to [0001] after annealing at 1000^{o}C, 1100^{o}C, and 1200^{o}C were (503 +/- 62), (449 +/- 43), and (468 +/ 40) GPa respectively. Overall, the annealed beams had a modulus of (476 +/- 53) GPa. This corresponded very well with both the results of the unannealed beams and the results from Wachtman's elastic constants [215]. Hence, the annealing had no effect on the stiffness.

Overall, the microcantilever beam technique yielded modulus results in good accordance with the expected values for a variety of different ceramics.

9.1.4. Microcantilever beams - strength

The strength of microcantilever beams in various materials was determined in this project. The strengths were considerably higher than in macroscopic tests due to the vast differences in the fracture origin. Rather than failing from polishing or sintering defects, beams failed at grain boundaries. Fracture strength measurements are an excellent method to determine the inherent strength of grain boundaries in different engineering ceramics.

In this work, the strength of thermally etched ceramics are considered. To quantitatively measure the grain boundary strength, the contributions to the strength require consideration. There are two contributions (assuming an absence of a defect): the grain boundary strength itself and the thermal groove. The former is obviously the most important factor in determining the failure strength; in the absence of thermal grooving, beams still fail at the

grain boundaries [228, 229]. However, to quantify the fracture strength of microcantilever beams, the contribution of the thermal groove needs consideration.

Using Equation 3.8, the strength of the diffusion bonded boundary was found to be (5.2 +/- 0.1) GPa (Section 7.1.2.). The thermal groove (Figure 4.30) was of a consistent shape and depth along the bicrystal, suggesting a similar stress intensity factor contribution for all beams failed at the grain boundary. The depth of the notch (from Figure 4.24b) was ≈ 130 nm. Noting that K_{I0} of the bicrystal boundary was 0.7 $MPam^{1/2}$ and using the relationship between the toughness and strength for an surface flaw ($K = 1.12\sigma\sqrt{\pi\alpha}$), the strength contribution due to the groove was ≈ 1GPa. The effect on the measured strength is significant, and illustrates the importance of accounting for such features if quantitative strength values are required.

This is further emphasised when considering materials such as thermally etched AES-11C and TM-DAR aluminas. The mean failure strength and standard deviation from the seventeen beams AES-11C failed at the grain boundaries was (3.9 +/- 0.7) GPa. Conversely, for a purer alumina such as TM-DAR, the strength was (5.9 +/- 0.6) GPa. Whilst there is a significant difference between these mean values, the thermal etches were different between the two: 1450^{o}C for TM-DAR and1550^{o}C for AES-11C. As a result, the thermal grooves were likely to be different depths. AES-11C, with a heavier etch, is likely to have a greater strength reduction due to the groove; this is emphasised by the lower strength.

However, the extent of the thermal groove will also depend upon the grain boundary energy [69, 70] (itself due to composition and structure), and thus there is likely to be different thermal groove depths and shapes across an alumina sintered at one temperature. In AES-11C, for example, TEM-EDX of the grain boundaries (Section 4.8.1.) showed that there was a range in the amount of silicon at the grain boundaries: (0.14 +/- 0.08) at%, and SEM showed that abnormal grain growth occurred (Section 4.1.1). Such effects are typical of there being grain boundaries of different energies in the material [53]; this in turn can lead to

different thermal groove depths [69, 70]. As a result, to quantitatively determine the fracture strength of the grain boundary, the thermal groove depth and shape of each grain boundary of interest need to be determined prior to failure.

One important feature of all experiments was the analysis of the fracture surfaces. In the diffusion bonded sapphire, the fracture surfaces were smooth due to failure directly along the boundary (Figure 7.3). In AES-11C, the cracks were predominately intergranular (Figure 8.5); this corresponded very well with the macroscopic fracture surfaces (Figure 5.3). In silicon nitride, the beams often did not fall away from the fixed end (Figure 8.15); this was indicative that, whilst the beam had failed, there was enough grain bridging to cause the beam to not fall away. One interesting property of silicon nitride beams was the kink in the load-displacement curve followed by a change in compliance (Figure 8.13); this was due to a crack propagating along the grain boundary phase and subsequently being arrested by the elongated grains lying across the crack path. The stress needed to be increased to propagate the crack further. This phenomenon did not occur every test, and was dependent upon the microstructure under the surface. Presumably the microstructure was such that the grain boundary phase had failed but the elongated grains were still holding the fracture surfaces together. This was analogous to the work of microcantilever beams of carbon nanotubes in borosilicate glass [220] whereby the glass failed in loading but the nanotubes held the fracture surface together.

Overall, the failure strengths of the microcantilever beams in polycrystalline samples were very high. Qualitative comparison of the strengths and fracture surfaces correlated well with the macroscopic properties. Quantitative comparisons would require an understanding of the thermal groove of each boundary (as well as the residual stress due to the gallium implanted region). It might be possible to simply not perform the thermal etching stage; however, in doing so, effect such as failure from polishing defects may still be an issue [228, 229]. Hence, whilst some further work is required to assess how the quantitative values were

affected by these different contributions, the technique is highly useful for assessing many of the inherent properties of engineering ceramics.

9.1.5. Microcantilever beams – notch types

Four different notch types were used in this project and assessed using a sapphire bicrystal: straight through, controlled flaw, and chevron notch, and pseudo-chevron notch.

Chevron and Pseudo-chevron

The chevron notch and pseudo-chevron notch were discounted as viable methods due to the lack of stable crack growth prior to failure (Figure 7.1.4.). The most likely cause of the lack of stable crack growth was the residual stress (due to the gallium implanted region). This imparted an additional stress intensity factor on the notch such that, when the notch tip crack did propagate through the implanted region, the applied stress intensity factor was much greater than the toughness of the underlying material. Hence, the crack propagated rapidly through the material and the beam failed. This instability restricted the extent of stable crack growth in all notch types, and was most obvious for notches types that were only produced to induce such crack growth. However, as shown with the annealed beams (Section 7.5), stable crack growth may be possible once the residual stress was removed (although it is unclear whether stable crack growth or plasticity was the cause of the compliance change prior to failure). Thus, although such notch shapes were experimentally difficult to produce (especially aligning both sides of the notch across the beam), they could be useful to use in the future. However, due to a lack of time to produce such notches and anneal before testing, their usability was not tested further in this work.

Straight through notches

The straight through notch was generally produced to a depth of around 0.3µm using a beam current of 10pA. In single crystal and diffusion bonded sapphire, the notch was straight and parallel sided (Figure 7.4). In polycrystalline samples, the notch was often less so (Figure

8.6), although fracture surfaces may have appeared rougher due to pull-out of grains at failure. The stress intensity factor was determined using a compliance calibration method, following similar work of other authors [89, 141, 211-214], using compliance measurements from Finite Element simulations of microcantilever beams (Section 6.1). To the author's knowledge, this is the first full description and calculation of the stress intensity factor of a triangular shaped microcantilever beam.

The straight through notches were utilized in various ways. In materials such as diffusion bonded sapphire and AES-11C with large grains, straight through notches were placed across the boundary and the crack propagated along a specific boundary. In finer grained materials such as TM-DAR and silicon nitride, straight through notches were placed across many grains and the crack nucleated at the lowest toughness feature under the notch. Such notches were used in these fine grained materials for following reasons. Due to the lack of the channelling contrast in the ceramic materials, it was difficult to determine the microstructure underneath the top surface. Using controlled flaws, it was possible that the notch may not intersect a grain boundary at all. In silicon nitride, for example, controlled flaws often finished in a crystalline grain and thus the beam failed away from the notch. As such, straight through notches were very useful in fine grain materials as the likely of a crack nucleating along a grain boundary was high. Also, due to the nature of the simulations and the calculations, this notch type was also the most rigorous described.

Controlled Flaws

Controlled flaws were produced at boundaries in a variety of materials. These were fairly rectangular in shape (Figure 7.7). Initially, these were analysed following the procedure by Matoy et al [118]. This assumed that the material-bridges (Figure 2.14) failed first in loading (at low loads), and the microcantilever beam failed from a sharp, straight through notch of the depth of the initial FIB flaw. Hence, the stress intensity factor at failure is calculated using an equation for a straight through notch. There were issues with this approach:

1) The authors show load-displacement curves that do not have a change in compliance; this would be expected if there was crack extension prior to failure. The authors do not present any conclusive evidence that the material bridges fail first.
2) Using the Matoy approach on the ceramics tested in this work, the applied stress intensity factor at failure was significantly larger than those of genuine straight through notches: (4.7 +/- 0.2) and (2.9 +/- 0.1) $MPam^{1/2}$ respectively.

Hence, this approach was not used in this work.

Instead, the stress intensity factors were determined using an analytical equation from Strobl et al [144] (Equation 6.26) using the factors given in full in Appendix 6.1. The Strobl equations were for elliptical flaws, but they were used here in lieu of suitable equations for the shaped flaws produced by the FIB. Ideally, Finite Element simulations of controlled flaws would have been performed and a calculation for the stress intensity factor determined. However, due to time constraints, it was not possible in this work. For each controlled flaw, the dimensions of the flaw needed to be analysed. As the Strobl equations were based on only certain values of $\frac{\alpha}{b}, \frac{\alpha}{h^*}, \frac{b}{w}$ (α = notch depth, w = half width of beam, h* = $^2/_3$ height of beam, b = half width of notch), only certain notch dimensions were acceptable; the criteria for the use of these equations were defined in Section 6.2.

Nonetheless, the controlled flaws were very useful in the polycrystalline ceramics such as AES-11C; these could be placed on a given boundary and so the toughness of a specific boundary could be ascertained. The straight through notches across many grain boundaries was useful for many materials, but fracturing from a specific boundary was also useful in this work and, as such, controlled flaws were very useful.

These equations were deemed to be valid for this work. As the width of the flaw was small relative to the beam width, the flaw acted like a surface flaw independent of the beam shape. To ensure that this was the case, additional criteria were given (Section 6.2) beyond those from Strobl et al [144].

In order to confirm that these equations were valid, direct comparison between straight through notches (using Equation 6.25) and controlled flaws (using Equation 6.26) was made for the sapphire bicrystal: (0.7 +/- 0.2) and (0.5 +/- 0.1) $MPam^{1/2}$ respectively. The controlled flaw analysis method also gave consistent results for other materials: for example, fracturing on the a-plane (Table 8.2), c-plane (Table 8.4), in AES-11C (Tables 8.9 and 8.10). Thus, whilst the equations used to determine the stress intensity factors of the controlled flaws were for semi-elliptical flaws, the results validated the technique.

9.1.6. Microcantilever beams – stress intensity factors at failure

Analysis of the use of microcantilever beams to determine the toughness of ceramics was discussed in this work in view of several key aspects of the Focussed Ion Beam milling process:

1) Moisture assisted sub-critical crack growth
2) Residual stress in the gallium implanted region at tip of notch
3) Sharpness of the notches
4) Redeposited material at tip of notch and around the beam

Most microcantilever beam studies, both in metals and in silicon, have been performed without consideration of all of these factors (see Section 2.6.5 and 2.6.6.)). Hence, the following sections form one of the first thorough descriptions of the consideration of the microcantilever beam testing.

9.1.6.1. Moisture assisted subcritical crack growth

Several key experiments considered if environmental assisted sub-critical crack growth could occur and, if so, what the stress intensity factors at failure were.

1) Theoretical model to assess which region beams should fail in in air
2) Beams broken in water; these can be compared to literature values of K_{I0}
3) Beams broken in oil: these can be compared to literature values of K_{Ic}.

Numerical analysis predictions of the crack growth (Section 7.4) showed that the beams should fail in Region I (i.e. undergoing moisture assisted sub-critical crack growth) and the stress intensity factor at failure should be close to K_{I0}. At it is difficult to estimate the crack velocity at failure, comparison with the date in Figure 2.20 is problematic.

Material	Environment	K_{fail} ($MPam^{1/2}$)	$K_{fail} \approx ?$	Literature value ($MPam^{1/2}$)	Literature Value ($MPam^{1/2}$)
Sapphire, fract m-plane	Submerged in water	0.9 +/- 0.2	K_{I0}	0.9 [222]	1.5 [178]
Sapphire, fract m-plane	Submerged in silicone oil	3.4 +/- 0.6	K_{Ic}	3.14 +/- 0.30 [147]	2.35 +/- 0.07 [231]
Sapphire, fract m-plane	In air, 50% relative humidity	1.5 +/- 0.2	$K_{I0, air}$	0.9 [222]	1.5 [178]

Table 9.2: Comparison of stress intensity factors of microcantilever beams in different environments with literature values for the stress intensity factors at failure.

The stress intensity factors at failure (after correcting for notch bluntness and residual stress) in different environments are given in Table 9.2, together with the expected values. The key results are that:

1) The stress intensity factors are in the order Water < Air < Oil, as expected.
2) The stress intensity factor at failure of beams submerged in water corresponded well to the literature values of K_{I0}.
3) The stress intensity factor at failure of beams submerged in silicone oil corresponded well to the literature values of K_{Ic}.
4) Points 2) and 3) suggest that the corrections for bluntness and residual stress are sound.
5) The variation between the values tested in air and water was related to the increase in the number of active reaction sites [5, 223]; such variation in stress intensity factors at failure are seen elsewhere [176, 178, 232, 233].

The majority of microcantilever beams tested in this work were tested in air, giving a stress intensity factor of $K_{I0,\,air.}$ Table 9.2 shows that the corrections for notch bluntness and residual stress are reasonable, and the resultant stress intensity factors for beams submerged in oil and water are close to the literature values. Hence, whilst there is often no direct comparison for $K_{I0,\,air}$ in the literature, the corrections can be used with confidence.

It should be noted that there is often significant scatter in the values of K_{I0} measured macroscopically; this is clear from Table 9.2. For fracture on the r-plane from [178], for example, K_{i0} is between 0.8 and 1.6 $MPam^{1/2}$. Microcantilever beams, submerged in water, may offer a far more accurate and reproducible measure of K_{I0} in a variety of different ceramics.

9.1.6.2. Residual stress & Notch bluntness

Corrections for residual stress and notch bluntness were used in this project (Section 7). The key factors defining the use of these corrections are:

1) The radii of the notches, and the effect on stress intensity factor at failure
2) The magnitude of the residual stress under the notch tip.
3) The characteristic notch tip crack length dα

These characteristics are intrinsically interlinked, and all need to be determined if quantitative values of the stress intensity factors at failure are required.

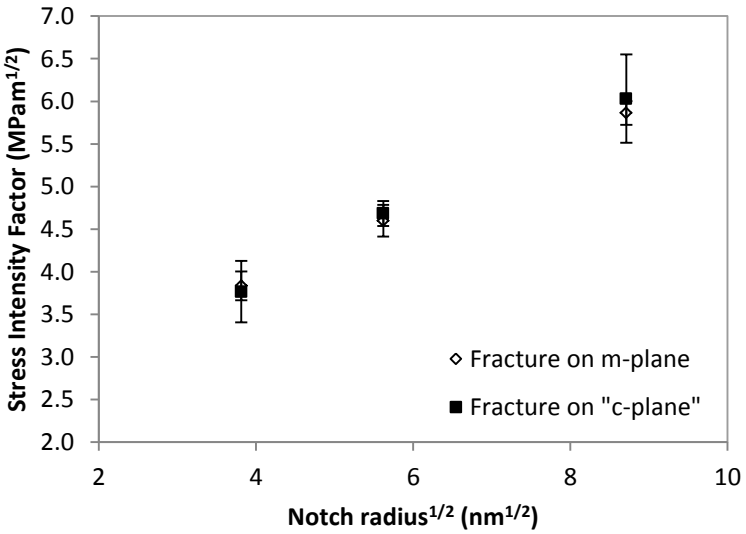


Figure 9.3: Stress intensity factor against square root of notch radii for beams on the surface of a-plane sapphire notched parallel to the m- and c-planes

Preliminary work (Section 7.1) with diffusion bonded sapphire showed that the applied stress intensity factors at failure (using Equation 6.25) were much higher than K_{I0}. This was true of all notch radii tested (Figure 9.3, compared to literature values in Table 9.2). Furthermore, applied stress intensity factors at failure (using Equation 6.25) increased with notch radius; Figure 9.3 looks very similar to plots from macroscopic tests [151, 212] for blunt notches. Hence, a correction term for the notch bluntness needed to be considered. However, there was also an effect of the residual stress at the notch tip due to the gallium implanted region (Section 9.1.3). These two effects are inter-related, and both are causing the stress intensity factor to be overestimated.

Correcting for notch bluntness using Picard's [148] method was erroneous as

1) the correction term for a FIB-milled notch of 15nm is ≈ 1, which cannot explain why the applied stress intensity factors (Figure 9.3) were larger than K_{I0}.
2) the method cannot explain the change in measured stress intensity factor at failure with notch radius; notches of 32 and 76nm also have correction terms of ≈ 1. This does not corroborate with Figure 9.3.

It is unclear why the Picard et al [148] method is so poor at explaining this FIB results. It could be that there is no consideration of the notch tip residual stress (the authors developed the equation for macroscopic specimens, so this was not a consideration). The correlation between the predicted and experimental results (Figure 2.15) is also not strong, suggesting that the equations may not even be valid for macroscopic specimens. Hence, this method is not considered further.

Instead, the method of Fett and Munz [149, 150] was used. There were two correction factors: 1) a weighted tanh function for the notch bluntness and 2) a stress intensity factor contribution due to the residual stress. These were outlined and discussed in Section 7. These corrections relied on several assumptions. Firstly, it was assumed that there was a sharp notch tip crack of length dα in front of the notch. Secondly, it was assumed (for

sapphire) that dα was smaller than the implanted region and thus the crack was being affected by the residual stress (if dα is larger than the implanted region, the residual stress will act behind the crack tip and thus give a smaller stress intensity factor contribution). Thirdly, it was assumed that the value dα was the same for all notch radii and thus the value could be determined from the overlap of the curves (Figure 7.14). Whilst these assumptions appeared to be valid for aluminium oxide, they did not appear to hold for silicon nitride (Section 8.5.2.).

One key question is what the physical meaning of dα is. Macroscopically, it was assumed to be related to machining damage and dependent on the microstructure of the ceramic [151]. Clearly, in materials such as sapphire, there is no microstructure so such an assumption cannot be made. Even in polycrystalline samples where the dimensions of the beams are on the order of the grain size, a crack of the order of 2 – 3 times the grain size [151] is not present. Hence, the interpretation of dα in microcantilever beams is fundamentally different to macroscopic specimens.

One possibility is that the residual stress is not uniform in the implanted region (due to the non-uniform penetration of ions into the surface [234, 235]), and dα relates to the some critical penetration depth of gallium ions. A more exciting possibility is that the length relates to some atomic scale bond breaking. If the theoretical strength of the material could be estimated as being E/10 [5], then some critical distance in front of the blunt notch, r_c, (beyond which no bonds have broken) can be estimated using Equation 9.3.

$$\sigma = \frac{E}{10} = \frac{K_c}{\sqrt{2\pi r_c}} \tag{9.3}$$

Using K_{Ic} of (3.4 +/- 0.6) MPam$^{1/2}$ (Table 9.3) and E of 400GPa, r_c = (1.2 +/- 0.4) nm. However, this assumes that the crack is sharp.

Alternatively, the Creager and Paris [221] equation A7.1.1. for a blunt notch could be used. This takes r = 0 ρ/2 behind the notch tip. Hence, $r_c \approx$ 4nm. The estimated value of dα for

sapphire was (7 +/- 2) nm (from Figures 7.14 and 7.15). Hence, it is possible that dα is related to some critical distance dependent upon the breaking of atomic bonds.

Another explanation for the fracture was that there was no notch tip crack, but instead the failure occurred in front of the implanted region. Noting that the implanted region was around 20nm and using the Creager and Paris [221] equation, the stress in front of this would be around 11GPa. This is lower that the theoretical strength of the material, but still represents a high stress. If a flaw is present in front of the notch tip, it is possible that the sample would fail under this stress in front of the implanted region. In silicon nitride, for example, there was a number of features (low strength boundaries, pores etc.) that the sample may have failed from; as a result dα was likely to be larger than the implanted region and dependent upon the microstructure, flaw density etc.

Further investigation is required to elucidate the nature of dα, especially in single crystals which do not have identifiable flaws in front of the notch tips. What is likely is that dα will be different for each material, and would need identification for each material to ascertain quantitative toughness values. Whilst the physical interpretation of the characteristic notch tip crack length was not determined here, the method for determining the corrections factors for the notch bluntness and residual stress (which use dα) resulted in stress intensity factors in good accordance with the results measured elsewhere (Section 9.1.6.1.).

9.1.6.3. Effect of annealing

Beams were annealed in vacuum to attempt to remove the residual stress (Section 7.5) (previous work [169] showed that the stress due to implantation in sapphire decreased by up to 80% after annealing at 900^{o}C). Those with straight through notches away from the boundary underwent a compliance change prior to failure (Figure 7.18) but those notched at the boundary did not (Figure 7.19).

Notched at the boundary

For beams notched at the boundary (where no compliance change was detected), the stress intensity factor at failure for beams notched at the boundary (three beams) was (0.9 +/- 0.2) $MPam^{1/2}$. This was in good accordance with the beams notched at the boundary without annealing of (0.7 +/- 0.2) $MPam^{1/2}$, despite no correction for notch bluntness being used for annealed beams (as dα was not known).

Notched away from the boundary

There were two possibilities for the compliance change during loading: plasticity or crack extension. Table 9.3 highlights evidence for and against the two hypotheses.

Whilst there was no conclusive physical evidence from fracture surfaces to suggest either crack extension or plasticity, the most likely cause was notch tip plasticity. If plasticity was occurring, the stress intensity factors at failure were close to $K_{I0,\ air}$ measured before annealing. If the crack was extending, the stress intensity factor at failure would be significantly larger than before annealing. This is the most conclusive evidence for plasticity being the cause of the compliance change.

From Section 9.1.6.2., the stress in front of the notch tip is around 11GPa. This is a high stress and, considering that basal twins were expected to form between 7.3GPa [32] or 7.7GPa [36] and rhombohedral twins between 3GPa [23] and 3.6GPa [32] (Section 2.1.2.), it is possible that some plasticity is occurring prior to failure More work (such as that suggested in Section 10) is required to determine if plasticity is occurring and, if so, the plastic zone size. If plasticity was occurring, then dα may be related to the plastic zone size and failure may occur from some plasticity feature.

Hypothesis	Evidence for	Evidence against
Plasticity	(1) Stress Intensity Factors at failure (1.7 +/- 0.2) ≈ those before annealing (1.5 +/- 0.2) $MPam^{1/2}$ (2) Explains difference in behaviour between "at" and "away" from boundary (plasticity unlikely at grain boundary) (3) Stress at notch tip high (and > critical stress for plasticity, see Section 2.1.2.).	(1) No evidence from SEI of fracture surfaces.
Crack Extension	(1) Some evidence from SEI of fracture surfaces (1000°C anneal) (2) Similar effect seen in silicon nitride.	(1) No evidence from SEI of fracture surfaces (1100, 1200°C anneal) (2) K_{fail} (2.6 +/- 0.3) $MPam^{1/2}$ > before annealing (1.5 +/- 0.2) $MPam^{1/2}$ (3) No physical interpretation of extension ≈ 0.2 μm before failure; (4) Difference in behaviour between "at" and "away" from boundary; may not expect difference if extension

Table 9.3: Evidence for and against cause of compliance change prior to failure in annealed sapphire microcantilever beams.

One further complication is what happens to the gallium ions during annealing. Significant diffusion/volatilisation of gallium may affect the microcantilevers. These are considered.

Diffusion of gallium in sapphire

The extent of diffusion during annealing can be considered using Equation 9.4. The diffusion coefficient, D_{ga}, is 3.89 x 10^{-20} m^2/s at 1400°C [236] (in lieu of data at lower temperatures, this value was used). The concentration at a given depth and time $C(x, t)$ is given by:

$$C(x,t) = \frac{Q}{\sqrt{\pi D_{ga} t}} \exp\left(-\frac{x^2}{4Dt}\right) \quad (9.4)$$

where Q is the number of supplied atoms per unit area (this was estimated from the density and composition of the redeposited material which was assumed, for simplicity, to be an un-depleting source). The anneal time was 3600s. The relative change in Q with distance was estimated (Figure 9.4); there was very little gallium diffusion into the sapphire surface, even with using the overestimated value of D_{ga}. This was confirmed from the TEM-EDX of an annealed notch (Section 4.9) which showed that the gallium was localised to the tip of the

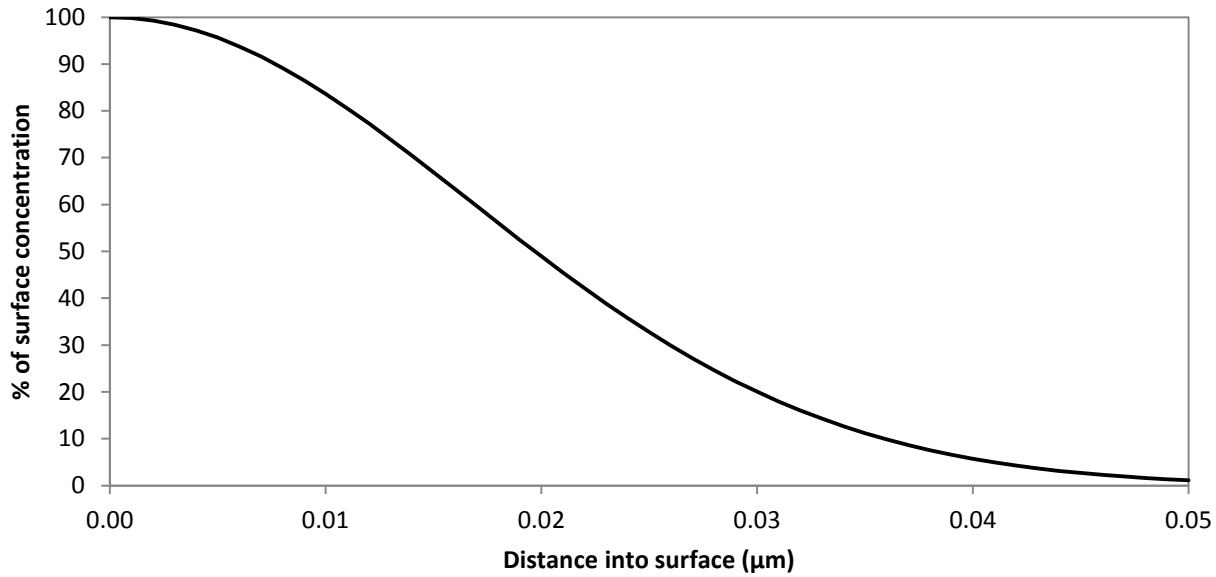


Figure 9.4: Estimation of relative concentration of gallium ions into the surface during annealing

notch. Hence, diffusion of gallium during annealing was not a critical effect.

Volatisation

Another possibility was that the gallium volatised during the annealing. Previous work [170] shows that, whilst heating FIB milled $BaTiO_3$ in air causes the formation of gallium oxide, the extent of gallium oxide reduces during a vacuum anneal at 700^{o}C. This was confirmed by other work that shows that gallium depletion (on the surface of $La_3Ga_5SiO_{14}$) occurred during vacuum anneal at 1000^{o}C due to the formation of a volatile Ga_2O oxide [237]. As the redeposited material included elemental gallium, it was possible that such a volatile oxide could form during annealing. There was still a significant amount of redeposited material present after annealing (Figure 4.49); it was probable that this was gallia-alumina solid solution which had a lower propensity to volatilise during annealing. The overall effect of annealing on the gallium rich regions needed further investigation, but was likely to be minimal.

Summary

There were some encouraging results from the annealed beam series. The stress intensity factors at failure of beams notched at the boundary corresponded well to those before annealing, despite no correction for notch bluntness. If plasticity was occurring in beams notched away from the boundary, the stress intensity factors at failure were in good accordance to those without annealing. However, there were some key unknowns that need further investigation before quantitative values can be confidently given: 1) the value of dα, 2) the residual stress (i.e. if all was removed), 3) the structure and gallium content at the notch tip.

9.1.7. Microcantilever beams – Summary

The microcantilever beam method was very successful to measure various mechanical properties on the microscale. Quantitative values can be obtained using the microcantilever beam technique, providing that correction factors are used (Table 9.4). The microcantilever results discussed in the following sections are corrected in the appropriate manner.

Mechanical Property	Correction Factor	Material(s) tested to determine validity	Comparison with literature values
Young's modulus	Flexure in the fixed end (value dependent on aspect ratio of beam)	Sapphire, polycrystalline alumina, silicon nitride	In good accordance with literature values (Section 9.1.3.)
Fracture Strength	None, although need to assess effect of residual stress (gallium implantation)	Sapphire bicrystal, polycrystalline alumina, silicon nitride	Higher, due to small flaw sizes.
Stress Intensity Factor at failure	1) Residual stress at notch tip 2) Bluntness of notch radius	Sapphire, sapphire bicrystal	If submerged in oil ≈ K_{Ic} If submerged in water ≈ K_{I0} In air, good accordance with $K_{I0,\ air}$

Table 9.4: Summary of mechanical properties, measured using microcantilever beams, with details of the corrections required and how the corrected values compare to literature data.

The following sections discuss microcantilever beams results, as well as the macroscopic mechanical properties, composition, and characteristics for the following materials:

- Section 9.2: Sapphire
- Section 9.3: Polycrystalline alumina (AES-11C v TM-DAR)
- Section 9.4: Polycrystalline alumina with and without carbon
- Section 9.5: Polycrystalline alumina with and without chromium doping
- Section 9.6: Rare-earth doped silicon nitride

9.2. Sapphire

Some of the key sapphire results are discussed previously (e.g. Sections 9.1.6.1.) due to the material being used to validate the technique.

$K_{I0,air}$ was determined for a variety of single crystal sapphire planes (Section 8.1). Notches were produced parallel to a-, m-, and c-plane sapphire as well as away from low-index planes. The stress intensity factors at failure for a- and m-plane sapphire (50% relative humidity) were close to each other and to data from previous work with similar humidities [178]: (1.4 +/- 0.2) and (1.5 +/- 0.2) $MPam^{1/2}$ respectively. When notched with the 10pA beam current, fracture surfaces were smooth due to fracture along the specific plane (fracture surface roughness increased with notch radius due to increased crack bifurcation). This gives confidence that the fracture of these beams is occurring in the expected manner.

Notching away from low-index planes (i.e. parallel to the c-plane, and 30^o and 60^o away from the c-axis) produced very facetted fracture surfaces (Figures 8.3, for example). As no low-index fracture plane was readily available, the crack propagated by diverting between different planes. However, the $K_{I0,air}$ values were close to the values for a- and m-planes: (1.5 +/- 0.2) $MPam^{1/2}$ notched parallel to the c-plane, (1.7 +/- 0.3) and (1.6 +/- 0.2) $MPam^{1/2}$ notched 30^o and 60^o from the c-axis. Whilst there was more faceting, the stress intensity factor to *initiate* crack propagation was the same regardless of the resultant crack path thereafter. This nicely illustrates the difference between long and short crack toughness; a tortuous crack path would affect the long crack toughness (as the crack extends energy is dissipated by the faceting), but the short crack toughness (i.e. to start fracture) will be similar.

This testing in sapphire also shows that, whilst a- and m-plane are low-index planes, their toughness is fairly similar to random orientations in sapphire. From Finite Element Analysis of fracture on different cleavage planes during thermal shock [238] and molecular dynamics simulations [239], there is a difference in fracture toughness between different fracture planes in sapphire. However, as the fracture (when notched away from low-index planes)

does not occur along one specific plane, it is not surprising that the measured toughnesses are very different to those estimated from FEA. Using the predicted values of K_{Ic} for seventeen different planes [238], the mean predicted K_{Ic} is (3.2 +/- 1.2) $MPam^{1/2}$. By noting that the ratio between $K_{Ic}/K_{I0,air}$ is (2.3 +/- 0.5) (Section 9.1.6.1) the estimated mean values of K_{I0} from this Finite Element Analysis [238] is ≈ 1.4 $MPam^{1/2}$. Hence, the values of K_{I0} for fracturing on random sapphire planes determined in this work are close to what might be expected theoretically.

Overall, the sapphire results show that:

1) Beams fractured in air (50% relative humidity) undergo moisture assisted sub-critical crack growth.
2) The values are close to previous results performed macroscopically.
3) Beams fractured away from low-index planes have facetted fracture surfaces, but the stress intensity factors at failure are the same as for low-index planes.
4) The technique could be a viable alternative to macroscopic testing to determine K_{I0} at different humidities, and improve on the scatter seen in previous work [178, 222]

9.3. AES-11C and TM-DAR alumina

In order to compare and contrast the properties of these two aluminas, the various properties (compositional, microstructural, mechanical) are summarised in Table 9.5. The following sub-sections focus on various important characteristics of the two aluminas, in order to explain the properties shown in Table 9.5. After considering the composition and microstructure of the materials, the mechanical properties are considered.

Property	Section	AES-11C	TM-DAR
Powder Purity (%)	3.1.1., 3.1.2.	99.8	> 99.99
Grain Boundary Composition	4.8.1., 4.8.3.	(0.14 +/- 0.08) at% Si (TEM-EDX)	No impurities detected (TEM-EDX & EELS)
Relative Density (%)	4.2.1., 4.2.3.	1600^{o}C: 99.7 +/- 0.7 1750^{o}C: 99.9 +/- 0.6	1600^{o}C: 99.8 +/- 0.8 1750^{o}C: 99.7 +/- 0.4
Grain Size (µm)	4.1.1., 4.1.4.	1600^{o}C: 2.7 +/- 0.9 1750^{o}C: 7.6 +/- 2.1	1600^{o}C: 4.3 +/- 0.7 1750^{o}C: 5.1 +/- 0.9
Microstructural Description	4.3.1., 4.3.2.	Twinned grains, abnormal grain growth	Some abnormal grain growth
GB Toughness ($K_{I0,\ air}$) (MPam$^{1/2}$)	8.2.6., 8.4.1.2.	0.6 +/- 0.1	0.7 +/- 0.1
Microcantilever Strength (GPa)	8.2.1., 8.4.1.1.	3.9 +/- 0.7 (Thermal Etch: 1550^{o}C)	5.9 +/- 0.6 (Thermal Etch: 1450^{o}C)
Macroscopic fracture toughness (K_{Ic}) (MPam$^{1/2}$)	5.3	3.5 +/- 0.2	3.8 +/- 0.1
Uniaxial Compression Strength (GPa)	5.4.1.1.	1600^{o}C: 3.2 +/- 0.3 1750^{o}C: 1.7 +/- 0.1	1600^{o}C: 3.7 +/- 0.3 1750^{o}C: 2.6 +/- 0.2
Flaw Density (= N_A) (µm^{-2})	5.4.3.1.	1600^{o}C: 0.03 1750^{o}C: 0.003	1600^{o}C: 0.006
D_0 (=$\pi a^2 N_A$) (a = ½ mean grain size)	Equation 2.9	1600^{o}C: 0.16 1750^{o}C: 0.15	1600^{o}C: 0.09

Table 9.5: Comparison of characteristics of two aluminas, AES-11C and TM-DAR.

9.3.1. Grain boundary composition and microstructure

The characteristics discussed in this sub-section are:

1) The grain boundary composition and the spatial resolution in measuring it.
2) Characterising the aluminas and tentative estimation of complexion classes
3) The presence of twins, and their structure
4) The presence of spinel grains in TM-DAR
5) Flaw size and distribution

Grain Boundary Composition

It was assumed that the silicon detected at grain boundaries (using TEM-EDX, Table 9.5) was present as SiO_2. Previous work [28] showed that the grain boundary phase of liquid phase sintered alumina had around 30 wt% SiO_2. The extent at the grain boundaries was considerably lower than this. Hence, in order to fully analysis the spectra, the spatial resolution needs consideration. The spatial resolution is:

$$R_s = \frac{B_d + R_{max}}{2} \tag{9.5}$$

where $R_{max} = (B_d{}^2 + B_s{}^2)^{1/2}$ [66], B_d the beam diameter and B_s the beam spreading. From [73]:

$$B_s = 7.21 \times 10^5 \frac{Z}{E_0}\left(\frac{\rho}{A}\right)^{\frac{1}{2}} t^{\frac{3}{2}} \tag{9.6}$$

where t is the foil thickness (in cm), E_0 the beam energy (in eV), ρ the density (in g/cm^3), A the atomic weight, Z the atomic number.

The beam diameter (JEOL 2000FX, Spot size 5L) was approximately 74nm. Noting the various constants for Al_2O_3, the spatial resolution (Equation 9.5) is estimated to be 78nm. Hence, as the grain boundary was significantly narrower than this (e.g. Figure 4.24b), much of the signal emanated from the grain either side. As a result, the silicon concentration at the grain boundary will have been considerably higher than presented here. Furthermore, some

silicon may have been present at TM-DAR grain boundaries but, as much of the x-ray signal came from the grains, the silicon peak could not be resolved.

Characterising the alumina

There was a large variation in silicon measured on different AES-11C boundaries, suggesting a variety in the type of grain boundary complexions (as shown in [71] for silica doped alumina). As silicon was at the grain boundaries in AES-11C, it could be characterised as a liquid-phase sintered alumina (although HRTEM would be required to confirm this). This was further suggested by consideration of microstructure (Figure 4.1); the triple point angle was often around 90^{o} which is only possible if a wetting phase is present. Liquid-phase sintered alumina often contains basal annealing twins [26, 27], as detected here (Section 4.3.5.). The boundary of AES-11C was probably complexion class IV - VI (Figure 2.4) (although HRTEM, such as shown in [71], would be required to confirm this). As discussed in Section 2.3, there may have been a range of complexions in the alumina to cause abnormal grain growth; the range in grain boundary silicon also eluded to a range of grain boundary complexions.

TM-DAR had no detectable silicon (or other impurities) at the grain boundaries using TEM-EDX. Electron energy-loss spectroscopy (EELS) was used to measure the composition of TM-DAR boundaries. Whilst it was possible to detect edges for aluminium and oxygen (Figures 4.36 and 4.37), no other grain boundary impurities were detected. As the extent of abnormal grain growth was lower than in AES-11C, the range in the complexions type was expected to be lower; it was expected that complexions would be in the class I – III range (Figure 2.4). High-resolution TEM would be required to confirm this.

The difference in the propensity for abnormal grain growth to occur was highlighted in the difference in grain sizes between 1600 and 1750^{o}C anneal (Table 9.5). Whilst AES-11C had a finer gran size than TM-DAR at 1600^{o}C, the grain size was much larger than TM-DAR after

1750^{o}C anneal. Much more abnormal grain growth occurred in AES-11C during the 1750^{o}C anneal, thus drastically increasing the mean grain size

Twins

Twin-matrix boundaries in AES-11C had (3 +/- 1) at% potassium with some calcium present (Section 4.3.4.); whilst this was not given as an impurity in AES-11C (Section 3.1.1.), the purity of the alumina was 99.8% and so some cation impurity was likely. There were two possible explanations for the twins.

Firstly, they were basal annealing twins in an α-Al_2O_3 grain; previous work has shown that basal facets [203] or twins [29, 240, 241] tended to be preferred sites for cations. TEM work showed that, as the amount of chromium increased, the number of twinned grains decreased (Section 4.3.3). Chromium oxide reduced the sinterability of the alumina (as seen by the change in relative density, Figure 4.11); if these twinned grains were annealing twins, it would be expected that a reduced sinterability would inhibit the growth of these.

Secondly, the structure may have been a β-Al_2O_3 structure with alternating twin planes with ordered impurities between (e.g. Figure 2.2) [29]. The effective repeating unit of the β-Al_2O_3 was around 2nm [29]. This was similar to twins imaged in this project (Figure 4.15): (2.1 +/- 0.4) nm. Such a structure may also explain the high number of additional diffraction spots (Section 4.3.5.) when most diffraction patterns of twins give rise to only one or two [26, 27, 187].

Based on the number of diffraction spots and the amount of potassium, the more likely explanation was that the grains were β-Al_2O_3 formed of basal chemical twins. Furthermore, as TM-DAR is a purer alumina (and thus fewer impurities to form such grains), it would explain why twins were not present. HRTEM would be required to assess the structure of the twin. Overall, the low frequency of these through the material suggested that, whilst an interesting feature of AES-11C, it was not hugely important to the mechanical properties.

Spinel in TM-DAR

In TM-DAR, one grain had a strong magnesium edge (Figures 4.42). It was probable that this grain was some magnesium-aluminium structure (possibly $MgAl_2O_4$ spinel, although electron diffraction would be required to confirm this). It was unclear whether this was a pre-existing particle due to the powder processing or formed during sintering. If a significant amount of the magnesium was being used to form such particles, the grain boundary concentration would be substantially lower than originally expected. This would explain why, despite the additional of 0.25 wt% magnesium (suggested by Coble [55]), there was still some abnormal grain growth and some triple point angles at 90^o (Figure 4.6).

Flaw size and distribution

Low magnification TEM was used to determine the type, size, and distribution of flaws. In AES-11C, the flaws per unit area were different between 1600 and 1750^oC sinters (due to the difference in grain size). However, as expected, the damage factors D_0 were the same[2] (Table 9.5). These factors were around double that of TM-DAR, suggesting that the flaw density in TM-DAR is lower. The grain boundary flaws in alumina may have been a thick layer of liquid phase (Figure 5.17 suggests this); this would explain the difference in flaw density between TM-DAR and AES-11C (the latter of which has more liquid phase present).

Summary

Overall, TM-DAR had 1) a higher purity than AES-11C, 2) no detectable silicon (or other impurities) at the grain boundaries, 3) more normal grain growth than AES-11C (although some abnormal grain growth still present) and 4) had no basal twins. As such, it was less likely than AES-11C to be a liquid phase sintered alumina.

[2] These factors were determined using Equation 2.8 by assuming that 1) all the flaws were of the same size and shape, 2) the mean flaw size (= 2a) was equal to the mean grain size, such that "a" could be determined, 3) the keys flaws were those at the grain boundaries (i.e. pores were not significant).

The following sections consider how these differences in compositions affect the mechanical properties on the micro- and macro-scale.

9.3.2. Mechanical Properties

Fracture Toughness

The stress intensity factors at failure for the grain boundaries, $K_{I0,\ gb}$ (air), measured from microcantilever beams (using the corrections discussed in 9.1.6.2.) were (0.6 +/- 0.1) and (0.7 +/- 0.1) $MPam^{1/2}$ for AES-11C and TM-DAR respectively. To the author's knowledge, this is the first direct measurement of K_{I0} of grain boundaries in alumina and, as such, comparisons with literature values are difficult. Experiments on alumina using "short cracks" (20 - 60μm) give K_{I0} of (1.2 +/- 0.3) $MPam^{1/2}$ [242], but this must also include some long-crack stress intensity contributions (e.g. crack deflection, micro-crack toughening [243], and crack bridging by un-fractured grains [244]). TM-DAR was tested elsewhere submerged in water [245] with K_{I0} between 2.5 and 3.0 $MPam^{1/2}$; again, long crack stress intensity factor contributions were present.

Whilst it was difficult to compare directly with literature values, the good accordance for K_{I0} for sapphire (Section 9.2) with literature work suggests that grain boundary values should also be in good accordance with the true values. Furthermore, previous work [246] showed that the ratio between fracture energies for non-special grain boundaries and the sapphire matrix was ≈ 0.54. In this project, the ratio $K_{I0,\ gb}$ / $K_{I0,\ sapp}$ was (0.5 +/- 0.1). This further suggests that the measured boundary toughnesses were close to the true values.

There are some literature values and estimations for K_{Ic} of grain boundaries of alumina. Some estimates are 2.1 $MPam^{1/2}$ [247], and between 2.1 and 2.5 $MPam^{1/2}$ [248]. These still use macroscopic techniques which probably include some additional toughness contributions. An estimate of K_{Ic} of the grain boundaries could be made by using the ratio K_{Ic} / $K_{I0,\ air}$ of sapphire: (2.3 +/- 0.5) (Section 9.1.6.1). Using this value as a conversion between $K_{I0,\ air}$ and K_{Ic}, $K_{Ic,\ gb}$ for AES-11C and TM-DAR was estimated to be (1.4 +/- 0.4) and (1.6 +/-

0.4) MPam$^{1/2}$ respectively. These values are lower than the literature values of K_{Ic} due to the lack of long-crack toughening mechanisms.

$K_{I0,gb}$ of TM-DAR and AES-11C are within the error of each other, despite the differences in the grain boundary composition (Table 9.5). There are several possibilities for this effect. Firstly, it could that there *is* a difference in the grain boundary toughness, but the errors are relatively large and thus the values cannot be distinguished. Secondly, although there was a difference in the silicon concentration measured at the grain boundaries (Table 9.5), there was silicon at boundaries in both TM-DAR and AES-11C boundaries (but the amount in TM-DAR was lower than could be detected by either EDX or EELS) and as such the grain boundary toughness was similar. Thirdly, there was a difference in the grain boundary composition but the grain boundary toughness is unaffected by the composition.

Consideration of the long crack fracture toughness (K_{Ic}) (Table 9.5) suggests that there is a small difference in fracture toughness between TM-DAR and AES-11C (both sets of values corresponded well with previous data [210]). However, as the microstructures (grain size, extent of abnormal grain growth) were different (Table 9.5), the long crack toughening mechanisms may be different and, as such, the variation in the long-crack toughness may not simply be down to a difference in the grain boundary toughness.

Overall, the most likely explanation is that, whilst the grain boundary composition may be different between the two aluminas, the grain boundary toughness is fundamentally the same. As a result, the difference in the macroscopic fracture properties must be due to other factors such as defects and flaw distributions.

Uniaxial Compression Strength

The compressive strengths in Table 9.5 corresponded well to literature values [15, 182, 210]. There was a noticeable difference in the uniaxial compression strength between the sintering temperatures (1600 and 1750^{o}C) and between AES-11C and TM-DAR (Table 9.5). The most likely cause of this was the internal flaw defect distribution and the damage factor D_0 (the

polishing and surface finish should be consistent, so this is likely to not be an effect). There is evidence to suggest that final failure during uniaxial compression is related to the growth and coalescence of microcracks. There was a significant amount of acoustic emission before failure (Figure 5.15) which showed the Felicity effect due to the inelastic behaviour of the material. Loading to just before failure often resulted in a sample that crumbled into many small pieces, suggesting a significant amount of microcrack growth. Hence, the difference in the compressive strength is likely to be related to the internal flaw distribution and how the microcracks coalesce during loading.

To understand the behaviour of microcracks during loading, the model of Ashby and Hallam was used [14]. The failure strength in uniaxial compression σ_f can be estimated (Equation 2.8) from the value of D_0 and the stress at which wing cracks are nucleated (Equation 2.5); this assumes that the wing cracks grow under loading and, at a certain length, interact and propagate unstably until the sample fails. This model was used to assess the compression failure of the two aluminas (Table 9.6). The assumptions used here are:

1) The average flaw size, a, is half the mean grain size (as an average flaw, 2a, is the length of the mean grain boundary).
2) The coefficient of friction is 0.4 [210]
3) The initiation stress, σ_i, is the stress at which K on the flaw (using Equation 2.5) > $K_{Ic,gb}$ (and not the long crack K_{Ic} which the model [14] originally used).
4) The initiation of wing cracks and the coalescence of microcracks in a polycrystalline material follow that of a continuum material (which the model was constructed for).
5) There is some macrocrack growth from the platen / sample interface but the growth of these cracks does not affect microcrack nucleation and propagation.

Alumina	D_0	Average Flaw Size (μm)	σ_i (GPa)	Estimated σ_f (GPa)	Real σ_f (GPa)
AES-11C, 1600°C	0.16	1.4	1.8	2.4	3.2 +/- 0.3
AES-11C, 1750°C	0.15	3.8	1.1	1.4	1.7 +/- 0.1
TM-DAR, 1600°C	0.09	2.2	1.6	2.3	3.7 +/- 0.3
TM-DAR, 1750°C	0.09	2.6	1.5	2.1	2.6 +/- 0.2

Table 9.6: Consideration of the uniaxial compression failure using the model of Ashby and Hallam [14].

In general, the results from Table 9.6 show that the model underestimates the failure strength. The most likely cause is that there is less microcrack coalescence during loading than the model predicted. This is considered in most detail in the Section 9.3.3.. Qualitatively, however, there is a correlation between the estimated and measured failure strengths suggesting that microcrack propagation and coalescence has a role in the final failure of these ceramics. Moreover, the behaviour in Table 9.6 cannot be explained by the difference in the grain boundary toughness or the surface defect population (due to polishing) and must instead be due to a difference in the flaw distribution.

Microcantilever Beam Fracture Strength

Many of the microscale fracture properties of the two ceramics are discussed in Section 9.1.4.. In general, whilst there was a significant difference between the fracture strengths (Table 9.5), the difference in the thermal etch meant that it was difficult to fully interpret the results. Further work would be required to measure the thermal groove depths, determine the stress contribution due to this (as performed in Section 9.1.4.), and assess the grain boundary strengths.

Summary

There was no measurable difference between the grain boundary toughnesses of AES-11C and TM-DAR alumina (using microcantilever beams), despite the difference in grain

boundary composition. There was a difference in the long crack fracture toughness K_{Ic} (measured from SEVNB), although there may have been differences in the extent of long crack toughening mechanisms such as crack bridging (summarised in [243]) due to the differences in the microstructure. The difference in the uniaxial compression strength between aluminas and sintering temperatures could not be explained using the grain boundary toughness; the more likely explanation was the flaw distribution (although there was a discrepancy between the expected values using the model by Ashby and Hallam and the experimental results). This is the focus of the next section.

9.3.3. AES-11C – Damage Evolution

In order to assess the damage evolution during uniaxial compression, AES-11C samples were compressed to a known load and subsequently unloaded. Several techniques were used to assess the damage: acoustic emission (during loading), optical microscopy, optical fluorescence microscopy, and transmission electron microscopy.

As discussed in Section 9.3.2., there was evidence to suggest microcrack growth and coalescence. These phenomena were considered further in this section. The following key terms are used:

- **Flaw**: The initial grain boundary defect
- **Wing crack**: The small section of crack nucleated at the grain boundary flaw
- **Microcrack**: The crack which has propagated through the material along many grain boundaries (i.e. when a wing crack is long)
- **Macrocrack:** A crack propagating parallel to the compressive stress direction from the sample surface, which can be imaged optically.

It is probable that the final stages of loading and final failure are related to the instable coalescence of microcracks. To understand this, failure strength could be estimated using Equation 2.8 (as shown in Table 9.6). One consideration of whether microcrack coalescence is occurring is whether the microcrack length required for interaction can be achieved during

Assumption	Drawback	Effect on conclusion
Average flaw size, a, half mean grain size	(1) Given abnormal grain growth, flaws may be much larger than this (2) Largest flaws may dominate	This assumption underestimates flaw size, and so overestimates σ_i and D_0. ➔ σ_f overestimated
D_0 can be determined from TEM	(1) As cracks are planar, not all present in sample may be in orientation to be imaged in TEM (2) Assumes D_0 is constant in material	If not all flaws were detected in TEM, σ_f is overestimated
Coefficient of friction is 0.4	(3) AES-11C may have different value (4) Each grain boundary may have different value (5) As microcrack propagates, this may change	If μ is increased, σ_i is increased. ➔ Without knowing true value for AES-11C, difficult to assess effect
Wing crack initiation stress found numerically (Equation 2.6) for when $K > K_{Ic,gb}$	(1) Relies upon the accuracy of microcantilever beam testing, and validating of converting $K_{I0,air}$ to K_{Ic} (2) Assumes all grain boundaries have average toughness	If use K_{Ic} (from SEVNB) instead, σ_i increased (factor of ≈ 2) ➔ σ_f increased (factor of ≈ 2).
Macrocrack formation not affecting microcracking	(1) If stress relaxation occurs due to macrocracks, stress on flaw changes. (2) Microcrack may interact with macrocrack during propagation	Difficult to determine, due to lack of knowledge of macro / microcrack interaction
Model can be used for polycrystalline fracture	(1) As crack propagates, crack opening displacements are not explained by model	See following text

Table 9.7: Consideration of assumption in using Ashby and Hallam [14] model to estimated microcrack coalescence and predict final failure

loading. Considering the plots in Ashby and Hallam [14], if $D_0 \approx 0.1$, the crack propagates unstably (due to microcrack interactions) when L (the wing crack length, l, divided by the half-width of the flaw, a) ≈ 1. Using Equation 2.6 with β = 1.5 (from [89], as used by the authors in [14]), μ of 0.4 [210], an applied stress of 3.5GPa, and a flaw size of 1μm, L ≈ 0.6 before the stress intensity factor is less than $K_{Ic,\ gb}$ (i.e. when the microcracks stop propagating due to the applied stress not being high enough). Hence, it is probable that these microcracks would propagate far enough that they interact, then propagate unstably and lead to failure.

Whilst the correlation between the predicted failure strength and measured failure strength was good (Table 9.6), the model underestimated the failure strength suggesting that there was less microcrack coalescence than predicted for the given damage factor D_0. The assumptions were given in Table 9.7 together with some consideration of how the factors affect the predicted failure strength. In general, there is some validity of the assumptions used in the model. The most likely cause of the discrepancy between the predicted and measured failure strength was the use of the model on polycrystalline samples. The model

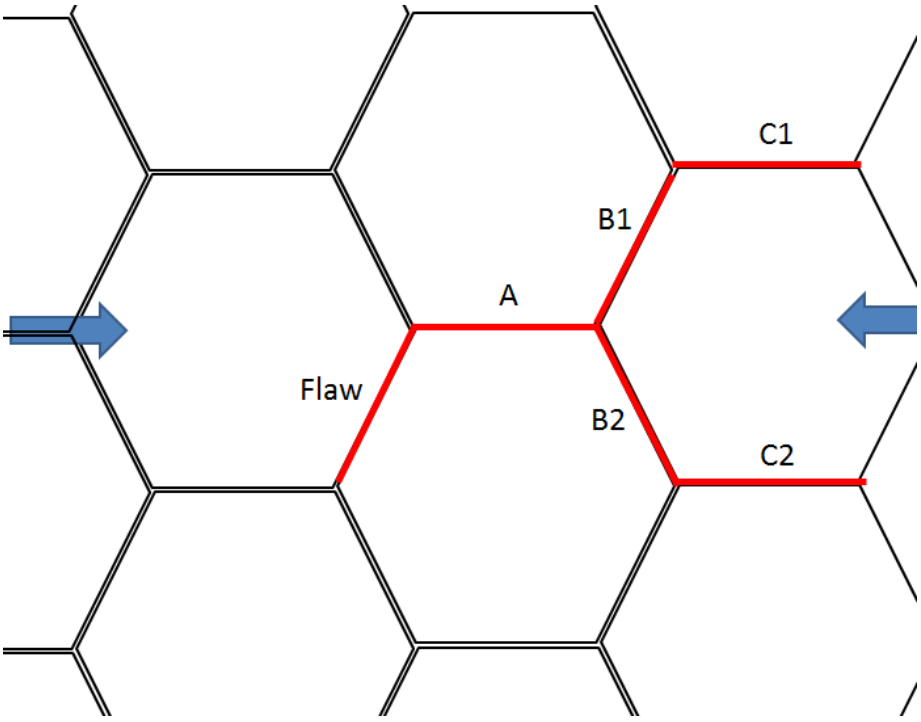


Figure 9.5: Schematic of wing crack nucleation and propagation in polycrystalline ceramic. Uniaxial compression direction indicated with arrows

was generated using a continuum material without grain boundaries where the microcracks can propagate parallel to the uniaxial compression direction (see Figure 2.8 for example of growth in isotropic material). In materials with grain boundaries, such uniform growth is not possible. Instead, cracks transverse around grains whilst growing parallel to the applied stress direction (Figure 9.5). A microcrack propagating on B1 boundary (and then C1) will not necessarily have the same stress intensity factor propagating the crack as propagating on B2 (and then C2). Whilst a simplistic case, it illustrates that the propagation of microcracks in the polycrystalline material may not be well explained by the Ashby and Hallam model. Furthermore, the microcracks will probably propagate with more difficulty than in the isotropic material (due to the tortuous path on the micro-scale) and thus a higher stress is required for microcrack coalescence to occur. This is the most likely explanation for why the failure strength is higher than that predicted by the model.

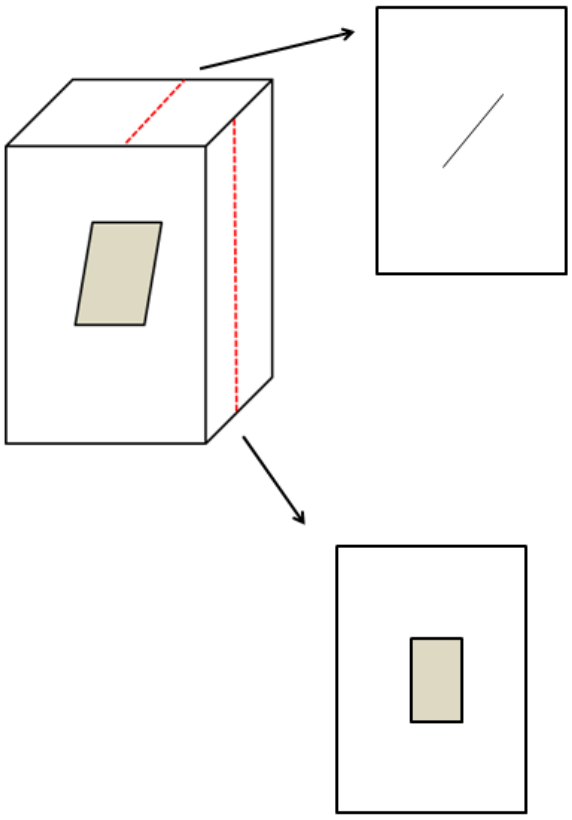


Figure 9.6: Schematic of imaged crack depending on sample preparation

Overall, it is likely that microcracking occurred during loading and the coalescence of these microcracks is related to the final failure. To investigate the microcracking, TEM images were taken and the damage evolution on the small scale investigated (Section 5.4.4.). The criteria for assessing these microcracks are given in Section 5.4.4. None of the microcracks imaged in the TEM could be corroborated with the Ashby and Hallam [14] model. It is worth noting that the cracks are planar and not linear, but the TEM images do not convey this (e.g. Figure 9.6, showing two

ways a crack may look depending on how the TEM foil is made). Hence, analysis of the flaws from TEM using the Ashby and Hallam [14] model has some inherent drawbacks. Furthermore, the microcracks were assessed by estimating the initial flaw. This was often difficult to determine.

Results from TEM also show that microcracks did not propagate parallel to the applied stress direction (Figure 5.25). Even if the model [14] has soon issues when applied to polycrystalline samples, this is clear evidence that these cracks cannot have formed during loading; there is no mechanism in the literature that could explain this behaviour. The most likely explanation for their presence was that they formed during TEM sample production. As discussed in Section 3.2.1., ion beam milling was used to thin the TEM sample. There were likely to be some microcracks in the foil due to the load (as discussed above) but, as the TEM foil became fragile as it became very thin, cracks may have formed between these microcracks. The cracks imaged in TEM were likely to be these cracks. This would explain why they were unrelated to the compressive direction and why there was no correlation between the applied stress and the resultant number of microcracks (Table 5.6).

There were no deformation twins in any of the compressed samples, both undoped and chromia doped. Previous work by Lankford [15, 39] presented many of these twins in alumina after compression, and stated that they were related to microcracking in the material. However, the absence of such features in any of the TEM images suggests that they were neither a feature of uniaxial compression nor were involved in microcracking in AES-11C. The most likely discrepancy between this work and that performed previously was the grain size; this was considerably smaller (Section 4.1.1.) than the work of Lankford [15] of ≈ 25μm. Other work showed that there was a critical grain size (≈ 20μm) below which deformation twins do not form [42]. As deformation twinning is related the double cross-slip [36, 37, 249] and movement of partial dislocations [36], the small grains may restrict the abilities for these mechanisms to occur; the critical grain size for twinning to occur was discussed for aluminium in [250]. Using the equations in [250] and the constants for sapphire

in [249], the critical grain size for twinning was 50 – 100nm. This does not correlate with the previous work [42], but does show that there is a critical grain size below which deformation twins cannot form.

Overall, whilst microcracking is expected to occur during uniaxial compression of polycrystalline alumina & the coalescence of these lead to failure, the cracks imaged in TEM were not such microcracks. There were no deformation twins formed as a result of the loading, unlike previous work, probably due to the grain size restricting the mechanisms related to the formation of twins.

9.4. TM-DAR with and without carbon

The key characteristics of the two materials are summarised in Table 9.8

Characteristic	Section	TM-DAR	0.012wt% carbon doped TM-DAR
Grain size (µm)	4.1.5., 4.1.6.	2.2 +/- 0.2	2.4 +/- 0.2
Relative density (%)	4.2.4., 4.2.6.	99.997 +/- 0.002	100.01 +/- 0.01
Grain boundary composition	4.7.2.	No impurities detected (EELS)	No impurities detected (EELS)
Macroscopic fracture toughness ($MPam^{1/2}$)	5.3	3.8 +/- 0.1	4.3 +/- 0.1
$K_{I0,\ air}$ ($MPam^{1/2}$)	8.4.1.2., 8.4.2.	0.7 +/- 0.1	1.3 +/- 0.2
Fracture mode	8.4.1.2., 8.4.2., 5.3	Intergranular	Transgranular

Table 9.8: Summary of properties in undoped and carbon doped TM-DAR

Electron energy-loss spectroscopy (EELS) of undoped and 0.012wt% carbon doped TM-DAR, sintered in vacuum, was performed. Previous work [68] showed that carbon was localised to the grain boundaries in TM-DAR. However, it was not possible to detect any carbon at the grain boundaries using EELS.

The minimum mass fractions (MMF) of the different elements were determined for EELS. This was the minimum amount of the element that could be detected (with the set of conditions outlined in Section 3.3.5.). This was considered using EELSAdvisor (aided by Dr Adam Papworth, Department of Materials, University of Oxford). In general, with a 10s exposure time, a minimum of 0.5 at% carbon would be required under the probe for an edge to be detected (Figure 9.7). This was far more than was measured from atom probe tomography (Figure 2.5), estimated to be half a monolayer [10]. Whilst the obvious solution was to increase the exposure time, this resulted in an increased probability of drifting.

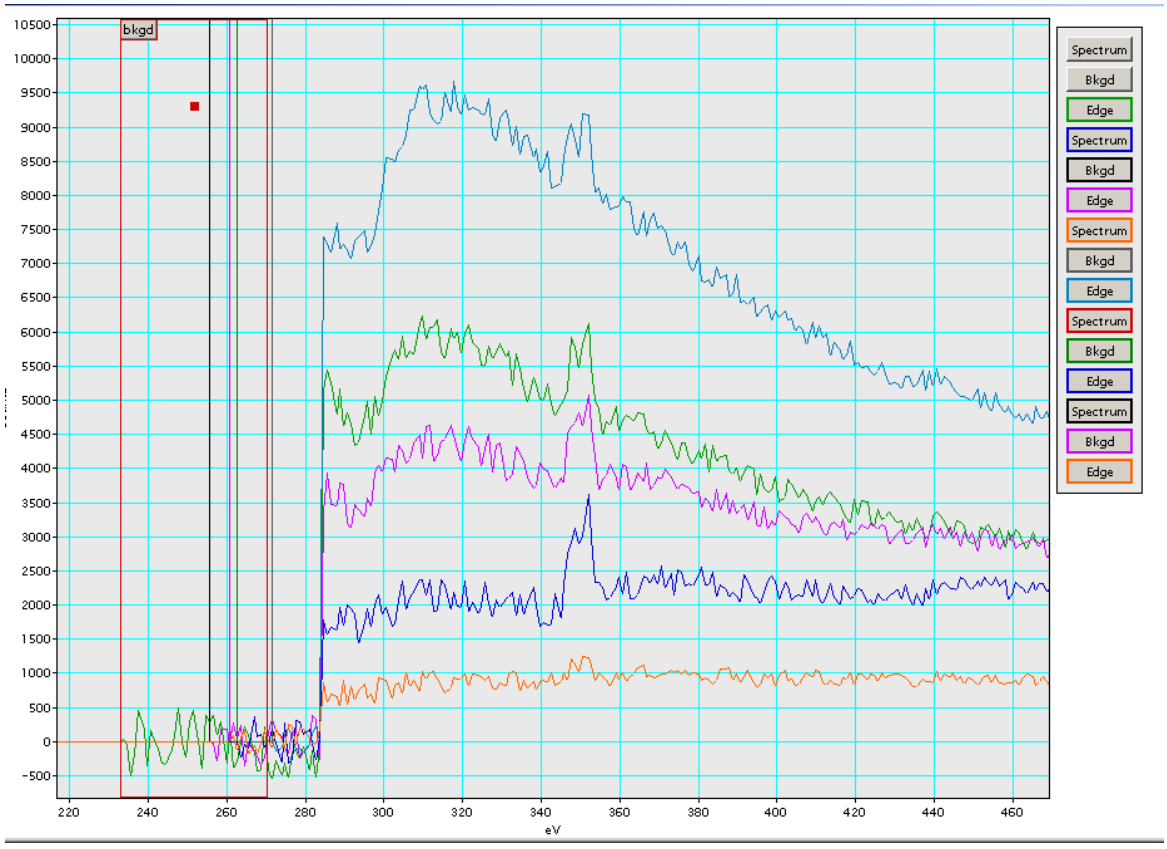


Figure 9.7: Simulated EELS spectra for carbon (edge at 293eV) in alumina (using experimental parameters in Section 3.3.5.). From top: 2%, 1.5%, 1%, 0.5% (all with 30s exposure), 0.5% with 10s exposure

This was similar for the other elements considered in this work: magnesium, silicon, calcium, and potassium. Thus, it was impossible to determine the compositional differences between the doped and undoped TM-DAR using EELS with the conditions used in this work. This is discussed further in Chapter 10.

Whilst it was not possible to determine compositional variations in the grain boundaries of doped and undoped TM-DAR, there were significant differences in the mechanical properties. K_{Ic} from macroscopic SEVNB was (3.8 +/- 0.1) and (4.3 +/- 0.1) $MPam^{1/2}$ for undoped and 0.012wt% carbon doped TM-DAR respectively. The fracture mode was transgranular for the carbon doped (Figure 5.8), as seen elsewhere for the same materials [10]. The conclusion is that the grain boundaries are tougher due to the carbon addition.

The same increase in fracture toughness was seen on the microscale (Table 9.8). Notched microcantilever beams had $K_{I0,\ air}$ of (0.7 +/- 0.1) and (1.3 +/- 0.2) $MPam^{1/2}$ for undoped and 0.012wt% carbon doped respectively. The fracture surfaces showed more transgranular fracture for the carbon doped (Figure 8.12) than the undoped (Figure 8.11). The value of $K_{I0,\ air}$ for carbon doped was similar to that for single crystal sapphire. This suggests that the grain boundary toughness is increased due to the carbon, to the point that the toughness is similar to that of the alumina grains. This explains why it fractures transgranularly; if the toughness of the grains and boundaries are the same, the crack propagates without influence of the microstructure.

The increase in fracture toughness due to the change in fracture mode (from inter- to trans-granular) was estimated to be 1.58 [251] by considering the fracture energies at and away from grain boundaries. From the microcantilever beams, the ratio $K_{I0,\ air}$ (doped) / $K_{I0,\ air}$ (undoped) was (1.9 +/- 0.4). Hence, the difference in the microcantilever fracture toughness between undoped and carbon doped alumina can be attributed to the difference in fracture mode due to the increased grain boundary strength because to the presence of the carbon.

It was interesting the note that, whilst the difference in the microscale toughness was large, there was a relatively smaller change in the macroscopic fracture toughness, K_{Ic}. As discussed previously, K_{Ic} (measured from SEVNB) has contributions from various toughening mechanisms: crack deflection, micro-crack toughening [243], and crack bridging by un-fractured grains [244]. The latter was a key toughening mechanism in alumina [244]; it is

likely to occur more readily if the crack propagated intergranularly. Hence, whilst the intrinsic grain boundary toughness may have been increased by the inclusion of carbon, there may have been a reduction in the extent of the long crack toughening mechanisms due to the change from inter- to trans-granular fracture.

Overall, whilst work in this project could not conclusively show that carbon was situated at the grain boundaries, the doping had a large effect on the mechanical properties. It is likely that the half a monolayer of carbon [10] was altering the grain boundary complexion (Section 2.3) which increased the grain boundary strength. However, which type(s) of complexion classes were present in the material is unclear, and only HRTEM will elucidate this.

9.5. Chromium oxide doping

The key characteristics of the undoped and chromium doped aluminas used in this project are given in Tables 9.9 (in AES-11C). Many of the characteristics of these materials, plus other doping levels and those of TM-DAR, are summarised in Table 5.7. For simplicity, a direct comparison of only undoped and 2wt% Cr_2O_3 doping is summarised in Table 9.9.

Chromium in corundum lattice

The introduced chromium substituted onto the aluminium oxide lattice, as seen elsewhere [203]. TEM-EDX (Figure 4.9.4.), the increase in the unit cell volume (Section 4.2.2.), and optical fluorescence microscopy (Section 4.4.4.) all showed that chromium was situated in the lattice.

Relative Density

The relative density decreased significantly with the addition of chromia (Figure 4.11). As chromium oxide has a high melting point (≈ 2300^{o}C) achieving full density in pure Cr_2O_3 was found difficult by previous authors [252]. Sintering at 1600^{o}C as used here was clearly not enough to produce a fully dense material (Table 9.9). The reduced sinterability also affected

Characteristic	Section	Undoped	2wt% Cr_2O_3
Grain Boundary Composition	4.8.1., 4.8.4.	(0.14 +/- 0.08) at% Si (TEM-EDX)	(0.3 +/- 0.2) at% Si (TEM-EDX)
Relative Density (%)	4.2.1., 4.2.2.	1600°C: 99.7 +/- 0.7 1750°C: 99.9 +/- 0.6	1600°C: 99.2 +/- 0.7 1750°C: 99.3 +/- 0.3
Grain Size (µm)	4.1.1., 4.1.3.	1600°C: 2.7 +/- 0.9 1750°C: 7.6 +/- 2.1	1600°C: 2.1 +/- 0.4 1750°C: 10.6 +/- 2.9
Microstructural Description	4.3.1., 4.3.3.	Twinned grains, abnormal grain growth	Fewer twinned and abnormal grains
Microscale Toughness ($K_{I0, air}$) ($MPam^{1/2}$)	8.2.6., 8.3	GB: 0.6 +/- 0.1 Grain: 1.5 +/- 0.3	GB: 0.8 +/- 0.2 Grain: 1.6 +/- 0.3
Macroscopic fracture toughness (K_{Ic}) ($MPam^{1/2}$)	5.3	3.5 +/- 0.2	3.7 +/- 0.2
Uniaxial Compression Strength (GPa)	5.4.1.1.	1600°C: 3.2 +/- 0.3 1750°C: 1.7 +/- 0.1	1600°C: 2.4 +/- 0.1 1750°C: 2.3 +/- 0.3
Weibull modulus (Comp)	5.4.1.1.	1600°C: 18, 3	1600°C: 9, 3
Flexural Strength (MPa)	5.5.	331 +/- 13	266 +/- 7
Weibull modulus (Flexural)	5.5.	12, 3	11

Table 9.9: Comparison of characteristics for undoped and Cr_2O_3 doped AES-11C

the grain size; the mean grain size and distribution decreased with the chromium addition due to grain coarsening being reduced. There were significantly fewer abnormal grains (although several still existed, such as in Figure 4.3) and fewer twinned grains. Both the latter were presumably related to grain coarsening and annealing.

Grain Boundary Toughness

The chromium oxide doping seemingly had little impact on the grain boundary composition in AES-11C; there was the same amount of silicon at both types of boundaries. As a result, $K_{I0,air}$ was the same as that for doped and undoped AES-11C (Table 9.9). The addition of the chromium had no effect on the fracture mode; cracks propagated mostly intergranularly with and without chromium (Figure 5.7). Any change in the mechanical properties discussed herein was not related to the grain boundary toughness.

Change in mechanical strength

The addition of chromia reduced the flexural and the uniaxial compression strength (Table 5.7). The most probable cause was the reduction in relative density with chromia (Figure 9.8). With a reduced density, the flaw distribution and D_0 (discussed in Section 9.3.3.) are likely to increase. Even though the grain size, and thus mean flaw size, decreases with chromia addition (Table 9.9), the increased factor D_0 results in microcracks having to propagate less far before interacting and extending unstably. This is apparent from Equation 2.8. The fracture of chromia doped alumina is fundamentally the same as without chromia; the critical difference is the flaw distribution and D_0.

Twinning

Overall, the key reason for using the chromium oxide was to investigate the relationship between chromium and the propensity to from deformation twins. As discussed in Section 2.1.3., the effect of chromium on deformation twinning was ambiguous. Twins were either more [43, 45] or less [44, 45] likely to form with chromium, depending on doping. However, there was no evidence of twins on the macroscale after uniaxial compression, with or without chromium additions. On the microscale, there was no evidence of twinning.

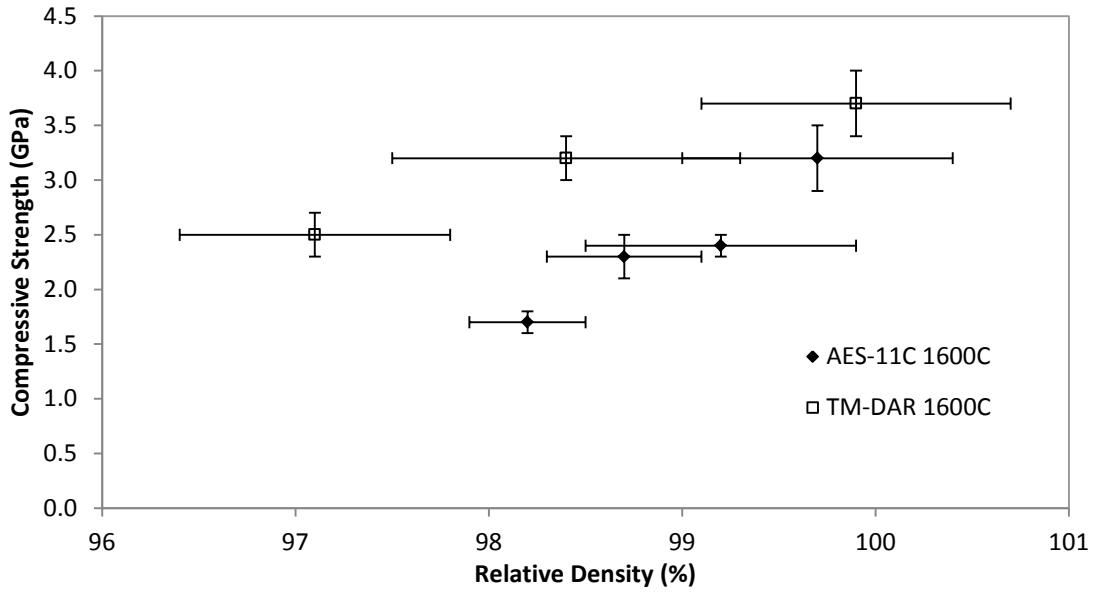


Figure 9.8: Relationship between relative density and compressive strength for different chromia doped AES-11C and TM-DAR alumina (doped at 1600°C)

Summary

The key phenomenon affecting the macroscopic mechanical properties of chromia doped alumina was the reduced sinterability, leading to 1) a lower relative density, 2) a higher flaw density, 3) coalescence of microcracks at a lower stress and thus a lower failure strength. The grain boundary properties were seemingly unaffected by the doping. Twinning was not present after loading, as was also the case for the undoped alumina.

9.6. Silicon Nitride

The key considerations for analysis of the rare-earth doped silicon nitrides are:

1) The grain boundary strength
2) The grain boundary toughness
3) Crack extension prior to failure
4) How these qualitative values explain the macroscopic fracture properties.

Strength

The grain boundary strength in silicon nitride varied with rare-earth dopant; the mean values for Lu- and La-doped silicon nitrides were (3.0 +/- 0.2) and (2.1 +/- 0.4) GPa respectively.

Toughness

The correction factors (for notch bluntness and residual stress) were discussed for sapphire in Section 7.3.3. In silicon nitride, the value of the sharp notch tip crack length dα was not known, and so only qualitative values of the fracture toughness could be determined.

The stress intensity factor at failure was (2.9 +/- 0.2) and (2.4 +/- 0.2) $MPam^{1/2}$ for Lu- and La-doped silicon nitride respectively. This corresponds well to previous work; using Vickers indents and measured the angle of incidence required to cause debonding, Lu-doped had tougher boundaries than La-doped [50].

The stress intensity factor was determined at the onset of crack extension in La-doped silicon nitride: (1.5 +/- 0.1) $MPam^{1/2}$. This may have been a more accurate measure of the toughness of the La-doped grain boundary material. The stress intensity factor at failure may have had additional ("long-crack") contributions from the microstructure, such as frictional bridging.

One further consideration was whether the silicon nitride undergoes environment assisted sub-critical crack growth. As discussed in Section 2.6.7., there was differing views on the sensitivity of silicon nitride to slow crack growth. More analysis is required (such as testing the beams submerged in water) to confirm this.

Crack extension prior to failure

Whilst there was no crack extension prior to failure in notched Lu-doped beams, there was some crack extension in the La-doped silicon nitride; the extension before failure was (0.17 +/- 0.06) μm. Considering the previous work on this material [11], the grain diameter for La-

doped silicon nitride was (0.3 +/- 0.2) µm. Hence, the crack presumably extended around a silicon nitride grain and was arrested due to elongated grains across the fracture plane. Further applied stress was required to propagate the crack further through the material. This was analogous to the work of microcantilever beams of carbon nanotubes in borosilicate glass [230] whereby the glass failed in loading but the nanotubes held the fracture surface together.

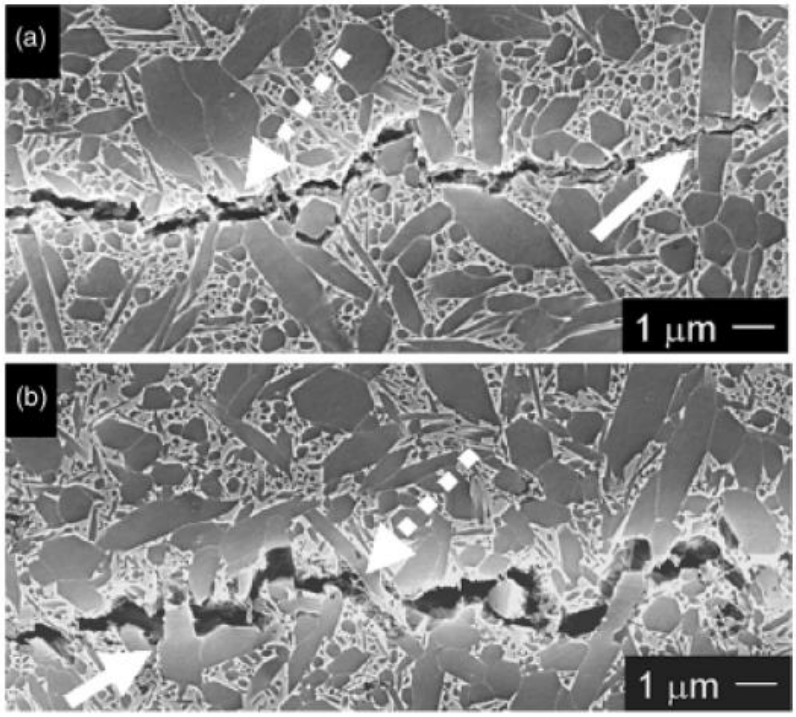


Figure 9.9: Crack path in a) Lu- and b) La-doped silicon nitride showing the difference between the propensity to crack through or around elongated grain. From [11]. Permission to reproduce this figure has been granted by John Wiley & Sons, Inc.

In Lu-doped silicon nitride, the boundary was stronger than in La-doped, and the crack was more likely to propagate through the grains than in La-doped. This was why no crack extension was seen prior to failure in the notched beams – the notch tip crack was more likely to propagate through the beam regardless of the microstructure under the notch.

Comparison to macroscopic results

The values for rare-earth doped silicon nitride correlated well with the macroscopic properties of these materials; K_{Ic} for long cracks was (5.5 +/- 0.3) $MPam^{1/2}$ and (7.0 +/- 0.2) $MPam^{1/2}$ for the Lu and La-doped silicon nitrides respectively [11]. In the La-doped, the lower grain boundary strength & toughness resulted in the crack having a greater propensity to propagate around the elongated grains rather than through them [11]. As a result, there was

more pull-out and frictional bridging in the La-doped silicon nitride (Figure 9.9) and thus a greater long crack fracture toughness.

Chapter 10 Conclusions and Further Work

1) Microcantilever Beam Validation

- The stress intensity factor for a straight through notch on the surface of a triangular cross-sectional beam was ascertained using a compliance calibration method (Section 6.1).
- The applied stress intensity factors at failure of Focussed Ion Beam produced microcantilever beams were too high (Section 7.1, Figure 9.3), due to the notch bluntness and notch tip residual stress (due to gallium implantation).
- Both redeposited (nanocrystalline, formed of both solid solution alumina-gallia and elemental gallium) and gallium implanted (crystalline, with 3 at% gallium) materials were present on the top surface and at the base of the FIB notch.
- A correction term to the notch bluntness was ascertained (following the method of Fett and Munz [149, 150]) using a characteristic notch tip crack length dα: (7 +/- 2) nm in sapphire.
- The residual stress in sapphire was measured using optical fluorescence microscopy as (13 +/- 5) GPa; the stress intensity factor contribution due to this was accounted for by noting the notch tip crack length, dα.
- The corrected stress intensity factors at failure in sapphire were comparable to K_{Ic} and K_{I0} values measured in the literature when submerged in silicone oil and water respectively. When tested in air, beams underwent moisture assisted sub-critical crack growth and the correction stress intensity factors at failure in sapphire were close to $K_{I0,\ air}$ measured in the literature.
- After annealing, beams underwent a compliance change prior to failure when notched away from the boundary. This was due to either plasticity or crack extension. Due to a

lack of data on the value of dα, only qualitative stress intensity factors could be determined.

To the author's knowledge, this is the first reported use of the microcantilever beams to qualitatively measure the toughness of alumina and silicon nitride ceramics, as well as the first to report a method to quantitatively determine the toughness in any material. It is also the first to thoroughly report and discuss issues such as notch bluntness and residual stress in any material.

The project showed that K_{Ic} and K_{I0} of sapphire and other ceramics can be measured directly using notched beams submerged in different liquids. Measuring sub-critical crack growth macroscopically can often be difficult; microcantilever beams can a useful alternative to measure K_{I0} accurately in different ceramics.

2) <u>Using the microcantilever beam technique for different ceramics</u>

- The Young's moduli of microcantilever beams in different materials (sapphire, polycrystalline alumina, and silicon nitride), calculated using simple beam theory equation (Equation 3.7) and corrected for flexure in the fixed end (Appendix 3.2), corresponded well to the macroscopic values.
- The fracture strength and toughness was ascertained for two grades of polycrystalline alumina (TM-DAR and AES-11C). Despite a difference in the grain boundary composition, there was no measurable difference in the grain boundary toughness.
- There was no difference in grain and grain boundary toughness with chromia doping in polycrystalline alumina.
- The addition of carbon in polycrystalline TM-DAR alumina increased the grain boundary toughness; this resulted in a change of fracture mode from intergranular to transgranular.
- The microscale fracture strength and grain boundary toughness was lower for La-doped silicon nitride than Lu-doped, which corresponded well to literature results as

well as macroscopic fracture properties measured elsewhere. La-doped beams underwent crack extension prior to failure, but Lu-doped did not, due to the different propensities for crack to propagate around the grains.

To the author's knowledge, this is the first reported direct & quantitative measurement of the grain boundary toughness in alumina (i.e. excluding long-crack toughening mechanisms). It is also the first direct (but qualitative) measurement of the grain boundary toughness of rare-earth doped silicon nitride.

3) Macroscopic properties of different ceramics

- The long crack fracture toughness, K_{Ic}, was the same for the two aluminas used in this work. There was no change in K_{Ic} with chromia doping. Carbon doping increased K_{Ic}; the crack propagated transgranularly and not intergranularly. All these results mirror those determined on the microscale. Toughness values were larger on the macroscale due to long crack toughening mechanisms such a crack bridging.
- The flexural and compressive strength of alumina decreased with chromia doping, due to the decreased relative density.

4) Damage Evolution during uniaxial compression

- The macroscopic damage increased with applied load, and the damage correlated with the acoustic emission.
- Microcracking played a role in the final failure. The measured fracture strength was compared to the predicted value (using the Ashby and Hallam microcracking model, noting the original extent of damage in the material and the grain boundary toughness using microcantilever beams). There was a correlation between the values, but the model underestimated the strength. This was most likely due to difficulties in applying the model, developed for a continuum material, to a polycrystalline ceramic.

Specifically, the crack opening displacements were likely to be different to those predicted by the model, due to the tortuous crack path as the crack propagates intergranularly.

- Microcracks were imaged using TEM after loading to different stresses and unloading. These could not have formed during loading, and instead formed during TEM sample production.
- There was no deformation twinning after loading; in the AES-11C alumina, twinning was not related to the final failure. The lack of twins was related to the relatively small grain size and was likely to be due to the restriction of the double cross-slip mechanism.

Further work

A) **Controlled Flaws:** A suitable equation to determine the stress intensity factors of controlled flaws is required. Finite Element Analysis simulations of a range of controlled flaw depths and widths (as well as positions from the fixed end) should be performed and a compliance calibration method undertaken.

B) **Quantitative fracture strength:** Further work is required to assess the effect of the residual stress (due to the gallium implantation) on the fracture strength. Using dual-beam FIB (and imaging the beams with SEM rather than the gallium ions) will help to reduce the implantation on the top surface. The beams should also be annealed to determine if the fracture strengths and strength distribution are altered.

C) **Notch tip crack length:** Extensive work is required to understand the physical interpretation of dα. Using low and high-resolution TEM, the size and meaning of this notch tip crack should be analysed in different polycrystalline ceramics and in single crystals.

D) **Compliance Change:** Annealed beams showed a compliance change prior to failure. Further investigation is required to determine the reason for this (plasticity or crack

extension). Beams should be loaded until the compliance change, but before fracture, and unloaded. If plasticity occurred, there will be a displacement offset when the load is removed. Furthermore, TEM foils (parallel to the beam) should be manufactured when loaded to just before failure; TEM analysis should show whether crack extension or whether plasticity has occurred.

E) **Grain boundary structure:** Electron energy-loss spectroscopy (EELS) was inconclusive at determining the difference between undoped and 0.012wt% carbon doped TM-DAR. High-resolution TEM should be performed to determine the structure (or complexion) of the grain boundaries for the two materials. Such analysis should also be performed on materials such as polycrystalline AES-11C and the sapphire bicrystal to fully understand the relationship between the complexion and fracture toughness.

F) **Annealing Twins:** High-resolution TEM should be performed on the twinned grains detected in polycrystalline AES-11C in order to ascertain whether they were β-Al_2O_3 (with ordered potassium between alumina planes) or heavily twinned α-Al_2O_3 (with potassium in gaps in the oxygen sub-lattice) grains.

G) **Deformation twins:** Macroscopic and microscopic experiments could not detect whether deformation twins were involved in the ambient temperature fracture and what involvement the chromium ions had on the production of the twins. Microcantilever beams on specific planes in ruby should be performed to determine if twinning could occur during loading.

Appendices

Appendix 3.1 – Mechanical Properties of microcantilever beams

The displacement recorded during nanoindentation was a combination of the displacement of the beam, and the indentation of the tip into the top surface of the beam. The indentation depth into the top surface was related to the hardness (Equation A3.1.1):

$$H_n = 0.0018544 \frac{F}{d^2} \quad \text{(A3.1.1)}$$

where d is the mean length across the Berkovich indent (i.e. tip-to-base of the triangular indent) in mm, F the load from the indenter tip in N, and H_n the hardness from nanoindentation (41GPa for a depth of 100nm). Rearranging and noting that the ratio between the diagonal length and the depth is 7 for a perfect Berkovich tip:

$$D_{true} = D_{total} - \frac{\sqrt{A_c}}{7}\left(\frac{0.0018544\ F}{41GPa}\right)^{0.5} \quad \text{(A3.1.2)}$$

where D_{true} is the true displacement of the beam at the point of contact with the tip, D_{total} the displacement of the nanoindenter tip outputted by the software, and A_c the area correction due to tip bluntness (3.17 from Section 3.7.2).

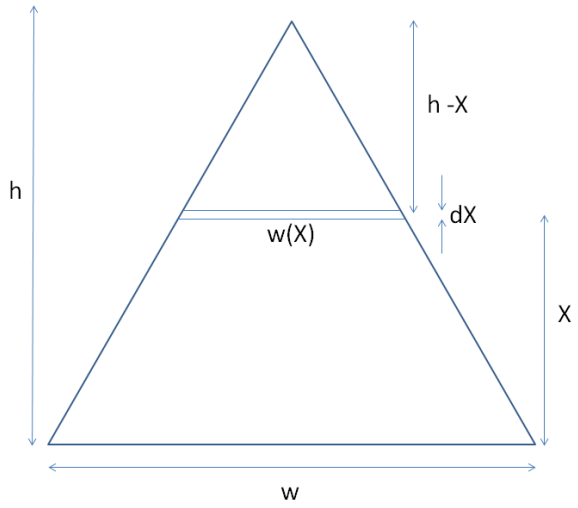


Figure A3.1.1: Schematic of cross-section of microcantilever beam

The Young's Modulus is calculated initially using simple beam theory. The second moment of area, I, of the triangle is found.

Using the dimensions from Figure A3.1.1., the second moment of area of a small increment away from the neutral axis $dI = X^2 dA$ where $dA = w(X)dX$.

Using similar triangles,

$$\frac{w(X)}{w} = \frac{h - X}{h} \tag{A3.1.3}$$

Substituting for $w(X)$ into $dA = w(X)dX$,

$$dA = \frac{w(h - X)}{h} dX \tag{A3.1.4}$$

Therefore,

$$I = \int X^2 dA = \int_0^h X^2 \frac{w(h - X)}{h} dX \tag{A3.1.5}$$

$$I = \frac{w}{h} \int_0^h X^2 h - X^3 \, dX \tag{A3.1.6}$$

$$I = \frac{w}{h} \left[\frac{hX^3}{3} - \frac{X^4}{4} \right]_0^h \tag{A3.1.7}$$

$$I = \frac{wh^3}{12} \tag{A3.1.8}$$

Using parallel axis theorem, the second moment of area about the triangles centroid or neutral axis, I_c, is related to the second moment of area about a non-centroidal plane, I, by:

$$I_c = I - A\delta^2 \tag{A3.1.9}$$

where A is the area of the triangle and δ the distance from the centroid. The centroid plane or neutral axis for a triangle is a $^1/_3h$ [253] and so, by noting that the area of the triangle is $wh/2$, the second moment of area around the neutral axis is:

$$I_c = \frac{wh^3}{12} - \frac{wh}{2}\left(\frac{h}{3}\right)^2 = \frac{wh^3}{36} \tag{A3.1.10}$$

Using the second moment of area, the Young's modulus is found by considering the beam deflection, D_{true}. As $M = EI/R$ and $1/R = d^2D_{true}/d\lambda^2$, where λ was an arbitrary distance along the length of the deflecting beam, then:

$$\frac{d^2D_{true}}{dx^2} = \frac{M}{EI_c} = \frac{36F(L_{el} - \lambda)}{h^3wE} \quad \text{(A3.1.11)}$$

where L_{el} is the length from the fixed end to the position of the indenter tip. Performing the first integration, where $dD_{true}/d\lambda = 0$ when $\lambda = 0$,

$$\frac{dD_{true}}{d\lambda} = \frac{36F}{h^3wE}\left(L_{el}\lambda - \frac{\lambda^2}{2}\right) \quad \text{(A3.1.12)}$$

Performing the second integration, with $D_{true} = 0$ at $\lambda = 0$,

$$D_{true} = \frac{36F}{h^3wE}\left(\frac{L_{el}\lambda^2}{2} - \frac{\lambda^3}{6}\right) \quad \text{(A3.1.12)}$$

As the maximum deflection occurs when $\lambda = L_{el}$,

$$D_{true} = \frac{12FL_{el}^3}{h^3wE} \quad \text{(A3.1.13)}$$

Rearranging,

$$E = \frac{F}{D_{true}}\frac{12L_{el}^3}{wh^3} \quad \text{(A3.1.14)}$$

Hence, using A3.1.2 to determine D_{true} from the outputted displacement, the Young's modulus was determined.

The normal stresses in the beam, $\sigma = MX/I$ [3]. Following the above approach using I from A3.1.10 and using $X = h$ (i.e. stress on the top surface of the beam),

$$\sigma(L_{fr}) = \frac{12FL_{fr}}{wh^2} \quad \text{(A3.1.15)}$$

At failure

$$\sigma_f(L_{fr}) = \frac{12F_{max}\,L_{fr}}{wh^2} \quad \text{(A3.1.16)}$$

where L_{fr} was the distance from the indenter tip to the point of fracture on the tensile surface of the beam, and F_{max} was the maximum load at failure.

Appendix 3.2 – Correlation of correction factor for Young's modulus with aspect ratio of microcantilever beams

Finite Element simulations (LS-DYNA) were performed (Simone Falco, Department of Engineering, University of Oxford) to determine the error between the encastré beam and the beam with flexibility in the fixed end. This was correlated with aspect ratio of the beam (Figure A3.2.1).

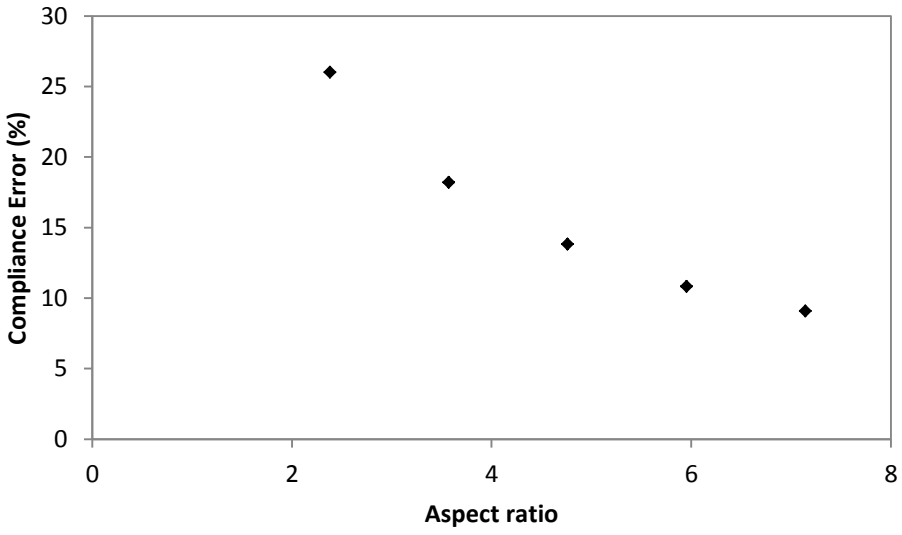


Figure A3.2.1: Correlation with compliance error between encastré and supported beam against aspect ratio, from Finite Element Analysis

Noting Equation 2.10 [115], the ratio between the compliance from the correction term (second part) to that of simple beam theory (first part) was $1/L$. By plotting Figure A3.2.1. with logarithmic axes, this relationship was apparent thus validating the simulations.

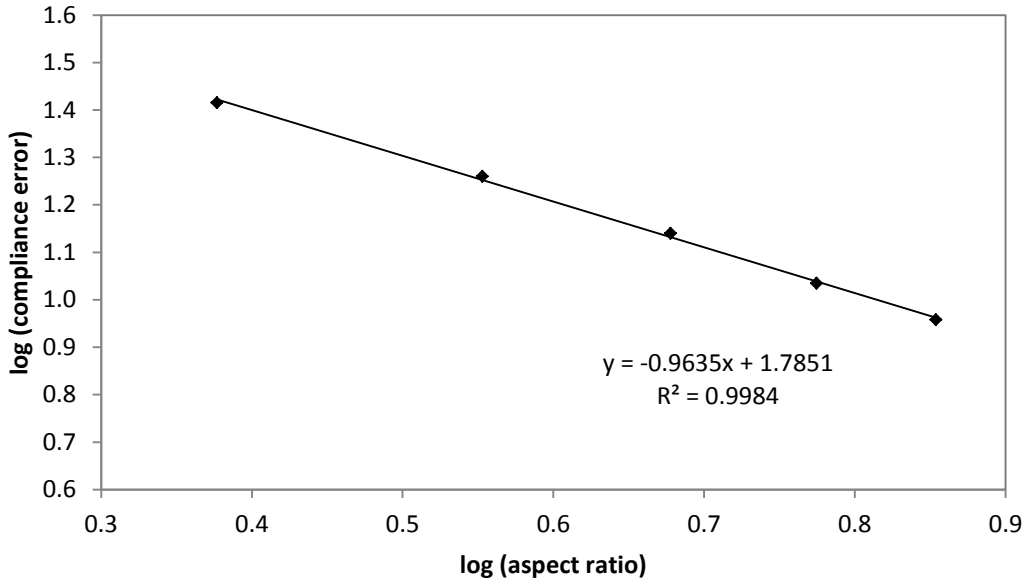


Figure A3.2.2: Correlation with log of the compliance error between encastré and supported beam against log of the aspect ratio, from Finite Element Analysis

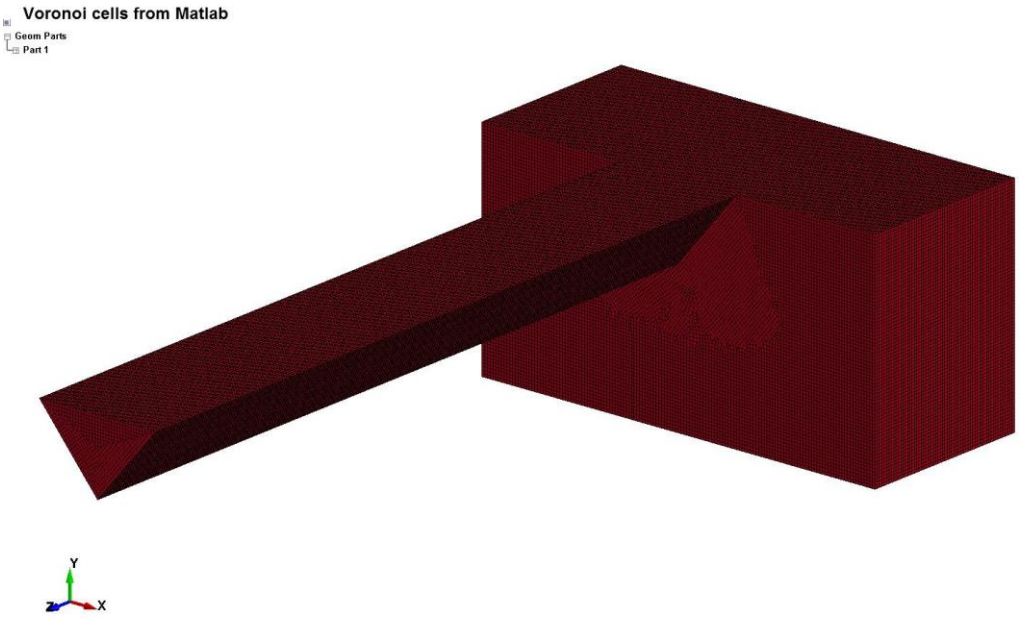


Figure A3.2.3: Finite Element Analysis construction used to determine Young's modulus correction

Appendix 4.1 - Calibrations of the JEOL 2000FX TEM

Image-to-diffraction pattern

Clockwise rotation (in degrees) of diffraction spot to image

Magnification x10³	Camera Length (cm)				
	80	100	150	200	250
20	4.8	5.0	4.1	3.8	3.3
40	6.9	6.8	6.2	5.6	5.3
50	7.2	7.1	6.6	5.6	5.3
80	7.1	6.7	6.1	5.1	4.2
100	7.5	7.5	7.2	6.8	6.5
150	8.9	8.7	8.3	7.7	7.4
200	9.0	9.2	8.9	8.0	8.2
250	11.2	10.9	10.2	9.4	9.5
400	12.1	12.7	12.3	11.5	10.9

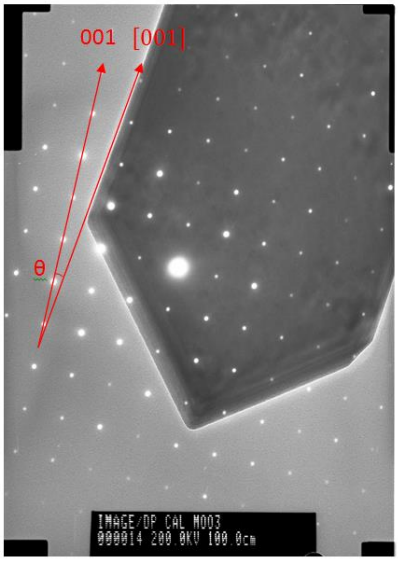


Figure A4.1.1: Calibration of the JEOL 2000FX image-rotation for a variety of magnifications and camera lengths using MoO_3 crystals.

Camera Length Calibration

Equation used:

$$Rd = \lambda L$$

- R = separation of direct and diffracted beam from DP
- d = d-spacing of diffracting plane
- λ = relativistic electron wavelength (2.5pm for 200kV)
- L = camera length

Averaging for different diffracted planes, the values in the table were determined.

Selected camera length (cm)	Measured camera length (cm)	Camera Constant (mm Å)
80	84	2.11
100	100	2.51
150	152	3.80
200	199	4.98

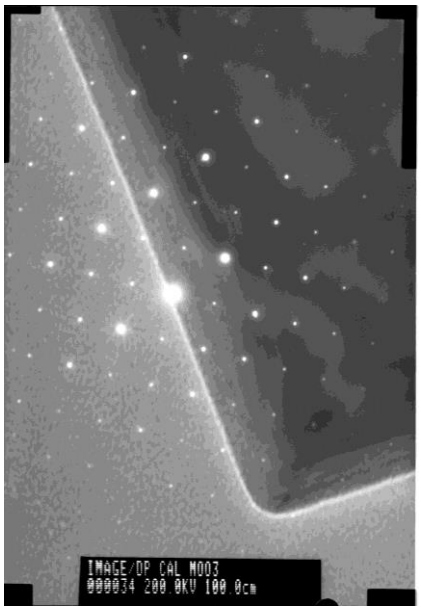


Figure A4.1.2: Diffraction pattern of standard MoO_3 crystal

X- and y-displacements

In the TEM it was not always apparent which way the sample was orientated. This was vitally important for determining how features, such as cracks, were oriented relative to the uniaxial compression direction. Two corrections needed to be considered in order to ensure that the image-to-compression direction were correct.

1) **Sample in holder**: The orientation of the sample in the TEM holder was required. This was achieved by image analysis of a digital camera photo prior to the holder being placed into the TEM. The angle between the edge of the sample (i.e. parallel to the compression direction) and the holder was measured (black lines in Figure A4.1.3.).

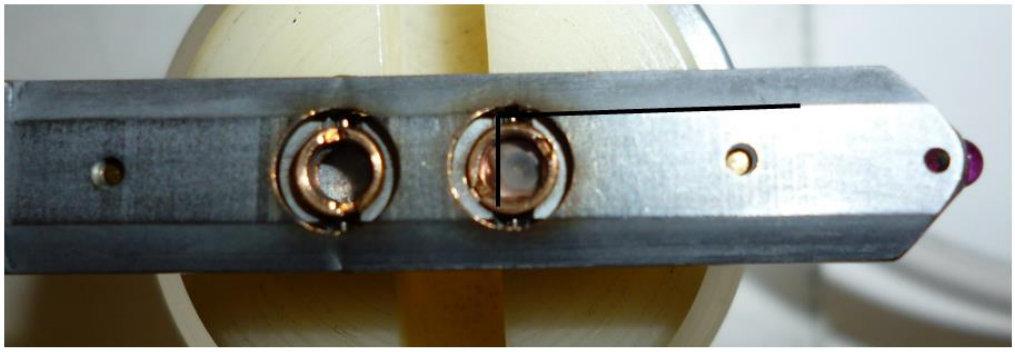


Figure A4.1.3: Uniaxially compressed sample place in the holder of 2000FX, where the black lines indicate the angle between the edge of the sample and the holder.

2) **Rotation of the image relative to the holder**: If there was no image rotation, as the holder was moved in and out of the microscope, there would be no movement of a feature in the y-direction. If the negatives and holder were aligned, then the feature would only move in the x-direction. Image analysis was used to measure the angle from negatives (such as Figure A4.1.4), and hence correct for the image rotation. As with the rotational difference between the diffraction pattern and the image, the image rotation was dependent upon the magnification. Thus, features in the same sample, but imaged at different magnifications, need to be calibrated separately.

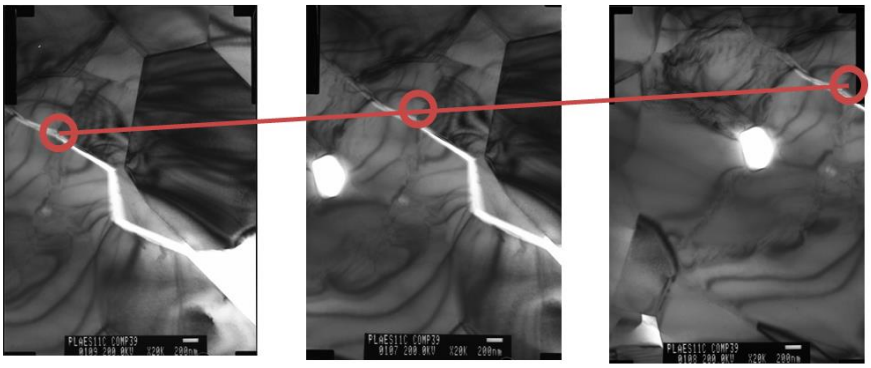


Figure A4.1.4: Three TEM images used to correct the image rotation.

These two corrections were combined to ensure that the angle between the uniaxial compression direction and the feature was accurately determined.

Appendix 4.2 – Standard EELS spectra

Aluminium

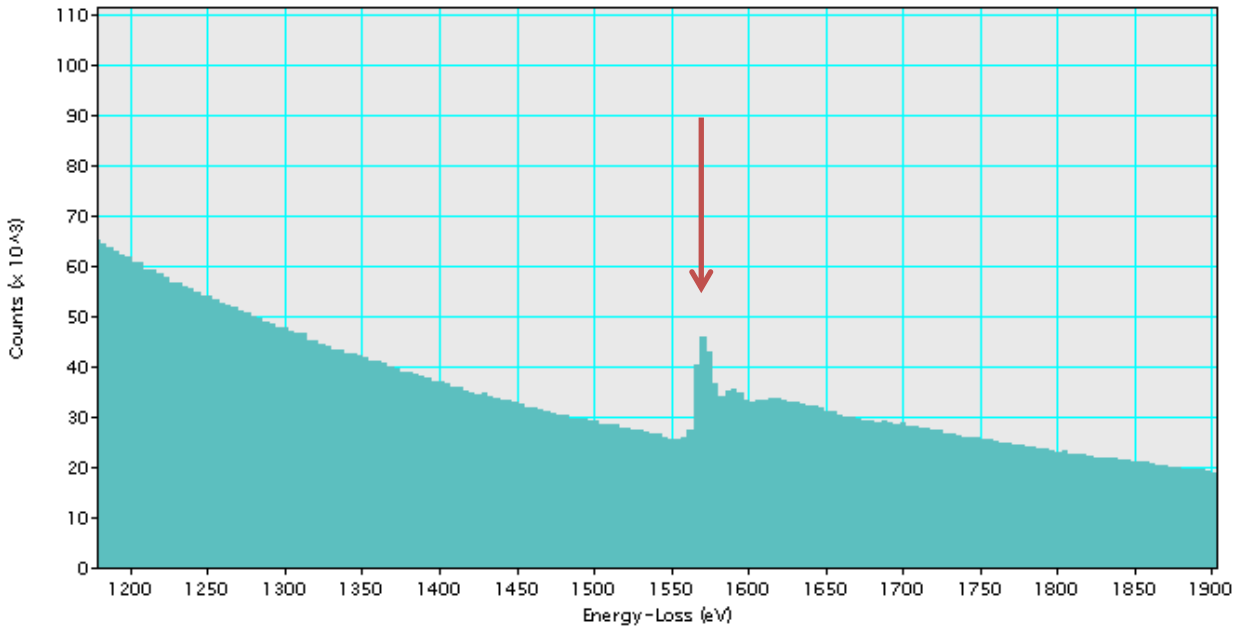


Figure A4.2.1: Aluminium edge in aluminium oxide (indicated with an arrow) from a standard material (from DM).

Figure A4.2.1 shows the standard edge for aluminium in aluminium oxide. The edge onset energy is at approximately 1560eV.

Oxygen

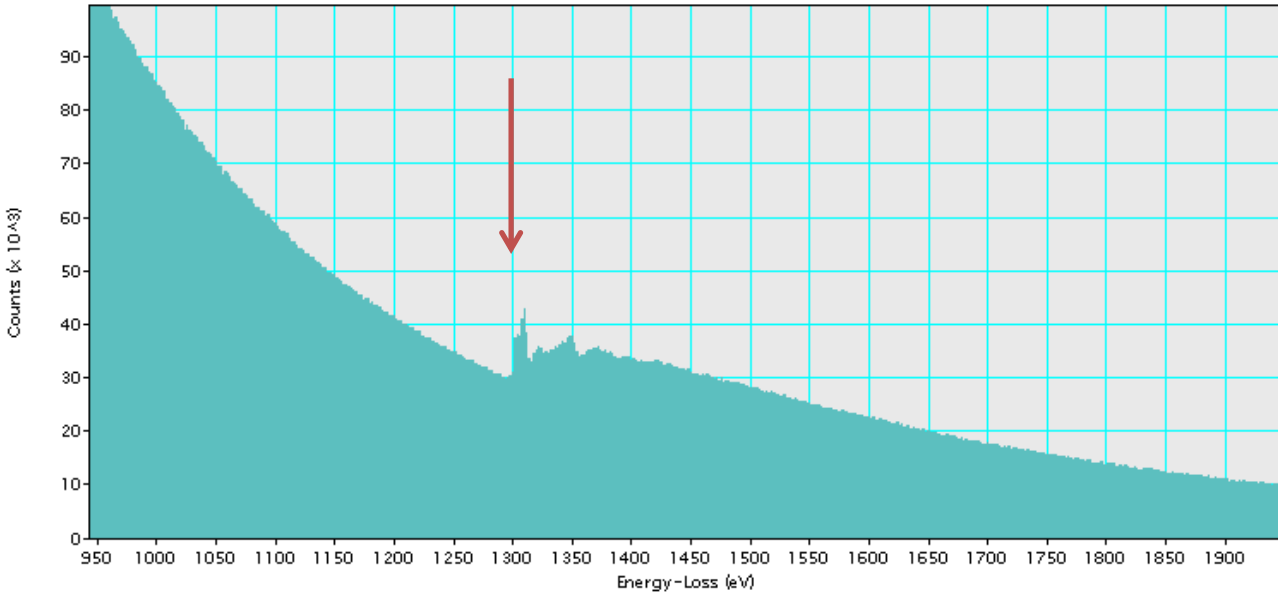


Figure A4.2.2: Magnesium edge in magnesium oxide (indicated with an arrow) from a standard material (from DM)

Magnesium

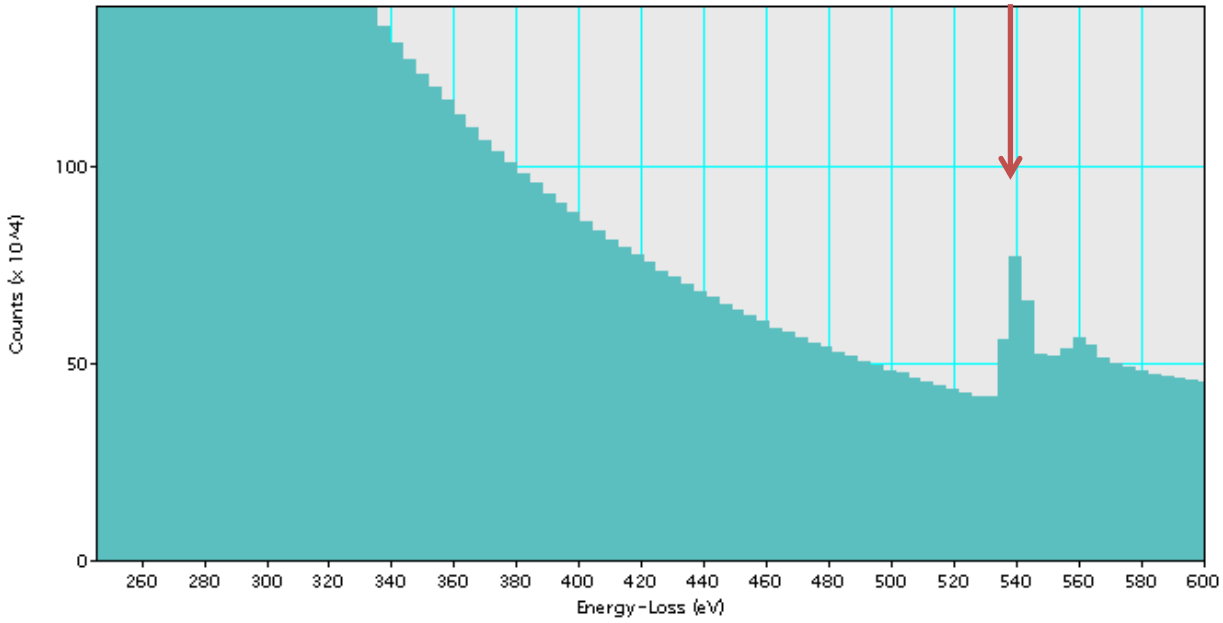


Figure A4.2.3: Oxygen edge in aluminium oxide (indicated with an arrow) from a standard material (from DM)

Silicon

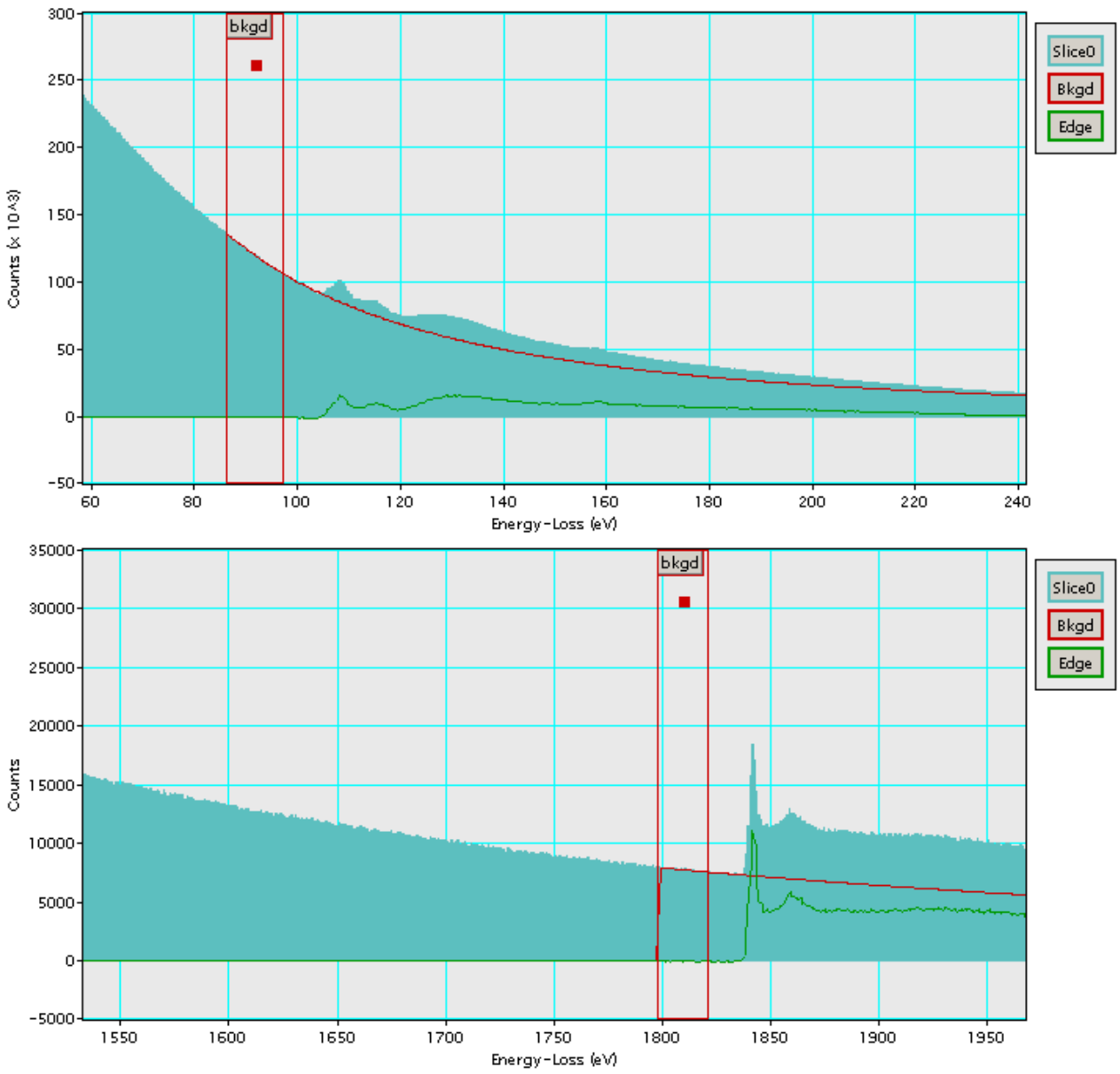
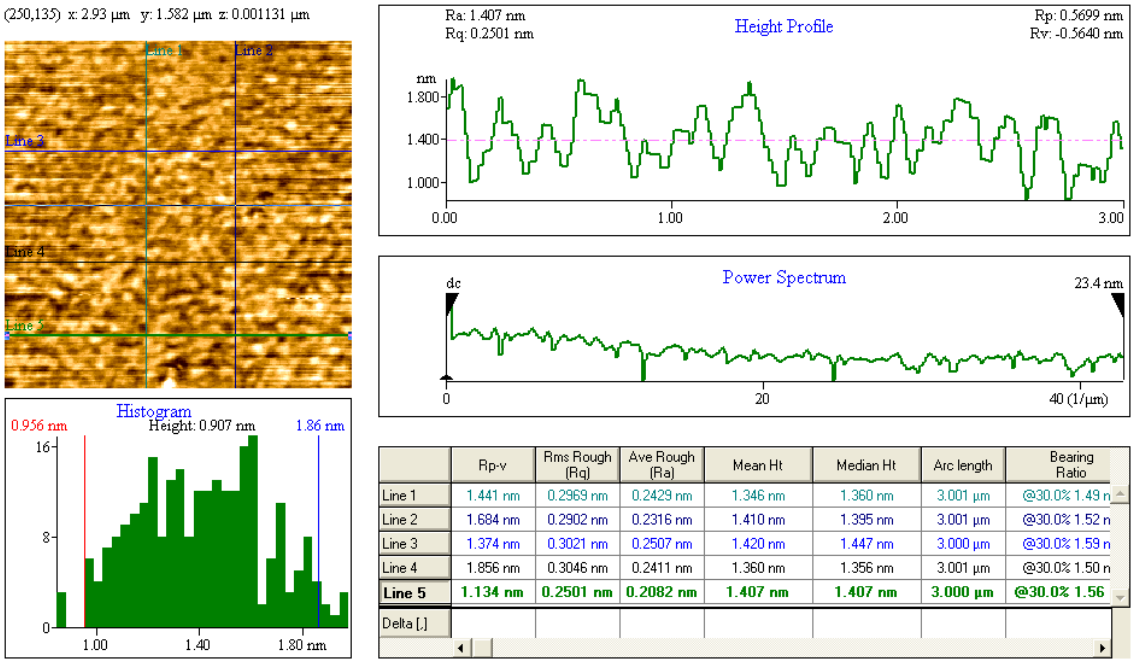


Figure A4.2.4: Two silicon edges in SiO a) low energy-loss and b) high energy-loss from a standard material (from DM)

There were two silicon edges in EELS. The low energy-loss edges (Figure A4.2.4a) had an onset energy-loss of approximately 104eV and, in SiO_2, showed some fine structure at higher energy-losses.

Appendix 4.3 – Atomic Force Microscopy of c-plane sapphire



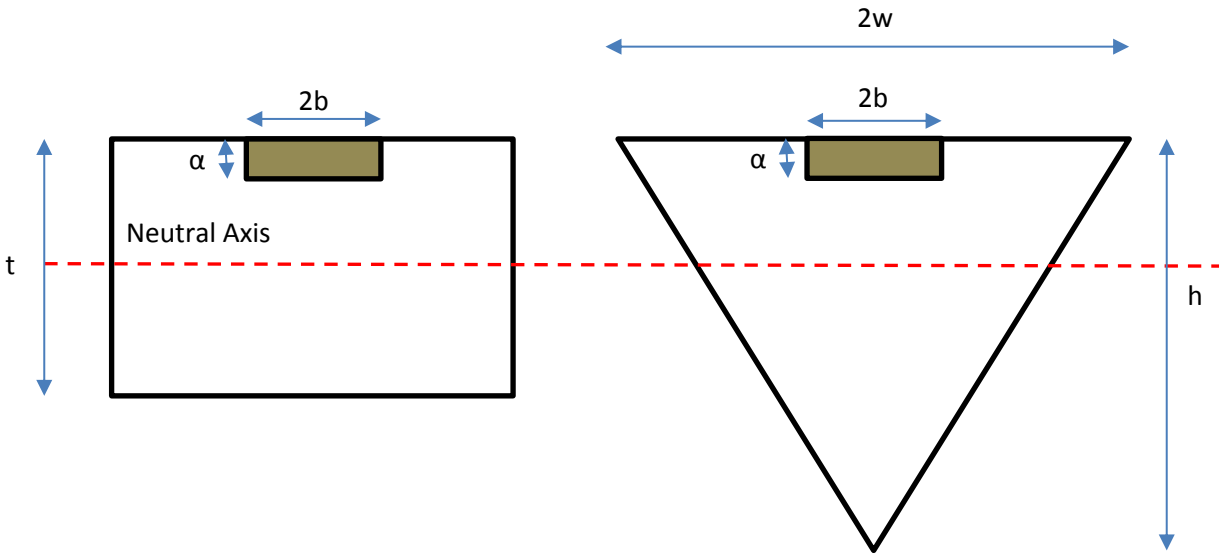
	Rp-v	Rms Rough (Rq)	Ave Rough (Ra)	Mean Ht	Median Ht	Arc length	Bearing Ratio
Line 1	1.441 nm	0.2969 nm	0.2429 nm	1.346 nm	1.360 nm	3.001 µm	@30.0% 1.49 n
Line 2	1.684 nm	0.2902 nm	0.2316 nm	1.410 nm	1.395 nm	3.001 µm	@30.0% 1.52 n
Line 3	1.374 nm	0.3021 nm	0.2507 nm	1.420 nm	1.447 nm	3.000 µm	@30.0% 1.59 n
Line 4	1.856 nm	0.3046 nm	0.2411 nm	1.360 nm	1.356 nm	3.001 µm	@30.0% 1.50 n
Line 5	**1.134 nm**	**0.2501 nm**	**0.2082 nm**	**1.407 nm**	**1.407 nm**	**3.000 µm**	**@30.0% 1.56**
Delta [.]							

Figure A4.3.1: AFM image and analysis of top of c-plane sapphire.

Four AFM scans across the top of the c-plane sapphire were taken, and 5 line scans per scan generated. The 5 scans were averaged to given a value of Ra (average roughness) per scan. The Ra value, averaged over the four scans, was (0.16 +/- 0.05) nm.

Appendix 6.1 - Geometric function M for semi-elliptical surface flaws

The following equations are by Strobl et al [144] and used in this project to determine the stress intensity factors for FIB produced controlled flaws. The original work was for rectangular beams. To be able to apply the equations to triangular beams, the neutral axes for the rectangular and triangular beams need to be equated.



$$\frac{t}{2} = \frac{h}{3} \quad \overset{so}{\rightarrow} \quad h = \frac{3}{2}t$$

To differentiate between the measured height (from SEM) and the height used in the equations in this section, the following conversion is used:

$$h^* = \frac{2}{3}h$$

h^* is used in the following equations along with:

K = stress intensity factor

Y = geometric function

α = flaw depth

w = half width of microcantilever beam

b = half width of controlled flaw

χ = angle between elliptical flaw and top surface

v = Poisson's ratio.

$$K = \sigma\sqrt{\pi\alpha}\,M = \sigma\sqrt{\pi\alpha}\,f\,f_b\,f_\nu\,f_\chi\,f_\theta \qquad \text{(A6.1.1)}$$

$$f\left(\frac{\alpha}{b},\frac{\alpha}{h^*}\right) = \left(1.11 + 1.71\left(\frac{\alpha}{b}\right)^{1.42}\right)^{-0.5}\left(1.16 - \frac{0.094\alpha}{b} + \left(-1.67 + \frac{0.174}{0.256 + \left(\frac{\alpha}{b}\right)}\right)\frac{\alpha}{h^*} + \left(-0.09 - 0.045\left(1 - \frac{\alpha}{b}\right) + \frac{0.316}{0.14 + \left(\frac{\alpha}{b}\right)}\right)\left(\frac{\alpha}{h^*}\right)^2 - 0.186\left(\frac{\alpha}{h^*}\right)^3\right)$$

$$f_b\left(\frac{\alpha}{b},\frac{\alpha}{h^*},\frac{b}{w}\right) = \left(\cos\left(1.04\left(\frac{b}{w} - 0.1\right)\left(\frac{2\alpha}{h^*}\right)^{0.5} 90^o\right)\right)^{-0.5}\left(1 + \left(\frac{\alpha}{b} - 0.41\right)\left(\frac{b}{w} - 0.1\right)\left(-0.38\left(\frac{\alpha}{b}\right)^2 + 1.4\right)\left(0.074 + 1.26\left(\frac{\alpha}{h^*}\right)^3\right)\right)$$

$$f_\nu\left(\frac{\alpha}{b},\frac{\alpha}{h^*},\nu\right) = 1 + 0.97\nu\left(-0.15\left(\frac{\alpha}{b}\right) + 0.13\left(\frac{\alpha}{b}\right)^2\right)\left(6.43\frac{\alpha}{h^*} - 6.15\left(\frac{\alpha}{h^*}\right)^{0.5}\right) 0.68\nu^2\left(0.68 - 0.09\left(\frac{\alpha}{b}\right)^2\right)\left(1 - \frac{1.8\alpha}{h^*} + 9.12\left(\frac{\alpha}{h^*}\right)^2\right)$$

$$f_\chi\left(\frac{\alpha}{b},\frac{\alpha}{h^*},\chi\right) = 1 - 0.31\left(\frac{\alpha}{b}\right)^{1.7}\left(-1.46 - 4.25\left(\frac{\alpha}{h^*}\right)^2\right)\left(1 - \left(\frac{90}{\chi}\right)^{0.72}\right)$$

$$f_\theta\left(\frac{\alpha}{b},\frac{\alpha}{h^*},\frac{b}{w},\nu,\theta\right) = \left(\left(\frac{\alpha}{b}\right)^2(\sin\theta)^2 + (\cos\theta)^2\right)^{0.25}\left(1 + \left(0.11\left(1.9 - \frac{\alpha}{b}\right)\left(1 + \frac{\alpha}{h^*}\right) - \frac{0.02}{\frac{\alpha}{b}}\sin\left(\frac{\alpha}{h^*}360\right)\right)\left(1 + 11\nu\left(\frac{\alpha}{h^*}\right)^6\left(0.11 - \left(0.13 - \frac{\alpha}{h^*}\right)^2\right)\right)\left(\frac{\theta}{90}\right)^3 + 0.05(1 - 3.7\nu)\left(\frac{\theta}{90}\right)^{10} + \frac{0.085}{\frac{\alpha}{b}}(1 - 2.3\nu)\left(\frac{\theta}{90}\right)^{20} - \frac{0.05}{\frac{\alpha}{b}}\left(\frac{\theta}{90}\right)^{50}\right)\left(1 + \left(0.28\left(\frac{2\alpha}{h^*}\right)^{0.9} + 0.72\left(\frac{2\alpha}{h^*}\right)^{\left(1+\frac{2.3\alpha}{b}\right)}\right)\left(0.69\left(\frac{\alpha}{h^*} + 0.25\right)\right)\left(\left(2.15 - \frac{0.28b}{w}\right)\left(\left(\frac{\theta}{90}\right)^{\left(3.9-\frac{1.99\alpha}{h^*}\right)} + \left(\frac{\theta}{90}\right)^3\left(1 - \frac{\theta}{90}\right)\right)\right)\right)\left(1 + 1.8\left(1 - \frac{\theta}{90}\right)\left(\left(-0.54\nu + \frac{0.07b}{w}\right)\left(\frac{\theta}{90}\right)^6 + \left(1 - \frac{2\alpha}{h^*}\right)\left(\frac{\left(1.2 - \frac{\alpha}{h^*}\right)}{0.8}\right)^4 0.7\left(\frac{\theta}{90}\right)^{2.5} - 3\left(\frac{\left(1.2 - \frac{\alpha}{h^*}\right)}{0.8}\right)\exp\left(-19.5\left(1 - \frac{\theta}{90}\right)\right)\right)\right)$$

Appendix 7.1 - Determining the stress intensity factors for blunt notches with residual stress at the tip due to gallium implantation

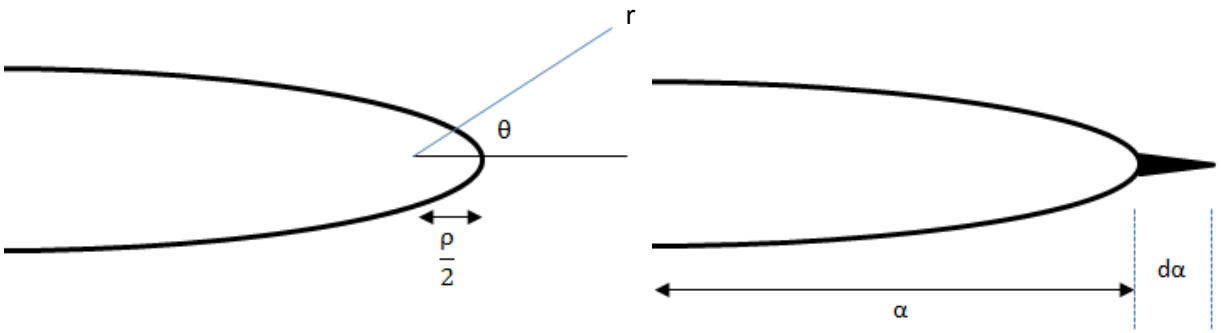


Figure A7.1.1: a) Schematic of blunt notch used to determine stress a given distance r from the tip, b) showing the small increment of crack from the front of the blunt notch.

The stress intensity factor correction for a blunt notch was determined. From Creager and Paris [221], the stress at a blunt tip, taking the origin a distance $\frac{\rho}{2}$ behind the notch tip is :

$$\sigma_y = \frac{K_{app}}{(2\pi r)^{\frac{1}{2}}} \cos\frac{\theta}{2}\left[1 + \sin\frac{\theta}{2}\sin\frac{3\theta}{2}\right] + \frac{K_{app}}{(2\pi r)^{\frac{1}{2}}}\frac{\rho}{2r}\cos\frac{3\theta}{2} \qquad \text{(A7.1.1)}$$

where K_{app} is the externally applied stress intensity factor. Taking $\theta = 0^o$ and $r = \frac{\rho}{2}$ (i.e. considering the stress at the notch tip),

$$\sigma_y = \frac{2K_{app}}{(\pi\rho)^{\frac{1}{2}}} \qquad \text{(A7.1.2)}$$

In front of the blunt notch a small length of crack, dα, could nucleate and propagate (Figure A7.1.1). The stress intensity for this notch tip crack, K_{nt}, is related to the stress in front of the notch, σ_y, and the length of the crack, $d\alpha$, using Equation A7.1.3.

$$K_{nt} = \frac{2K_{app}}{(\pi\rho)^{\frac{1}{2}}}\ \psi\sqrt{\pi\, d\alpha} \qquad \text{(A7.1.3)}$$

where ψ is a geometric parameter (1.12 for a through thickness edge crack).

Thus, the relationship between the stress intensity for the notch tip crack and the externally applied stress intensity factor is:

$$\frac{K_{nt}}{K_{app}} = 2\,\psi\,\sqrt{\frac{d\alpha}{\rho}} \qquad \text{(A7.1.4)}$$

Following previous work [149-151], a weighting function was considered. At small values of dα, the bluntness of the notch has a huge impact on the stress intensity factor of the notch tip crack. At large values of dα, the stress intensity tends towards the externally applied value. This was considered graphically (Figure A7.1.2) using Equation 6.25 for the externally applied stress intensity factor.

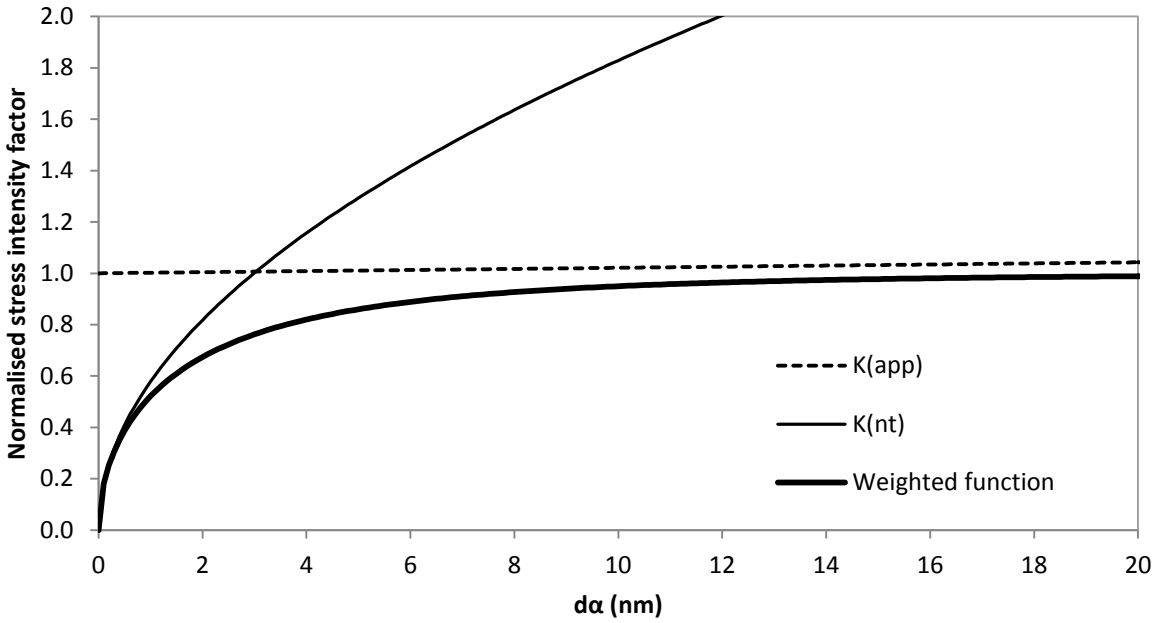


Figure A7.1.2: Normalised stress intensity factor against notch tip crack length dα for: K(nt) (using Equation A7.1.4 with ρ = 15nm) & K(app) (using Equation 6.25 where α = α_0 + dα). The weighted function was given in Equation A7.1.5

The value of the crack length for K_{app} is $\left(\alpha_0 - \frac{\rho}{2}\right) + d\alpha$, where α_0 is the original notch depth. In Damani et al [151], the final notch depth is used in the equation for K_{app}; this resulted in the weighted function tending strongly towards $Kapp$ at high values of dα.

The weighted function that reconciled the two curves is (from [132-134]):

$$\frac{K_{nt}}{K_{app}} = \tanh\left(2\,\psi\sqrt{\frac{d\alpha}{\rho}}\right) \qquad \text{(A7.1.5)}$$

This gave a good fit for the data in the work of Damani et al [151].

Due to the gallium implantation, there was a residual stress at the notch tip (Figure A7.1.3).This reduced the stress intensity factor on the notch tip crack (Equation A7.1.6). The reduced value of the stress intensity factor was termed $K_{nt,r}$.

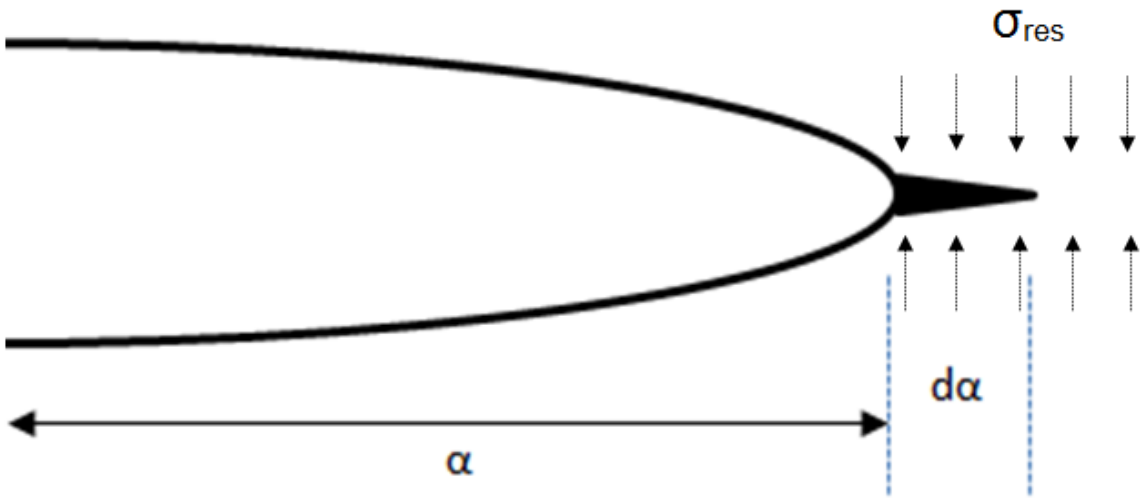


Figure A7.1.3: Schematic of notch tip crack with residual stress due to gallium implantation

$$K_{nt,r} = K_{app}\,\tanh\left(2\,\psi\sqrt{\frac{d\alpha}{\rho}}\right) + \sigma_{res}\,\psi\sqrt{\pi\,d\alpha} \qquad \text{(A7.1.6)}$$

where σ_{res} is negative (i.e. compressive) If the notch tip crack is short, the stress intensity due to the blunt notch is more significant. If the tip crack is long, the residual stress term becomes more significant such that, at a very large $d\alpha$, the stress intensity factor becomes negative. In practice, the value of dα was small enough that the stress intensity factor was large and positive at the onset of fracture.

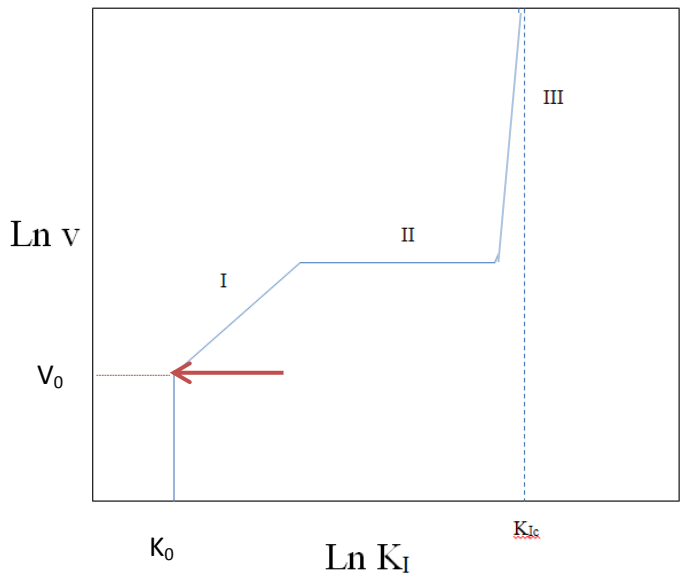


Figure A7.2.1: Crack tip velocity against applied stress intensity factor. Arrow shows start of Region I with the values of K_0 and V_0.

Appendix 7.2 - Deriving the crack extension with dynamic loading due to moisture assisted sub-critical crack growth in Region I

The following was related to the work presented by Evans [177]. However, owing to errors in the original paper, the following was presented in full to correct for those typographical errors.

The stress-intensity factor, K, can be related to the stress, σ, and the crack length, α, by the equation:

$$K = \psi\sigma(\pi\alpha)^{\frac{1}{2}} \tag{A7.2.1}$$

ψ is a factor that depends on the crack geometry. For a constant stress-rate condition, the crack velocity $d\alpha/dt$ is:

$$\frac{d\alpha}{dt} = \left(\frac{\partial\alpha}{\partial\sigma}\right)_{K,t}\frac{d\sigma}{dt} \tag{A7.2.2}$$

From [177]. Rearranging:

$$d\sigma = \frac{\dot{\sigma}}{V}d\alpha \tag{A7.2.3}$$

where V is the crack tip velocity and $\dot{\sigma}$ the loading rate.

Charles [254] found $V \propto K^n$ in Region I. Hence, assuming that the crack growth velocity, V, is related to the stress intensity factor, K, at any given point by:

$$V = V_0 \left(\frac{K}{K_0}\right)^n \tag{A7.2.4}$$

where V_0 and K_0 are the stress intensity factor and crack tip velocity at the start of Region I, respectively, and n the power constant. The stress intensity factor is related to the crack length and the stress during Region I by:

$$K = K_0 \left(\frac{\alpha}{\alpha_0}\right)^{\frac{1}{2}} \left(\frac{\sigma}{\sigma_0}\right) \tag{A7.2.5}$$

Combining A7.2.4. and A7.2.5:

$$V = \frac{V_0 K_0}{{K_0}^n} \left(\frac{\alpha}{\alpha_0}\right)^{n/2} \left(\frac{\sigma}{\sigma_0}\right)^n \tag{A7.2.6}$$

Hence, substituting into equation A7.2.3:

$$d\sigma = \frac{\dot{\sigma} {K_0}^{n-1}}{V_0} \left(\frac{\alpha_0}{\alpha}\right)^{\frac{n}{2}} \left(\frac{\sigma_0}{\sigma}\right)^n d\alpha \tag{A7.2.7}$$

Rearranging and integrating between σ and σ_0:, and α and α_0:

$$\left[\frac{\sigma^{n+1}}{n+1}\right]_{\sigma_0}^{\sigma} \frac{1}{\dot{\sigma}} = \frac{{\alpha_0}^{\frac{n}{2}} {\sigma_0}^n {K_0}^{n-1}}{V_0} \left[-\frac{2\alpha^{1-\frac{n}{2}}}{n-2}\right]_{\alpha_0}^{\alpha} \tag{A7.2.8}$$

$$\sigma^{n+1} = {\sigma_0}^{n+1} + \frac{2\dot{\sigma} {\alpha_0}^{\frac{n}{2}} {\sigma_0}^n {K_0}^{n-1} (n+1)}{V_0 (n-2)} \left[{\alpha_0}^{1-\frac{n}{2}} - \alpha^{1-\frac{n}{2}}\right] \tag{A7.2.9}$$

By noting that $\sigma_0 = \frac{K_0}{\psi(\pi\alpha_0)^{\frac{1}{2}}}$ for a surface crack,

$$\sigma^{n+1} = \left(\frac{K_0}{\psi(\pi\alpha_0)^{\frac{1}{2}}}\right)^{n+1} \left[1 + \frac{2\dot{\sigma}\pi^{\frac{1}{2}} \alpha_0^{\frac{n+1}{2}} (n+1)}{V_0 K_0 (n-2)} \left[{\alpha_0}^{1-\frac{n}{2}} - \alpha^{1-\frac{n}{2}}\right]\right] \tag{A7.2.10}$$

Hence:

$$\sigma = \left(\frac{K_0}{\psi(\pi\alpha_0)^{\frac{1}{2}}}\right)\left[1 + \frac{2\dot{\sigma}\pi^{\frac{1}{2}}\alpha_0{}^{\frac{n+1}{2}}(n+1)}{V_0K_0(n-2)}\left[\alpha_0{}^{1-\frac{n}{2}} - \alpha^{1-\frac{n}{2}}\right]\right]^{\frac{1}{n+1}} \qquad \text{(A7.2.11)}$$

Or,

$$\alpha = \left[\alpha_0{}^{1-\frac{n}{2}} - \left(\left(\frac{\sigma\psi(\pi\alpha_0)^{\frac{1}{2}}}{K_0}\right)^{n+1} - 1\right)\frac{V_0K_0(n-2)}{2\dot{\sigma}\pi^{\frac{1}{2}}\alpha_0{}^{\frac{n+1}{2}}(n+1)}\right]^{\frac{1}{1-\frac{n}{2}}} \qquad \text{(A7.2.12)}$$

Appendix 7.3 – Relating change in compliance with crack growth

From Section 6.1,

$$Y = \left[\frac{1}{2}\frac{dC'}{d\alpha'}\right]^{\frac{1}{2}} \tag{A7.3.1}$$

Using Equations 6.19 and the value of η from Equation 6.25,

$$\left[\frac{1}{2}\frac{dC'}{d\alpha'}\right]^{\frac{1}{2}} = 13.44\sqrt{\pi}\frac{L_{fr}}{h}\left(\frac{h}{w}\right)^{\frac{1}{2}}\sqrt{\alpha'(1-\alpha')}\ \left(1 + 0.123\alpha' + 5.456\alpha'^{2} + 0.073\alpha'^{3} - 0.023\alpha'^{4}\right) \tag{A7.3.2}$$

$$\int_{C'_1}^{C'_2} C' = 2\left(13.44\sqrt{\pi}\frac{L_{fr}}{h}\left(\frac{h}{w}\right)^{\frac{1}{2}}\right)^{2}\int_{\alpha'_1}^{\alpha'_2}\alpha'(1 - \alpha')\ \left(1 + 0.123\alpha' + 5.456\alpha'^{2} + 0.073\alpha'^{3} - 0.023\alpha'^{4}\right)^{2}\ d\alpha' \tag{A7.3.3}$$

Let $A = 2\left(13.44\sqrt{\pi}\frac{L_{fr}}{h}\left(\frac{h}{w}\right)^{\frac{1}{2}}\right)^{2}$, B = 0.123, C = 5.456, D = 0.073, E = -0.023

$$[C']_{C'_1}^{C'_2} = -A\left(\frac{1}{5}\alpha'^{5}(B^2 - 2BC + 2C - 2D) - \frac{1}{4}\alpha'^{4}(B^2 - 2B + 2C) + \frac{1}{7}\alpha'^{7}(2(B(D - E) + E) + C^2 - 2CD) - \frac{1}{6}\alpha'^{6}(-2BC + 2BD + C^2 - 2D + 2E) - \frac{1}{8}\alpha'^{8}(-2EB + 2C(E - D) + D^2) + \frac{1}{3}(1 - 2B)\alpha'^{3} + \frac{1}{9}\alpha'^{9}(2EC + D^2 - 2ED) - \frac{1}{10}E(E - 2D)\alpha'^{10} + \frac{1}{11}E^2\alpha'^{11} - \frac{1}{2}\alpha'^{2}\right)_{\alpha'_1}^{\alpha'_2} \tag{A7.3.4}$$

By noting the increase in C' during loading, the increase in the reduced notch depth α' is calculated and, using the height of the beam, the crack extension determined.

References

1. A. A. Griffith, “The Phenomena of Rupture and Flow in Solids,” *Philosophical Transactions of the Royal Society of London. Series A, Containing Papers of a Mathematical or Physical Character* 221 (1921): 163-198.
2. T. Nishida, Y. Hanaki, and G. Pezzotti. “Effect of Notch-Root Radius on the Fracture Toughness of a Fine-Grained Alumina.” *Journal of the American Ceramic Society* 77, no. 2 (1994): 606–608.
3. David J. Green, *An introduction to the mechanical properties of ceramics*, 1st ed., Cambridge Solid State Science Series (Cambridge University Press).
4. Fracture Toughness, Iron and Steel Institute, ISI Publication 121
5. B. R. Lawn and T. R. Wilshaw, *Fracture of Brittle Solids*, 1st ed. (Cambridge University Press, 1975).
6. G. D. Quinn and R. Morrell, “Design Data for Engineering Ceramics: A Review of the Flexure Test,” *Journal of the American Ceramic Society* 74, no. 9 (1991): 2037-2066.
7. R. Bermejo, Y. Torres, A.J. Sánchez-Herencia, C. Baudín, M. Anglada, and L. Llanes. “Residual Stresses, Strength and Toughness of Laminates with Different Layer Thickness Ratios.” *Acta Materialia* 54, no. 18 (2006): 4745–4757.
8. A. H. Heuer. “Transformation Toughening in ZrO2-Containing Ceramics.” *Journal of the American Ceramic Society* 70, no. 10 (1987): 689–698.
9. P. F. Becher, C-H Hsueh, K. B. Alexander, and E. Y Sun. “Influence of Reinforcement Content and Diameter on the R-Curve Response in SiC-Whisker-Reinforced Alumina.” *Journal of the American Ceramic Society* 79, no. 2 (1996): 298–304.
10. N. A. Yahya and R. I. Todd. “Influence of C Doping on the Fracture Mode and Abrasive Wear of Al2O3.” *Journal of the European Ceramic Society* 32, no. 16 (2012): 4003–4007.

11. R. L. Satet and M. J. Hoffmann. “Influence of the Rare-Earth Element on the Mechanical Properties of RE–Mg-Bearing Silicon Nitride.” *Journal of the American Ceramic Society* 88, no. 9 (2005): 2485–2490.
12. D. Di Maio, and S.G. Roberts. “Measuring Fracture Toughness of Coatings Using Focused-ion-beam-machined Microbeams.” *Journal of Materials Research* 20, no. 2 (2005): 299–302.
13. D. E. J. Armstrong, A.J. Wilkinson, and S.G. Roberts. “Micro-mechanical Measurements of Fracture Toughness of Bismuth Embrittled Copper Grain Boundaries.” *Philosophical Magazine Letters* 91, no. 6 (2011): 394–400.
14. M. F. Ashby and S.D. Hallam (Née Cooksley). “The Failure of Brittle Solids Containing Small Cracks Under Compressive Stress States.” *Acta Metallurgica* 34, no. 3 (1986): 497–510
15. J. Lankford, “Compressive strength and microplasticity in polycrystalline alumina,” *Journal of Materials Science* 12, no. 4 (1977): 791-796
16. G. S. Rohrer, *Structure and Bonding in Crystalline Materials*, 1st ed. (Cambridge University Press).
17. P Auerkari, “Mechanical and physical properties of engineering alumina ceramics,” *Technical Research Centre of Finland* 1792 (1996): 1-26.
18. J. J Cleveland and C. W. Fritsch Jnr, “FINE GRAIN TRANSLUCENT ALUMINA,” US Patent 3,834,915, 1974.
19. P. J. Hazell, N. A. Fellows, and J. G. Hetherington, “A note on the behind armour effects from perforated alumina/aluminium targets,” *International Journal of Impact Engineering* 21, no. 7 (1998): 589-595.
20. M. L. Kronberg, “Plastic deformation of single crystals of sapphire: Basal slip and twinning,” *Acta Metallurgica* 5, no. 9 (1957): 507-524.
21. J. B. Wachtman, *Mechanical Properties of Ceramics*, 1st ed. (Wiley-Interscience).
22. D. W. Budworth, *An Introduction to Ceramic Science*, 1st ed. (Pergamon Press)

23. R. M. Cannon, “Mechanical Properties of MgO and Al_2O_3,” in *Proceedings of an international symposium on structure and properties of MgO and Al_2O_3 ceramics, MIT, June 13-16 1983.* (The American Ceramic Society), 818-838.
24. K. P. D. Lagerlöf et al., “Slip and Twinning in Sapphire (α-Al_2O_3),” *Journal of the American Ceramic Society* 77, no. 2 (1994): 385-397.
25. I. Levin and D. Brandon, “Metastable Alumina Polymorphs: Crystal Structures and Transition Sequences,” *Journal of the American Ceramic Society* 81, no. 8 (2005): 1995-2012.
26. Y. R. Shiue and D. S. Phillips. “The Crystallography of Annealing Twins in Alumina Ceramics.” *Philosophical Magazine A* 50, no. 5 (1984): 677–702.
27. D. S. Phillips and Y. R. Shiue. “Grain-Boundary Microstructures in Alumina Ceramics.” In *Structure and Properties of MgO and Al_2O_3 Ceramics*, 10:357–367. Advances in Ceramics
28. S. C. Hansen and D. S. Phillips. “Grain Boundary Microstructures in a Liquid-phase Sintered Alumina (α-Al2O3).” *Philosophical Magazine A* 47, no. 2 (1983): 209–234.
29. C. B. Carter and M. G. Norton. *Ceramic Materials: Science and Engineering*. Springer, 2007.
30. P. S. Nicholson “Synthesis of Polycrystalline H_3O^+ and NH^{4+}-β’’/β-Al_2O_3 and Potential Applications in Steam-electrolysis/fuel-cells.” In *Proton Conductors*. Chemistry of Solid State Materials. Cambridge University Press, 1992.
31. Seong-Jai Cho et al., “The transition from mild to severe wear in alumina during sliding,” *Acta Metallurgica et Materialia* 40, no. 1 (1992): 185-192.
32. J. D. Clayton, “A continuum description of nonlinear elasticity, slip and twinning, with application to sapphire,” *Proceedings of the Royal Society A: Mathematical, Physical and Engineering Science* 465, no. 2101 (2009): 307-334.
33. J. D. O. Barceinas-Sánchez and W. M. Rainforth, “On the role of plastic deformation during the mild wear of alumina,” *Acta Materialia* 46, no. 18 (1998): 6475-6483.

34. P. F. Becher, “Abrasive Surface Deformation of Sapphire,” *Journal of the American Ceramic Society* 59, no. 3 (1976): 143-145.
35. T. Geipel, K.P.D. Lagerlöf, P. Pirouz, and A.H. Heuer. “A Zonal Dislocation Mechanism for Rhombohedral Twinning in Sapphire (α-Al_2O_3).” *Acta Metallurgica et Materialia* 42, no. 4 (1994): 1367–1372.
36. P. Pirouz et al., “On Basal slip and basal twinning in sapphire (α-Al_2O_3)--II. A new model of basal twinning,” *Acta Materialia* 44, no. 5 (1996): 2153-2164.
37. P. Pirouz. “Deformation Mode in Silicon, Slip or Twinning?” *Scripta Metallurgica* 21, no. 11 (1987): 1463–1468.
38. A. H. Heuer, “Deformation twinning in corundum,” *Philosophical Magazine* 13, no. 122 (1966): 379.
39. J. Lankford, “Tensile failure of unflawed polycrystalline Al_2O_3,” *Journal of Materials Science* 13, no. 2 (1978): 351-357.
40. J. Lankford, “Temperature-strain rate dependance of compressive strength and damage mechanisms in aluminium oxide,” *Journal of Materials Science* 16, no. 6 (1981): 1567-1578.
41. I. Zarudi, L. Zhang, and Y-W. Mai, “Subsurface damage in alumina induced by single-point scratching,” *Journal of Materials Science* 31, no. 4 (1996): 905-914.
42. F. Guiberteau, N. P. Padture, and B. R. Lawn. “Effect of Grain Size on Hertzian Contact Damage in Alumina.” *Journal of the American Ceramic Society* 77, no. 7 (1994): 1825–1831.
43. W.C. Levengood, “Quantitative Aspects of Twinning Deformation in Sapphire and Ruby Single Crystals,” in *Crystal Growth: Proceedings of an International Conference on Crystal Growth, Boston, 20-24 June, 1966.* (Pergamon Press), 93-97.
44. M. Castillo-Rodríguez, A. Muñoz, J. Castaing, P. Veyssière, and A. Domínguez-Rodríguez. “Chromium Influence on Rhombohedral Twinning in Sapphire.” *Journal of Materials Science* 46, no. 23 (2011): 7431–7436.

45. B. Müller and D. Schulze. “Basal Twinning as a Room Temperature Plastic Deformation Mode of Chromium- and Titanium-doped Sapphire Crystals.” *Crystal Research and Technology* 19, no. 12 (1984): 1597–1602.
46. W. Walkosz. “Silicon Nitride Ceramics.” In *Atomic Scale Characterization and First-Principles Studies of Si_3N_4 Interfaces*, by Weronika Walkosz, 1–10. New York, NY: Springer New York, 2011.
47. P. F. Becher et al. “Microstructural Design of Silicon Nitride with Improved Fracture Toughness: I, Effects of Grain Shape and Size.” *Journal of the American Ceramic Society* 81, no. 11 (1998): 2821–2830.
48. F. L. Riley. “Silicon Nitride and Related Materials.” *Journal of the American Ceramic Society* 83, no. 2 (2000): 245–265.
49. F. F. Lange, “Relation Between Strength, Fracture Energy, and Microstructure of Hot-Pressed Si3N4.” *Journal of the American Ceramic Society* 56, no. 10 (1973): 518–522.
50. S. Fünfschilling et al. “Mechanisms of Toughening in Silicon Nitrides: The Roles of Crack Bridging and Microstructure.” *Acta Materialia* 59, no. 10 (2011): 3978–3989.
51. T. Ohji, K. Hirao, and S. Kanzaki. “Fracture Resistance Behavior of Highly Anisotropic Silicon Nitride.” *Journal of the American Ceramic Society* 78, no. 11 (1995): 3125–3128.
52. C. W. Li et al. “R-Curve Behavior and Strength for In-Situ Reinforced Silicon Nitrides with Different Microstructures.” *Journal of the American Ceramic Society* 75, no. 7 (1992): 1777–1785.
53. S. J. Dillon et al., “Complexion: A new concept for kinetic engineering in materials science,” *Acta Materialia* 55, no. 18 (2007): 6208-6218.
54. S. J. Dillon and M. P. Harmer, “Demystifying the role of sintering additives with "complexion",” *Journal of the European Ceramic Society* 28, no. 7 (2008): 1485-1493.

55. R. L. Coble, “Sintering Crystalline Solids. II. Experimental Test of Diffusion Models in Powder Compacts,” *Journal of Applied Physics* 32, no. 5 (1961): 793.
56. S. J. Bennison and M. P. Harmer, “Grain-Growth Kinetics for Alumina in the Absence of a Liquid Phase,” *Journal of the American Ceramic Society* 68, no. 1 (1985): C-22-C-24.
57. K. A. Berry and M. P. Harmer, “Effect of MgO Solute on Microstructure Development in Al_2O_3,” *Journal of the American Ceramic Society* 69, no. 2 (1986): 143-149.
58. W. A. Kaysser et al., “Effect of a Liquid Phase on the Morphology of Grain Growth in Alumina,” *Journal of the American Ceramic Society* 70, no. 5 (1987): 339-343.
59. C. A. Handwerker, P. A. Morris, and R. L. Coble, “Effects of Chemical Inhomogeneities on Grain Growth and Microstructure in Al_2O_3,” *Journal of the American Ceramic Society* 72, no. 1 (1989): 130-136.
60. S. Baik and J. H. Moon, “Effects of Magnesium Oxide on Grain-Boundary Segregation of Calcium During Sintering of Alumina,” *Journal of the American Ceramic Society* 74, no. 4 (1991): 819-822.
61. E. Dörre and H. Hübner, *Alumina: processing, properties, and applications* (Springer, 1984).
62. S. I. Bae and S. Baik, “Sintering and grain growth of ultrapure alumina,” *Journal of Materials Science* 28, no. 15 (1993): 4197-4204.
63. G. Rossi and J. E. Burke, “Influence of Additives on the Microstructure of Sintered Al_2O_3,” *Journal of the American Ceramic Society* 56, no. 12 (1973): 654-659.
64. S. J. Bennison and M. P. Harmer, “Effect of MgO Solute on the Kinetics of Grain Growth in Al_2O_3,” *Journal of the American Ceramic Society* 66, no. 5 (5, 1983): C-90-C-92.
65. S. J. Dillon, M. P. Harmer, and G. S. Rohrer. “The Relative Energies of Normally and Abnormally Growing Grain Boundaries in Alumina Displaying Different Complexions.” *Journal of the American Ceramic Society* 93, no. 6 (2010): 1796–1802.

66. H. Gu, R. M. Cannon, and M. Rühle. “Composition and Chemical Width of Ultrathin Amorphous Films at Grain Boundaries in Silicon Nitride.” *Journal of Materials Research* 13, no. 02 (2011): 376–387.
67. N. Shibata, G. S. Painter, R. L. Satet, M. J. Hoffmann, S. J. Pennycook, and P. F. Becher. “Rare-earth Adsorption at Intergranular Interfaces in Silicon Nitride Ceramics: Subnanometer Observations and Theory.” *Physical Review B* 72, no. 14 (2005): 140101. http://dx.doi.org/10.1103/PhysRevB.72.140101
68. E. A. Marquis, N. A. Yahya, D. J. Larson, M. K. Miller, and R. I. Todd. “Probing the Improbable: Imaging C Atoms in Alumina.” *Materials Today* 13, no. 10 (2010): 34–36.
69. S. A. Bojarski et al “The Relationship Between Grain Boundary Energy, Grain Boundary Complexion Transitions, and Grain Size in Ca-Doped Yttria.” *Materials Science Forum* 753 (2013): 87–92.
70. S. A. Bojarski et al “Changes in the Grain Boundary Character and Energy Distributions Resulting from a Complexion Transition in Ca-Doped Yttria.” *Metallurgical and Materials Transactions A* 43, no. 10 (2012): 3532–3538.
71. S. J. Dillon and M. P. Harmer. "Relating Grain Boundary Complexion to Grain Boundary Kinetics II: Silica-Doped Alumina." *Journal of the American Ceramic Society* 91 no. 7 (2008): 2314-2320.
72. M. F. Ashby and C. G. Sammis. “The Damage Mechanics of Brittle Solids in Compression.” *Pure and Applied Geophysics* 133, no. 3 (1990): 489–521.
73. G. R. Holzhausen and A.M. Johnson. “Analyses of Longitudinal Splitting of Uniaxially Compressed Rock Cylinders.” *International Journal of Rock Mechanics and Mining Sciences & Geomechanics Abstracts* 16, no. 3 (1979): 163–177.
74. G. Ravichandran, and G. Subhash. “A Micromechanical Model for High Strain Rate Behavior of Ceramics.” *International Journal of Solids and Structures* 32, no. 17–18 (1995): 2627–2646.
75. C. G. Sammis and M.F. Ashby. “The Failure of Brittle Porous Solids Under Compressive Stress States.” *Acta Metallurgica* 34, no. 3 (1986): 511–526.

76. H. Horii and S. Nemat-Nasser. “Compression-induced Microcrack Growth in Brittle Solids: Axial Splitting and Shear Failure.” *Journal of Geophysical Research: Solid Earth* 90, no. B4 (1985): 3105–3125.
77. S. Nemat-Nasser, “Mechanics of Brittle Failure in Compression.” *Computers & Structures* 20, no. 1–3 (1985): 235–237.
78. S. Nemat-Nasser and H. Deng. “Strain-rate Effect on Brittle Failure in Compression.” *Acta Metallurgica et Materialia* 42, no. 3 (1994): 1013–1024.
79. B. Cotterell and J. R. Rice. “Slightly Curved or Kinked Cracks.” *International Journal of Fracture* 16, no. 2 (1980): 155–169.
80. S. Nemat-Nasser and H. Horii. “Compression-Induced Nonplanar Crack Extension With Application to Splitting, Exfoliation, and Rockburst.” *Journal of Geophysical Research* 87, no. B8 (1982): PP. 6805–6821.
81. M. Basista and D. Gross. “The Sliding Crack Model of Brittle Deformation: An Internal Variable Approach.” *International Journal of Solids and Structures* 35, no. 5–6 (1998): 487–509.
82. H. Deng and S. Nemat-Nasser. “Dynamic Damage Evolution in Brittle Solids.” *Mechanics of Materials* 14, no. 2 (1992): 83–103.
83. G. Subhash and G. Ravichandran. “Mechanical Behaviour of a Hot Pressed Aluminum Nitride Under Uniaxial Compression.” *Journal of Materials Science* 33, no. 7 (1998): 1933–1939.
84. B. Lauterbach and D. Gross. “Crack Growth in Brittle Solids Under Compression.” *Mechanics of Materials* 29, no. 2 (1998): 81–92.
85. F. Lehner and M. Kachanov. “On Modelling of ‘winged” Cracks Forming Under Compression.” *International Journal of Fracture* 77, no. 4 (1996): R69–R75.
86. W. A. Nixon. “Wing Crack Models of the Brittle Compressive Failure of Ice.” *Cold Regions Science and Technology* 24, no. 1 (1996): 41–55.

87. G. Vekinis, M.F. Ashby, H. Shercliff, and P.W.R. Beaumont. “The Micromechanisms of Fracture of Alumina and a Ceramic-based Fibre Composite: Modelling the Failure Processes.” *Composites Science and Technology* 48, no. 1–4 (1993): 325–330.
88. P. S. Steif, “Crack Extension Under Compressive Loading.” *Engineering Fracture Mechanics* 20, no. 3 (1984): 463–473.
89. H. Tada, P.C. Paris , and G. R. Irwin. *The Stress Analysis of Cracks Handbook, Third Edition*. Three Park Avenue New York, NY 10016-5990: ASME, 2000.
90. E. G. Bombolakis, “Study of the Brittle Fracture Process Under Uniaxial Compression.” *Tectonophysics* 18, no. 3–4 (1973): 231–248.
91. H. D. Espinosa and P. D. Zavattieri. “A Grain Level Model for the Study of Failure Initiation and Evolution in Polycrystalline Brittle Materials. Part I: Theory and Numerical Implementation.” *Mechanics of Materials* 35, no. 3–6 (2003): 333–364.
92. H. D. Espinosa and P. D. Zavattieri. “A Grain Level Model for the Study of Failure Initiation and Evolution in Polycrystalline Brittle Materials. Part II: Numerical Examples.” *Mechanics of Materials* 35, no. 3 (2003): 365–394.
93. Y. H. Zhao et al "Real-time SEM observations of the microfracturing process in rock during a compression test." In *International journal of rock mechanics and mining sciences & geomechanics abstracts*, vol. 30, no. 6, pp. 643-652. Pergamon, 1993.
94. P. Merkert, M. Hoffman, and J. Rödel, “Detection of prefracture micro-cracking in Al_2O_3 by acoustic emission,” *Journal of the European Ceramic Society* 18, no. 12 (1998): 1645-1654.
95. A. G. Evans, M. Linzer, and L.R. Russell, “Acoustic emission and crack propagation in polycrystalline alumina,” *Materials Science and Engineering* 15, no. 2 (1974): 253-261.
96. A. G. Evans and M Linzer, “Acoustic Emission in Brittle Materials,” *Annual Review of Materials Science* 7, no. 1 (1977): 179-208.
97. C. U. Grosse and M. Ohtsu, *Acoustic Emission Testing* (Springer, 2008).
98. R. V. Williams, *Acoustic Emission*. 1st ed. Adam Hilger Ltd, 1980.

99. H. M. Tensi, "The Kaiser-effect and its scientific background." *J. Acoust. Emission* 22 (2004): S1-S16.

100. M. Ettouney and S. Alampalli. *Infrastructure Health in Civil Engineering*. CRC Press, 2012.

101. A. Lavrov, “The Kaiser Effect in Rocks: Principles and Stress Estimation Techniques.” *International Journal of Rock Mechanics and Mining Sciences* 40, no. 2 (2003): 151–171.

102. A. Nair, and C.S. Cai. “Acoustic Emission Monitoring of Bridges: Review and Case Studies.” *Engineering Structures* 32, no. 6 (2010): 1704–1714.

103. C. Li and E. Nordlund. “Experimental Verification of the Kaiser Effect in Rocks.” *Rock Mechanics and Rock Engineering* 26, no. 4 (1993): 333–351.

104. S. I. Likhatski and S.G. Nicholski, “Acoustic emission monitoring of strength in brittle materials,” *Ultrasonics* 24, no. 1 (1986): 31-35.

105. S. Johansson et al “Fracture Testing of Silicon Microelements in Situ in a Scanning Electron Microscope.” *Journal of Applied Physics* 63, no. 10 (1988): 4799–

106. S. Sundararajan et al. “Mechanical Property Measurements of Nanoscale Structures Using an Atomic Force Microscope.” *Ultramicroscopy* 91, no. 1–4 (2002): 111–118.

107. T. Namazu, Y. Isono, and T. Tanaka. “Evaluation of Size Effect on Mechanical Properties of Single Crystal Silicon by Nanoscale Bending Test Using AFM.” *Journal of Microelectromechanical Systems* 9, no. 4 (2000): 450–459.

108. K. Komai, K. Minoshima, and S. Inoue. “Fracture and Fatigue Behavior of Single Crystal Silicon Microelements and Nanoscopic AFM Damage Evaluation.” *Microsystem Technologies* 5, no. 1 (1998): 30–37.

109. J. McCarthy, Z. Pei, M. Becker, and D. Atteridge. “FIB Micromachined Submicron Thickness Cantilevers for the Study of Thin Film Properties.” *Thin Solid Films* 358, no. 1–2 (2000): 146–151.

110. F. A. Stevie, L. A. Giannuzzi, and B. I. Prenitzer. “The Focused Ion Beam Instrument.” In *Introduction to Focused Ion Beams: Instrumentation, Theory, Techniques and Practice*. Springer.

111. L. A. Giannuzzi, B. I. Prenitzer, and B. W. Kempshall. “Ion-Solid Interactions.” In *Introduction to Focused Ion Beams: Instrumentation, Theory, Techniques and Practice*. Springer.

112. D. E. J. Armstrong, M.E. Rogers, and S.G. Roberts. “Micromechanical Testing of Stress Corrosion Cracking of Individual Grain Boundaries.” *Scripta Materialia* 61, no. 7 (2009): 741–743.

113. J. Gong, and A. J. Wilkinson. “Investigation of Elastic Properties of Single-crystal α-Ti Using Microcantilever Beams.” *Philosophical Magazine Letters* 90, no. 7 (2010): 503–512.

114. J. Gong and A. J. Wilkinson. “Anisotropy in the Plastic Flow Properties of Single-crystal α Titanium Determined from Micro-cantilever Beams.” *Acta Materialia* 57, no. 19 (2009): 5693–5705.

115. D. E. J. Armstrong, A. J. Wilkinson, and S. G. Roberts. “Measuring Anisotropy in Young’s Modulus of Copper Using Microcantilever Testing.” *Journal of Materials Research* 24, no. 11 (2009): 3268–3276.

116. Y. L. Chan, A. H. W. Ngan, and N. M. King. “Use of Focused Ion Beam Milling for Investigating the Mechanical Properties of Biological Tissues: A Study of Human Primary Molars.” *Journal of the Mechanical Behavior of Biomedical Materials* 2, no. 4 (2009): 375–383..

117. C. Motz, T. Schöberl, and R. Pippan. “Mechanical Properties of Micro-sized Copper Bending Beams Machined by the Focused Ion Beam Technique.” *Acta Materialia* 53, no. 15 (2005): 4269–4279.

118. K. Matoy et al. “A Comparative Micro-cantilever Study of the Mechanical Behavior of Silicon Based Passivation Films.” *Thin Solid Films* 518 (2009): 247–256.

119. S. Wurster, C. Motz, and R. Pippan. “Notched-cantilever and –tensile Testing on the Micrometer Scale – Effects of Constraints on Plasticity and Fracture Behaviour.” In *ECF18, Dresden 2010*, 2013.

120. S. Massl, W. Thomma, J. Keckes, and R. Pippan. “Investigation of Fracture Properties of Magnetron-sputtered TiN Films by Means of a FIB-based Cantilever Bending Technique.” *Acta Materialia* 57, no. 6 (2009): 1768–1776.

121. K. Takashima, and Y. Higo. “Fatigue and Fracture of a Ni–P Amorphous Alloy Thin Film on the Micrometer Scale.” *Fatigue & Fracture of Engineering Materials & Structures* 28, no. 8 (2005): 703–710.

122. J. C. Ye, J. Lu, Y. Yang, and P. K. Liaw. “Extraction of Bulk Metallic-Glass Yield Strengths Using Tapered Micropillars in Micro-Compression Experiments.” *Intermetallics* 18, no. 3 (2010): 385–393.

123. C. J. Lee, Y. H. Lai. “Mechanical Behavior of Au-Based Metallic Glass in MicroScale at Ambient and Elevated Temperatures.” *Materials Transactions - MATER TRANS* 50, no. 12 (2009): 2795–2800.

124. C. J. Lee, Y. H. Lai, J. C. Huang, X. H. Du, L. Wang, and T. G. Nieh. “Strength Variation and Cast Defect Distribution in Metallic Glasses.” *Scripta Materialia* 63, no. 1 (2010): 105–108.

125. C. J. Lee, J. C. Huang, and T. G. Nieh. “Sample Size Effect and Microcompression of $Mg_{65}Cu_{25}Gd_{10}$ Metallic Glass.” *Applied Physics Letters* 91, no. 16 (2007): 161913.

126. Y. H. Lai, C. J. Lee, Y. T. Cheng, H. S. Chou, H. M. Chen, X. H. Du, C. I. Chang, et al. “Bulk and Microscale Compressive Behavior of a Zr-Based Metallic Glass.” *Scripta Materialia* 58, no. 10 (2008): 890–893.

127. B. E. Schuster, Q. Wei, T. C. Hufnagel, and K. T. Ramesh. “Size-Independent Strength and Deformation Mode in Compression of a Pd-Based Metallic Glass.” *Acta Materialia* 56, no. 18 (October 2008): 5091–5100.

128. Y. Yang, J. C. Ye, J. Lu, F. X. Liu, and P. K. Liaw. “Effects of Specimen Geometry and Base Material on the Mechanical Behavior of Focused-Ion-Beam-Fabricated Metallic-Glass Micropillars.” *Acta Materialia* 57, no. 5 (March 2009): 1613–1623..

129. C. Niederberger, W. M. Mook, X. Maeder, and J. Michler. “In Situ Electron Backscatter Diffraction (EBSD) during the Compression of Micropillars.” *Materials Science and Engineering: A* 527, no. 16–17 (2010): 4306–4311.

130. Jian, Sheng-Rui, T. -H Sung, J.C. Huang, and Jenh-Yih Juang. “Deformation Behaviors of InP Pillars under Uniaxial Compression.” *Applied Physics Letters* 101, no. 15 (2012): 151905–151905–4.

131. N.H. Takata, H. Ghassemi Armaki, Y. Terada, M. Takeyama, and K. S. Kumar. “Plastic Deformation of the C14 Laves Phase $(Fe,Ni)_2Nb$.” *Scripta Materialia* 68, no. 8 (2013): 615–618.

132. N. Takata, H. Ghassemi-Armaki, Y. Terada, M. Takeyama, and S. Kumar. “Effect of Dislocation Sources on Slip in Fe_2Nb Laves Phase with Ni in Solution.” *MRS Online Proceedings Library* 1516 (2013): 269–274.

133. C. Shih et al “Determination of Interfacial Mechanical Properties of Ceramic Composites by the Compression of Micro-pillar Test Specimens.” *Journal of Materials Science* 48, no. 15 (2013): 5219–5224.

134. G. Dehm, H. P. Wörgötter, S. Cazottes, J. M. Purswani, D. Gall, C. Mitterer, and D. Kiener. “Can Micro-Compression Testing Provide Stress–strain Data for Thin Films?: A Comparative Study Using Cu, VN, TiN and W Coatings.” *Thin Solid Films* 518, no. 5 (2009): 1517–1521.

135. C. Shin, Hyung-Ha Jin, Weon-Ju Kim, and Ji-Yeon Park. “Mechanical Properties and Deformation of Cubic Silicon Carbide Micropillars in Compression at Room Temperature.” *Journal of the American Ceramic Society* 95, no. 9 (2012): 2944–2950.

136. Zhang, Xinan, Qiuhong Zhao, Siqun Wang, Rosa Trejo, Edgar Lara-Curzio, and Guanben Du. “Characterizing Strength and Fracture of Wood Cell Wall through Uniaxial Micro-Compression Test.” *Composites Part A: Applied Science and Manufacturing* 41, no. 5 (2010): 632–638.

137. H. J. Yang, Y. T. Pei, G. M. Song, and J. Th. M. De Hosson. “Healing Performance of Ti_2AlC Ceramic Studied with in Situ Microcantilever Bending.” *Journal of the European Ceramic Society* 33, no. 2 (2013): 383–391.

138. Liu, S., J. M. Wheeler, P. R. Howie, X. T. Zeng, J. Michler, and W. J. Clegg. “Measuring the Fracture Resistance of Hard Coatings.” *Applied Physics Letters* 102, no. 17 (2013): 171907.

139. F. Ericson, and J. A. Schweitz. “Micromechanical Fracture Strength of Silicon.” *Journal of Applied Physics* 68, no. 11 (1990): 5840–5844.

140. M. W. Phaneuf, “FIB for Materials Science Applications - A Review.” In *Introduction to Focused Ion Beams: Instrumentation, Theory, Techniques and Practice*. Springer.

141. J. D. Landes and R. P. Wei. “The Kinetics of Subcritical Crack Growth Under Sustained Loading.” *International Journal of Fracture* 9, no. 3 (1973): 277–293.

142. I. S. Raju and J.C. Newman Jr. “Stress-intensity Factors for a Wide Range of Semi-elliptical Surface Cracks in Finite-thickness Plates.” *Engineering Fracture Mechanics* 11, no. 4 (1979): 817–829.

143. J. C. Newman Jr. and I. S. Raju. “An Empirical Stress-intensity Factor Equation for the Surface Crack.” *Engineering Fracture Mechanics* 15, no. 1–2 (1981): 185–192.

144. S. Strobl, P. Supancic, T. Lube, and R. Danzer. “Surface Crack in Tension or in Bending – A Reassessment of the Newman and Raju Formula in Respect to Fracture Toughness Measurements in Brittle Materials.” *Journal of the European Ceramic Society* 32, no. 8 (2012): 1491–1501.

145. J. Bagdahn et al. “Fracture Toughness and Fatigue Investigations of Polycrystalline Silicon.” In *Micromachining and Microfabrication* (pp. 159-168). International Society for Optics and Photonics (2001) 159–168

146. D. Miyaguchi, M. Otsu, K. Takashima, and M. Takeyama. “Microscale Fracture Toughness Testing of TiAl PST Crystals.” *MRS Proceedings* 1128 (2011): pp. 1128-U05

147. M. Iwasa, and R. C. Bradt. “Fracture Toughness of Single-Crystal Alumina.” *Structure and Properties of MgO and Al_2O_3 Ceramics*. Vol. 10

148. D. Picard, D. Leguillon, and C. Putot. “A Method to Estimate the Influence of the Notch-root Radius on the Fracture Toughness Measurement of Ceramics.” *Journal of the European Ceramic Society* 26, no. 8 (2006): 1421–1427.

149. T. Fett et al “Fracture Toughness Test with a Sharp Notch Introduced by Focussed Ion Beam.” *International Journal of Fracture* 153, no. 1 (2008): 85–92.

150. T. Fett and D. Munz “Stress Intensity Factors and Weight Functions”, *Computational Mechanics Publications*, Southampton, 1997.

151. R. Damani, R. Gstrein, and R. Danzer. “Critical Notch-root Radius Effect in SENB-S Fracture Toughness Testing.” *Journal of the European Ceramic Society* 16, no. 7 (1996): 695–702.

152. D. Kiener, C. Motz, M. Rester, M. Jenko, and G. Dehm. “FIB Damage of Cu and Possible Consequences for Miniaturized Mechanical Tests.” *Materials Science and Engineering: A* 459, no. 1–2 (June 25, 2007): 262–272.

153. G. Dehm, C. Motz, C. Scheu, H. Clemens, P. H. Mayrhofer, and C. Mitterer. “Mechanical Size-Effects in Miniaturized and Bulk Materials.” *Advanced Engineering Materials* 8, no. 11 (2006): 1033–1045.

154. H. Bei, S. Shim, M. K. Miller, G. M. Pharr, and E. P. George. “Effects of Focused Ion Beam Milling on the Nanomechanical Behavior of a Molybdenum-alloy Single Crystal.” *Applied Physics Letters* 91, no. 11 (September 14, 2007): 111915–111915–3.

155. S. Rajsiri, B. Kempshall, S. Schwarz, and L. A. Giannuzzi. “FIB Damage in Silicon: Amorphisation or Redeposition?” *Microscopy and Microanalysis* 8, no. Supplement S02 (2002): 50–51.

156. M. Nastasi, D. Lilienfeld, H. H. Johnson, and J. W. Mayer. “Stability of Metallic CsCl-structured Alloys Under Ion Irradiation.” *Journal of Applied Physics* 59, no. 12 (1986): 4011–4016.

157. B. I. Prenitzer, C A Urbanik-Shannon, L A Giannuzzi, S R Brown, R B Irwin, T L Shofner, and F A Stevie. “The Correlation Between Ion Beam/material Interactions and Practical FIB Specimen Preparation.” *Microscopy and Microanalysis* 9, no. 3 (2003): 216–236.

158. T. L. Matteson, S. W. Schwarz, E. C. Houge, B. W. Kempshall, and L. A. Giannuzzi. “Electron Backscattering Diffraction Investigation of Focused Ion Beam Surfaces.” *Journal of Electronic Materials* 31, no. 1 (2002): 33–39.

159. J. P. McCaffrey, M. W. Phaneuf, and L. D. Madsen. “Surface Damage Formation During Ion-beam Thinning of Samples for Transmission Electron Microscopy.” *Ultramicroscopy* 87, no. 3 (2001): 97–104.

160. J. Mayer, L. A. Giannuzzi, Takeo Kamino, and Joseph Michael. “TEM Sample Preparation and FIB-Induced Damage.” *MRS Bulletin* 32, no. 05 (2007): 400–407.

161. N. I. Kato, “Reducing Focused Ion Beam Damage to Transmission Electron Microscopy Samples.” *Journal of Electron Microscopy* 53, no. 5 (October 1, 2004): 451–458.

162. J. M. Cairney, and P. R. Munroe. “Redeposition Effects in Transmission Electron Microscope Specimens of FeAl-WC Composites Prepared Using a Focused Ion Beam.” *Micron* 34, no. 2 (2003): 97–107.

163. T. Hioki, A. Itoh, M. Ohkubo, S. Noda, H. Doi, J. Kawamoto, and O. Kamigaito. “Mechanical Property Changes in Sapphire by Nickel Ion Implantation and Their Dependence on Implantation Temperature.” *Journal of Materials Science* 21, no. 4 (1986): 1321–1328.

164. P. J. Burnett, and T. F. Page. “An Investigation of Ion Implantation-induced Near-surface Stresses and Their Effects in Sapphire and Glass.” *Journal of Materials Science* 20, no. 12 (1985): 4624–4646.

165. C. J. McHargue, M. E. O’Hern, C. W. White, and M. B. Lewis. “Ion Implantation in Ceramics-residual Stress and Properties.” *Materials Science and Engineering: A* 115 (1989): 361–367.

166. C. J. McHargue, “Structure and Mechanical Properties of Ion Implanted Ceramics.” *Nuclear Instruments and Methods in Physics Research Section B: Beam Interactions with Materials and Atoms* 19–20, Part 2 (1987): 797–804.

167. H. Gnaser, A. Brodyanski, and B. Reuscher, “Focused ion beam implantation of Ga in Si and Ge: fluence-dependent retention and surface morphology”. *Surface and Interface Analysis*, *40* no 11 (2008): 1415-1422.

168. B. Prével, J.-M. Benoit, L. Bardotti, P. Mélinon, A. Ouerghi, D. Lucot, E. Bourhis, and J. Gierak. “Nanostructuring Graphene on SiC by Focused Ion Beam: Effect of the Ion Fluence.” *Applied Physics Letters* 99, no. 8 (2011): 083116.

169. G. B. Krefft, and E. P. EerNisse. “Volume Expansion and Annealing Compaction of Ion-bombarded Single-crystal and Polycrystalline α-Al_2O_3.” *Journal of Applied Physics* 49, no. 5 (1978): 2725–2730.

170. A. Schilling, T. Adams, R. M. Bowman, and J. M. Gregg. “Strategies for Gallium Removal after Focused Ion Beam Patterning of Ferroelectric Oxide Nanostructures.” *Nanotechnology* 18, no. 3 (2007): 035301.

171. P. R. Howie, S. Korte, and W. J. Clegg. “Fracture Modes in Micropillar Compression of Brittle Crystals.” *Journal of Materials Research* 27, no. 01 (2012): 141–151.

172. S. Korte, R. J. Stearn, J. M. Wheeler, and W. J. Clegg. “High Temperature Microcompression and Nanoindentation in Vacuum.” *Journal of Materials Research* 27, no. 01 (2012): 167–176.

173. J. R. Greer, H. Espinosa, K. T. Ramesh, and E. Nadgorny. “Comment on “Effects of Focused Ion Beam Milling on the Nanomechanical Behavior of a Molybdenum-alloy Single Crystal”. *Applied Physics Letters* 92, no. 9 (2008): 096101–096101–1.

174. J. R. Greer, and W. D. Nix. “Nanoscale Gold Pillars Strengthened through Dislocation Starvation.” *Physical Review B* 73, no. 24 (2006): 245410.

175. P. R. Howie, *Measuring plasticity in brittle materials,* PhD Thesis, University of Cambridge, 2012

176. S. M. Wiederhorn. “Moisture Assisted Crack Growth in Ceramics.” *International Journal of Fracture Mechanics* 4, no. 2 (1968): 171–177.

177. A. G. Evans, “Slow Crack Growth in Brittle Materials Under Dynamic Loading Conditions.” *International Journal of Fracture* 10, no. 2 (1974): 251–259

178. J. A. Salem. “Slow Crack Growth and Fracture Toughness of Sapphire for the International Space Station Fluids and Combustion Facility.” *National Aeronautics and Space Administration*.

179. A. Bhatnagar, M. J. Hoffman, and R. H. Dauskardt. “Fracture and Subcritical Crack-Growth Behavior of Y-Si-Al-O-N Glasses and Si3N4 Ceramics.” *Journal of the American Ceramic Society* 83, no. 3 (2000): 585–596.

180. D. S. Jacobs and I-W Chen. “Mechanical and Environmental Factors in the Cyclic and Static Fatigue of Silicon Nitride.” *Journal of the American Ceramic Society* 77, no. 5 (1994): 1153–1161.

181. K. D. McHenry, T. Yonushonis, and R. E. Tressler. “Low-Temperature Subcritical Crack Growth in SiC and Si3N4.” *Journal of the American Ceramic Society* 59, no. 5–6 (1976): 262–263.

182. L. Grabner. “Spectroscopic Technique for the Measurement of Residual Stress in Sintered Al2O3.” *Journal of Applied Physics* 49, no. 2 (1978): 580–583.

183. Q. Ma and D.R. Clarke. “Optical Fluorescence from Chromium Ions in Sapphire: A Probe of the Image Stress.” *Acta Metallurgica et Materialia* 41, no. 6 (1993): 1811–1816.

184. Q. Ma and David R. Clarke. “Stress Measurement in Single-Crystal and Polycrystalline Ceramics Using Their Optical Fluorescence.” *Journal of the American Ceramic Society* 76, no. 6 (1993): 1433–1440.

185. J. He and D. R. Clarke. “Determination of the Piezospectroscopic Coefficients for Chromium-Doped Sapphire.” *Journal of the American Ceramic Society* 78, no. 5 (1995): 1347–1353.

186. S. Guo, A. Limpichaipanit, and R. I. Todd. “High Resolution Optical Microprobe Investigation of Surface Grinding Stresses in Al_2O_3 and Al_2O_3/SiC Nanocomposites.” *Journal of the European Ceramic Society* 31, no. 1–2 (2011): 97–109.

187. S. Guo and R.I. Todd. “Quantitative Optical Fluorescence Microprobe Measurements of Stresses Around Indentations in Al_2O_3 and Al_2O_3/SiC Nanocomposites: The Influence of Depth Resolution and Specimen Translucency.” *Acta Materialia* 59, no. 7 (2011): 2637–2647.

188. S. Guo and R. I. Todd. “Confocal Fluorescence Microscopy in Alumina-based Ceramics: Where Does the Signal Come From?” *Journal of the European Ceramic Society* 30, no. 3 (2010): 641–648.

189. S. Guo and R. I. Todd. “Cr3+ Microspectroscopy Measurements and Modelling of Local Variations in Surface Grinding Stresses in Polycrystalline Alumina.” *Journal of the European Ceramic Society* 30, no. 12 (2010): 2533–2545.

190. M. I. Mendelson. “Average Grain Size in Polycrystalline Ceramics.” *Journal of the American Ceramic Society* 52, no. 8 (1969): 443–446.

191. J. B. Nelson and D. P. Riley. “An Experimental Investigation of Extrapolation Methods in the Derivation of Accurate Unit-cell Dimensions of Crystals.” *Proceedings of the Physical Society* 57, no. 3 (1945): 160.

192. H. P. Klug and L. E. Alexander. *X-ray Diffraction Procedures for Polycrystalline and Amorphous Materials*. 1st ed. John Wiley & Sons Inc.

193. W. E. Lee and K. P. D. Lagerlof. “Structural and Electron Diffraction Data for Sapphire (α-al2o3).” *Journal of Electron Microscopy Technique* 2, no. 3 (1985): 247–258.

194. G. Cliff and G. W. Lorimer. “The Quantitative Analysis of Thin Specimens.” *Journal of Microscopy* 103, no. 2 (1975): 203–207.

195. J. Kübler "Fracture toughness of ceramics using the SEVNB method; round robin." *ECF13, San Sebastian 2000*. 2013.

196. W. Weibull, "A statistical distribution function of wide applicability." *Journal of applied mechanics* 18.3 (1951): 293-297.

197. U. Genschel and W. Q. Meeker. "A comparison of maximum likelihood and median-rank regression for Weibull estimation." *Quality Engineering* 22.4 (2010): 236-255.

198. http://www.weibull.nl/weibullstatistics.htm (Accessed 29th June 2013)

199. J. B. Wachtman, W. R. Cannon, and M. J. Matthewson. *Mechanical Properties of Ceramics*. Wiley, 2009

200. A. Tsirk, “Fractography Lessons from Knapping.” In *Fractography of Glasses and Ceramics VI*, John Wiley & Sons, Inc. (2012). 123–132.

201. J.-P. Jan, S. Steinemann, and P. Dinichert. “Les Paramètres Du Réseau et La Densité Du Rubis.” *Helvetica Physica Acta* 33 (1960): 123.

202. D. B. Williams, and C. B. Carter. *Transmission Electron Microscopy: a Textbook for Materials Science*. Plenum Press.

203. C. B. Carter and K.J. Morrissey. “Grain-Boundary Structure in Al_2O_3.” In *Structure and Properties of MgO and Al_2O3 Ceramics*. Vol. 10. Advances in Ceramics. The American Ceramic Society, 1984.

204. A. A. Kaplyanskii, et al, *Concentration-Dependent Line-Shift in Optical spectra of ruby.* Soviet Physics – Solid State, Vol. 10 no 8. (1969)

205. R. Brydson, *Electron Energy Loss Spectroscopy*. 1st ed. BIOS Scientific Publishers Ltd,

206. D. C. Joy, A. D. Romig, and J. I. Goldstein. *Principles of Analytical Electron Microscopy*. Plenum Press.

207. J. F. Al-Sharab, F. Cosandey, A. Singhal, G. Skandan, and J. Bentley. “TEM Characterization of Nanostructured $MgAl_2O_4$ Synthesized by a Direct Conversion Process from γ-Al2O3.” *Journal of the American Ceramic Society* 89, no. 7 (2006): 2279–2285.

208. The Influence of Surface Roughness on Instrumented Indentation Testing (IIT), *Advanced Mechanical Surface Testing,* CSM Instruments.

209. V. M. Malhotra and N. J Carino. *Handbook on Nondestructive Testing of Concrete*. Boca Raton, Fla.: CRC Press, 2004.

210. R. G. Munro, “Evaluated Material Properties for a Sintered alpha-Alumina.” *Journal of the American Ceramic Society* 80, no. 8 (1997): 1919–1928.

211. R. T. Bubsey, D. Munz, W. S. Pierce, and J. L. Shannon Jr. “Compliance Calibration of the Short Rod Chevron-notch Specimen for Fracture Toughness Testing of Brittle Materials.” *International Journal of Fracture* 18, no. 2 (1982): 125–133.

212. D. Munz, R. T. Bubsey, and J. L. Shannon. “Fracture Toughness Determination of A12O3 Using Four-Point-Bend Specimens with Straight-Through and Chevron Notches.” *Journal of the American Ceramic Society* 63, no. 5–6 (1980): 300–305.

213. D. Munz, R. T. Bubsey, and J. E. Srawley. “Compliance and Stress Intensity Coefficients for Short Bar Specimens with Chevron Notches.” *International Journal of Fracture* 16, no. 4 (1980): 359–374.

214. F. Iqbal, J. Ast, M. Göken, and K. Durst. “In Situ Micro-Cantilever Tests to Study Fracture Properties of NiAl Single Crystals.” *Acta Materialia* 60, no. 3 (2012): 1193–1200.

215. J. B. Wachtman, W. E. Tefft, D. G. Lam, and R. P. Stinchfield. “Elastic Constants of Synthetic Single-Crystal Corundum at Room Temperature.” *Journal of the American Ceramic Society* 43, no. 6 (1960): 334–334.

216. G. G. Stoney, “The Tension of Metallic Films Deposited by Electrolysis.” *Proceedings of the Royal Society of London. Series A, Containing Papers of a Mathematical and Physical Character* 82, no. 553 (1909): 172–175.

217. G. C. A. M. Janssen et al. "Celebrating the 100th anniversary of the Stoney equation for film stress: Developments from polycrystalline steel strips to single crystal silicon wafers." *Thin Solid Films* 517.6 (2009): 1858-1867.

218. D.M. Lipkin, D.R. Clarke, M. Hollatz, M. Bobeth, W. Pompe, Stress development in alumina scales formed upon oxidation of (111) NiAl single crystals, Corrosion Science 39 no. 2, (1997): 231-242

219. V. G. Hill, R. Roy, and E. F. Osborn. “The System Alumina-Gallia-Water.” *Journal of the American Ceramic Society* 35, no. 6 (1952): 135–142.

220. J. E. Field, “Brittle Fracture: Its Study and Application.” *Contemporary Physics* 12, no. 1 (1971): 1–31.

221. M. A. Creager and P. C. Paris. “Elastic Field Equations for Blunt Cracks with Reference to Stress Corrosion Cracking.” *International Journal of Fracture* 3, no. 4 (1967): 247–252.

222. S. M. Wiederhorn, *Fracture of Ceramics*, Mechanical and Thermal Properties of Ceramics, April 1-2 1968.

223. Z. Han et al. “Effects of Thickness and Substrate on the Mechanical Properties of Hard Coatings.” *JCT Research* 1, no. 4 (2004): 337–341.

224. S. Suresh, T.-G. Nieh, and B.W. Choi. “Nano-indentation of Copper Thin Films on Silicon Substrates.” *Scripta Materialia* 41, no. 9 (1999): 951–957.

225. G. Hobler et al. “Fundamentals of Focused Ion Beam Nanostructural Processing: Below, At, and Above the Surface,” *MRS bulletin* 32.05 (2007): 424-432.

226. H. H. Yu and J. W. Hutchinson. “Influence of Substrate Compliance on Buckling Delamination of Thin Films.” *International Journal of Fracture* 113, no. 1 (2002): 39–55.

227. S. Guo et al “Hot-pressed Silicon Nitride Ceramics with Lu2O3 Additives: Elastic Moduli and Fracture Toughness.” *Journal of the European Ceramic Society* 23, no. 3 (2003): 537–545.

228. N. A. Yahya, *Micromechanical Testing and Carbon Doping of Aluminium Oxide,* PhD thesis, University of Oxford, 2012 (in review)

229. N. A. Yahya et al, *Micromechanical testing of Al_2O_3 based materials,* Paper in Preparation

230. G. Otieno, *Processing & Properties of Aligned Carbon Nanotube / Glass Ceramic Composite.* PhD Thesis, University of Oxford, 2012.

231. Y. Mitamura, and Y. Wang. “Fracture Toughness of Single Crystal Alumina in Air and a Simulated Body Environment.” *J Bio Mat Res* 28 no. 7 (1994): 813–817

232. S. M. Wiederhorn, “Subcritical Crack Growth in Ceramics.” In *Fracture Mechanics of Ceramics*,. Springer US, (1974). 613–646

233. A. H. De Aza, J. Chevalier, G Fantozzi, M Schehl, and R Torrecillas. “Crack Growth Resistance of Alumina, Zirconia and Zirconia Toughened Alumina Ceramics for Joint Prostheses.” *Biomaterials* 23, no. 3 (2002): 937–945.

234. C. A. Volkert and A. M. Minor. “Focused Ion Beam Microscopy and Micromachining.” *MRS Bulletin* 32, no. 05 (2007): 389–399.

235. T. Kamino et al “Evaluation of TEM Samples of an Mg-Al Alloy Prepared Using FIB Milling at the Operating Voltages of 10 kV and 40 kV.” *Journal of Electron Microscopy* 53, no. 5 (2004): 459–463.

236. V. Apostolopoulos, L. M. Hickey, D. A. Sager, and J. S. Wilkinson. “Gallium-diffused Waveguides in Sapphire.” *Optics Letters* 26, no. 20 (2001): 1586–1588.

237. M. D. Malinkovich et al “XPS Study of Gallium Loss from Langasite Crystal Surface Under Vacuum Annealing.” *Sensors and Actuators A: Physical* 180 (2012): 63–66.

238. T. Vodenitcharova et al “The effect of anisotropy on the deformation and fracture of sapphire wafers subjected to thermal shocks”. *Journal of Materials Processing Technology*, 194 no. 1 (2007): 52-62.

239. W. Wunderlich et al, “Molecular Dynamics-Simulations of the Fracture Toughness of Sapphire”. *Progress of Theoretical Physics Supplement*, 138, (2000). 156-158.

240. C. Elsässer and A.G. Marinopoulos. “Substitutional Cation Impurities in α-Al2O3: Ab-initio Case Study of Segregation to the Rhombohedral Twin Boundary.” *Acta Materialia* 49, no. 15 (2001): 2951–2959.

241. I. Milas, B. Hinnemann, and E. A. Carter. "Structure of and ion segregation to an alumina grain boundary: Implications for growth and creep." *Journal of Materials Research* 23 no. 5 (2008): 1494.

242. J. J. Kruzic, W. R. M. Cannon, and R. O. Ritchie. “Effects of Moisture on Grain Boundary Strength, Fracture and Fatigue Properties of Alumina.” *J. Am. Ceram. Soc,* 88 no. 8 (2005): 2236 - 2245

243. J. W. Hutchinson, "Mechanisms of toughening in ceramics." *Theoretical and applied mechanics* (1989): 139-144.

244. G. Vekinis, M.F. Ashby, and P.W.R. Beaumont. “R-curve Behaviour of Al_2O_3 Ceramics.” *Acta Metallurgica et Materialia* 38, no. 6 (1990): 1151–1162.

245. A. Krell et al. "Subcritical crack growth in Al_2O_3 with submicron grain size." *Journal of the European Ceramic Society* 23 no. 1 (2003): 81-89.

246. J. F. Shackelford and W. D. Scott. “Relative Energies of Tilt Boundaries in Aluminum Oxide.” *Journal of the American Ceramic Society* 51, no. 12 (1968): 688–692.

247. S. J. Cho et al “Grain-Size and R-Curve Effects in the Abrasive Wear of Alumina.” *Journal of the American Ceramic Society* 72, no. 7 (1989): 1249–1252.

248. S. J. Bennison and B. R. Lawn. "Role of interfacial grain-bridging sliding friction in the crack-resistance and strength properties of nontransforming ceramics." *Acta Metallurgica* 37, no. 10 (1989): 2659-2671.

249. A. He, K. P. D. Lagerlöf, J. Castaing, and A. H. Heuer. “Considerations of the Double-cross-slip Mechanism for Basal and Rhombohedral Twinning in Sapphire (α-Al_2O_3).” *Philosophical Magazine A* 82, no. 15 (2002): 2855–2867.

250. M. Chen et al. “Deformation Twinning in Nanocrystalline Aluminum.” *Science* 300, no. 5623 (2003): 1275–1277.

251. T. Hansson, R. Warren, and J. Wasén. “Fracture Toughness Anisotropy and Toughening Mechanisms of a Hot-pressed Alumina Reinforced with Silicon Carbide Whiskers.” *Journal of the American Ceramic Society* 76, no. 4 (1993): 841–848.

252. W. D. Callister, M. L. Johnson, I. B. Cutler, and R. W. Ure. “Sintering Chromium Oxide with the Aid of TiO_2.” *Journal of the American Ceramic Society* 62, no. 3–4 (1979): 208–211.

253. R. Rosing, R. Reichenbach, and A. Richardson. “Generation of Component Level Fault Models for MEMS.” *Microelectronics Journal* 33, no. 10 (2002): 861–868.

254. R. J. Charles, “Dynamic Fatigue of Glass.” *Journal of Applied Physics* 29, no. 12 (1958): 1657–1662.